Spatial distribution, carbon stocks and diversity of peat swamp forests in the central Congo Basin

Bart Jonathan Crezee

Submitted in accordance with the requirements for the degree of

Doctor of Philosophy

The University of Leeds

School of Geography

June 2022

The candidate confirms that the work submitted is his own, except where work which has formed part of jointly-authored publications has been included. The contribution of the candidate and the other authors to this work has been explicitly indicated below. The candidate confirms that appropriate credit has been given within the thesis where reference has been made to the work of others.

<u>Chapter 5 and 6:</u>

Crezee, B., Dargie, G.C., Ewango, C.E.N., Mitchard, E.T.A., Emba B., O., Kanyama T., J., Bola, P., Ndjango, J-B.N., Girkin, N.T., Bocko, Y.E., Ifo, S.A., Hubau, W., Seidensticker, D., Batumike, R., Imani, G., Cuní-Sanchez, A., Kiahtipes, C.A., Lebamba, J., Wotzka, H-P., Bean, H., Baker, T.R., Baird, A.J., Boom, A., Morris, P.J., Page, S.E., Lawson, I.T. & Lewis, S.L. (2022). Mapping peat thickness and carbon stocks of the central Congo Basin using field data. *Nature Geoscience*, 15, 639-644. https://doi.org/10.1038/s41561-022-00966-7.

*S.L.L., E.T.A.M., I.T.L., G.C.D., and S.E.P. conceived the study; **B.C.**, G.C.D., S.L.L., E.T.A.M., I.T.L., S.E.P., S.A.I., C.E.N.E. and T.R.B. developed the study; **B.C.**, G.C.D., S.L.L. C.E.N.E., O.E.B., P.B., J.K.T., N.T.G., and J-B.N.N. organised and conducted the fieldwork; Y.E.B., S.A.I., W.H., D.S., R.B., G.I., A.C-S., C.A.K., J.L and H-P.W. provided additional data; **B.C.**, G.C.D., A.B. and H.B. performed laboratory analyses; **B.C.** and E.T.A.M. analysed the remote sensing data and developed the models; **B.C.**, S.L.L., E.T.A.M., G.C.D., A.J.B., T.R.B., P.J.M. and C.A.K. evaluated the results. **B.C.** and S.L.L. wrote the paper, with input from all co-authors.*

Acknowledgements

Scientific research is very much a collaborative effort, and perhaps even more so in the case of tropical ecology, which often requires large teams to collect field data. I am very grateful to all who have contributed to this project. The work that I present in this thesis would not have been possible without the effort, support, or advice from many people, some of whom I would like to explicitly thank here.

Principally, I want to thank my main supervisor Prof Simon Lewis for his professional guidance and close engagement throughout this project. I am very thankful to Simon for providing me with the opportunity to study the fascinating peat swamp forests of the Congo Basin, and for supporting me on my fieldwork campaigns in the Democratic Republic of the Congo. This thesis would not have been possible without his pragmatic, but critical approach. Simon's focus on getting the best possible research done under sometimes challenging field conditions, and his efforts to communicate scientific results clearly with the wider world have been particularly inspiring.

I would also like to thank my second supervisor Prof Tim Baker for his very kind support and feedback over the course of many years. By bringing an expertise in peatlands of the Peruvian Amazon, I have especially appreciated Tim's outside-perspective on my work in the Congo Basin. Our discussions comparing peatlands across continents gave lots of food for thought.

Furthermore, I am very grateful to Dr Greta Dargie, without whose impressive work this project would not have existed in the first place. Studying a largely undocumented ecosystem means that my thesis principally builds on Greta's pioneering study of the central Congo Basin peatlands, as will be clear from the many references to Dargie et al. (2017). Greta, thank you for introducing me to your research, teaching me how to work and live in the Congolese swamps, and helping me out on numerous occasions. I have especially enjoyed our fieldwork trip up the Ruki River, a journey I will not easily forget.

This project involved a lot of fieldwork that was only possible thanks to a large number of wonderful people in the DRC. First and foremost, I wish to thank the many communities that hosted and assisted with my fieldwork: Lokolama, Bosukela, Mpama, Befale, Bonsole, Mweko, Mpeka, Bondamba, Bolengo, Boleke and Pombi. Without their approval and support, none of the field data that this thesis is built on could have been collected. I am hugely indebted to all of

Thanks also to the following people: Dave Roe for helping organize fieldwork equipment, never without a cheerful smile; Rachel Gasior, David Ashley, Dave Wilson and Martin Gilpin for their assistance and advice with laboratory analysis at the School of Geography; Dr Adam Hastie for providing modelling advice; Dr David Milodowski for his support with developing the HAND-index; and Prof Guy Ziv for commenting on my vague early plans when I didn't know how this project would turn out.

The modelling of peatland distribution and peat thickness would not have been possible without other researchers sharing their hard-won data from across the Congo Basin with me: Dr Wannes Hubau, Dr Dirk Seidensticker, Rodrigue Batumike, Gérard Imani, Dr Aida Cuní-Sanchez, Dr Chris Kiahtipes, Dr Judicaël Lebamba and Prof Hans-Peter Wotzka. Thanks also to Christelle Gonmadje, Claire Delvaux, Connie Clark, David Harris, Elizabeth Kearsley, Faustin Mbaya Mpanya Lukasu, Hans Beeckman, Hans Verbeek, Innocent Liengola, Jacques Mukinzi, Jan Bogaert, Jean-Remy Makana, Jefferson Hall, John Poulsen, John Tshibamba Mukendi, Lee White, Oliver Phillips, Omari Ilambu, Pascal Boeckx, Peter Umunay, Terry Brncic, Terry Sunderland, Thales de Haulleville and Vincet Medjibe for allowing me access to their *ForestPlots.net* vegetation data. Furthermore, Dr Greta Dargie was so kind to share crucial data and peat samples with me from the Boboka, Ipombo, Lobaka, Bolombo, and Bonzembo transects along the Congo River, collected as part of fieldwork by the CongoPeat consortium. Moreover, thanks to Dr Chris Kiahtipes for his critical comments and our discussions on the role of geomorphology in peat formation across the basin.

I would also like to express my gratitude to all members of the *Centre de Recherche en Écologie et Foresterie* (CREF) in Mabali, DRC, for hosting me at their historic research site on the shores of Lake Tumba. The dedication and determination that has been shown by the staff of CREF Mabali in collecting a unique dataset of weather data through many difficult decades is truly astonishing. In particular, thanks to Ikali Monkengo-mo-Mpenge, Ngubu Mompongo, Boika Mola Sandoka, and Nsala Mboyo Agastino for generously sharing their data and knowledge with me. I hope to have done your hard work justice and wish that it may be recognized and valued by the wider world.

Lastly, I want to thank my family and friends back home, whom I always could rely on, even though I moved abroad for multiple years. I am particularly grateful to my parents, John and Marijke, who have always supported me, whatever faraway or unknown destinations I chose to pursue. It means a lot to me that John is still able to celebrate the completion of this thesis with me.

My deepest thanks go to my partner Annemiek, who has encouraged and supported me from the first application to final submission. Lieve Annemiek, your love kept me sane during a pandemic, multiple lockdowns and almost two years of working from home. I am sorry for the endless conversations about peat that I got you bogged down in, as well as the terribly broken satellite calls from the depths of the rainforest. Thank you for being there for me.

Abstract

In 2017, scientists announced that the world's largest tropical peatland complex was found in the central Congo Basin, covering 145,500 km^2 and storing 30 Pg C belowground in peat (30×10^{15} g C). However, these results were extrapolations from field data limited to rain-fed interfluvial basins in the Republic of the Congo (ROC). How peat formation is affected by different hydrological conditions, particularly river inundations, is currently unknown. Here, I present the first extensive field surveys of peat in the Democratic Republic of the Congo (DRC), which covers two-thirds of the estimated peatland area. I sampled 50 km of transects in geomorphologically-distinct river systems in DRC, finding deep peat deposits (mean 3.2 m; maximum 7.0 m) and a new seasonally inundated, mixed peat swamp forest type. These peatlands receive seasonal river water input, in contrast to the rain-fed interfluvial basin peatlands of the ROC, yet remain very nutrient-poor. Radiocarbon dating shows that some DRC peatlands began forming ~42,000 calibrated years Before Present, over 20,000 years earlier than ROC peatlands. I used field-based observations and remotely-sensed data to produce a 50-m resolution map of the central Congo peatlands, which cover 167,600 km^2 (95% confidence interval, 159,400-175,100 km^2). Using field data, I derived the first basin-wide maps of peat thickness (mean ± standard deviation, 1.7±0.9 m; maximum 5.6 m) and peat carbon density (mean 1,712±634 Mg C ha^{-1}; maximum 3,970 Mg C ha^{-1}). In total, 29.0 Pg C is stored belowground in peat across the region (95% confidence interval, 26.3-32.2 Pg C). These field-based constraints give high confidence that the central Congo Basin holds the world's largest tropical peatland complex, ~36% of all tropical peatlands, and stores a globally significant ~28% of the world's tropical peat carbon. However, only 8% of this peat carbon lies within protected areas, suggesting vulnerability to land-use change.

Table of contents

List of figures

List of tables

List of abbreviations

aboveground biomass	AGB
aboveground carbon	AGC
accelerator mass spectrometry	AMS
Advanced Land Observation Satellite	ALOS
Alaska Satellite Facility	ASF
Advanced Spaceborne Thermal Emission and Reflection Radiometer	ASTER
balanced accuracy	BA
calibrated year Before Present	cal yr BP
climatic water balance	CWB
confidence interval	CI
cross-validation	CV
Democratic Republic of the Congo	DRC
diameter at breast height	DBH
digital elevation model	DEM
electrical conductivity	EC
Enhanced Thematic Mapper +	ETM+
enhanced vegetation index	EVI
European Space Agency	ESA
Food and Agriculture Organization of the United Nations	FAO
Global Digital Elevation Map	GDEM
Global Forest Watch	GFW
Gini-Simpson diversity index	GS
height above nearest drainage point	HAND
high-water fraction	HWF
inductively coupled plasma - mass spectrometry	ICP-MS
inductively coupled plasma - optical emission spectrometry	ICP-OES
Intergovernmental Panel on Climate Change	IPCC
Japan Aerospace Exploration Agency	JAXA
Last Glacial Maximum	LGM
long-term rate of carbon accumulation	LORCA
loss-on-ignition	LOI
Matthews correlation coefficients	MCC
Ministry of Economy, Trade and Industry (Japan)	METI

Multi-Error-Removed Improved-Terrain (DEM)	MERIT
Maximum Likelihood	ML
moderate resolution imaging spectroradiometer	MODIS
MultiSpectral Instrument	MSI
National Aeronautics and Space Administration (US)	NASA
near infrared	NIR
non-metric multidimensional scaling	NMDS
organic matter	OM
Observatoire Satellital des Forêts d'Afrique Centrale	OSFAC
phased array L-band synthetic aperture radar	PALSAR
permutational multivariate analysis of variance	PERMANOVA
petagram carbon (10^{15} g C)	Pg C
rate of change	RC
Random Forest	RF
Republic of the Congo	ROC
standard deviation	s.d.
synthetic aperture radar	SAR
species richness	SR
Shuttle Radar Topography Mission	SRTM
Support Vector Machine	SVM
Shannon-Wiener index	SW
short-wave infrared	SWIR
Upper Continental Crust	UCC
United States Geological Survey	USGS

Chapter 1: Introduction and literature review

1.1 Thesis rationale

Peatlands are exceptionally carbon-rich ecosystems. Even though they cover only 3% of Earth's land surface (Xu et al., 2018), they store an estimated 600 petagram (Pg, or 10^9 tonnes) of carbon (Leifeld & Menichetti, 2018; Yu et al., 2010). This is equivalent to more than one-third of Earth's soil carbon (Scharlemann et al., 2014). While most peatlands are located in the temperate and boreal zones (Xu et al., 2018), recent research is revealing the existence of vast tropical peatlands with high carbon densities (Page et al., 2011; Ribeiro et al., 2021; Xu et al., 2018; Yu et al., 2010). Although most of the world's tropical peatlands are located in Southeast Asia (Page et al., 2011), new scientific discoveries over the past decade of large peat deposits in both the Peruvian Amazon and Central Africa show that peatland ecosystems of considerable size can be found across all major tropical regions (Dargie et al., 2017; Draper et al., 2014; Lähteenoja et al., 2011). One study recently mapped peatlands in the central depression of the Congo Basin (the 'Cuvette Centrale' region), which appear to be particularly extensive. Based on a combination of field and remotely-sensed data, Dargie et al. (2017) estimate the size of this peatland area to be 145,500 km^2, making it the largest tropical peatland complex in the world.

The total carbon (C) stock of this peatland complex is estimated to be 30.6 Pg C, equivalent to approximately three years of current global fossil fuel emissions, or 29% of the total tropical peat carbon stock (Dargie et al., 2017). Protecting this vast carbon stock is highly important within the context of the global climate crisis. Although currently largely undisturbed, the peatlands of the Cuvette Centrale are at risk of loss or degradation due to future climate change – particularly changes in the hydrological cycle – and land use changes incured by oil exploration, logging, mining or agriculture (Dargie et al., 2019).

However, although the work of Dargie et al. (2017) is based on extensive field research, this occurred in only one part of a large wetland region, hence considerable uncertainties remain around the total peatland area and peat carbon stock of the central Congo Basin. For example, data collection was confined to large interfluvial basins, which appear to be largely rain-fed and ombrotrophic-like, i.e. low in nutrient status (Dargie et al., 2017). Nothing is known about potential peatland areas in other environmental settings. Furthermore, Dargie et al. (2017) report a 95% confidence interval (CI) for total belowground carbon stocks of 6.3 - 46.8 Pg C. The wide interval range of more than 40 Pg indicates that it is unclear if the central Congo Basin

peatlands truly store globally significant quantities of carbon. The large uncertainty is attributed to uncertainty in peat thickness, total peatland area, peat bulk density, and peat carbon concentrations. Reducing uncertainties in these figures is paramount in reducing the overall uncertainty in peat carbon stock estimates of the central Congo Basin (Dargie, 2015; Dargie et al., 2017).

The uncertainty in peatland area is particularly concerning, given that others have come up with different peatland distribution maps for the same region. Gumbricht et al. (2017), for example, published a peatland map for the wider Congo Basin region with a smaller area, at 125,440 km^2, and a very different geographical distribution. The spatial discrepancy between the two maps, together with the uncertainty in total peatland area reported by Dargie et al. (2017), highlights the need to better understand peatland distribution in the central Congo Basin.

Furthermore, it is important to note that the results of Dargie et al. (2017) are based on field data from the north of the Republic of the Congo (ROC) only. Yet they predict that two-thirds of the central Congo Basin peatlands are to be found in the neighbouring Democratic Republic of the Congo (DRC), sometimes hundreds of kilometres from existing field data. Only a handful of observations of peat cores have been documented in the Cuvette Centrale area of the DRC (S.L. Lewis, *pers. comm.*, 2014; Kiahtipes & Schefuß, 2019), and no field-based evidence of extensive peat deposits has yet been provided. Thus, it is unclear if the central Congo Basin peatlands are truly as extensive or deep as suggested.

Uncertainties are further compounded by a limited understanding of the processes that determine peat formation in the central Congo Basin, particularly the peatlands' hydrology (Alsdorf et al., 2016; Dargie et al., 2017). Peat has only been systematically documented in interfluvial basins in ROC, where an absence of annual flood waves (Dargie et al., 2017), modest domes (Davenport et al., 2020), and remotely-sensed water-table depths (Lee et al., 2011) all suggest that these peatlands are largely rain-fed and receive little river water input. However, the peat deposits that are predicted in the DRC are located in different hydro-geomorphological settings, including what appear to be river-influenced regions close to the Congo River mainstem and dendritic-patterned valley-floors along some of its left-bank tributaries (Dargie et al., 2017). Remotely-sensed data indicates that these areas of swamp forest are likely partly seasonally inundated (Rosenqvist, 2009), with inundation depths of up to 1.5 m during the main wet season

(Lee et al., 2015). This suggests seasonal river flooding and/or upland runoff as key sources of water. Whether peat accumulates under these river-influenced conditions is currently unknown. If seasonally inundated peat swamps exist in these parts of the central Congo Basin, this would indicate a greater diversity of peatland types than described so far by Dargie et al. (2017). Understanding the diversity of peat swamp forests in terms of vegetation and hydro-geomorphological setting is important, as river-influenced peatlands might respond differently to future hydrologic changes compared to rain-fed interfluvial basin peatlands. Studying peat deposits in the DRC's part of the central Congo Basin is therefore vital for the conservation of what is likely the largest tropical peatland complex in the world.

Therefore, the principal aim of this thesis is to understand if peatlands exist in seasonally inundated river valley bottoms in DRC, and if so, to understand the diversity of these ecosystems in order to better map the region's peatland extent and the regional carbon stocks in peat. In brief, the objectives of this thesis are to (i) investigate whether peat forms in areas adjacent to rivers in the DRC, via a series of field campaigns; (ii) analyse how (river-influenced) inundation patterns affect swamp forest vegetation and peat characteristics; (iii) map the spatial distribution of peat presence and peat thickness across the central Congo Basin; and (iv) estimate the amount of carbon that is stored in peat.

1.2 Literature review

Soils often store large quantities of carbon in the form of soil organic matter. Globally, soil organic matter contains at least three times as much carbon as can be found in either the atmosphere or terrestrial plant biomass (Schmidt et al., 2011). It is generally estimated that this enormous carbon pool holds up to 1,500 Pg of carbon, although large uncertainties surround this figure (Scharlemann et al., 2014). About 40% of this carbon stock is made up by the global peatland carbon pool, which is estimated to be approximately 600 Pg in recent global syntheses (Leifeld & Menichetti, 2018; Yu et al., 2010), again with large uncertainties attached. This large fraction of the global soil carbon pool is stored in a relatively small area, as peatlands cover only approximately 3% of Earth's land surface (Leifeld & Menichetti, 2018; Xu et al., 2018). This means that peatlands are exceptionally carbon-rich ecosystems. Combining these afore-mentioned estimates of global peatland area and carbon stock, the average carbon density of peatlands around the world can be estimated to be 1,300-1,400 Mg C ha^{-1}, considerably more than the average of other carbon-dense ecosystems such as mangrove forests (937 Mg C ha^{-1}; Alongi, 2012), or aboveground biomass in tropical rainforests (approx. 140-200 Mg C ha^{-1}; Sullivan et al., 2017).

Peatlands are able to attain high carbon densities because of a long-term imbalance between input and loss of carbon. Peatlands are wetland ecosystems in which the rate of production of organic matter from plant and animal detritus generally exceeds the rate of decomposition of these same materials. The result is a net accumulation of semi-decomposed organic material in the soil (Page et al., 2006; Rydin & Jeglum, 2006). Typically, decomposition of organic matter is impeded by waterlogging of the soil and/or low temperatures. Because of the latter condition, most of the world's peatlands are found in either the temperate or boreal zones (Kaat, 2009; Page et al., 2011; Rydin & Jeglum, 2006; Xu et al., 2018). In particular, peat accumulation at these latitudes is strongly determined by the amount of photosynthetically active radiation over the growing season, suggesting longer and warmer growing seasons due to climate change could increase carbon accumulation of northern peatlands (Gallego-Sala et al., 2018). However, if impeded drainage causes waterlogged conditions throughout a sufficiently long time-period, peatlands can also develop in the tropics. Generally, this requires very nutrient-poor conditions to slow down the higher microbial decomposition rates that characterize warmer climates (Yule & Gomez, 2009). Contrary to northern peatlands, warming has a negative impact on peat accumulation in the tropics, likely because it further stimulates microbial decay, which is not fully offset by increased plant growth (Gallego-Sala et al., 2018). Thus, sufficiently well-

inundated and nutrient-poor locations with high organic matter production are the most likely sites for peat formation in the tropics.

Most tropical peatlands are located in Southeast Asia (Page et al., 2011), although recent discoveries of large peat deposits in the Peruvian Amazon and the Congo Basin show that peatland ecosystems can be found across all major tropical regions (Dargie et al., 2017; Draper et al., 2014; Lähteenoja et al., 2011). However, both the extent and carbon storage, as well as the ecological functioning of most of these tropical peatlands remains poorly understood. As they store a large part of the global soil carbon pool, improving our knowledge of tropical peatlands is an important research priority (Lawson et al., 2015).

1.2.1 Peat definitions

There is no internationally agreed-upon definition of what constitutes a peatland, or peat soil more specifically. Many studies, organizations and government agencies apply their own definitions, which makes comparisons of regional or global peatland areas and carbon stocks difficult. Comparative analyses are further complicated by the fact that many studies do not explicitly mention the peat definition that has been used (e.g., Householder et al., 2012; Draper et al., 2014; Uda et al., 2017).

In general, peat soils are defined by two aspects, namely (i) the organic matter content of the soil, and (ii) the thickness of this organic matter layer (Osaki et al., 2016). Organic matter (OM) content is the percentage of organic matter found in the peat soil, in contrast to the non-organic mineral content of the soil (also referred to as ash). The International Mire Conservation Group and the International Peat Society use these two aspects to define peat as sedentarily accumulated material consisting of at least 30% dry mass of dead organic material, with a minimal thickness of 30 cm at the surface (Joosten & Clarke, 2002). However, major international organisations such as the United Nations' Food & Agriculture Organization (FAO) do not explicitly define peat. Rather the FAO sees peat soils as part of a larger group of organic soils called histosols (FAO, 2006). Histosols are defined by the organization as soils having an H horizon of at least 40 cm of organic matter (FAO-Unesco, 1974). In this definition, the H horizon is defined as having an organic matter content of at least 30% if the mineral fraction contains more than 60% clay, or an organic matter content of at least 20% if the mineral fraction contains no clay. Like the FAO, the Intergovernmental Panel on Climate Change (IPCC) does not provide

definitions of peat or peatlands. In the IPCC's Wetlands Supplement, peatlands are considered to be included in 'land with organic soil' (IPCC, 2014). For determining organic soils, the IPCC largely follows the definition of histosols as provided by the FAO, but omits the minimum thickness requirement to allow for historically determined, country-specific definitions (Osaki et al., 2016). Particularly in Northern Hemisphere countries, large variations exists in the minimum thickness of peat layers, with Germany using 20 cm, Ireland applying 30 or 45 cm (for drained or undrained soils, respectively), the Scandinavian countries choosing 30 cm, and Canada opting for 40 cm in medium or well decomposed deposits, or even 60 cm in weakly decomposed peats (Bord na Móna, 1984). Between these countries, there traditionally is less variation in the required threshold of organic matter content, which has normally been set as at least 50% (Bord na Móna, 1984). 50% is also the OM threshold that Gumbricht et al. (2017) used in a more recent study of global tropical peatland distribution. However, this is considerably higher than the 20 to 30% used by the International Mire Conservation Group, the International Peat Society and the FAO. According to Andriesse (1988), older soil classification systems have traditionally taken 65% organic matter content as the minimum definition of peat soils. This is also the figure that Page et al. (2011) have used in a study of global tropical peatland distribution. They define peat as the surface layer of soil, consisting mostly of partially decomposed vegetation, with an organic content of at least 65% and a minimum thickness of 30 cm. Zulkifley et al. (2013) go even further and take 75% as minimum organic matter content of tropical peatlands, with the thickness criterium set at minimum 50 cm. Thus, around the world, substantial differences remain with regards to both the organic matter aspect of the peat definition (ranging from 20 to 75%), as well as the minimum thickness of the peat layer required (20 to 60 cm).

To complicate matters, a third criterion is sometimes proposed as part of the definition of peat, namely the soil organic carbon content. The dry weight percentage of organic carbon is traditionally used in soil science to distinguish organic from mineral soils, with typical minimum values of 12-18% carbon in organic soils, depending on clay content (Barthelmes, 2018; Osaki et al., 2016). However, organic matter content and organic carbon content scale linearly in most peatland types (Klingenfuß et al., 2014; Wüst et al., 2003), meaning that there is no apparent benefit from using both criteria simultaneously. In particular, Wüst et al. (2003) have shown how tropical peat soils in Malaysia with OM content greater than 45% all had organic carbon contents of at least 18% as well. Therefore, as OM content is generally easier to measure than organic carbon content (De Vos et al., 2007; Heiri et al., 2001), using only the former to set a criterion for defining peat appears preferable.

Using organic matter content as the crucial criterion appears particularly appropriate, given that some agreement on a minimum organic matter content seems to have emerged in tropical peatland countries over the past few years. While Wüst et al. (2003) initially defined tropical peat in Indonesia as soil with at least 45% organic matter content, Wetlands International (2010) opted for a definition of 65% organic matter content in studies of Malaysian peat soils, following the definition of the USDA Soil Taxonomy. After Page et al. (2011) completed a comparative analysis of tropical peatlands globally using this same figure, the 65% OM threshold seems to have become commonplace in tropical peatland studies in other regions as well. Both Lähteenoja et al. (2011) and Dargie et al. (2017) used this criterion in their studies of the largely newly documented Peruvian and Congolese peatlands, respectively, referring back to the choice of Page et al. (2011). This means that the 65% OM threshold now appears commonplace in all three major tropical peatland areas around the world.

In the case of the second aspect of the definition, minimum peat thickness, some agreement seems to be emerging among tropical peatland scholars as well. In 2010, Wetlands International chose 50 cm as threshold in their study of Malaysian peatlands. However, since then, 30 cm seems to have become more common. Both Page et al. (2011) and Gumbricht et al. (2017) decided on 30 cm in their assessments of tropical peatland extent. This threshold value was also applied in more regional studies by Lähteenoja et al. (2011) and Dargie et al. (2017) in the Peruvian Amazon and Central Africa, respectively. It has yet to be fully accepted though, as Osaki et al. (2016) again proposed the 50 cm threshold for tropical peatland ecosystems in Indonesia. Overall, it thus becomes clear that in the case of tropical peatlands, 65% is currently the most common threshold used for organic matter content, but that disagreement remains on what the minimum thickness should be. This is especially relevant, given that with shallower peat thickness and lower organic matter thresholds, the estimated areas and carbon stocks of peatlands could increase substantially.

Apart from defining peat, it is also important to provide a definition of a peatland. This is relevant in a policy context, given that most policy decisions will likely concern landscape or ecosystem types, rather than soil types. A clear definition of peatlands is lacking in both academic and policy contexts, but according to the Ramsar Convention on Wetlands (2002), the key characteristic of a peatland is either the presence of peat or the presence of vegetation that is capable of forming peat. This means that peatlands are ecosystems with peat deposits, that may or may not have vegetation cover (Osaki et al., 2016). On the other hand, this also means that ecosystems with

vegetation capable of forming peat, but currently without a sufficient peat layer, would potentially constitute a peatland as well.

For the remainder of this thesis, and in line with Dargie et al. (2017)'s choice for the Congo Basin peatlands, I will define peat as having at least 65% organic matter content and a minimum depth of 30 cm. A peatland is then defined as any geographical area that harbours peat according to this definition, irrespective of land cover.

1.2.2 Tropical peatlands

1.2.2.1 Tropical peatlands around the world

For a long time in the early history of peatland research, it was thought that no peatlands could be found in the tropics. Organic matter decomposition was considered to occur too fast in the warmer climates of the tropics to allow peat accumulation to happen. Only in 1909 did Henri Potonié manage to convince other peatland researchers that tropical peatlands did indeed exist in Southeast Asia. However, he mistakenly thought that tropical peatlands could only be fed by groundwater. Betje Polak was the first to argue convincingly in 1933 that many tropical peatlands in Southeast Asia are in fact fed by rainwater (Joosten, 2016). Since then, Southeast Asia has remained the focus of most tropical peatland research (Lawson et al., 2015), as large peat swamps can be found across the islands of the archipelago, spanning a total of 250,000 km^2 (Page et al. 2011). Only in recent years has it become clear that extensive peat deposits can also be found in other tropical regions outside Southeast Asia, particularly in the western Amazon in Peru and the Congo Basin in Central Africa (Dargie et al., 2017; Draper et al., 2014; Lähteenoja et al., 2011).

Although the term is much used, there is no agreed-upon definition of what constitutes a tropical peatland. Some authors define the prefix 'tropical' by referring to high precipitation and temperature values, which includes sub-tropical areas such as the Florida Everglades as well (e.g. Andriesse, 1988). Most commonly though (e.g. Page et al., 2011; Lawson et al., 2015), tropical peatlands are defined as those peatlands found between the Tropic of Cancer and Tropic of Capricorn (23.5°N and 23.5°S, respectively). However, a potential problem with this definition is that it includes both warm lowland and cool upland (mountainous) peatlands in the tropics, with the latter bearing greater resemblance to temperate or boreal peatlands. In this thesis, I will

normally use the term tropical peatlands to refer to lowland (warm) tropical peatlands, unless specified otherwise.

Inconsistencies in the definitions of peat can result in markedly different outcomes in terms of peatland area and volume (Xu et al., 2018). For example, before the recent discovery of new peatlands in the Congo basin, Page et al. (2011) reported that African peatlands covered an area of 55,860 km^2. This figure is considerably lower than the 72,476 or even 178,814 km^2 that was found in FAO's Harmonized World Soil Database or WWF's Global Lakes and Wetland Database, respectively (Xu et al., 2018). However, irrespective of their exact extent, it is clear that tropical peatlands can be found across the lowland moist forests of Southeast Asia, Amazonia, Central America and Central Africa (Lawson et al., 2015). In 1992, the total tropical peatland area was estimated to be 382,950 km^2, or 10-12% of global peatland area (Immirzi et al., 1992). In a more recent global synthesis of tropical peatland distribution, Page et al. (2011) estimated the extent of these peatlands to be slightly higher at 441,025 km^2, which still accounted for approximately 11 percent of the estimated global peatland area at that time. Of this area, 56% (247,778 km^2) was thought to be located in Southeast Asia (Page et al. 2011), while South-America was thought to hold the second-largest peatland area (107,486 km^2; 24%), followed by Africa (55,860 km^2; 13%) and the Central American and Caribbean region (23,374 km^2; 5%).

In terms of peat volume, tropical peatlands are thought to take up a slightly larger share of the globally estimated peat volume, namely 1,758 Gm^3, or approximately 18–25% (Page et al. 2011). This is mainly due to the fact that tropical peatlands, and particularly those in Southeast Asia, are generally deeper than boreal or temperate peatlands. Of the tropical peat volume, 77% (1,359 Gm^3) was estimated by Page et al. (2011) to be found in Southeast Asia, 11% in South-America (192 Gm^3) and only 8% in Africa (138 Gm^3).

In terms of carbon stored in tropical peatlands, Page et al. (2011) also showed that the tropical peatland carbon pool was larger than previously thought, with a best estimate of 88.6 Pg (81.7–91.9 Pg range), which they estimated to be equal to 15–19% of the global peat carbon pool (Page et al. 2011). Again, this was estimated before the more recent mapping of the central Congo Basin peatlands. Of this tropical peat carbon stock, 77% (68.5 Pg) was estimated to be in Southeast Asia, equal to 11–14% of global peat carbon, followed by South-America (9.7 Pg, 11%) and Africa (6.9 Pg, 8%). Indonesia has the largest share of tropical peat carbon (57.4 Pg, 65%) in Page et al.'s (2011) assessment, followed by Malaysia (9.1 Pg, 10%).

Recently, though, a study by Gumbricht et al. (2017) reported much larger tropical peatland areas and carbon stocks than estimated before. These authors modeled areas and depths of tropical wetlands and peatlands using a rules-based, or so-called 'expert system' approach. That approach incorporates several biophysical indicaters, namely (i) the inter-annual water balance, to detect areas in which the water supply exceeds atmospheric water demand; (ii) the intra-annual phenology of soil wetness, to differentiate between annually or seasonally water-logged soils; and (iii) hydro- and geomorphological indices that show landscape locations such as depressions where water can be supplied and retained. In this study, peatlands were defined as any soil having at least 30 cm of decomposed or semi-decomposed organic material with at least 50% of organic matter content. However, in practice in their model, peatlands were seperated from wetlands by applying a set of expert rules to the biohysical indicators. For example, one rule stated that precipitation must exceed reference evapotranspiration in all forested peat domes. The result is a prediction of unprecedentedly large peatland areas across the global tropics. Gumbricht et al. (2017) found a total pantropical peatland area of 1.7 million km^2, more than three times the roughly 440,000 km^2 found by Page et al. (2011). The new figures are particularly striking for the Brazilian Amazon, which according to Page et al. (2011) harbours 25,000 km^2 of peatland, while Gumbricht et al. (2017) report 312,250 km^2, more than ten times this figure. In terms of peat volume, Gumbricht et al. (2017) find 7,268 km^3 across the tropics - more than four times the volume reported by Page et al. (2011).

These differences can partly be explained by the fact that Gumbricht et al. (2017) applied a finer spatial scale than previous modelling studies. As such, they were potentially able to detect smaller peatland areas that together add up to significantly larger areas. In addition, Gumbricht et al. (2017) argue that their modelling approach is better at capturing inundated areas under dense forest cover. However, their results are not based on any field verifications. Because of this, and as the authors themselves already note, estimates of peat thickness in their study are likely substantially overestimated. The vast differences in estimation methods – those based on geomorphological indicators and those based on past reports of peat – show that uncertainties in peatland area and volume remain exceptionally large and that the chosen method has a considerable impact on the reported outcomes.

The fact that we are only beginning to understand the full extent of tropical peatlands was underscored by the relatively recent mapping of the world's largest tropical peatland complex in the Cuvette Centrale region, a low-lying swamp area in the heart of Central Africa's Congo

basin (Dargie et al., 2017). The mapping of this tropical peatland complex, which accounts for approximately 29% of the total tropical peat carbon stock, substantially changed the tropical peatland distribution as previously reported by Page et al. (2011). The Congolese peatlands are estimated to cover 145,500 km^2 (95% CI; 131,900-156,400), roughly equivalent to the size of England, and estimated to store approximately 30.6 Pg carbon (95% CI, 6.3-46.8), approximately half the area and half the carbon stored in peat in Southeast Asia (Dargie et al., 2017). Thus, the peatland complex in central Congo is larger than any other continuous peatland area in the tropics, because the Southeast Asian peatlands occur as separate areas across several islands including Borneo, Java and Sulawesi.

Combining their data on the Congolese peatlands with the global estimates of Page et al. (2011), Dargie et al. (2017) estimated the total contemporary tropical peat carbon stock to be 104.7 Pg C (69.6 – 129.8 range). Of this, 34.4 Pg C is located across the African continent, instead of the 8 Pg reported earlier by Page et al. (2011). In terms of both peatland area and peat carbon stocks, the Democratic Republic of the Congo (90,800 km^2 of peat, with 19.1 Pg C) and the Republic of the Congo (54,700 km^2 of peat, with 11.5 Pg C) take up second and third place after Indonesia as most important peatland countries in the tropics. Together, these two countries store approximately 5% of the estimated global peat carbon stock (Dargie et al., 2017).

Similarly, research by Lähteenoja et al. (2011) and Draper et al. (2014) on a previously understudied peatland area in the Pastaza-Marañón Foreland Basin in the lowland Peruvian Amazon revealed that this part of South-America harbours extensive peatlands as well. Hastie et al. (2022) recently estimated these peatlands to cover an area of ~43,600 km^2, storing approximately 4.1 Pg C belowground. Together, these new insights from Africa and Amazonia have challenged the long-standing notion that tropical peatlands are rare outside Southeast Asia. As more peatlands are expected to be found across the tropics, it is likely that current estimates of tropical peatland extent are an underestimation (Xu et al. 2018).

1.2.2.2 Tropical peatland characteristics

Peat accumulation is the net result of a larger organic matter production than decomposition (Osaki & Tsuji, 2016; Page et al., 2006; Rydin & Jeglum, 2006). The rate of organic matter decomposition thus plays an important role in determining how much peat can accumulate. Decomposition rate is influenced by various factors, including temperature and moisture conditions, chemical composition of the litter material, and the structure of the decomposer

community of bacteria, fungi and soil fauna (Liski et al., 2003; Powers et al., 2009). Of these different factors, temperature has long been recognized as the primary driver of decomposition rates (Bothwell et al., 2014; Powers et al., 2009). In boreal and temperate areas, peatlands can form under high-precipitation and low-temperature conditions where microbial decomposition is naturally slow. However, with the right regional environmental and topographic conditions, peatlands can also develop in the high-precipitation and high-temperature climates of the tropics (Page et al., 2006). This normally requires near-permanent inundation of the soils, sufficiently large organic matter input, and low nutrient concentrations (Hooijer, 2006; Rydin & Jeglum, 2006; Takada et al., 2016). Permanent inundation of tropical peat soils results in oxygen deficiencies, which inhibit oxidation of organic carbon and thus prevent complete decomposition of the litter material. At the same time, a low nutrient status has been associated with reduced decomposition rates, as high acidity and high levels of polyphenols and fulvic acids in the humus and soil water can have unfavourable or directly toxic effects on soils microbes (Takada et al., 2016), significantly slowing down microbial decomposition. In addition, it has recently been shown how surface peat in the tropics has less labile carbohydrates and more recalcitrant aromatic contents than surface peat at high-latitudes, which inhibits anaerobic decomposition (Hodgkins et al., 2018). This higher aromatic content is mostly due to the presence of lignin, as tropical peat is largely made up of woody material from fallen trees, branches, and dead roots. What's more, it has been suggested that the presence of woody vegetation itself induces a shift in microbial communities to slow-growing microbes, thereby further reducing decomposition rates (Wang et al., 2021). These forested tropical peatlands contrast with many boreal or temperate peatlands, which are normally covered by bryophytes, most commonly *Sphagnum* species, as well as grasses, sedges and shrubs (Page et al., 2006).

1.2.2.3 Tropical peat initiation and formation

Inundation is a key requirement for peat formation, both in the tropics and at higher latitudes. Peat formation under wet conditions can occur in different ways. Terrestrialisation is the process by which water-filled depressions, such as lakes, are being gradually filled in with peat deposits that result from the accumulation of organic matter near the lake's margins. Paludification, on the other hand, is the process of peat accumulating on top of mineral soils. When poorly-drained, flat surfaces are consistently water-saturated, partly decomposed organic matter can overflow onto mineral soil. Both processes are often related to shifts in precipitation or hydrology, although with opposite directions. Terrestrialisation is generally associated with a shift to dryer conditions over initially waterlogged depressions, while paludification is normally

the result of a shift to wetter conditions over mineral soils (Cameron et al., 1989; Håkan Rydin & Jeglum, 2006).

Globally, peat has been forming since at least 130,000 years ago, particularly during warmer interglacial periods at higher latitudes. However, this extremely old peat was buried again during the Last Glacial Period as icesheets advanced (Treat et al., 2019). In the tropics, peat burial appears to be insensitive to these glacial-interglacial temperature variations, but rather driven by sea level changes and regional hydrology. Peatlands have been persistently present in the tropics throughout various climatic conditions over the last 50,000 years (Treat et al., 2019). For example, inland peatlands in Borneo show initiation dates of up to 30,000 years ago, and sometimes even 47,000 years ago (Ruwaimana et al., 2020). This tells us that tropical peat initiation is not necessarily a feature of the Holocene only, but occurred from the late Pleistocene to the Late Holocene (Page et al., 2006). As the global climate moved from the Last Glacial Maximum (LGM, ca. 18,000 years ago) to the current interglacial, the Bornean peatlands have gone through a series of increases and decreases in peat accumulation, most likely as a result of changes in sea level, precipitation and seasonality of climate (Page et al., 2004). This is in line with a study by Morris et al. (2018), who found that rising temperatures and declining seasonality of both temperature and precipitation were significant predictors of peat initiation in Southeast Asia. In Africa and Latin-America, on the other hand, peat formation was not significantly predicted by any paleoclimatic variable in their study. Rather, Morris et al. (2018) suggest that the creation of waterlogged depressions due to tectonic subsidence could be a more plausible driver of peat initiation in these regions. This corresponds with current understanding about the drivers of peat initiation in the Peruvian Amazon. According to Baker et al. (2019), peat swamps occur in the Pastaza-Marañón Foreland Basin because tectonic activity and ongoing subsidence during the Quaternary has created the depressions that allow water to accumulate. However, this appears to be in contrast with recent field data from the world's most extensive tropical peatland complex in the central Congo Basin. Radiocarbon dating of basal samples from interfluvial basin peatlands in Republic of the Congo suggests that peat initiation in this region began approximately 10,500 years ago (Dargie et al, 2017). The authors point out that this initiation date coincides with a known increase in humidity across the basin known as the African Humid Period (ca. 11,000-8,000 years ago). This indicates that a shift in precipitation, rather than tectonic subsidence, was the most likely cause of peat formation in this part of the tropics (Dargie, 2015). Nonetheless, this highlights how hydrology, whether

because of changes in precipitation or geomorphology, is crucial to peat formation and preservation in the tropics.

1.2.2.4 Tropical peat composition and properties

Peat consists of three main components, namely organic matter, mineral or inorganic matter, and water. Water content of undisturbed tropical peatlands is generally high with values of 90% at saturation (Wösten et al., 2008). To account for this, organic and mineral matter content is usually expressed as a dry weight value. As discussed, dry weight organic matter content needs to be at least 65% in order to classify as true peat in most tropical peatland studies. This leaves the mineral (or inorganic or ash) content to range between 0 and 35%. Less than 1% ash content is common in most true peatlands, although values between 10-15% can often be found in shallow peat deposits that are flooded by river water (Page et al. 2006). As carbon constitutes a large proportion of the organic matter content, the organic carbon content of tropical peat soils is usually greater than 50% (Page et al., 2006; Page et al., 2011; Wüst et al., 2003).

The relative proportions of organic and mineral materials in peat determine its bulk density value, which is one of the most important physical characteristics of peat (Andriesse, 1988). Bulk density is defined as the dry weight of a given volume of soil, normally expressed as grams per cubic centimetre. Globally, values typically range from 0.05 g cm^{-3} in very fibric, undecomposed soil to less than 0.5 g cm^{-3} in well-decomposed soils (Andriesse, 1988). However, in the tropical peatlands of Indonesia and the Peruvian Amazon, values are typically lower and range between 0.02 and 0.2 g cm^{-3} (Lawson et al., 2015). This corresponds with a list of pantropical bulk density values for tropical peatlands published by Page et al. (2011), which generally fall between 0.05 and 0.25 g cm^{-3}, although values up to 0.70 g cm^{-3} are given for sites in Kalimantan in Indonesia. In the central Congo Basin peatlands, Dargie et al. (2017) found a mean bulk density of 0.19 g cm^{-3}, with values ranging between 0.1 and 0.32 g cm^{-3}. This mean bulk density value is considerably higher than the mean values that were reported for the Central Kalimantan or the Peruvian Amazon peatlands, which are both 0.11 g cm^{-3} (Dargie et al., 2017). Whilst bulk density is related to mineral content, this does not account for these higher bulk density values alone. According to Dargie (2015), these higher values in the Cuvette Centrale are more likely caused by a higher degree of compaction, which is a result of a higher degree of decomposition. Higher rates of decomposition result in lower rates of peat accumulation, which has been observed for the Cuvette Centrale peatlands (Dargie et al., 2017). Furthermore, Dargie (2015) shows that these peatlands have a relatively high mean ratio of carbon to nitrogen (C/N), which is also

characteristic of high decomposition rates. The cause of these higher rates of decomposition in central Congo, relative to other tropical peatland areas, remains unclear. One possibility is that greater decomposition is related to the relatively dry climate over central Congo Basin (mean annual precipitation ~1700 mm yr^{-1}), compared to other tropical peatland regions (e.g., ~2,500-3,000 mm yr^{-1} in Northwest Amazonia and Southeast Asia; Malhi & Wright, 2004), which could indicate reduced surface wetness and resulting higher decomposition.

Part of the bulk density variation can be explained by variation in the average peat thickness of these locations. Dargie (2015) reports a significant negative relationship in the central Congo Basin between both total peat thickness of a core and mean bulk density of that core, as well as between bulk density and OM content. This means that thicker peat deposits have lower mean bulk density values. This corresponds with general reports of decreasing bulk density with peat thickness (Andriesse, 1988; Page et al., 2006). However, as a general pattern, all sites sampled by Dargie (2015) individually showed bulk density values increasing towards the base of the core. This pattern was also described by Rydin and Jeglum (2006), who state that bulk density generally increases with depth below the surface. Lähteenoja et al. (2009b) also found increasing bulk density with increased depths for one of their Peruvian Amazon peatland sites, while Page et al. (2004) found that bulk density first increases between 50 and 100 cm depth, than decreases again after 200 cm, after which it finally increases again near the base of the peat core at 800 cm. It thus appears that conflicting trends in bulk density with peat thickness can be observed (Lewis et al., 2012), likely depending on site characteristics.

Variations in bulk density are further related to factors such as the botanical composition of the peat, drainage history and measurement method. However, distribution and number of samples are often not well designed to capture these effects across a peatland area (Lawson et al., 2015). Furthermore, many studies on tropical peatlands only report mean or median bulk density values per region and no variation within or between sites (e.g. Householder et al., 2012; Draper et al., 2014; Dargie et al., 2017). As bulk density has repeatedly been shown to be among the most important drivers of uncertainty in tropical peat carbon stocks estimates (Dargie et al., 2017; Draper et al., 2014), this might cause assessments of tropical peatland carbon pools to vary by an order of magnitude (Lawson et al., 2015). Especially in the tropics, more research is needed to determine how bulk density varies spatially within sites and between different regions (Lawson et al., 2015; Yu, 2012).

1.2.2.5 Tropical peatland hydrology

Nutrient composition of peatlands can vary significantly depending on the origin of the peatland's water input. Traditionally, a distinction is made between ombrotrophic peat systems, which are hydrologically detached from their surroundings and receive water input from precipitation alone, and minerotrophic peat systems, which receive water input from rivers, streams or groundwater (Cameron et al., 1989; Håkan Rydin & Jeglum, 2006; Wheeler & Proctor, 2000). Because nutrient input in ombrotrophic peatlands is entirely dependent on rainwater, these systems generally receive less nutrients and are therefore more acidic in nature. Minerotrophic peatlands are generally more alkaline, as they are subject to higher nutrient inputs from surrounding surface or groundwater (Rydin and Jeglum, 2006; Lähteenoja et al. 2009a). In the Peruvian Amazon, it was found that minerotrophic peat has particularly higher Ca levels and Ca/Mg ratios compared to ombrotrophic peat (Lähteenoja et al. 2009a).

In poorly-drained depressions such as basins and valleys, terrestrialisation can eventually result in peatlands growing above the original waterline. This can cause a shift from what often used to be a minerotrophic peatland to an ombrotrophic system with a characteristic dome-shape (Takada et al., 2016). Ombrotrophic peatlands are therefore often surrounded by peripheral minerotrophic bands, or they overlay minerotrophic peat layers that can be found at greater depths. These distinct differences in nutrient status can result in a mosaic of both minerotrophic and ombrotrophic peatland systems and increase the regional habitat diversity of a tropical peatland complex (Lähteenoja et al. 2009a).

The majority of peat swamps in Southeast Asia are domed, ombrotrophic systems, which feature a typical convex shape (Page et al, 2006). These ombrotrophic peat swamps are not subject to river flooding, generally have a pH of less than 4 and an organic matter content above 75%. On the other hand, minerotrophic peat is generally formed in freshwater swamps that are regularly flooded by river water in the wet season. These peatlands have pH values higher than 4 and an organic matter content below 75%. Because the higher nutrient content in freshwater swamps enhances decomposition, these swamps are generally less deep than ombrotrophic peat swamps (Takada et al., 2016).

Ombrotrophic peat domes that have grown out above the initial waterline are entirely dependent on water input from precipitation. Yet growth of the peat dome is bound by river channels at its margins. As a result, the carbon uptake of a peatland system is proportional to

the area of the still-growing interior of the peat dome (Cobb et al., 2017). However, because peat accumulates only below the water table, the shape of the peat dome is a reflection of the shape of the water table, and thus its hydrology (Winston, 1994). Since the peat dome requires a stable peat surface, dome height is limited by the maximum stable water table within the external boundaries. This shape parameter, a function of rainfall and groundwater flow, specifies the ultimate stable morphology of the peat dome, and therefore, the maximum amount of carbon storage possible within a peatland area (Cobb et al., 2017).

The flow of water through peatlands is determined by the peat's hydraulic conductivity. Especially in drained peatlands, hydraulic conductivity of the surface peat layer affects the peatland water table, and thus which parts of the peatland are exposed to aerobic decomposition (Baird et al., 2017). The relationship between bulk density and hydraulic conductivity is not straightforward and depends on the amount of peat degradation and type of peat-forming plants (Liu & Lennartz, 2019). However, it has been known for several decades that there exists a relationship between the rate of decomposition of peat soils and their saturated hydraulic conductivity, with the latter decreasing pronouncedly with increasing decomposition (Bloemen, 1983; Wong et al., 2009). As the degree of decomposition generally increases with depth below the surface, this means that the peat surface layer is most important peat layer for groundwater flow of water through a peatland (Clymo, 2004; Rezanezhad et al., 2016). Baird et al. (2017) found that the hydraulic conductivity of near-surface peat in ombrotrophic peat domes in Panama was particularly high, resembling the permeability of unconsolidated gravel. This contrasts with lower values obtained by Kelly et al. (2014) in floodplain peatlands of the Peruvian Amazon, suggesting that hydraulic conductivity might be different depending on the type of peatland and their water source. However, both studies concluded that most rainwater input must leave the peatland via overland flow, as the hydraulic gradient in the deeper peat layer is very low. As such, an effect of groundwater flow on water tables is likely only to be seen near the peatland's margins, while water tables at the centre of a peat dome can be expected to be relatively stable (Baird et al., 2017).

If the water table temporarily drops, for example due to drought, various self-regulated hydraulic mechanisms can prevent the peat surface layer from drying out (Dommain et al. 2010). In intact tropical peat domes, water is stored above the peat surface in depressions between hummocks around tree trunks, as well as between spreading buttress roots. This differentiation – between hummocks with limited hydraulic conductivity and depressions with high water

storage capacity – resembles the typical hummock-hollow patterning of temperate or boreal *Sphagnum* bogs. Dommain et al. (2010) showed that buttressed trees play a key role in providing the structural elements for this self-regulation. As part of a concentric zonation of forest types around a peat dome, buttressed trees in Southeast Asian peatlands are typically more present on steeper margins where they prevent water runoff. Additionally, other irregularities at the surface, such as tip-up pools where peat has been removed by uprooting trees, can fill up with water and prevent the peat surface layer from drying out (Dommain et al., 2015). Together with the fact that most excess water leaves a peat dome via overland flow due to the peat surface's lower hydraulic conductivity, these mechanisms help to stabilise the water tables of tropical peatlands, and ultimately contribute to the maintenance of peat that has accumulated.

1.2.2.6 Classifying tropical peatlands

Tropical peatlands occur in a number of types. According to Page et al. (2006), the majority of peatlands in Southeast Asia are domed rain-fed peatlands. These ombrotrophic peatlands can largely be divided in three major types according to location: coastal peatlands; basin or valley peatlands; and high, interior or watershed peatlands. Coastal peatlands can be found along the maritime edge or in deltaic areas where they have developed over marine sediments, slightly above sea level. Basin or valley peatlands are found inland along river valleys at slightly higher elevations, and often in backswamp situations behind alluvial levees, where they can grow up to 20m thick. High, interior, or watershed peatlands are found in Central Kalimantan where they cover interfluvial basins between major rivers. These watershed peatlands are dome-shaped (up to 13m) and extent over large areas in a gently sloping manner analogous to temperate blanket peat (Page et al., 2006). In comparison with Southeast Asia, a potentially larger diversity of peatland types exists in the Peruvian Amazon. Peatlands in the Pastaza-Marañón Foreland Basin in northern Peru harbour extensive minerotrophic sites in seasonally flooded river floodplains, characterized by markedly increased nutrient concentrations. Together with nutrient-poor ombrotrophic domes, this points towards a gradient from nutrient-poor to nutrient-rich peatlands in the Peruvian Amazon (Lähteenoja & Page, 2011).

Apart from location, morphology or nutrient status, tropical peatlands can be classified by vegetation type. It has long been recognized that peatland characteristics such as water table height and nutrient-status have a considerable impact on the vegetation structure of the peat swamp forest (Page et al., 1999; Phillips & Bustin, 1998). Local gradients in nutrient-status and inundation levels can typically be found from the margin towards the centre of a peat dome,

which often corresponds with a similar variation in vegetation types. For example, part of the peatland complex in the Peruvian Amazon shows concentric zonation, with tall pole forest in the centre of a domed peatland area, and swamp forest dominated by the *Mauritia flexuosa* palm tree in marginal peatland areas surrounding this dome (Lähteenoja & Page, 2011). Thus, peatlands can often by classified according to distinct vegetation types.

Similarly to the Peruvian Amazon, Anderson (1963) described a sequence of vegetation communities in concentric zones on ombrotrophic peat domes in Sarawak and Brunei. In Southeast Asia, tall, floristically diverse and structurally complex forest generally covers shallow peat at the margins of a peatland, while less diverse, low-canopy pole forest with small diameters can be found to cover the thicker, interior parts of a peatland (Page et al., 1999). Many of the peat swamp forest trees found in these areas are specialists that are not found in other ecosystems (Page et al., 2006).

However, contrary to Amazonia and Southeast Asia, no spatial arrangement in vegetation types has so far been identified for the Cuvette Centrale peatland complex in the Congo basin. Here, only two vegetation types are associated with peatlands, namely palm-dominated swamp forest (typically *Raphia laurentii*) and diverse hardwood swamp forest (Dargie et al., 2017). A thorough understanding of structural differences between these vegetation types and the region's vegetation history is currently lacking. In addition, it is unclear whether minerotrophic peatlands or floodplain peatlands with a different morphology than ombrotrophic peat domes can be found in the Congo Basin. Improving our understanding of the Congolese peatlands' ecological functioning is an important research priority, as identifying any relationship between aboveground vegetation types and belowground peat characteristics could potentially assist in mapping peat carbon stocks (Lawson et al., 2015).

1.2.2.7 Tropical peatland carbon dynamics

Given the importance of waterlogging for peat formation, peatlands are very sensitive to changes in the water table. Particularly in the tropics, water table depth is recognized by many experts as the main driver of long-term peat accumulation (Loisel et al., 2021). When groundwater levels drop more than 40 cm below the surface, tropical peatlands in Southeast Asia show increased subsidence due to oxidation, as well as increased susceptibility to fire (Wösten et al., 2008). Because of this, drainage of peat swamp forests for conversion to oil palm plantations has led to large-scale emissions of CO_2 to the atmosphere (Hooijer et al., 2010).

Carbon emissions from widespread burning of peat and vegetation during the 1998 El Niño event in Indonesia were estimated to be between 0.8 and 2.6 Pg, equivalent to 13–40% of the mean annual global carbon emissions from fossil fuels at the time (Page et al., 2002). Similarly, the total carbon emissions from forest and peatland fires in Indonesia during the more recent 2015 El Niño event are estimated to be 0.28 Pg C (Huijnen et al., 2016). The six largest fire events between 2004 and 2015 together are thought to have caused a total economic loss of almost 100 billion US dollars (Kiely et al., 2021). In addition, exposure to particulate matter pollution caused by (peatland) forest fires has been estimated to have caused more than 44,000 excess deaths in 2015 alone (Kiely et al., 2020).

The large-scale conversion and degradation of peat swamp forests in Peninsular Malaysia, Sumatra and Borneo have now shifted this ecosystem type from being a long-term carbon sink to being a large carbon source, emitting around 146 Mt C yr^{-1} in 2015 (Miettinen et al., 2017). However, there is some evidence to suggest that even relatively undisturbed peatlands in Southeast Asia are already a net source of carbon to the atmosphere, due to higher temperatures and lower water tables. For example, Hirano et al. (2012) measured a mean net ecosystem CO_2 exchange of 174 g C m^{-2} yr^{-1} in a relatively intact peat swamp forest in Central Kalimantan with little drainage. Furthermore, they suggested that annual CO_2 emissions increase with 79–238 g C m^{-2} with every 10 cm of lowering of the water table. Similarly, Tang et al. (2020) recently found that a relatively undisturbed peat swamp forest in Sarawak was a net source of CO_2 to the atmosphere. However, these measurements exclude methane emissions and other carbon pathways out of the system, so total ecosystem carbon exchange was not specified. Peat swamps typically switch from a CH_4 sink during the dry season to a CH_4 source during the wet season. But because annual CH_4 fluxes of an undrained peat swamp forest studied in Central Kalimantan were typically low, Sakabe et al. (2018) concluded that these forests could potentially be regarded as CH_4-neutral at the ecosystem-scale. However, controls on peat carbon sequestration are likely considerably more complex than suggested by these studies, given that there is palaeo-evidence that indicates that drought can also lead to increased peat accumulation. A study of Peruvian peatlands by Swindles et al. (2018) observed increases in long-term (millennial) net peat accumulation rates during historic drought phases. The authors suggested this could possibly be driven by a strong increase in plant productivity as water tables are lowered, which might have offset the loss of already formed peat carbon due to increased aerobic decay. Thus, there could be opposite short- and long-term effects of hydraulic changes on carbon sequestration in peat swamp forests, although much remains unknown. Especially in

the Congo Basin, no data currently exists on net ecosystem exchanges, or how plant productivity would be affected by changes to hydrology. This causes large uncertainties around how these ecosystems will respond to future land use and climate change (Dargie et al., 2019).

1.2.3. The central Congo Basin peatlands

The central Congo Basin peatlands are found in the 'Cuvette Centrale' (central depression), a large wetland area located within the Congo Basin. Here I first describe the regional setting, then the central Congo Basin peatlands specifically.

1.2.3.1. The Congo Basin rainforest

The Congo River Basin is the second largest river basin in the world after that of the Amazon, covering about 4 million km^2 from 09° 15' N to 13° 28' S and 11° 18' E to 31° 10' E. It occupies almost all of the Democratic Republic of the Congo (DRC) and much of the Republic of the Congo, as well as large portions of Cameroon, the Central African Republic, Zambia, and Angola (Harrison et al., 2016). Although the terms are often used interchangeably, this area does not entirely overlap with the Central African forest region, which typically covers all forests found in the eight countries of Central Africa: DRC, ROC, Cameroon, Central African Republic, Gabon, Equatorial Guinea, Burundi and Rwanda (Verhegghen et al., 2012). This area is home to the second largest rainforest on the planet, which covers about half (46%) of the total land area of these eight countries. With an estimated area of about 1.87 million km^2, this forest is primarily made up of dense moist forest (1.69 million km^2), in addition to 0.13 million km^2 of edaphic (seasonally or permanently flooded) forest, as well as smaller amounts of mangroves, mountainous and submontane forests. These forests and other vegetation types are an important carbon stock, storing an estimated 49 Pg of C in aboveground biomass (Verhegghen et al., 2012). Although this is smaller than that of the Amazon Basin forest, the forests of the Congo River Basin are thought to be a six times stronger net carbon sink, owing to lower deforestation emissions and stronger carbon uptake in undisturbed forests. Overall, the Congo River Basin forests take up a net amount of 0.61 Pg CO_2-equivlent per year (consisting of 1.1 Pg CO_2-eqv. gross removals and 0.53 Pg CO_2-eqv. gross emission; Harris et al., 2021b).

African tropical forests have relatively more aboveground biomass (AGB) per area than those in South America (mean 389 and 297 Mg ha^{-1}, respectively; Sullivan et al., 2017). Central African forests store even more carbon per area than African tropical forests in general, with mean AGB

values of 429 Mg ha^{-1} (Lewis et al., 2013). This is similar to that of Bornean forests (445 Mg ha^{-1}, but substantially higher than that of Amazonian forests (341 Mg ha^{-1}; Lewis et al., 2013).

However, Central African forests are characterized by a considerably lower stem density of 425 stems ≥ 10 cm diameter per hectare (cf. ~600 stems ha^{-1} in Amazonia and Borneo). This means that mean tree size in Central Africa is greater than elsewhere in the tropics. According to Lewis et al. (2013), this is because Central African forests experience relatively few disturbances, allowing trees to grow tall and stands to self-thin. This also corresponds with the relative extensive presence of monodominant forests in Central Africa, compared with other tropical regions (Peh et al., 2011). While a rarity in otherwise diverse Amazonian forests (Ter Steege et al., 2019), monodominant stands of typically *Gilbertiodendron dewevrei* can be found to extend over kilometres in Central Africa (Peh et al., 2011), likely because there is a low-level disturbance regime over the long term (Lewis et al., 2013).

Apart from lower stem density, African rainforests are also characterized by a lower tree species diversity compared with the Amazon rainforest (Parmentier et al., 2007; Sullivan et al., 2017). Parmentier et al. (2007) speculate that this lower diversity may be caused by the fact that the number of species in African forests that is adapted to warm and wet conditions is smaller than in Amazonia, due to past extinction events specific to Central Africa. This appears to be confirmed by a recent study of Hagen et al. (2021), who show that there is no correlation of forest diversity with present-day climate. Rather, geological processes shaped species diversity on this continental scale, notably aridity in African forests during the Cenozoic.

Although low in plant species diversity compared to Amazonia and Southeast Asia, the Congo rainforest has a remarkably high diversity of animals, because Africa experienced markedly less Late Pleistocene extinctions of megafauna than other continents (Barnosky et al., 2004). The swamp forest is known to have high population densities of great ape species such as the western lowland gorilla (*Gorilla gorilla gorilla*), chimpanzee (*Pan troglodytes*) and bonobo (*Pan paniscus;* Miles et al., 2017). Bonobos are known to live in the swamp forest east of the Congo River in DRC (Inogwabini et al., 2013), while the critically endangered western lowland gorillas occur to the west of the river in ROC (Rainey et al., 2009). Lowland gorillas in particular have been documented to occur at high densities in swamp forests, in contrast with chimpanzees that typically have lower densities in the swamps (Strindberg et al., 2018). In addition, the African dwarf crocodile (*Osteolaemus tetraspis*) is known to prefer the swamps as habitat, where it has

been recorded using the peat soil to construct its nests (Riley & Huchzermeyer, 1999). Another species known to be present in the swamps of the Cuvette Centrale is the African forest elephant (*Loxodonta cyclotis*), which is thought to have shaped the rainforest's structure and composition by causing a selective disturbance of relatively small trees. This leads to a reduction in stem density and favours fewer and larger trees with higher wood density, thereby increasing overall aboveground biomass (Berzaghi et al., 2019). The decline of forest elephant populations by more than 60% during the first decade of this century (Maisels et al., 2013) therefore not only threatens faunal diversity, but also potentially the forest's vegetation composition and carbon dynamics. The rivers, lakes and swamps of the central Congo Basin are also abundant in fish, although fish stocks are threatened by overfishing for the commercial market (Inogwabini, 2014). However, very little is known about other aspects of biodiversity in the central Congo Basin. In particular, there is a great lack of data about diversity of fish, reptiles, birds and insects.

1.2.3.2. Geological history of the Congo Basin

The Cuvette Centrale region is a low-lying area straddling the equator in the central part of the Congo Basin. Geologically, the Cuvette Centrale forms a shallow bowl-shaped depression within the larger Congo Basin (Figure 1.1), one of the largest intracratonic sedimentary basins in the world (Becker et al., 2014). The Cuvette Centrale has elevations between 200 and 350 m above sea level and is bordered on all sides by a range of mountains and plateaus. West and southwest of the Cuvette Centrale lie the Chaillu mountains (900 m) and Batéké plateau (600-800 m), while the Adamawa plateau (1500 m) lies to the northwest. The Bongo massif (1300 m and more) and the Central African rift (600-700 m) are located to the north of the Cuvette Centrale. In the east, the volcanic foothills of the East African rift (2000 – 3000 m) form the highest border rim, while the Katanga and Lunda plateaus (1000 – 1500 m) close the depression on the southern side (Becker et al., 2014). The current depression forms the lowest part of the Congo Basin, which evolved over 800 Ma as a result of different geodynamic processes such as extension and subsidence related to stretching (Owusu Agyemang et al., 2016).

Little seismic exploration has taken place in the Congo Basin. According to Delvaux et al. (2021) most of the current surface geology in the Cuvette Centrale, particularly West of the Congo River and along its Eastern tributaries, is of Quaternary origin (< 2.6 million years ago). On the other hand, the higher uplands East of the Congo River are thought to be of Tertiary origin (2.6-66 million years ago). This is because the current river drainage pattern is superimposed on a crystalline basement that likely formed in the early Tertiary (Deffontaines & Chorowicz, 1991).

More specifically, most of the lowland Quaternary geology of the Cuvette Centrale consists of Holocene alluvium, deposited since the end of the Last Glacial Period, i.e. more recently than 11,700 years ago (Master, 2010).
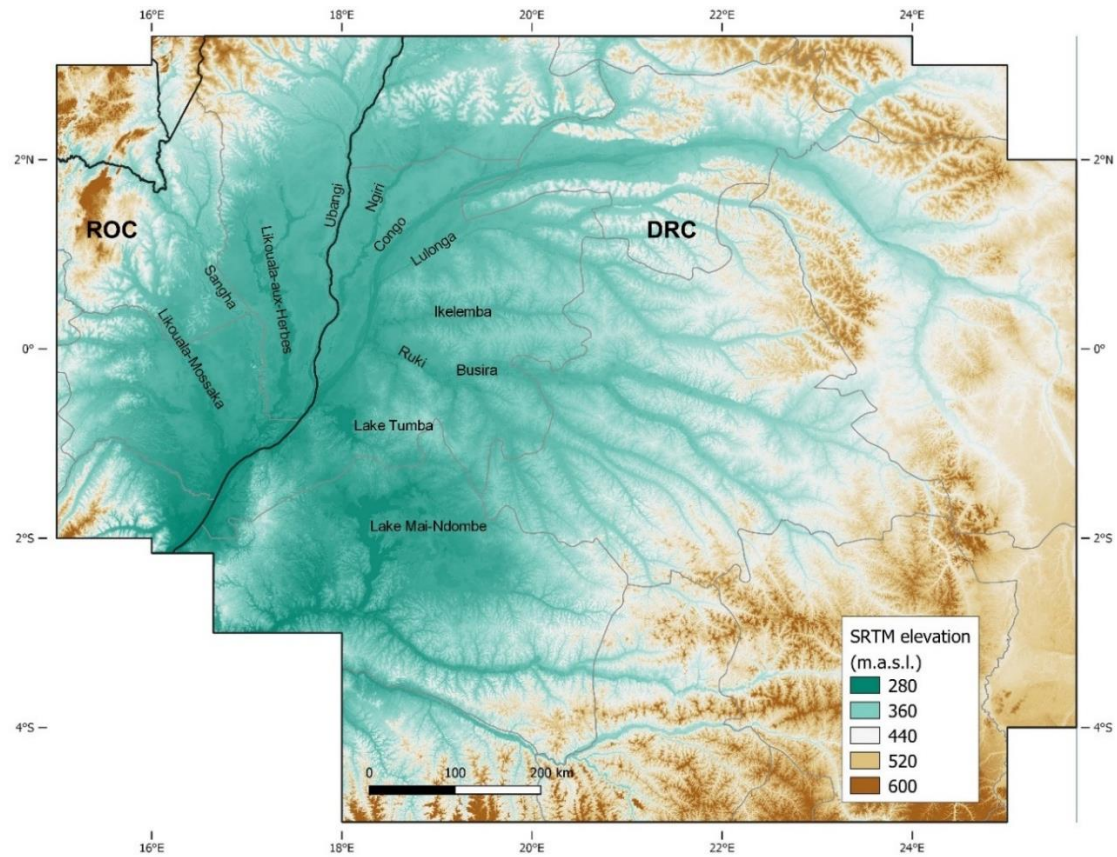
Figure 1.1. Topographic map of the central Congo Basin. *The map is based on the Digital Elevation Model (DEM) derived from the Shuttle Radar Topography Mission (SRTM) and shows elevation in meter above sea level (m.a.s.l.) across parts of the Republic of the Congo (ROC) and Democratic Republic of the Congo (DRC). Black lines represent country boundaries; grey lines represent sub-national administrative boundaries. The names of the most important rivers and lakes are provided.*

Given the very shallow gradients in the bowl-shaped depression, the Cuvette Centrale region is characterized by very low erosion rates (Laraque et al., 2009). More generally, the wider Congo Basin is characterized by very low levels of sediment (Coynel et al., 2005; Mushi et al., 2019), likely because the Congo Basin catchment area has experienced intense weathering in the past (Garzanti et al., 2019; Guillocheau et al., 2015). It has been suggested that sediment transport by the Congo River has been relatively stable during different climatic periods, possibly as a result of sediment trapping in the Cuvette Centrale wetlands that buffer suspended sediment fluxes (Molliex et al., 2019). However, there is some evidence that suggests an increase in sediment concentration in river waters in recent years, possibly due to deforestation (Mushi et al., 2019), although this needs to be confirmed by more research.

The wetlands in the Cuvette Centrale are interspersed by the presence of a few very shallow lakes, such as Lake Télé in ROC, and Lake Tumba and Lake Mai-Ndombe in DRC. Several theories have been proposed as to their possible origin. Lake Télé, which has a strikingly round shape, was once proposed to be an ancient impact crater (Laraque et al., 1998), but this theory has been refuted by Master (2010). Instead, Master (2010) has proposed that the presence of this and other lakes is more likely related to the blockage of local drainage patterns due to reactivated old tectonic fault lines. Alternatively, it has been proposed that during the Tertiary, the basin was covered by a large water body, of which Lake Tumba and Lake Mai-Ndombe are present-day remnants (Goudie, 2005). However, there is little evidence to support this theory (Dargie, 2015).

More recently during the Quaternary, the Congo Basin wetlands and forests have experienced considerable changes. During the Last Glacial Maximum, when temperatures where about 5 degrees lower than today and Central Africa was drier than today, the area of evergreen and semi-deciduous forest in Africa is estimated to have been reduced by 84% (Anhuf et al., 2006). Much of the current Central African rainforest extent would have been savanna.

During the warmer Holocene Period that followed since ~11,600 years ago, the Central African rainforests were affected once more by major forest contractions. In particular, the forests were affected by the Late Holocene Rainforest Crisis, which developed between 2,500 and 2,000 years ago. This crisis caused major perturbations at the forest core, leading to forest disturbance and fragmentation with a rapid expansion of pioneer-type vegetation, and increased erosion rates. It has been suggested that this crisis was triggered by extensive anthropogenic impacts, possibly related to large-scale expansion of Bantu farmers into Central Africa (Garcin et al., 2018). However, debate about the exact contributions of climatic or anthropogenic drivers in this rainforest crisis continues and remains unresolved (Bayon et al., 2019; Giresse et al., 2020). It has been proposed that the present-day low level plant diversity of the Central African rainforest, compared with climatically similar rainforests in Amazonia or Asia, is a result of these repeated forest contractions during drier periods, leaving only a limited species pool surviving in smaller forest 'refugia' (Hardy et al., 2013; Maley et al., 2018).

1.2.3.3. Hydrology of the Congo Basin

The Congo Basin has a wet tropical climate with mean annual temperatures between 25 and 27°C and a permanent Atlantic monsoon. Annual rainfall is high with more than 1600 mm of

precipitation throughout the basin and more than 2000 mm in some of the basin's central areas (Campbell, 2005). Rainfall tends to show a bi-annual seasonal pattern that follows from the passage of the Intertropical Convergence Zone. Thus, the Congo Basin is generally characterized by two wet seasons from March to May (MAM) and September to November (SON), and two dry seasons from June to August (JJA), and December to February (DJF; Dyer et al., 2017). However, the local pattern can diverge slightly form this, as the relative strength of the dry seasons are opposite, north and south of the equator: DJF is the main dry season in the northern hemisphere, while JJA is the main dry season in the southern hemisphere.

Figure 1.2 presents multidecadal weather data from the CREF Mabali research station on the shore of Lake Tumba in DRC. This figure shows that the main wet season is SON, but that the wet season already starts in August and runs over into December. Both August and December receive as much precipitation as the monthly average of the minor wet season in MAM. The main dry season is then concentrated in June and July.
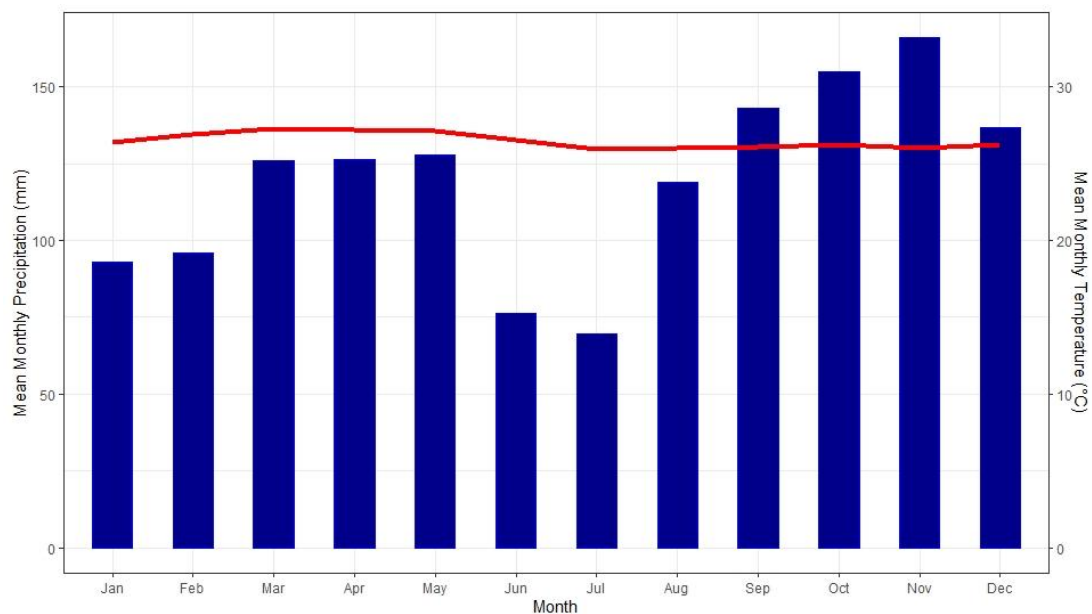
Figure 1.2. Mean monthly temperature and precipitation at CREF Mabali station in DRC. *Temperature is given by the red line (°C), precipitation by the blue bars (mm). Data represents 40-year (temperature; 1979-2018) or 50-year (precipitation; 1970-2019) timespans, excluding data gaps. Mean (± s.d.) total annual precipitation is 1436 ± 264 mm (n=44 years). Mean annual temperature is 26.5 ± 0.4 °C (n=39 years).*

The Congo river, which runs through the centre of the Cuvette Centrale, drains a catchment area of 3,747,320 km^2, making the Congo basin the second largest river basin on Earth (Runge, 2008). Using satellite altimetry, Becker et al. (2014) studied regional variability of surface water level anomalies across the basin and described how water levels in the Cuvette Centrale wetlands

have a bimodal distribution, similar to the rainfall seasonal pattern. Because the Congo River system is fed from both north and south of the Equator, the wetlands experience their main low-water period in July and August, corresponding with the prevailing dry season in the southern hemisphere. Water levels then begin to rise in August and September due to increased rainfall in the south. This reaches a short-lived peak in December, after which a secondary low-water period occurs in March, corresponding with the occurrence of the northern hemisphere dry season (Becker et al., 2014).

Congo River tributaries that originate in the southern hemisphere, such as the Ruki River, show a similar bimodal pattern in river discharge, with a peak from November to January, and a lesser peak in MAM. However, some of the tributaries that originate north of the equator, such as the Ubangi and Ngiri Rivers, show unimodal discharge patterns with a peak in October and November. Still others, such as the Sangha or Likouala-aux-Herbes Rivers, show bimodal patterns with a lesser peak in May (Campbell, 2005). Because the Congo River itself receives water from tributaries on either side of the equator, its seasonal discharge pattern is less pronounced. It is characterized by two periods of high flows (October-January and April-May) and two periods of low flows (February-March and June-September) (Laraque et al., 2020).

A study by O'Loughlin et al. (2020) found that interactions between the river channel and floodplain have only a limited impact on the annual bimodal flood wave pattern of the Congo River. River discharge is largely dominated by meteorologically factors (rainfall), rather than hydraulically-controlled features such as floodplain interactions and river width constrictions. However, the study found that channel-floodplain interactions do occur extensively along the Congo's middle reach, with over 2,100 km out of 13,000 km of the channel network being identified as zones where water is actively exchanged between channels and floodplains. This is nearly the entire middle reach of the main stem. This is largely in line with work by Lee et al. (2011) who suggests that a considerable contribution of river channel water to wetlands occurs. Laraque et al. (2020) also identify the Cuvette Centrale wetlands as behaving like a 'buffer' for river discharge, meaning they store water in the wet season to be more slowly discharged at later stages. More specifically, Datok et al. (2021) conclude based on a model simulation that the Congo River supplies about one-third of the water input to Cuvette Centrale, with precipitation supplying another one-third. Right- and left-bank tributaries together contribute the remaining one-third. Datok et al. (2021) report that only in October and April is there a surplus of water entering the Cuvette Centrale, while in other months there is a deficit, meaning

the floodplains and wetlands then act as a storage of water supplying the Congo River downstream. Because of the interaction between river water and wetlands, the Cuvette Centrale supplies vast amounts of carbon to the Congo River, both in the form of dissolved organic matter (Laraque et al., 2009) and dissolved greenhouse gases (Borges et al., 2019). By dating the age of organic matter that is discharged by the Congo River into the Atlantic Ocean, Schefuß et al. (2016) found that the Congo River Basin has been releasing aged organic matter for thousands of years. From this, even before peatlands were first mapped in the central Congo Basin, they inferred that the Cuvette Centrale wetlands must be an important terrestrial store of carbon that would have global climatic effects. Thus, it is clear that there are significant interactions between wetlands and rivers in the Cuvette Centrale, with implications for the accumulation of globally significant amounts of carbon. However, the exact flow directions and quantifies of water fluxes between wetlands and rivers still remain poorly specified.

1.2.3.4. Swamp vegetation in the Congo Basin

Wetlands in sub-Saharan Africa are widespread and cover an estimated 1.4 million km^2 (Rebelo et al., 2010), making up between 4.6 and 6% of the total sub-Saharan Africa land mass (Lehner & Döll, 2004). Although many wetlands are characterized by seasonal fluctuations in rainfall and surface water levels, permanently inundated swamp forests can be found throughout the Congo basin wetlands (Hughes & Hughes, 1992; Mayaux et al., 2002). The Cuvette Centrale region in particular has long been classified as an important wetland area with extensive swamp forest cover, although without there being any explicit indication of the presence of peatlands (Campbell, 2005; Hughes & Hughes, 1992a). For example, in 1984, the Irish Peat Development Authority analysed the potential of peat as fuel in developing countries around the world and concluded that 'various types of swamps are extremely abundant in Africa, [but] true peatlands are comparatively rare' (Bord na Móna, 1984). It was thought that the extensive swamp forests of the Cuvette Centrale region hardly contained any peat due to the high temperature and fluctuating water tables, "characteristic of many of these swamp areas".

Other studies have also commented on the extensive swamp forests in the Cuvette Centrale, without describing them as peatlands. Early descriptions of flooded forests are available from Belgian and French scholars during the colonial period. Among the most well cited is a study by Lebrun and Gilbert (1954), who classified swamp forest in the Congo Basin into five classes based primarily on the length of inundation period, e.g. permanently inundated swamp forest, seasonally inundated forest, riverine forests with long periods of flooding, continually flooded

riparian shrub forest, and well-drained alluvial-valley forests. Evrard (1968) built on these classes to create a classification of wetlands forest principally organised around vegetation type, but which combines aspects of the inundation period. As a starting point, Evrard (1968) used the three most important classes identified by Lebrun and Gilbert (1954): permanent swamp forests (*forêts marécageuses*), seasonally inundated forest (*forêts inondables*), and riparian shrub forest (*forêts ripicoles colonisatrices*). Across these classes, Evrard (1968) then identified five main vegetation alliances or associations:

- Permanent swamp forests:
  1: alliance of *Raphia laurentii* palms;
  2: alliance of *Coelocaryon botryoides* and *Entandrophragma palustre* trees;
- Seasonally inundated forest:
  3: association of *Oubanguia africana* and *Guibourtia demeusei* trees;
- Riparian shrub forest:
  4: alliance of *Alchornea cordifolia* shrubs;
  5: alliance of *Uapaca heudelotii* trees.

Partly based on the seminal work of Evrard (1968), White (1983) included extensive swamp and riparian forests in the Congo region as part of his assessment of African vegetation types. Like with Evrard (1968), these forests were said to include *Coelocaryon botryoides, Entandrophragma palustre, Oubanguia africana, Guibourtia demeusei, Raphia* spp. and *Uapaca* spp., as well as other species. However, although most of these species are not confined to swamps alone, White (1983) identifies *Carapa procera* and *Symphonia globulifera* as additional species that are typically confined to lowland swamps, and thus highly characterized of these vegetation types. Yet like his predecessors, peat deposits or carbon-rich soils are not explicitly mentioned as characteristics of these ecosystems.

Tathy et al. (1992) are likely the first to have measured methane fluxes from the flooded forests in the Cuvette Centrale. Although this suggests a focus on soil carbon dynamics, and although they rely extensively on scholarship of northern peatlands, their work focuses on surface samples only. Again, they do not mention that considerable peat deposits are found below the flooded surface of the Cuvette Centrale swamps.

Nonetheless, Tathy et al. (1992) make a rudimentary distinction between flooded soils, wet soils and dry (*terra firme*) soils. According to their distinction, flooded soils in the Cuvette Centrale have water tables between 10 and 40 cm above the surface, while wet soils have water tables of 10-20 cm below the surface. They also map three different vegetation types in the Republic of Congo: swamps, flooded forest and dry forest. The flooded forests are defined as forested wetlands close to the Congo and Ubangi Rivers, which they estimate to cover 100,000 km^2. Swamps, on the other hand, are defined as a mix of flooded forests and herbaceous wetlands (i.e., likely containing flooded savannas), for which they do not provide an area estimate.

It is unclear how exactly the vegetation map of Tathy et al. (1992) was produced. However, spatially explicit maps of swamp forests were typically first produced via manual photointerpretation or by analysing cloud-free optical remote sensing data (Vancutsem et al., 2009). In recent years, however, a focus has shifted to the use of active radar sensors as well. This started at the turn of the century when De Grandi et al. (1998) and Mayaux et al. (2002) constructed the first spatially explicit maps of Central African wetlands by using active radar data. Bwangoy et al. (2010) then combined both approaches by using optical remote sensing data from the Landsat Thematic Mapper (TM) and Enhanced Thematic Mapper Plus (ETM+) sensors with L-band active Synthetic Aperture Radar data (SAR) from the JERS-1 mission and topographical data from the Shuttle Radar Topography Mission (SRTM). Landsat ETM+ and SRTM data have long been used effectively to map wetlands across the tropics (Islam et al., 2008). L-band SAR data has also been used effectively to map wetlands in Africa with high accuracy. Its effectiveness stems from the fact that radar data is unaffected by the frequent cloud and smoke cover in the equatorial area, and that it has high temporal resolution which allows a study of hydrological dynamics (Rebelo, 2010). L-band radar in particularly is very useful for inundation mapping in the tropics given that it's relatively long wavelength (15-30 cm) is able to penetrate the forest canopy (Ottinger & Kuenzer, 2020).

Analysing these different remote sensing datasets, Bwangoy et al. (2010) estimated a wetland landcover of 360,000 km^2, which makes up 32% of the Cuvette Centrale watershed (Figure 1.3). The Lake Télé-Lake Tumba landscape in the western part of the central Congo Basin is mapped to be the area most dominated by wetlands (56% of the local landscape). Although relative local elevational differences proved to be the most important factor in discriminating wetland cover, the study showed that a combination of different kinds of data sources (optical, radar, and topography) can be used successfully to map wetland vegetation (Bwangoy et al., 2010).
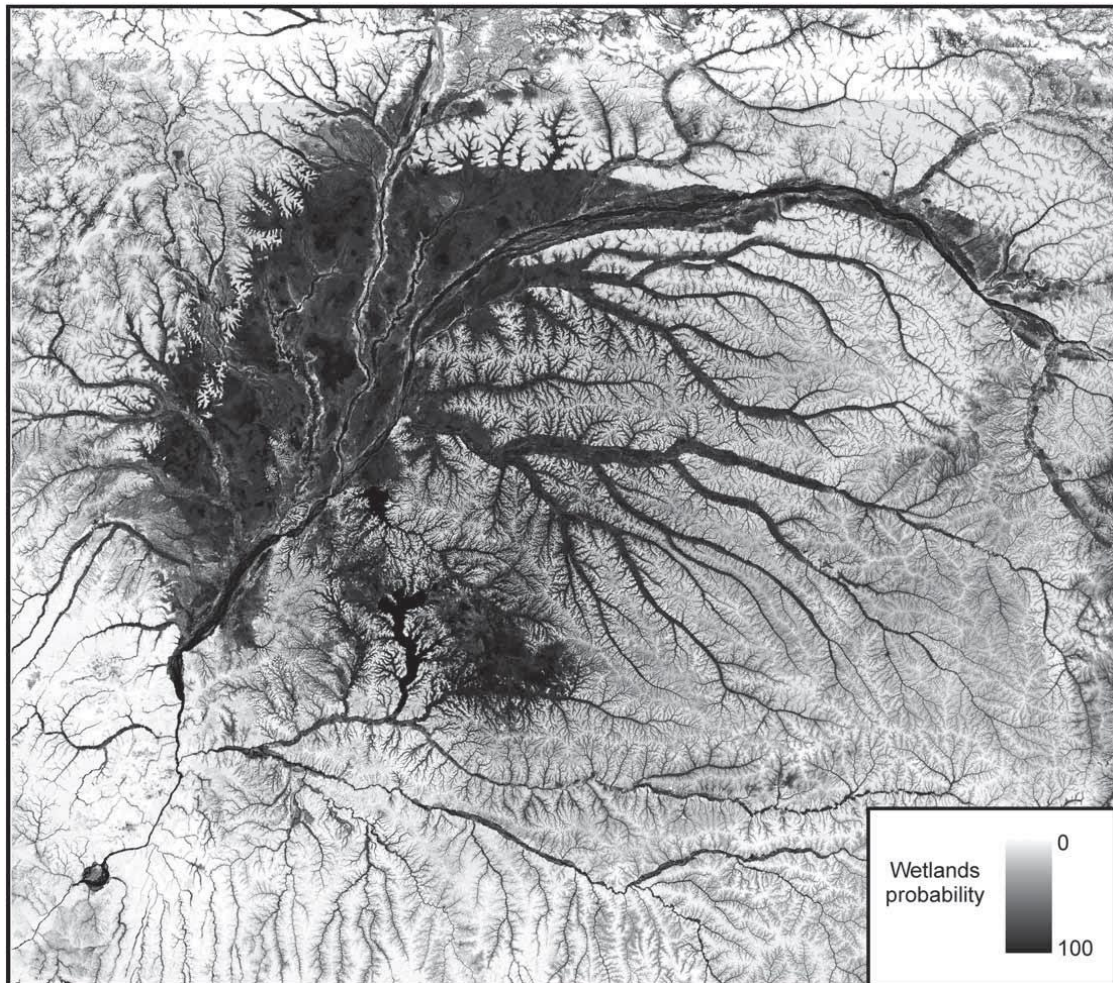
Figure 1.3. Bangoy et al.'s (2010) wetland probability map for the Cuvette Centrale. *The probability map is developed with a combination of optical, radar and topographic data. Figure reproduced from Bwangoy et al. (2010). © 2010 Elsevier.*

In recent years, L-band SAR data from the Advanced Land Observation Satellite (ALOS) with Phased Array L-band Synthetic Aperture Radar (PALSAR) has become a popular choice for active remote sensing of wetland areas. Betbeder et al. (2014) were able to construct a first spatial distribution of four different forested wetland types, based on combining ALOS PALSAR data on flooding with maps of vegetation classes derived using the Enhanced Vegetation Index (EVI) from the optical MODIS sensor (Moderate Resolution Imaging Spectroradiometer). They distinguished three vegetation classes of flooded forests as identified by Evrard (1968), as well as a non-flooded forest class (Figure 1.4). Together the three flooded forests classes are estimated to cover 230,000 km^2. This is considerably less than the estimate of Bwangoy et al. (2010), but mostly because these latter authors included a wider study area. Like Bwangoy et al. (2010) found, the spatial extent of the forested wetlands in the Cuvette Centrale turned out to be largely controlled by topography, which determines the extent of flooding, but also by the time and intensity of flooding events. Phenology of the forested wetlands was both determined

by flooding events, as well as changes in light intensity as a result of the bimodal seasonality in weather (Betbeder et al., 2014).

However, not all of Evrard's (1968) wetland classes are suitable for peat formation. As tropical peatlands require both sufficient organic matter input as well as anoxic conditions, forests with water tables close to the surface throughout most of the year are most likely to harbour peat (Lawson et al., 2015). This means that the vegetation class of permanent swamp forest subjected to stable water levels (characterized by *Entandrophragma palustre-Coelocaryon botryoide* or *Raphia laurentii* palms) is the most likely vegetation indicator of peat presence. Assuming this corresponds with the 'forests subjected to stable water level' as mapped by Betbeder et al. (2014), their map would suggest about 85,000 km^2 of likely peat swamps in the Cuvette Centrale.
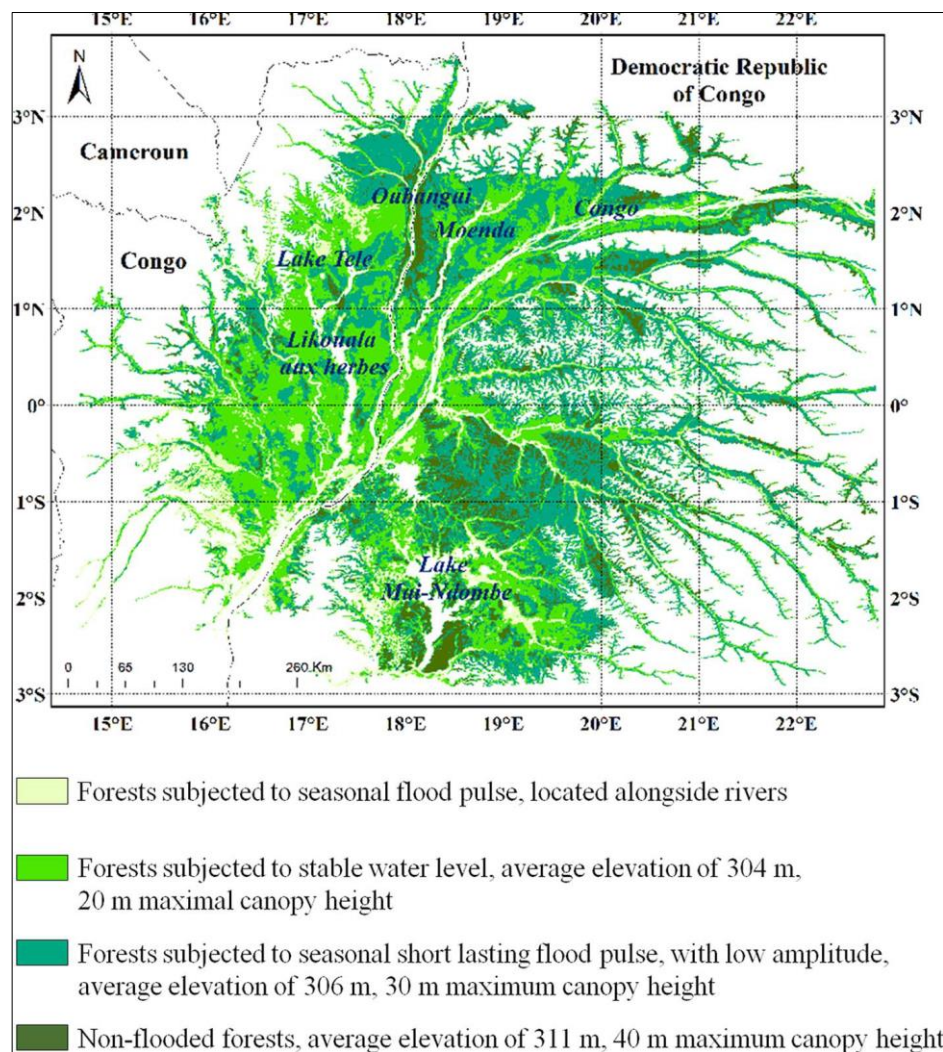
Figure 1.4. Betbeder et al.'s (2014) spatial distribution of wetland types. *The map is derived using an unsupervised classification of the MODIS Enhanced Vegetation Index (EVI), while taking into account ALOS PALSAR radar data. Figure reproduced from Betbeder et al. (2014). © 2014 IEEE.*

Although long suspected (e.g., Hughes & Hughes, 1992), actual field observations of peat presence underneath this vegetation type in the Congo basin are rare (Joosten et al., 2012; Lawson et al., 2015). To fill this data gap, Dargie (2015) and Dargie et al. (2017) undertook extensive field studies in the north of the Republic of the Congo, in the western part of the Cuvette Centrale wetland area. They discovered peat deposits underneath two types of swamp forest with relatively stable water tables, which they classified as hardwood-dominated swamp forest and palm-dominated swamp forest. This classification appears to correspond with the two permanent swamp forest alliances originally identified by Evrard (1968). However, in contrast to Evrard's (1968) alliance of *Coelocaryon botryoides* and *Entandrophragma palustre*, documented in DRC, Dargie et al. (2017) report that their hardwood swamp type is commonly characterized by *Uapaca paludosa, Carapa procera*, *Symphonia globulifera* and *Xylopia rubescens*. Nonetheless, their palm-dominated swamp forest types does corresponds with Evrard (1968), being characterized by large *Raphia laurentii* monodominant stands. They also found that a much rarer type of *Raphia hookeri* palm-dominated swamp forest was sometimes associated with the presence of peat in channels or fluvial features. In addition, savanna vegetation was found to overlie peat in only one sample point, thus appearing to be extremely rare.

Dargie (2015) also report seasonally flooded forests, often dominated by *Guibourtia demeusei* and *Dialium pachyphyllum*, which does not form peat, as it is normally only flooded during the major wet season. According to Bocko et al. (2016), who also reported vegetation characteristics in more detail from the same region in the Likouala department in the Republic of the Congo, seasonally flooded forests are additionally dominated by *Diospyros crassiflora* and *Lophira alata*. More specifically, Ifo et al. (2018) make a distinction between seasonally flooded forests dominated by *Guibourtia demeusei* and seasonally flooded forests dominated by *Lophira alata*. According to these authors, *Guibourtia*-dominated forests are flooded during longer periods of time (up to five months), and greater depth (up to two metres), than *Lophira*-dominated forests. Although many species are shared between the different flooded forest types, Bocko et al. (2016) identify *Symphonia globulifera, Xylopia rubescens, Garcinia smeathmannii, Drypetes principum* and *Entandrophragma palustre* as species that are uniquely common to permanent swamp forest only, and thus are likely to be characteristic species of peat swamps. On the other hand, they report that *Parinari excelsa, Gardenia imperatis, Albizia laurentii* and *Trichilia prieuriana* are uniquely common to seasonally flooded forests only.
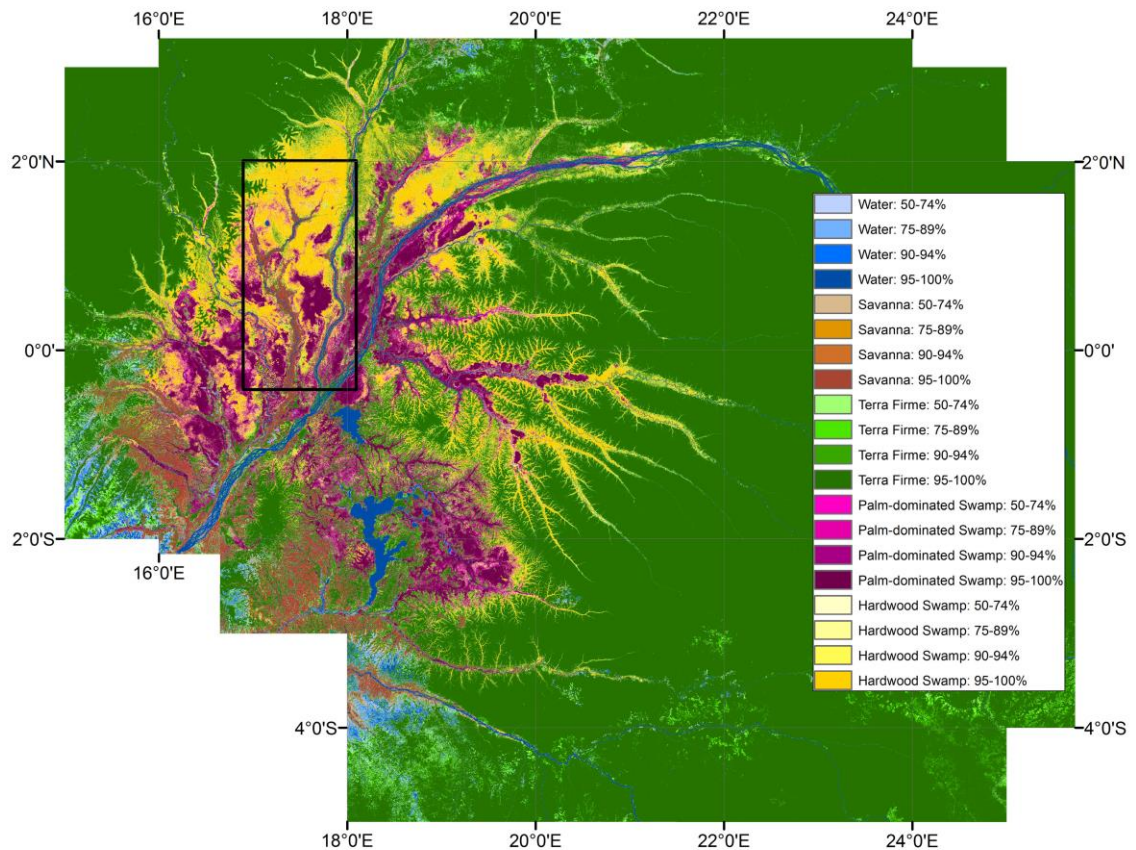
Figure 1.5. Dargie et al.'s (2017) probability map of peat swamp vegetation types. *Probability is derived from 1000 supervised Maximum Likelihood classifications based on optical, radar and topographic data. The black rectangle indicates the approximate area of field sampling in interfluvial basins in ROC. Figure reproduced from Dargie et al. (2017).*

Dargie (2015) and Dargie et al. (2017) were the first to combine field verification of associations between vegetation and the presence of peat (primarily hardwood-dominated and *Raphia laurentii* palm-dominated swamp forest) with multiple remote sensing data products. They used optical data from the Landsat 7 ETM+ satellite (short-wave infrared [SWIR], near infrared [NIR] and Red bands), radar data from ALOS PALSAR (HH and HV polarizations and the ratio), and SRTM-derived maps of elevation and slope. They then applied 1,000 supervised Maximum Likelihood classifications to map these vegetation classes associated with the presence of peat across the central Congo Basin (Figure 1.5). They estimated that the peat swamp forests together cover 145,500 km^2 (95% CI, 131,900 − 156,400 km^2). Hardwood-dominated swamp forest is estimated to be the most common, covering 79,042 km^2 (95% CI, 68,100 − 90,500), while palm-dominated swamp forest covers 66,300 km^2 (95% CI, 56,900 − 74,700 km^2).

These field-based estimates are not very different from the rules-based model developed by Gumbricht et al. (2017), who reported an exceptionally large pantropical peatland area of 1.7 million km^2, but only 125,440 km^2 of peatlands in the Congo Basin region (Table 1.1).

Study	Wetland area (km²)	Peatland area (km²)	Notes
Bwangoy *et al.* (2010)	360,000	-	Supervised classification of optical, radar, and topographic data, using manual photo-interpretation
Betbeder *et al.* (2014)	230,000	-	Unsupervised classification of MODIS-Enhanced Vegetation Index (EVI), taking into account ALOS PALSAR radar data
Gumbricht *et al.* (2017)	-	125,440	Rules-based model combining biophysical indicators from hydrological modelling and optical and topographic data
Dargie *et al.* (2017)	-	145,500	Supervised classification of optical, radar, and topographic data, using field-based ground-truth data

Table 1.1. Recent estimates of the extent of the Cuvette Centrale peatlands or wetlands. *Wetlands include peatland areas, but not vice versa. Table reproduced from a review by Biddulph et al. (2021).*
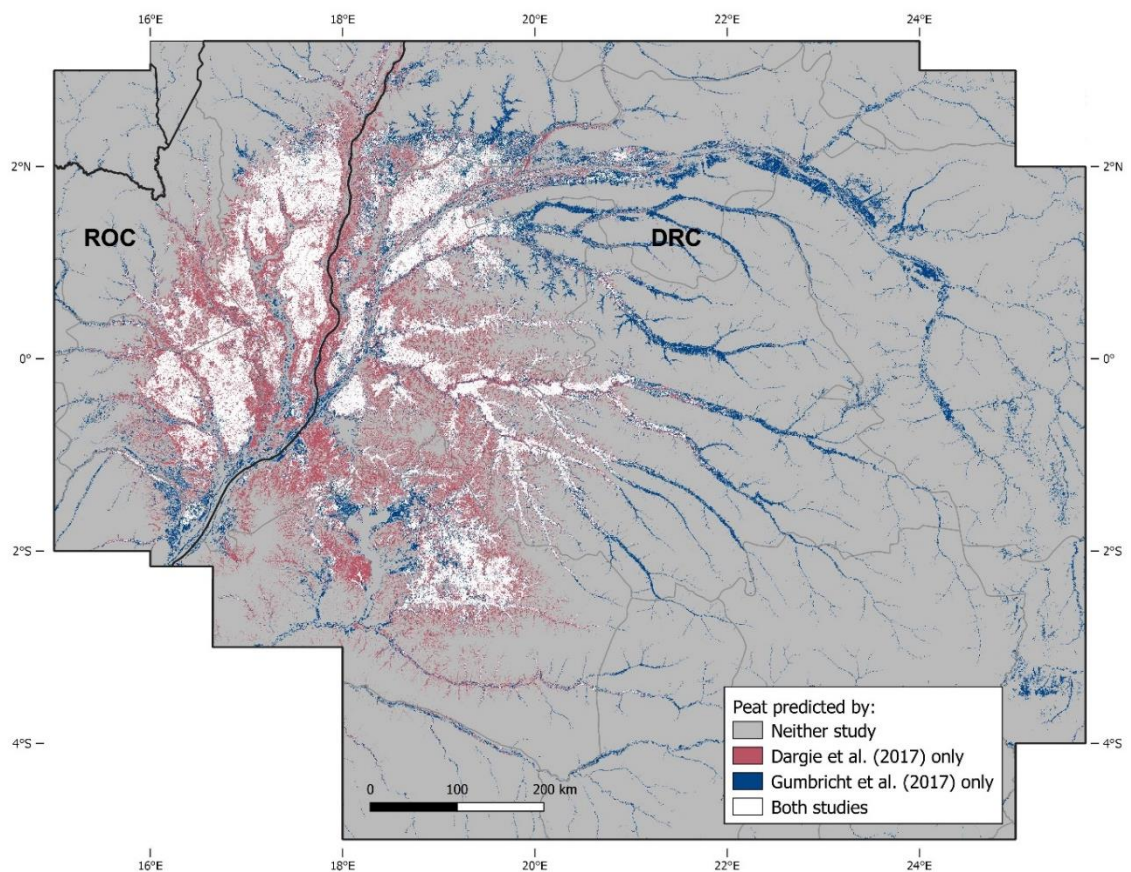
Figure 1.6. Comparison of peatland predictions by Dargie et al. (2017) and Gumbricht et al. (2017). *White indicates peat predicted by both studies; red indicates peat predicted by Dargie et al. (2017) only; blue indicates peat predicted by Gumbricht et al. (2017) only; grey indicates that neither study predicts peat. Black lines represent country boundaries; grey lines represent sub-national administrative boundaries.*

In comparison with the areas mapped by Dargie et al. (2017), the peatland map by Gumbricht et al. (2017) generally shows that peatlands extend further upriver along the Congo River mainstem and its eastern tributaries (Figure 1.6). In particular, the map identifies riverine peatland areas along the Lomami River in the east of the basin, south-west of the city of Kisangani, as well as further upstream along the different headwaters of the Lulonga and Ruki Rivers, which have not been mapped by Dargie et al. (2017). On the other hand, the peatlands predicted by Dargie et al. (2017) in the interfluvial basins in the centre of the Cuvette Centrale, such as along the Ubangi, Likouala-aux-Herbes and Sangha Rivers, are wider and denser than what is predicted by Gumbricht et al. (2017), which explains why the former's overall peatland area is still larger than that of the latter. From this comparison, it is clear that considerable uncertainty surrounds the spatial distribution of peatlands in the central Congo Basin. In particular, the extend of peatlands upstream along the Congo River and some of its tributaries remains unclear. More field verification is thus needed to reconcile these two different maps.

1.2.3.5. Climate change in the Congo Basin

There are well documented negative trends in precipitation across the Congo Basin region since at least the 1970's (Alsdorf et al., 2016; Malhi & Wright, 2004). In particular, Samba et al. (2008) report a shift in rainfall over the Republic of Congo around 1968-1970. The 1950's to 1960's were characterized by an increase in rainfall, relative to the long-term mean, followed by a relative decline between the 1970's and 1990's. This corresponds with discharge measurements of the Congo River. According to Laraque et al. (2001), the Congo River experienced higher discharge in the 1960's, followed by two successive phases of lower discharge from 1971 onwards.

These dry phases appears to have continued into the 21st century, as Asefi-Najafabady & Saatchi (2013) report an increasing drying trend in Central Africa, characterized by recent strong negative water deficit anomalies in 2005-2007. Furthermore, Jiang et al. (2019) provided evidence for a widespread increase in the length of the summer dry season (June-August) over the Congo Basin since the 1980s. According to their study, the dry season length increased by 6.4–10.4 days per decade between 1988 and 2013, mostly due to an earlier dry season onset and a delayed dry season end. An earlier onset of the summer dry season in the months of April, May and June was also detected by Hua et al. (2016), who propose that this is likely related to changing sea surface temperatures over the Indo-Pacific region. Temperature changes over the Indian Ocean appear particularly relevant for the climate of the Congo Basin, as moisture from

the Indian Ocean is thought to be the dominant source of precipitation in the basin, followed by local evaporation and moisture from terrestrial evaporation outside the Congo Basin (Dyer et al., 2017). Cook et al. (2020) also showed a robust drying in the summer months of June-August, as well as negative trends in mean annual precipitation between 1979-2017. However, contrary to Hua et al (2016), they state that these trends are likely not related to shifts in moisture transport from the Atlantic or Indian Ocean, nor local surface warming, but rather linked to a warming trend over the Sahara region.

Irrespective of the driving factor, it is clear that a drying trend is manifesting itself locally in the Cuvette Centrale wetland region too. Inogwabini et al. (2006) and Imbole et al. (2016) analysed multidecadal weather data from the CREF Mabali research centre (*Centre de Recherche en Écologie et Foresterie*), located approximately 15 km south of the town of Bikoro, on the eastern shores of Lake Tumba in DRC (18.1221°E, 0.8825°S). The Mabali research centre was founded in 1954 by IRSAC, the Belgian *Institut pour la Recherche Scientifique en Afrique Central* (BESTOR, 2021) and is currently being managed by the DRC's Ministry of Scientific Research and Technology. Although the centre has received little funding for decades, dedicated local employees have preserved daily records since at least the 1970's. Inogwabini et al. (2006) analysed data from 1970-2005 and concluded that annual precipitation had dropped considerably after 1990. However, this trend was not properly tested for significant long-term changes. Imbole et al. (2016), on the other hand, studied a more recent dataset of precipitation from the same weather station for 1980-2012. Like Inogwabini et al (2006), they found a downward trend in annual precipitation (-3.9 mm yr^{-1}), as well as the number of rainfall events per year (-0.97 days yr^{-1}) since 1980.

As of 2019, an unprecedented 50-year dataset is available for rainfall (1970-2019) from CREF Mabali, while an equally impressive 40-year dataset is available for temperature (1979-2018), providing long-term local weather data from the heart of the Cuvette Centrale peatland complex. Gaps in the rainfall record are present only for the years 1991, 1993, 1996, 1997, 1999 and 2002 (annual precipitation), and 1991, 1993, 1996, 1997, and 2002 (rainfall events), due to the civil unrest and war that took place in the DRC at the time. For temperature, only Oct-Dec 2017 is missing from the 40-year record.

Mean (± s.d.) total annual precipitation is 1436 ± 264 mm (n=44 years). However, a significant decline is observed over the 50-year timespan (Sen's slope = -5.417 mm yr^{-1}; $p<0.01$; Figure 1.7).

Interestingly, both 1970 and 1971 were exceptionally wet years characterized by > 2000 mm yr^{-1}, after which the decline sets in. When removing these two potential outlier years, a more significant, but less steep decline of -3.408 mm yr^{-1} is found (p<0.001), indicating that precipitation has been steadily declining in the centre of the Cuvette Centrale since the start of the 1970's.

Significant declines in total precipitation are also found on a monthly basis in January, April, August, October, November, and December, with monthly reductions ranging from -0.449 mm yr^{-1} in December to -1.892 mm yr^{-1} in October. The month of June, however, shows a slight, but significant increase in monthly precipitation of 0.479 mm yr^{-1} (Table 1.2). Additionally, all seasonal trimesters show significant declines. However, the total reduction in rainfall appears to be much more severe in the main wet season trimester of September, October and November (-2.912 mm yr^{-1}), compared with the other trimesters (-1.219, -1.317, and -1.097 mm yr^{-1} for DJF, MAM and JJA, respectively).
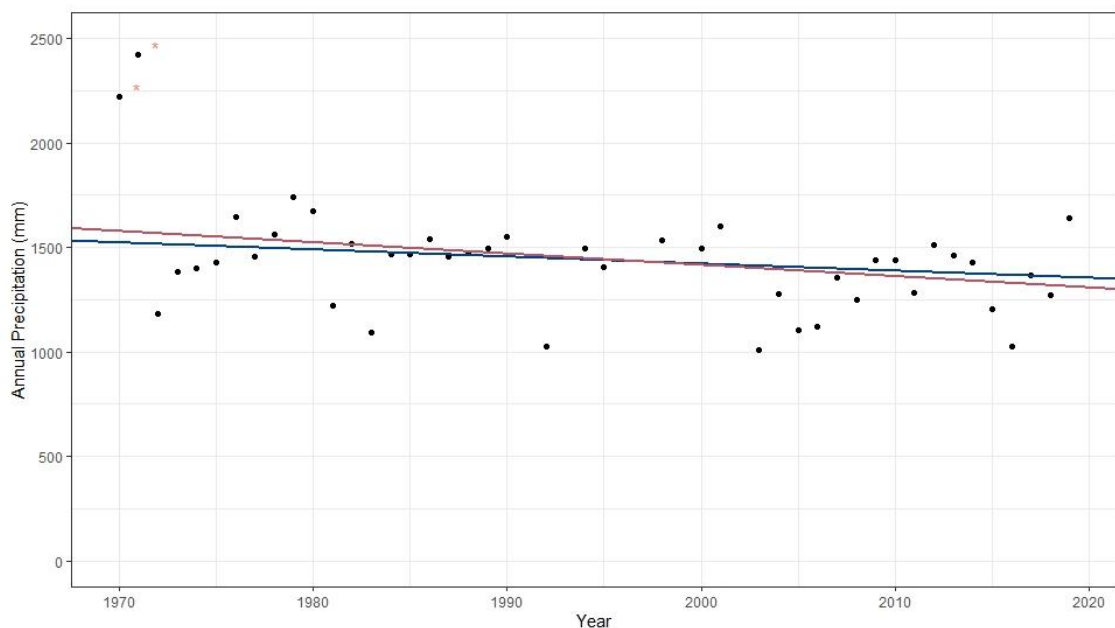
Figure 1.7. Trend in annual precipitation at the CREF Mabali station in DRC. *Trend direction and strength are estimated using Sen's non-parametric, rank-based approach (Sen, 1968). To account for the potential effect of serial autocorrelation in climate data (Wang et al., 2020), a modified Mann-Kendall test based on the Variance Correction Approach was implemented (Yue & Wang, 2004), using the mmky function in the modifiedmk package in R (version 1.6; Patakamuri, 2021). The blue line includes the exceptionally wet years 1970-1971, marked by red asterisks (Sen's slope -5.417 mm yr^{-1}; p<0.01), while these years are excluded in the red line (Sen's slope -3.408 mm yr^{-1}; p<0.001).*

In addition to the decline in total precipitation, a significant decline in the total number of rainfall events per year is found (Sen's slope = -0.833 events yr^{-1}; p<0.001). The mean (± s.d.) number of rainfall events is 100.4 ± 15.3 per year (n=45). However, rainfall events decline from about 100-125 events per year during most of the 1970's, 80' and 90's, to between 75-100 events per year since 2000. This decline is mirrored in the monthly and seasonal means, with a significant reduction found in almost all months: January, March, April, May, June, July, August, September, October, and November (Table 1.2). Declines range from 0.024 rainfall events less each year in April to 0.121 events less each year in October. Likewise, all trimesters show strongly significant declines, with the largest reductions occurring during the wet seasons (-0.200 and -0.263 events per year in MAM and SON, respectively) while smaller reductions occur in the dry seasons (-0.107 and -0.178 events per year in DJF and JJA, respectively).

	Trend in total precipitation (mm yr^{-1})	Trend in rainfall events (events yr^{-1})	Trend in rainfall intensity (mm event^{-1} yr^{-1})	Trend in mean temperature (°C yr^{-1})
Annual	-5.417**	-0.833***	0.081**	
DJF	-1.219**	-0.107***		
MAM	-1.317***	-0.200***	0.058***	
JJA	-1.097***	-0.178***	0.089**	0.015***
SON	-2.912***	-0.263***		0.014***
January	-1.129***	-0.078***		
February				
March		-0.071***	0.092**	
April	-1.000***	-0.024**	-0.035*	
May		-0.091***	0.100***	0.020***
June	0.479*	-0.048***	0.219***	
July		-0.053***	0.137***	0.022***
August	-1.044***	-0.071***		0.021***
September		-0.053***	0.118*	0.018***
October	-1.892***	-0.121***		0.016***
November	-0.905**	-0.057***		0.011*
December	-0.449*			

Table 1.2. Overview of significant climatic trends at the CREF Mabali station in DRC. *Trends reflect 40-year (temperature; 1979-2018) or 50-year (rainfall; 1970-2019) timespans, separated out on a monthly, seasonal and annual basis. Trend direction and strength are estimated using Sen's non-parametric, rank-based approach (Sen, 1968). To account for the potential effect of serial autocorrelation in climate data (Wang et al., 2020), a modified Mann-Kendall test based on the Variance Correction Approach was implemented (Yue & Wang, 2004), using the* mmky *function in the* modifiedmk *package in R (version 1.6; Patakamuri, 2021). Data includes potential outliers, with* p<0.05; ** p<0.01; *** p<0.001.*

As the number of rainfall events is declining, mean annual rainfall intensity (14.6 ± 2.8 mm per event, n=44) is found to be going up by 0.081 mm per event per year (p<0.01). When the two high-rainfall years of 1970/1971 are excluded as potential outliers, this effect becomes even stronger (Sen's slope = 0.105 mm event^{-1} yr^{-1}; p<0.001). A significant increase in rainfall intensity is also observed in the months of March, May, June, July, and September (Table 1.2). The strength of these intensifications ranges from 0.092 mm per event per year in March, to 0.219 mm per event per year in June. On the other hand, a slight, but significant decline in rainfall intensity is seen in April (Sen's slope = -0.035 mm event^{-1} yr^{-1}; p<0.05). Again, these monthly trends are reflected in the seasonal trends (Table 1.2), with significant increases in rainfall intensity found in MAM (0.058 mm event^{-1} yr^{-1}) and JJA (0.089 mm event^{-1} yr^{-1}). No significant effect was found in the DJF and SON trimesters.

Thus, based on this updated 50-year dataset, there appears to have been a major shift towards lower rainfall patterns since the 1970's, consistent with the discontinuity in rainfall trends observed around 1970 (Laraque et al., 2001; Samba et al., 2008). In the Lake Tumba region, the discontinuity apparently manifests itself after 1971. While 1971 was the wettest year on record (2423 mm), a significant, decline in precipitation is observed in the four decades since this date. The negative trend can be observed throughout all four seasons but is particularly strong during the main wet season from September to November. Furthermore, the drying appears associated with a particularly strong shift towards less rainfall events around 2000. At the same time, an increase in rainfall intensity in both the small wet season of March-May, and the summer dry season of June-August is observed. This suggests precipitation in the region is becoming more erratic, with longer dry periods interspersed by more intense rainfall events.

In addition, trends in mean annual surface air temperatures as measured at CREF Mabali on the shore of Lake Tumba are available over an updated 40-year timespan between 1979 and 2018. This dataset shows that the late 90's and early 2000's were relatively cold years, while temperatures were about a degree higher in the decade after 2005 (Figure 1.8). However, over the full 40-year timespan between 1979 and 2018 a slightly positive, but non-significant warming trend is found (Sen's slope = 0.012 °C yr^{-1}; p= 0.07). Individually, however, the months of May, July, August, September, October, and November can all be identified as having significant upwards trends (Table 1.2), ranging from 0.011 °C yr^{-1} (November) to 0.022 °C yr^{-1} (July). This is reflected in trimester trends, with both JJA and SON showing significant warming (0.015 and 0.014 °C yr^{-1}, respectively). Thus, there appears to be a slight warming trend in the

centre of the Cuvette Centrale, which is most manifested in the summer dry season and long wet season. This mirrors an irregular, but generally increasing trend that has been observed across the Republic of Congo (Samba et al., 2008), suggesting this is likely a regional trend that affects the whole central Congo Basin.
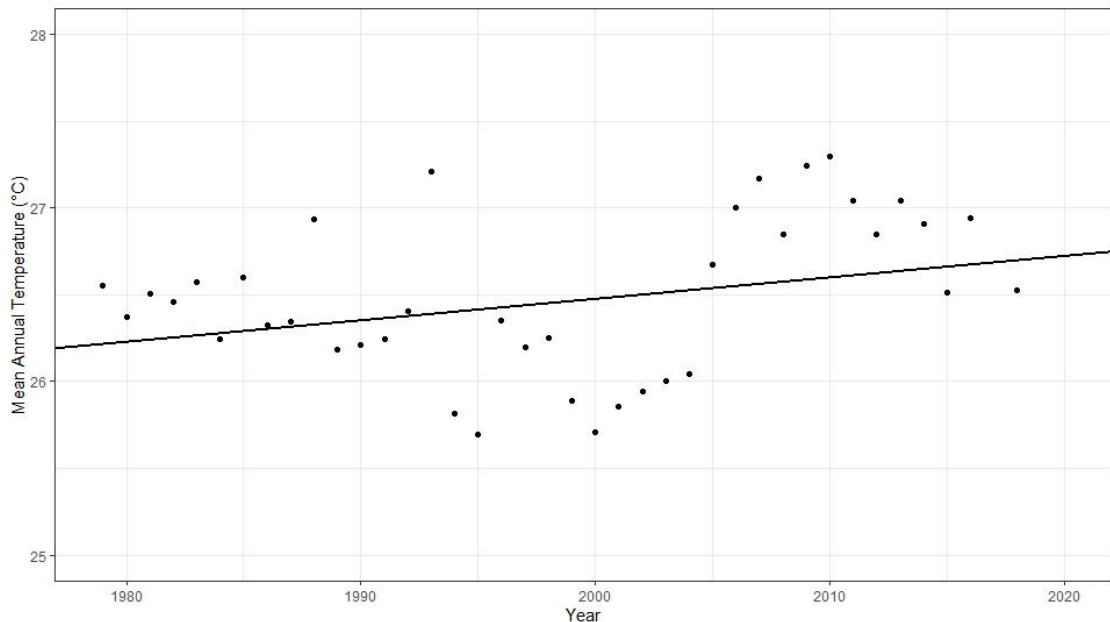
Figure 1.8. Trend in mean annual temperature at the CREF Mabali station in DRC. *The trend line indicates a slightly positive, but non-significant warming (Sen's slope = 0.012 °C yr^{-1}; p= 0.07). Trend direction and strength are estimated using Sen's non-parametric, rank-based approach (Sen, 1968). To account for the potential effect of serial autocorrelation in climate data (Wang et al., 2020), a modified Mann-Kendall test based on the Variance Correction Approach was implemented (Yue & Wang, 2004), using the mmky function in the modifiedmk package in R (version 1.6; Patakamuri, 2021).*

1.2.3.6. Threats to the central Congo Basin peatlands

The vast carbon stocks of up to 30.6 Pg C that have been identified in the Cuvette Centrale make these peatlands a central component of the global carbon cycle. At present, these peatlands are relatively intact and have not been degraded yet. However, in a recent synthesis of potential threats to the Congo basin peat carbon stocks, Dargie et al. (2019) identify climate change as a particularly pressing concern.

Although climate models for the Central African region are known to be uncertain due to a lack of ground-based data (Washington et al., 2013), it is extremely likely that the region will warm as a result of anthropogenic climate change (Dargie et al., 2019). This warming will likely result in a decrease of the carbon sink of peatlands in this region (Gallego-Sala et al., 2018). However, the extent to which a temperature rise will impact the peat's carbon is strongly determined by

the prevalence of waterlogged conditions. Climate change's biggest impact on the Congo Basin peatlands will therefore likely come from changes to rainfall patterns. It has already been shown that the start of peat accumulation and its cessation in the Cuvette Centrale coincided with the start and end of the African Humid Period across the region (Dargie et al., 2017). Potential reductions in rainfall or changes in the temporal distribution of rainfall are therefore likely to have strong negative impacts on the peat carbon stocks. This is particularly likely since the Congo Basin peatlands are relatively dry, compared with other tropical peatland regions (Malhi & Wright, 2004), and possibly close to their hydrological limits (Garcin et al., 2022). However, a true understanding of the potential impact of climate change on these ecosystems is lacking due to a major lack of knowledge about how the peatland complex has responded to climate changes in the past, what its current hydrology is like, and what the future Congo Basin rainfall regime will be (Dargie et al., 2019).

The impacts from climate climate on the Cuvette Centrale peatlands could be accelerated or exacerbated by the negative impacts of potential land-use changes (Dargie et al., 2019). Much of the Cuvette Centrale peatlands is currently protected on paper by some form of conservation designation, most notably the Ramsar Convention on Wetlands and the Brazzaville Declaration on peatlands. However, Dargie et al. (2019) and Miles et al. (2017) showed that there are still large possibilities of hydrocarbon exploration, logging, agricultural plantations and other forms of land disturbances that could significantly damage the peatland ecosystems. In general, tropical peat swamp forest that have been disturbed by drainage become a net carbon source to the atmosphere, due to oxidation of organic matter and increased loss of fluvial organic carbon (Moore et al., 2013), particularly in the first 100 years after construction of drainage ditches (Young et al., 2017). Thus, keeping the recently described Congo Basin peatlands wet is vital in the face of both land use changes and climate change (Cole et al., 2022).

Additionally, both land use and climate change pose a threat to aboveground forest vegetation and the carbon stored there-in. African rainforests are threatened by climate change because, generally, they are already close to their hydrological limits (James et al., 2013). However, a recent analysis of 100 long-term monitoring plots in African tropical forests of six countries showed that these forests remained a carbon sink during the 2015 El Niño event (Bennett et al., 2021), suggesting that the African rainforests could be more resilient than previously thought. Whether these findings hold for peat swamp forest communities as well is currently unknown.

Because of these future threats to the Cuvette Centrale peatlands, it is critical to start ensuring the conservation of these ecosystems today. Dargie et al. (2019) suggest that protective measures could be funded through a combination of climate, biodiversity and development funding. In order to ensure that these approaches are most effective, a better understanding of the ecological functioning, hydrology and history of these peatlands is critically needed, which is the focus of this thesis.

1.3 Thesis aims and objectives

As the literature review has shown, there are considerable uncertainties regarding the true extent of peatlands and the size of peat carbon stocks in the central Congo Basin. These uncertainties are associated with a limited understanding of the processes that determine peat formation and maintenance in the Cuvette Centrale, particularly related to hydrology (Alsdorf et al., 2016; Dargie et al., 2017). Peat has so far only been systematically documented in largely rain-fed, nutrient-poor swamp forests in interfluvial basins in ROC (Dargie et al., 2017; Davenport et al., 2020). However, peat is also predicted in other hydro-geomorphological settings (Dargie et al., 2017), including what appear to be river-influenced regions close to the Congo River mainstem and dendritic-patterned valley floors along some of its left-bank tributaries. These forest areas are likely seasonally inundated to depths of up to 1.5 m during the main wet season (Rosenqvist, 2009; Lee et al., 2015), suggesting seasonal river flooding and/or upland run-off as key sources of water. Whether peat accumulates under these river-influenced conditions, and how this would affect overall peatland extent and peat carbon stocks, is currently unknown. Therefore, this thesis aims to improve the ecological understanding of peat swamp forest ecosystems in the central Congo Basin by studying these river-influenced settings in the Democratic Republic of the Congo. In doing so, I intend to answer three main research questions:

- How much carbon is stored in the Cuvette Centrale peatlands?
- Where exactly is this carbon located?
- How is peat formation and maintenance affected by inundation patterns?

By investigating the spatial distribution and characteristics of swamp forests in different hydro-geomorphological settings, such as river-influenced settings in DRC, a better understanding of the ecological diversity of the central Congo Basin peatlands can be obtained. This will help us to understand why peat is found in some locations and not in others. Together with an expanded set of datapoints, this should enable much-improved mapping of the Cuvette Centrale peatlands and their carbon stocks. Furthermore, broadening our understanding of the various hydrological conditions under which peatlands exist in the central Congo Basin will help us comprehend how these ecosystems might have developed in the past, and could possibly change in the future.,

Thus, the objectives of this thesis are to (i) investigate whether peat forms in areas adjacent to rivers in the DRC, via a series of field campaigns; (ii) analyse how (river-influenced) inundation patterns affect swamp forest vegetation and peat characteristics; (iii) map the spatial

distribution of peat presence and peat thickness across the central Congo Basin; and (iv) estimate the amount of carbon that is stored in peat.

The bulk of the new data for this thesis is obtained from a series of field campaigns to the swamp forests of the Cuvette Centrale area in the DRC between January 2018 and January 2020, visiting peatlands adjacent to a series of tributaries of the Congo River. It is hoped that this new data and understanding will contribute to improved management of the peatlands, including the conservation of the vast carbon stocks and biodiversity that are present in the world's largest tropical peatland complex.

1.4 Thesis outline

The remainder of this thesis is composed of five data chapters, and a conclusions chapter.

Chapter 2: Describing the river-influenced peat swamp forests of the central Congo Basin

This data chapter describes the field sites that were visited as part of this PhD project. It provides the first field-based evidence of extensive peat presence in the Cuvette Centrale region of the DRC. This chapter shows that in addition to wide interfluvial basins that are common in the Republic of the Congo, peatlands are also found along the bottoms of smaller river valleys, predominately in the DRC, broadening our understanding of where peat forms in the central Congo Basin.

Chapter 3: Characterising peat swamp forest vegetation types in the central Congo Basin

This chapter presents an analysis of vegetation types that were identified in the DRC's peat swamp forests. I compare forest structure and compositional diversity across different peat swamp forest types, identifying a distinct vegetation type in seasonally inundated peat swamps. I combine this with vegetation types previously identified in the Republic of the Congo to derive an overview of known peat swamp vegetation types in the central Congo Basin.

Chapter 4: Understanding the hydrology, geochemistry and age of river-influenced peatlands in the DRC

This chapter aims to analyse how peat formation and maintenance is affected by inundation patterns. It contrasts the seasonally inundated peatlands in river valleys in DRC with non-river-influenced peatlands in both DRC and ROC. This analysis shows that like interfluvial basins peatlands, river-influenced peatlands in DRC are very nutrient-poor, allowing them to attain similar peat thickness despite experiencing greater water table fluctuations. This chapter also presents evidence that the river-influenced peatlands are among the oldest tropical peat deposits in the world, with peat initiation commencing ~42,000 calibrated years Before Present (Present being 1950).

Chapter 5: Mapping the peat swamp forests of the central Congo Basin

In this chapter, I develop a model of peatland distribution in the central Congo Basin by combining field data on peat-vegetation associations and remotely-sensed data, producing a 50-meter resolution map of the central Congo peatlands. For this model, I compare optical, radar and topographic datasets, finding that the addition of relative elevation as input product

significantly improves predictions of peatland distribution. With triple the ground-truth data, I find the total peatland area, at 167,600 km^2, to be 15% larger than previously estimated by Dargie et al. (2017). This chapter also presents a map of inundation frequency derived from multitemporal radar data, which is overlaid with the peatland map to locate the newly identified seasonally inundated mixed peat swamp forest type.

Chapter 6: Modelling peat thickness, carbon density and carbon stocks of the central Congo Basin

The final data chapter uses the collected *in situ* data on peat thickness to develop a new methodology, based on Random Forest regression, for mapping peat thickness and carbon stocks. This allows me to make the first ever map of peat thickness for the central Congo Basin peatlands. By combining the peat thickness map with laboratory data on peat carbon stocks, I then produce a first ever map of peat carbon density for the Cuvette Centrale peatlands. I use this map to estimate that the central Congo Basin peatlands store 29.0 Pg C in the peat, with a much-narrowed 95% confidence interval of 26.3-32.2 Pg C. Lastly, overlaying the peat carbon density map with maps of protected areas and industrial logging, mining, palm oil or hydrocarbon concessions, I compare the levels of protection of the peat carbon stocks and their threats.

Chapter 7: Conclusion

This final chapter summarizes all study results and presents the overall conclusions. I also discuss the limitations of this work and present priorities for future research directions.

Chapter 2: Describing the river-influenced peat swamp forests of the central Congo Basin

2.1 Abstract

The presence of large peatland areas has previously been predicted in the Democratic Republic of the Congo, but never assessed in the field. Therefore, peat cores were sampled, and peat thickness and vegetation characteristics were measured along seven long transects and four shorter transects in Équateur province, DRC. These transects are located across three major river systems and in one region away from rivers, totalling almost 50 kilometres in length. Peat was found along all seven long transects that were used to assess likely peatland areas predicted by Dargie et al. (2017). For the shorter transects, which were used to assess and improve mapping capabilities by targeting uncertain areas, no peat was found along two transects, while the other two transects only had very shallow peat deposits. These four shorter transects are located in seasonally inundated swamps or on the margins of larger peatland areas, showing that Dargie et al.'s (2017) predictions are generally accurate for major peat swamp forest areas near DRC's rivers, but less accurate near the peatland's margins. Field-measured peat thickness in the DRC is 3.2 ± 1.7 m (n=159, peat defined as ≥ 30 cm thickness of ≥ 65% organic matter), significantly greater than the 2.4 ± 1.6 m reported for ROC. Peat thickness increases more quickly with distance from the peatland margin in DRC than in ROC. Thus, thick peat deposits in the central Congo Basin are not confined to wide interfluvial basins, but can also be found in narrower peatlands in geomorphologically distinct river valleys systems. However, typically shallow peat deposits are found in sites experiencing large wet season inundations, closest to the major rivers or streams. This shows that peat formation is not confined to permanently waterlogged swamps with stable water tables, but also occurs in swamps that are characterized by greater water table fluctuations. These seasonally inundated peat swamps are as acidic as other peatlands, and appear at least as nutrient-poor.

2.2 Introduction

Tropical peatlands are carbon-rich ecosystems that play an important role in the global carbon cycle (Ribeiro et al., 2021). In the central depression of the Congo Basin (also known as the 'Cuvette Centrale'), the presence of peatlands has long been suspected, but was only confirmed in recent years (Dargie et al., 2017). The only field-verified peatland map available suggests that peat underlies 145,500 km^2 of swamp forests, making the central Congo peatlands the world's largest tropical peatland complex (Dargie et al., 2017). The field data used in this estimate originates from one department in the northern Republic of the Congo, yet two-thirds of the central Congo Basin peatlands are predicted to be found in neighbouring Democratic Republic of the Congo, sometimes hundreds of kilometres away from the field data used to obtain this estimate (Fig. 2.1a). Similarly, peat carbon stocks were estimated to be 30.6 Pg C based on the only field data available, but the lower confidence interval was just 6.3 Pg C (Dargie et al., 2017). Thus, it is unclear if the central Congo peatlands are truly as extensive or deep as suggested, and whether they store globally significant quantities of carbon.

Uncertainties in peat area and peat carbon stock estimates are further compounded by a limited understanding of the processes that determine peat formation in this region, particularly its hydrological functioning (Alsdorf et al., 2016; Dargie et al., 2017). In the central Congo Basin, peat has only been systematically documented in interfluvial basins in the Republic of the Congo (Dargie et al., 2017; Kiahtipes & Schefuß, 2019), where an absence of annual flood waves (Dargie et al., 2017), the presence of modest peat domes (Davenport et al., 2020), and water tables that are higher than that of nearby rivers (Lee et al., 2011) all suggest these peatlands are permanently waterlogged, largely rain-fed and independent of river water inputs.

However, peat is predicted by Dargie et al. (2017) in other hydro-geomorphological settings, including what appear to be river-influenced regions close to the main Congo River and dendritic-patterned river valleys along some of its major left-bank tributaries (Fig. 2.1a). Topographic maps show that these river valleys are characterized by larger elevation gradients than those found in the shallow interfluvial basins further west (Fig. 2.2c). This is likely to strongly influence local hydrological patterns. According to radar data, some riverine swamp forests are seasonally inundated for parts of the year (Figure 2.1c; Rosenqvist, 2009). Other radar data has shown that these inundations can reach heights of up to 1.5 m above the surface during the main wet season (Figure 2.1b; Lee et al., 2015). This points to seasonal river flooding

or upland runoff from *terra firme* forests as key sources of water into these swamp forests. Whether peat accumulates under these conditions is currently unknown.
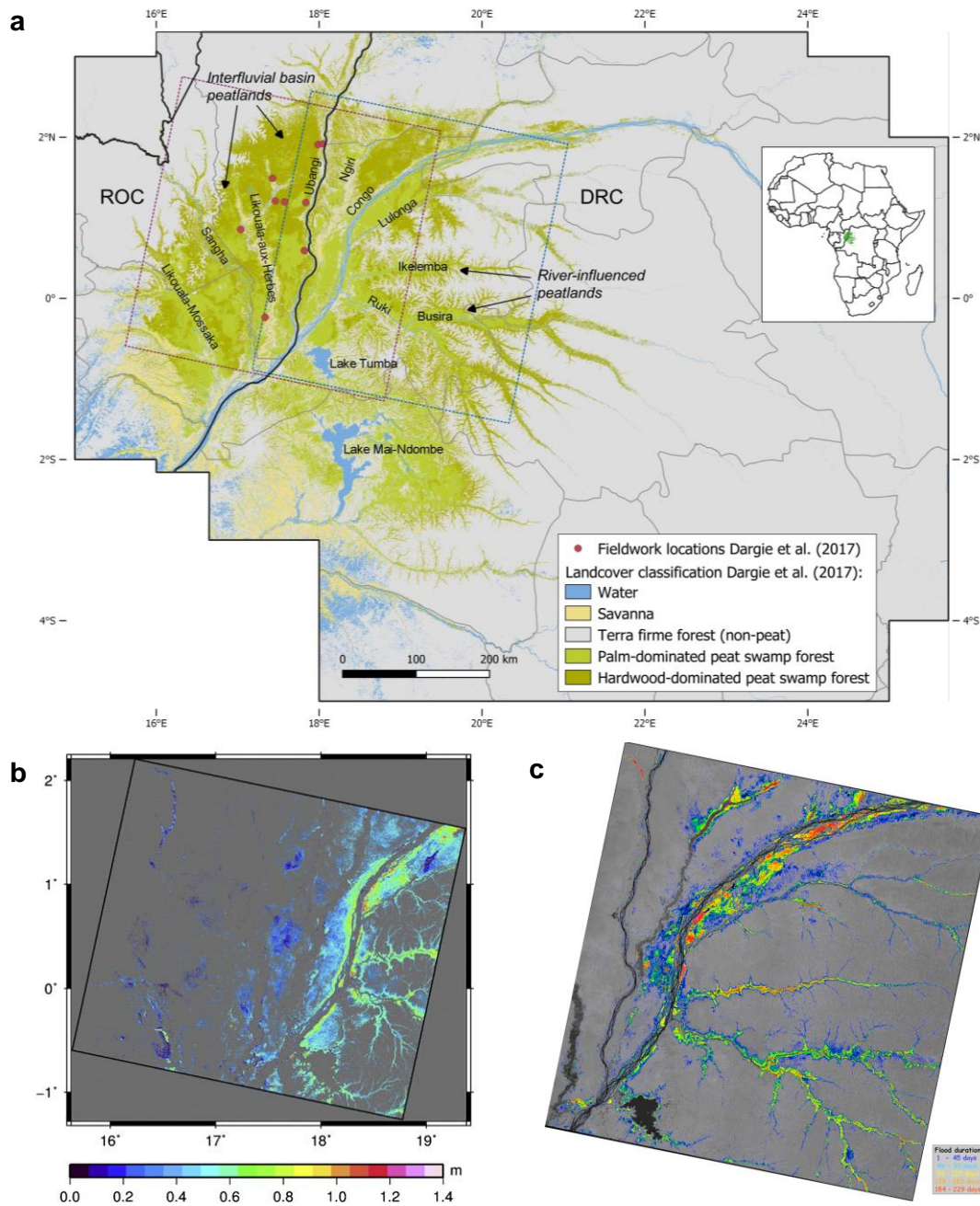
Figure 2.1. Maps of peat swamps and water tables in the central Congo Basin. a, *Map of peat swamp forest predictions (shades of green) and field site locations (red dots) by Dargie et al. (2017). Interfluvial basin peatlands are predominantly found on western side of the basin (ROC), while likely river-influenced peatlands are predominantly found on the eastern side of the basin (DRC). Names of the major rivers and lakes are shown. Black lines represent country boundaries; grey lines represent sub-national administrative boundaries.* ***b,*** *Map of inundation height (m) above the surface in December 2008, reproduced from Lee et al. (2015). © 2015 Elsevier.* ***c,*** *Map of inundation duration (number of days) between July 2007 and March 2008, reproduced from Rosenqvist (2009). Map location of* ***b*** *and* ***c*** *is indicated in* ***a*** *by the red and blue dashed rectangle, respectively.*

Little is also known about the types of vegetation that are found in these likely river-influenced swamps. The field study of peat swamp forests in the Republic of the Congo by Dargie et al. (2017) describes three different types of peatland vegetation, namely hardwood-dominated peat swamp forest, in which *Uapaca paludosa, Carapa procera* and *Xylopia rubescens* are common; peat swamp forest dominated by the *Raphia laurentii* palms; and a much rarer peat swamp forest dominated by *Raphia hookeri* palms that is found in abandoned river channels. Mapping of hardwood-dominated and the common palm-dominated (*R. laurentii)* peat swamp forests predicts that both are present in the hydro-geomorphologically distinct river-influenced wetlands of DRC (Dargie et al., 2017). However, no field verification of this prediction has so far taken place. Understanding whether similar vegetation types are found in the swamp forests of the DRC is crucial for peatland mapping efforts, as peat presence in the tropics is primarily mapped indirectly based on vegetation characteristics (Lawson et al., 2015). As forest structure and composition are likely to be different between swamps with seasonal inundations and swamps with more stable water tables (Targhetta et al., 2015), landcover predictions from Dargie et al. (2017) are potentially less accurate in river-influenced settings from which they did not include any datapoints as training data in their models. Thus, field observations of peat are necessary to assess if peat really exists under swamp forests along river valleys in the Democratic Republic of the Congo (DRC). This is particularly important given that the Dargie et al. (2017) predict that two-thirds of the peat area of the central Congo basin is in DRC.

2.3 Chapter aims

The aim of this chapter is to use field observations to test the predictions of the presence of peat swamp forests in the central Democratic Republic of the Congo, particularly in river-influenced settings. The specific objectives of this chapter are (i) to describe the rationale behind the chosen field locations (transects) that were used to test peat predictions in DRC; (ii) to describe the fieldwork methodologies used in assessing peat swamp forests, including peat thickness measurements; and (iii) to describe and compare the field locations in terms of vegetation, water table heights, pH/electrical conductivity and peat thickness characteristics as observed in the field.

2.4 Methods

2.4.1 Transect selection

The only published map of peatland distribution that is based on field data, developed by Dargie et al. (2017), was used as a guide to identify suitable field locations for peat prospecting in the Democratic Republic of the Congo. Each field site served multiple purposes, namely: (i) to test the predictions of peat presence made by Dargie et al. (2017); (ii) to assess and classify peat swamp vegetation types, developed further in Chapter 3; (iii) to test hypotheses of peat formation, development and maintenance (long transects) or to assess mapping capabilities (short transects), detailed in Table 2.1 and developed further in Chapter 4; (iv) to collect ground-truth points for further peatland distribution mapping, developed in Chapter 5; and (v) to measure peat carbon and peat thickness that will be used to model the spatial variation in peat thickness and carbon density across the Cuvette Centrale, developed in Chapter 6.

Fieldwork was conducted in the peat swamp forests of Équateur province, Democratic Republic of the Congo, across three field seasons, in January - March 2018, June - August 2019 and January 2020. All fieldwork sites were either accessed by car or boat from the provincial capital Mbandaka. An overview of the different field campaigns, including locations, field team members, and the type of data collected, is included in Appendix I.

A total of 11 transects were installed across the three field seasons, identical to Dargie et al.'s (2017) transect approach. These included seven "long" transects (4-11 km), targeted in locations highly likely to contain peat according to Dargie et al.'s (2017) map, which were used to test hypotheses about the role of vegetation, surface wetness, nutrient status, and topography in peat accumulation (detailed in Table 2.1). Additionally, four "short" transects (0.5-3 km) were installed to assess the mapping capabilities of peatland distribution models (see Chapter 5), by testing suspected false predictions of peat presence from Dargie et al.'s (2017) map, because of the geomorphological setting at higher relative elevation above the nearest river, or conflicting results from preliminary remote sensing models (detailed in Table 2.1).

All but one of the 11 new transects are located in the geomorphologically distinct river-influenced landscape of the Cuvette Centrale, east of the Congo River mainstem (Figure 2.2). This includes a group of transects (Mpeka, Bondamba, Bolengo, Ikelemba, Pombi and Boleke) that is located perpendicular to the major left-bank tributaries of the Congo River, namely the

Ruki, Busira and Ikelemba rivers. A smaller group of transects (Boloko and Tumba) is located in places not directly adjacent to one of these major tributaries, but rather in the valley bottoms of smaller dendritic channels or branches of the drainage system that dominate this eastern part of the peatland complex (Figure 2.2).
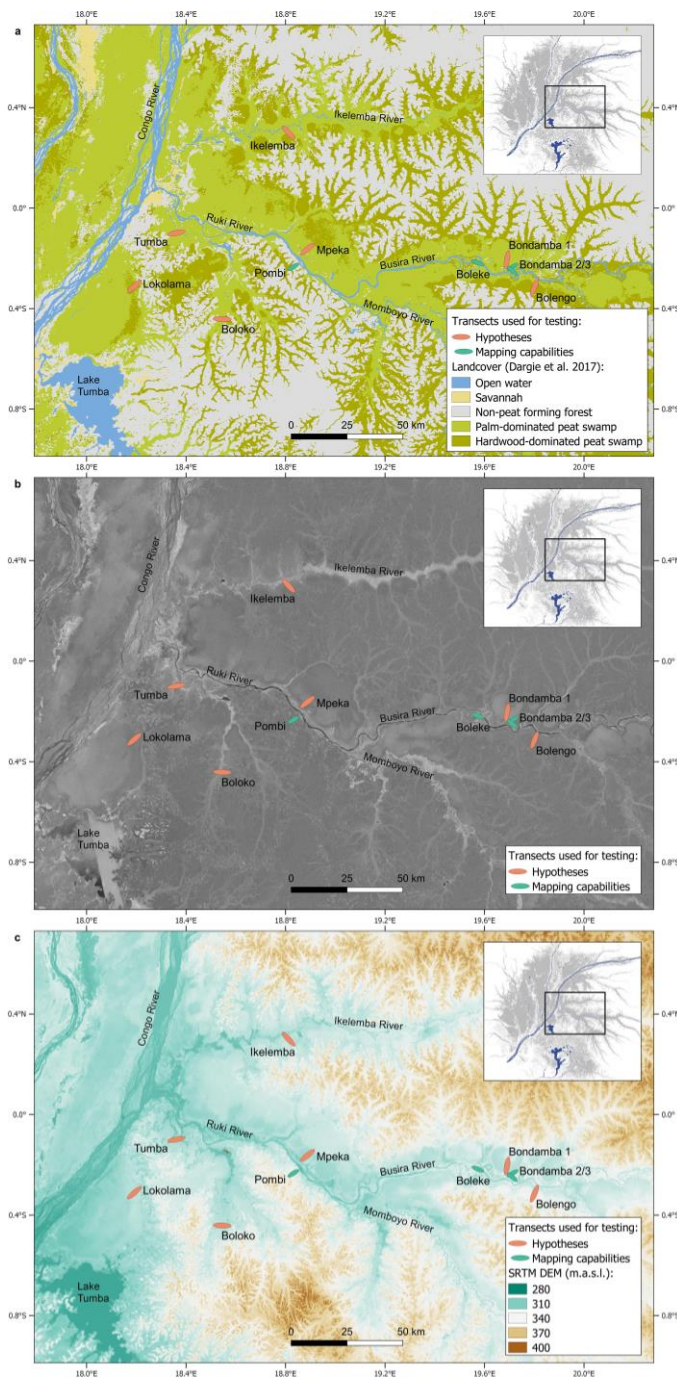
Figure 2.2. Transect locations in Équateur province, DRC. *Transects (not to scale) are indicted by red (testing hypotheses) or green (testing mapping capabilities) markers. Upper-right corner insets: image location within the wider peatland complex (grey shading) and river network (blue).* ***a****, Background image of the smoothed (7x7 majority filter) landcover map of Dargie et al. (2017).* ***b****, Background image of the HV/HH-ratio of multi-date ALOS PALSAR radar data developed by*

*Dargie et al. (2017) to differentiate between inundated (light grey) and non-inundated (dark grey) forests. **c,** Regional SRTM Digital Elevation Model (DEM; meter above sea level, m.a.s.l.).* One transect (Lokolama) is not located in a river-influenced setting, but on the edge of what appears to be a likely (shallow) peat dome, given its markedly round shape (Figure 2.2). However, it is unclear if this peatland area can be classified as an 'interfluvial basin' like shallow peat domes in ROC (Davenport et al., 2020), as it is adjacent to the Congo River mainstem on one side and *terra firme* upland, some 20 km away, on the other side. Therefore, this peatland area may be different from the interfluvial basin peatlands found previously in ROC (Dargie et al., 2017) and was additionally included in the sampling.

It was hypothesized that a general trend in peat thickness and vegetation types could be detected along the transects that run perpendicular to rivers, with shallower peat deposits found closer to the river because of more seasonal inundation patterns. The vegetation in swamps with seasonally fluctuating water tables was hypothesized to be different from swamps with stable water tables further away from the river. Furthermore, greater peat thickness was hypothesized towards the centre of suspected peat domes. The specific justifications and hypotheses/peat predictions for each of the 11 transects are presented in more detail in Table 2.1.

I selected the location of each transect by first assessing the predicted vegetation types (hardwood-dominated peat swamp forest, palm-dominated peat swamp and non-peat forming *terra firme* forest) from the landcover map previously developed by Dargie et al. (2017; Figure 2.2a). Transects used for hypothesis testing were selected in such a way that most transects have a high predicted probability of peat presence (typically > 90%), but also cross more than one vegetation type to ensure that all vegetation types are included in the sampling. Hypotheses about peat formation are further based on surface wetness indications from ALOS PALSAR radar data (multi-date HV/HH-ratio; Figure 2.2b), or SRTM topographic data (Figure 2.2c). The radar data was used to select transects in locations characterised by what appear to be concentric pattern formations (Bondamba transect) or in locations that cross smaller branches of the drainage network (Tumba and Boloko transect; Figure 2.2b). In addition, topographic data obtained from the SRTM Digital Elevation Model (DEM) was used to select transects on relatively higher elevation (> 340 m.a.s.l.), where no sampling had taken place before but which is characteristic of the south bank of the Ruki/Busira River (Bolengo and Pombi transects; Figure 2.2c). Finally, for the purpose of assessing mapping capabilities, preliminary supervised Maximum Likelihood classification models based on either SRTM DEM, SRTM HAND (Height

Above Nearest Drainage point) or SRTM DEM+HAND as elevation data (with a subset of ground-truth data; see Chapter 5) were used to select the locations of shorter transects that could help differentiate the modelling effect of these topographic products.

Transect name (code)	Transect purpose	Length (km)	Transect description	Hypothesis / Peat prediction
Mpeka (PEK)	Testing hypotheses	10.0	This transect runs perpendicular to the Ruki River towards the interior of a likely low-lying floodplain, with mostly palm swamp predicted. However, it first traverses a river levee, before entering a likely depression. Potential effects of nutrient gradient or inundation levels (river-influenced) on peat thickness could be found.	Because of the depression behind a levee, water tables are more stable here than along other transects close to the river, resulting in deeper peat deposits.
Bolengo (BNG)	Testing hypotheses	8.0	This transect crosses through seemingly higher elevation on the left-bank of the Busira River, providing crucial insight in peat formation at higher elevations. It traverses mostly hardwood swamp, perpendicular to the river, before ending in likely upland *terra firme* forest, which is predicted as peat by one of the preliminary models (see Ch. 5). The potential effect of a nutrient gradient could be detected when moving away from the river, or inundation effects from upland *terra firme* runoff.	This transect is less wet and has shallower peat than other transects, because of the higher elevation. Additionally, towards the upland *terra firme* at the end of the transect, no peat is found contrary to what is predicted by one preliminary model (Ch. 5).
Bondamba (BDM)	Testing hypotheses	7.0	Concentrating patterns are visible in optical and radar data along the right-bank of the Busira River, indicating potential peat domes (see Fig. 2.2). This transect runs from the margin to the centre of one of these potential domes, mostly traversing palm swamp forest.	Increasing peat thickness is found towards the interior of the peat dome, where water tables are more stable.
Ikelemba (IKE)	Testing hypotheses	5.0	This transect crosses the floodplain along the Ikelemba River, traversing both predicted hardwood and palm swamp forest before ending in upland *terra firme* forest. Potential effects of nutrient gradients or inundation levels (river-influenced or runoff) on peat thickness could be detected. The transect provides crucial ground verification further away along a second Congo tributary, in addition to the Ruki River.	Shallower peat deposits are found closer to the river, because of more fluctuating water tables.
Lokolama (LOK)	Testing hypotheses	5.0	This transect is on the edge of a peat basin next to the Congo River mainstem, which could potentially be domed. However, seasonal radar data indicates more inundation than in interfluvial basins in ROC (see Ch. 5), meaning it could be partly river-influenced from the west or experience more *terra firme* runoff from the east. The transect traverses first likely	Increasing peat thickness is found towards the interior of the peat dome, where water tables are more stable.

			hardwood swamp, before palm swamp forests closer towards the interior.	
Boloko (BEL)	Testing hypotheses	4.5	This transect crosses a small, dendritic river valley (Boloko River, tributary of the Ruki River), of which many are found in this part of the peatland complex. Ground verification at these locations is therefore crucial. Part of the peatland water likely originates as upland runoff from surrounding *terra firme* forest.	Even though the area is very small, peat has formed here because of the high water levels in small dendritic river valleys.
Tumba (TUM)	Testing hypotheses	4.0	This transect crosses a likely low-lying floodplain site between the Bonsole and Boloko Rivers (both tributaries of the Ruki River), with little elevation change. It traverses predicted palm swamp. This provides useful data from low-lying floodplains along smaller river channels.	No peat is found here, because the floodplain is likely seasonally inundated or experiences erosion from migrating rivers.
Pombi (POM)	Assessing mapping capabilities	3.0	This short transect is located opposite the Mpeka transect on the left-bank of the Ruki River, on higher elevation in a likely small channel of the dendritic drainage system. It crosses sites either predicted as peat or not by different models (see Ch. 5), giving a good chance to distinguish between the models.	This site is likely a false positive prediction of peat by Dargie et al. (2017), because it is at a higher relative elevation above the river.
Boleke (BLK)	Assessing mapping capabilities	2.0	This short transect is located in a floodplain on an island in a bend of the Busira River. It crosses expected savanna, *terra firme* forest and palm and hardwood swamp. Peat is predicted by some models, but not all (see Ch. 5), giving a good chance to distinguish between models.	Shallow peat is expected because of frequent inundations in this low-lying floodplain, but with potential effects of river erosion.
Bondamba 2 (BDM2)	Assessing mapping capabilities	0.5	This short transect is close to the main Bondamba peat dome, but with potential *terra firme* present. It traverses an area predicted as peat by some models, but not all (see Ch. 5), giving a good chance to distinguish between these models.	This site is likely a false positive prediction of peat by Dargie et al. (2017), because it is located at higher relative elevation above the river.
Bondamba 3 (BDM3)	Assessing mapping capabilities	0.5	This short transect is close to the main Bondamba peat dome, but with potential *terra firme* present. It runs in a different direction than BDM2. It traverses an area predicted as peat by some models, but not all (see Ch. 5), giving a good chance to distinguish between these models.	This is likely a false positive prediction of peat by Dargie et al. (2017), because it is located at higher relative elevation above the river.

Table 2.1. Description and justification of the 11 transect locations in DRC. Each transect tests a hypothesis about peat formation ('Testing hypotheses'), or the ability of preliminary classification models to accurately predict peat ('Assessing mapping capabilities'). The hypotheses or peat predictions, respectively, are listed in the last column. Expected landcover types are from Dargie et al. (2017; Figure 2.2a). Hypotheses about peat formation are further based on surface wetness indications from ALOS PALSAR radar data (Fig. 2.2b), or SRTM topographic data (Fig. 2.2c). Preliminary supervised Maximum Likelihood classification models based on either SRTM DEM, SRTM HAND (Height Above Nearest Drainage point) or SRTM DEM+HAND as elevation data (with a subset of ground-truth data) were used to select the locations of short transects that could help differentiate the modelling effect of these topographic products (see Chapter 5).

2.4.2 Field sampling

The 11 field sites identified in section 2.4.1 were visited to collect peat samples and assess peat, water and vegetation characteristics along straight transect lines. The location, direction, and length of each transect were predetermined before entering the field using QGIS software (version 3.10). In the field, navigation towards and along transects was done using a GPS (Garmin GPSMAP 64s) and compass.

Peat presence/absence was recorded every 250 m along each transects. If peat was present, peat thickness was measured using a series of metal poles inserted into the peat soil until the underlying mineral substrate was reached, identical to Dargie et al.'s (2017) pole-method. The total length of the pole from peat surface to the point on the pole where the first visible signs of mineral substrate were seen was then measured. A total of 206 peat thickness measurements was taken using the pole-method across all 11 transects.

In addition to this pole-method, for the seven hypothesis-testing transect, a core of the full peat profile was extracted every kilometre, using a 50 cm-long Russian-type peat corer (52-mm stainless steel Eijkelkamp model). Each peat core was subdivided in the field by cutting up the 50 cm core segments into 10 cm pieces using a knife and metal spatula, whilst still inside the corer, and then placing each subsample inside sealed plastic bags for transportation out of the field. These cores served to collect peat samples for laboratory analysis to assess carbon content (Chapter 6), and for calibration of the pole-method peat thickness measurements based on more accurate laboratory measurements. A total of 40 peat cores was collected every kilometre along the seven transects. Additionally, two more peat cores were collected together with a pole-method measurement, one located away from the main Lokolama transect (LOK_Extra), and one located in a seasonally inundated channel that crossed near the end of the Tumba transect at 3.93 km (TUM_3.93). As such, a total of 42 full peat cores was collected at locations where peat thickness was also measured via the pole-method, to allow a correction of pole-measured peat thickness from extracted peat cores (see section 2.4.4).

Every 250 m along each transect, at the same locations where peat presence/absence was recorded, landcover was classified as one of six classes: water, savanna, *terra firme* forest (TF), non-peat forming seasonally inundated forest (SIF), palm-dominated peat swamp forests (PS), or hardwood-dominated peat swamp forests (HS). Peat swamp forest was classified in the field

as palm-dominated, instead of hardwood-dominated, when > 50% of the canopy, estimated by eye, were identified as *Raphia* palms.

In addition to this basic classification, a more detailed description of forest structure, vegetation type and species composition was recorded every 250 m along each transect. This included a description of the most dominant canopy and understory species present, identified within a ~10 m radius by local expert botanists (Prof Corneille Ewango and Joseph Kanyama of the University of Kisangani, and Pierre Bola of ISP-Mbandaka). The height of the five trees that most dominate the canopy at the GPS location of the site was also measured using a laser hypsometer (manufacturer: Nikon, Kingston upon Thames, UK; model: Forestry Pro Laser Rangefinder). These five height measurements could then be used to estimate the average tree height at each location.

The vegetation descriptions were further complemented by vegetation plots of 20 x 40 m (800 m^2) that were installed every kilometre along the seven hypothesis-testing transects, regardless of whether peat was present or not, where all trees with a diameter of ≥ 10 cm were measured. A relatively small plot size of 800 m^2 was used for speed, to increase the overall number of plots, and because swamp forests typically have lower biomass values and tree species diversity than *terra firme* forest (Dargie, 2015; Ifo et al., 2019). They are therefore likely more homogeneous at smaller scales than a typical *terra firme* forest. These vegetation plots were used for a more detailed characterization of vegetation types, developed in Chapter 3.

Furthermore, alongside descriptions of peat and vegetation, the local hydrology and flood regime was characterized every 250 m along each transect. For this, I first measured the local water table depth with respect to the peat surface at the time of visit (in cm; positive if above the peat surface, negative if below). Care was taken to avoid measuring the water table depth directly after rainfall events. Because the field visit corresponded with the dry season (particularly the Ruki river transects were sampled at the height of the main dry season in July/August 2019), this variable was cautiously regarded as a proxy for the maximum dry season water table depth.

I also derived an estimate of the maximum inundation level at the peak of the wet season (in metres), from marks left on trees by the water, with assistance from the knowledge of local field assistants. This estimated inundation level was cautiously regarded as a proxy for the maximum

wet season inundation height. I then used both measures to calculate the estimated water table fluctuation, which is the absolute difference between maximum wet season and dry season water table levels. I also used the maximum inundation level to calculate a High-Water Fraction (HWF) for each transect, which is defined as the proportion of peat sites along each transect with estimated maximum inundations > 50 cm, out of all peat sites along that transect. A threshold of 50 cm was chosen, because sites that are very unlikely to experience seasonal river flooding (such as the Lokolama transect), were found to have relatively stable maximum inundation levels that do not exceed 50 cm.

To get an insight into the nutrient availability of the peatland sites, measurements of pH and electrical conductivity (EC; in μS/cm) were taken of the peat pore or surface water at all sites at which a full peat core was collected, every kilometre along each long transect. Measurements of pH give an indication of the presence of organic acids, which are produced during the decomposition of organic matter but are neutralised by base cations. EC measurements of peat pore or surface water are a proxy of the concentration of total dissolved solids (TDS), the sum of dissolved major ions and organic matter (Allen & Castillo, 2007; Theimer et al., 1994). Both higher EC (more TDS) and higher pH (more base cations, notably Na^+, K^+, Ca^{2+} and Mg^{2+}) are related to nutrient presence in peat surface waters, which are an important indication of the peatland's water source (Chesworth et al., 2006; Weiss et al., 2002). In particular, alkali and alkaline earth metals such as Na^+, K^+, Ca^{2+} and Mg^{2+} generally originate from the weathering of silicate and carbonate minerals, therefore their presence indicates water that has interacted with sedimentary rocks (Allen & Castillo, 2007; Berner & Berner, 2012). Acidity is also related to impediment of microbial activity (Yule et al., 2018; Yule & Gomez, 2009), thus affecting peat decomposition and accumulation rates.

To measure pH and EC, I used a portable combined pH/EC-meter (manufacturer: Hach Company, Loveland, Colorado, USA; model: Hach HQd Portable Metre) that was calibrated every day before use. However, at the Bolengo and Bondamba transects, a less accurate Hanna Combo metre was used (manufacturer: Hanna Instruments, Smithfield, Rhode Island, USA; model: Hanna HI 98129), as the Hach metre had broken. All pH/EC-measurements were taken only as long as sufficient pore water was present to permit a measurement (generally, up to depths of ~40 cm below the surface). Statistical testing of pH and EC was based on measurements taken in peat swamp forest only, excluding measurements taken in non-peat forming seasonally inundated or *terra firme* forests.

Finally, every 250 m along each transect, topography, natural disturbance levels from treefall, and human activities (logging, fire, hunting) were also recorded. The data collected from the transects is listed in Table 2.2. All field protocols are identical to or adapted from those used previously for peatland research in the central Congo Basin in the Republic of the Congo (Dargie, 2015).

Item	What was recorded
1. **General plot and peat measurement description**	- Site and plot name/code - Date - Latitude/longitude - Altitude (m.a.s.l.) - GPS model and accuracy (± m) - Total pole method peat thickness (m) - Description of base material (clay, sand, etc) - Depth of litter cover (cm)
2. **Forest type**	One option is selected for each: - Forest /Savanna/Transition - Primary/Logged/Secondary - Evergreen/Semideciduous/Deciduous
3. **General description of vegetation**	One of the following is selected: - Savanna - Non-peat forming seasonally inundated forest - *Terra firme* forest - Hardwood-dominated peat swamp forest - Palm-dominated peat swamp forest Plus: dense or open forest structure? Lianas present? Percentage canopy cover?
4. **Species composition**	Which species dominate? What are common species in canopy and understory?
5. **Tree height measurements**	Tree height (m) of 5 most dominant trees is recorded.
6. **Vegetation Photo No.**	Four photos are taken in all four parallel and perpendicular directions along the transect.
7. **Microtopography**	Whether the terrain is flat or undulating. If undulating, an estimate is made by eye of size and frequency of undulations (i.e., hummocks > 1 m, hummocks < 1m)
8. **Inundation regime**	One of the following is selected: - Rarely inundated / *Terra firme* - Seasonally inundated - Seasonally inundated, but only in major wet season (Sept. to Dec.) - Permanently inundated (swamp)
9. **Hydrology**	Estimated maximum inundation level (m) in the wet season is recorded from marks on trees or based on local knowledge of field assistants. If there is surface water, descriptions are made (some rare pools, or hollows regularly filled with water, etc)
10. **Water table depth**	Water table level (cm) above (+) or below (-) peat surface is recorded.
11. **Pore/surface water measurements (every km of long transects only)**	The following is recorded: - Pore/surface water pH - Pore/surface water temperature (°C) - Pore/surface water electrical conductivity ($\mu S\ cm^{-1}$)

12. Disturbance: Human	A record was made of whether there were signs of: -Hunting -Non-timber forest product harvesting -Trails (footpaths) -Trees < 10cm DBH cut -Trees > 10 cm DBH cut
13. Disturbance: Fire	One of the following was selected: -None -Surface -Surface and trees
14. Disturbance: Tree Fall	One of the following was selected: -None -Minor (tree < 40 cm DBH), plus location recorded -Major (tree > 40 cm DBH), plus location recorded

Table 2.2. Overview of field data recorded every 250 m along each transect. *All field protocols are identical to or adapted from those used previously for peatland research in the central Congo Basin in the Republic of the Congo (Dargie, 2015).*

2.4.3 Laboratory analysis

Throughout this thesis, peat is defined as having an organic matter (OM) content of ≥ 65% and a thickness of ≥ 30 cm, in line with previous definitions of tropical peat by Page et al. (2011) and Dargie et al. (2017). Except for occasional minor mineral intrusions (< 65% OM) into the main peat columns, collected soil samples that did not fit this definition were excluded from further analyses.

The definition implies that the OM content of peat needs to be measured in order to accurately assess peat thickness. For this, the organic matter content of each 0.1-m thick peat sample of each peat core was estimated via Loss-On-Ignition (LOI) analysis at the School of Geography laboratory at the University of Leeds. Subsamples of approximately 0.5-1 g of wet peat were dried for 24 hours in an oven at 105°C, after first thoroughly mixing the entire sample inside its plastic bag to ensure sample homogeneity. The dry mass of each subsample was then weighed after cooling off to room temperature in a desiccator. The subsample was then heated for 4 hours in a furnace at 550°C, whilst placed inside a ceramic crucible. It was then weighed again after cooling off to room temperature in a desiccator. Because organic matter is oxidised to carbon dioxide and ash at 500–550°C (Heiri et al., 2001), the mass fraction lost after heating was used as an estimate of total OM content (% of dry mass), using the following equation:

$$OM = \left(\frac{(m_{105} - m_{550})}{m_{105}}\right) * 100 \qquad \text{[Eq. 2.1]}$$

Here, m_{105} is the dry mass remaining after heating to 105°C, and m_{550} is the dry mass remaining after heating to 550°C. This approach is in line with similar measurements by Dargie et al. (2017)

and follows the recommendation of Heiri et al. (2001). If OM content dropped below the 65% threshold but would later increase again to over 65% at greater depths, this was interpreted as indicating a mineral intrusion into the peat layer, rather than the base of the peat layer. Total peat thickness was recorded as the depth in the profile at which OM content dropped below 65% and did not reach this threshold again.

2.4.4 Peat thickness measurements

All peat cores collected every kilometre that had ≥ 30 cm of peat based on the LOI measurements were included in the analyses of peat thickness (n=41, one site had < 30 cm with OM ≥ 65%). For all sites every 250 m without a peat core, only pole-method thickness measurements were available. Dargie (2015) and Dargie et al. (2017) have noted how the pole method significantly overestimates peat thickness in the peat swamp forests of ROC. This was also found to be the case at the locations sampled in DRC, particularly if the underlying mineral substrate consisted of soft, riverine alluvium.

I therefore fitted a linear regression between all paired LOI-verified and pole-method peat thickness measurements sampled at the same locations in DRC. Of the 41 sites with LOI-verified peat thickness ≥ 30 cm, one site along the Mpeka transect (PEK_10.0) was excluded as influential outlier because it was found to have a Cook's distance > 4 times the mean Cook's distance. Cook's distance is a measure of how influential an outlier is in affecting a regression equation, by measuring the change in the regression coefficients that would occur if that datapoint were to be omitted from the regression (Stevens, 1984). The remaining 40 pairs of LOI and pole-method thickness measurements were used to fit a simple linear regression model (R^2 = 0.94, p<0.001; Figure 2.3). This model was then used to correct all pole-method thickness measurements in DRC for which no LOI-verified measurement was available (n=164), comparable to the method used by Dargie (2015) and Dargie et al. (2017) in ROC.

For this, the following equation was used:

$$T_{corr} = 0.8741 * T_{pole} - 0.554 \qquad \text{[Eq. 2.2]}$$

Here, T_{corr} is the corrected peat thickness (m) and T_{pole} is the pole-measured peat thickness (m).
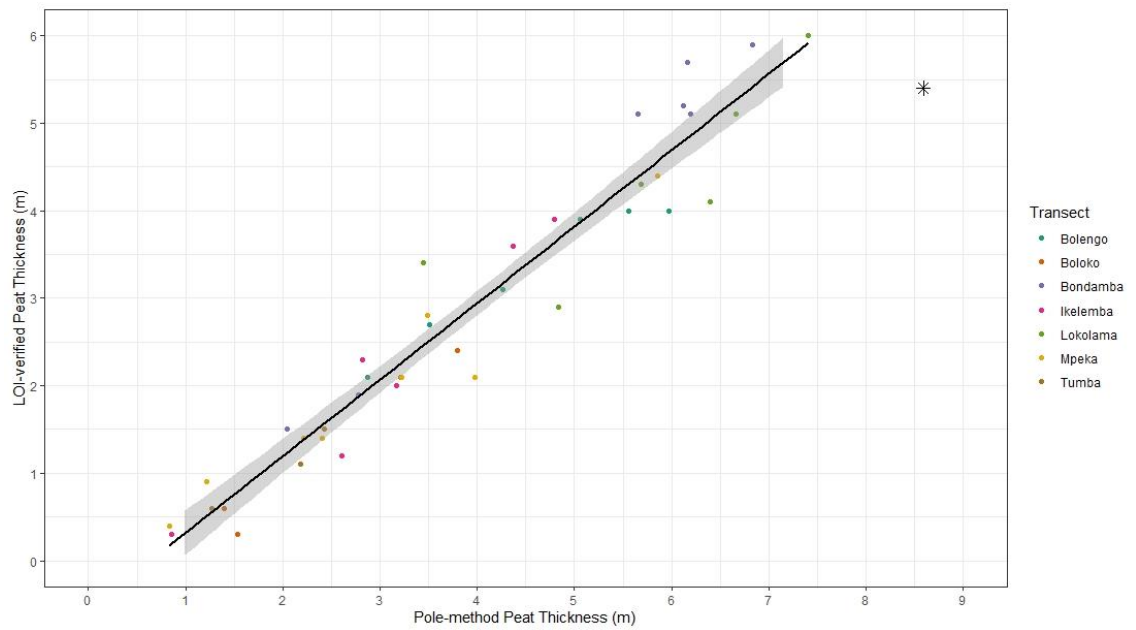
Figure 2.3. Linear regression model to correct pole-method peat thickness measurements in river-influenced peat swamps in DRC. *The plot shows the relationship between peat thickness (m) estimated using the pole-method and laboratory-verified peat thickness (m) using Loss-On-Ignition (LOI) for all hypothesis-testing transects. Datapoints are coloured by transect. Best-fitting line: Corrected peat thickness = 0.8741 x (pole-method thickness) – 0.554; n=40, R^2 = 0.94; p<0.001. Shaded grey shows the 95% confidence interval. One outlier (PEK_10.0, indicated by the star) with > 4x the mean Cook's distance (pole-method: 8.6 m, LOI-verified: 5.4 m) is excluded from the regression model.*

2.5 Results

2.5.1 Transect descriptions

Peat was found along all seven hypothesis-testing transects that were predicted to be peatland by Dargie et al. (2017). All seven transects had a high (81% to 97%, mean 89%) percentage of sites correctly predicted as peat swamp or not by Dargie et al. (2017) (Table 2.3). Along these seven transects, mean peat thickness was 3.2 ± 1.7 m (n=159, with thickness ≥ 30 cm). A maximum thickness of 7.0 m was found at 6.5 km along the Bondamba transect. In general, it was observed that peat thickness increases with distance along the transect, and that a thickness of 5-7 m can be reached within several kilometres of the start of a transect in *terra firme* forest.

Transect name (code)	Transect purpose	Length (km)	Proportion (%) correctly predicted by Dargie et al. (2017)
Mpeka (PEK)	Testing hypotheses	10.0	80.5
Bolengo (BNG)	Testing hypotheses	8.0	97.0
Bondamba (BDM)	Testing hypotheses	7.0	86.2
Ikelemba (IKE)	Testing hypotheses	5.0	95.2
Lokolama (LOK)	Testing hypotheses	5.0	91.3
Boloko (BEL)	Testing hypotheses	4.5	86.7
Tumba (TUM)	Testing hypotheses	4.0	83.3
Pombi (POM)	Assessing mapping capabilities	3.0	46.2
Boleke (BLK)	Assessing mapping capabilities	2.0	22.2
Bondamba 2 (BDM2)	Assessing mapping capabilities	0.5	33.3
Bondamba 3 (BDM3)	Assessing mapping capabilities	0.5	33.3

Table 2.3. Proportion of correctly predicted peat sites by Dargie et al. (2017). *Each proportion reflects the correctly predicted number of sites (peat/non-peat) per transect. Peat is defined as ≥ 30 cm of soil with ≥ 65% organic matter content. Thickness measurements used to identify peat include both LOI-verified and corrected pole-method measurements.*

Along the four transects used to investigate areas with a low-probability of peat, and to test possible false positive predictions by Dargie et al. (2017), peat was found only at the two Bondamba transects (BDM2 and BDM3). Both contained at least one location where peat was found (BDM2_0.25 and BDM3_0.50), albeit in the form of shallow deposits (~1-1.5 m). No peat was found along the Pombi transect, likely due to its well-drained, higher elevation location. No peat was found along the Boleke transect either, contrary to what was predicted (Table 2.3). This lack of peat formation is probably due to the fact that this site is seasonally inundated by river water, but also likely well-drained in the dry season. Furthermore, as it is located on an

island in the Busira River, it is unlikely to receive any upland runoff, which could make it less likely to form peat than other seasonally inundated sites located on riverbanks. No direct signs of erosion were seen along this transect. At all other locations along the shorter map-testing transects, non-peat forming seasonally inundated forest was found, in contrast to what was sometimes predicted by Dargie et al. (2017).

Regarding the seven hypothesis-testing transects, some are largely dominated by either hardwood (Ikelemba, Boloko) or palm peat swamp forest (Bondamba) alone, while other transects are characterised by a mixture of the two. Hardwood swamp, of which an example is shown in Figure 2.4, was found at least once along each transect. Palm swamp, of which an example is shown in Figure 2.5, was generally found at least once along each transect as well, except for the Boloko transect, which is fully dominated by hardwood swamp. Each of the seven hypothesis-testing transects is discussed in more detail below. A list of all species names that are mentioned, including author names, is provided in Appendix II.

Figure 2.4. Example of hardwood-dominated peat swamp forest. Hardwood swamp generally has a dense understory with numerous juveniles, while many trees are supported by buttress or stilt roots (such as Uapaca corbisieri *in this photo taken near the end of the Ikelemba transect). Photo taken by the author.*

Figure 2.5. Example of palm-dominated peat swamp forest. *Palm swamp is typically dominated by large* Raphia laurentii *palms, which can attain heights of up to 15 m (such as in this photo taken along the Mpeka transect). The understory is generally sparse, characterized by smaller* Raphia sese*,* Sclerosperma mannii *or* Pandanus candelabrum*, with few to no hardwood trees present. Photo taken by the author.*

Mpeka transect (PEK)

Figure 2.6. Mpeka transect overview, *showing from top to bottom: mean* in situ *tree height (m), field-estimated maximum inundation (m), dry season water table depth (cm), peat pore/surface water pH and electrical conductivity (µS cm^{-1}), SRTM digital elevation (m.a.s.l.) and estimated peat thickness (m; incl. LOI-verified and corrected pole-method measurements). Colours indicate field-identified vegetation types (on top in bold), with the tree most abundant species listed every full kilometre. All y-axes are similar across transect figures (Figs. 2.6-2.12), except for the pore/surface water EC and SRTM elevation scales. Note that the x-axis (distance along transect) differs per transect (Figs. 2.6-2.12).*

The Mpeka transect (Figure 2.6), located on the north bank of the Ruki River, was chosen to run perpendicular to the river towards the interior of what appeared to be a large floodplain. The transect starts in seasonally inundated forest that does not form peat, and then traverses a levee covered in *terra firme* forest (characterized by *Guibourtia demeusei* and a dense understory of rattan species). This is followed by a small depression covered by hardwood- and palm-dominated forest with shallow peat deposits. The transect then traverses a non-peat forming seasonally inundated forest that is located on a second elevated ridge (characterized by

Guibourtia demeusei, *Oubanguia africana* and an understory of rattan species) at 1.0 km along the transect. The actual peat swamp then starts from 1.25 km along the transect, with shallow peat deposits of generally between 1 and 3 m. This section is mostly characterised by *Raphia laurentii*-dominated palm swamp vegetation, although between 2.25 and 2.75 km, a short and mixed hardwood swamp forest is found, characterized by an understory of *Raphia sese*, *Sclerosperma mannii* and many rattan species. Between 3.0 and 8.0 km, the palm swamp forest dominated by *Raphia laurentii* returns, with peat thickness gradually increasing further along the transect. After 9.0 km, this changes permanently into a hardwood-dominated swamp forest, characterized by *Carapa palustris, Uapaca corbisieri* and *Entandrophragma palustre*. This shift largely coincides with higher elevations, greater tree height and greater peat thickness (up to 6.6 m at 9.75 km). This segment of the transect is also where the largest tree height of all transects is observed (31.3 m at 9.50 km).

The mineral layer below the peat deposits is initially characterized by light grey clay with a slight grit. Between 4.0 and 8.25 km, occasionally more silt or sandy deposits are detected. From 8.5 km onward, very soft, dark grey clay is found, likely riverine alluvium, coinciding with greater peat thickness.

The estimated maximum inundation was found to reach ~1 m above the peat surface between 2 and 4 km away from the river, but gradually diminishes after 4.5 km until the water table reaches no more than just above the peat surface from 7.0 km onwards. Thus, the deepest peat is found furthest away from the river, overlain with hardwood swamp forest, where the soil is permanently waterlogged but experiences no (seasonal) inundation.

Peat pore water pH shows consistent acidic conditions (ranging between 2.8 and 3.5), but no clear trend with distance along the transect. However, electrical conductivity almost doubles between 2.0 and 5.0 km (from 96 to 177 $\mu S\ cm^{-1}$), after which it stays above 120 $\mu S\ cm^{-1}$ throughout the transect.

Apart from a few trails and signs of fishing activities, no major human disturbances were observed along the Mpeka transect.

Bondamba transect (BDM)

Figure 2.7. Bondamba transect overview, *showing from top to bottom: mean* in situ *tree height (m), field-estimated maximum inundation (m), dry season water table depth (cm), peat pore/surface water pH and electrical conductivity (µS cm^{-1}), SRTM digital elevation (m.a.s.l.) and estimated peat thickness (m; incl. LOI-verified and corrected pole-method measurements). Colours indicate field-identified vegetation types (on top in bold), with the tree most abundant species listed every full kilometre. All y-axes are similar across transect figures (Figs. 2.6-2.12), except for the pore/surface water EC and SRTM elevation scales. Note that the x-axis (distance along transect) differs per transect (Figs. 2.6-2.12).*

The Bondamba transect (Figure 2.7) is located further upriver from Mpeka, on the north bank of the Busira River. It was chosen to run from the margin to the centre of a potential peat dome that displays concentric patterning formation in radar images (Figure 2.2b). The transect does not start directly at the river's edge, but close to a small side channel that is located about 1.5 km from the actual river, at the margin of the suspected dome. The transect firstly traverses a short patch of very tall, but open seasonally inundated forest (characterized by *Oubanguia africana* and little understory). Here, the estimated maximum inundation reaches close to 2 m above the peat surface.

After a brief (transitioning) hardwood swamp forest (with *Guibourtia demeusei* and *Oubanguia africana*), the transect enters a monodominant *Raphia laurentii* swamp forest of very low stature and limited inundation levels, which extends for six kilometres. This palm forest is often characterized by small chandelier-like screw palms (*Pandanus candelabrum*) that dominate in the understory. It is truly monodominant, with sometimes not a single hardwood tree species present inside the 20x40 m vegetation plots, at 2 and 4 km. From 3.0 km onwards, maximum inundation levels remain at (or close to) the peat surface. However, during the field visit at the height of the dry season in August 2019, water tables were consistently 20-40 cm below the peat surface.

Peat thickness is considerable along the Bondamba transect, increasing with distance from the margin up to 7.0 m at 6.5 km along the transect. This is the deepest field-measured peat deposit found in the entire Cuvette Centrale peatland complex. After 7.0 km, the *Raphia*-dominated vegetation slowly changes to a mixed, hardwood swamp forest at slightly higher elevation, which appears to be the centre of what is potentially a modest peat dome.

The mineral layer below the peat is initially characterized by soft grey clay. Between 1.5 and 2.0 km, however, find sand is found, after which it becomes clay again. Between 3.0 and 7.0 km, alternations of sand and clay are observed more often, which coincides with greater peat deposits.

Peat pore water pH is relatively high (4.0) in the seasonally inundated forest at the start of the transect, while EC is relatively low (90 μS cm^{-1}). However, throughout the *Raphia*-dominated forest, pH values are more acidic (ranging between 2.7 and 3.3), while EC values are higher (ranging between 125 and 150 μS cm^{-1}). No further trend with distance along the transect is observed.

The Bondamba transect crosses several hunting trails and fishing nets, but no major human disturbances are observed.

Bolengo transect (BNG)

Figure 2.8. Bolengo transect overview, *showing from top to bottom: mean* in situ *tree height (m), field-estimated maximum inundation (m), dry season water table depth (cm), peat pore/surface water pH and electrical conductivity (μS cm⁻¹), SRTM digital elevation (m.a.s.l.) and estimated peat thickness (m; incl. LOI-verified and corrected pole-method measurements). Colours indicate field-identified vegetation types (on top in bold), with the tree most abundant species listed every full kilometre. All y-axes are similar across transect figures (Figs. 2.6-2.12), except for the pore/surface water EC and SRTM elevation scales. Note that the x-axis (distance along transect) differs per transect (Figs. 2.6-2.12).*

The Bolengo transect (Figure 2.8) is located close to Bondamba, but on considerably higher elevation on the southern bank of the Busira River, which was mostly predicted to be hardwood swamp. It was additionally chosen because different machine learning models (see Chapter 5) provided divergent predictions of peat presence towards the end of the transect.

At the start, the transect was found to briefly traverse a modest levee covered in seasonally inundated forest (*Albizia glaberrima, Oubanguia africana, Cynometra simplicifolia*), where no peat was formed. It then enters a peat swamp forest that is largely dominated by hardwood vegetation, with some *Raphia laurentii*-dominated vegetation between 1 and 2 km along the

transect. The hardwood swamp extends until 6.5 km along the transect. Common tree species here are *Cryptosepalum congolanum, Entrandrophragma palustre, Carapa palustris, Coelocaryon botryoides, Uapaca corbisieri, Daniellia pynaertii* and *Cleistanthus* spp. However, between 1 and 2 km along the transect, some *Raphia laurentii*-dominated vegetation can be found. Peat thickness increases with distance along the transect, reaching 4 m or more from 2.75 km onwards (maximum 5.2 m at 4.75 km).

The estimated maximum inundation is almost 2 m in the seasonally inundated forest at the start of the transect, close to the river, but rapidly decreases to below 1 m in the 1st km of the transect. After this, maximum inundation levels remain consistently close to or just above the peat surface. Contrary to the dry Bondamba transect, water table depths were also close to the peat surface at the height of the dry season in August 2019.

These changing inundation patterns correspond with a gradual shift towards higher elevation as the transect approaches *terra firme* upland, which is reached after 6.5 km. From here, the transect traverses 1.5 km of *terra firme* forest without peat formation and year-round dry soils. This upland area is characterized by *terra firme* forest (*Uapaca guineensis, Staudtia kamerunensis, Donella pruniformis*, with thick understories of *Hypselodelphys scandens*). At 7.0 km, a recent manioc field is also found, as well as patches of secondary forest dominated by *Musanga cecropioides*. The transect then again descends into a small depression at 8.0 km from the start, where shallow peat deposits of 1.0 m are found, overlain by hardwood swamp forest (*Daniellia pynaertii, Symphonia globulifera*).

The mineral layer underneath the peat is initially characterised by very soft brown clay. After 2.0 km, this becomes light-grey clay with more grit, which turns completely to sand at 4.0 km. However, between 4.5 and 6.5 km, very soft grey clay is found again, coinciding with the thickest peat deposits. After the *terra firme* forest, the peat swamp at 8 km is again overlying a sandy mineral layer.

Peat pore water pH and EC both show gradual increases along the transect. pH increases from 2.6 to 3.7 between 1.0 and 6.0 km, while EC increases from 118 to 165 µS cm^{-1} between 1.0 and 5.0 km, before dropping again to 129 µS cm^{-1} at 6.0 km. The less acidic conditions further along the transect, together with more dissolved solids, could indicate increased presence of nutrients and minerals when moving away from the river towards *terra firme* upland.

The Bolengo transect is characterized by large human influences, with many signs of hunting, fishing and trapping present in the peat swamp forest, as well as signs of larvae and honey collection. Several trails are present that connect the riverbank with upland agricultural fields. The *terra firme* forest between 6.5 and 8.0 km is furthermore characterized by many recent and older forest clearings, burned areas, shifting manioc fields, and regrowth of secondary *Musanga cecropioides*.

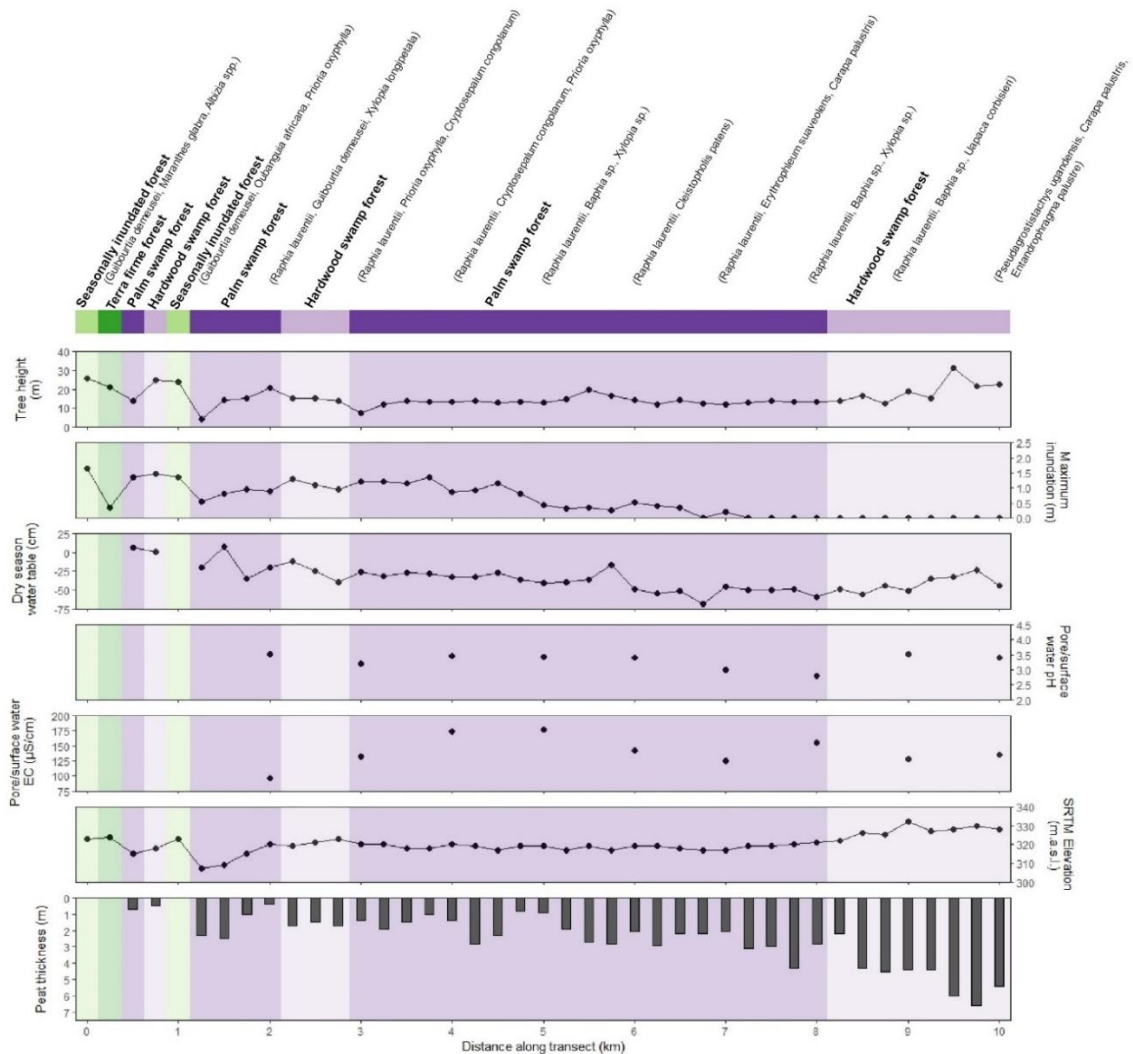***Figure 2.9. Ikelemba transect overview,*** *showing from top to bottom: mean* in situ *tree height (m), field-estimated maximum inundation (m), dry season water table depth (cm), peat pore/surface water pH and electrical conductivity (µS cm^{-1}), SRTM digital elevation (m.a.s.l.) and estimated peat thickness (m; incl. LOI-verified and corrected pole-method measurements). Colours indicate field-identified vegetation types (on top in bold), with the tree most abundant species listed every full kilometre. All y-axes are similar across transect figures (Figs. 2.6-2.12), except for the pore/surface water EC and SRTM elevation scales. Note that the x-axis (distance along transect) differs per transect (Figs. 2.6-2.12).*

The Ikelemba transect (Figure 2.9) is located in what appeared to be a floodplain area south of the Ikelemba River, a second major tributary of the Congo River. Like the Bolengo transect, it runs perpendicular to the river towards *terra firme* upland. Just before the start of the transect, at the riverbank, a small river levee was found that houses a fisherman's camp. The transect was started just after this levee, in a relatively open, seasonally inundation forest characterized by a canopy of tall *Oubanguia africana* and *Guibourtia demeusei*, with juvenile *Raphia sese* and *Palisota mannii* dominating the understory. Even though this start of the transect is in seasonally inundated forest, a shallow peat deposit of 0.3 m could be found here. However, the transect

was not inundated during a first field visit in March 2018, with water tables ~20-30 cm below the peat surface. The estimated maximum inundation during the wet season is ~1.5 m, which was confirmed during a second visit at the end of the wet season in January 2020, when the forest was entirely flooded. This seasonally inundated forest extents for two km along the transect, after which the maximum inundation level remains close to or at the peat surface. This shift coincides with a small increase in elevation towards higher *terra firme* uplands. Peat thickness gradually increases with distance along the transect, reaching a first maximum of 4.0 m at the end of the inundated area after 2.25 km. It then becomes shallower again, before reaching a second maximum of 4.6 m just before the end of the transect after 4.75 km. The mineral layer underneath the peat starts off as largely white or grey sand and silt, indicating riverine deposits. However, towards the end of the transect, from 3.75 km onward, this becomes softer grey clay, coinciding with mostly thicker peat deposits.

Vegetation along the Ikelemba transect is almost entirely characterized by hardwood swamp or open, seasonally inundated forest. The shift from peat-forming, seasonally inundated forest to hardwood-dominated peat swamp forest is marked by a brief dominance of *Raphia laurentii* palms at 2.0 km. After this, the hardwood peat swamp forest extents until 5.0 km, characterized by *Coelocaryon botryoides*, *Uapaca guineensis, Symphonia globulifera*, and *Entrandrophragma palustre*.

Peat pore water pH values are slightly higher along the first two kilometres of the transect (3.4 and 3.3), after which they drop to between 3.1 and 3.2. Pore water EC, however, shows an opposite trend, with increasing EC further along the transect. During the first two kilometres, EC is relatively low at 123 and 136 μS cm^{-1}. This changes considerably after two km, with values ranging between 188 and 205 μS cm^{-1} for the remainder of the transect. Like at Bolengo, greater EC could indicate the presence of more nutrients and minerals when moving away from the river towards *terra firme* upland. However, this is not reflected by the slightly opposite trend in pH.

Considerable human impact on the forest was observed along the Ikelemba transect. In particular, the hardwood tree species *Daniella pynaertii* is selectively logged for timber during the dry season. As this tree species is relatively lightweight, it is then floated out towards the river during the wet season, for transport towards Mbandaka. In addition, many fishing nets were observed. Hunting is also practiced along this transect, as indicated by hunting trails and the occasional sounds of gunshots.
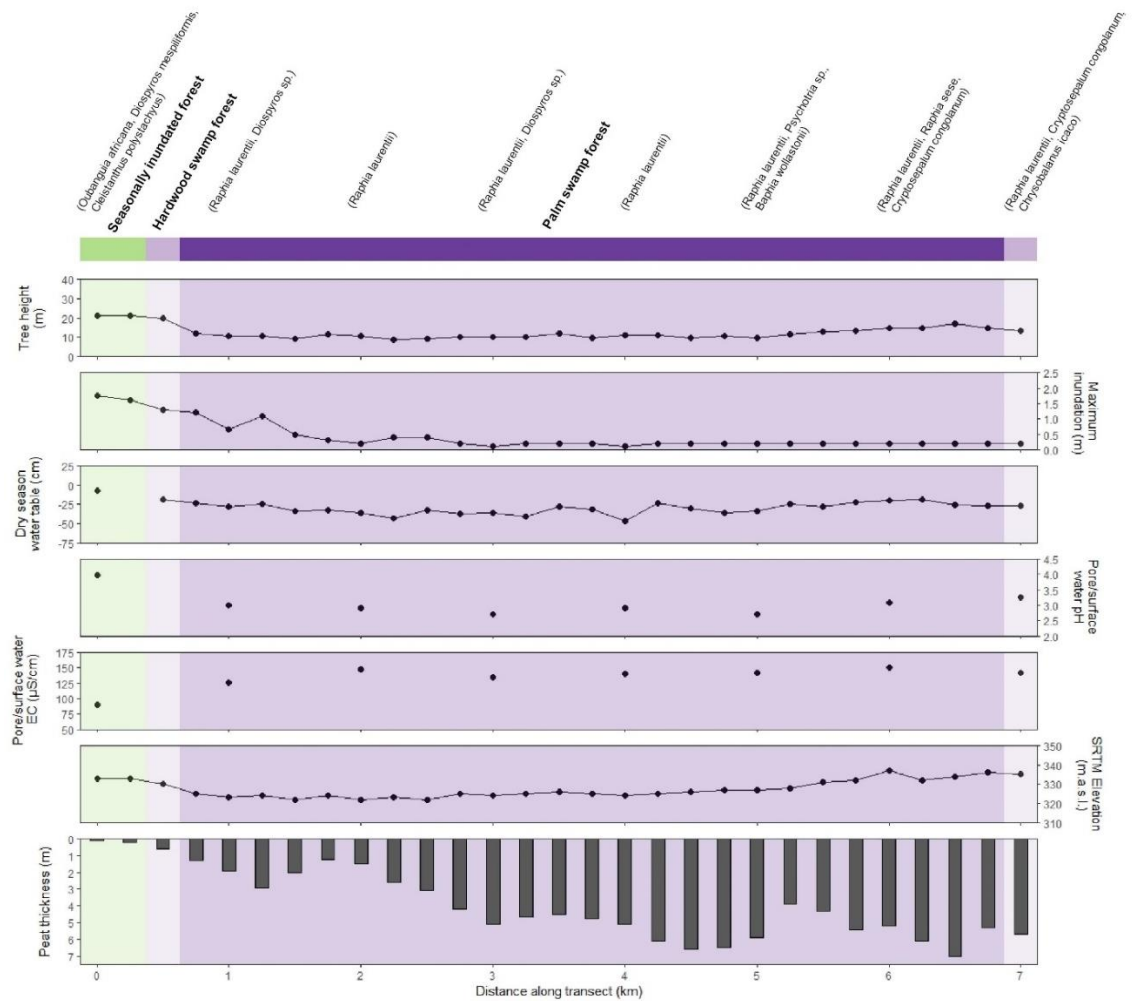
Boloko transect (BEL)
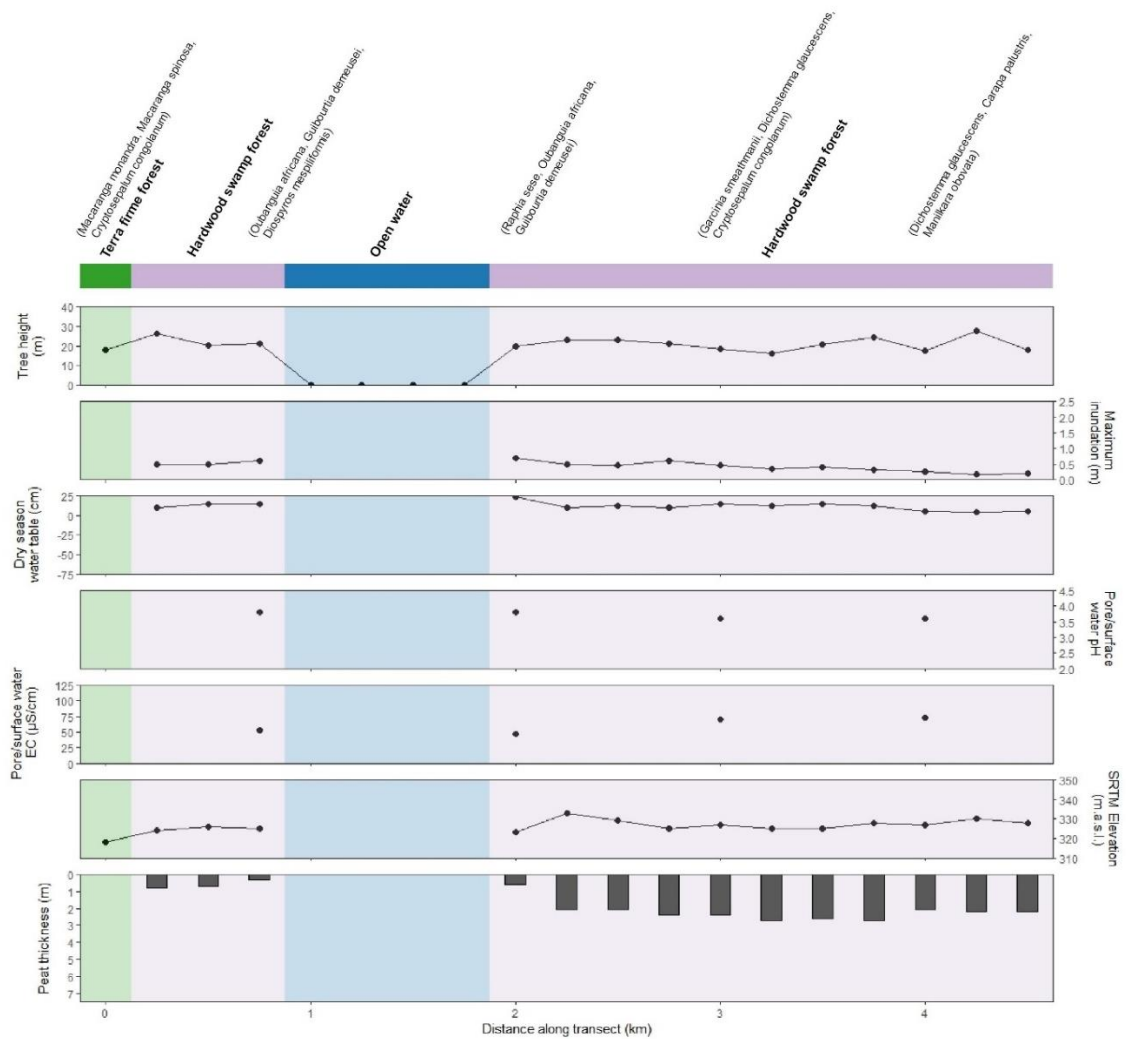
***Figure 2.10. Boloko transect overview**, showing from top to bottom: mean* in situ *tree height (m), field-estimated maximum inundation (m), dry season water table depth (cm), peat pore/surface water pH and electrical conductivity (μS cm⁻¹), SRTM digital elevation (m.a.s.l.) and estimated peat thickness (m; incl. LOI-verified and corrected pole-method measurements). Colours indicate field-identified vegetation types (on top in bold), with the tree most abundant species listed every full kilometre. All y-axes are similar across transect figures (Figs. 2.6-2.12), except for the pore/surface water EC and SRTM elevation scales. Note that the x-axis (distance along transect) differs per transect (Figs. 2.6-2.12).*

The Boloko transect (Figure 2.10) crosses the Boloko River, a side-channel of the Ruki River. It was chosen to assess peat formation in the smaller, dendritic valley bottoms of the drainage system. The transect starts on *terra firme*, in what is part primary and part secondary forest (characterized by *Macaranga* spp. and *Cryptosepalum congolanum*). It then enters a hardwood peat swamp forest with shallow peat deposits < 1 m thick. Here, vegetation is characterized by *Oubanguia africana, Guibourtia demeusei* and *Diospyros mespiliformis*. This part of the forest is likely inundated year-round, because of its proximity to the river, although maximum inundation levels reach only 0.6 m. After 0.75 km, the swamp gives way to the Boloko River itself, which

extends for a kilometre m along the transect. Inundated swamp vegetation can be found along some parts of this river segment, but no measurements were possible due to the high water levels.

At 2.0 km from the start of the transect, traversable hardwood peat swamp forest is encountered again, which extends for a further 2.5 km. This swamp forest is first characterized by species commonly found in seasonally inundated locations, such as *Raphia sese*, *Oubanguia africana* and *Guibourtia demeusei*. Further away from the river, the swamp forest is characterized by *Garcinia smeathmannii, Cryptosepalum congolanum, Symphonia globulifera, Carapa palustris, Manilkara obovata, Dichostemma glaucescens* and *Coelocaryon botryoides*. Again, inundation is likely year-round but of limited height, reaching a maximum of ~0.5 m. This gradually diminishes when moving away from the river. Peat thickness remains relatively low throughout the transect, with a maximum of 2.7 m after 3.75 km. The mineral layer underneath the peat is characterised by grey silt on either side of the Boloko River. However, towards the end of the transect, further away from the river, this becomes very soft clay.

Surface water pH is slightly higher directly on either side of the Boloko River (both 3.8) than further away along the transect (3.6 at both 3.0 and 4.0 km). This is opposite to the trend in surface water EC, which is lower on either side of the river (53 and 48 μS cm^{-1}), compared with further away (70 and 73 μS cm^{-1} at 3.0 and 4.0 km, respectively).

Many signs of fishing activities were observed in the first 750 m of the transect, before crossing the Boloko River. In particular, many fishing nets were observed, as well as the presence of the common oil palm (*Elaeis guineensis*) whose seeds are often used as fishing bait. This contrasts with the transect segment on the other side of the river, where little human disturbance was observed.
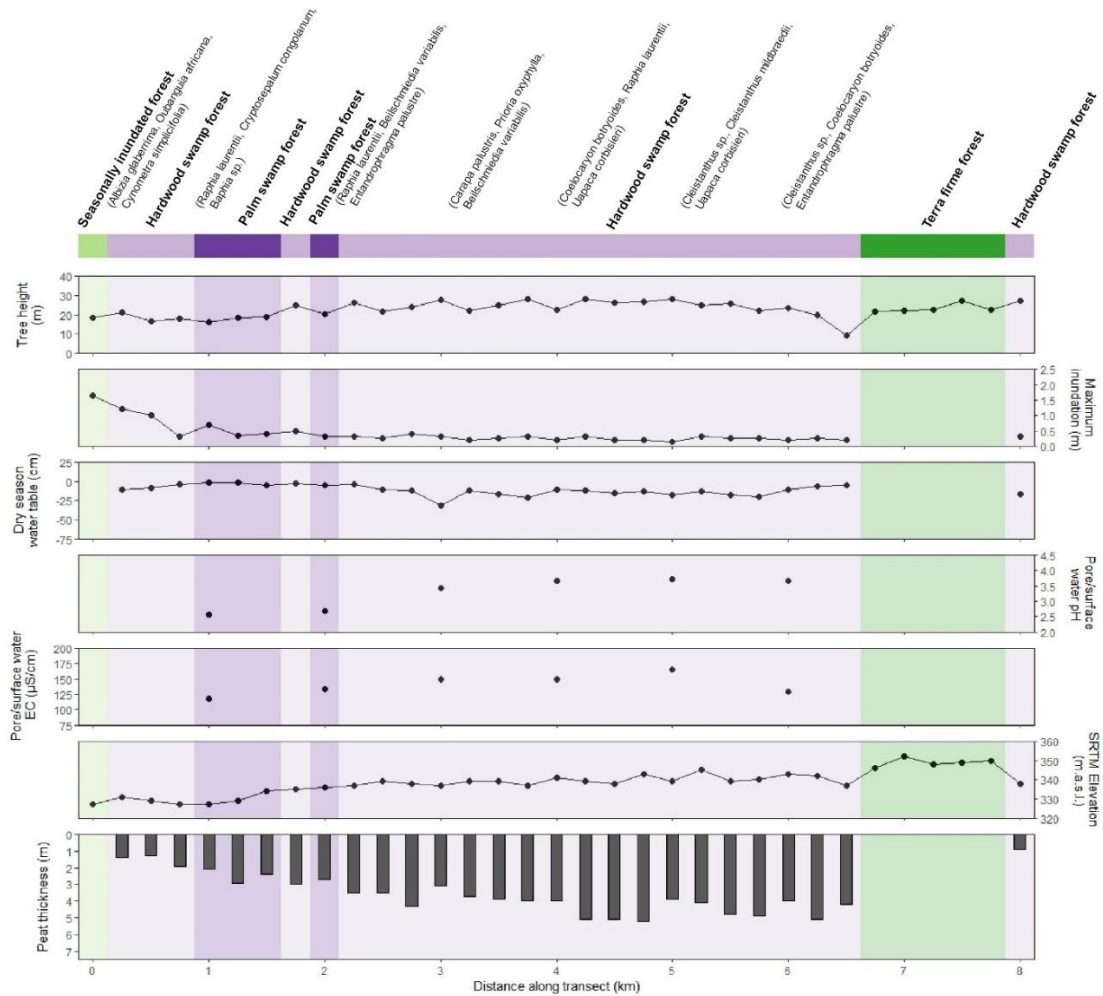
Tumba transect (TUM)
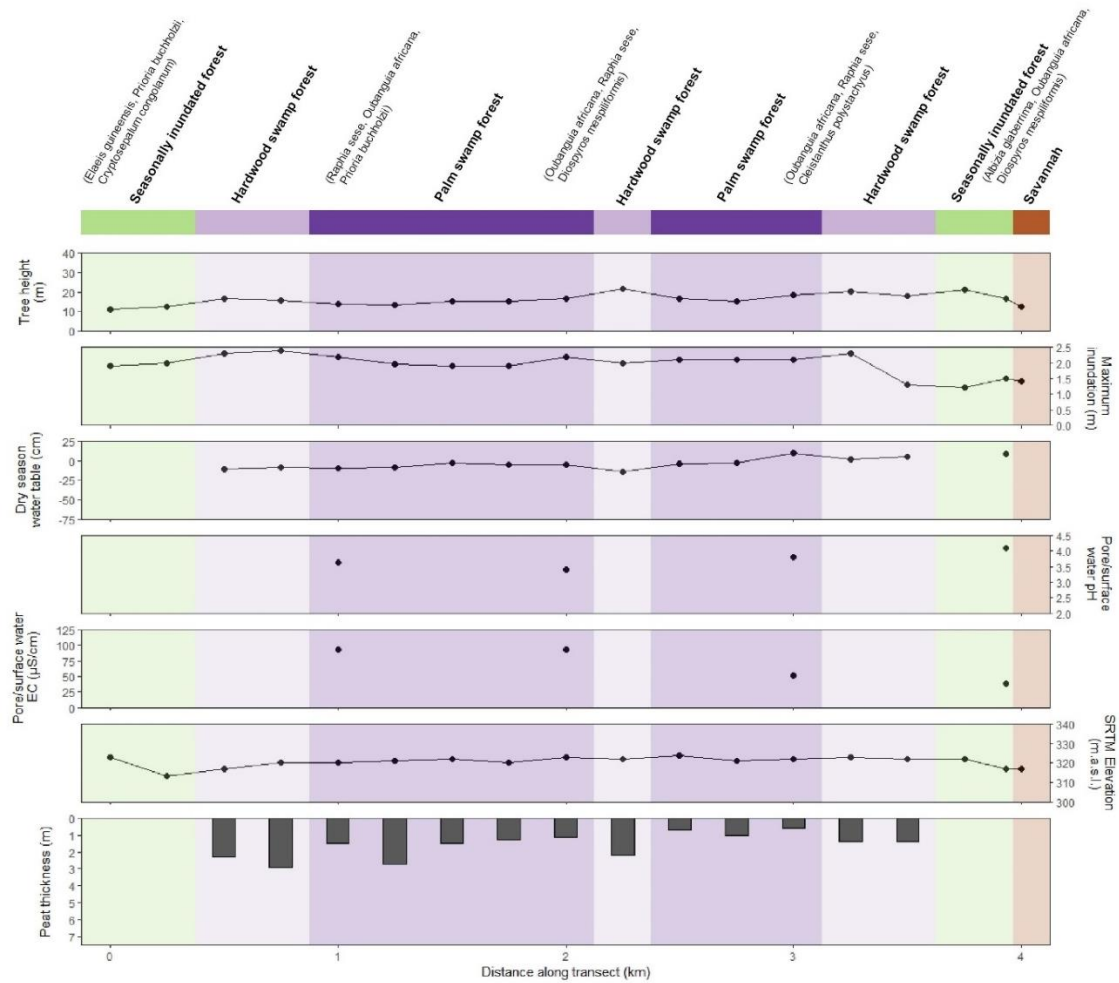
Figure 2.11. Tumba transect overview*, showing from top to bottom: mean* in situ *tree height (m), field-estimated maximum inundation (m), dry season water table depth (cm), peat pore/surface water pH and electrical conductivity (µS cm⁻¹), SRTM digital elevation (m.a.s.l.) and estimated peat thickness (m; incl. LOI-verified and corrected pole-method measurements). Colours indicate field-identified vegetation types (on top in bold), with the tree most abundant species listed every full kilometre. All y-axes are similar across transect figures (Figs. 2.6-2.12), except for the pore/surface water EC and SRTM elevation scales. Note that the x-axis (distance along transect) differs per transect (Figs. 2.6-2.12).*

The Tumba transect (Figure 2.11) is located in a low-lying floodplain between the Bonsole and Boloko Rivers (both tributaries of the Ruki River). It was chosen to investigate if peat forms in these seasonally inundated floodplains, or is potentially eroded away by shifting rivers. The transect starts on a small levee in non-peat forming seasonally inundated forest. Here, secondary forest vegetation can be found that is dominated by *Elaeis guineensis, Prioria buchholzii* and *Cryptosepalum congolanum*. After 0.5 km, the forest transitions to a seasonally inundated hardwood peat swamp, initially characterized by *Oubanguia africana, Guibourtia demeusei* and *Englerophytum laurentii*, which dominate the canopy, with an open understory dominated by *Raphia sese*. This seasonally inundated swamp was not inundated during the field

visit at the height of the dry season in March 2018 (water tables ~ 10 cm below the surface) but experiences an estimated maximum inundation of close to 2.5 m at the height of the wet season. These maximum inundation levels remain consistently high until 3.25 km along the transect. Throughout, the vegetation remains a mix of open hardwood swamp and palm-dominated swamp, with *Oubanguia africana, Guibourtia demeusei, Prioria buchholzii, Diospyros mespiliformis* and *Cleistanthus polystachyus* dominating the canopy, while *Raphia sese* dominates in the understory. Peat deposits are shallow, with a maximum of only 2.9 m after 0.75 km and gradually decreasing towards the end of the transect. The mineral layer underneath this peat is characterized by grey clay throughout the transect, with alternations of brown, organic-rich sand.

After 3.5 km, the transect enters an area of seasonally inundated forest that does not form peat, with maximum inundation levels slightly lower at ~1-1.5 m. The vegetation is characterized by *Albizia glaberrima, Oubanguia africana* and *Diospyros mespiliformis* in the canopy, with an understory dominated by rattans like *Laccosperma secundiflorum* and juvenile *Raphia sese* palms.

The transect ends again on a river levee next to the Boloko River, which is the site of a local fishermen's camp. As such, significant human disturbance can be observed, with many paths and hunting trails, signs of tree cutting, logging and fishing, as well as the presence of a charcoal pit. Because of this charcoal pit, the last vegetation plot and pH/EC measurements were taken in a seasonally inundated channel just before the levee, at 3.93 km, instead of 4.0 km.

Peat pore water pH in the peat-forming swamp ranges between 3.4 (at 2.0 km) and 3.8 (at 3.0 km). This goes up to 4.1 in the non-peat forming seasonally inundated channel at 3.93 km. Pore water EC, on the other hand is relatively higher at the start of the transect (94 µS cm^{-1} at both 1.0 and 2.0 km), which drops to 51 and 39 µS cm^{-1} at 3.0 and 3.93 km, respectively.
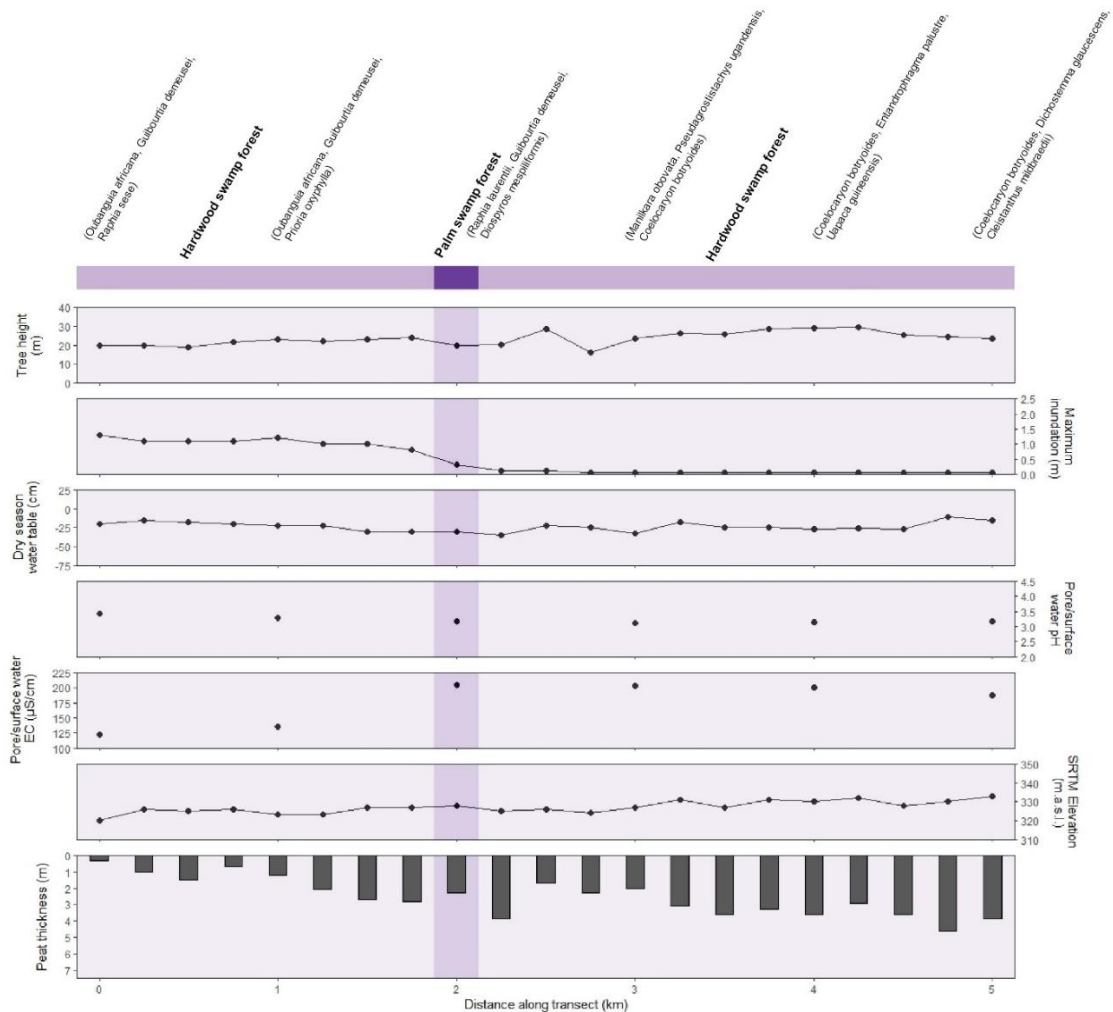
Lokolama transect (LOK)
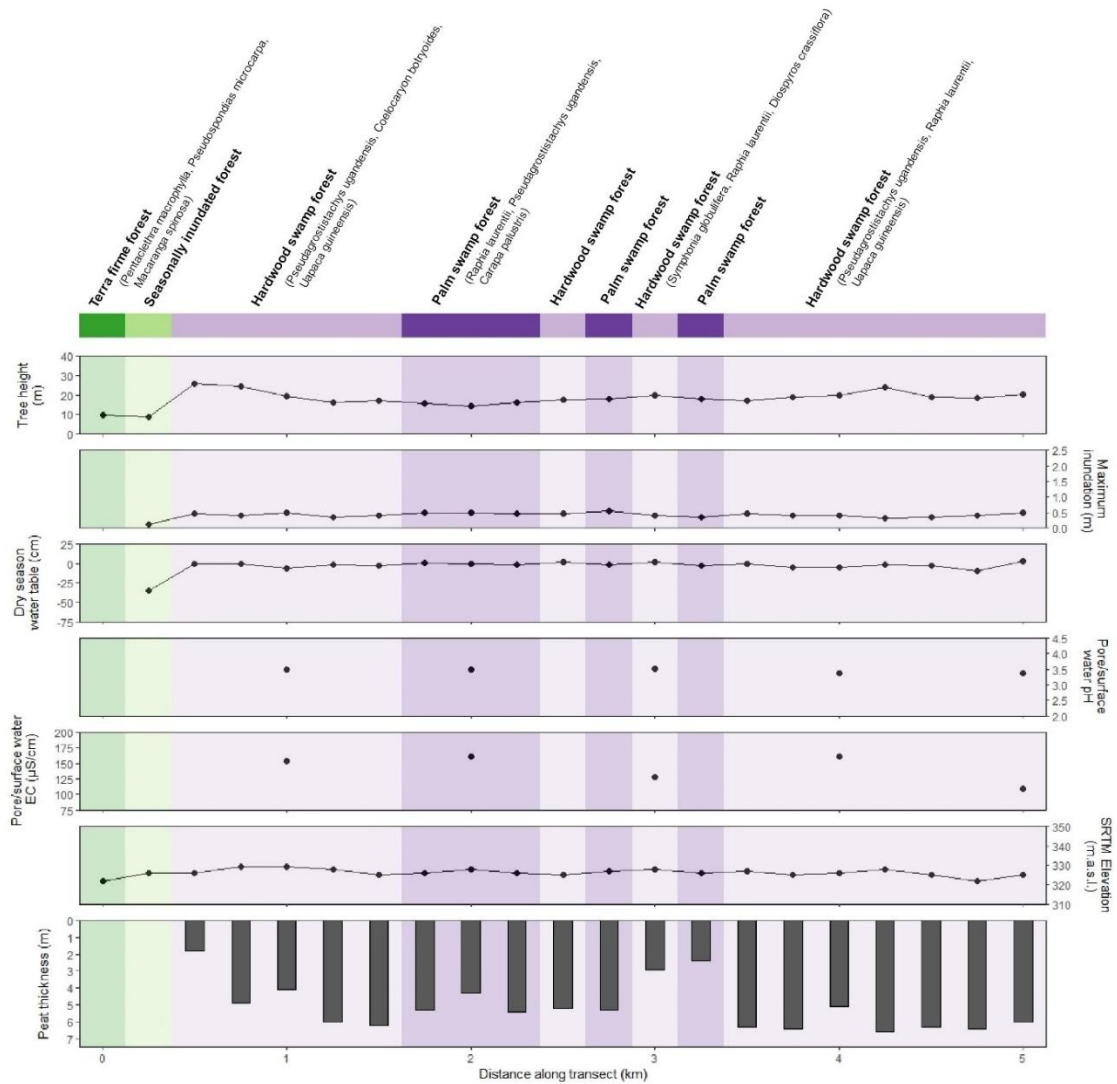
Figure 2.12. Lokolama transect overview, *showing from top to bottom: mean* in situ *tree height (m), field-estimated maximum inundation (m), dry season water table depth (cm), peat pore/surface water pH and electrical conductivity (µS cm⁻¹), SRTM digital elevation (m.a.s.l.) and estimated peat thickness (m; incl. LOI-verified and corrected pole-method measurements). Colours indicate field-identified vegetation types (on top in bold), with the tree most abundant species listed every full kilometre. All y-axes are similar across transect figures (Figs. 2.6-2.12), except for the pore/surface water EC and SRTM elevation scales. Note that the x-axis (distance along transect) differs per transect (Figs. 2.6-2.12).*

Contrary to the other transects, the Lokolama transect (Figure 2.12) is not located adjacent to a river or in a floodplain. Rather, this transect is located on the margin of a suspected (ovoid) interfluvial basin next to the Congo River mainstem, which could potentially be domed. The transect starts on the edge of an agricultural field and enters a hardwood-dominated peat swamp forest after 0.5 km. Here, vegetation is characterized by *Pseudagrostistachys ugandensis, Coelocaryon botryoides* and *Uapaca guineensis*. This changes after 1.5 km, when palm swamp forest dominated by *Raphia laurentii* can intermittently be found. Additional

hardwood tree species present here are *Carapa palustris, Symphonia globulifera, Entandrophragma palustre, Daniellia pynaertii* and *Diospyros crassiflora*, while *Scelorosperma mannii* and *Palisota mannii* dominate the understory. From 3.5 km onward, a hardwood-dominated peat swamp forest returns, with the occasionally *Raphia laurentii* found in the understory.

A slight variation in tree height can be observed which corresponds with shifts between hardwood- and palm- dominated peat swamp vegetation. Irrespective of vegetation type, however, deep peat deposits can be found. Already after 750 m, a peat thickness of 4.9 m is measured. After this, peat deposits of 4-6 m thick extend throughout the transect, except between 3.0 and 3.25 km, where peat thickness is < 3.0 m. The mineral layer underneath the peat is characterized by soft brown/grey clay throughout the transect.

The estimated maximum inundation is very stable, generally being just above the peat surface (0-50 cm) throughout the length of the transect. During the field visit in the dry season of February/March 2018, water tables were just below (> -10 cm) the peat surface. This stable inundation pattern could be explained by the relatively flat topography, as no major change in elevation are observed.

Peat pore water pH is stable throughout the transect. During the first three kilometres of the transect a consistent pH of 3.5 is observed, which drops slightly to 3.4 in the last two kilometres. Pore water EC show a little more variation, but without a clear trend. EC is generally between 155 and 160 μS cm^{-1}, except at 3.0 and 5.0 km, when it drops to 128 and 110 μS cm^{-1}, respectively.

The Lokolama transect is not characterized by major human disturbances. However, several hunting trails can be found that lead from the agricultural fields at the swamps edge towards fishing camps next to the Congo River on the other side of the peatland area.

2.5.2 Transect comparisons

Mean peat thickness, tree height, estimated maximum inundation height, and dry season water table depth varied significantly between the seven hypothesis-testing transects (p<0.001, Kruskal-Wallis rank sum test for all four variables), as detailed in each section below. To easily distinguish among transects that experience different levels of inundations, transects shown in these figures are ordered by increasing High Water Fraction, which reflects the proportion of peat sites along each transect with estimated maximum inundations of > 50 cm.

Peat thickness

It can be observed that peat deposits are significantly thicker in Lokolama, Bolengo and Bondamba than along the other four transects (Fig. 2.13). This difference corresponds with an increasing gradient in High Water Fraction, with these three transects all having proportionally less high-water-sites than the Boloko, Ikelemba, Mpeka or Tumba transects. A significant difference in peat thickness is also found between low- and high-water sites (Mann–Whitney U test, p<0.001), with low-water sites (≤ 50 cm maximum inundation) having a mean thickness of 3.9 m (max = 7 m; s.d. = 1.6 m; n=109), compared with a mean thickness of 1.6 m in high-water sites (max. 5.3 m; s.d. = 0.9; n=50). A linear regression model of peat thickness and estimated maximum inundation, corrected for interaction effects of transect groups, also provides a clear negative correlation (R^2 = 0.35; p<0.001), showing that shallower peat is found at sites with greater inundation levels.

Similarly, peat thickness has a significant positive correlation with SRTM elevation (R^2=0.19, p<0.001, including transect interaction effects). This is likely because maximum inundation itself is negatively correlated with elevation (R^2=0.32, p<0.001, including transect interaction effects).

Mean peat thickness of hardwood-dominated peat swamp is 3.3 m (max = 6.6 m; s.d. = 1.7 m), while the mean peat thickness of palm-dominated peat swamp is slightly lower, at 3.0 m (max = 7.0 m; s.d. = 1.7 m). Thus, no overall statistical difference in peat thickness is found between hardwood- and palm-dominated peat swamp vegetation, as classified in the field (n=90 and 69, respectively; Mann–Whitney U test, p=0.26). When testing this difference within individual transects, significantly greater peat thickness is only found for hardwood-dominated sites than palm-dominated sites in Mpeka and Bolengo (both p<0.05).
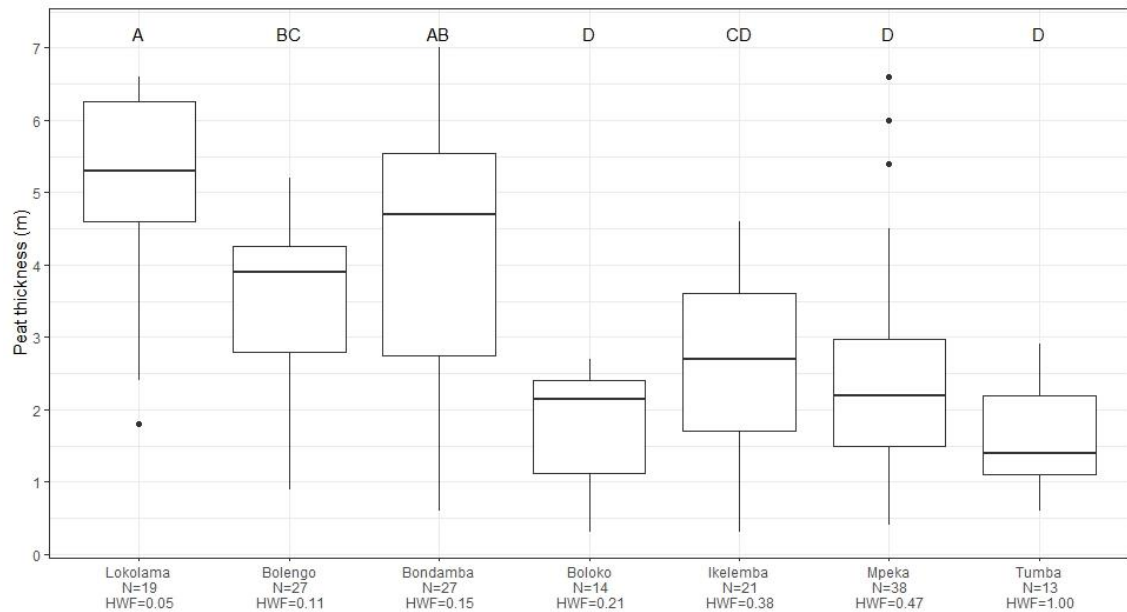
Figure 2.13. Boxplot of peat thickness across the seven hypothesis-testing transects. *The black line shows the median value (m). The box shape shows the upper and lower quartiles. The vertical lines show the minimum and maximum values. Circles represent outlying values. Transects that do not share a common letter are significantly different (p<0.05, Dunn's Kruskal-Wallis multiple comparison test, p-values adjusted with the Benjamini-Hochberg method). Transects are ordered by increasing High-Water Fraction (HWF), i.e. from no river impact to high seasonal river flooding.*

Tree height

Mean tree height across all peat swamp vegetation is 18.1 ± 5.6 m (n=159), the mean of the five trees samples every 250 m across all 11 transect. Maximum tree height was 31.3 m, recorded towards the end of the Mpeka transect (PEK_9.50). However, considerable differences in mean tree height are observed across the seven transects (Figure 2.14). Trees of 25 m or more are found in Bolengo, Boloko and Ikelemba, transects that are all characterized by large areas of hardwood swamp forest. On the other hand, particularly low tree height of generally less than 15 m is found in Bondamba, which is almost entirely characterized by palm-dominated swamp forest. Mean tree height for hardwood-dominated swamp along the seven transects is 21.5 m (max = 31.3m ; s.d. = 4.5 m; n=90), significantly higher than the 13.6 m found for palm-dominated swamp (max = 20.6 m; s.d. = 3.2 m; n=69; Mann–Whitney U test, p<0.001). This significant difference also holds within individual transects, such as Lokolama, Bolengo, Tumba (p<0.05) and Mpeka (p<0.01).

A weak, but significant negative correlation is found between mean tree height and estimated maximum inundation (R^2=0.05, p<0.05, including transect interaction effects). On the other hand, tree height is positively correlated with higher water tables as measured in the dry season

(R^2 = 0.13, p<0.001, including transect interaction effects). This suggest that tree height of peat swamp forest is negatively affected by large inundations, and deep dry season water tables. However, no significant correlation is found between mean tree height and peat thickness (p=0.25, including transect interaction effects).
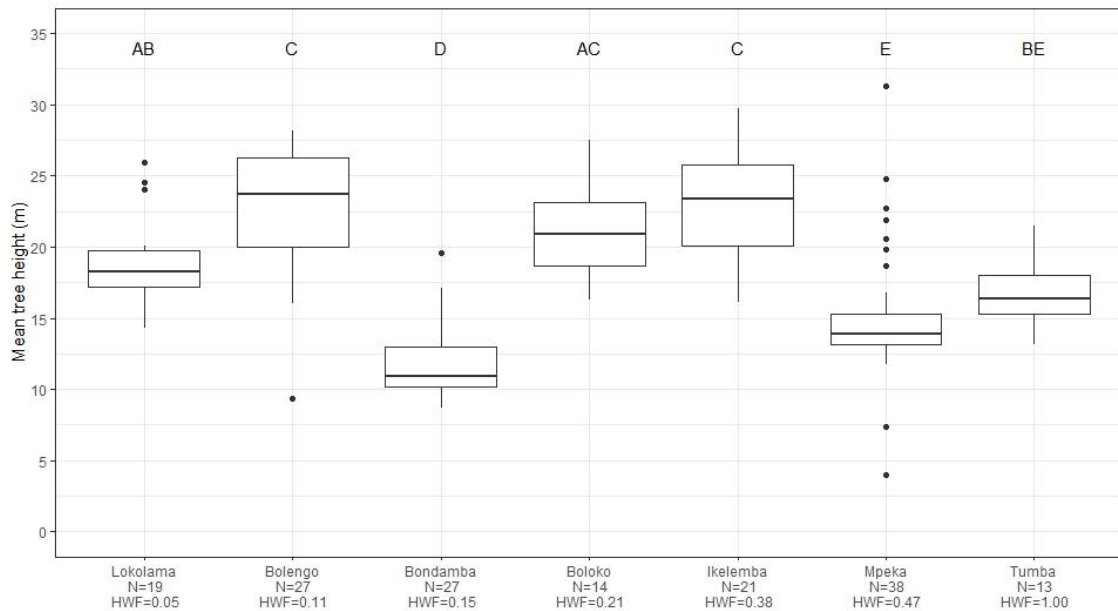
Figure 2.14. Boxplot of tree height across the seven hypothesis-testing transects. *Measurements include the mean of the five trees (m) recorded every 250 m along each transect if peat was present. The black line shows the median value. The box shape shows the upper and lower quartiles. The vertical lines show the minimum and maximum values. Circles represent outlying values. Transects that do not share a common letter are significantly different (p<0.05, Dunn's Kruskal-Wallis multiple comparison test, p-values adjusted with the Benjamini-Hochberg method). Transects are ordered by increasing High-Water Fraction (HWF), i.e. from no river impact to high seasonal river flooding.*

Maximum inundation height

Mean estimated maximum inundation does not vary significantly between the majority of transects (Figure 2.15). The only exception is Tumba, which has significantly higher maximum inundation levels than all the other transects. However, it must be noted that some transects, in particular Mpeka and Ikelemba, show large variability, which is the result of considerable gradients in inundation along these transects.

No significant difference in maximum inundation was found between hardwood- or palm-dominated swamp forest across all seven transects (n=90 and 69, respectively; Mann–Whitney U test, p=0.18). None of the individual transects showed a significant difference in inundation between these two vegetation types either.
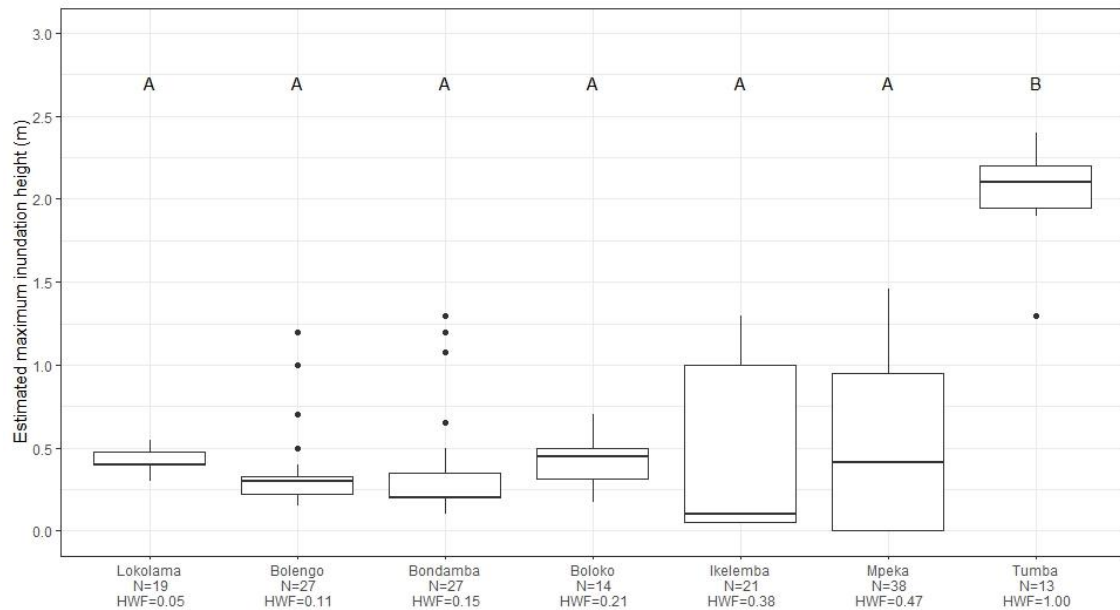
Figure 2.15. Boxplot of estimated maximum inundation height (m) across the seven hypothesis-testing transects. *The black line shows the median value. The box shape shows the upper and lower quartiles. The vertical lines show the minimum and maximum values. Circles represent outlying values. Transects that do not share a common letter are significantly different (p<0.05, Dunn's Kruskal-Wallis multiple comparison test, p-values adjusted with the Benjamini-Hochberg method). Transects are ordered by increasing High-Water Fraction (HWF), i.e. from no river impact to high seasonal river flooding.*

Water table depths

Mean water table depths at the time of sampling in the dry season show larger differences than estimated maximum inundation (Figure 2.16; positive if above the peat surface, negative if below). Water tables were consistently close or above the peat surface in the three transects not adjacent to one of the two main rivers (Lokolama, Boloko and Tumba; mean +2 cm; n=46). This contrasts significantly with the other four transects that are perpendicularly located to either the Ruki or Ikelemba River (Mpeka, Bolengo, Bondamba and Ikelemba), which had water tables largely below the peat surface (mean -26 cm; n=113; Mann–Whitney U test, p<0.001). In particular, deep water tables (> 25 cm below the peat surface) were regularly found along the Mpeka, Bondamba and Ikelemba transects at the time of sampling. This includes river-influenced sites with maximum inundations of > 1 m above the peat surface, suggesting considerable differences in water table heights between the wet and dry season in these locations.

Water table depths were also significantly lower in palm-dominated swamps at the time of sampling (mean -25 cm; n=69), compared with hardwood-dominated swamps (mean -12 cm; n=90; Mann–Whitney U test, p<0.001). However, this may be an effect of the transect sampling

design, as within-transect statistical differences were only found in the Bolengo transect (Mann–Whitney U test, p<0.01) and no other transect.
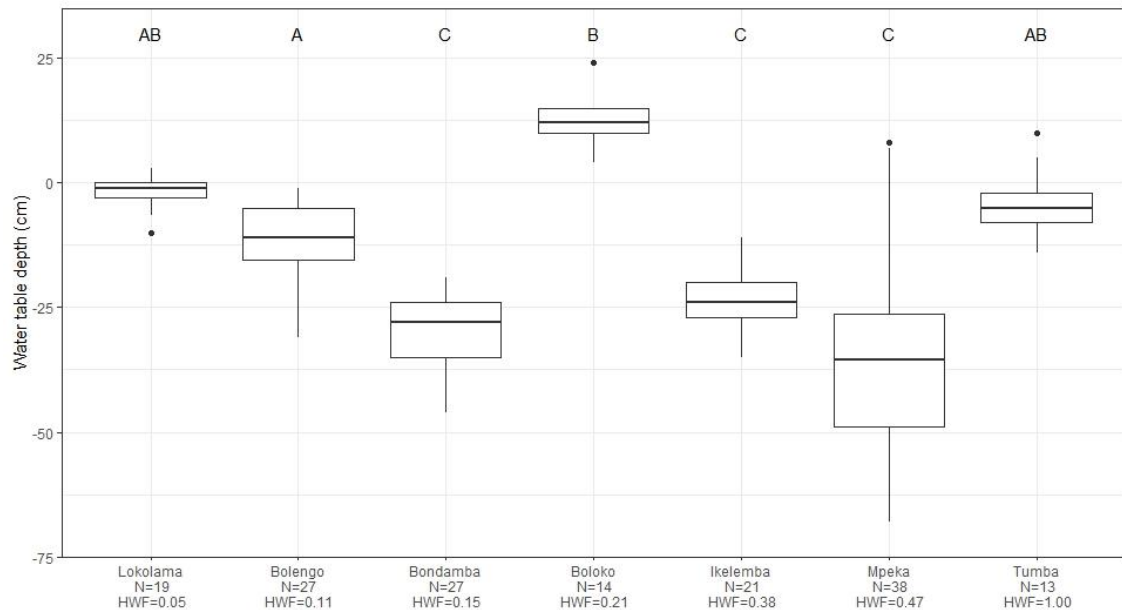
Figure 2.16. Boxplot of dry season water table depth (cm) across the seven hypothesis-testing transects. *Positive (negative) values indicate water tables above (below) the peat surface. The black line shows the median value. The box shape shows the upper and lower quartiles. The vertical lines show the minimum and maximum values. Circles represent outlying values. Transects that do not share a common letter are significantly different (p<0.05, Dunn's Kruskal-Wallis multiple comparison test, p-values adjusted with the Benjamini-Hochberg method). Transects are ordered by increasing High-Water Fraction (HWF), i.e. from no river impact to high seasonal river flooding.*

pH and electrical conductivity

All 40 peat swamp locations where pH/EC-measurements were taken are strongly acidic, with pore/surface water pH values ranging between 2.6 and 3.8 and a mean value of 3.3 ± 0.3 (n=40). Pore/surface water electrical conductivity ranges between 48 and 205 µS cm^{-1}, with a mean value of 134 ± 39 µS cm^{-1}.

However, like with water table depths, differences between the four transects connected directly to the Ruki or Ikelemba Rivers and those unconnected to them can also be observed for pH and electrical conductivity. Peat pore water pH is found to be lower, on average, along the Mpeka, Bolengo, Bondamba and Ikelemba transects connected directly to the main rivers (mean 3.20 ± 0.32) than the Lokolama, Boloko and Tumba transect unconnected from them (mean 3.58 ± 0.17; Mann–Whitney U test, p<0.001). No significant difference, however, is observed

between high-water and low-water sites (maximum inundations either > 50 or ≤ 50 cm, respectively), either across all transects groups or within individual transects.

Palm-dominated peat swamps are characterized by lower pH (mean 3.15 ± 0.36, n=20) than hardwood-dominated peat swamps (mean 3.47 ± 0.21, n=20; Mann–Whitney U test, $p<0.01$). However, this may be an effect of the transect sampling design, as no significant within-transect differences are observed.

Five transects showed no clear gradient in pH when moving along the transect: the three transects unconnected to either the Ruki or Ikelemba River (Lokolama, Boloko and Tumba), and Bondamba and Mpeka. The other two river-influenced transects showed opposing trends. Along the Bolengo transect, higher pH is found when moving away from the river towards the interior, which corresponds with higher elevations, lower water table fluctuations and a shift towards hardwood vegetation before reaching *terra firme* uplands. Along the Ikelemba transect, on the other hand, pH decreases slightly when moving away from the river towards *terra firme* uplands.

In terms of peat pore/surface water electrical conductivity, it is observed that the three transects not connected to either the Ruki or Ikelemba River have, on average, lower EC values (mean 100 ± 43 µS cm^{-1}) than the group of four transects that is directly located along one of these two rivers (mean 148 ± 27 µS cm^{-1}; Mann–Whitney U test, $p<0.005$). EC is also significantly lower in sites with high maximum inundations (mean 107 ± 39 µS cm^{-1}) than in sites with low maximum inundations (mean 147 ± 33 µS cm^{-1}; Mann–Whitney U test, $p<0.01$). However, again, this is likely an effect of transect grouping, as no significant within-transect differences are observed. No significant differences in electrical conductivity, either across all transects groups or within individual transects, are observed between hardwood- and palm-dominated peat swamps.

As with pH, five transects showed no clear gradient in electrical conductivity, including the three transects unconnected to either the Ruki or Ikelemba River. The Ikelemba and Bolengo transects both have increasing EC with distance from the river, when moving towards *terra firme* upland.

A general summary of the variation between transects is provided in Table 2.4 below. The same variables were also compared between hardwood- and palm-dominated peat swamp forests sites, an overview of which is presented in Table 2.5.

Variable	Mean ± s.d. across transects	Basic pattern description	Interpretation
Peat thickness (m)	3.2 ± 1.7 (max = 7.0)	Thicker in Lokolama, Bolengo and Bondamba	Sites with heavy wet season inundation have shallower peat
Tree height (m)	18.1 ± 5.6 (max = 31.3)	Highest in Bolengo, Boloko and Ikelemba; lowest in Bondamba.	Sites with heavy wet season inundations, or deep dry season water tables, have lower tree height
Wet season maximum inundation height (cm)	57 ± 58	Higher in Tumba than all other transects	Gradient within transects, with highest inundation closest to rivers
Dry season water table depth (cm)	-18 ± 18	Near the surface in Lokolama, Boloko and Tumba; deep in Mpeka, Bondamba and Ikelemba	Transects perpendicular to major rivers show a gradient, with deep water tables in sites experiencing heavy inundation
pH	3.31 ± 0.33	Lower in Mpeka, Bolengo, Bondamba and Ikelemba	Sites along the main rivers are possibly more acidic than smaller tributaries
Electrical conductivity (µS cm^{-1})	134 ± 39	Higher in Mpeka, Bolengo, Bondamba and Ikelemba	Sites along the main rivers possibly have more nutrients, or dissolved organic matter

Table 2.4. Summary of significant differences in field characteristics between transects. All variables show significant differences between transects (p<0.001, Kruskal-Wallis rank sum test). n=159 for peat thickness, tree height, wet season maximum inundation height and dry season water table depth; n=40 for pH and electrical conductivity.

Variable	Hardwood-dominated peat swamp forest (mean ± s.d.)	Palm-dominated peat swamp forest (mean ± s.d.)
Peat thickness (m)	3.3 ± 1.7 (max. 6.6)	3.0 ± 1.7 (max. 7.0)
Tree height (m) ***	21.5 ± 4.5 (max. 31.3)	13.6 ± 3.2 (max. 20.6)
Wet season maximum inundation height (cm)	59 ± 56	70 ± 61
Dry season water table depth (cm) ***	-12 ± 16	-25 ± 18
pH **	3.47 ± 0.21	3.15 ± 0.36
Electrical conductivity (µS cm^{-1})	132 ± 43	135 ± 33

Table 2.5. Comparison of field characteristics between peat swamp vegetation types. Hardwood-dominated and palm-dominated peat swamp forest vegetation types were identified in the field. n=90 and n=69, respectively, for peat thickness, tree height, wet season maximum inundation height and dry season water table depth. n=20 and n=20, respectively, for pH and electrical conductivity. Asterisks indicate statistically significant differences (is p<0.05, ** is p<0.01, *** is p<0.001; Mann–Whitney U test).*

2.6 Discussion

The field data presented in this chapter show for the first time that extensive peat swamp forests are found in the lowland forested wetlands of DRC's Cuvette Centrale. These swamp forests have a mean peat thickness of 3.2 ± 1.7 m (n=159, with ≥ 30 cm of ≥ 65% OM), which is significantly greater (p<0.001) than the mean thickness of 2.4 ± 1.6 m that was reported for ROC (Dargie et al., 2017).

Peat thickness generally increases with distance along the transect. Maximum peat thickness was found to be 7.0 m, measured close to the end of the 7.0 km-long Bondamba transect. This is slightly thicker than the maximum of 5.9 m recorded in ROC (Dargie et al., 2017). However, this maximum ROC peat thickness was found 20 km from the start of a transect in the centre of a wide interfluvial basin. In the DRC, on the other hand, thick peat deposits are recorded along transects that have approximately one quarter the length of this. In contrast with interfluvial basin peatlands in ROC, peat thickness of 5-7 m can already be reached in the DRC's river-influenced peatlands within several kilometres of encountering peat on the transects, for example along the Bondamba transect (Figure 2.7). These deeper peats are found in the floodplain areas of the major river valleys of the Ruki or Ikelemba Rivers, between the rivers and upland *terra firme* forest or croplands. Narrower, river valleys along upstream rivers and streams, such as the Boloko transect (Figure 2.10), appear to have shallower peat deposits.

It must be noted though, that the maximum measurement of peat thickness (7.0 m at Bondamba) is based on the corrected pole-method, rather than laboratory-method using Loss-On-Ignition. The linear regression used for the pole-method correction is dependant on the dataset of matched pole method and LOI-verified thickness measurements. The correction used here (Figure 2.3) applies to the river-influenced DRC transects, and is therefore different from the correction used by Dargie et al. (2017). If applying the ROC-based regression model from Dargie et al. (2017), or a basin-wide regression model including data from both DRC and ROC (Chapter 5), slightly different peat thickness estimates will be obtained. Maximum peat thickness measurements reported for the Congo Basin peatlands will therefore be uncertain unless LOI measurements are taken. Nonetheless, the maximum LOI-derived thickness measurement in the DRC (6.0 m at LOK_5.0) is still greater than the maximum LOI-derived value in the ROC (5.5 m at 16 km along the Centre transect; Dargie et al., 2017), confirming that thicker peat deposits are found in DRC.

Average peat thickness in the central Congo Basin, and particularly in its river-influenced peatlands, appears to be slightly deeper than in the Pastaza-Maranon Foreland Basin in the Peruvian Amazon, where Hastie et al. (2022) report a mean thickness of 2.19 m (95% CI, 1.94-2.40 m). However, maximum peat thickness appears larger in Peru, where Draper et al. (2014) report a maximum value of 6.6 m, while Lähteenoja et al. (2011) mention 7.5 m in one of their study sites. Compared with Southeast Asia, however, both peatland areas are relatively shallow. Average peat thickness in Southeast Asia is estimated to be 5-8 m (Page et al., 2022), with maximum observed values of up to 18 m (Ruwaimana et al., 2020).

The gradient in peat thickness with increasing distance along the transect tends to correspond with increasing distance from the river, as most of the transects are located perpendicular to major rivers. This suggests that peat swamp forests that are seasonally inundated by river water have shallower peat deposits than those characterized by more stable water tables. This is confirmed by the negative correlation that was observed between peat thickness and estimated maximum inundation ($R^2 = 0.35$; p<0.001). This highlights how mapping water table fluctuations or seasonal patterns in inundation could be critical to understanding spatial patterns of peat thickness.

Neither peat thickness, nor maximum inundation, was found to vary significantly between hardwood- and palm-dominated peat swamp vegetation (Table 2.5). This shows that the gradients in peat thickness and inundation levels do not neatly overlap with shifts from one of these vegetation types to the other. This confirms what is visually observed from the transect descriptions in Figures 2.6-2.12, namely that seasonally inundated peat swamps close to the river and peat swamps further away from the river with stable water tables can be found in combination with both hardwood vegetation (e.g., Ikelemba and Bolengo), as well as *Raphia*-dominated palm vegetation (e.g., Bondamba and Mpeka). While no difference in peat thickness was found between the hardwood and palm-dominated peat swamp forests in ROC, a visual inspection of the maps by Dargie et al. (2017) shows that palm swamp vegetation is typically predicted further from the margin of the peatlands, indicating the possibility of deeper peat under palm-dominated swamp forest. However, much larger sample sizes will be required to test this hypothesis. Furthermore, it is likely that different processes and patterns may be seen in the interfluvial basin and river-influenced peatlands. Indeed, possibly four peat swamp types could be detected in the DRC peatlands, depending on both vegetation and environment: hardwood swamp either seasonally influenced by the river or not, and palm swamp either

seasonally influenced by the river or not. This intersection of vegetation type and hydrology will be further explored in Chapter 3.

The peat swamps forests in the DRC are found to be strongly acidic, with peat pore/surface water pH values ranging between 2.6 and 3.8 and a mean value of 3.31 ± 0.3 (n=40). This is similar to what was observed in the ROC, where Dargie (2015) recorded a pH of 3.24 ± 0.2 (n=33) in peat pore/surface water. However, electrical conductivity in the DRC ranges between 48 and 205 μS cm^{-1}, with a mean value of 134 ± 39 μS cm^{-1} (n=40), considerably lower than the 171 ± 36 μS cm^{-1} measured in ROC (n=28). This lower EC value could indicate either lower nutrient concentrations (less dissolved major ions), or less organic acids (Allen & Castillo, 2007; Theimer et al., 1994). In this case, since pH values are comparable between the DRC and ROC peat swamps, this finding implies less dissolved ions in the river-influenced peatlands. As EC concentrations were also found to be lower in sites with higher maximum inundations (i.e., closest to the river), this could indicate that seasonally inundated peat swamps along rivers are even more nutrient-poor than peatlands further away from rivers. This appears in line with the observation of greater EC values closer to the *terra firme* uplands, such as observed along the Ikelemba and Bolengo transects, suggest a supply of dissolved solids (cations) from upland runoff. This points towards a possible trend of greater nutrient concentrations on the edges of floodplain peat swamps towards more nutrient-poor conditions closer to the river.

However, it must be noted that pH values are heavily influenced by local rain events, which typically have a pH close to neutral (Allen & Castillo, 2007). This may make these values less representative than they might be. Also, some equipment failures meant that I had to rely on less accurate pH/EC-probes, which likely has made the results less precise. Furthermore, it must be noted that some of the pH/EC-measurements along the Ikelemba, Tumba and Bondamba transect were taken at depths of > 30 cm below the peat surface, given that water tables were low at the height of the dry season. This could have increased the acidity or concentrations of dissolved solids in the peat water, since evaporation will have likely concentrated the presence of peat tannins, organic acids, and base cations. Alternatively, it could be that peat at greater depths is already more decomposed, and therefore results in less organic acids. To investigate whether lower nutrient concentrations are really characteristic of the river-influenced peat swamps in DRC, concentrations of base cations will be further explored in Chapter 4.

2.7 Conclusion

This chapter sought to present an overview of the field site locations used in this study. Specifically, it aimed to show if there is peat in the swamp forests of the geomorphologically-distinct riverine setting in the central Democratic Republic of the Congo, and to make a first test of the peatland map of Dargie et al. (2017). Peat was found in the geomorphologically-distinct riverine setting along all hypothesis-testing transects, as predicted by Dargie et al. (2017). These transects had between 80.5 and 97.0% accuracy in predicting the presence of peat. However, peat was not always found along the shorter transects used for assessing mapping capabilities. Often, these transects were located in seasonally inundated swamps toward the margins of larger peatland areas. Together, this shows that the peatland map by Dargie et al. (2017) is generally accurate for predicting peat in major swamp forest areas near DRC's rivers, but less accurate near the peatland's margins.

The fieldwork presented in this chapter shows that peat deposits in the river valleys of the DRC are, on average, thicker than those found in the interfluvial basins in the Republic of the Congo. The largest peat thickness measurement in the central Congo Basin originates from the Bondamba transect in the DRC, where 7.0 m thick peat was recorded, a record for the central Congo Basin peatland complex. However, in contrast to what has previously been observed in ROC, peat thickness in DRC increases faster with distance from the peatland margin. Thus, thick peat deposits in the central Congo Basin are not confined to wide interfluvial basins, but can also be found in narrower peatlands in geomorphologically different river valleys systems.

The shallowest peat deposits are found in sites experiencing large wet season inundations, typically close to major rivers or streams. These sites can sometimes be characterized by deep water tables in the dry season as well, indicating major seasonal water table fluctuations. This combination of high wet season inundations and relatively deep dry season drawdown appears largely to take place in floodplain sites along the major rivers (e.g., as opposed to the Tumba transect, which has the largest inundations, but dry season water tables closer to the surface). These sites show how peat formation is not confined to permanently waterlogged swamps with stable water tables close to the peat surface, but also occurs in swamps that experience larger water table fluctuations on a seasonal basis. These seasonally inundated peat swamps appear as acidic as other peatlands, but may possibly be characterized as more nutrient-poor, due to their lower electrical conductivity.

Two distinct vegetation types have been described in the DRC peatlands, namely hardwood-dominated and palm-dominated peat swamp forests, which are comparable in peat thickness. However, it was observed that both types can be found in seasonally inundated riverine settings, as well as more permanently waterlogged sites further from rivers. This highlights how peat swamp forest vegetation types are likely more diverse than this dichotomy between hardwood and palm swamps suggests.

Chapter 3: Characterising peat swamp forest vegetation types in the central Congo Basin

3.1 Abstract

The vegetation of the central Congo Basin peatlands has so far been classified as either hardwood-dominated or palm-dominated peat swamp forest, based on fieldwork in northern ROC (Dargie et al., 2017). However, the data presented in Chapter 2 shows how peat swamps occupy very distinct river-influenced settings in DRC which have not been described in ROC. As forest structure and species composition are strongly related to inundation patterns (Targhetta et al., 2015), the peat swamp forest types of the DRC may be expected to differ from those described in ROC. In this chapter, I present the results of a first analysis of vegetation patterns in the largely river-influenced peat swamp forests of the DRC. Detailed vegetation characteristics were obtained from 48 vegetation plots (20x40 m) across seven transects, of which 40 were located in peat swamp forests and 8 in *terra firme* forest. Mean aboveground carbon stock across all 40 peat swamp forest plots in DRC is 97.8 Mg C ha^{-1}. Using a combination of unsupervised clustering and non-metric multidimensional scaling (NMDS) ordinations, I identify two key gradients that drive peat swamp forest vegetation types in DRC: one related to hydrology (ranging from stable water tables to large seasonal inundation patterns), and one related to the proportion of palm-dominance. This results in the identification of four distinct vegetation types in DRC's peat swamp forests: a diverse hardwood-dominated peat swamp forest; a *Raphia laurentii* palm-dominated peat swamp forest; a mixed (hardwood and palm tree) peat swamp forest characterized by *Cryptosepalum congolanum*; and a mixed peat swamp forest characterized by *Ouganbuia africana* and *Guibourtia demeusei*. The distinction between the *Oubangia-Guibourtia*-associated mixed peat swamp forest and the other types is driven by the gradient in river-influenced inundation patterns. However, the distinction between the other three peat swamp forest vegetation types is driven by a second gradient related to palm-dominance. It remains unclear what is driving this gradient. The diverse hardwood-dominated peat swamp and *R. laurentii* palm-dominated peat swamp appear similar to those forest types found by Dargie et al. (2017) in ROC. Given that they also identified a *R. hookeri* palm-dominated vegeation in abandoned river channels in ROC, this suggests that at least five peat swamp forest vegetation types can be distinguished in the central Congo Basin peatlands when adding the *Cryptosepalum congolanum*- and *Oubangia-Guibourtia*-associated mixed peat swamp forests.

3.2 Introduction

The first attempt at classifying peat swamp forest vegetation in the central Congo Basin defined two common types: a hardwood- and palm-dominated swamp forest (Dargie et al., 2017). In Chapter 2, I showed how both hardwood- and palm-dominated peat swamp forest can be found in seasonally inundated riverine settings in DRC, as well as at more permanently waterlogged sites further from rivers in DRC. However, although swamp forest was classified in the field as belonging to either one of these two landcover classes, forests in riverine settings in DRC may be very distinct from the vegetation types described in the ROC. This may be because different species have different tolerances for the duration and depth of flooding. For example, in the non-peat forming wetlands of the Igapó blackwater forest of the Amazon basin, longer inundation periods are typically associated with lower species richness, forest height and aboveground biomass (Targhetta et al., 2015). This suggests that flood tolerance might restrict species diversity in such wetland habitats. Alternatively, it may be the species' tolerance to the drier dry season conditions which determines species composition: when Lopez and Kursar (2003) compared species-poor seasonally flooded forests with more species-rich *terra firme* forests in Panama, they found no evidence that these two forest types differed in their response to flooding specifically. Rather, a species' ability to tolerate dry conditions following severe flood events was found to be equally important for surviving in seasonally inundated sites (Lopez & Kursar, 2003).

In the Congo Basin specifically, there is evidence to suggest that seasonally inundated swamps are structurally different from swamps with more stable water tables. In a remote-sensing study of Central African vegetation structure, Gond et al. (2013) identified two separate swamp forest types, which do not appear to overlap with the distinction between hardwood- and palm-dominated swamps made by Dargie et al. (2017). Using seasonal profiles of the MODIS-derived enhanced vegetation index (EVI), which quantifies photosynthetic activity throughout the year, Gond et al. (2013) distinguished between 'swamp forests located in the Congo Basin' and 'swamp located at the valley bottom in the Congo Basin and long rivers in Cameroon and Gabon', with the latter type having significantly lower basal area than the former. The identification of a separate swamp type in 'valley bottoms in the Congo Basin', distinct from Congo Basin 'swamp forests' suggest that river-influenced peat swamp vegetation in DRC could be different from the peat swamp vegetation types found in interfluvial basins in ROC.

Early literature from the Cuvette Centrale, such as Evrard (1968), typically only considered the swamps as wetlands and not as peatlands. Nonetheless, Evrard (1968) reports several different wetland swamp forest vegetation types, some of which may overlie peat. In addition to permanently inundated swamp forests, Evrard (1968) identified a seasonally inundated forest type that is associated with *Oubanguia africana* and *Guibourtia demeusei* species. Furthermore, in addition to a class of permanently inundated *forêts marécageuses*, Lebrun and Gilbert (1954) also identified a seasonally inundated forest type (*forêts périodiquement inondées*) that they describe as being characterized by *Oubanguia africana* and *Guibourtia demeusei.* Similarly, Betbeder et al. (2014) report a forest type subjected to seasonal short lasting flood pulses of low amplitude that is characterised by *Guibourtia deumeusei* and *Oubanguia africana*. These reports seems to correspond with the initial vegetation descriptions of the field transects (Chapter 2), in which *Oubanguia africana* and *Guibourtia demeusei* were often encountered in some peatlands, suggesting this could be a separate peat-forming swamp vegetation class.

There is thus a need to describe the diversity of peat swamp forest vegetation types of the Cuvette Centrale in more detail than is capture by the binary classification of hardwood- and palm-dominated swamp. Given that valley bottom swamp forests (Gond et al., 2013) and seasonally flooded forests (Betbeder et al., 2014) are reported to have different spectral signatures, a better understanding of the vegetation characteristics of river-influenced peatlands will likely also facilitate efforts to better map peat swamp forests. Furthermore, improved understanding of vegetation types in the Cuvette Centrale peat swamps will likely help to reduce uncertainties in estimates of the amount of carbon stored aboveground in trees.

3.3 Chapter aims

The aim of this chapter is to compare the characteristics of the different peat swamp forest vegetation types in the central Congo Basin. The specific objectives of this chapter are: (i) to classify the vegetation of DRC's peat swamp forests based on forest structure and diversity; (ii) to classify the vegetation of DRC's peat swamp forests based on species composition; and (iii) to estimate aboveground carbon stocks of peat swamp forests in river-influenced settings in the DRC. I then compare this DRC classification with descriptions of peat swamp forest vegetation in ROC to derive a characterization of vegetation types across the total central Congo Basin peatland complex.

3.4 Methods

3.4.1 Vegetation plot measurements

Vegetation plots of 20x40 m were installed every kilometre along the seven hypothesis-testing transects (Chapter 2) to collect detailed data on aboveground biomass, forest structure and diversity, and species composition. This was done identically to the approach by Dargie et al. (2017), to provide a consistent dataset across the region.

Vegetation plots were installed regardless of whether peat was present or not, except for the final plot on the Lokolama and Bolengo transects, which are missing due to time constraints imposed by the significant field challenges in reaching these locations. In addition, two non-peat sites lack vegetation plots because they were highly disturbed: the penultimate kilometre of the Bolengo transect (BNG_7.0) lacks a vegetation plot due the presence of a manioc field, while the end point of the Tumba transect (TUM_4.0) lacks a vegetation plot because it was located in secondary forest surrounding a charcoal pit. On the other hand, two additional vegetation plots were installed at two locations where extra peat cores were collected (see Chapter 2, section 2.4.2), ensuring that every peat core had a corresponding vegetation plot. One of these plots was located away from the main Lokolama transect (LOK_Extra), and one in an old fluvial channel that crossed near the end of the Tumba transect (TUM_3.93). As such, a total of 48 vegetation plots was installed, of which eight were in non-peat forming seasonally inundated or *terra firme* forest and 40 in peat swamp forest (20 hardwood-dominated and 20 palm-dominated swamp plots).

In each plot, the diameter of all tree stems with a diameter at breast height (DBH) ≥ 10 cm was measured at a height of 1.3 m from the ground. If stilt roots, buttresses or deformities were present, the diameter was measured 30 cm above these deformations. Branched stems from the same tree with individual stems DBH ≥ 10 cm were measured separately.

Because *Raphia laurentii* palms do not typically form trunks at breast height, the diameter of the single basal stem near the ground (D_{base}) was measured instead. This was done for all *R. laurentii* specimens with a distinctly identifiable D_{base} ≥ 10 cm, after the stem base was being cleared with a machete of any dead fronds or curly black fibres that typically cover the trunk. Care was taken to measure each *Raphia* stem base individually, despite them often occurring in dense multi-individual clusters. If grouped together in such a way that individual stems were not

immediately apparent, *Raphia laurentii* stems were assigned to the same cluster, similar to how branched stems of a hardwood tree were assigned to the same individual.

The cross-sectional ground area occupied by each tree stem (basal area) was calculated as:

$$BA = \pi * \left(\frac{D}{200}\right)^2 \qquad \text{[Eq. 3.1]}$$

where *BA* stands for stem basal area (m^2) and *D* is the basal diameter near the ground (cm) in the case of *R. laurentii*, or the trunk diameter at breast height (cm) in the cases of hardwood species and all other palms.

Individual trees were identified to species level, where possible, or failing that, to genus or family level. For this, vouchers of all unique tree species were collected for botanical identification and verification at the herbarium of the Faculty of Sciences of the University of Kisangani in DRC. Botanical identification and verification were performed by local expert botanists Joseph Kanyama and Prof Corneille Ewango from the University of Kisangani, with help from Pierre Bola from ISP-Mbandaka. A list of all species names that are mentioned, including author names, is provided in Appendix II.

Height measurements of each tree stem with DBH ≥ 10 cm were taken with a laser hypsometer (manufacturer: Nikon, Kingston upon Thames, UK; model: Forestry Pro Laser Rangefinder). These measurements were used in canopy height estimations (both hardwood and palm trees) and AGB allometric equations (hardwood trees only). If no laser measurement was available for hardwood trees (n=66 out of 1,423), I estimated tree height from DBH (see 3.4.2). If no laser measurement was available for palm trees, I estimated the height of the largest palm frond by eye (n=151 out of 759 *Raphia laurentii* palms), or I estimated the trunk height by eye (n=8 out 94 *Raphia sese* palms).

3.4.2 Estimating aboveground carbon stocks

I used allometric models developed from destructively harvested and measured trees and palms to estimate total aboveground live biomass in each vegetation plot. For this, I used three equations, one for hardwood trees (Chave et al., 2014), one for the R. *laurentii* palm (Y.E. Bocko, *pers. comm.* of unpublished data, 2021), and one for other palms with trunks (largely *R. Sese;* Goodman et al., 2013). The allometric model for hardwood trees uses an estimate of stem diameter, tissue density, and height, while both palm models rely only on stem diameter.

Many different allometric equations exist for hardwood trees in local, regional or global ecosystems, including for the Congo Basin specifically (Fayolle et al., 2018). However, these are not based on trees of the central Congo Basin peat swamp forests, or tropical peat swamp forests elsewhere. Therefore, I used the pantropical allometric equation developed by Chave et al. (2014), as this model has been found to perform well across different vegetation types:

$$AGB = 0.0673 * (\rho * DBH^2 * H)^{0.976} \hspace{2cm} \text{[Eq. 3.2]}$$

where *AGB* stands for estimated aboveground biomass (kg), ρ is wood specific gravity (g cm^{-3}), *DBH* is trunk diameter at breast height (cm), and *H* is total tree height (m). This pantropical model was also used by Dargie (2015) and Dargie et al. (2017), making this model preferable for comparisons across the peatland complex.

I applied a species-specific allometric equation to all *Raphia laurentii* measurements (n=759), which was recently developed by Dr. Yannick Bocko of the University of Marien Ngouabi through destructive harvesting of 90 *Raphia laurentii* palms in the peat swamps of the Republic of the Congo (adj-R^2 = 0.86; *pers. comm.* of unpublished data, 2021):

$$AGB = e^{-6.308 + 3.211 * \ln(D_{base})} * 1.02 \hspace{2cm} \text{[Eq. 3.3]}$$

Here, *AGB* stands for estimated aboveground biomass (kg) and D_{base} is the diameter of the palm stem measured at ground base (cm). Diameter at ground base was used as a reliable metric, rather than diameter at breast height or the combined diameter of all palm fronds, as most *Raphia laurentii* stems do not reach breast height.

The single-stemmed *Raphia sese* species does form a clearly identifiable 'woody' trunk of considerable height (typically up to 10 m). This trunk contains most of the aboveground biomass of this species, as its crown often has only a few small palm fronds. Because of this different shape, the *Raphia laurentii*-specific equation in Eq. 3.3 is thought to be unsuited for *Raphia sese* trees. Instead, I used the general family-level (Arecaceae-specific) allometric model developed by Goodman et al. (2013) for all *Raphia sese* trees (n=94), which is only dependent on DBH:

$$AGB = e^{-3.3488 + 2.7483 * \ln(DBH)} \hspace{2cm} \text{[Eq. 3.4]}$$

Here, *AGB* stands for estimated aboveground biomass (kg) and *DBH* is trunk diameter at breast height (cm). This equation was also used for any other palm-species identified, such as the common oil palm (*Elaeis guineensis*), a relatively rare species in the peat swamp forests of the central Congo Basin (n=13).

Tree height for input into the hardwood allometric equation (Eq. 3.2) was measured for all, except 66 out of 1,423 trees. For this relatively small sample of hardwood trees, total tree height was estimated from measured DBH values by developing a local diameter-height model from all available paired measurements of DBH and height across the plots (n=1,357 non-palm trees; R^2 = 0.54, p<0.001; Figure 3.1a):

$$H = 7.395 * \ln(DBH) - 7.62$$ [Eq. 3.5]

where *H* is total tree height (m) and *DBH* is trunk diameter at breast height (cm).
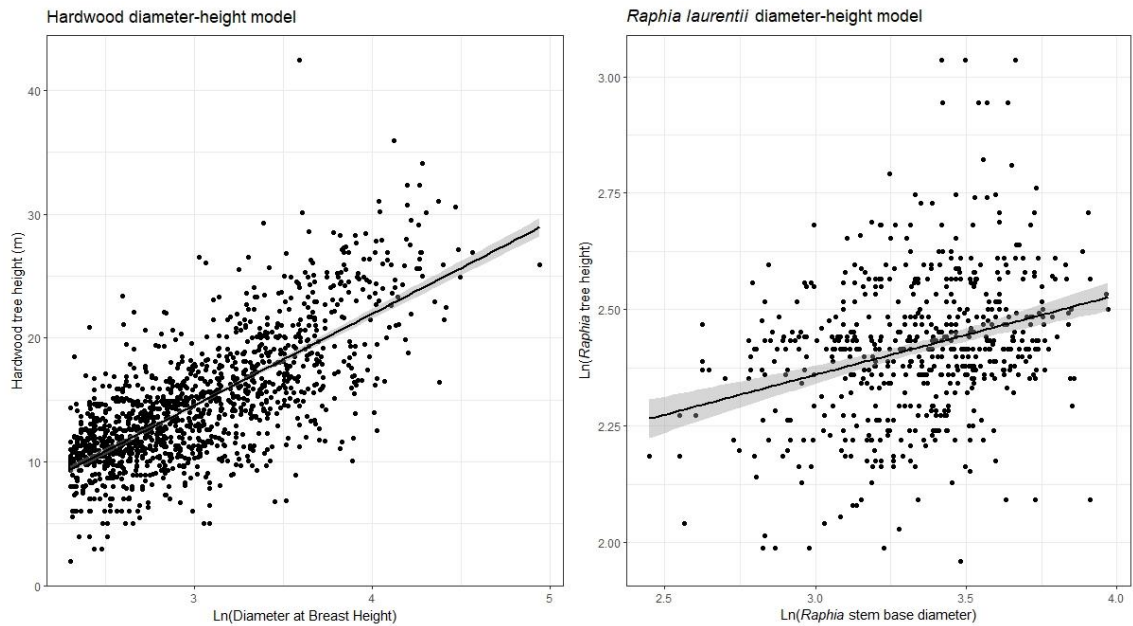
Figure 3.1. Diameter-height models for hardwood and* Raphia *palm trees. *The plots show the relationship between hardwood tree height (m) measured using the laser hypsometer and the natural logarithm of hardwood DBH (**a**), or between the natural logarithm of* Raphia laurentii *tree height (m) measured using the laser hypsometer and the stem base diameter of* Raphia laurentii *palms (**b**). Black lines show the best-fitting linear regressions (n=1,357, R² = 0.54, p<0.001; and n=588, R² = 0.09, p<0.001, respectively). Shaded grey shows the 95% confidence intervals.*

The only predictor variable required in the *Raphia laurentii*-specific model (Eq. 3.3) is the diameter of the palm stem at ground base. However, for a small selection of *Raphia laurentii* palms (n=23), no measurement of stem diameter at ground base was available. For these palms, I developed a reversed, local diameter-height model based on the diameter-height relationship of all *Raphia laurentii* palms for which both stem base diameter and accurate height measurements from the laser hypsometer were available (n=588, R^2 = 0.09, p<0.001; Figure 3.1b):

$$D_{base} = e^{2.063 + 0.5279 * \ln(H)}$$ [Eq. 3.6]

Here, D_{base} is the diameter of the *Raphia* palm stem at ground base (cm) and H is the total estimated palm height (m). The explanatory power (R^2) of this model is very low. However, this was judged not to be too problematic, as this is only used to estimate D_{base} for 3% of *Raphia laurentii* specimens. Furthermore, both biomass and total palm height of *R. laurentii* are low and exhibit much less variation than hardwood trees. Therefore, the uncertainty and potential bias introduced in the aboveground biomass of a plot by applying this reversed diameter-height model to a limited number of palm trees is thought to be small.

Wood specific density of hardwood species was obtained from a specific swamp dataset from northern Republic of the Congo (Bibi-Loumoni, 2019), the Global Wood Density Database (Chave et al., 2009; Zanne et al., 2009), or the Central African wood density database (Momo et al., 2020; Ploton et al., 2020b).

No tissue density was required in the allometric models of palm species. Nonetheless, density values were assigned to estimate mean tissue specific density per vegetation plot. For this, I used a mean genus-specific value of 0.23 g cm^{-3} for both the common *Raphia laurentii* and *Raphia sese* palm species, obtained by Dr. Yannick Bocko of the University of Marien Ngouabi from direct measurements of 90 *Raphia laurentii* palms (*pers. comm.* of unpublished data, 2021). For the occasional presence of the common oil palm tree (*Elaeis guineensis*), I used the species-specific value of 0.395 g cm^{-3} reported by Porankiewicz et al. (2006).

As wood density is highly species-specific (Phillips et al., 2019), mean wood density values at species-level were used as much as possible. If trees were not identified at species-level, or no species-specific wood density values were available, the mean value at genus-level was used. If trees were not identified at genus-level, or no genus-specific wood density values were available, the mean value at family-level was used. If trees were not identified at family-level, or no family-specific wood density values were available, the mean plot value was used to estimate wood density.

Total aboveground live biomass of each plot (AGB, in Mg dry mass ha^{-1}) was calculated by summing the estimated AGB of all individual trees. Finally, estimates of AGB were converted to aboveground live carbon stocks (AGC, in Mg C ha^{-1}) by multiplying by a factor 0.47, the mean observed carbon fraction in tropical angiosperms (Thomas & Martin, 2012).

3.4.3 Estimating species diversity

Species diversity of each vegetation plot was first assessed by calculating species richness (*SR*), the absolute number of unique species found in each plot (*S*), including distinct morphospecies in a plot that did not have a formal identification to species level:

$$SR = S \qquad\qquad \text{[Eq. 3.7]}$$

However, species richness only represents one important component of species diversity. Besides richness, another component of diversity is evenness: the distribution of species' relative abundances in a community, which is expressed as the number of individual trees counted for each species as a fraction of the total number of trees per site (Daly et al., 2018). Therefore, I calculated two other common metrics of species diversity: the Gini-Simpson diversity index (*GS*) and the Shannon-Wiener index (*SW*). The Gini-Simpson diversity index represents the probability that two individual specimens randomly selected from the population represent different species. It was calculated by summing the squared relative abundances of each species, using the following equation:

$$GS = 1 - \sum_{i=1}^{N}\left(\frac{n_i}{N}\right)^2 \qquad\qquad \text{[Eq. 3.8]}$$

Here, *n* is the total number of individuals of the *i*th species at the site, and *N* is the total number of individuals of all species at that site. By subtracting the summation over all species from 1, the index has a positive relationship with diversity, meaning the greater the value, the greater the species diversity. The Shannon-Wiener index was calculated from the same relative abundance data, using the following equation:

$$SW = -\sum_{i=1}^{N}\left(\frac{n_i}{N} * \ln\left(\frac{n_i}{N}\right)\right) \qquad\qquad \text{[Eq. 3.9]}$$

Here, *n* is again the total number of individuals of the *i*th species at the site, and *N* is the total number of individuals of all species at that site. Like with the GS diversity index, the greater the SW index value, the greater the species diversity. Theoretically, the Shannon-Wiener index measures the uncertainty (entropy) in predicting the species identity of a randomly sampled tree within a plot. Generally, it is seen as giving more weight to richness, while the Gini-Simpson index gives relatively more weight to evenness (Daly et al., 2018). Both the Gini-Simpson index and the Shannon-Wiener index were calculated from relative abundance data whereby multi-stemmed (hardwood) or clustered (*R. laurentii* palm) stems were counted as the same individual.

3.4.4 Classifying vegetation by forest structure and diversity

Forest structure was characterized for each peat swamp plot (n=40) along the seven hypothesis-testing transects based on the following eight variables: stem density; stem density excluding *Raphia laurentii*; the proportion of palms; total basal area; mean tree height; mean DBH; mean wood specific gravity; and total aboveground biomass.

Because of the clustered nature of *Raphia laurentii* palm trees, individuals of this species were treated differently than hardwood trees or other palm species in the calculation of these variables. For stem density (the total number of stems per hectare) multi-stems of the same hardwood tree with DBH ≥ 10 cm were counted as separate stems, while *Raphia laurentii* individuals with *Dbase* ≥ 10 cm were counted as separate stems, irrespective of how clustered these palm stems were. Since this can heavily skew stem density towards *Raphia laurentii*-dominated plots, which sometimes contain a large number of stems in a small number of clusters, I also calculated a stem density that excludes *Raphia laurentii* (but includes *Raphia sese* or *Elaeis guineensis*).

The proportion of palms (% *Raphia* or *Elaeis* individuals out of total number of individuals) was calculated based on relative abundances. Like multi-stemmed hardwood trees, clustered *Raphia laurentii* palms were counted as if originating from the same individual, to prevent skewing of the data by the presence of a small number of clusters with many individuals.

Total basal area (m^2 ha^{-1}) was obtained by applying Eq 3.1 to each individual stem, including multi-stemmed hardwood trees or clustered *R. laurentii* palms. Similarly, mean tree height (m), mean DBH (cm), and mean wood specific gravity (g cm^{-3}) were calculated by treating every multi-stemmed or clustered stem as a separate datapoint.

The eight forest structure variables were then combined with the three measurements of species diversity (species richness, Gini-Simpson diversity index and Shannon-Wiener index) into one dataset to group plots according to similar vegetation types. For this, I used k-means clustering, which is an unsupervised machine learning approach to divide datasets into a pre-specified number of distinct clusters. It has the advantage over other clustering approaches, such as hierarchical clustering, that it can produce a useful two-dimensional visualization of the proximity between datapoints (Tan et al., 2019).

I tested multiple pre-specified numbers of clusters, each corresponding with a distinct hypothesis: (i) two clusters to test the hypothesis that a difference between hardwood- and palm-dominated peat swamps can be found; (ii) three clusters to test the hypothesis that an additional subdivision between riverine and non-riverine vegetation can be detected within either one of the palm- or hardwood-dominated peat swamp type; and (iii) four clusters to test the hypothesis that both hardwood- and palm-dominated peat swamps can each be subdivided in a riverine and non-riverine type.

I used the *factoextra* package in R (version 1.0.7; Kassambara & Mundt, 2020) to implement k-means clustering and visualization, using the default Euclidian distance to measure the (dis)similarity of observations, and with *nstart* set to 25. This provides the best clustering result out of 25 initial start configurations. All data was standardized (scaled), such that each variable has a mean of zero and a standard deviation of one to make them comparable.

3.4.5 Classifying vegetation by species composition

Both the Gini-Simpson and Shannon-Wiener indices used here represent alpha-diversity, the species richness at the local plot scale. Beta-diversity, on the other hand, is the rate of change in the species composition of communities between plots (typically over distance within a larger landscape or along an environmental gradient). Together, alpha- and beta-diversity determine gamma-diversity, which is the total species diversity at regional scale (Tuomisto, 2010). To analyse beta-diversity among the different peat swamp forests sites in the Cuvette Centrale, the (dis)similarity in floristic composition between pairs of vegetation plots was calculated using the Bray-Curtis dissimilarity statistic, which measures the proportion of the total species abundances in which two plots differ (Ricotta & Podani, 2017). The Bray-Curtis dissimilarity statistic is defined as:

$$BC_{UV} = \frac{\sum_{i=1}^{N}|A_{Ui}-A_{Vi}|}{\sum_{i=1}^{N}(A_{Ui}+A_{Vi})} \qquad \text{[Eq. 3.10]}$$

Here, BC_{UV} is the Bray-Curtis dissimilarity statistic for the two plot sites *U* and *V* that are being compared, with A_{Ui} and A_{Vi} being the abundance values of the ith species at each site, and *N* is the total number of species across both sites combined.

The Bray-Curtis statistic was chosen as it has been used to analyse similar swamp forest vegetation types in Peruvian peatlands (Honorio Coronado et al., 2021), as well as in seasonally flooded and *terra firme* forests in northern Republic of Congo (Ifo et al., 2018). To calculate the

Bray-Curtis statistic for each plot combination, a species matrix was first constructed, where each column represents a unique species found across the entire dataset, and each row represents one vegetation plot. Species composition was recorded in the matrix as abundance counts of individual specimens, whereby branched (hardwood) or clustered (palm) stems were counted as the same individual.

Following similar analyses of compositional diversity in the peat swamp forests of the Amazon basin (Draper et al., 2018; Honorio Coronado et al., 2021), the dissimilarity matrix for all plot combinations was then used to create non-metric multidimensional scaling (NMDS) ordinations optimized for two axes, in order to visualize the compositional diversity between plots and within transect groups and identified clusters. NMDS is a rank-based approach to ordination, meaning the absolute Bray-Curtis dissimilarities are replaced by ranks, which makes it a flexible technique that is suitable for often incomplete ecological datasets (Clarke, 1993).

A non-parametric permutational multivariate analysis of variance (PERMANOVA; Anderson, 2001) was conducted to test the significance of the variation in species composition among different groups. These groups are: (i) the seven transects; (ii) the field-identified hardwood- and palm-dominated swamp classes; and (iii) the clusters in forest structure and diversity identified through k-means clustering. The Bray–Curtis dissimilarity matrix was used as the response variable. However, since the data has been collected in a semi-nested design, with vegetation plots grouped in correlated transects that will exhibit spatial autocorrelation, a correction is applied when testing the significance of variation among the identified clusters. This is done by adding transect group as additional predictor variable to the permutational multivariate analysis. Post-hoc comparisons between the identified groups were subsequently analysed using a pairwise comparison (Dunn's Kruskal-Wallis multiple comparison test with Benjamini-Hochberg-adjusted p-values), again with transect group as additional predictor variable.

All dissimilarity and ordination analyses were conducted in the R statistical environment (R Core Team, 2019), using the *adonis* function in the *vegan* package (version 2.5-7; Oksanen et al., 2013), with 999 permutations. For pairwise comparison, I used the *pairwise.adonis2* function in the *pairwiseAdonis* package (version 0.4; Martinez Arbizu, 2020), again with 999 permutations.

Indicator species that are driving dissimilarities between groups and characterise identified clusters were subsequently analysed with the *multipatt* function from the *indicspecies* package (version 1.7.9; De Cáceres et al., 2020), again with 999 permutations. This function implements a multi-level pattern analysis using a method developed by De Cáceres et al. (2010). In this analysis, I compared indicator species for each cluster separately, following Dufrêne and Legendre (1997), as well as for possible combinations of clusters.

To study what environmental predictors are driving species composition, environmental factors were overlaid onto the NMDS ordination plots produced. For this, I used the *envfit* function in the *vegan* package (version 2.5-7; Oksanen et al., 2013), with 999 permutations. As environmental factors, I used six variables measured in the field (peat thickness, pH, EC, estimated maximum inundation height during the wet season, maximum water table depth as measured during the dry season, and the absolute water table fluctuation), as well as six remotely-sensed climatological and topographic variables (annual precipitation, precipitation seasonality, temperature, potential evapotranspiration, SRTM elevation and slope). The three climatic variables (annual precipitation [mm yr^{-1}], precipitation seasonality [coefficient of variation], and temperature [°C]) were obtained from the WorldClim database (Fick & Hijmans, 2017). Potential evapotranspiration (mm yr^{-1}) was obtained from the Global Aridity Index and Potential Evapotranspiration Database (Trabucco & Zomer, 2019). Pre-processed SRTM-derived elevation and slope products (USGS, 2006), void-filled with ASTER GDEM data (NASA/METI, 2011), were obtained for the central Congo Basin from Dargie et al. (2017). All datasets were resampled to 50 m resolution, using a nearest neighbour resampling method in IDL-ENVI geospatial software (version 8.7-5.5).

3.5 Results

3.5.1 Aboveground carbon stock of peat swamp forests

Mean aboveground live carbon stock across all measured peat swamp forest plots in DRC is 97.8 Mg C ha^{-1} (median 91.0 Mg C ha^{-1}; s.d. 41.1 Mg C ha^{-1}; n=40). However, the aboveground live carbon stock of hardwood-dominated peat swamps (mean 114.1 Mg C ha^{-1}; median 117.1 Mg C ha^{-1}; s.d. 32.2 Mg C ha^{-1}; n=20) is significantly higher than that of palm-dominated peat swamps (mean 81.5 Mg C ha^{-1}; median 70.1 Mg C ha^{-1}; s.d. 45.2 Mg C ha^{-1}; n=20; Mann–Whitney U test, p<0.005), as shown in Figure 3.2.
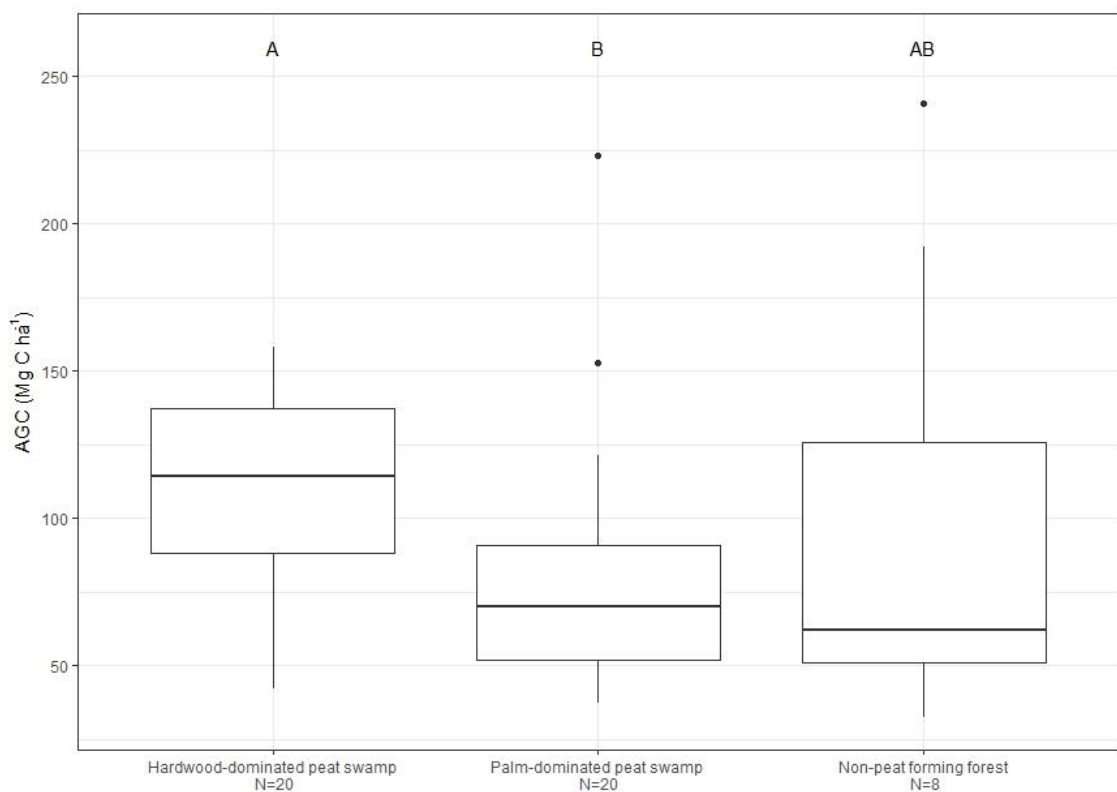
Figure 3.2. Boxplot of aboveground live carbon stocks (AGC) per vegetation class. *The black line shows the median value. The box shape shows the upper and lower quartiles. The vertical lines show the minimum and maximum values. Circles represent outlying values. Classes that do not share a common letter are significantly different (p<0.05, Dunn's Kruskal-Wallis multiple comparison test, p-values adjusted with the Benjamini-Hochberg method). Non-peat forming forest includes both* terra firme *and non-peat forming seasonally inundated forest.*

When testing the AGC difference between hardwood- and palm-dominated swamp plots within individual transects, to correct for the influence of the nested transect design, none of the transects shows a statistical difference. Similarly, a linear regression model that includes transect interaction effects provides a significant correlation (adj-R^2 = 0.56, p<0.001), but only

because some of the interaction effects are significant. This indicates that differences in AGC between transects are due to a predominance of certain peat swamp types in specific transects. For example, it can be observed that AGC is significantly lower along the Bondamba transect on the one hand, than along the Bolengo, Ikelemba, Boloko and Tumba transects on the other (Figure 3.3). This effect is largely driven by the dominance of palm trees with lower biomass in Bondamba. However, the variation within individual transect groups can be large, such as in the case of Tumba (n=3), especially given the relatively low sample size per transect.
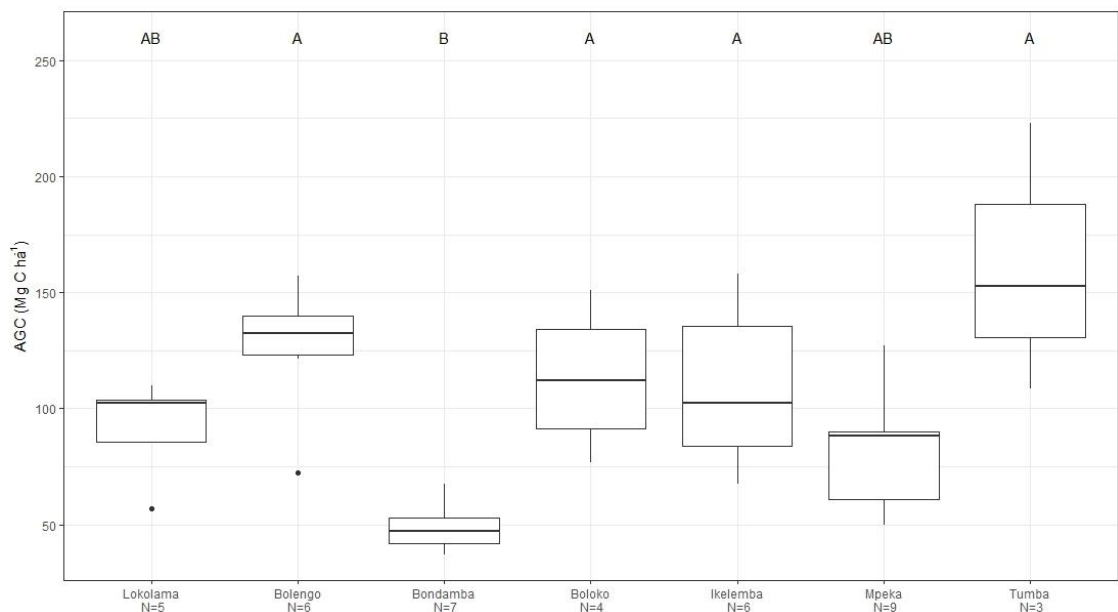
Figure 3.3. Boxplot of aboveground carbon stocks (AGC) per transect. *The black line shows the median value. The box shape shows the upper and lower quartiles. The vertical lines show the minimum and maximum values. Circles represent outlying values. Classes that do not share a common letter are significantly different (p<0.05, Dunn's Kruskal-Wallis multiple comparison test, p-values adjusted with the Benjamini-Hochberg method). Transects are ordered by increasing High-Water Fraction (HWF).*

A marginally significant difference is found between the AGC of peat swamp vegetation in transects adjacent to the Ruki and Ikelemba rivers (mean 89.6 Mg C ha^{-1}; n=28) and transects not adjacent to one of the two major rivers (mean 116.9 Mg C ha^{-1}; n=12; Mann–Whitney U test, p=0.06). However, again, this effect is likely driven by the low aboveground carbon values found in the palm swamps of the Bondamba transects, which runs perpendicular to the Ruki transect.

Similarly, mean AGC is slightly higher in high-water sites with maximum inundations > 50 cm (mean 115.1 Mg C ha^{-1}; n=13) than in low-water sites (mean 88.3 Mg C ha^{-1}; n=27). This suggests a predominance of hardwood trees in seasonally inundated forests, although the difference is only marginally significant (Mann–Whitney U test, p=0.09).

Finally, no significant differences are found between the two peat swamp forest classes and the non-peat forming forest class. However, this latter class has a low sample size (n=8) so this not unexpected. Therefore, the rest of this chapter will focus on the 40 plots that are located in peat swamp vegetation only.

3.5.2 Peat swamp forest vegetation types

A total of 152 species was encountered across the 40 peat swamp forest vegetation plots. Within this group, *Raphia laurentii* and *Oubanguia africana* clearly dominate, as these two species alone account for a quarter of all individuals counted (Figure 3.4a). Furthermore, just six other species make up another quarter, together accounting for half of all peat swamp trees encountered. These eight species are, from high to low relative abundance: *Raphia laurentii* (16.8% of all individuals)*, Oubanguia africana* (8.5%)*, Raphia sese* (5.3%)*, Guibourtia demeusei* (4.9%)*, Cryptosepalum congolanum* (4.0%)*, Pseudagrostistachys ugandensis* (3.9%)*, Coelocaryon botryoides* (3.6%) and *Carapa palustris* (2.9%). A further total of ten species makes up another 18%, together covering two-thirds of all individuals counted. On the other hand, 49 trees are represented by a single individual (2.75% of all individuals), while 18 species are represented by just two individuals (2.0% of all individuals).

For genera (Figure 3.4b), there are 101 genera counted across the 40 plots. *Raphia* (22.1%) and *Oubanguia* (8.5%) again dominate. Together with *Diospyros* (6.1%), *Guibourtia* (4.9%), *Cryptosepalum* (4.0%) and *Coelocaryon* (3.9%), these genera make up half of all individuals. This contrasts with 26 genera that are represented by a single individual (totalling 1.5%).

For families (Figure 3.4c), there are 40 families counted across the 40 plots. The *Arecaceae* (palm) family clearly dominates with 22.8% of all individuals. However, the *Fabaceae* family is the most dominant among the hardwood species (20.7%), followed by *Lecythidaceae* (8.6%), *Phyllanthaceae* (6.9%), *Euphorbiaceae* (6.2%) and *Ebenaceae* (6.1%). These five families together account for almost half of all individuals encountered, while 12 families are represented by a single individual (totalling 0.7%).
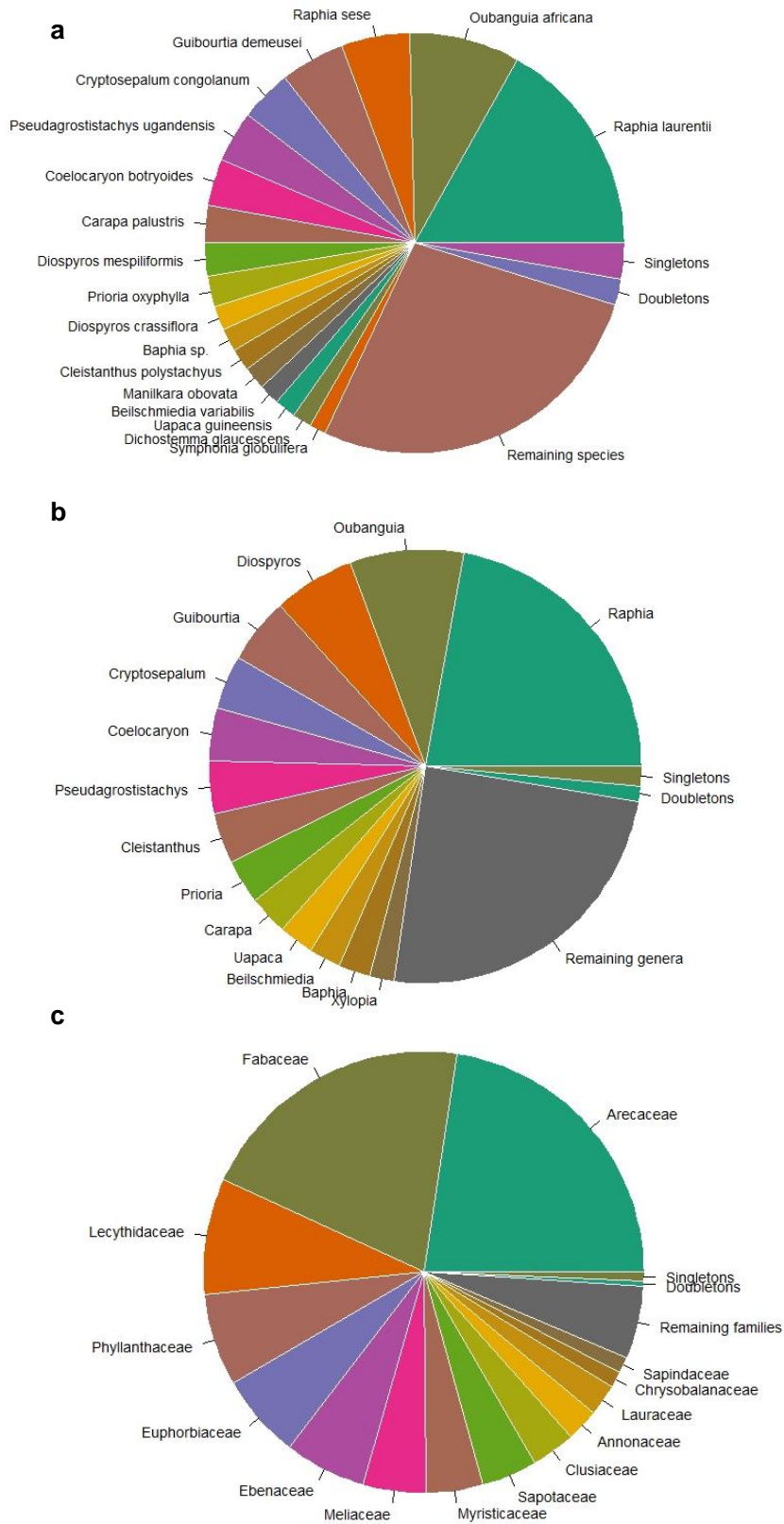
Figure 3.4. Distribution of species, genera and families in peat swamp forest plots. *Each pie charts showing the distribution of most abundant species (**a**), genera (**b**) and families (**c**) in 40 peat swamp forest vegetation plots. Remaining species/genera/families includes singletons and doubletons.*

3.5.2.1 Clustering of forest structure and diversity

Figure 3.5 shows the results of k-means clustering of the 40 peat swamp plots based on 11 variables of forest structure and diversity. Each panel (Fig. 3.4a-c, respectively) shows the resulting clusters based on 2, 3 or 4 pre-specified number of clusters. The closer two points are in each of the diagrams, the more similar these vegetation plots are. The two dimensions plotted in each of the four panels together explain 83.0% of variability in the dataset. It can be observed that dimension 1 along the x-axis (explaining 72.1% of variability) consistently separates cluster 1 (dark green) from the other plots. This dimension can be thought of as separating hardwood- from palm-dominated vegetation types (from left to right), as cluster 1 contains nine vegetation plots that were identified as palm-dominated in the field. This cluster includes all palm-dominated swamp sites along the Bondamba transect, as well as some palm-dominated sites along the Mpeka transect. On average, the nine plots in cluster 1 consist of 86% palm trees, and are characterised by lower mean tree height, wood specific gravity, species diversity (SR, GS and SW) and AGB, as well as higher mean DBH, basal area and stem density (Table 3.1).
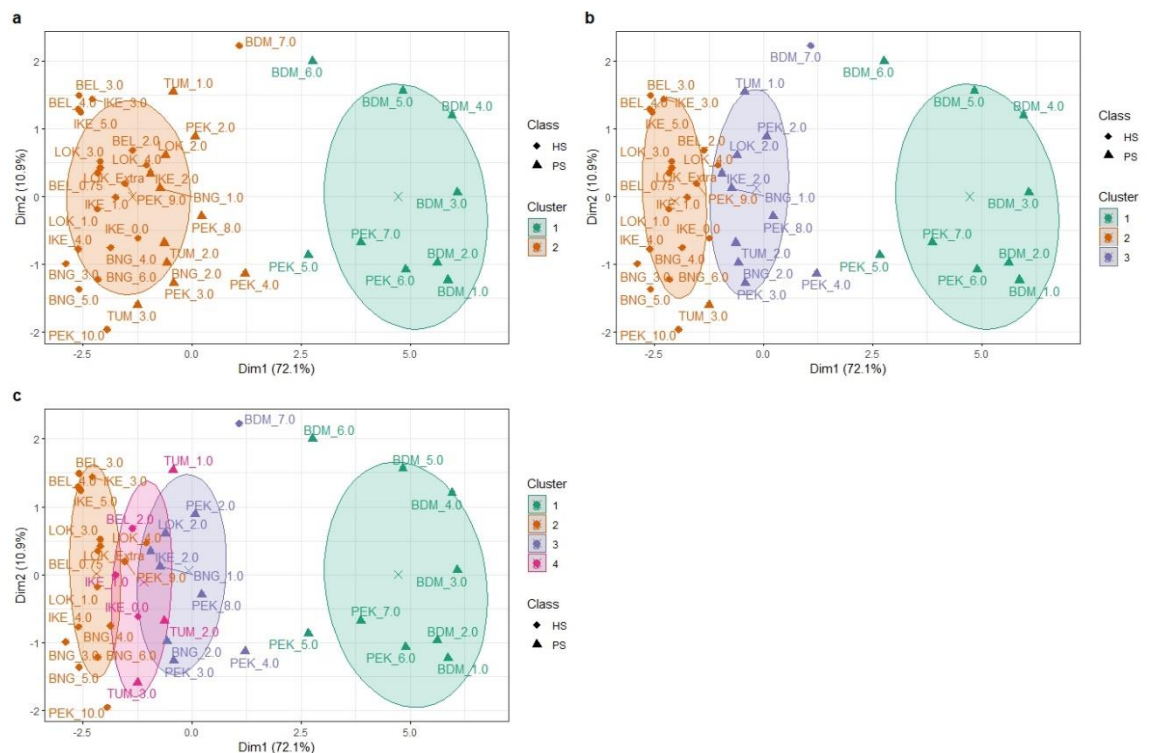
Figure 3.5. k-Means clustering of 40 peat swamp vegetation plots along two principal axes, based on forest structure and diversity. *The number of clusters was pre-specified as 2 (**a**), 3 (**b**), or 4 (**c**). The two principal components (Dim1 and Dim2) together explain 83% of variability. Ellipses represent the 1-sigma (68%) confidence interval for a multivariate t-distribution per cluster, with a cross showing the central points.*

However, not all field-identified palm swamp sites are part of cluster 1, as 11 palm-dominated plots are included in cluster 2. This second group (cluster 2 in orange in Fig. 3.4a) represents sites with hardwood-dominated and mixed vegetation, consisting on average of only 15% palm trees, and having higher mean tree height, wood specific gravity, species diversity and AGB, in combination with lower mean DBH, basal area and stem density (Table 3.1).

Figure	Cluster	n =	Height	DBH	WSG	BA	Stem density	Stem density excl. *R. laurentii*	Palms	AGB	SR	GS index	SW index
3.4a	1*	9	11.0	29.2	0.259	60.4	856	75	86	114	3.8	0.27	0.58
	2	31	14.1	24.3	0.561	34.4	577	491	15	233	15.5	0.86	2.34
3.4b	1*	9	11.0	29.2	0.259	60.4	856	75	86	114	3.8	0.27	0.58
	2	20	14.8	23.5	0.598	32.9	562	537	7	258	17.3	0.87	2.46
	3	11	12.8	25.7	0.494	37.0	605	407	30	187	12.3	0.84	2.12
3.4c	1*	9	11.0	29.2	0.259	60.4	856	75	86	114	3.8	0.27	0.58
	2	16	15.2	23.4	0.594	31.0	548	516	5	233	18.1	0.90	2.58
	3	9	12.8	26.1	0.489	36.7	583	342	29	167	12.4	0.85	2.17
	4	6	13.0	24.1	0.581	39.9	646	646	22	331	13.2	0.78	1.98

Table 3.1. Overview of 11 forest structure and diversity metrics for different k-means clusters of 40 peat swamp vegetation plots. *The number of pre-specified clusters is 2, 3 or 4 (Fig. 3.4a-c, respectively). All values are cluster averages of vegetation plot means. n indicates the number of vegetation plots per cluster. Height is mean plot tree height (m). DBH is mean plot diameter at breast height (cm). WSG is mean plot wood specific gravity (g cm^{-3}). Basal area is total plot basal area (m^2 ha^{-1}). Stem density is total number of stems per plot (ha^{-1}), either with or without* Raphia laurentii. *Palms is the proportion (%) of palm species (Raphia or Elaeis) per plot. AGB is total plot aboveground biomass (Mg ha^{-1}). SR is species richness. GS index is the Gini-Simpson diversity index. SW is the Shannon-Wiener index. Rows identified by * are identical clusters.*

The second cluster can be further separated into two subgroups when applying 3-means clustering. A first subgroup (cluster 2 in orange in Fig. 3.4b) has few palms present (the average plot has 7% palms). It can be contrasted with a second subgroup (cluster 3 in blue in Fig. 3.4b) that has medium palm dominance (30%). Thus, with three pre-specified clusters, a palm-dominated swamp type, a hardwood-dominated swamp type and a mixed palm/hardwood swamp type can be identified. This grouping largely corresponds with how these plots were described in the field. All plots from cluster 1 were correctly identified in the field as palm-dominated based on visual observation only, while 19 out of 20 plots from cluster 2 where correctly identified as hardwood-dominated. However, the third mixed swamp cluster tends to

be described as palm-dominated in the field, with ten out of 11 plots being identified as palm-dominated based on visual inspection only.

The hardwood-dominated swamp in cluster 2 is characterized by the greatest species diversity of all clusters and consists of relatively tall and slim trees with high aboveground biomass stocks (Table 3.1). This group is mostly made up of the hardwood swamp sites along the second half of the Boloko transect and the second half of the Ikelemba transect. The mixed swamp type, cluster 3, on the other hand, is characterized by lower species diversity, shorter tree height, and lower aboveground biomass, because of a larger presence of palm species. It is mostly found along the start of the Mpeka and Bolengo transects, and the endpoint of the Bondamba transect.

When using 4-means clustering, the picture becomes even more nuanced, with the hardwood-dominated swamp and mixed swamp clusters fragmenting even further. Another mixed swamp type of six plots is identified (cluster 4 in pink in Fig. 3.4c). This vegetation type is characterised by medium palm presence (22%), but with the greatest aboveground biomass (331 Mg ha^{-1}). However, mean stem density of this cluster is the same when including or excluding *Raphia laurentii* palms, indicating that the palms present here are mostly *Raphia sese*. This vegetation type is made up of plots along the Tumba transect and the first half of the Ikelemba transect that are strongly inundated during the wet season. In the field, based on visual observation only, half of the plots in this cluster were identified as palm-dominated, and half as hardwood-dominated.

3.5.2.2 Comparing species composition

To understand how these clusters relate to floristic diversity, it is useful to study the results of the NMDS ordination of species composition, shown in Figure 3.6. The closer two points are in these diagrams, the more similar they are in terms of species composition. Figure 3.6a shows the NMDS ordination diagram with all plot IDs grouped by transect. It can be observed that most transect are clustered, meaning that vegetation plots resemble other vegetation plots along the same transect in terms of floristic diversity. The only exception is the Ikelemba transect (light green), which is notably spread out across the second NMDS dimension (y-axis). In addition, a similar pattern as with forest structure (Figure 3.5) can be seen, with most field-identified palm-dominated sites (triangles) clustered together on the left, while mostly hardwood-dominated sites (diamonds) are clustered on the right (note the reversal of orientation along the x-axis, compared with Figure 3.5).

Figure 3.6b-d show the same ordination diagram, but then with all vegetation plots grouped by the four clusters identified through k-means clustering in Figure 3.5c. The ordination diagram in the upper right panel (Figure 3.6b) shows plot IDs, while the diagrams on the bottom row are overlaid with either the 11 forest structure variables in ordination space (Figure 3.6c), or ten environmental variables (Figure 3.6d). It can be observed from the 1-sigma (68%) confidence intervals around each cluster that cluster 1 (*Raphia laurentii* palm-dominated) and 4 (mixed swamp forest) are clearly distinct of the other clusters in terms of floristic diversity. However, cluster 2 (hardwood-dominated) and 3 (mixed swamp forest) share a slight overlap, indicating more floristic similarity between these clusters.
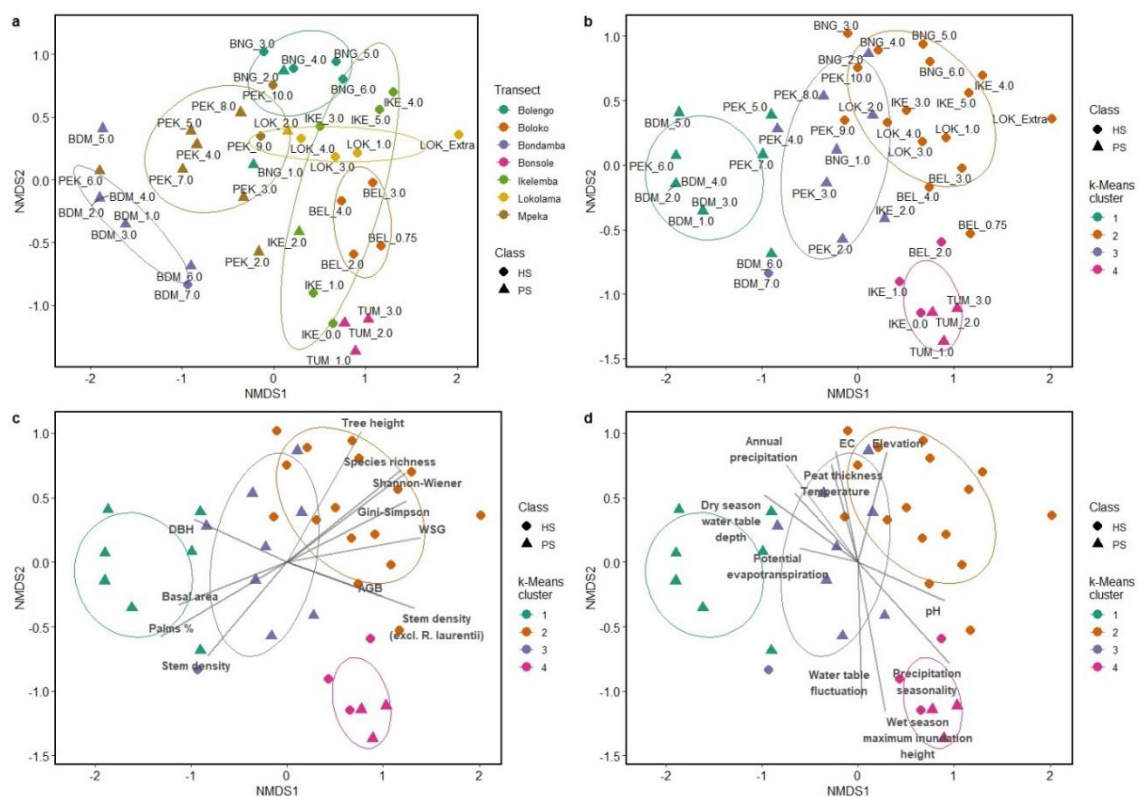
Figure 3.6. NMDS ordination of floristic dissimilarity among 40 peat swamp forest plots. *Panels show plots coloured by transect group (**a**), or coloured by the four clusters identified through k-means clustering (**b-d**). Ellipses represent the 1-sigma (68%) confidence interval for a multivariate t-distribution per transect or cluster. **a/b** show plot IDs, while **c** is overlaid with 11 forest structure variables and **d** is overlaid with 11 significantly correlated environmental variables (p<0.01). The length of the arrows in panel **c/d** indicates the strength of the association. In all panels, point shapes (triangles and diamonds) differentiate between field-identified vegetation classes (HS: hardwood-dominated peat swamp, PS: palm-dominated peat swamp). All ordination diagrams are optimized for two dimensions.*

A separation of palm-dominated plots (left) from hardwood-dominated plots (right) can generally be seen along the x-axis (NMDS1) in Figure 3.6c. Palm-dominated swamps tend to have lower species diversity, wood specific gravity and tree height, but greater basal area, stem

density when including *R. laurentii*, and average DBH. Hardwood-dominated swamps, on the other hand, tend to have greater species diversity, wood specific gravity, tree height, AGB and stem density, when excluding *R. laurentii.* However, there are some palm-dominated plots on the right of this axis, in cluster 4 (pink), which appear to differ from this pattern. This could partly be because cluster 4 is a mixed swamp type with medium palm presence (22%). Even so, part of this is likely explained by the fact that some of these plots could have been misclassified in the field due to a dominance of juvenile palms in the understory. The canopy of these sites is in fact largely dominated by hardwood trees, meaning these sites should probably have been classified as hardwood-dominated in the field.

A second pattern can be seen on the right side of the ordination diagrams, where hardwood swamp plots appear to be stretched out along the y-axis (NMDS2), with denser and more biomass-rich sites towards the bottom of the ordination space, and less dense, but taller and more diverse sites towards the top of the ordination space. The former group, associated with cluster 4, includes typically seasonally inundated plots from Tumba and the first half of the Ikelemba transect, while the latter group, associated with cluster 2, includes plots with lower inundation levels from Bolengo, Lokolama and the second half of the Ikelemba transect.

PERMANOVA analysis, to detect significant differences in species composition between groups of plots, indicates how the sampling design, in the form of seven transect groups, explains about half of the variability in species composition (R^2 = 0.52; p<0.001). However, after correcting for this grouping factor, a significant difference between the field-identified hardwood- and palm-dominated swamp types is still observed (R^2 = 0.16; p<0.001).

Eight significant indicator species (De Cáceres et al., 2010) are found that drive the difference between hardwood- and palm-dominated swamp forests types as identified in the field. *Raphia laurentii* is a significant indicator of palm-dominated swamp forest (p<0.001), while *Coelocaryon botryoides, Cleistanthus mildbraedii, Dichostemma glaucescens* (all p<0.01), *Carapa palustris*, *Symphonia globulifera, Uapaca corbisieri* and *Manilkara obovata* (all p<0.05) are significant indicators of hardwood-dominated swamp forest.

PERMANOVA analysis, again correcting for the transect design, shows that the four identified clusters are also significantly different from each other in terms of species composition (R^2 = 0.15; p<0.001). Post-hoc analysis shows that the pairwise differences between each of the

possible cluster combinations are significantly different when correcting for the transect design (all p<0.001). This shows that species composition is not only significantly different between clusters 1 and 4, clusters 1 and 2/3, and clusters 4 and 2/3, of which the ellipses do not overlap in Figure 3.6, but also between cluster 2 and 3, which have partially overlapping ellipses.

Twenty-one significant indicator species are identified when analysing the four k-means clusters. In the case of cluster 1, the palm-dominated peat swamp type, this is *Raphia laurentii* (p<0.001), often in association with *Cleistopholis patens* (n.s.). In the case of cluster 2, the hardwood-dominated peat swamp type, the indicator species are *Coelocaryon botryoides* (p<0.001), *Cleistanthus mildbraedii*, *Dichostemma glaucescens* (both p<0.01)*, Uapaca corbisieri* and *Pseudagrostistachys ugandensis* (both p<0.05). In the case of cluster 3, the mixed peat swamp type, the indicator species is *Cryptosepalum congolanum* (p<0.001). However, cluster 2 and 3 share *Carapa palustris* and *Entandrophragma palustre* (both p<0.05) as common indicator species too. Finally, in the case of cluster 4, the mixed peat swamp type that is typically found in seasonally inundated sites, the indicator species are *Oubanguia africana*, *Cleistanthus polystachyus, Raphia sese, Baphia laurentii* (all p<0.001), *Homalium africanum, Prioria buchholzii, Garcinia ovalifolia, Isoberlinia doka, Guibourtia demeusei* (all p<0.01), *Chionanthus* sp., *Crotonogynopsis* sp. and *Albizia altissima* (all p<0.05).

When overlaying the ordination diagram with the 12 selected environmental variables (Figure 3.6d), 11 of these were found to be significantly correlated (all p<0.01). Only slope was not significantly correlated and therefore left out of the diagram. It can be observed that the y-axis corresponds with a gradient from stable water tables (top) to fluctuating water tables (bottom). The fourth cluster of mixed swamp vegetation is strongly related to larger water table fluctuations, greater maximum inundation height, as well as greater precipitation seasonality. In opposite direction along the y-axis, it can be seen that cluster 2, the hardwood-dominated swamp, is related to higher elevations, greater electrical conductivity, greater peat thickness, less acidic conditions (greater pH), and potentially greater annual precipitation.

The environmental differentiation along the x-axis is less clear-cut. However, it appears that palm-dominated sites in cluster 1 (to the left of the diagram) are related to lower water table depths, as measured during the dry season, as well as possibly greater potential evapotranspiration and more acidic conditions (lower pH).

3.6 Discussion

Peat swamp forests in the DRC are characterized by relatively low levels of aboveground carbon, storing 97.8 Mg C ha^{-1} on average. This is about half of the mean AGC found in Central African tropical forests (~202 Mg C ha^{-1}; Lewis et al., 2013). Like Dargie et al. (2017), it was found that mean AGC is significantly higher in hardwood-dominated peat swamps (114.1 Mg C ha^{-1}) than in palm-dominated peat swamps (81.5 Mg C ha^{-1}). However, this difference is smaller than the difference reported by Dargie et al. (2017) for ROC swamps, who measured 123.6 and 67.0 Mg C ha^{-1} for the two vegetation types, respectively. This might suggest that the AGC estimates of palm-dominated swamps by Dargie et al. (2017) are an underestimation, potentially caused by the use of a generic rather than species-specific palm allometric equation. However, mean AGC of vegetation cluster 1 in the DRC swamps, which was found to represent largely monodominant palm swamps and thus likely provides the best estimate of truly palm-dominated vegetation, is only 54 Mg C ha^{-1}, in line with the findings of Dargie et al. (2017). One cause of the higher AGC observed across DRC plots classified in the field as palm-dominated appears to be that some DRC sites have been incorrectly classified in the field. This seems to be specifically the case for seasonally inundated swamp forests, such as cluster 4 of the k-means clustering, which often have an understory composition largely made up of small palms, causing them to be classified as palm-dominated in the field, while the canopy is in fact dominated by tall hardwood tree. The AGC of palm-dominated plots in DRC, excluding those in cluster 4 (n=3) is only 68 Mg C ha^{-1}, suggesting that the incorrect labelling of this mixed swamp type as palm-dominated in the field has considerably increased the average AGC of the field-identified palm-dominated class. This highlights the difficulty of applying a binary classification system onto an ecosystem that exhibits more complexity in the field.

To better understand the complexity of peat swamp forest vegetation, unsupervised k-means clustering of forest structure variables was performed, followed by an NMDS ordination analysis of compositional diversity. Based on this, four distinct vegetation types were identified in DRC's mostly river-influenced peatlands. Firstly, it is clear from both the k-means clustering and species ordination that *Raphia laurentii*-dominated palm swamp forms a distinct vegetation type (cluster 1; Table 3.1). This vegetation type, with 88% of individuals being palms, is mostly found further away from the Ruki River along the Bondamba and Mpeka transects. It appears partly associated with lower pH and less water availability during the dry season, potentially driven by efficient drainage of floodplain areas further from the river.

This palm-dominated swamp type corresponds well with Evrard's (1968) seral forest association of *Raphia laurentii*, and Dargie et al.'s (2017) main palm-dominated peat swamp forest type dominated by *Raphia laurentii*. To a certain degree, it also corresponds with Lebrun and Gilbert's (1954) class of permanently inundated *forêts marécageuses* and Betbeder et al.'s (2014) EVI-2 class of forests subject to stable water levels. However, this overlap is less distinct, as both authors use hydrology to group *Raphia* palms and hardwood trees together in a permanently inundated swamp forest class, rather than identifying a specific *Raphia*-dominated swamp type based on vegetation alone. No direct comparison can be made with Gond et al.'s (2013) swamp forest classes, as this study does not mention the presence of *Raphia* species or palms at all.

Secondly, a hardwood-dominated peat swamp type (cluster 2), most prominently characterized by *Coelocaryon botryoides* and very few palms, but with the highest species diversity of the four groups, can also be identified as a distinct vegetation type (Table 3.1). This swamp type appears related to more stable water table depths closer to the peat surface, which are either potentially driven by greater precipitation, or possibly upland runoff (as indicated by greater EC and higher elevations). It is largely found on higher elevations along the Bolengo and Ikelemba transect, along part of the Boloko transect, as well as most of the Lokolama transect which is not adjacent to any of the rivers.

This hardwood-dominated vegetation type corresponds well with the *Entandrophragma palustre-Coelocaryon botryoides* alliance of mature swamp forest identified by Evrard (1968). Like with palm-dominated peat swamps, this vegetation type also partly corresponds with Lebrun and Gilbert's (1954) class of permanently inundated *forêts marécageuses*, and Betbeder et al's (2014) EVI-2 class of forests subject to stable water levels. Both authors mention the presence of *Entandrophragma palustre* and *Coelocaryon botryoides*, among other species, in their respective classes. However, since their distinction is primarily based on hydrology, *Raphia* palms with stable water tables are also included in these classes. Thus, contrary to this study and Dargie et al. (2017), these authors do not make the explicit distinction between palm- (cluster 1) and hardwood-dominated (cluster 2) swamps. Furthermore, it is possible that both cluster 1 and cluster 2 correspond with the swamp forest class identified by Gond et al. (2013). However, they do not provide any species data to properly make a comparison.

Dargie (2015) and Dargie et al. (2017) describe a hardwood-dominated swamp forest in ROC, although this forest type differs in species composition to cluster 2, because neither

Entandrophragma palustre or *Coelocaryon botryoides* were recorded. Instead, they report *Uapaca paludosa, Carapa procera* and *Xylopia rubescens* as commonly present. However, Bocko et al. (2016) mentions this hardwood-dominated peat swamp forest from the same region in ROC, in association with the presence of *Entandrophragma palustre*. Some of the differences between my results and those of Dargie (2015) and Dargie et al. (2017) may be a result of different botanical traditions: for example, records of *Carapa procera* in ROC are likely to be the same species as identified by *Carapa palustris* in this study in the DRC. The taxonomy of the genus *Carapa*, and especially the place of *C. procera* in it, is controversial and has been the subject of extensive discussions and revisions. After a revision by Kenfack (2011), *C. procera* is now seen as a West-African *terra firme* species, while *C. palustris* is thought to be found in Central African swamps and riparian environments. Thus, it is very likely that the species that Dargie (2015), Dargie et al. (2017) and Bocko et al. (2016) identified as *C. procera* should be recorded as *C. palustris*.

In addition to *Carapa*, the hardwood peat swamp forest of cluster 2 identified in DRC also shares species of the genera *Xylopia* and *Uapaca* with Dargie et al.'s (2017) hardwood-dominated swamp type in ROC. Thus, it is possible that the Congo River may be a barrier to some species, with different species of the same genera occupying the hardwood peat swamp forest on either side of this barrier. Overall, it is therefore likely that the hardwood peat swamp forest, cluster 2 identified in this study, largely corresponds with the hardwood-dominated swamp forest identified by Dargie et al. (2017), even though the presence of *Coelocaryon botryoides* has not been reported in ROC swamps. Given that this swamp forest type tends to be the most diverse of all peat swamps encountered, and that the ROC and DRC sampling sites are far apart and separated by the ecological boundary of the Congo River, it is not surprising to find a diverse set of species characteristic for this forest type.

Thirdly, a mixed hardwood and palm swamp type (cluster 3) can be identified, with 29% of stems being palm, which is characterized by the presence of *Cryptosepalum congolanum*. However, this cluster is less distinct than the other clusters, as it also shares *Carapa palustris* and *Entandrophragma palustre* as indicator species with cluster 2. There are also no clear environmental variables associated with this cluster. Like cluster 1, most of the sites in this cluster were identified in the field as palm-dominated. However, unlike the monodominant palm swamp forest that are typical of cluster 1, this mixed hardwood/palm vegetation type is characterized by the presence of a diverser group of hardwood trees. This vegetation type is

often found at the transition zone from hardwood- to palm-dominated sites, such as along the Mpeka transect, at the start of the Bolengo transect, or at the endpoint of the Bondamba transect. It is unclear, from published sources, whether this vegetation type is found in ROC, but it is clear that there are long, shallow environmental gradients in the interfluvial basins (Dargie 2015), and that there is a gradient from palm-dominated to hardwood-dominated peat swamp forest (S. Lewis and G. Dargie, *pers. comm.*). This mixed peat swamp forest does not simply map onto any of the vegetation classes of either Evrard (1968), Lebrun and Gilbert (1954), Betbeder et al. (2014), or Gond et al. (2013). Furthermore, none of these, including Dargie et al. (2017), explicitly mention the presence of *Cryptosepalum congolanum* in relation to a swamp forest vegetation type. It may be the case that there is a gradient from hardwood-dominated to palm-dominated peat swamp forest, with authors identifying ideal end-member types, and my new classification attempting to show this gradient by making an intermediate cluster.

Finally, a second mixed hardwood/palm swamp forest type (cluster 4) can be identified as a distinct vegetation type, most prominently characterized by the presence of *Ouganbuia africana* and *Guibourtia demeusei* in the canopy, in association with *Raphia sese* and juvenile *Raphia laurentii* species in the understory. This swamp type appears to be found mostly in river-influenced sites with seasonal inundations during the wet season, which are located at lower elevations close to rivers or streams. For example, this vegetation type is largely found at the start of the Ikelemba transect, close to the Ikelemba River, and along the Tumba transect, located in a floodplain between two tributaries. Based on overlaying the NMDS ordinations with environmental variables, it appears further characterized by shallow peat deposits with low electrical conductivity and less acidic conditions. However, the fact that this cluster is also related to greater precipitation seasonality suggests that some of these inundations could be partially related to rainfall patterns, rather than geomorphology alone.

The seasonally inundated, mixed swamp forest type corresponds well with Evrard's (1968) description of the seasonally flooded *Oubanguia africana-Guibourtia demeusei* association. It is also very likely related to Lebrun and Gilbert's (1954) classes of *forêts périodiquement inondées*, which was described as being dominated by *Oubanguia* and *Guibourtia* and having little to moderate peat soil accumulation. In addition, it corresponds well with Betbeder et al.'s (2014) EVI-1 class of forests subjected to seasonal flood pulse, which is also located alongside rivers, and described as being characterised by *Oubanguia africana* and *Guibourtia deumeusei.*

Furthermore, cluster 4 possibly corresponds with the Gond et al.'s (2013) swamp type located in valley bottoms of the Congo Basin, although no further description is provided.

Seasonally flooded forests dominated by *Guibourtia demeusei* are described for the ROC by Ifo et al. (2018), although these are also not peat-forming and not in association with *Oubanguia africana*. Rather, the seasonally flooded forests in ROC are typically associated with *Dialium pachyphyllum* (Bocko et al., 2016; Dargie, 2015; Ifo et al., 2018), a species which was only occasionally observed in DRC. Ifo et al. (2018) also report a *Lophia alata*-dominated seasonally flooded forest, which was not encountered in the river-influenced swamps of DRC at all. Thus, it appears that the seasonally flooded forest types in ROC are different from the seasonally inundated mixed swamp in DRC, which is typically characterized by both *Oubanguia* and *Guibourtia* and does form peat. Overall, the particular inundation patterns in a location, including both depth and duration of wet season inundation and dry season water table drawdown, alongside the chemical characteristics of the flood water, may alter which species can dominate. This could lead to a variety of vegetation types in seasonally inundated environments within the Cuvette Centrale, of which only some accumulate peat.

Evrard (1968) and Dargie et al. (2017) have additionally identified a *Raphia sese/Raphia hookeri*-associated riparian forest type, which was not identified along the transects studied in the DRC either. According to Dargie et al. (2017), the *R. hookeri* palm-dominated swamp type was found to occupy abandoned river channels in ROC, while Evrard (1968) reports stands of *R. sese* along streams in DRC. No clearly abandoned river channels with peat accumulation were identified in the DRC, which explains why a *Raphia sese*-dominated vegetation type was not found as part of this study. Nonetheless, *R. sese* was frequently encountered in association with the seasonally inundated swamp forest of cluster 4, although without dominating there. This is likely explained by the tendency of this species to grow in riparian or periodically inundated locations, which are ecologically similar to abandoned river channels.

Both *Raphia hookeri* and *Raphia sese* are characterized by curled fibres on a tall trunk, but primarily distinguished from one another by the type of 'beak' found at the apex of the yellowish fruit, which is tapering (long cylindrical point, +15mm) in specimens of *R. hookeri*, while more squat (6-9mm) and noticeably inflated in the middle in specimens of *R. sese* (Tuley, 1995). According to Tuley (1995), *R. hookeri* is a West African species occurring from Senegal to the Congo Basin, while *R. sese* is reported to be native to central and north-eastern DRC. This

suggests that these are different species that fill similar ecological niches on either side of the Congo River, with the river acting as an ecological barrier.

Assuming cluster 1 identified here is similar to the palm-dominated swamp type described by Dargie et al. (2017) in ROC, and cluster 2 is largely similar to the hardwood-dominated swamp type described by these same authors in ROC, at least five different vegetation types can be identified across the central Congo Basin:

- hardwood-dominated peat swamp forest, with a diverse set of species, mostly characterised by *Entandrophragma palustre, Coelocaryon botryoides* and *Carapa palustris* in DRC, or *Uapaca paludosa, Carapa procera* (likely *C. palustris)* and *Xylopia rubescens* in ROC;

- *Raphia laurentii* palm-dominated peat swamp forest, often characterized by monodominant stands, or in association with *Cleistopholis patens*;

- mixed peat swamp forest, likely intermediate between the hardwood-dominated and palm-dominated peat swamp forest types, with medium palm presence and characterised by *Cryptosepalum congolanum*, so far only documented in DRC but likely existing in ROC as well;

- seasonally inundated mixed peat swamp forest, characterised by *Oubanguia africana* and *Guibourtia demeusei* in association with *Raphia sese,* often found in riparian settings and so far only documented in the DRC;

- *Raphia hookeri* palm-dominated peat swamp forest, found in abandoned river channels and along streams, so far only documented in ROC.

These vegetation classifications were derived without including data on the presence of rattans, small woody shrubs, or small monocots. For example, some seasonally inundated swamp vegetation was heavily characterized by extensive understory coverage of rattan palms (typically *Eremospatha wendlandiana, Eremospatha haullevilleana* or *Laccosperma secundiflorum*), or woody shrubs (typically *Alchornea cordifolia)*. Furthermore, *Raphia laurentii*-dominated palm swamps were typically characterized by an understory of trunkless palms (*Sclerosperma mannii*) or chandelier-like screw palms (*Pandanus candelabrum*). As these understory species normally did not reach the threshold of DBH ≥ 10 cm, they were excluded from aboveground biomass estimates and other indicators of vegetation structure and diversity. Including these may further help delimit vegetation types in the peat swamps of the Cuvette Centrale. Moreover, the exclusion of these species could lead to a small underestimation of AGB if the understory of

some vegetation plots was found to be dominated by rattan palms. Further work on classifying peat swamp forest vegetation, including the smaller (< 10 cm DBH) plant species, is therefore needed in the future.

Difficulties in assessing vegetation characteristics are further compounded by the fact that both Dargie et al. (2017) and this study used a relatively small vegetation plot of 20x40 m. While the orientation and location of the plot was pre-determined before the fieldwork commenced, to avoid bias, small plots necessarily have greater uncertainty attached, as treefall gaps and other small-scale environmental heterogeneities may affect the results. This tends to produce less stable ordination patterns (Otypková & Chytrý, 2006) and could cause the analysis to miss out on potentially rare but important large trees (Harris et al., 2021a). Specifically, given the low prevalence of hardwood trees in *Raphia laurentii*-dominated swamp forests, 20x40 m is likely too small to capture the relatively rare occurrences of hardwood species in this vegetation type. Ideally, species-area relationships would be calculated in the future to assess what plot size and how many plots are required to accurately assess large-scale vegetation patterns (Plotkin et al., 2000).

Furthermore, the applicability of the Bray-Curtis statistic used for NMDS ordination analysis has recently been called into question. The Bray-Curtis statistic is related to the Sørensen-Dice index, which has recently been criticized for being oversensitive to species prevalence, potentially causing misleading conclusions (Mainali et al., 2022). Mainali et al. (2022) state that this index is especially problematic if sample sizes are small and species distributions are skewed, such as in the palm-dominated plots that were assessed in DRC. Since the Bray-Curtis metric is one of the most popular abundance-based dissimilarity metrics among ecologists (Anderson et al., 2011), and has been used to analyse similar swamp forest vegetation types in Peruvian peatlands (Honorio Coronado et al., 2021) and seasonally flooded forests in northern Republic of Congo (Ifo et al., 2018), it was decided to still apply it here. To reduce the potential issue of a strongly skewed distribution of *Raphia laurentii* in palm-dominated plots, multi-stemmed clusters of this palm species were treated as the same individual, like multiple stems ≥ 10 cm DBH originating from the same hardwood tree. Similarly, the negative effect of overprevalence by multi-stemmed *Raphia laurentii* palms was countered in the k-means clustering by including stem density without *Raphia laurentii* as separate variable, and by calculating the proportion of palm trees based on individuals, rather than stems. The fact that the NMDS ordination results correspond well with the clustering results obtained from k-means-clustering gives confidence

in the identified vegetation types. Nonetheless, given the status of debate about the use of Bray-Curtis similarity metric, the results reported here should be interpreted as broad vegetation descriptions only.

Environmental drivers of swamp forest vegetation types

From the transect descriptions in Chapter 2 it can be observed that there are clear gradients in vegetation types along some transects, especially when moving away from the rivers. Overlaying the NMDS ordination with environmental variables in Figure 3.6d confirms that these gradients are often related to inundation levels. The seasonally inundated mixed swamp type (cluster 4) is strongly correlated with both large fluctuations in water table depth throughout the year and greater inundation heights during the wet season. Increased exposure to oxidation therefore likely explains why this peat swamp type has relatively shallow peat deposits. On the other hand, the hardwood-dominated swamp type (cluster 2) is strongly correlated with stable water tables and low levels of wet season inundation. Here, permanent anoxic conditions likely explain the greater peat deposits observed.

Although the NMDS ordination partly points towards a climatic effect of annual precipitation and precipitation seasonality, differences in inundation patterns are likely to also be determined by landscape geomorphology and distance from the major rivers and drainage points. This makes these factors highly relevant for mapping of peat thickness across the basin.

However, contrary to what was hypothesized for palm swamps, there isn't a clear distinction between inundated and non-inundated palm swamp forests. Rather, palm-dominance in my sampling in DRC appears partly related to greater dry season water table depths, with monodominant *Raphia laurentii* swamps experiencing lower water tables than mixed swamp forests which have a medium palm presence. Additionally, palm-dominance appears partly associated with two climatic factors, namely greater annual precipitation and potential evapotranspiration (Figure 3.6d). Larger potential evapotranspiration could partly explain the association with lower water tables in the dry season. Palm-dominance in peatlands with low water tables appears counter-intuitive, given that some of the deepest peat deposits throughout the central Congo Basin have been recorded in monodominant palm swamp forest (Dargie, 2015; Dargie et al., 2017). However, the controls on peat carbon accumulation are complex, and drought does not necessarily need to lead to less carbon accumulation, as has been suggested for seasonally inundated tropical peatlands in Amazonia (Swindles et al., 2018). It is also possible

that (i) my sampling is limited and the low water tables are not a true reflection of the environmental conditions of the *Raphia laurentii* peat swamp forest vegetation type; (ii) *Raphia laurentii* palms provide considerably more biomass input into the peat and peat surface compared with hardwood trees, which could cause greater gross peat accumulation if the inputs more than offset an increased decomposition from oxidation due to lower dry season water tables; or (iii) *Raphia laurentii* stands represent a late successional stage in peatland development, forming on top of previously formed deep deposits. The first suggestion is plausible, given that palm-dominated swamp vegetation has been mapped across a wide geographical range in both interfluvial basins and river-influenced settings by Dargie et al. (2017). The second suggestion could also be plausible, given the large amount of litter and dead palm fronds that typically characterize a palm-dominated swamp. The third suggestion would contrast with the classification by Evrard (1968), who regarded *Raphia laurentii* swamps as seral forest, in contrast with hardwood and seasonally inundated swamps that were described as mature forests. Additionally, Evrard (1968) has suggested that monodominant *Raphia laurentii* stands could partly be the result of human interference, as *Raphia* palms are used for building materials and to make palm wine. More research is thus required to understand the factors that drive palm-dominance in Central African peat swamp forests.

3.7 Conclusion

The aim of this chapter was to compare the characteristics of the different peat swamp forest vegetation types in the central Congo Basin. A diverse set of vegetation types was observed across 40 vegetation plots (0.08 ha each) in the largely river-influenced peatlands in DRC. Mean aboveground carbon stock across all measured peat swamps in DRC was found to be 97.8 Mg C ha^{-1}. However, a lot of variation was observed between and within transects. Field-identified hardwood-dominated peat swamp forests have a mean value of 114.1 Mg C ha^{-1}, which is significantly greater than that of palm-dominated peat swamps forests, who have a mean value of 81.5 Mg C ha^{-1}. Species diversity in the peat swamp forests is high, with 152 species and 101 genera encountered across a total plot area of 3.2 ha. Nonetheless, some species clearly dominate, with *Raphia laurentii, Oubanguia africana, Raphia sese, Guibourtia demeusei, Cryptosepalum congolanum, Pseudagrostistachys ugandensis, Coelocaryon botryoides* and *Carapa palustris* accounting for over half of all individual trees recorded.

Based on an unsupervised clustering analysis of 11 forest structure and diversity metrics, four distinct vegetation types were identified in the swamp forests of the DRC. NMDS ordination subsequently showed that these vegetation clusters are characterized by significantly different species composition. These four types are: a hardwood-dominated peat swamp forest, a *Raphia laurentii* palm-dominated peat swamp forest, a mixed peat swamp forest characterized by *Cryptosepalum congolanum*, and a mixed peat swamp forest characterized by *Oubanguia africana* and *Guibourtia demeusei*. Contrary to what was hypothesized, these did four types did not correspond with a subdivision of both hardwood- and palm-dominated swamps into a river-influenced and non-river-influenced class. Overlaying the ordination plot with environmental factors showed that the distinction between the hardwood-dominated peat swamp and the *Oubanguia-Guibourtia*-associated mixed peat swamp is indeed driven by a gradient in river-influenced inundation patterns, with the latter type associated with greater water table fluctuations and strong wet season inundation. However, the distinction between the hardwood-dominated, *Raphia laurentii* palm-dominated and the *Cryptosepalum congolanum*-associated mixed swamp type is not. Rather, these three vegetation types occupy a second gradient from strongly hardwood- to palm-dominated vegetation. Although palm-dominance appears partly associated with lower water tables in the dry season, it remains unclear what is driving this gradient in palm-dominance.

Combining the results of this analysis in DRC with earlier vegetation descriptions of peat swamps in ROC, I identify at least five distinct forest types in the central Congo Basin peatlands. These are: a hardwood-dominated peat swamp, a *Raphia laurentii* palm-dominated peat swamp, a mixed peat swamp with *Cryptosepalum congolanum*, a seasonally inundated mixed peat swamp with *Oubanguia africana* and *Guibourtia demeusei*, and a *Raphia hookeri* palm-dominated peat swamp in abandoned fluvial channels.

Chapter 4: Understanding the hydrology, geochemistry and age of river-influenced peatlands in the DRC

4.1 Abstract

In this chapter, I describe the hydrological, geochemical and radiocarbon characteristics of peatlands in the DRC. In particular, I compare the seasonal inundation patterns, nutrient status and basal ages of river-influenced peatlands along the Ikelemba transect with the non-river-influenced peatlands of the Lokolama transect, as well as interfluvial basin peatlands previously analysed in ROC. This is done to understand what has been driving peat initiation in the central Congo Basin, and which factors are sustaining contemporary peat formation and maintenance. The river-influenced peatlands in DRC are found to be extremely nutrient-poor, with a mean (± s.d.) Ca/Mg-ratio of surface peat samples of 1.76 (± 0.74), which is typically lower than that of either peat pore/surface water, river water or rainwater. However, these nutrient-poor peatlands receive seasonal river water input through overbank flow from blackwater rivers, as indicated by large seasonal fluctuations in water table height of close to a meter along the Ikelemba transect. This contrasts with lower water table fluctuations in the non-river-influenced peatland of Lokolama. In addition, there is evidence to suggest that the river-influenced peatlands might episodically receive some water input through (sub)surface runoff from *terra firma* uplands. The river valley peatlands were likely formed during the Late Pleistocene, with radiocarbon dating of the base of the thickest Ikelemba peat core revealing an age of between 41,200 and 43,800 calibrated years Before Present. This is over 20,000 years before the formation of ombrotrophic peat domes started in interfluvial basins in the ROC. Radiocarbon dating of the base of the thickest Lokolama peat core, which is not river-influenced, gives an age of between 10,300 and 10,600 calibrated years Before Present, similar to reported basal dates from interfluvial basins in the ROC. The presence of extensive nutrient-poor, but seasonally inundated peatlands in DRC, in addition to the previously known ombrotrophic-like interfluvial basin peatlands, reveals that there is an additional geomorphological setting in the central Congo region where peat is formed. The pre-Holocene age of the river valley peatlands also indicates that peat formation was not limited to the warmer and wetter conditions following the Last Glacial Maximum.

4.2 Introduction

Peatlands in the Republic of the Congo are found mostly in interfluvial basins, bounded from the rivers by patches of *terra firme* forest and savanna. Although supra-annual river flooding cannot be excluded, Dargie et al. (2017) have shown that these peatlands are mostly ombrotrophic-like (nutrient-poor), being largely fed by rainwater. However, as has been described in Chapter 2, some peatlands in the Democratic Republic of the Congo are located immediately adjacent to rivers and characterised by high inundation levels. Vegetation analysis (Chapter 3) has additionally shown that a specific peat forest type can be observed in these seasonally inundated peatlands. These findings suggest that a different peatland type can occur in river-influenced settings that is different from the rain-fed peatlands identified by Dargie et al. (2017).

Typically, peatlands fed by river water are minerotrophic in nature, owing to the nutrient-rich conditions of most rivers (Clymo, 1987; Rydin & Jeglum, 2006). However, it is unclear if this is the case in the river-influenced peatlands of the DRC. Although a wide range of biogeochemical signatures can be detected within the watershed (Bouillon et al., 2014), the Congo Basin rivers typically have very low concentrations of dissolved metal cations, a high proportion of dissolved organic carbon, and some of the most acidic river conditions in the world (Dupré et al., 1996). In particular, the eastern tributaries of the Congo River, such as the Ruki and Ikelemba River, are known as typical blackwater rivers with low quantities of suspended matter and pH values close to or even below 4 (Berg, 1961; Borges et al., 2019). This makes them potentially even more acidic than the Negro River in the Amazon Basin, the classic example of a blackwater river with pH values in the range of 4-5 (Junk et al., 2011). This suggests that even if river water from these tributaries is feeding into the peatlands of the central Congo Basin, this would not necessarily alter the chemical composition or nutrient status of the peatlands.

Apart from nutrient status, the inundation pattern itself can be expected to influenced peat swamps as well, in particular through its effect on species diversity and forest structure (Targhetta et al., 2015), as was observed in Chapter 3. Seasonal and interannual variation in inundation is also crucial in determining the amount of peat accumulation that takes place (Ise et al., 2008; Kurnianto et al., 2015; Mezbahuddin et al., 2015) and carbon emissions to the atmosphere (Hirano et al., 2007; Mitsch et al., 2010), by determining the balance between accumulation and decay through aerobic decomposition.

However, the height of a water table not only depends on the amount of precipitation, river water input, and soil water retention characteristics, but also on the presence of microrelief (Dettmann & Bechtold, 2016). Water storage in hummocks and hollows has wide implications for the hydrological functioning of the peatland, playing a key role in the hydrological self-regulation of domed peatlands in Southeast Asia (Dommain et al., 2010). Studying microtopography can also help understand slope directions in shallow, domed peatlands, where elevation gradients are not immediately apparent in the field (Lampela et al., 2014, 2016), such as in the Congo Basin. Thus, it is important to study in more detail both the seasonal inundation dynamics, as well as the microtopography of DRC transects that have been identified to be impacted by river flooding.

If DRC peatlands are strongly influenced by river dynamics, their developmental histories might have been very different from those found in interfluvial basin peatlands in ROC. The interfluvial basin peatlands in the Republic of the Congo are likely of early-Holocene age, with published initiation dates obtained through radiocarbon (^{14}C) dating typically ranging between 7,100 and 10,500 cal yrs BP (calibrated years Before Present, where 'present' is defined as AD 1950; Dargie et al., 2017), but occasionally up to 17,500-20,400 cal yrs BP (Garcin et al., 2022). This generally coincides with the onset of the African Humid Period, a period of higher rainfall across Central Africa (Shanahan et al., 2015), which underscores the important role of precipitation in peat formation in the central Congo Basin. Further down-core radiocarbon dating of these ROC peat deposits showed 0.57-0.80 m of peat accumulation over the past 1,500-2,600 cal yrs BP, indicating that peat has continued to accumulate since after the end of the African Humid Period (~3,000-5,000 years BP; Dargie et al., 2017).

However, the vast extent of the Cuvette Centrale, and the varying hydrologies described in Chapter 2 indicate that our current understanding of the region's formation history, based on a small number of sites in interfluvial basins alone, is unlikely to be representative of the entire peatland complex. Comparative studies with multiple transects across a wider basin have previously proven useful in the study of Southeast Asian and Amazonian peatlands (Brady, 1997; Kelly et al., 2020; Lähteenoja & Page, 2011; Morley, 1981). Particularly in the Peruvian Amazon, it has been shown that initiation and development of fluvial peatlands has been very different from peatlands without riverine influence (Kelly et al., 2020; Lähteenoja & Page, 2011). For example, river-influenced tropical peatlands in the Peruvian Amazon are characterised by the burial and erosion of peat due to migrating river channels (Lähteenoja et al., 2011). In some of

these peatlands, the flood regime appears to be the dominant control on ecosystem functioning and development (Roucoux et al., 2013). Furthermore, tropical peatlands in Southeast Asia are known to be of varying ages, with coastal peatlands that formed as a result of Late-Holocene sea level stabilization and regression typically being less than eight thousand years old, while some inland peat domes formed during the Late Pleistocene (Dommain et al., 2011) and can be up to 48,000 years old (Ruwaimana et al., 2020). Therefore, divergent basal ages in hydrologically and geomorphologically different peatland systems of the central Congo Basin are to be expected. Obtaining radiocarbon dates from riverine peatlands in the DRC is thus critical for a more complete understanding of the region's history.

In this chapter, I specifically decided to compare the Lokolama (non-river-influenced) and Ikelemba (river-influenced) transects in DRC, because of their contrasting geomorphologies and hydrologies. It is hypothesized that the non-river-influenced peatland at Lokolama is of similar age as the interfluvial basin peatlands in ROC. If confirmed, this would suggest a common initiation time across the Cuvette Centrale region. As LOK_5.0 is the deepest peat core sampled so far across the region, with a LOI-measured thickness of 6.0 m, it is also hypothesized that the base of this core could potentially hold the oldest peat sampled so far in the Cuvette Centrale peatland complex.

An additional hypothesis is that since the river-influenced peat deposits at Ikelemba are shallower than those at Lokolama, riverine peat deposits are likely younger than non-riverine peat deposits. This could indicate that peat initiation in Ikelemba may have started at a different time as a result of river-induced hydrological changes, rather than basin-wide climatic conditions such as the African Humid Period. Thus, by comparing both Ikelemba and Lokolama from DRC with interfluvial basin peatlands in ROC it is hoped that the effects of river-induced and climate-induced hydrological changes can be determined.

Radiocarbon dating of the Lokolama and Ikelemba cores further makes it possible to study how carbon accumulation rates have differed over time in riverine and interfluvial peat swamps. In particular, one core from Ekolongouma in ROC (EKG_9.0) shows that very little peat has survived between ~2,000 and ~7,500 BP, in contrast with thicker deposits of younger and older peats (Dargie et al. 2017). This could indicate a potential slowdown of litter accumulation or an increase in decomposition rates during these 5,000 years, a later severe decomposition or erosion event that removed peat carbon from the peat profile, or a combination of all these

factors (Dargie et al., 2017; Garcin et al., 2022). If this pattern is seen in both DRC sites, it would suggest a basin-wide event. The alternative hypothesis is that this was a local event in one interfluvial peatland only. In addition, it is hypothesized that the slope of the age-depth relationship will vary more strongly in Ikelemba, as a result of advancing and retreating riverine influences.

Contrary to interfluvial basin transects such as Ekolongouma in ROC, Lokolama experiences a sharp increase in peat thickness close to the peatland margin, which remains large throughout the transect. This does likely not correspond with a scenario of peat formation through paludification, which is expected to result in increasingly younger basal dates (and thus shallower deposits) towards the peatland edge. Rather, it is hypothesized that the Lokolama basin could be the result of the terrestrialisation of a previous lake or waterlogged depression. This idea corresponds well with the markedly round shape of the eastern basin border, but would set it apart from the interfluvial basins that have been studied so far in the ROC. Along the Ikelemba transect, on the other hand, a gradient in basal dates is likely to be found, as peat thickness increases with distance from the river. It is hypothesized that this is the result of a paludification process, whereby peat forms on a poorly drained, continuously wet mineral surface (Cameron et al., 1989).

4.3 Chapter aims

The aims of this chapter are to characterise and classify the hydrology, geochemistry and age of river-bound peatlands in the DRC. The specific objectives are to measure *in situ* water tables, microtopography, peat pore and river water inorganic chemistry, peat surface and downcore inorganic chemistry, and radiocarbon dates across a number of transect, based on hypotheses described in Chapter 2, section 2.4.1, and summarised in Table 2.1. The focus is a comparison of the river-influenced Ikelemba transect and the non-river-influenced Lokolama transect. In addition to the Ikelemba and Lokolama transects, pore water, river water and peat chemistry will also be compared with the three Ruki River transects Mpeka, Bondamba and Bolengo. All these sites will further be compared with published data from the interfluvial basin sites in the Republic of the Congo (Dargie, 2015; Dargie et al., 2017).

4.4 Methods

4.4.1 Water table measurements

Two transects were chosen for the collection of year-round *in situ* water table measurements: Lokolama and Ikelemba. These transects were chosen because ALOS PALSAR radar data (HV/HH ratio) showed contrasting hydrological differences between the transects (Figure 4.1). The Ikelemba transect can be seen to have a high backscatter coefficient close to the Ikelemba River, indicating significant inundations. The Lokolama transect, on the other hand, has relatively low backscatter coefficients near the edge of a potential round peat dome, indicating limited standing water above the peat surface. These remotely-sensed insights were confirmed upon visit in the field, as described in Chapter 2, with some Ikelemba sites having maximum estimated inundation heights well beyond 1 m, while at Lokolama maximum inundation was generally estimated to be 20-30 cm above the peat surface.
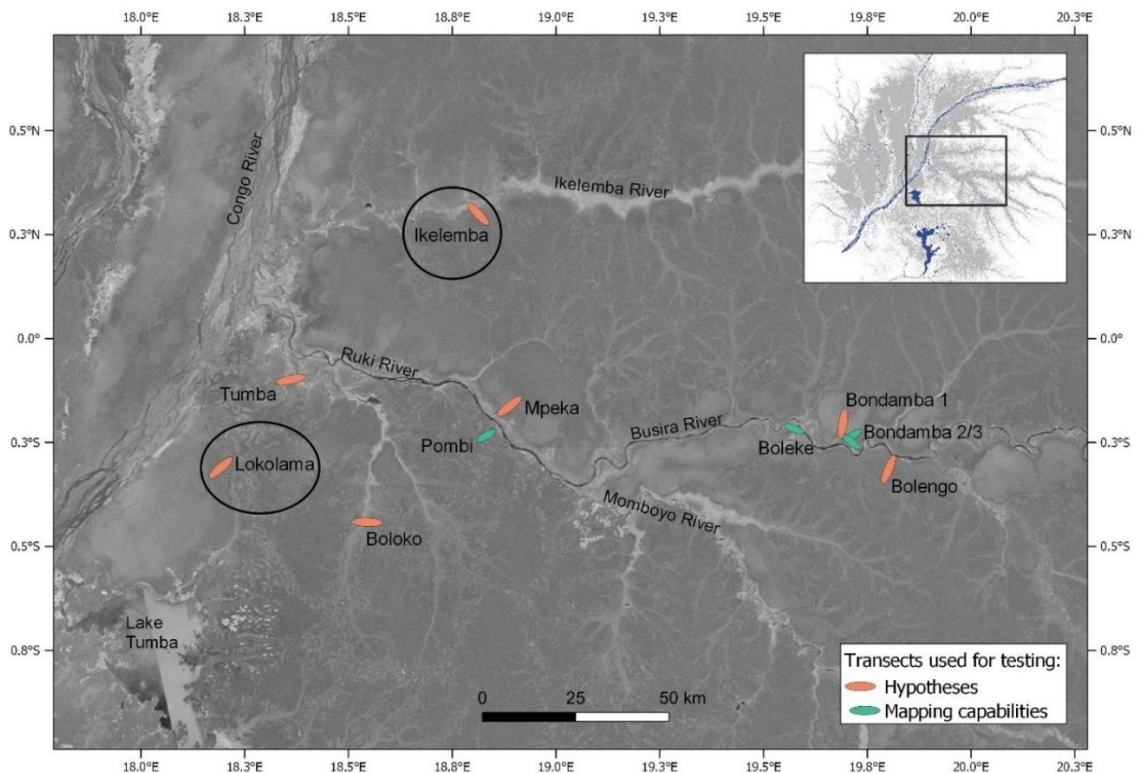
Figure 4.1. Location of the Ikelemba and Lokolama transects for *in situ* water table measurements. *Background image of the HV/HH-ratio of ALOS PALSAR radar data developed by Dargie et al. (2017) to differentiate between inundated (light grey) and non-inundated (dark grey) forests. Lighter colours indicate relatively larger HH backscatter due to the double-bounce mechanism in flooded forests. Upper-right corner insets: image location within the wider Cuvette Centrale peatland complex (grey shading) and river network (blue).*

Based on the field observations (Chapter 2), it is hypothesized that at IKE_1.0, close to the river, large fluctuations in water table heights can be observed, ranging from > 1 m above the surface to > 30 cm below the peat surface. At IKE_3.0, the fluctuations will likely be much more limited, given this is the site where riverine influence appears to end. Given the relatively large elevation gradient at Ikelemba, it is hypothesized that water table depths at IKE_5.0 would not increase much above the peat surface, as any excess water above the peat surface would drain away as overland flow. It is further hypothesised that water table depths at IKE_5.0 should show stronger increases during rainfall events than at Lokolama, as the water table likely rises both from local precipitation, as well as runoff from higher *terra firme* ground.

At Lokolama, on the other hand, no runoff from higher ground is expected, given the peat dome is likely elevated higher than the surrounding *terra firme* forest. It is hypothesized that the observed differences between LOK_1.0 and LOK_3.0/LOK_4.0 are limited, as elevation gradients are small and there is no runoff. Furthermore, because of this lack of elevation gradients, it is hypothesized that belowground drops in water table fluctuations are likely smaller than at Ikelemba, as drainage capacity will be limited.

To obtain continuous water table measurements across these two transects, six belowground pressure sensors (manufacturer: Solinst, Georgetown, Canada; model: Levellogger Edge 3001 M5 and M10) were installed every other kilometre along each transect. This way, changes in water table fluctuations along the transect (i.e., when moving away from the river at Ikelemba, or moving away from the *terra firme* forest edge at Lokolama) could be observed. At Ikelemba, the sensors were installed in March 2018 at 1, 3, and 5 km along the transect. However, at Lokolama, the sensors were installed in February 2018 at 1, 3, and 4 km along the transect, as this transect hadn't yet been extended towards 5 km at the time.

Each pressure sensor was suspended below the peat surface using a metal wire inside a ~5 cm-wide perforated plastic tube, similar to Dargie et al.'s (2017) approach. Each tube was closed at the top using a small tin can and duct tape to prevent it from clogging up with leaf litter (Figure 4.2). The pressure sensors were installed at a fixed depth below the peat surface that was thought to be well below the lowest water table depth at the height of the dry season. The distance between the sensor and the water table depth at the time of installation, as well as between the sensor and the peat surface was measured to allow calibration of the recorded data.

Figure 4.2. Example of a water pressure logger installed in the peat surface along the Lokolama transect. *The plastic tube was capped with a tin can and duct tape. Sticks were placed around the tube to try to keep animals out. Photo by the author.*

Because the belowground pressure sensors measure absolute pressure, which is a combination of water pressure and atmospheric pressure, two barologgers (manufacturer: Solinst, Georgetown, Canada; model: Barologger Edge 3001 M1.5) were installed in the air along each transect as well, to correct for atmospheric pressure fluctuations. At Ikelemba, the two barologgers were installed in between the three water pressure sensors, at 2 and 4 km along the transect. At Lokolama, the two barologgers were installed at 2 and 4 km along the transect. Each barologger was attached to a tree trunk at 2.5 m above the peat surface, using a nail and metal wires, whilst inside a 25 cm-long perforated plastic tube for protection (Figure 4.3).

Both the absolute belowground pressure sensors and the barologgers were set to record pressure every 20 minutes. The data was then retrieved again from the field in January 2020. The recorded data was extracted using an optical reader (manufacturer: Solinst, Georgetown, Canada; model: Levelogger Optical Reader) and Solinst Levelogger software (version 4.4.0). However, upon visiting the field sites in January 2020, the belowground pressure sensor installed at IKE_3.0 was missing. Furthermore, the belowground pressure sensor installed at IKE_1.0 was broken upon retrieval and no data could be extracted from it. Hence, at Ikelemba, only data from at 5 km along the transect is available.

Upon retrieval of the barologgers, it also turned out that the two barologgers installed at Ikelemba were corrupted due to likely exposure to extremely high temperatures (potentially during transport out of the field). Because of this, no useful atmospheric pressure data is available from this transect from August 2018 onward, only five months after the start of the measurements. Similarly, the two barologgers at Lokolama also showed some corrupted data from November 2018 onwards, although to a lesser extent than at Ikelemba and for small periods of time only.

Figure 4.3. Example of a barologger attached to a tree trunk along the Lokolama transect. The *plastic tube was capped with a tin can and duct tape. Photo by the author.*

As no other records of surface atmospheric pressure exists with sufficient local accuracy on hourly or daily timescales, it was decided to combine atmospheric pressure records from different transects to fill in these data gaps. All belowground pressure data collected between the start of measurements in February 2018 and the end of August 2018 was corrected with atmospheric pressure data from LOK_4.0. From September 2018 onward, I used atmospheric pressure data from LOK_2.0, with some small data gaps in Nov/Dec 2018 and Jan/Feb 2019. From 15 March 2019 until 21 April 2019, barometric data from the Ekolongouma site EGK_3.0 in the Republic of the Congo was used. From 21 April 2019 until the end of all measurements on 21 December 2019, data from the adjacent Ekolongouma site EKG_2.0 was used (both *pers. comm.*, Greta Dargie). This approach assumes that the atmospheric pressure measured at Lokolama is representative of the Ikelemba transect (~90 km distance) during the first year of

measurements. Furthermore, from 15 March 2019 onward, it assumes that the atmospheric pressure measured at Ekolongouma in ROC is also representative of both Lokolama (~180 km) and Ikelemba (~150 km) in DRC. Even though the barologgers are only accurate within a 30 km radius, according to the manufacturer, these assumptions are thought to be sufficiently valid for the purpose of this analysis, given the generally small variation in atmospheric pressure in the region. Mean barometric pressure over the entire data period from the four barologgers combined is 992.3 cm (97.3126 kPa), with a standard deviation of only 2.4 cm. The minimum and maximum recorded pressure values throughout this period are 982.8 and 1007.0 cm, respectively. This suggest that any error introduced in the water table records is no larger than the maximum seasonal difference of 24 cm. On a daily and hourly basis, this range is likely much less. The mean pressure range at EKG_3.0 over five random 24-hr timespans in March and April 2019 is only 7.0 cm. The mean absolute pressure difference between EKG_3.0 and overlapping LOK_2.0 data during these same 24-hr periods is 4.7 cm on average. Seasonal changes in water table depth at each site should therefore still be observable, assuming a roughly 5 cm error introduced by the atmospheric pressure correction.

To calculate water table heights, all atmospheric pressure data was first converted from kPa to water height (in cm) by multiplying each value with a barometric constant of 10.1972 kPa. This barometric pressure was then subtracted from the belowground absolute pressure data (in cm) to obtain the height of the water table above the pressure sensor. The water table depth with respect to the peat surface was then calculated by subtracting the distance between the pressure sensor and the peat surface (as measured at the time of installation) from the recorded water table height above the pressure sensor.

In total, corrected water table measurements were available for more than 1.5 years across four sites: from 5 February 2018 (LOK_1.0), 11 February 2018 (LOK_3.0) and 13 February 2018 (LOK_4.0) until 21 December 2019 (all Lokolama sites); and from 25 March 2018 until 4 November 2019 (IKE_5.0).

To compare changes in water table fluctuations, I subsequently calculated the rate of change in water table height (RC; cm hr^{-1}) across the timeseries of each pressure sensor using the following equation:

$$RC = (b - a) * 3 \qquad \text{[Eq. 4.1]}$$

Here, *a* is the water table at the start of each 20-minute interval, and *b* is the water table at the end of each 20-minute interval.

Owing to the effect of specific yield of the peat, whereby the water table rise within a peat profile is dependent on the peat's pore space and hydraulic conductivity (Lv et al., 2021), water table changes will be much higher below than above the peat surface, if receiving the same amount of rainfall. Because the water table at IKE_5.0 was below the peat surface most of the time, which was not the case at Lokolama, I only calculated RC values for each pressure sensor if both *a* and *b* were below the peat surface. This approach assumes that the peat specific yield at Lokolama and Ikelemba is comparable, yet avoids comparing belowground fluctuations from Ikelemba with aboveground fluctuations from Lokolama.

Finally, mean values from the three Lokolama sites were compared with the single Ikelemba site.

4.4.2 Measuring surface microtopography

Microtopography was measured along the Ikelemba and Lokolama transects, at the same sites where water table pressure loggers were installed (section 4.4.1). At every other kilometre along each transect, a quadrat of 4x4 m (16m^2) was installed to measure microtopography, ensuring that there were three quadrats per transect. Along the Ikelemba transects, quadrats were located at 1, 3 and 5 km along the transect. Along the Lokolama transect, however, quadrats were located at 1, 3, and 4 km, as the transect hadn't been extended yet to 5 km at the time.

In each quadrat, I measured the ground surface height of the peat soil along two axes that crossed in the centre of the quadrat. One axis of 4 m was located parallel to the transection direction, and one axis of 4 m was located perpendicular to the transect direction. Along each axis, peat surface height with respect to the quadrat's centre point was measured every 20 cm. As such, there were 20 measurements along each axis, and 40 measurements in total.

To accurately measure small changes in peat surface height, I used a battery-powered, self-levelling laser line (Hanmer LV2 Portable Red Light Laser Cube) that was positioned in the centre of the quadrat using a lightweight tripod. The laser line was directed in turn in each of the primary four directions, i.e. parallel and perpendicular to the transect direction. I then measured the distance from the horizontal laser line to the ground surface to the nearest cm using a

measuring tape. From these measurements, all relative differences with respect to the ground surface at the quadrat's centre could be calculated. Care was taken to not disturb the peat surface along the measured lines while installing the laser.

This quadrat approach is a simplified version of the plot methodology described by Lampela et al. (2016). To save time in the field, measurements were taken along the two principal laser axes only, compared with the more detailed sampling approach described by Lampela et al. (2016), which uses 30x30 cm grids within each quadrat. Because of the bright forest light, the red laser line was only visible up to 2 m distance, hence a relatively small quadrat design of 4x4 m had to be used. An alternative would be to measure relative ground surface along a single 50 m long line that runs parallel to the transect direction. The tripod and laser can then be moved and recalibrated every 2 m to collect relative height differences. This approach is favoured by Lampela et al. (2016), because the plot approach is likely more biased, given that plots are not randomly located. Additionally, the longer transect approach could shed light on the relative orientation of microtopography with respect to the centre of peat domes. However, to accurately measure ground surface heights along a 50 m long laser line at all six sites would have been very time-consuming and was not possible during this fieldwork, given the time-constraints in the field.

One of the six sites (IKE_1.0km) was inundated with ~ 70 cm of water at the time of measurement in January 2020. Hence, the laser line could not be used at this site. Instead, I used the water surface itself as a horizontal reference line. I measured the distance from the ground surface with respect to the water surface from a fixed dugout canoe, by sticking a stick vertically into the water until it reached the ground surface and measuring its length. Care was taken not to disturb the water surface by accidentally moving the canoe.

As it should not matter for a relative comparison if the quadrat's centre point is located in a hollow or at a hummock, all height differences were converted to absolute differences with respect to the quadrat's centre point. Hence, a mean (± s.d.) of the absolute height differences could be calculated for each quadrat, in which differences of -5 or +5 cm are given equal weight.

All 40 microtopography measurements per quadrat were further used to calculate fractional inundation patterns at the microtopographic scale, based on the water table depths measured at the same sites (4.4.1). First, for each water table depth ranging between -30 and +50 cm, the

percentage of ground surface measurements below that depth was calculated. This indicates the fraction of each quadrat that would have been under water if the water table was at that specific depth. From this, the minimum depths required to cover 10, 25, 50 and 75% of each quadrat could be found. Using the *in situ* water table depths measured during 1.5 years at LOK_1.0, LOK_3.0, LOK_4.0 and IKE_5.0, the amount of time per year at which the water table rises above these minimum depths could be calculated.

4.4.3 Measuring peat and river water inorganic chemistry

Samples of peat pore water and river water were collected at a selected number of sites to measure metal cation concentrations of the elements Al, Ca, Fe, K, Mg, Mn and Na. Peat pore water samples were taken every full kilometre along the Mpeka (n=9), Bondamba (n=7), Bolengo (n=6), Ikelemba (n=6) and Lokolama (n=5) transects, if peat was present (Figure 4.4). Per site, three pseudo-replicates were collected in 12 ml glass vials from a single hole in the ground. If the water table was above the peat surface, surface water samples were taken instead of pore water samples. Since the fieldwork was conducted in the dry season, peat pore water samples were generally taken after extensive periods without any rain. To ensure that the collected samples are most comparable, care was taken not to take any peat pore water samples directly after a rain event.

River water samples were collected on three occasions (yellow triangles in Figure 4.4) using the same 12 ml glass vials: once from the Ruki River, near the start of the Bolengo transect (-0.28549, 19.81397); once from a small side channel that drains from the swamp forest into the Ruki River, near the start of the Bondamba transect (-0.23583, 19.68660); and once form the Ikelemba River, near the start of the Ikelemba transect (0.31722, 18.79605). Each sample was taken in the middle of the respective river or stream, at 20 cm depth. Three pseudo-replicates were taken at the same site from the Ikelemba River, while only single samples were taken from the Ruki River and its side stream. After sampling, all water samples (both pore and river water) were wrapped in aluminium foil and stored in a cool and dark place until transportation to the UK.
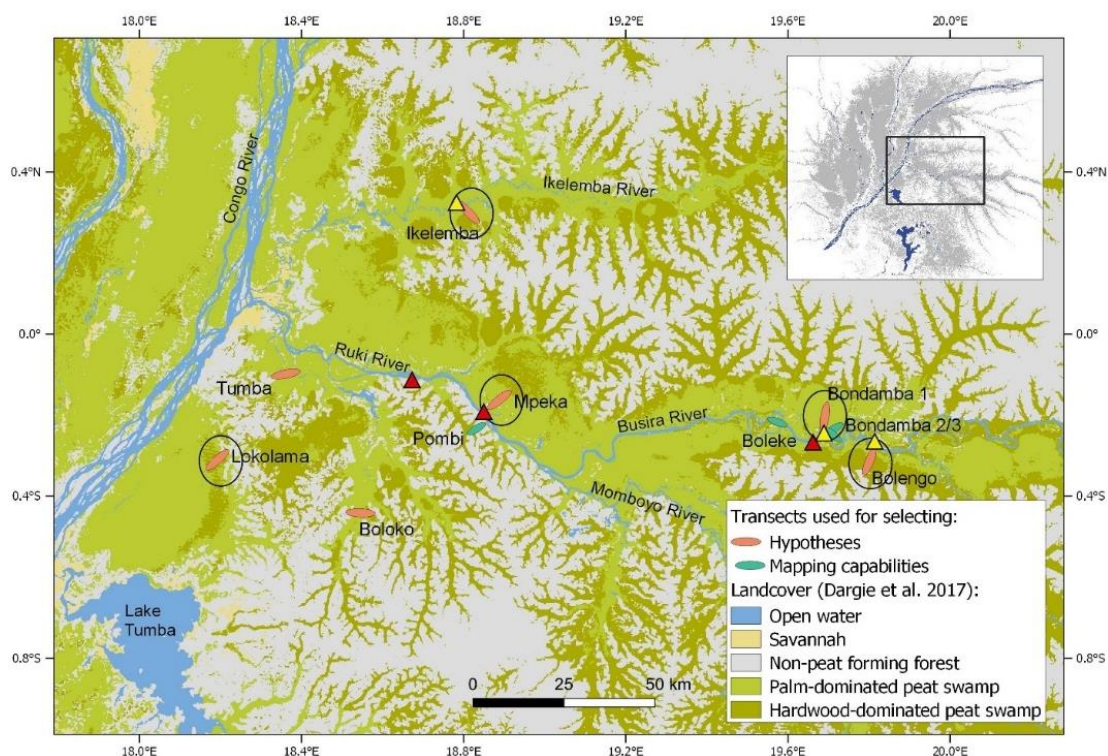
Figure 4.4. Locations of river and pore water sampling for inorganic chemistry. *All transects encircled in black had pore water samples collected every kilometre. Yellow triangles indicate locations were both river/stream water was collected for chemical analysis, as well as* in situ *pH/EC was measured. Red triangles indicate locations were only* in situ *pH/EC-measurements were taken.*

At the School of Geography laboratory of the University of Leeds, 10 ml of each pore/surface or river water sample was filtered with a 0.45 µm nylon syringe filter and acidified with 167 µl of concentrated nitric acid (HNO_3). Ideally, all samples would have been filtered and acidified with nitric acid at the time of sampling in the field, in order to enhance preservation conditions. However, this was not possible, as no analytical grade quantitative filter paper (Whatman 542) was available in the field because of a loss of luggage. As a result of these poor preservation conditions and the high concentrations of dissolved organic carbon in pore water samples, brown precipitate had formed at the bottom of some of these samples. Pore water samples with brown precipitate were therefore additionally treated with 100 µl of concentrated HCl just before analysis, in order to dissolve the precipitate. This was not necessary for river water samples.

Total metal cation concentrations in each of the water samples were then measured using an Inductively Coupled Plasma - Optical Emission Spectrophotometer (ICP-OES; manufacturer: Thermo Fisher Scientific, Bremen, Germany; model: iCAP 7600 Duo). Elemental concentrations of Al, Fe and Mn were measured using Axial configuration, while Ca, K, Mg and Na were

measured using Radial configuration. Mean blank concentrations obtained from three blanks per ICP batch were subtracted from the measured sample concentration. Detection limits were calculated per element as the mean of all blanks, plus 3x the standard deviation of all blanks. However, to prevent a loss of information, measured values below the detection limit were retained in the dataset if not negative or zero.

Raw concentration values (in mg L^{-1}) were corrected for the dilution factor from acidification (in ml), by multiplying with either 1.0167 if only HNO_3 was added, or 1.0267 if both HNO_3 and HCl were added. Peat pore water concentrations were averaged across the three pseudo-replicates to derive a mean value per site. For each sample, a Ca/Mg ratio was then calculated, which can act as a useful indicator of the water source (Lähteenoja et al., 2009a; Muller et al., 2006; Weiss et al., 2002).

Additionally, pH and electrical conductivity (EC, in µS cm^{-1}) of river and stream water was measured at six sites across the Ikelemba and Ruki Rivers (yellow and red triangles in Figure 4.4). These measurements were similar to the pH/EC-measurements of peat surface/pore water (see Chapter 2, section 2.4.2). At the middle of the Ikelemba River, near the start of the Ikelemba transect, pH/EC was measured in March 2018 using the portable combined pH/EC-meter (manufacturer: Hach Company, Loveland, Colorado, USA; model: Hach HQd Portable Metre). At the Ruki River, pH/EC was measured at four sites increasingly upstream along the Ruki River (July-August 2019), taken with the less accurate Hanna Combo metre (manufacturer: Hanna Instruments, Smithfield, Rhode Island, USA; model: Hanna HI 98129). Additionally, pH/EC was measured with the Hanna Combo metre at the side stream of the Ruki River near the start of the Bondamba transect. All measurements were taken in the middle of the following river/stream as much as possible, at ~ 20 cm depth.

4.4.4 Measuring peat surface inorganic chemistry

Surface peat samples across the same transects that were targeted for pore water collection were analysed for concentrations of the same metal cations: Al, Ca, Fe, K, Mg, Mn and Na. Surface samples of 50-100 g were collected every kilometre along the Mpeka, Bondamba and Bolengo transects (n=9, 7 and 6, respectively), and every other kilometre along the Ikelemba and Lokolama transects (n=3 for both; Figure 4.5). At each site, four or five replicates were

collected from the upper 10 cm of peat (excluding leaf litter), whilst taking care to ensure a representative selection across the local microtopography (hummocks and hollows).
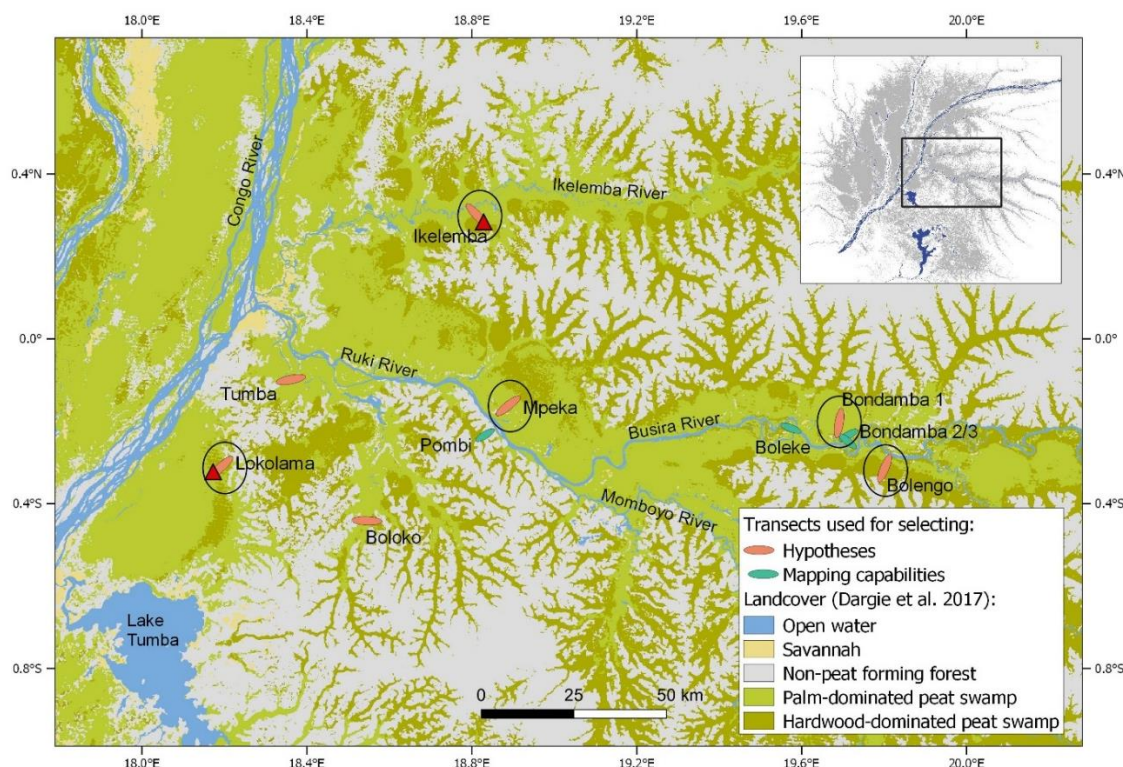
Figure 4.5. Locations of peat surface and downcore sampling for inorganic chemistry. *All transects encircled in black had peat surface samples collected every kilometre (Mpeka, Bondamba and Bolengo) or every other kilometre (Ikelemba, Lokolama). Red triangles indicate the locations of the Lokolama (LOK_4.0) and Ikelemba (IKE_5.0) cores used for downcore sampling.*

Each surface sample was analysed using a nitric acid digestion followed by ICP measurement. This was done by Dr Nick Girkin and Haley Curran at the School of Biosciences laboratory of the University of Nottingham. Samples were first oven-dried at 105°C for 24 hours. Approximately 0.2 g of oven-dried sample was then placed inside a 50 ml polypropylene digestion tube. On a heating block, 8 ml of concentrated nitric acid (HNO_3) and 2 ml of concentrated hydrogen peroxide (H_2O_2) were added, after which the tubes were covered with a watch glass. This was left to stand overnight in a fume cupboard. The next day, the samples were digested by heating at 95°C for 2 hours. After having cooled down, the samples were diluted to 50 ml solution.

The digestion solutions were then analysed for the required elemental concentrations using Inductively Coupled Plasma - Mass Spectrometry (ICP-MS; manufacturer: Thermo Fisher Scientific, Bremen, Germany; model: iCAP-Q and iCAP-TQ). Mean blank concentrations obtained from five blanks per ICP batch were subtracted from the measured sample concentration. Like

with ICP-OES (see section 4.4.3), detection limits were calculated per element as the mean of all blanks, plus 3x the standard deviation of all blanks. However, ICP-MS has greater sensitivity (up to parts per trillion) compared with ICP-OES (up to parts per billion), and no samples were found to be below detection limits.

Raw concentration values (in mg L^{-1}) were corrected for the dilution factor from the acid digestion by multiplying with 50 ml. Concentrations were then converted to soil concentrations (in mg kg^{-1}) by dividing this by the oven-dried sample weight (in g).

A mean value per site was calculated from the four or five surface replicates. Like with pore and river water samples, Ca/Mg ratios were then calculated for each sample to infer information about the water's origins (Lähteenoja et al., 2009a; Weiss et al., 2002).

Additionally, the pH and electrical conductivity (EC, in μS cm^{-1}) of all surface peat samples was measured by Dr Nick Girkin at the University of Nottingham. For this, a suspension of peat was created by mixing the peat with deionised water in a 1:2.5 ratio, an end-over-end shaker for 1 hour. After this, pH and EC were measured using a standard laboratory pH/EC-meter.

4.4.5 Measuring downcore peat inorganic chemistry

In addition to surface peat samples, two peat profiles from Ikelemba and Lokolama (red triangles in Figure 4.5) were measured downcore using ICP-OES, to compare the developmental histories of these two peatlands. In addition to the elements Al, Ca, Fe, K, Mg, Mn and Na analysed for surface samples, measurement of Ti concentrations was added to the analysis as well.

Peat cores can provide reliable records of the changing rates of atmospheric metal deposition from dust or aerosols (Martínez Cortizas et al., 2002; Shotyk, 1996). Ti is typically derived from weathering of the Earth's crust and thus of terrestrial origin (Weiss et al., 2002). As it is essentially immobile in the peat profile, it can be related to historic deposition rates (Novak et al., 2011; Weiss et al., 2002).

The deepest cores of both the Lokolama and Ikelemba transects were selected for this analysis. This includes the IKE_5.0 core (3.9 m) from Ikelemba. However, as the Lokolama transect had not been extended yet to 5 km at the time of the laboratory analysis, the LOK_4.0 core (5.1 m)

was used for this transect, instead of the slightly deeper core from LOK_5.0 (6.0 m). Downcore sampling of additional peat profiles from the other transects used for surface sampling (Mpeka, Bondamba and Bolengo) was not possible due to lab closures and subsequent time constraints as a result of disruption due to the Covid-19 pandemic.

In contrast to the analysis of surface chemistry, downcore samples were prepared using a hydrofluoric-perchloric-nitric acid digestion. This is because the complete breakdown of the high concentrations of organic matter in peat samples requires the presence of perchloric acid. However, hydrofluoric acid (HF) is also essential for the acid dissolution of silicates (Allen, 1989). HF acid digestions have been shown to be more effective in extracting total metal concentrations from soils than nitric acid digestion (Gaudino et al., 2007; Rajashekhar Rao et al., 2011). As downcore samples are likely more enriched with sand or clay, especially samples that are close to the underlying mineral substrate, hydrofluoric-perchloric-nitric acid digestion was applied.

Subsamples of wet peat were dried inside an oven at 40°C for 48 hours. From this, approximately 0.1 gram of dried sample was taken and ground to < 100 µm using a mixer mill (manufacturer: Retsch, model: MM301). Each ground sample was then placed in a PTFE beaker and weighed. It was moistened with a little deionised water, after which 3mL of concentrated nitric acid (69% HNO_3) was added. This was left to stand overnight in a fume cupboard. The next day, 1 mL 60% perchloric acid ($HClO_4$) was added using a dispenser pump, whilst swirling the beakers gently. Next, 7 mL of 40% hydrofluoric acid (HF) was added using a dispenser pump. Each beaker was covered with an acid-washed PTFE watch glass and placed on a hotplate (sand bath) which was slowly increased in temperature. When vapour started to rise and condense on the watch glass (reflux conditions), the temperature was maintained for two hours. After two hours, the beakers were moved to a heat-proof mat and allowed to cool. The underside of the watch glasses was rinsed using deionised water and the beaker left to evaporate. 1mL of concentrated sulphuric acid (98% H_2SO_4) was then added, after which the beaker placed on the hotplate again to drive off the perchloric acid. The remaining sulphuric acid solution was diluted to 30 ml and the sediment-free supernatant was decant onto a filter paper (Whatman 542) and into a 50 mL centrifuge tube. Finally, the solution was further diluted to 50 ml.

Each hotplate batch of 14 samples contained two reagent blanks, two duplicate samples and a digestion of NJV942 peat, a certified reference sample of peat with known metal cation concentrations.

Total metal cation concentrations (Al, Ca, Fe, K, Mg, Mn, Na and Ti) present in the sulphuric acid solutions were measured using Inductively Coupled Plasma - Optical Emission Spectrophotometer (ICP-OES; manufacturer: Thermo Fisher Scientific, Bremen, Germany; model: iCAP 7600 Duo). Radial configuration was chosen to measure Al, while all other elements were measured using Axial configuration, as the latter is preferably for smaller concentrations (< 1 ppm; *pers. comm.*, R. Gasior). However, most Ca, K and Na concentrations were found to be below detection limits, and therefore left out of any further analysis. For the other elements, a small number of measurements below the detection limit was retained in the final dataset if the concentration values were not negative or zero. Values of exactly zero were left out those likely represent oversaturated measurements.

Mean blank concentrations were calculated for each element from 16 blank measurements. Because of the sensitivity for detection limits, I tested for outliers among the blanks using Grubb's test, after which a maximum of one or two outliers were excluded per element. Grubb's test calculates Z, the absolute deviation from the sample mean in units of the sample standard deviation (Grubbs, 1969):

$$Z = \frac{|\text{ sample mean} - \text{sample value }|}{sample\ standard\ deviation}$$

[Eq. 4.2]

Samples with Z > 2.59 (the critical value for n=16 samples) were identified as outliers. Detection limits were calculated per element as the mean of all blanks, plus 3x the standard deviation of all blanks, after excluding outliers. For duplicate peat samples, a mean concentration value is reported per element. If one of the duplicates was found to have a value below the detection limit, only the duplicate with a value above the detection limit was used.

Raw ICP values (in mg L^{-1}) were corrected for blank concentrations by subtracting the mean of the blanks (in mg L^{-1}). This was further corrected for dilatation by multiplying with the dilution factor (50 ml). It was then converted to soil concentrations (in mg kg^{-1}) by dividing this by the oven-dry weight of each sample (in g). Since the samples were only dried at 40 °C, and not oven-dried at 105 °C, each sample weight was additionally corrected for total moisture content, to derive the correct oven-dry weight:

$$ODW = W * \frac{(1 - M)}{1}$$

[Eq. 4.3]

Here, *ODW* is the oven dry weight (g), *W* is the weight of the sample as dried at 40°C (g), and *M* is the moisture content expressed as fraction (see Chapter 6 for details).

Elemental concentrations of Al, Fe, Mg and Mn were normalized with respect to Ti by calculating the Al/Ti, Fe/Ti, Mg/Ti and Mn/Ti ratios. This compensates for natural variations in the amount of dust supplied to the peatland and for bulk density differences within the peat profile (Weiss et al., 2002). Ratios were then compared with typical values from the Upper Continental Crust (UCC; McLennan, 2001).

4.4.6 Radiocarbon dating

Peat samples from the Lokolama and Ikelemba transects were radiocarbon dated to understand if river-influenced peatlands have similar basal ages and accumulation rates as non-river-influenced peatlands in DRC, or as interfluvial basin peatlands in ROC. Basal samples from the lowest 10 cm of a peat core were dated every other kilometre along each transect, totalling three basal dates from Ikelemba and three basal dates from Lokolama. At Ikelemba, these were collected from 1.0, 3.0 and 5.0 km along the transect, at depths of 1.2, 2.0 and 3.9 m, respectively. At Lokolama, basal samples were collected from 1.0, 3.0 and 5.0 km along the transect, at depths of 4.1, 2.9 and 6.0 m, respectively.

In addition, three extra peat samples were dated downcore from the deepest core of each transect (IKE_5.0 and LOK_5.0), to assess changes in accumulation rates over time. These so-called rangefinder dates were selected to coincide as much as possible with observed changes in the downcore inorganic chemistry (see section 4.5.5) or organic matter concentrations (see Chapter 2, section 2.4.3 for details). Samples were located at 100-110, 260-270 and 440-450 cm depth (LOK_5.0) and 140-150, 200-210 and 300-310 cm depth (IKE_5.0). Organic matter concentrations of LOK_5.0 showed very little variations downcore, so inorganic chemistry was used to guide the choice of rangefinder depths. Since downcore inorganic chemistry was only analysed at 4.0 km along the Lokolama transect (as the LOK_5.0 core had not been collected at the time), it was assumed that the cation concentrations of this core are representative of LOK_5.0 as well. Observed changes at LOK_4.0 included a relative peak in Fe and Ti at 100-110 cm depth; an increase in Al and relative peak in Ti at 260-270 cm; and a very strong increase in Al at 440-450 cm. At IKE_5.0, there was more variation in organic matter concentrations downcore. Sampling depths were chosen because of a sudden increase in Al, Fe, Mg and TI at

140-150 cm; a strong drop in organic matter concentration to below 80% at 200-210 cm, indicating a layer with higher sediment concentrations; and a peak in Al and sudden increase in Fe at 300-310 cm, before a mineral intrusion (< 65% OM) between 320 and 370 cm depth.

As such, a total of 12 peat samples (6 basal dates, and 6 additional rangefinders) were radiocarbon (^{14}C) dated using accelerator mass spectrometry (AMS), following the same protocols as Dargie et al. (2017). Samples were processed and analysed at the Natural Environmental Isotope Facility (NEIF) environmental radiocarbon laboratory and the Scottish Universities Environmental Research Centre (SUERC) AMS laboratory in East Kilbride, Scotland.

Because the sampled peat is generally very humified and mostly lacks wood fragments, seeds or macrofossils that can be easily dated at a fixed depth, bulk samples of peat were used. Each sample was mixed thoroughly inside the plastic bag in which it was sampled to ensure homogeneity, after which a subsample of approximately ~2 cm^3 was taken. Each sample was sieved at 180 µm to remove fine roots that would give younger ages than the peat itself. Small peat fragments were washed through the sieve using deionised water. Between each sample, the sieve was flamed with a Bunsen burner to burn off any remaining organic matter, and then washed clean with deionised water. Samples were then centrifuged to remove any excess water.

At the NEIF facility, the samples were further pre-treated with HCl-KOH-HCL to extract carbon. Samples were first digested in 0.5M HCl (at 80°C for 2 hours), washed free from mineral acid with deionised water, and then digested in 0.5M KOH (again at 80°C for 2 hours). This digestion was repeated using deionised water until no further humic substances were extracted. The residue was rinsed free of alkali, digested in 0.5M HCl (at 80°C for 1 hour), then rinsed free of acid, dried and homogenised. The total carbon in a known weight of the pre-treated sample was then recovered as CO_2 by heating with CuO in a sealed quartz tube. This gas was converted to graphite by Fe/Zn reduction, after which the graphite was analysed for the percentage modern carbon (^{14}C/^{12}C) at the SUERC AMS laboratory.

The AMS results obtained represent conventional radiocarbon years Before Present (BP, relative to AD 1950), expressed at the ± 1 σ level of analytical confidence. However, because the atmospheric ^{14}C concentration has not been stable over time, these dates need to be calibrated.

Previously, radiocarbon dates from Ekolongouma in ROC (1.20° north) were calibrated by Dargie et al. (2017) using the IntCal13 Northern Hemisphere atmospheric calibration curve (Reimer et al., 2013). However, Lokolama and Ikelemba are located closer to and on either side of the Equator (Ikelemba at 0.28° north, Lokolama at -0.33° south). Therefore, radiocarbon dates for these transects were calibrated using a mixed calibration curve consisting of 50% IntCal20 (the updated Northern Hemisphere curve; Reimer et al., 2020) and 50% SHCal20 (the updated Southern Hemisphere curve; Hogg et al., 2020). Both the IntCal20 and SHCal20 curves use an updated statistical methodology (Monte Carlo Markov Chains), compared with the IntCal13 approach (Heaton et al., 2020). To facilitate proper comparison between the DRC dates sampled here and the dates for the interfluvial basin site in ROC (Ekolongouma), I recalibrated all ROC dates obtained by Dargie et al. (2017) using the same mixed IntCal20/SHCal20 curve. The results from Lokolama and Ikelemba were then compared with each other, as well as with the recalibrated ROC results.

All calibrations were implemented in the online programme OxCal (version 4.4; Bronk Ramsey, 2009), using the default settings for a Poisson mediated deposition model (Bronk Ramsey, 2008; Bronk Ramsey & Lee, 2013). All calibrated ages are median values obtained from the modelled calibration, reported as calibrated years Before Present, relative to AD 1950 (cal yr BP), alongside a 2σ (95%) confidence interval.

Peat and carbon accumulation rates were estimated following the methods of Clymo et al. (1998) and Korhola et al. (1995). First, a peat accumulation rate (r, mm yr^{-1}) was calculated using:

$$r = \frac{h}{t} \qquad \text{[Eq. 4.4]}$$

where h is the total peat thickness (mm) and t is the number of years between the top and bottom of the peat layer. From this, the dry mass accumulation rate (A, g m^{-2} yr^{-1}) was calculated using the following equation:

$$A = r * \rho * 1000 \qquad \text{[Eq. 4.5]}$$

Here, r is the peat accumulation rate (mm yr^{-1}) and ρ is the mean bulk density (g cm^{-3}) as sampled evenly across the peat layer. From this, a long-term rate of carbon accumulation over the whole peat core (*LORCA*, g C m^{-2} yr^{-1}) can be calculated using the following equation:

$$LORCA = A * C \qquad \text{[Eq. 4.6]}$$

Here, A is the dry mass accumulation rate (g m^{-2} yr^{-1}) over the whole peat core and C is the mean carbon fraction sampled evenly across all layers. Further details about the laboratory analysis of dry bulk density and carbon concentration can be found in Chapter 6, sections 6.4.1 and 6.4.2.

To study how carbon accumulation rates have changed throughout the peatland's development, it is possible to calculate apparent carbon accumulation rates (aCAR, g C m^{-2} yr^{-1}) over shorter segments of the peat profile. However, it is argued by Young et al. (2021) that aCAR should not be used to compare accumulation rates across different time periods in the peatland's development, as it is dependant on the age of the respective layers. Older layers will have lost more mass due to continuing decay, thereby reducing their apparent accumulation rates relative to younger layers. Furthermore, aCAR can only ever provide positive values of carbon accumulation over time, thereby obscuring potential losses of peat. Thus, aCAR values are not representative of true accumulation rates, and should not be used to compare past accumulation rates according to Young et al. (2021). This is especially true when analysing apparent accumulation rates in the acrotelm layer near the peat surface, as this top part of the peat profile is not yet as decomposed as lower peat layers. This can result in deceptively high accumulation rates for near-surface peats (Young et al., 2019).

Despite these limitations, aCAR can be a potentially useful tool in comparing accumulation rates at greater depths across different sites, as long as these peat layers span the same timeperiods to ensure that they have experienced the same amount of 'decay time'. Thus, I calculated aCAR values for each peat layer between the available rangefinder samples, for both Lokolama and Ikelemba as well as Ekolongouma, using only the mean bulk density and C concentration values of the respective layers. Additionally, I plot age-depth curves (i.e., peat age against thickness) to help understand past changes in peat development. Because aCAR is mathematically the first derivate of the age-depth curve, this is the preferential approach to show this information, as it avoids associating a dimension of carbon accumulation rates (in g C m^{-2} yr^{-1}) with past developments, which can easily be misinterpreted.

4.5 Results

The following section presents the results of the analyses of peatland hydrology, geochemistry and age. In discussing these results, the focus is on comparing the river-influenced Ikelemba transect and the non-river-influenced Lokolama transect. However, pore water, river water and peat chemistry will also be compared with the three Ruki River transects Mpeka, Bondamba and Bolengo. For ease of reference, a summary of all transect descriptions is presented in Figure 4.6. This figure represents a condensed version of the individual transect descriptions as presented in Figure 2.6-2.12.
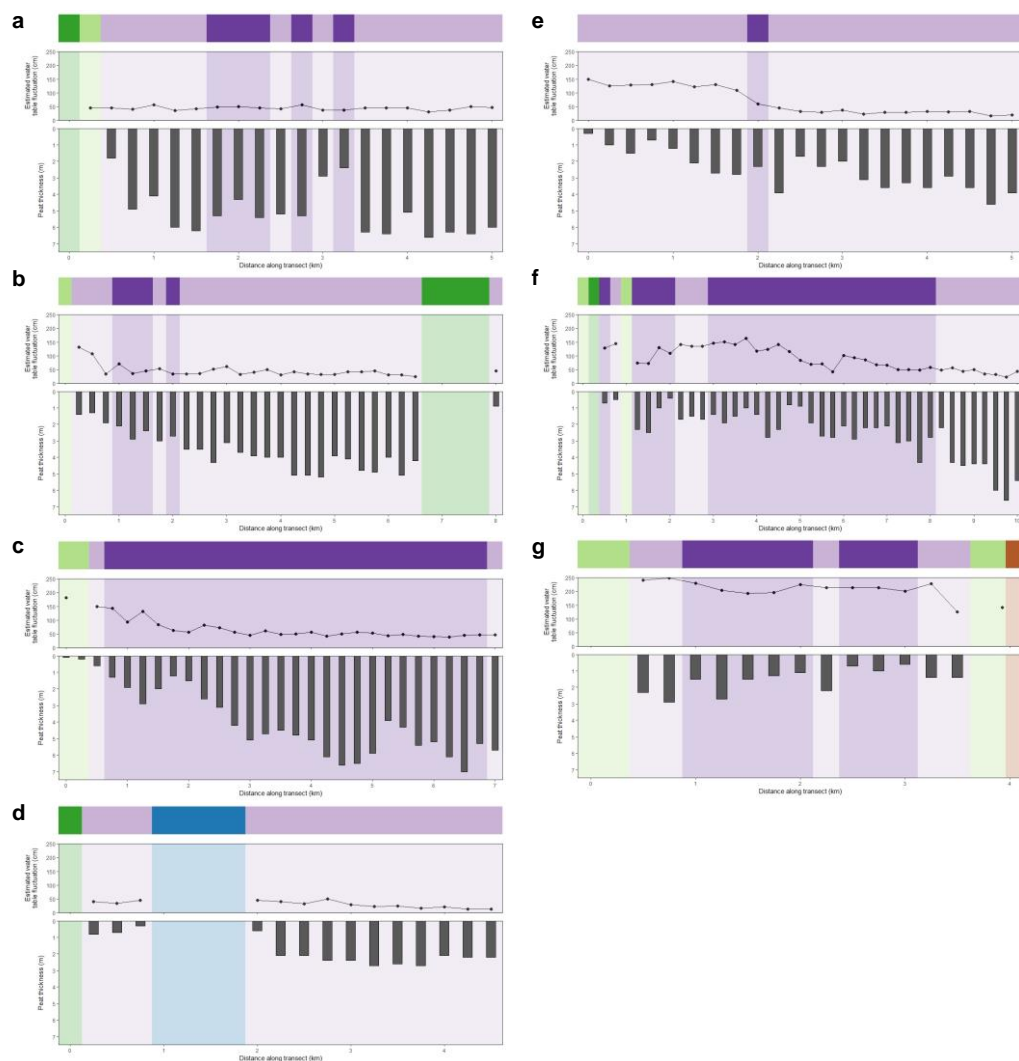
Figure 4.6. Condensed transect overview. *Each panel shows landcover types (top bar), estimated water table fluctuation (middle row; absolute difference between estimated maximum inundation height and dry season water table depth, cm), and peat thickness (bottom row, m). Purple is palm swamp forest, pink is hardwood swamp forest, dark green is* terra firme *forest, light green is non-peat forming seasonally inundated forest, blue is open water, and brown is savanna. Panels are ordered by increasing High-Water Fraction, i.e. from relatively little river impact to high seasonal river flooding: Lokolama (**a**), Bolengo (**b**), Bondamba (**c**), Boloko (**d**), Ikelemba (**e**), Mpeka (**f**) and Tumba (**g**). Note the differences in x-axis length.*

4.5.1 Peatland water tables

The Ikelemba transect, which runs perpendicular from the Ikelemba River towards *terra firme* upland, was expected to show considerable water table fluctuations between the dry and wet seasons, particularly at 1 and 3 km from the river. It was observed at the time of the first visit in March 2018, during the small dry season, that the water table at IKE_1.0 was 22 cm below the peat surface. That same site was inundated by 70 cm of water above the peat surface at the end of the major wet season during the second visit in January 2020 (Figure 4.7). This confirms that this site at 1 km from the Ikelemba River at least occasionally experiences water table fluctuations of close to a metre difference between the dry and wet season. Unfortunately, the loss of sensors from the field meant no year-round water table data could be collected at both the IKE_1.0 and IKE_3.0 sites.

This major wet season inundation of IKE_1.0 contrasts with the inundation levels recorded further along the transect at 5 km from the Ikelemba River. Inundation levels at IKE_5.0, 5 km from the river and documented using the pressure sensors every 20 minutes, are much lower with a maximum recorded water table height of only 10 cm above the peat surface during the major wet season in December 2019 (green line in Figure 4.8). On the other hand, this site experiences very low water tables that can occasionally exceed more than 60 cm below the peat surface during dry periods. Thus, both IKE_1.0 and IKE_5.0 are characterised by relatively large water table fluctuations, but resulting from different patterns.

Throughout the 1.5 years of measurement, water table depths at IKE_5.0 are below the peat surface 98.2% of the time. This compares markedly with the 45.4% measured on average across the three Lokolama sites (blue, pink and yellow lines in Figure 4.8). The three sites at Lokolama all follow the same pattern, characterised by relatively shallow fluctuations around the peat surface. The minimum recorded values across the three Lokolama sites is -37 cm and the maximum 20 cm, which differs markedly from the minimum and maximum recorded values of -65 and 10 cm at IKE_5.0, respectively. Mean (± s.d.) water table depth across the three Lokolama sites is also considerably higher with -0.2 (± 8.6) cm, compared with -18.6 (± 12.2) cm at IKE_5.0. However, both Lokolama and Ikelemba show a strong drawdown of water between March and May 2019, indicating potentially severe drought conditions across the wider region (Figure 4.8).

Figure 4.7. Example of seasonal inundation at 1 km from the Ikelemba River. *The photo above shows the IKE_1.0 site during the dry season in March 2018. The photo below shows approximately the same site at the end of the wet season in January 2020. Photos taken by the author.*

Figure 4.8. Water table heights along the Lokolama and Ikelemba transects. *Water tables were measured at four sites at Lokolama (LOK_1.0, LOK_3.0, LOK_5.0) and Ikelemba (IKE_5.0). Positive (negative) water table depths are above (below) the peat surface. Measurements were taken every 20 minutes between February/March 2018 and November 2019. Small artefacts from missing data (in the form of unnatural straight lines) are visible in February 2019, due to corrupted atmospheric pressure data.*

Apart from having deeper water tables, belowground rates of change (RC) in water table height are also more variable at Ikelemba. Mean (± s.d.) RC across the three sites in Lokolama is 0.00089 (± 0.86579) cm hr^{-1}, compared with 0.00046 (± 1.06071) cm hr^{-1} at IKE_5.0. Thus, on average, refill of the belowground water table is about twice as fast at Lokolama as at 5 km along the Ikelemba transect, and the higher standard deviation indicates more extreme fluctuations at Ikelemba. In particular, the maximum recorded drop in belowground water table at Ikelemba is 53.0 cm hr^{-1}, almost twice the maximum drop of 28.5 cm hr^{-1} recorded on average across the three Lokolama sites. The maximum rate of belowground water refill is slightly larger at Lokolama (41.4 cm hr^{-1} on average) than at Ikelemba (33.4 cm hr^{-1}).

4.5.2 Peat surface microtopography

Inundation fractions of each quadrat, as caused by microtopography variation, are plotted in Figure 4.9 for different levels of water table depth. All six sites that were analysed across the Lokolama and Ikelemba transects show a rapid increase in inundation fraction as water table depths rise from approximately 5 cm below the peat surface to 20 cm above. This is because the mean height differences measured in the 16 m^2-quadrats are generally low (mean 8.6 ± 9.0 cm across all sites, n=240; Table 4.1).
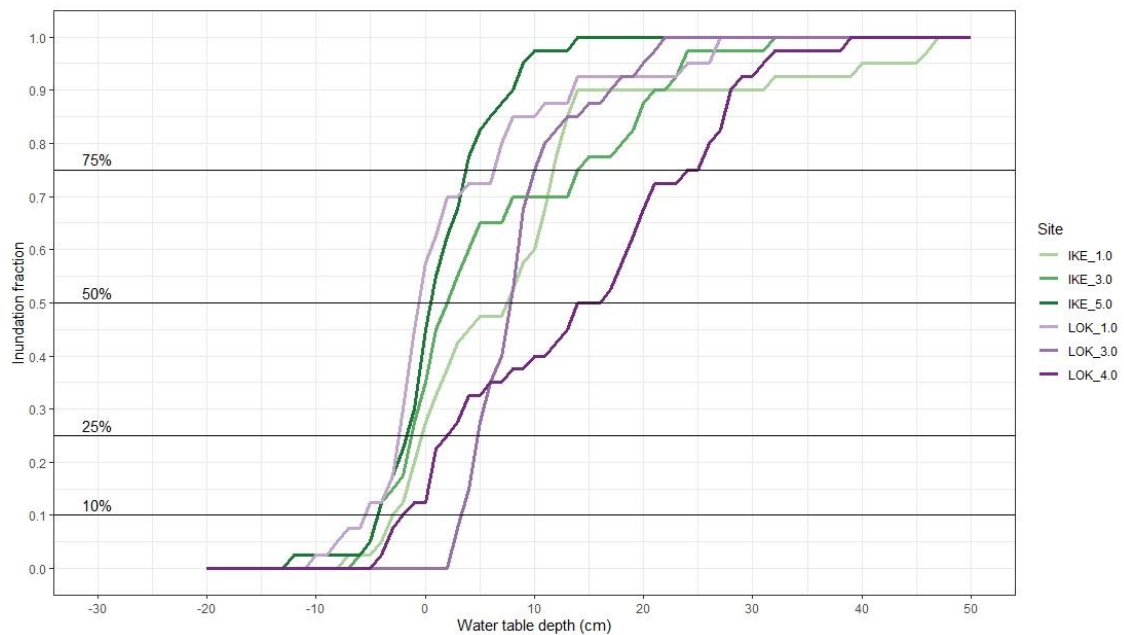
Figure 4.9. Inundation fractions per water table depth at Lokolama and Ikelemba. *Inundation fractions are based on the fraction of 40 surface height measurements in a quadrat that is inundated at each water table depth. Six quadrats installed ever other kilometre across the Lokolama and Ikelemba transects. The black horizontal lines indicate the water table levels at which 10, 25, 50 or 75% of each quadrat (40 measurements) is covered by water.*

However, the average microtopographic height difference at Lokolama (9.6 cm, n=120) is found to be about 30% higher than at Ikelemba (7.3 cm, n=120; Mann-Whitney U test, p<0.01). As such, higher minimum water table depths are required at Lokolama than at Ikelemba to inundate 10, 25, 50 or 75% of each quadrat's surface area.

Strikingly, the Lokolama and Ikelemba transects show an opposite gradient in microtopography, with both mean and standard deviation of the absolute height differences increasing along the Lokolama transect but decreasing along the Ikelemba transect. This means that LOK_1.0 and IKE_5.0, both located about 1 km from a peatland edge with transition to *terra firme* forest, have relatively little microtopographic height differences. However, further away from the *terra firme*

edge (either 4 km away at LOK_4.0 or 5 km away at IKE_1.0), microtopography variation appears to increase, as measured by the mean and standard deviation of the absolute height differences.

Site	Mean absolute surface height differences (cm)	SD of absolute surface height differences (± cm)	Maximum absolute surface height difference (cm)	Minimum required water table depth (cm) per inundation fraction			
				10%	25%	50%	75%
LOK_1.0	5.6	6.9	27	-6	-2	0	7
LOK_3.0	9.1	4.9	22	4	5	8	10
LOK_4.0	15.0	10.9	39	-2	2	14	24
Mean LOK	9.6	8.9	39	-2	1	7	14
IKE_1.0	10	11.5	47	-3	0	8	12
IKE_3.0	8.1	8.6	32	-4	-1	2	14
IKE_5.0	3.7	3.4	14	-4	-1	1	4
Mean IKE	7.3	9.0	47	-4	-1	2	10
Mean LOK+IKE	8.6	9.0	47	-4	-2	0	2

Table 4.1. Statistics of microtopographic variation. *Microtopographic variation is measured as the absolute difference peat surface height (cm). Each site includes 40 measurements per quadrat. Mean values across transects are based on 120 measurements (LOK or IKE), or 240 (both). Minimum required water table depths (cm) reflect the horizontal lines in Figure 4.9.*

4.5.3 Peat and river water inorganic chemistry

The Ruki River has a mean (± s.d.) pH of 3.04 (± 0.59) and electrical conductivity of 32 (± 6.6) μS cm^{-1} (n=4, excluding the Bondamba side stream). This is slighter lower than the Ikelemba River, which has a pH of 3.66 and EC of 69 μS cm^{-1}, as measured near the Ikelemba transect (n=1). Mean pH across all six river water samples is 3.20 (± 0.54), while mean electrical conductivity is 39.5 (± 14.7) μS cm^{-1}.

However, the four Ruki River measurements are very site specific, with more than a unit difference in pH between the Bolengo and Bondamba sampling sites, which are only 20 km apart. In general, though, a downstream trend towards more acidic conditions is detected along the Ruki River (Table 4.2), likely because the acidic content of the river scales with the peatland area being drained. However, no downstream trend is detected for electrical conductivity (Table 4.2).

The main difference in water inorganic chemistry between the different sampling sites is the much higher K concentration in the Ruki River, and similarly in the Ruki side stream near Bondamba, compared to the order of magnitude lower K concentration in the Ikelemba River (Table 4.2). Sodium concentration is also higher in the Ruki River and its side stream, compared to the Ikelemba River. The other elements AL, Ca, Fe, Mg, and Mn all have similar concentrations across the two rivers and the side stream.

The Ca/Mg ratio of the Ikelemba River is 2.19, while the Ruki River has a ratio of 2.51 as measured at Bolengo. Only the Bondamba side stream has a higher Ca/Mg ratio of 3.39, owing to a lower Mg value.

Site	Distance (km)	pH	EC (µS cm^{-1})	Al (mg L^{-1})	Ca (mg L^{-1})	Fe (mg L^{-1})	K (mg L^{-1})	Mg (mg L^{-1})	Mn (mg L^{-1})	Na (mg L^{-1})	Ca/Mg ratio
Ikelemba River											
Ikelemba (n=3)	100	3.66	69.2	0.330	0.230	0.293	0.345	0.105	0.0096	0.160	2.19
Ruki River											
Bolengo (n=1)	220	4.03	34	0.278	0.285	0.236	5.712	0.114	0.0109	0.248	2.51
Bondamba	200	2.89	23	-	-	-	-	-	-	-	-
Mpeka	80	2.64	41	-	-	-	-	-	-	-	-
Bokuma	60	2.58	29	-	-	-	-	-	-	-	-
Bondamba side stream											
Bondamba (n=1)	200	3.42	41	0.236	0.276	0.157	2.837	0.082	0.0079	0.667	3.39

Table 4.2. River water pH/EC-measurements and metal cation concentrations. Distance is the estimated river distance between the site and the river's confluence with the Congo mainstem. Samples sizes indicate the number of pseudo-replicates for cation concentrations only. All pH/EC-measurements have a sample size of 1.

Elemental concentrations in peat pore/surface water across the five transects that were analysed are very consistent, with very few significant differences found between transects (Figure 4.10). Only Na concentrations are different across transects, with Bondamba having significantly higher values than all other transects, and Ikelemba and Lokolama having significantly lower values than all Ruki River transects ($P<0.05$, one-way ANOVA with post-hoc Tukey HSD test).

It is notable how the Lokolama transect, which has the smallest sample size, has consistently low variations in elemental concentrations (indicated by the small boxplot heights in Figure

4.10), compared with the other transects. This is line with the expected shallow environmental gradients along this transect.
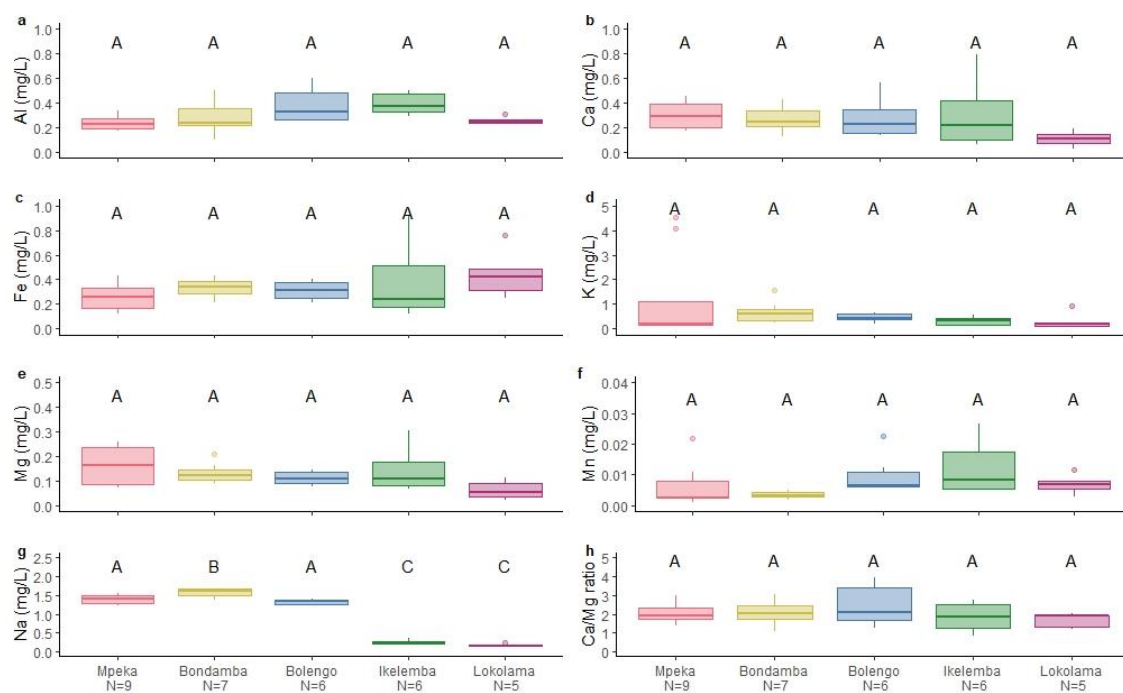
Figure 4.10. Boxplots of geochemistry of peat pore/surface water across five transects. *Panels show selected metal cation concentrations (in mg L^{-1}) and ratios (for Ca/Mg). Transects that share the same letter are not significantly different from each other (p<0.05, using one-way ANOVA with post-hoc Tukey HSD test for Al, Mg, Na and Ca/Mg; or Dunn's Kruskal-Wallis multiple comparison test, p-values adjusted with the Benjamini-Hochberg method, for Ca, Fe, K and Mn). Reported values for K at Mpeka include two samples below the detection limit (< 0.1.05 mg/L).*

On average, Na is the most abundant element of the measured cations in DRC peat water (mean 1.029 ± 0.587 mg L^{-1}), followed by K > Fe > Al > Ca > Mg > Mn (Table 4.3). Although no significant differences between transects are observed for K, there is considerable variation in the concentrations of this element, with some relatively large outliers of more than 4 mg L^{-1} measured at Mpeka (Figure 4.10f).

	Al (mg L^{-1})	Ca (mg L^{-1})	Fe (mg L^{-1})	K (mg L^{-1})	Mg (mg L^{-1})	Mn (mg L^{-1})	Na (mg L^{-1})	Ca/Mg ratio
Mean	0.305	0.262	0.334	0.656	0.127	0.008	1.029	2.045
St. Dev	0.113	0.161	0.167	0.987	0.066	0.006	0.587	0.710
Min.	0.094	0.028	0.118	0.041	0.023	0.001	0.133	0.830
Max.	0.603	0.790	0.915	4.555	0.303	0.027	1.689	3.984

Table 4.3. Geochemistry of peat pore/surface water in the DRC. *Concentrations are in in mg L^{-1} for all elements, plus the Ca/Mg ratio. N=33 for all elements (9 Mpeka, 7 Bondamba, 6 Bolengo, 6 Ikelemba, and 5 Lokolama). Reported values for K includes two samples from Mpeka below the detection limit (< 0.105 mg/L).*

The mean (± s.d.) of the measured Ca/Mg-ratios in peat pore water is 2.045 (± 0.710). The maximum observed Ca/Mg-ratio is close to 4, similar to the mean regional rainwater estimate obtained in ROC by Dargie (2015). However, this maximum value of 4 was only observed in peat pore water near the end of the Bolengo transect (Figure 4.11). All other transects are found to have values well below the regional rainwater estimate, and often even below 2, which is the minimum global average of continental rainwater (Berner & Berner, 2012). Rather than corresponding with rainwater, Ca/Mg-ratios in peat water samples are closer to the lower Ca/Mg-ratios for the Ruki (2.51) or Ikelemba (2.19) Rivers. Because the Ca/Mg-ratio is not larger than that of rainwater, it can be assumed that there is no additional non-atmospheric (minerotrophic) source of Ca into the peat water from nutrient-rich surface or groundwater (Lähteenoja et al., 2009a; Weiss et al., 2002).
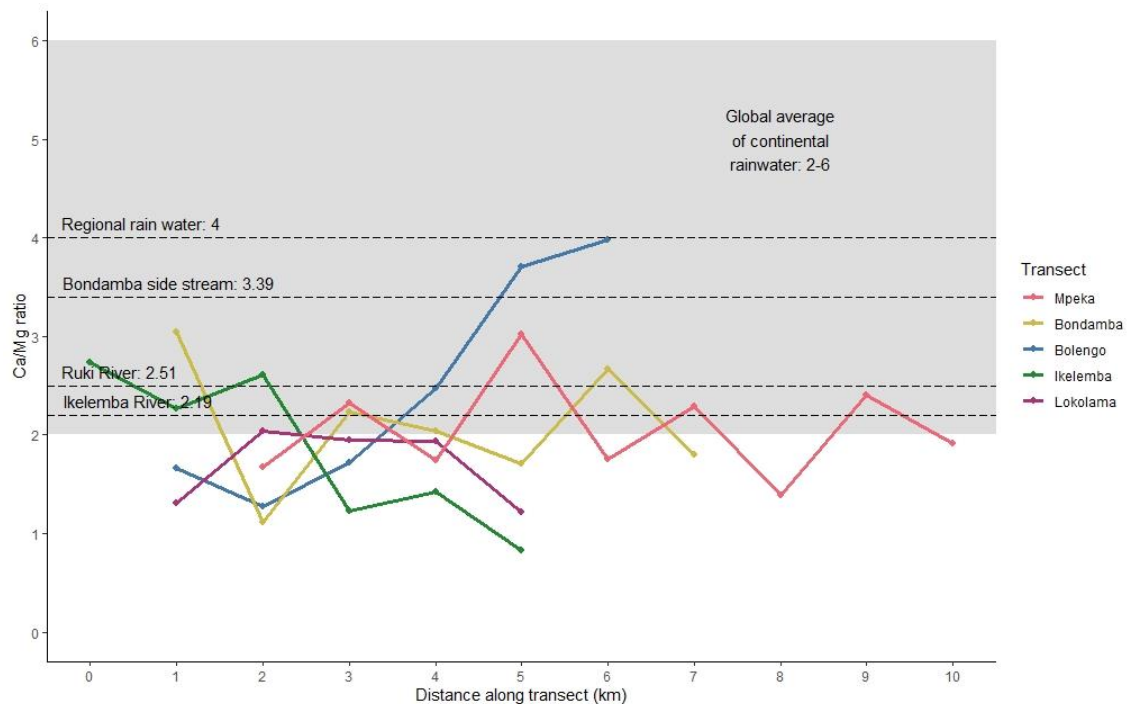
Figure 4.11. Ca/Mg-ratios of peat pore/surface water along five transects. *Grey shading indicates the global average of continental rainwater, from Berner and Berner (2012). The upper dashed line indicates the regional rainwater estimate in ROC, from Dargie (2015). The three lower dashed lines reflect local river water samples from Table 4.2.*

Nevertheless, seasonal hydrological changes that affect upland runoff or riverbank overflow likely result in small variations in Ca inputs. A clear upward trend is seen along the Bolengo transect, moving away from the river towards the *terra firme* forest edge, which could indicate potential Ca supply from upland runoff. However, an opposite trend is observed along the Ikelemba transect, which also runs from the river towards the *terra firme* forest edge, suggesting

upland runoff is not important there. The difference could reflect local hydrological conditions at the time of sampling, as the Bolengo transect was sampled just after rainfall at the end of the 2019 summer dry period. As the Ca/Mg-ratio does not reach above 4, this peak is thus most likely the result of a sudden increase in rainwater and upland runoff into the peatland. On the other hand, the Ikelemba transect was sampled during a dry period in January 2020 at the end of the major wet season. A temporal lack of rainwater could explain the lower Ca/Mg-ratios observed that are observed near the end of this transect, when moving away from the river. Finally, river flooding from the wet season had not entirely receded along the first few kilometres of this transect, explaining the relatively higher Ca/Mg ratios there, which mirror those of the river itself.

4.5.4 Peat surface inorganic chemistry

The most abundant metal cation element in peat surface samples is Al (mean 1,365 ± 591 mg kg^{-1}), followed by Fe > K > Ca > Mg > Mn > Na (Table 4.4). This order is generally similar to elemental abundance in peat pore and surface water samples, except that Na was the most abundant element in peat water, while it is the least abundant in surface peat. This suggests that Na concentrations are potentially sensitive to changes in the hydrologic cycle.

Mean pH of peat surface samples (3.77 ± 0.14) is higher than that of all river samples (mean 3.20). Similarly, mean EC of peat surface samples (77.9 ± 28.3 µS cm^{-1}) is higher than that of all river samples (mean 39.5 µS cm^{-1}). This pattern also holds when excluding the non-river-influenced Lokolama transect. This indicates that riverbank overflow does not have a buffering effect on the adjacent peat swamps. Rather it shows that acidic peat water, as it drains from the peat swamps, causes the rivers to become more acidic.

	pH	EC (µS cm^{-1})	Al (mg kg^{-1})	Ca (mg kg^{-1})	Fe (mg kg^{-1})	K (mg kg^{-1})	Mg (mg kg^{-1})	Mn (mg kg^{-1})	Na (mg kg^{-1})	Ca/Mg ratio
Mean	3.77	77.90	1,365	403.3	784.5	442.3	220.7	22.02	15.55	1.76
St. Dev	0.14	28.26	591	238.5	269.7	152.0	84.0	21.85	5.96	0.74
Min.	3.53	33.20	744	101.1	350.0	257.5	121.5	4.92	2.50	0.83
Max.	4.07	142.79	3,247	1,014.3	1,477.9	859.9	418.1	88.82	29.28	4.18

Table 4.4. Geochemistry of peat surface samples in the DRC. Electrical conductivity (EC) in µS cm^{-1}; concentrations of all elements in mg kg^{-1}, plus pH and Ca/Mg-ratios. N=28 for all elements (9 Mpeka, 7 Bondamba, 6 Bolengo, 3 Ikelemba, 3 Lokolama, with each sample the mean of 4 or 5 pseudo-replicates per site).

In contrast to the peat pore/surface water, which showed very little variation among transects, more variation is detected in metal cation concentrations of peat surface samples (Figure 4.12). For example, Al concentrations are significantly lower at Bondamba than at all other transects ($p < 0.05$, Kruskal-Wallis rank sum test). Fe concentrations at both Bondamba and Bolengo are also significantly lower than at Lokolama ($p < 0.05$, one-way ANOVA). Furthermore, Lokolama has significantly higher concentrations of K than all other transects, while Ikelemba has significantly lower concentrations of Na than the Mpeka and Bondamba transects (both $p < 0.05$, one-way ANOVA). These differences have likely also affected the pH and EC measurements, with significantly higher pH observed at Lokolama than at the three Ruki river transects of Mpeka, Bondamba and Bolengo. EC values are significantly lower at Bondamba, compared with Mpeka (both $p < 0.05$, one-way ANOVA). However, no significant differences are observed in Ca, Mg, Mn concentrations or Ca/Mg-ratios ($p > 0.05$, Kruskal-Wallis rank sum test).
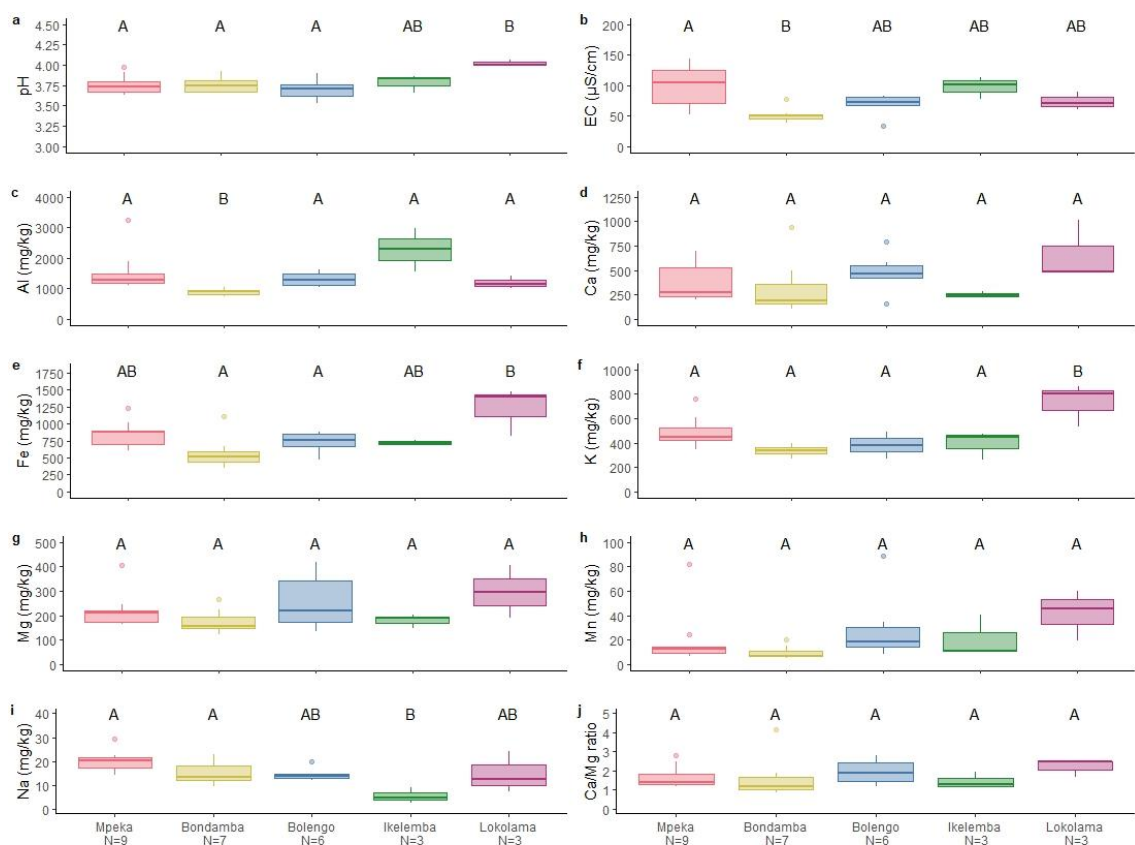
Figure 4.12. Boxplots of geochemistry of peat surface samples across five transects. *Panels show pH, electrical conductivity (EC, $\mu S\ cm^{-1}$), selected metal cation concentrations (mg kg^{-1}) and ratios (for Ca/Mg). Transects that share the same letter are not significantly different from each other ($p < 0.05$, using one-way ANOVA with post-hoc Tukey HSD test for pH, EC, Fe, K, and Na; or Dunn's Kruskal-Wallis multiple comparison test, p-values adjusted with the Benjamini-Hochberg method, for Al, Ca, Mg, Mn and Ca/Mg). Each sample is the mean of 4 or 5 replicates per site.*

Although often not statistically significant, it can be further observed from Figure 4.12 that Lokolama generally has more abundant metal cation concentrations (Ca, Fe, K, Mg, Mn, Na, and Ca/Mg-ratio) than Ikelemba, as well as many of the other river-influenced sites. This suggest that the river-influenced peatlands could be more nutrient-poor than non-river-influenced peatlands.

Mean Ca/Mg-ratio across the transects is 1.76 (± 0.74), which is lower than the values observed in peat pore/surface water (mean 2.045 ± 0.710), suggesting the latter values are likely higher due to additional Ca-input from rainwater with a Ca/Mg-ratio close to 4. No clear trends in Ca/Mg-ratios can be seen along the five transects (Figure 4.13), which indicates that additional non-atmospheric (minerotrophic) sources of Ca into the peatlands are unlikely (Lähteenoja et al., 2009a; Weiss et al., 2002).
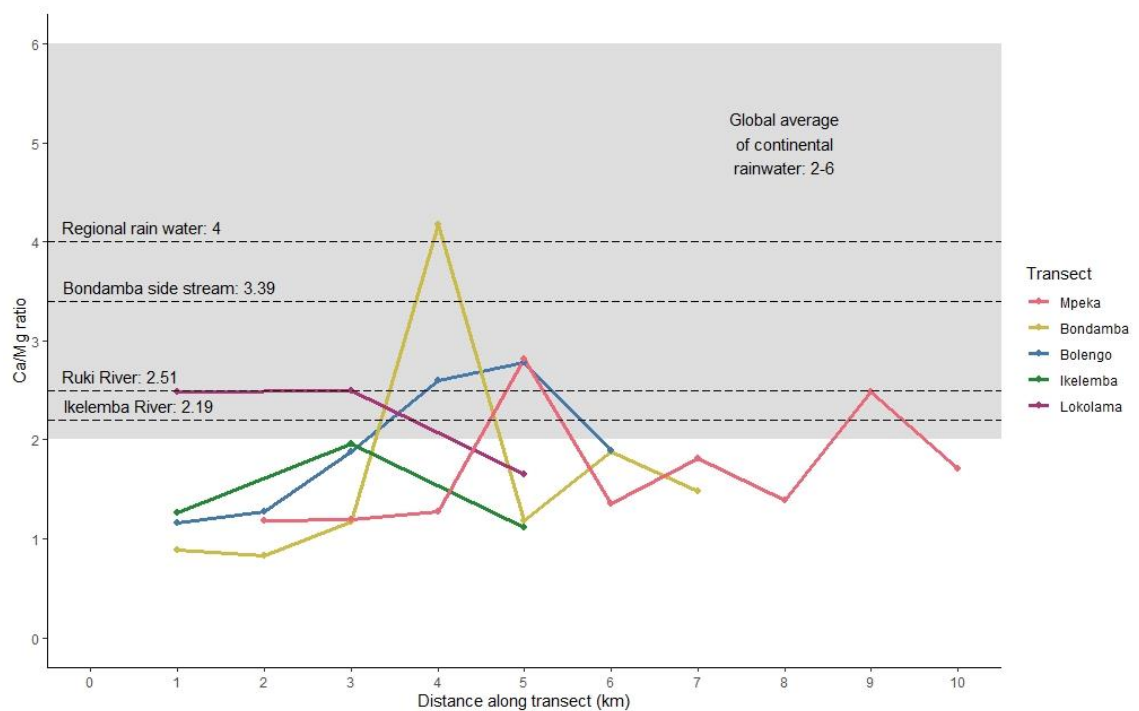
Figure 4.13. Ca/Mg-ratios of peat surface samples along five transects. *Grey shading indicates the global average of continental rainwater, from Berner and Berner (2012). The upper dashed line indicates the regional rainwater estimate in ROC, from Dargie (2015). The three lower dashed lines reflect local river water samples from Table 4.2.*

4.5.5 Downcore peat inorganic chemistry

Downcore metal cation concentrations for Al, Fe, Mg, Mn and Ti from one Lokolama and one Ikelemba core are shown in Figure 4.14. Downcore measurements of Ca, K and Na were typically

below the ICP-OES detection limits so cannot be reliably presented. This suggests that nutrient poor conditions as identified for surface peat samples are also characteristic of downcore peat samples, indicating nutrient-poor conditions throughout the peatlands' developmental histories.

Of the elements that showed reliable measurements (Al, Fe, Mg, Mn, Ti), Al is the most abundant, followed by Ti, Fe, Mg and Mn. Both Al and Ti reveal large increases towards the base of the peat core, with relatively low concentrations in the upper peat layers. Large peaks in Fe concentration can also be observed down the peat core, although this element shows increased concentrations again near the peat surface. In contrast, both Mg and Mn are mostly only present near the peat surface.

These patterns are observable both at Ikelemba and Lokolama. However, absolute elemental concentrations are generally much greater in Ikelemba than in Lokolama, particularly for Al and Ti. This potentially indicates either greater interactions with bedrock or (sub)surface sediments, or greater atmospheric depositions of metal cations.
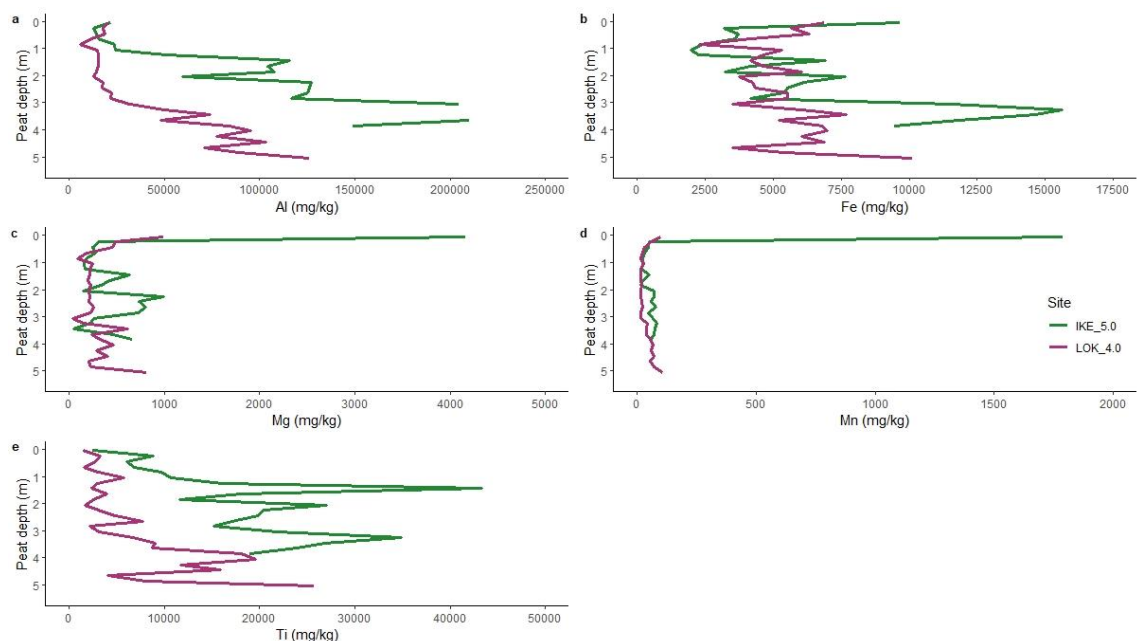
Figure 4.14. Downcore concentrations of Al, Fe, Mg, Mn and Ti at Ikelemba and Lokolama. Downcore samples are from the IKE_5.0 (green) and LOK_4.0 (pink) cores. Data on Ca, K and Na is left out because the concentrations of most of these elements was below the detection limits. Missing line segments for Al (panel a; 3-4 m depth) are due to ICP-OES oversaturation.

To investigate the origins of these elements, I plotted the same elemental concentrations normalized with respect to Ti-concentrations (Figure 4.15). This shows significant downcore enrichment of Al and Fe with respect to Ti. In particular, considerable Fe-enrichment is detected at Lokolama, which is not the case at Ikelemba. Both peat cores also show considerable Al-enrichment towards the base of the core, and this peak again appears greater at Lokolama than at Ikelemba. Thus, although absolute concentrations are larger at Ikelemba, enrichment with Al and Fe is greater at Lokolama.

However, neither of these Ti-normalized profiles crosses the typical ratios observed in the Upper Continental Crust (UCC; McLennan, 2001), which would have suggested enhanced atmospheric deposition of dust from highly-weathered tropical soils (Weiss et al., 2002). The Fe/Ti-ratio of LOK_4.0 does not correlate with absolute Al, Fe or Ti trends either, which further suggests its patterns are not due to changes in atmospheric deposition of the original material. Rather, local processes such as instability in the water table are more likely the cause of these patterns. Because Fe is sensitive to the peat's redox-state (Bhattacharyya et al., 2018; Steinmann & Shotyk, 1997), it has been suggested that alternating aerobic and anaerobic conditions in the peat profile could affect the solubility and speciation of Fe in peat soils (Weiss et al., 2002).

In contrast to Al and Fe, downcore peat samples are strongly depleted of Mg and Mn with respect to Ti, as shown in Fig. 4.15. This suggests that these elements do not accumulate in the peat profile but are instead quickly taken up by the surface vegetation (Weiss et al., 2002). However, both the absolute and the Ti-normalized values of Mg and Mn in near-surface peat are considerably larger at Ikelemba than at Lokolama, indicating more contemporary enrichment of these elements at Ikelemba. Mn in particular is known to be strongly enriched in near-surface peat layers due to bioaccumulation. Like Fe, it is relatively sensitive to changes in redox-state, with enhanced solubility in acidic, anaerobic water at lower depths (Damman, 1978; Shotyk et al., 1990). Thus, the greater presence of Mn in surface peat samples is likely related to the lower water tables that generally prevail at IKE_5.0, compared with LOK_4.0. It is suspected that a similar process affects Mg, although to a lesser extent.
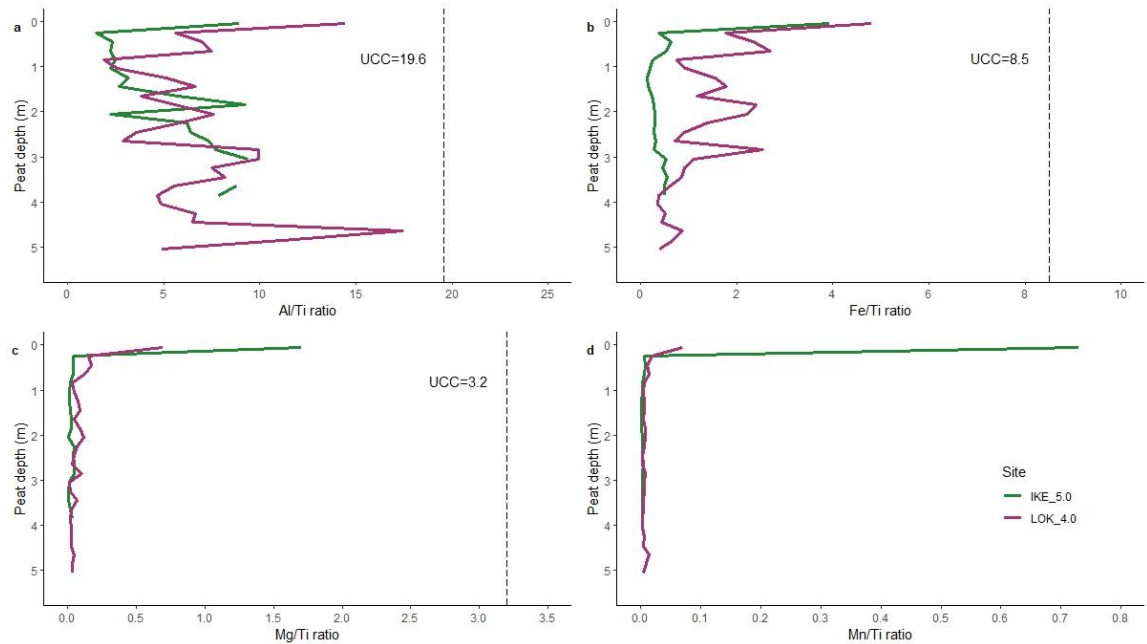
Figure 4.15. Downcore Ti-normalized concentrations of Al, Fe, Mg and Mn at Ikelemba and Lokolama. *Data is from the IKE_5.0 (green) and LOK_4.0 (pink) cores. Data on Ca, K and Na is left out because the concentrations of most of these elements was below the detection limits. Missing line segments for Al (panel **a**; 3-4 m depth) are due to ICP-OES oversaturation. Dashed lines indicates typical Ti-ratios in the Upper Continental Crust (UCC; McLennan, 2001).*

4.5.6 Basal radiocarbon dates and age-depth models

The AMS radiocarbon dates of six basal peat samples are presented in Table 4.5. Median calibrated age of the basal peat samples along the Lokolama transect ranges between 9,500 and 10,800 BP. By contrast, at Ikelemba, median peat basal ages range from 9,100 to 42,300 BP. This latter radiocarbon date of 42,3k cal yr BP (95% CI; 43,8k – 41,2k) was recorded at IKE_5.0 and represents by far the oldest peat found across the central Congo Basin so far. This date is more than 20,000 years older than the published peat samples dated in ROC (Dargie et al., 2017; Garcin et al., 2022), indicating that some areas of the central Congo Basin peatlands are much older than previously thought and harbour some of the oldest tropical peat deposits in the world (Ruwaimana et al., 2020).

A clear trend in basal age with distance from the river can be observed along the Ikelemba transect, with the peat basal age doubling every two kilometres. This contrasts strongly with the Lokolama transect, where all peat cores have the same age of approximately 10k cal yr BP.

Transect	Distance along transect (km)	Basal depth (m)	Sample code (SUERC-)	Conventional ^{14}C basal age (yr. BP)	Error (1 σ)	Median modelled calibrated basal age (cal yr BP)	2σ modelled calibrated age range (cal yr BP)
Lokolama	1.0	4.0-4.1	99679	9,497	39	10,783	11,073 – 10,590
Lokolama	3.0	2.8-2.9	99680	8,429	40	9,475	9,535 – 9,323
Lokolama	5.0	5.9-6.0	99687	9,285	42	10,480	10,644 – 10,296
Ikelemba	1.0	1.1-1.2	99688	8,124	39	9,079	9,268 – 8,992
Ikelemba	3.0	1.9-2.0	99689	1,8597	85	22,524	22,874 – 22,349
Ikelemba	5.0	3.8-3.9	99693	38,050	917	42,316	43,792 – 41,206

Table 4.5. Lateral basal ages of peat cores along the Lokolama and Ikelemba transects. *Modelled calibrated ages are obtained using a mixed calibration curve (50% IntCal20 and 50% SHCal20). Modelled calibrated age ranges represent a 2σ (95%) confidence interval.*

Table 4.6 shows the down-core AMS radiocarbon dates from the deepest core of each transect: LOK_5.0 at Lokolama, and IKE_5.0 at Ikelemba. Figure 4.16 shows the corresponding age-depth models of both cores. It can be observed that long-term apparent peat accumulation rates have been considerably larger at LOK_5.0, which has developed a ~50% deeper peat layer during roughly a quarter of the time that the peat profile at IKE_5.0 took to develop. However, both age-depth models show notable changes in slope between individual segments of each core. In particular, the slope is shallower during the third segment of LOK_5.0, between 7,500 and 2,200 cal yrs BP than before and after those dates. IKE_5.0 also has a shallower age-depth profile in the core's second segment, between 35,900 and 16,500 cal yrs BP.

Core	Peat depth (cm)	Sample code (SUERC-)	Conventional ^{14}C age (yr. BP)	Error (1 σ)	Median modelled calibrated age (cal yr BP)	2σ modelled calibrated age range (cal yr BP)
Lokolama 5km	1.0-1.1	99681	2,274	37	2,249	2,350 – 2,156
Lokolama 5km	2.6-2.7	99682	6,674	39	7,535	7,612 – 7,433
Lokolama 5km	4.4-4.5	99683	8,646	40	9,600	9,691 – 9,536
Lokolama 5km	5.9-6.0	99687	9,285	42	10,480	10,644 – 10,296
Ikelemba 5km	1.4-1.5	99690	9,884	43	11,285	11,401 – 11,203
Ikelemba 5km	2.0-2.1	99691	13,656	52	16,500	16,704 – 16,313
Ikelemba 5km	3.0-3.1	99692	31,630	412	35,927	36,886 – 35,199
Ikelemba 5km	3.8-3.9	99693	38,050	917	42,316	43,792 – 41,206

Table 4.6. Down-core peat ages at Lokolama and Ikelemba. *Samples are from the deepest core of each transect. Modelled calibrated ages are obtained using a mixed calibration curve (50% IntCal20 and 50% SHCal20). Modelled calibrated age ranges represent a 2σ (95%) confidence interval.*
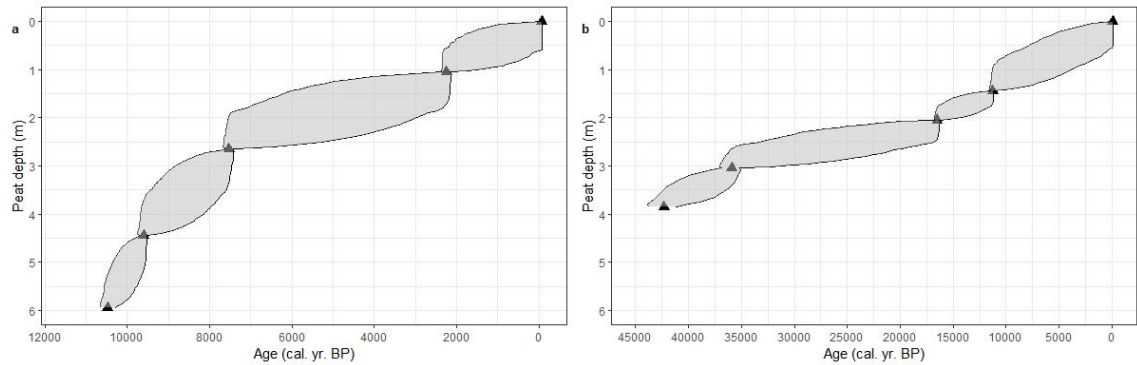
Figure 4.16. Age-depth models for the deepest peat cores from at Lokolama and Ikelemba.
*Both cores are taken at 5 km along the transect: LOK_5.0 (**a**) and IKE_5.0 (**b**). The x-axis shows peat depth (m) below the surface, the y-axis shows calibrated ages in years before present (cal yr BP, relative to 1950). Note the differences in x-axis range. The black triangles represent the median of the calibrated age ranges presented in Table 4.6. The grey shading represents the modelled 2σ (95%) confidence intervals. Modelled calibrated ages are obtained using a mixed calibration curve (50% IntCal20 and 50% SHCal20).*

Figure 4.17 shows a comparison of the age-depth models of both LOK_5.0 and IKE_5.0 with the deepest peat core sampled by Dargie et al. (2017) at the interfluvial basin site of Ekolongouma in ROC (EKG_9.0). It is clear from this figure that peat deposits of both Lokolama and Ekolongouma are of early-Holocene age, with peat initiation occurring in the early African Humid Period (shaded green). However, the slope of the age-depth curve is much steeper at Lokolama than at Ekolongouma, in particular during the peatland's initiation phase, resulting in the development of a total peat layer that is more than twice as thick. This could imply greater biomass inputs into the peat layer, lower decomposition rates, or a combination of the two at Lokolama compared to Ekolongouma. Alternatively, it is also possible that peat in Ekolongouma experienced secondary decomposition of formed peat at a later stage, for example, due to a temporary drying event or erosion, resulting in a less thick peat layer for the same age range. This hypothesis implies a regional event at Ekolongouma, rather than basin-wide climatic changes that would have impacted Lokolama as well.

Peat initiation at the river-influenced site of IKE_5.0, however, started much earlier during the Late Pleistocene. Here, peat was formed and retained over 40,000 years, including spanning the Last Glacial Maximum (shaded blue). With the start of the Holocene and the African Humid Period a similar, albeit shallower, age-depth slope is seen to the LOK and EKG cores.
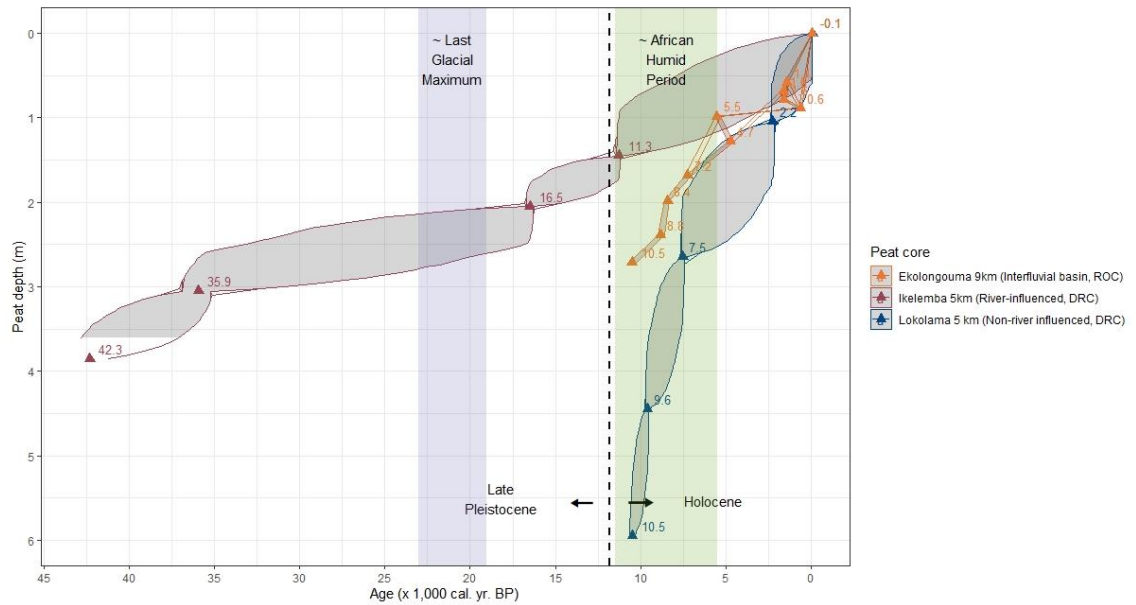
Figure 4.17. Comparison of age-depth models of Ikelemba, Lokolama and Ekolongouma. *Models included are from IKE_5.0 (dark red), LOK_5.0 (dark blue) and EKG_9.0 (orange). The x-axis shows peat depth (m) below the surface, the y-axis shows calibrated ages in 1,000 years before present (cal yr BP, relative to 1950). Data for the 9 km core from Ekolongouma is obtained from Dargie et al. (2017). In all cases, modelled calibrated ages are obtained using a mixed calibration curve (50% IntCal20 and 50% SHCal20). Triangles represent the median of the calibrated age ranges per core. Grey shading represents the modelled 2σ (95%) confidence intervals. The Last Glacial Maximum is indicated by shaded blue between 23,000 and 19,000 BP, and the African Humid Period by shaded blue between 11,500 and 5,500 BP (Collins et al., 2017). The vertical dashed line indicates the start of the Holocene (~11,650 BP; Walker et al., 2009).*

Overall, Table 4.7 shows that the long-term rate of carbon accumulation (LORCA) at Lokolama (36.79 g C m^{-2} yr^{-1}) is much greater than that of Ikelemba and Ekolongouma (11.80 and 18.84 g C m^{-2} yr^{-1}, respectively). The latter two sites have long-term rates of carbon accumulation that are much more similar, even though these sites differ strongly in terms of hydrology (river-influenced or interfluvial basin, respectively) and peat initiation age.

When looking only at the Holocene period in Figure 4.17, this pattern of greater net accumulation at Lokolama holds as well. Because of the age differences between Ikelemba and the other two cores, the timeframe of the upper surface segment of the Ikelemba core corresponds roughly with the timeframe of the full peat cores from Lokolama and Ekolongouma. The slopes of the age-depth curves during this Holocene period show that the apparent net peat accumulation rate (aCAR) of the surface peat at Ikelemba (segment 1; 13.41 g C m^{-2} yr^{-1}) is roughly comparable with the long-term rate of carbon accumulation (LORCA) at Ekolongouma (18.84 g C m^{-2} yr^{-1}), but not with that of Lokolama (36.79 g C m^{-2} yr^{-1}), which is much higher.

Compared with the Holocene period, the slope of the middle segment of the Ikelemba core (segment 3; 16,500 – 35,900 cal yrs BP), which incorporates the time of the Last Glacial Maximum, is much lower, corresponding with a lower apparent net peat accumulation rate (7.04 g C m^{-2} yr^{-1}). This could be the result of slow accumulation of peat due to lower biomass inputs and/or greater decomposition at this time. But since apparent accumulation rates only record what has remained from this period, it could also imply the loss of formed peat due to erosion or decay at a later stage.

More recently, the two non-riverine peat cores (Lokolama and Ekolongouma) show a relative decline in aCAR during the same mid-Holocene period after approximately 7,000 cal. yr. BP (segment 2 of both cores). However, this cannot be compared with Ikelemba, as the youngest date from this core originates from 11,300 cal. yr. BP.

Peat core	Segment	Depth (m)	Age ranges (cal. yr. BP)	Apparent peat accumulation rate (mm yr^{-1})	LORCA (g C m^{-2} yr^{-1})	aCAR (g C m^{-2} yr^{-1})
LOK_5.0	Full core	0 – 5.95	0 – 10,5k	0.5640	36.79 (36.23-37.45)	-
IKE_5.0	Full core	0 – 3.85	0 – 42,3k	0.0908	11.80 (11.40-12.12)	-
EKG_9.0	Full core	0 – 2.715	0 – 10,5k	0.2568	18.84 (18.53-19.30)	-
LOK_5.0	1	0.0 – 1.05	0 – 2,2k	0.4528	-	30.02
LOK_5.0	2	1.05 – 2.65	2,2k – 7,5k	0.3027	-	22.48
LOK_5.0	3	2.65 – 4.45	7,5k – 9,6k	0.8717	-	53.85
LOK_5.0	4	4.45 – 5.95	9,6k – 10,5k	1.7045	-	98.18
IKE_5.0	1	0.0 – 1.45	0 – 11,3k	0.1277	-	13.41
IKE_5.0	2	1.45 – 2.05	11,3k – 16,5k	0.1151	-	11.89
IKE_5.0	3	2.05 – 3.05	16,5k – 35,9k	0.0515	-	7.04
IKE_5.0	4	3.05 – 3.85	35,9k – 42,3k	0.1252	-	18.63
EKG_9.0	1	0.0 – 1.285	0 – 4,7k	0.2675	-	22.68
EKG_9.0	2	1.285 – 1.685	4,7k – 7,2k	0.1599	-	10.17
EKG_9.0	3	1.685 – 1.985	7,2k – 8,4k	0.2551	-	15.41
EKG_9.0	4	1.985 – 2.385	8,4k – 8,8k	0.9685	-	54.30
EKG_9.0	5	2.385 – 2.715	8,8k – 10,5k	0.1965	-	13.59

Table 4.7. Apparent and long-term rates of peat and carbon accumulation for the LOK_5.0, IKE_5.0 and EKG_9.0 cores. LORCA is the long-term rate of carbon accumulation over the full peat core, while aCAR is the apparent carbon accumulation rate of layer segments. Apparent peat accumulation rates are reported as either long-term rates for the full peat core, or per layer segment. Data for the EKG_9.0 core is obtained from Dargie et al. (2017) using a mixed calibration curve (50% IntCal20 and 50% SHCal20). Additional dates from EKG_9.0 between 0 and 1.285 m depth (segment 1) have been left out because of reversals in the age-depth profile.

4.6 Discussion

The aim of this chapter was to characterise and classify the hydrology, geochemistry and age of river-influenced peatlands in the DRC, and contrast this with non-river-influenced peatlands in DRC and ROC. Specifically, I aimed to compare the hydrology and age of the Ikelemba and Lokolama transects (see Table 4.8). In addition, I looked at the peatland's inorganic chemistry at Ikelemba and Lokolama (Table 4.8), as well as the Mpeka, Bondamba and Bolengo transects on the Ruki River.

		Ikelemba	Lokolama
Peatland type		River-influenced	Non-river-influenced
Location description		Running perpendicular from river to *terra firme* upland	Running from edge to centre of a suspected round peat dome
Vegetation description		Mostly hardwood swamp forest, but with seasonally inundated forest near the river	Mostly hardwood swamp forest, but with sections of *Raphia laurentii* dominance
Peat thickness	Mean (± s.d.) thickness	2.2 (± 1.1) m	4.5 (± 1.8) m
	Maximum thickness	4.0 m	6.0 m
Inundation description	General pattern	Seasonally inundated close to the river; near the surface further away	Stable water tables near the peat surface throughout
	Estimated max. inundation	~ 1.5 m	~ 0.5 m
Water table height (pressure sensors)	Mean (± s.d.) water table	-18.6 (± 12.2) cm	-0.2 (± 8.6) cm
	Mean (± s.d.) belowground water table rate of change	0.00046 (± 1.06071) cm hr^{-1}	0.00089 (± 0.86579) cm hr^{-1}
Microtopography	Mean (± s.d.) absolute height difference	7.3 (± 9.0) cm	9.6 (± 8.9) cm
Peat pore / surface water	Pore water metal cations	More variable	Less variable
	Mean pore water Ca/Mg	1.8 (± 0.7)	1.7 (± 0.3)
	Mean pore water pH	3.23 (± 0.10)	3.47 (± 0.05)
	Mean pore water EC	176 (± 34) µS cm^{-1}	151 (± 14) µS cm^{-1}
Surface peat	Surface peat metal cations	Lower	Higher
	Mean surface peat Ca/Mg	1.4 (± 0.4)	2.2 (± 0.4)
	Mean surface peat pH	3.78 (± 0.09)	4.02 (± 0.03)
	Mean surface peat EC	97 (± 15) µS cm^{-1}	74 (± 12) µS cm^{-1}
Downcore peat	Absolute Al, Fe, Ti conc.	Higher	Lower
	Ti-normalized Al, Fe conc.	Lower	Higher
Radiocarbon dating	Basal material	Sand-to-clay	Clay
	Oldest peat basal date	~ 42,300 cal yr BP	~ 10,800 cal yr BP
	Trend in lateral basal dates	Increasing with distance from river	All approximately 10k years ago
	LORCA	11.80 g C m^{-2} yr^{-1}	36.79 g C m^{-2} yr^{-1}

Table 4.8. Comparison of hydrology, geochemistry and peat radiocarbon dates along the Ikelemba and Lokolama transects. *Vegetation descriptions, peat thickness, inundation descriptions and peat pore/surface water pH/EC are from Chapter 2. All other data are reported in this chapter.*

Water table heights

Although no *in situ* water table measurements could be obtained from a clearly river-influenced site (IKE_1.0), personal observations from this and other sites along the Ikelemba and Ruki Rivers nonetheless make it clear that some of these river-bound peatlands experience large seasonal inundation patterns, with extensive flooding during the (end of the) wet season and deep water tables during the dry season. However, this does not necessarily mean that all this inundation is due to overbank flow from rivers. The one Ikelemba site that I was able to obtain year-round water table measurements from (IKE_5.0), which is located on higher ground towards the *terra firme* upland, shows little surface water inundation, even during the wet season. Rather, water table measurements show a relatively rapid drawdown of water, as revealed by the large negative rates of change of the water table at this site. This likely indicates effective drainage of water into lower-ground peatlands that are closer to the river. Thus, part of the inundating water that is observed closer to the river could actually be the result of (sub)surface runoff from higher-ground peatlands and *terra firme* upland.

These results from Ikelemba contrast with those from the Lokolama transect in DRC, as well as similar measurements made by Dargie et al. (2017) at Ekolongouma and Itanga in ROC. All those sites have higher water table levels closer to the peat surface and experience less fluctuations. This is expected, as both the Lokolama sites, as well as those in ROC, are located towards the edge of likely peat domes (Davenport et al., 2020). Thus, the dataloggers are located along very shallow environmental gradients away from the centre of a modest peat dome towards the peatland's edge, and so experience lower fluctuations, as the centre of the peat dome sheds excess water as overland flow which maintains relatively wet conditions near the margins.

Microtopography

However, surface wetness is not only determined by water flows, but also by the local microtopography (Dettmann & Bechtold, 2016). This chapter presented the first measurements of microtopography in the peatlands of the central Congo Basin and found that microtopography is lower at the peatland's edges next to seasonally inundated or *terra firme* forest. This was the case both at the edge of a likely peat dome at Lokolama (LOK_1.0), as well as in the river-bound peatland of Ikelemba (IKE_5.0). However, on average, Ikelemba exhibited less microtopography than Lokolama, with IKE_5.0 having the lowest local height differences of all sites that were measured. This supports the idea of more effective runoff at Ikelemba, as less pooling of water in hollows can be expected to allow for greater lateral discharge, either as overland flow or as

subsurface runoff through the top layer of peat (Dommain et al., 2010). At Lokolama, on the other hand, greater microtopography might be related to reduced runoff rates and the pooling of water, potentially explaining the wetter surface conditions that are found there. Given the relatively small water table fluctuations found at Lokolama, the influence of microtopography on surface wetness is also comparatively greater along this transect.

However, it is important to emphasize that these hydrological analyses include only a limited number of sites across two transects and that a causal relationship between microtopography and wetness is hard to establish. In particular, the lower microtopography near the peatland's edges contrasts with more extensive measurements by Lampela et al. (2016) in Central Kalimantan, Indonesia, who found no differences in microtopography patterns between areas near a peatland's margins and areas closer to the centre of a peat dome. The overall mean microtopographic surface elevation (8.6 ± 9.0 cm) is also lower than the 14.1 ± 2.2 cm reported by Lampela et al. (2016). More analyses over a wider range of sites in the central Congo Basin are needed to fully understand whether these differences are real.

Peat and river water inorganic chemistry

One way to separate out the different sources of flood water at the start of the Ikelemba transect is to analyse chemical signals in the water sources. In this chapter, I measured metal cation concentrations in both peat pore/surface water, river water, and peat surface samples. Unfortunately, only a limited number of river water samples is available, and no rainwater samples were taken in DRC, due to technical problems with the filtration of samples. Nonetheless, it can be concluded that both the Ikelemba and Ruki Rivers are extremely acidic and nutrient-poor. The pH-values measured at the Ikelemba (3.66) and Ruki Rivers (mean 3.04, n=4) are both lower than pH-values measured in the comparable blackwater Likoula-aux-Herbes River in ROC, which has a pH ranging between 3.80 and 4.65 (Dargie, 2015; Dupré et al., 1996; Laraque et al., 1998). This could be a reflection of greater connectivity between the river and the peatlands, indicating that tannin-rich, acidic water from the peatlands is draining into these left-bank tributaries of the Congo River. As expected, acidity of the Ruki River was also found to increase with closer distance towards the confluence with the Congo River, which suggests that the acidic content is related to the size of the peatland area that is being drained.

The most extreme acidic conditions observed on the Ruki River as part of this study were near the village of Bokuma, approximately 60 km from the confluence with the Congo River, where

pH was 2.6 and electrical conductivity was 29 μS cm^{-1}. However, river water chemistry is strongly affected by seasonality, as large amounts of precipitation (with a pH closer to neutrality) will dilute the acid content originating from dissolved organic matter (Clymo, 1987). Thus, less acidic conditions are expected during or near the end of the wet season. Still, strong acidic conditions have been observed at the same site near Bukoma on the Ruki River in October 2020, with a pH of 4.0 and EC of 61 μS cm^{-1} (measured with Hanna Combo metre; Ovide Emba, *pers. comm.*). This contrasts with pH-values of the Congo River mainstem, which is almost neutral during the wet season with a pH of around 6. It is also much lower than reported wet-season pH values of 4.7, 5.5 or 6.8 in the Likouala-Mossaka, Sangha and Ubangi Rivers that drain into the Congo River from the west (Dupré et al., 1996). Thus, this confirms the Ruki and Ikelemba Rivers as likely the most acidic of the central Congo Basin rivers.

The low pH and EC values in the Ikelemba and Ruki Rivers correlate with low levels of metal cation concentrations. In particular, Al, Ca, Fe and Na concentrations in the Ruki and Ikelemba Rivers are all lower than those observed in the Likoula-aux-Herbes River (Dargie, 2015). Ca and Na values are also lower than typical reference values reported for the blackwater Negro River in the Amazon Basin (ca. 400 and 700 mg L^{-1}, respectively; Wood et al., 2003). This confirms the Congo Basin rivers as having very low dissolved cation concentrations compared with other rivers (Dupré et al., 1996), likely making these as among the lowest concentrations in the world.

However, some extremely large K concentrations, more than ten times the values observed on the Ikelemba or the Likouala-aux-Herbes Rivers, have been measured in the Ruki River. This is likely an artefact from rainfall at the end of the dry season, as K is the least abundant and least variable of the major cations in river water. In this case, high K concentrations are likely due to forest burning or soil dust resulting in high K in rainwater inputs (Berner & Berner, 2012). The river water sample near Bolengo was taken just after heavy rain at the end of the dry season, which has likely caused a considerable deposition of soil dust, ultimately the result of more complete weathering of underlying rocks resulting in high K concentrations in the soil dust. This also explains the relatively higher pH value of river water at Bolengo, as well as the large outliers of K concentrations in peat surface samples at Mpeka.

Differences in the timing of sampling are likely also the cause of differences in Na concentrations measured in peat pore water. Metal cation concentrations measured in peat water samples along the five transects showed remarkably little variation, except for Na, which was found to

be significantly higher along the three Ruki transects. The higher concentrations of Na measured along the Ruki River are likely due to drought conditions towards the end of the summer dry season (Clymo, 1987), with evaporation having increased the relative concentrations of Na, compared with more diluted samples from Lokolama or Ikelemba that were measured at the end of the wet season. This is more likely than the alternative explanation of a sudden or regional difference in the deposition of sea salts, as Na is partly derived from marine aerosols containing sea salts in coastal areas (Berner and Berner, 2012). This is unlikely in the central Congo Basin, as it is located so far from the nearest coast.

More significant differences between the five transects were observed in peat surface samples, with significantly higher concentrations of Fe and K at the non-river-influenced site of Lokolama, corresponding with significantly higher pH values. However, this pattern is not consistent across all elements. In particular, no significant differences in Ca, Mg or Ca/Mg-ratio were observed across the transects. Both Ca and Mg originate almost entirely from the weathering of sedimentary rocks (J. D. Allen & Castillo, 2007). In the Congo Basin, rivers receive these elements mainly from wet deposition of aerosols during rainfall, or from carbonate dissolution in soils (Négrel et al., 1993). Elevated levels above those of rainfall are therefore a primary indicator for water sources that have come into contact with the ground or subsurface. In particular, the Ca/Mg-ratio of the surface peat can be compared with the local rainwater, the assumption being that peat with a Ca/Mg-ratio lower than or comparable to rainwater is ombrotrophic; otherwise, the peat must have had an additional, non-atmospheric source of Ca and is therefore minerotrophic (Muller et al., 2006; Weiss et al., 2002).

It was observed that Ca/Mg-ratios of both the Ruki (2.51) and Ikelemba (2.19) Rivers is higher than that of other central Congo Basin rivers, such as the Sangha, Ubangi, Kasai or Congo mainstem (2.0, 1.6, 1.2 or 0.7, respectively; Négrel et al., 1993). However, Dargie (2015) reports higher values of 2.3 in the Ubangi River and even 3.2 in the Likouala-aux-Herbes River. Nonetheless, overall Ca/Mg-ratios in Congo Basin rivers are lower than those of typical whitewater Amazon tributaries such as the Purus, Japurá, Juruá, Jutaí or Solimões Rivers that cross seasonally flooded forests (2.9, 3.4, 4.3, 5 and 5.8, respectively; Probst et al., 1994). This is because sedimentary carbonate rocks dominate in the Andes region where the Amazon tributaries originate, while forming a relatively smaller portion of the well-weathered Congo basin (Probst et al., 1994). Overall, this results in relatively low Ca/Mg-ratios in the region,

making the Ca/Mg-ratio potentially less indicative of minerotrophic input than in other peat swamp forests regions such as the Peruvian Amazion.

Even so, the Ca/Mg-ratios in both peat pore water and peat surface samples are generally even lower than those of the Ruki and Ikelemba Rivers themselves, indicating that there is likely no additional source of Ca from groundwater, river water or runoff into the peatlands. The only exception is the Ca/Mg-ratio of pore water along the Bolengo transect, which increases to 4.0 close to the *terra firme* upland (BNG_6.0). This is similar to the Ca/Mg-ratio observed in regional rainwater by Dargie (2015). Together with the fact that this increase in peat water samples is not mirrored in peat surface samples, this indicates that this increase in Ca/Mg could be due to a local rainfall event (or runoff from rainfall on *terra firme* uplands) that has temporarily altered the composition of the peat water. This is further confirmed by the fact that no increase in Ca/Mg is seen when moving towards *terra firme* upland along the Ikelemba transect. In fact, Ca/Mg-ratios in peat water decrease along the Ikelemba transect, because the first few kilometres were still inundated by receding riverbank overflow with higher Ca/Mg-ratios. This shows that local variation in Ca/Mg can be caused by seasonal rainfall or inundation events. Nevertheless, even in those cases, the Ca/Mg-ratio never reaches above the rainwater average of 4, confirming that these peatlands remain nutrient-poor. This contrasts strongly with peatlands in the Peruvian Amazon, which have been shown to be much more diverse in terms of nutrient status. According to Lähteenoja et al. (2009a), Amazonian peatlands in the Pastaza-Marañón Foreland Basin harbour both minerotrophic peatlands with Ca/Mg-ratios of 10-13, while ombrotrophic peatlands are encountered with Ca/Mg-ratios of < 6. Similarly, Southeast Asian peatlands, while being largely ombrotrophic, have also been shown to harbour some minerotrophic peatlands (Wüst & Bustin, 2004). Thus, given the data collected so far, the central Congo Basin peatlands appear unique among tropical peatlands in potentially being almost exclusively nutrient-poor.

Downcore peat inorganic chemistry

Ca/Mg-measurements are generally less reliable in the upper peat layer than further downcore, as vegetation may lead to a remobilisation of these elements via nutrient recycling in the root zone (Muller et al., 2006). However, Ca concentrations in downcore peat samples (and by extension Ca/Mg-ratios) were even lower than those in surface peats, with most values below the detection limits of ICP-OES. This suggest that contemporary nutrient-poor conditions have

been a long-term feature throughout the peatlands' development history in the central Congo Basin.

For this reason, no Ca/Mg ratio could be analysed downcore. Instead, I compared Ti-normalized ratios of Al, Fe, Mg and Mn for two deep cores of the Ikelemba and Lokolama transects. This showed considerable Fe-enrichment at Lokolama, compared with Ikelemba. Highly weathered tropical soils are typically enriched with Al and Fe, because these elements are most resistant to leaching. Thus, if the Ti-normalized ratios are above typical values for the upper continental crust (UCC), this would suggest significant wet deposition of atmospheric dust, or another form of mineral soil input into the peat layer (Weiss et al., 2002). Neither Al/Ti or Fe/Ti-ratios reach values that are higher than UCC values. Nonetheless Fe/Ti-ratio is markedly higher at Lokolama than at Ikelemba, particularly from halfway downcore to the peat surface. This would point towards a local process causing Fe-enrichment, rather than a regionwide event, given that this pattern is not visible in Ikelemba. Possible local effects could include increased pollution from metallurgy due to human settlements, or dust deposition associated with drought and/or climate impacts driving a shift in vegetation from forest to savanna around ~2,000 BP, known as the late-Holocene rainforest crisis (Giresse et al., 2020). However, since the Fe/Ti-ratio at Lokolama does not correlate with absolute Al, Fe or Ti trends, changes in atmospheric deposition are not the most likely explanation. Because Fe is sensitive to the peat's redox-state (Bhattacharyya et al., 2018; Steinmann & Shotyk, 1997), shifts in the aerobic and anaerobic conditions in the peat profile could affect the presence of Fe in peat soils as well (Weiss et al., 2002). Thus, it is perhaps more likely that Fe/Ti-trend at Lokolama reflects local hydrological changes, such as a potential shift from minerotrophic to ombrotrophic conditions as the peat profile got raised above the initial water table and water supply become rainfall-dependent. However, an alternative explanation would be that Fe is simply more mobile due to its solubility (Novak et al., 2011), making it a less reliable indicator of past conditions.

Absolute values of Al, Fe and Ti are generally higher in Ikelemba than in Lokolama. This is possibly explained by the fact that the peat profile represents a longer time period and thus could have accumulated a large concentration of these elements over time. Additionally, a larger peatland area such as Lokolama is likely to have a greater buffering capacity to store mineral input (Sjöström et al., 2020). Unfortunately, no downcore samples are available from Mpeka, Bolengo and Bondamba, which would provide useful to see if these patterns are replicated along other river-influenced sites.

In contrast to Al and Fe, both cores from Lokolama and Ikelemba show a consistent pattern for Mg and Mn, with elemental concentrations peaking near the peat surface. This could indicate rapid biological recycling of these elements by the root zone of active vegetation, rather than accumulation in the peat profile (Weiss et al., 2002). Interestingly, both the absolute and the Ti-normalized values of Mg and Mn in near-surface peat are considerably larger at Ikelemba than at Lokolama, indicating more contemporary enrichment of these elements at Ikelemba. As Mn is relatively sensitive to changes in redox-state (Damman, 1978; Shotyk et al., 1990), this greater presence of Mn in surface peat samples is likely related to the lower water tables that characterize the Ikelemba core. This corresponds with findings by Lawson et al. (2014) in Amazonian peatlands, who suggest that the Mn record is related to the depth of the aerobic surface layer. I hypothesize that a similar process could affect Mg, although to a lesser extent. However, the Mg and Mn peaks at Ikelemba were not replicated in the ICP-MS measurements of surface peat samples, suggesting this pattern could also be an artefact of the ICP-OES measurements.

Peat age and accumulation rates

This chapter presents the first radiocarbon basal dates from river-influenced peatlands in the DRC. Remarkably, results show that some peatlands in the central Congo Basin are of Late Pleistocene-age, and much older than those previously identified in ROC by Dargie et al. (2017). The oldest peat sample found in the basin has an age of approximately 42,300 cal yr BP, more than 20,000 years older than the oldest peat sample found so far in ROC (Dargie et al., 2017; Garcin et al., 2022). This date is close to the oldest tropical peat deposit found in the world of 47,800 cal yr BP (Ruwaimana et al., 2020), suggesting tropical peat formation in the Late Pleistocene was not restricted to Southeast Asia.

This basal peat sample at 380-390 cm depth is overlain by a mineral intrusion of 50 cm which has OM concentrations < 65%. Thus, by definition, the base of the peat core consists of 10 cm of peat, followed by 50 cm of mineral soil. As the next analysed peat sample at 300-310 cm depth was radiocarbon dated at ~ 35,900 cal yr BP, this shows that the early peat that had started forming was quickly submerged by a likely riverine deposit of sediment between 42.3k and 35.9k years ago. However, if taking 35,900 cal yr BP as the true start of peat formation at this site, that would still imply that peat formation started more than 20,000 years earlier than at either Lokolama in DRC or Ekolongouma in ROC.

Organic matter concentrations in the peat layer between 310 and 200 cm depth (35,9k - 16,5k cal yrs BP) were found to be relatively low, ranging between 70 and 80%. This indicates that there was still a relatively large mineral sediment input throughout this early phase of peat formation, most likely because of less dense vegetation and higher sediment concentrations during the LGM (Molliex et al., 2019). Only after ~ 16,500 cal yr BP (above 200 cm depth) does the OM concentration exceed above 90%, indicating little mineral deposition after this point.

Lateral basal dating along the Ikelemba transects furthermore reveals a gradient in peat initiation ages from 42.3k years ago near the *terra firme* uplands to 22.5k to 9k years ago closer to the river. This could suggest that peat formation at Ikelemba occurred through a process of paludification, with peat initiation likely happening in waterlogged soils in floodplain depressions caused by the overflowing river, after which a lateral spread towards the centre of the river valley took place. This idea corresponds with the presence of soft clay in the base layer below the peat, as detected at 5 km from the river, which gradually becomes silt and sand closer to the river. The presence of clay below the oldest peat deposits suggests a slow-flowing riverine environment, potentially from standing water left after riverbank overflow. The sand layer underneath the more recent deposits closer to the river suggest that this peat formed in a faster-flowing environment that is more impacted by the river itself (Swindles et al., 2018). However, the clay-to-sand-gradient along the transect is not uniform, and there are some short reversals back to clay in the basal layer closer to the river, implying shifting river positions and a potentially non-continuous process of peat initiation.

Nonetheless, given that very old peat deposits have survived in such a riverine environment, this suggests that the current position of the Ikelemba River has been relatively stable throughout the peatland's development, even though the Ikelemba is characterized by a relatively large number of small meanders, compared with other rivers in the central Congo Basin. This suggest this floodplain system is less dynamic than the floodplains in the Peruvian Amazon peatlands, which are much younger (Kelly et al., 2020). Furthermore, the fact that this old peat has survived the glacial-interglacial climate transition points towards a certain resilience to climatic perturbations at this site. The shallower age-depth profile observed between 35,9k and 16,5k cal yrs BP includes the Last Glacial Maximum, which points towards at least some preservation of peat during the LGM, as seen in some locations in Southeast Asian tropical peatlands as well (Ruwaimana et al., 2020).

However, the fact that large areas of swamp forest is found along dendritically-patterned river valleys of higher-order rivers and streams in the DRC (Dargie et al., 2017) suggests that the specific geomorphology of this drainage system east of the Congo mainstem plays a role in peat formation as well. These higher-order streams, such as the one crossed by the Boloko transect (see Chapter 2), are typically not characterized by meanders and floodplain depressions behind levees, as seen along the Ikelemba. Here, peat formation appears to have occurred directly in the waterlogged soils along streams, likely because they are characterized by very shallow slopes which facilitates the retention of water from seepage and upland runoff.

Contrary to the riverine environment of Ikelemba, similar peat initiation ages along the length of the Lokolama transect suggest that a process of terrestrialisation of a former lake or waterlogged depression took place there, rather than paludification on top of mineral soil. This conclusion is supported by the markedly round shape of the Lokolama peatland area, suggesting a round lake, which is only cut off by the Congo River on its western side. The base layer underneath the peat was also found to be consistently made up of clay, supporting the idea of a stable lacustrine environment.

Given that peat initiation at Lokolama started around 10,000 cal yr BP, this suggests that the Congo River mainstem obtained its contemporary position cutting through this peatland basin sometime after 10,000 BP. It has been proposed that the modern, 'sickle' shape of the Congo River was already established in the Early Pleistocene (~2 million years ago; Flugel et al., 2015), implying that this section of the river was previously located further to the west, before eroding away part of the Lokolama peat dome.

The long-term rate of carbon accumulation (LORCA) at Lokolama (37 g C m^{-2} yr^{-1}) is more than triple/double that at Ikelemba and Ekolongouma (12 and 19 g C m^{-2} yr^{-1}, respectively). Even though these latter two sites differ strongly in terms of hydrology and initiation age, their long-term rates of carbon accumulation are in line with the pantropical Holocene average of 12.8 g C m^{-2} yr^{-1} (Yu et al., 2010). The slope of the age-depth models also appears relatively similar during the Holocene for both Ikelemba and Ekolongouma. Given that peat formation at Lokolama and Ekolongouma started around the same time and these locations are just ~100 km apart, a climatic difference is not the likely explanation for the higher accumulation rates at Lokolama. The largest slopes in Lokolama's age-depth model are observed near the base of the core, suggesting either very wet conditions and low rates of decomposition, high rates of biomass

productivity, or a combination of both during peat initiation at this site. This corresponds with the hypothesized process of terrestrialisation of a former lake or waterlogged depression, which would imply very wet conditions in the early phase of formation. Biomass productivity is not expected to vary considerably between established peat swamp forests in Lokolama and Ikelemba, but it could be that the lacustrine vegetation during early peat formation at Lokolama was also more productive than the riparian vegetation that likely dominated at Ikelemba. Furthermore, if climate is not thought to be a sufficient explanation, site-specific geomorphological factors must play a role in sustaining the wetter conditions. In the case of Lokolama, it is likely that the ancient lake could have been connected to the Congo River before becoming terrestrialised, thereby guaranteeing sufficiently wet conditions throughout the early stages of the peatland's development. For example, it has been documented how the contemporary Congo River sometimes discharges into Lake Tumba during the high-water season. There are also reports of Congo River fish species being found several kilometres away from the river inside the Lokolama peatland area (R. Monsembula, *pers. comm.*), suggesting river water is sometimes feeding the western side of this peat dome during the wet season. Such a connection could imply more sustained waterlogging and therefore higher net apparent accumulation rates in the early Holocene, compared to Ekolongouma and Ikelemba. After ~ 7,500 cal yr BP (2.65 m depth), the slope of the age-dept model decrease at Lokolama, which coincides with a shift towards larger Fe/Ti-ratios. This could potentially be interpreted as a likely shift towards ombrotrophic conditions as the peat surface grows above the former lake's water table and becomes more susceptible to drought conditions related to rainfall. However, more detail dating of these three cores, as well as other cores from different sites, is needed to disentangle the local patterns from region-wide processes.

4.7 Conclusion

The aims of this chapter were to characterise and classify the hydrology, geochemistry and age of river-bound peatlands in the DRC. I have done so by comparing the seasonal inundation patterns, nutrient status, and basal ages of river-influenced peatlands along the Ikelemba transect with the non-river-influenced peatlands of the Lokolama transect, as well as with interfluvial basin peatlands from the Ekolongouma transect previously analysed in ROC (Dargie et al., 2017). I conclude that the river-influenced peatlands in DRC are extremely nutrient-poor, with a mean (± s.d.) Ca/Mg-ratio of surface peat samples of 1.76 (± 0.74), which is typically lower than that of either peat pore/surface water, river water or rainwater. However, these nutrient-poor peatlands receive seasonal river water input through overbank flow from blackwater rivers, as indicated by large seasonal fluctuations in water table height of close to a meter along the Ikelemba transect. This contrast with significantly lower water table fluctuations in the non-river-influenced peatland of Lokolama. This blackwater status of river water is indicated by the low river water pH of 3.20 (± 0.54), while mean electrical conductivity of river water is only 39.5 (± 14.7) $\mu S\ cm^{-1}$. The low-nutrient status of this river water explains why – contrary to what would be expected – peat can be found in river-influenced swamps. I therefore conclude that these peatlands are partially river-fed, yet do not classify as minerotrophic, given their poor nutrient-status.

In addition, there is evidence to suggest that the river-influenced peatlands might episodically receive water input through (sub)surface runoff from *terra firma* uplands. I analysed the first microtopography data from peat swamp forests in the central Congo Basin, finding that Ikelemba, on average, exhibited less microtopography than Lokolama, with IKE_5.0 having the lowest local height differences of all sites that were measured. This could suggest greater drainage efficiency along the Ikelemba transect. Together with the observed larger fluctuations in water table drawdown and recharge, as well as increase Ca/Mg-ratios along the Bolengo transect after rainfall, this points towards upland runoff as an additionally water supply to the river-influenced peatlands. However, more research is needed to quantify the relative importance of these different water fluxes.

The river valley peatlands started forming during the Late Pleistocene, with radiocarbon dating of the base of the thickest Ikelemba peat core revealing an age of between 41,200 and 43,800 calibrated years Before Present. This is over 20,000 years before the formation of ombrotrophic peat domes started in interfluvial basins in the ROC (Dargie et al., 2017; G. Dargie, *unpublished*

data). Radiocarbon dating of the base of the thickest Lokolama peat core, which is not river-influenced, gives an age of between 10,300 and 10,600 calibrated years Before Present, similar to reported basal dates from interfluvial basins in the ROC. This suggests that the Late Pleistocene peatland initiation was possibly restricted to river-influenced settings only. The discovery of extensive nutrient-poor seasonally inundated peat swamps in DRC, in addition to the previously known ombrotrophic-like interfluvial basin peatlands, reveals that there is an additional geomorphological setting in the central Congo Basin region where peat is formed. Based on the pre-Holocene age of the river valley peatlands, I also conclude that peat initiation was not limited to the warmer and wetter conditions following the Last Glacial Maximum, but to some extent also occurred under the different climatic conditions of the Late Pleistocene.

Chapter 5: Mapping the peat swamp forests of the central Congo Basin

5.1 Abstract

The Cuvette Centrale peatlands are estimated to cover an area of 145,500 km^2 (95% CI, 131,900 – 156,400 km^2) (Dargie et al., 2017). However, the field data used to calibrate and validate this prediction was limited to only one region in the north of the Republic of the Congo and to only one peatland type, rain-fed interfluvial basins. In this chapter, I develop a second-generation map of peatland distribution based on extensive new field data from the Democratic Republic of Congo, including from river-influenced peatlands. I use associations between peat and vegetation, and remotely-sensed data to produce maps of peatland distribution. I assessed optical, radar and topographic input variables and a series of possible algorithms to generate an improved map. The most accurate model included three optical bands (Landsat 7 ETM+ SWIR 1, NIR and Red), three radar bands (ALOS PALSAR HV and HH, and the ratio), absolute elevation (SRTM Digital Elevation Model), relative elevation (SRTM-derived Height Above the Nearest Drainage point) and slope (SRTM-derived). I also tested three supervised landcover classification algorithms: Maximum Likelihood (ML), Support Vector Machine (SVM) and Random Forest (RF). The more complex SVM and RF classifiers were not found to improve model performances compared with ML, based on their lesser ability to accurately predict peat in regions from which no training data was included, assessed via spatial cross-validation. The ML model, based on the new field data from both DRC and the original ROC data combined, predicts a median total peatland area of 167,600 km^2 (95% confidence interval, 159,400 - 175,100 km^2), based on 1,000 runs using two-thirds of the ground truth data as training data, giving a peatland probability map at 50 m resolution. This area estimate represents an increase of 15% compared with Dargie et al. (2017). The additional peatland areas are found at the fringes of the peatland complex in the DRC. Both maps consistently predict large areas of peatland in the central depression of the Cuvette Centrale. Overall model performance of my new model, as assessed using the Matthews correlation coefficient, is 78.0% (95% CI, 74.2-81.6%). In addition, the development of a map of inundation frequency highlights the regions where seasonally inundated river-influenced peatlands are expected to be found, mostly in DRC. Furthermore, a large and understudied area of permanently inundated palm swamp forest is detected east of Lake Mai-Ndombe in DRC. From this map of inundation frequency, it is estimated that about a quarter of the total peatland area is seasonally inundated, particularly along the Congo River and its eastern tributaries in

DRC, while about a fifth of the peatlands is estimated to be permanently inundated by standing water. Slightly over half of the peatland complex is estimated to be permanently waterlogged yet rarely experiencing inundations of standing water above the surface.

5.2 Introduction

Only two estimates of peatland area extent are available for the central Congo Basin. According to Dargie et al. (2017), the Congolese peatlands cover an estimated 145,500 km^2, which is the only published estimate so far that is based on field data. However, Dargie et al. (2017) report a 95% confidence interval of 131,900 – 156,400 km^2, highlighting the uncertainty that remains around this estimate. Independently, Gumbricht et al. (2017) have estimated the size of the Cuvette Centrale peatlands to be 125,440 km^2, using a rules-based approach based on hydrological modelling and remotely-sensed data alone. This figure falls outside the 95% confidence interval reported by Dargie et al. (2017), indicating that real uncertainty could be higher than reported and that robust mapping of peatland extent requires more field data on peat-vegetation associations, as to date no satellite can directly detect peat. Whilst the use of *in situ* data by Dargie et al. (2017) warrants more confidence in their estimate, uncertainty is reinforced by the fact that this estimate is based on field data from interfluvial basins in a single region of northern Republic of the Congo, whereas two-thirds of the Cuvette Centrale peatlands are estimated to be located in neighbouring Democratic Republic of Congo, including large areas with a different hydro-geomorphology.

Two types of uncertainty can be distinguished when assessing model predictions such as those of peatland extent: statistical (aleatoric) and systemic (epistemic) uncertainty. Statistical uncertainty derives from inherently random effects in the data. Systemic uncertainty derives from a lack of knowledge about either model structure and parameters, or forcing and response data (Beven, 2016; Hüllermeier & Waegeman, 2021). Systemic uncertainty is difficult to quantify, but can in theory be reduced by adding more data or by making the model structure more representative of reality. Statistical uncertainty, on the other hand, can be formally analysed with statistical probability distributions if normality assumptions are met (Hüllermeier & Waegeman, 2021). This means that statistical uncertainty around peatland area predictions can be quantified if sampling data is spatially representative, for example, using a well-designed random sampling approach (Olofsson et al., 2014).

Such a formal statistical approach to assess uncertainty is not possible in the case of the Congolese peatlands, however, where field data is highly clustered around transects that are not spatially representative, due to the logistical challenges of doing fieldwork in the region. Instead, Dargie et al. (2017) used 1,000 random Monte Carlo cross-validations (CV) to derive a 95% confidence interval around their area estimate. In this resampling approach, a stratified

random two-thirds of all ground-truth data is used to train the model, while the remaining one-third is used as validation data. This random separation of training and validation data is slightly different for each of the 1,000 model runs, producing a consensus classification with a spatial assessment of uncertainty (Lyons et al., 2018).

However, as the number of transects is limited, compared to the number of datapoints per transect, it is very likely that multiple datapoints from each transect are selected as part of the training dataset in each run. This means that the 1,000 runs do not differ significantly in the large-scale spatial distribution of their samples throughout the Cuvette Centrale (~100 km). Instead, the random Monte Carlo cross-validation more strongly tests how well the model performs on the transect scale (~10 km), at which spatial autocorrelation is likely to play an important role (Legendre, 1993; Ploton et al., 2020a). This means that spatial autocorrelation could dominate real environmental effects (Bahn & Mcgill, 2007; Parmentier et al., 2011). The 95% confidence interval that is reported by Dargie et al. (2017) therefore reflects statistical uncertainty from randomness, with more weight on the local scale, at the expense of capturing systemic uncertainty from a lack of data across large parts of the map area.

As random Monte Carlo cross-validation is not able to fully assess systemic uncertainties (Beven, 2016), true uncertainty in peatland area estimates will likely be larger than reported. To better assess these systemic uncertainties, different classification algorithms and model configurations need to be compared in order to assess uncertainty that stems from model choice. In addition, one has to test how well the models perform in areas far-away from any training data, in order to assess uncertainty from a lack of spatially representative input data. One way to do this is by applying a spatial cross-validation strategy (Ploton et al., 2020a; Roberts et al., 2017). In such an approach, rather than randomly selecting test data with the same spatial distribution as the training data, the test data is confined to a specific map region from which no training data was used. This can provide a better assessment of how well the model extrapolates into unknown map areas. Dargie et al. (2017) report that they tested Maximum Likelihood, minimum distance, Mahalanobis distance, neural networks and support vector machine algorithms, finding the best results for Maximum Likelihood. However, this was not tested using a spatial cross-validation approach, meaning it is unclear how well this model predicts in areas without any data.

However, there is considerable debate in geospatial ecology about the use of spatial cross-validation strategies for large-scale mapping purposes. For example, Wadoux et al. (2021)

recently argued explicitly against using spatial CV because it is inherently subjective, given the way that the partitioning is implemented. They further point to an inherent paradox in the spatial CV approach, as on the one hand it aims to exclude testing data that is geographically close to the training data, while it on the other hand also aims to avoid extrapolation in unknown geographic and covariate space. However, extrapolating in unknown space appears sometimes unavoidable, such as in the case of the Congo Basin, where design-based probability sampling is not possible.

One way to overcome this paradox is to first use spatial CV strategies to assess systemic modelling uncertainties from extrapolating into unknown space, while later using a random CV approach to include data from as many different regions as possible and get the best predictions across the entire map area. Furthermore, Meyer & Pebesma (2021, 2022) recommend that large-scale mapping studies that apply spatial CV need to provide reliable indication of prediction errors, or define 'areas of applicability' that prevent extrapolation outside predictor space. Moreover, Meyer et al. (2019) caution against the use of highly autocorrelated spatial predictor variables (such as geographic latitude/longitude) which can lead to considerable overfitting of the model.

In this chapter, I produce a new map of the central Congo Basin peatlands. I also test both statistical and systemic uncertainty in peatland distribution models for the central Congo Basin. I do so by adding new ground-truth data collected in the river-influenced swamps of the DRC to previous data collected in ROC by Dargie et al. (2017). I will then use this larger and spatially more representative dataset to assess systemic uncertainty stemming from (i) model configurations, by comparing multiple combinations of remote sensing input products and supervised classification algorithms; and (ii) from limited spatial representativeness of the data across the region, by using spatial CV to test how well different classification algorithms perform in areas from which they haven't been given any training data. I will use these comparisons to select the best model of peatland distribution in the central Congo Basin and derive a best new estimate of total peatland area using random CV.

Furthermore, since previous chapters have described the importance of seasonally inundated peat swamp forests in the DRC, I will use multi-temporal synthetic-aperture radar (SAR) data to develop a map of inundation frequency that can be used to assess the spatial distribution of this specific peat swamp vegetation type. Because multi-temporal SAR data is not available across

the whole of the central Congo Basin, and mindful of the uncertainties surrounding large-scale mapping studies as just discussed, this map will not feature as input in the peatland distribution models, and only serves as a first attempt to understand the distribution of this vegetation type across a portion of the central Congo peatlands.

5.3 Chapter aims

The overall aim of this chapter is to use ground-truth data from the Democratic Republic of the Congo to develop a more accurate map of peatland distribution across the central Congo Basin. In addition, it is aimed to develop a better understanding of the spatial distribution of the seasonally inundated mixed peat swamp forest type identified in DRC. The specific objectives of this chapter are: (i) to test various remote-sensing products and machine learning algorithms to construct a robust 50 m resolution landcover classification model of the central Congo Basin peatlands and surrounding region; (ii) to estimate the total extent of the peat swamp forests across the central Congo Basin; and (iii) to develop a first map of inundation frequency across a major part of the peatlands to delineate seasonally inundated mixed peat swamps.

5.4 Methods

5.4.1 Collection of ground-truth data

Satellites cannot detect peat directly. Therefore, field-based associations between peat and swamp forest vegetation have to be used to infer the presence of peat, in combination with geomorphological features (Lawson et al., 2015). Five landcover classes were used for the purpose of peatland mapping: water, savanna, palm-dominated peat swamp forest, hardwood-dominated peat swamp forest, and non-peat forming forest. In this classification, field recordings of non-peat-forming seasonally inundated forest (< 30 cm thickness of ≥ 65% OM) are grouped together with field recordings of *terra firme* forest, which also does not form peat, to form the non-peat-forming forest class. Field recordings of hardwood- or palm-dominated peat swamp forest, by definition, consist of all forest sites that were found to form peat, including any seasonally inundated forest that forms peat (≥ 30 cm of ≥ 65% OM).
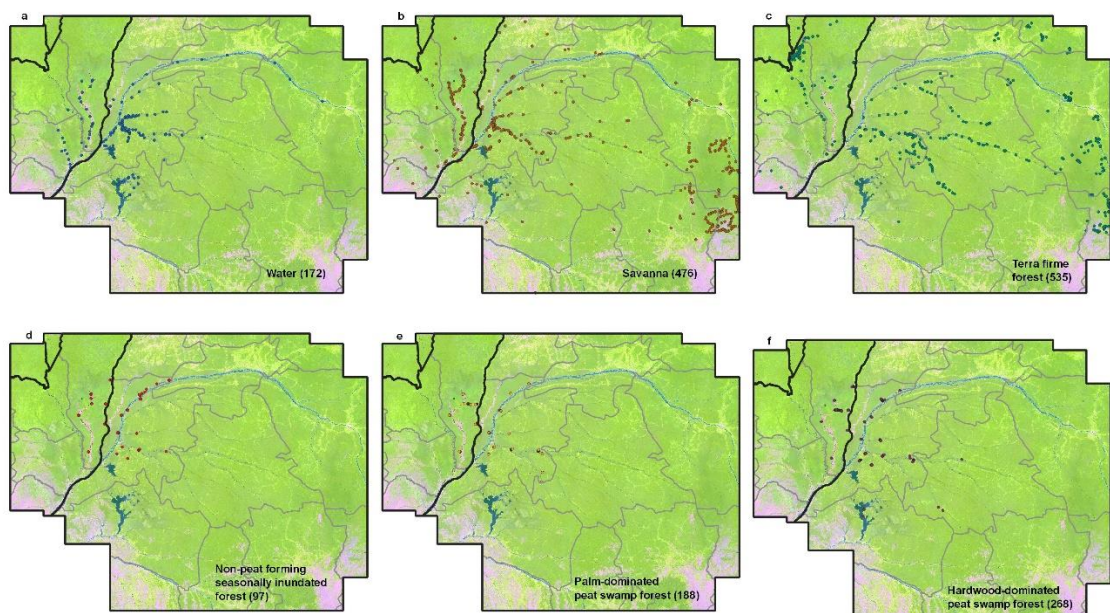
Figure 5.1. Spatial distribution of ground-truth datapoints used for mapping peatland distribution. *Only the palm-dominated and hardwood-dominated peat swamp forest classes (**e, f**) are associated with the presence of peat.* Terra firme *forest (**c**) and non-peat forming seasonally inundated forest (**d**) are combined into a single non-peat forming forest class for mapping purposes. The baselayer consists of three Landsat 7 ETM+ bands (SWIR 1, NIR and Red bands as red, green and blue, respectively), reflecting different forest types (shades of green), open savanna (pink), agricultural land (yellow) and open water (blue).*

A total of 1,736 ground-truth datapoints was used, more than triple the number used by Dargie et al. (2017). Of these, 172 are in water, 476 in savanna, 632 in non-peat forming forest (97 in non-peat forming seasonally inundated forest, and 535 in *terra firme* forest), 188 in palm-

dominated peat swamp forest, and 268 in hardwood-dominated peat swamp forest. The spatial

distribution of each class is shown in Figure 5.1.

Data source	Water	Savanna	Non-peat forming forest (incl. seasonally inundated forest)	Palm-dominated peat swamp forest	Hardwood-dominated peat swamp forest	Total peat swamp forest	Total
DRC fieldwork (Chapter 2, this thesis)	19	26	59 (9)	65	90	155	259
DRC Congo River (CongoPeat project)	0	6	46 (46)	25	46	71	123
ROC fieldwork (Dargie et al., 2017)	0	13	66 (34)	90	123	213	292
Archaeological database (Seidensticker, 2020; Seidensticker et al., 2021)	0	128	171	0	0	0	299
AfriTRON / ForestPlots.net (Lopez-Gonzalez et al., 2009, 2011; Hubau et al., 2020**)**	0	0	186 (1)	0	5	5	191
Forest and savanna sites around Lomami NP (*pers.comm.,* R. Batumike, G. Imani and A. Cuní-Sanchez, 2020).	0	134	95	0	0	0	229
Savanna around Lomami NP (Batumike et al., 2020).	0	24	0	0	0	0	24
Palaeo-archaeological research (Kiahtipes & Schefuß, 2019	0	2	9 (7)	8	4	12	23
Google Earth	153	143	0	0	0	0	296
Total	172	476	632 (97)	188	268	456	1,736

Table 5.1. Ground-truth sample sizes and data sources for mapping peatland distribution. Only hardwood- and palm-dominated swamp forest is associated with the presence of peat. Total peat swamp forest includes both hardwood- and palm-dominated peat swamp forest types. Non-peat-forming forests consist of terra firme*, as well as seasonally inundated forest that does not form peat (number of datapoints given in parentheses, if present).*

The 1,736 datapoints originate from nine sources, as detailed in Table 5.1. Firstly, ground-truth

locations were collected using a GPS (Garmin GPSMAP 64s) at all sites for which a landcover

class was recorded along the 11 transects in DRC, as presented in Chapter 2. This dataset totals

259 ground-truth datapoints. Secondly, I added 123 ground-truth datapoints from seven similar transects (0.5-11 km in length) along the Congo River mainstem, also in DRC (S. Lewis, G. Dargie and the CongoPeat consortium, unpublished data). These transects were sampled by a team of the CongoPeat project in Jan-Mar 2020, consisting of Dr. Greta Dargie, Joseph Kanyama, Pierre Bola and Ovide Emba, using the same field methodology as described in Chapter 2. The Congo River sites were included to increase the sample size of ground-truth data and provide another likely river-influenced region of sampling within the Cuvette Centrale. The locations of these seven additional transects are shown in Figure 5.4. Third, I added published ground-truth data from the nine transects sampled by Dargie et al. (2017), which are located in largely interfluvial basins in ROC (292 points). Fourth, I added 299 GPS locations of known savanna and *terra firme* forest landcover classes from archaeological research databases across the basin (Seidensticker, 2020; Seidensticker et al., 2021). Fifth, I added 191 GPS locations from permanent long-term forest inventory plots of the African Tropical Rainforest Observation Network (AfriTRON), retrieved in July 2018 from the *ForestPlots.net* database (Lopez-Gonzalez et al., 2009, 2011). These included mostly *terra firme* forest sites (Hubau et al., 2020). Sixth, 229 GPS datapoints from known *terra firme* forest and savanna locations in and around Lomami National Park were added (*pers. comm.,* R. Batumike, G. Imani and A. Cuní-Sanchez, 2020). Seventh, I also added 24 published savanna datapoints in and around Lomami NP (Batumike et al., 2020). Eighth, I added 23 published locations of savanna, *terra firme* forest, palm- or hardwood-dominated peat swamp forest in DRC wetlands (Kiahtipes & Schefuß, 2019). Nineth, I added 296 datapoints selected in Google Earth for unambiguous savanna and water sites (middle of lakes or rivers), distributed across the region. Together, as far as I aware, the data on peat swamp vegetation locations that I used represents all the known field data that is available from peat swamp forests across the region.

Because the landcover classification of swamp forest sites depends on the thickness of the measured organic matter layer (classified as peat swamp if ≥ 30 cm of ≥ 65% OM, otherwise classified as non-peat-forming forest), a representative calibration of the pole-method estimate is required. The calibration used here was a linear regression model between all LOI-verified and pole-method peat thickness measurements sampled at the same location across a wider dataset than the 40 sites analysed in Chapter 2. I used 96 sites from across ROC and DRC, including 18 from the Congo River transects in DRC and 37 from ROC, obtained from Dargie et al. (2017). Three measurements from DRC, with a Cook's distance > 4x the mean Cook's distance, were excluded as influential outliers that under- (BDM_7.0) or overestimate the correction (LOK_1.0

and PEK_10.0). The mean pole-method offset was found to be significantly higher in DRC (0.94 m) than along those in ROC (0.48 m; p<0.001), due to the presence of softer alluvium substrate in river-influenced sites in DRC. I therefore added this binary grouping as a categorical variable to the regression. The resulting model (adj-R^2 = 0.95, n=93, p<0.001; Figure 5.2) was used to correct all pole-method estimates of peat thickness across the central Congo Basin dataset of ground-truth points for which no LOI-verified peat thickness was available:

$$T_{corr} = 0.8626 * T_{pole} - 0.3248 * Country - 0.176 \qquad \text{[Eq. 5.1]}$$

Here, T_{corr} is the corrected peat thickness (m) and T_{pole} is the pole-measured peat thickness (m), while *Country* is dummy coded as either ROC (0) or DRC (1).
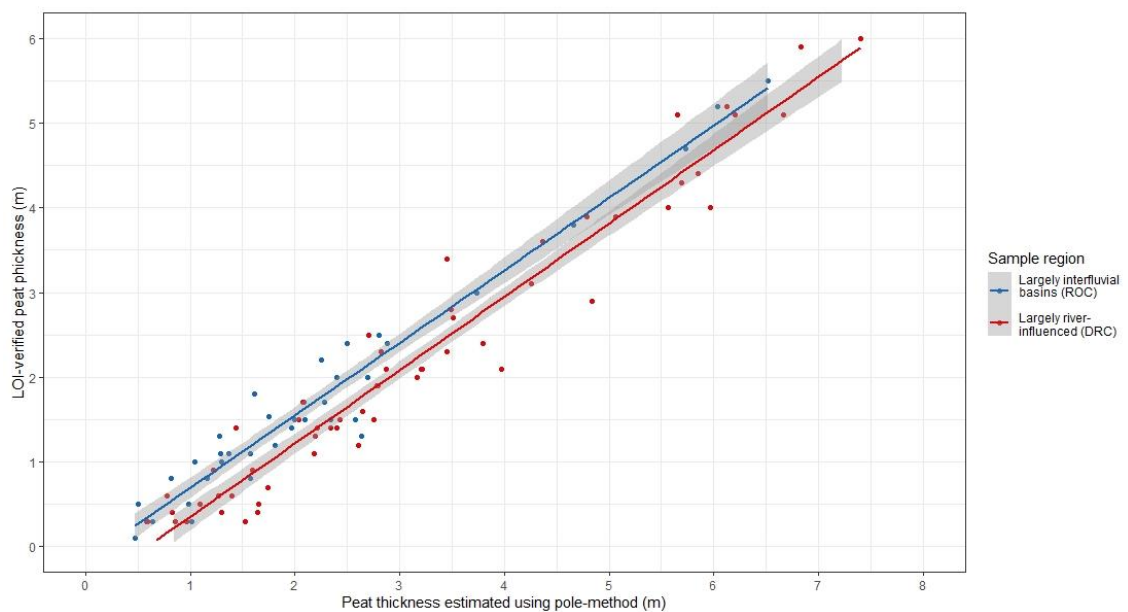
Figure 5.2. Linear regression model to correct pole-method peat thickness measurements across the central Congo Basin. The plot shows the relationship between peat thickness (m) estimated using the pole-method and laboratory-verified peat thickness (m) using Loss-On-Ignition (LOI). Datapoints are coloured by region. Best-fitting line: corrected peat thickness = -0.1760 + 0.8626 x (pole-method thickness) -0.3284 x (country); n=93, adj-R^2=0.95; p<0.001. Country is dummy coded as: ROC (0) and DRC (1). Shaded grey shows 95% confidence intervals. Outliers (n=3) with > 4x the mean Cook's distance are excluded from the analysis: LOK_1.0 (LOI: 4.1 m; pole-method: 6.1 m), BDM_7.0 (LOI: 5.7 m; pole-method: 6.2 m), and PEK_10.0 (LOI: 5.4 m; pole-method: 8.6 m).

5.4.2 Remote-sensing products

Various remote-sensing products were tested as input data for mapping peat distribution across the central Congo Basin. This was done by in turn changing either the optical (Landsat 7 ETM+), radar (ALOS PALSAR) or topographic (SRTM elevation and slope) data products used by Dargie

et al. (2017), while keeping all other remote sensing products the same, and comparing model performances against the unchanged combination of bands.

Specifically, I first made a comparison between models using either absolute or relative elevation products, or a combination of both. Secondly, I made a separate comparison of different sources of optical, radar and topographic dataproducts:

- Landsat 7 ETM+ vs. Sentinel-2 (optical bands);

- ALOS PALSAR vs. ALOS-2 PALSAR-2 (radar bands);

- SRTM vs. NASADEM vs. MERIT (topographic bands).

Each of these comparisons will be discussed in more detail below.

In all cases prior to running the models, remote-sensing products were processed in IDL-ENVI-software (version 8.7-5.5) and resampled to 50 m resolution using the 'cubic convolution' method. To limit computation time, principal component analysis (PCA) was then applied to reduce the different combinations of remote-sensing products to six uncorrelated principal components. I then tested 1,000 supervised Maximum Likelihood (ML) landcover classifications for each combination of remote sensing bands, based on an initial subset of 1,722 datapoints from DRC and ROC (174 water, 474 savanna, 610 non-peat-forming forest, 196 palm-dominated peat swamp forest, and 268 hardwood-dominated peat swamp forest). For each combination of input products, I used random Monte Carlo cross-validation to produce a consensus accuracy with assessment of uncertainty (Lyons et al., 2018), similarly to how Dargie et al. (2017) assessed model uncertainty. This was done by training each of 1,000 runs on a stratified random selection of two-thirds of all ground-truth datapoints (training data) and predicting landcover class for each of the remaining one-third datapoints (testing data). Model performance was then assessed by comparing the median Matthews correlation coefficients (MCC) of the binary peat/non-peat classifications from the 1,000 runs, alongside a 95% confidence interval. In the binary classification, predictions of hardwood- and palm-dominated peat swamp forest classes were combined into one peat class, while predictions of non-peat-forming forest, savanna and water were combined into a non-peat class, as this distinction is the most relevant for belowground carbon stock estimations.

Matthews correlation coefficient (MCC) was calculated with the following equation:

$$MCC = \frac{(TP*TN)-(FP*FN)}{\sqrt{(TP+FP)*(TP+FN)*(TN+FP)*(TN+TN)}} \qquad \text{[Eq. 5.2]}$$

Here, *TP* is the number of correctly classified peat datapoints (true positive), *TN* is the number of correctly classified non-peat datapoints (true negative), *FP* is the number of falsely classified peat datapoints (false positive), and *FN* is the number of falsely classified non-peat datapoints (false negative). I compared MCC, rather than popular metrics such as Cohen's kappa, F1-score or accuracy, because MCC takes into account both true and false positives and negatives, and is thought to be the most reliable evaluation metric for binary classifications (Chicco & Jurman, 2020; Powers, 2011).

The comparison between absolute and relative elevations was performed in IDL-ENVI software by generating peat predictions for the entire map area, to allow a comparison of peatland area estimates between the different models and with the results of Dargie et al. (2017). For this, predicted landcover classes were obtained as the most likely class per pixel (> 50%) out of 1,000 runs. All other comparisons for optical, radar and topographic products were performed in R software (using the *superClass* function from *RStoolbox* package, version 0.2.6) with the ground-truth datapoints only. To reduce computation times, these runs were used only to assess model performances by predicting landcover classes for the one-third validation dataset, and not to predict peatland distributions across the wider map area.

Absolute and relative elevation

Firstly, I tested whether prediction accuracy could be improved by changing the elevation data used in the model. Dargie et al. (2017) rely on absolute elevation above sea level, while Gumbricht et al. (2017) also include hydrological terrain relief, a potentially more useful topographic predictor variable of peat. Hydrological terrain relief is measured as height above the nearest drainage point (HAND), which normalises topography according to local relative heights along the drainage network (Nobre et al., 2011). This could be more useful than normalization with respect to sea level, given the Cuvette Centrale's location far away from the sea in an intracratonic basin. Previous studies have shown how the HAND-index is an important predictor of inundation potential (Aristizabal et al., 2020; Nobre et al., 2016) and peat attributes such as depth (Gumbricht et al., 2017). To optimize the peat prediction model, I therefore tested the addition of a HAND-index to the eight remote sensing products previously used by Dargie et al. (2017). This was done by comparing models that included just the SRTM DEM (absolute elevation only; similar to Dargie et al., 2017), just the HAND-index (relative elevation only), or both SRTM DEM and HAND (absolute and relative elevation combined). The HAND-index was derived from the SRTM DEM with Clubb et al.'s algorithm (2017), using the HydroSHEDS global

river network at 15s resolution as reference product of nearest drainage point (Lehner et al., 2008), which is one of the most frequently applied global hydrographic mapping products (Lindersson et al., 2020).

Optical products

Dargie et al.'s (2017) peatland distribution model was trained on pre-processed optical data from Landsat 7 ETM+ (SWIR 1, NIR and Red bands), which is freely available across the Congo basin (OSFAC, 2014). These dataproducts are seamless cloud-free mosaics at 60 m spatial resolution developed for either ROC (image composite of the medians of 2000, 2005 and 2010; OSFAC, 2014) or DRC (image composite of 2005-2010; Potapov et al., 2012; OSFAC, 2014). To test if model accuracy could be improved with more recent data at higher spatial resolution, I created new optical mosaics for the central Congo Basin with imagery from the European Spaca Agency's (ESA) Sentinel-2 MultiSpectral Instrument (MSI). Sentinel-2 MSI data is available since mid-2015 at 10 and 20 m resolution (ESA, 2021).

Three image composites of Sentinel-2 Level-1C products (bands 5, 8A and 11) were constructed from cloud-masked images over the same map area, which were acquisitioned between January 1, 2016 and January 1, 2021 (Copernicus Sentinel data, processed by ESA). Bands 5 (vegetation red edge), band 8A (narrow Near Infra-Red) and band 11 (Short Wave Infra-Red) were chosen to mirror the three Landsat 7 ETM+ bands used by Dargie et al. (2017). The images were obtained from Google Earth Engine (GEE), a free cloud-based platform for large-scale geospatial analysis (Gorelick et al., 2017), representing top-of-atmosphere (TOA) reflectance at 20 m spatial resolution. TOA reflectance was chosen, rather than atmospherically-corrected bottom-of-atmosphere (BOA) reflectance (Level-2A), because the Landsat 7 ETM+ imagery also includes TOA reflectance (Potapov et al., 2012; OSFAC, 2014). It has recently been shown that TOA imagery could be more accurate than BOA imagery in machine learning applications because the atmospheric correction causes a loss of information that affects the multispectral-*in situ* relationships (Medina-Lopez, 2020). Specifically, atmospheric correction seems to be smoothing out reflectance patterns that could be useful for training the machine learning model. Nonetheless, bidirectional reflectance effects resulting from differing surface reflectances between neighbouring images can cause stripy artefacts in optical remote sensing images, distorting the image classification. To reduce these artefacts in the new Sentinel-2 mosaics, I developed three normalised indices for each of three possible band combinations. Combining

bands 5 and 8A, bands 8A and 11, and bands 5 and 11, these indices were produced with the following band math calculation in IDL-ENVI software:

$$Normalised\ index\ bands\ X/Y = \frac{band\ X - band\ Y}{band\ X + band\ Y}$$ [Eq. 5.3]

Here, bands *X* and *Y* represent one of the three possible band combinations.

Radar products

Similar to the optical products, a more recent version of the ALOS PALSAR radar data was developed at higher spatial resolution. The ALOS PALSAR radar bands (HV, HH and HV/HH-ratio) used by Dargie et al. (2017) were mosaics of mean annual composites for the years 2007-2009 at 50 m resolution. To update this, I obtained freely-available yearly orthorectified HV and HH mosaics of ALOS-2 PALSAR-2 radar data at 25 m resolution from the Japan Aerospace Exploration Agency (JAXA) for the years 2015, 2016 and 2017 (JAXA, 1997). I mosaiced these into region-wide composites, after which they were converted from raw digital numbers to backscatter values in decibels (σ^0, sigma naught) using the following equation in IDL-ENVI software (Shimada et al., 2009):

$$\sigma^0 = 10 * log_{10}(DN^2) - 83$$ [Eq. 5.4]

Here, *DN* is the value of the HV or HH mosaic for each of the three years in digital numbers. Each yearly mosaic converted to decibels was then smoothed using an Enhanced Lee-adaptive filter with 3x3 kernel size (Lopes et al., 1990) to remove speckle. Similar to Dargie et al. (2017), the average of the three years was then calculated for both HV and HH composites in order to remove any annual temporal variation.
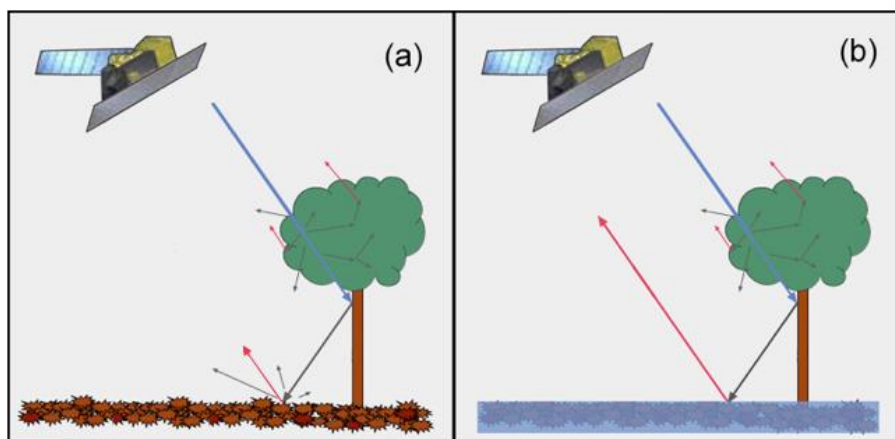
Figure 5.3. Illustration of L-band radar backscattering mechanisms. a, *In non-flooded forests, radar signals scatter in tree crowns and on the ground, resulting in limited backscatter (red arrows) and a darker image.* ***b***, *In flooded forests, a strong 'double bounce' mechanism of reflection on tree trunks and the water surface results in increased backscatter and a brighter image. The double bounce mechanism is stronger with single-polarized HH than with cross-polarized HV radar signals. Image reproduced from Rosenqvist (2009).*

A third band with HV/HH-ratios was then created using the following equation in IDL-ENVI:

$$\frac{HV}{HH} = (10^{\left(\frac{b1}{10}\right)})/(10^{\left(\frac{b2}{10}\right)})$$ [Eq. 5.5]

Here, *b1* is the mean HV σ-mosaic over three years and *b2* is the mean HH σ-mosaic over three years. This equation highlights the difference between HV and HH. Areas of flooded forest often have higher proportions of HH backscatter than non-flooded forests, due to the double-bounce mechanism whereby the radar signal first bounces off the tree trunks and is then reflected back from the surface by standing water, as shown in Figure 5.3 (Manavalan, 2018; Richards et al., 1987). However, this is not the case for cross-polarized HV signals, which result predominantly from volume scattering in tree tops (Martinis & Rieke, 2015; Wang et al., 1995). Hence, areas with lower ratios of HV over HH are likely indicative of flooded forests. Together with the primary HV and HH bands, this provides three ALOS-2 PALSAR-2 bands (HV, HH and HV/HH), to compare with the three ALOS PALSAR bands used by Dargie et al. (2017).

Topographic products

The DEM (absolute elevation) and slope maps used by Dargie et al. (2017) are derived from SRTM-data (USGS, 2006), which is void-filled with ASTER GDEM version 2 elevation data (NASA/METI, 2011) at 1-arc second resolution (equivalent to 30 m). SRTM elevation data has been shown to be prone to significant vertical errors, especially in heavily vegetated areas, due to the relatively weak penetration of C-band radar in canopy vegetation. This is likely to considerably affect inundation mapping in forested wetlands (Baugh et al., 2013; O'Loughlin et al., 2016). In order to overcome this limitation, I tested an error-adjusted version of the SRTM DEM that accounts for the known tree height bias, called the 'Multi-Error-Removed Improved-Terrain DEM' (MERIT DEM; Yamazaki et al., 2017). Multiple comparative studies have shown the improved accuracy of the MERIT DEM over SRTM DEM (e.g., Hirt, 2018; Tavares da Costa et al., 2019), particularly in (vegetated) floodplain sites (Hawker et al., 2018, 2019). A HAND-index has already been derived from MERIT DEM by these same authors (Yamazaki et al., 2019), which I used for comparison with the SRTM-derived HAND-index described above. Like Dargie et al. (2017) did with the SRTM DEM, I also derived a slope map (in degrees) based on the MERIT DEM. This was done using the Topographic Modelling tool in IDL-ENVI software, with default kernel size of 3. Similar to Dargie et al. (2017), the resulting file was converted to a byte file to reduce size, whereby all slope values ≤ 25 were multiplied by 10 and all values > 25 were given a value of 250.

In addition to the SRTM-derived and MERIT-derived sets of three topographic dataproducts (DEM, HAND and slope), I also tested a set of topographic products derived from NASADEM. NASADEM is a 30-m resolution, updated digital elevation model (NASA/JPL, 2020). It is derived from the same SRTM-data as the original SRTM DEM, but has improved data processing, elevation control, and void-filling. A slope and HAND-index were derived from NASADEM, similar to how the slope and HAND-index were derived from the original SRTM DEM.

5.4.3 Machine learning algorithms

In addition to remote sensing input products, I tested which classification algorithm to use, as more sophisticated algorithms might improve overall accuracy against the training dataset, yet might also reduce regional accuracy of the map in areas that are far away from test data, critical in this case given large areas of the central Congo Basin peatlands remain unsampled. Three supervised classification algorithms were tested in order of increasing complexity: Maximum Likelihood (ML), Support Vector Machine (SVM) and Random Forest (RF). Maximum Likelihood is one of the most common classification algorithms in remote sensing. It assumes that the statistics for each class in each band are normally distributed when calculating the probability that a given pixel belongs to a specific class (Richards & Jia, 2006). Support Vector Machine (SVM) is a more complex approach that aims to find a hyperplane that maximises the margin between data-points in N-dimensional space, where N equals the number of predictor variables (Burges, 1998). Finally, Random Forest (RF) is an ensemble machine learning method that combines multiple decisions trees that are trained using bootstrap aggregating and random feature selection (Breiman, 2001).

I assessed each classifier using both a random and spatial cross-validation approach (Meyer et al., 2019; Ploton et al., 2020a; Roberts et al., 2017). Random CV was implemented using a stratified two-thirds Monte Carlo selection (Lyons et al., 2018), similar to the way remote-sensing products were assessed in 5.4.2. Hereby, 1,000 times I randomly selected two-thirds of all datapoints per class as training data (n=1,157), to be evaluated against the remaining one-third per class as testing data (n=579).

Spatial CV was implemented using all transects datapoints (Table 5.1) obtained in both DRC (Chapter 2, this thesis; plus the Congo River transects, sampled by the CongoPeat project) and ROC (Dargie et al., 2017). These 673 datapoints were subdivided into four distinct hydro-

geomorphological regions: (i) five transects perpendicular to the blackwater Likouala-aux-Herbes River (n=179 datapoints); (ii) four transects perpendicular to the white-water Ubangi River (n=113; both from Dargie et al., 2017); (iii) seven transects perpendicular to the Congo River, intermediate between a black and white-water river (n=123; sampled by the CongoPeat project); and (iv) 11 transects perpendicular to the blackwater Ruki, Busira and Ikelemba Rivers, plus other nearby transects (collectively named the Ruki group; n=258; sampled for this PhD and presented in Chapter 2). The first two groups comprise the largely interfluvial basin transects in ROC that experience limited inundations. The last two groups compromise the largely river-influenced transects in DRC that experience larger seasonal inundations (Figure 5.4).
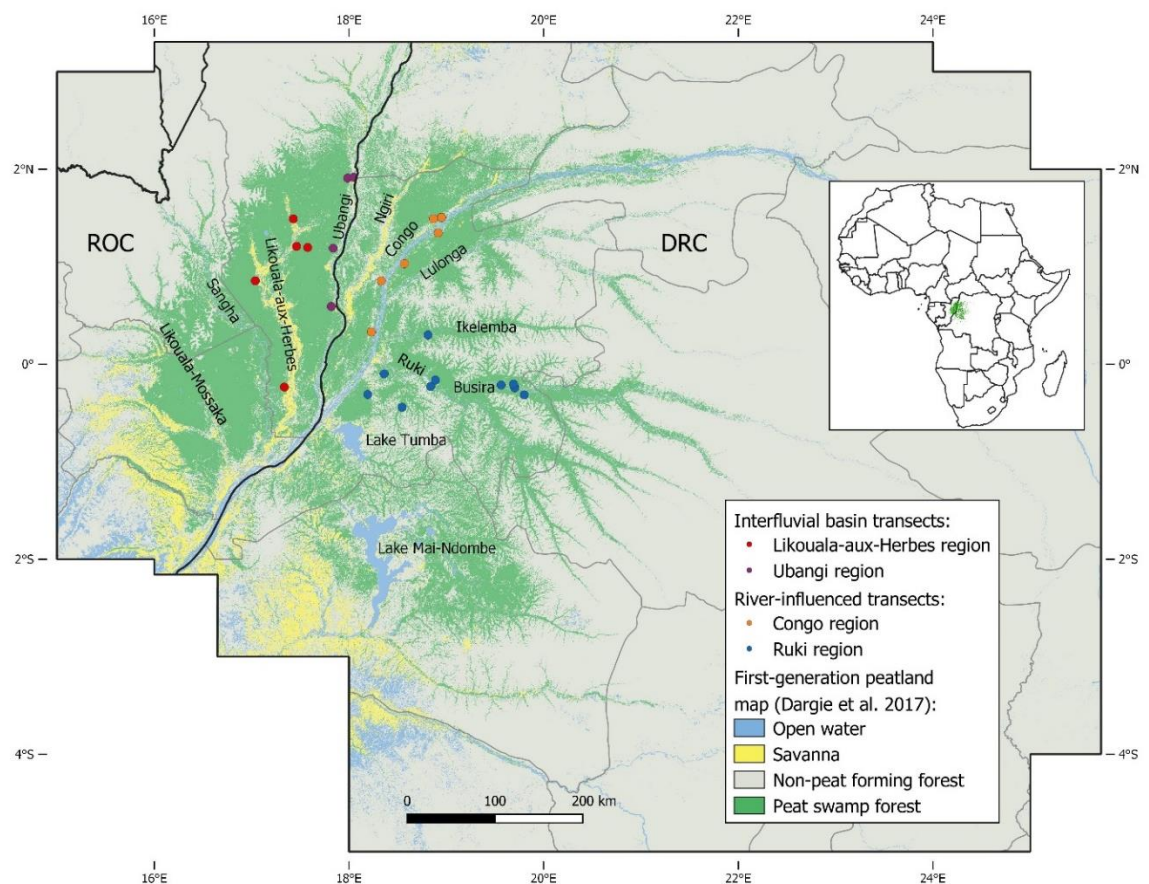
Figure 5.4. Location of transect groups for spatial cross-validation. *Points indicate transects, coloured by region. The Congo (orange) and Ruki River (blue) regional groups are in largely river-influenced peatlands, predominating in DRC, sampled for this study (Chapter 2) and by the CongoPeat project. The Likouala-aux-Herbes (red) and Ubangi River (pink) regional groups are in largely rain-fed interfluvial basins, predominating in ROC, obtained from Dargie et al. (2017). The base map, in green, shows the prediction of peat swamp forest (hardwood- or palm-dominated) by Dargie et al. (2017). Inset: Location of the central Congo Basin peatlands (shaded green) on the African continent. National boundaries are black lines; sub-national boundaries are grey lines.*

To each group I then added non-transect ground-truth datapoints from other data sources in Table 5.1 that belonged to the same map regions (n=82, 27, 20, 113, respectively), bringing the total datapoints used for spatial CV to 915. I then tested 1,000 times how well each classifier performs in each of the four map regions, in a 'leave one region out' type design, i.e. when trained only on a stratified two-thirds Monte Carlo selection of datapoints from the three other regional transect groups, plus all remaining ground-truth datapoints not associated with or near any transect group (n=821; for example, the savanna and *terra firme* forest datapoints in Lomami National Park in DRC which are far [> 300 km] from any transect group). Additionally, I applied spatial CV by training the model 1,000 times on a stratified two-thirds Monte Carlo selection of the two interfluvial basin regions combined (Likouala-aux-Herbes and Ubangi), plus all remaining ground-truth datapoints, and testing this against the left-out data from the river-influenced regions (Congo and Ruki), and vice versa.

Like with the assessment of remote-sensing products, model performance was based on Matthews correlation coefficient for binary peat/non-peat predictions (hardwood- and palm-dominated peat swamp forest classes combined into one peat class; water, savanna and non-peat forming forest combined into one non-peat class). I also computed balanced accuracy (BA) from random cross-validation to compare the new map results with the initial peatland map developed by Dargie et al. (2017). While less robust than MCC, BA is independent of imbalances in the prevalence of positives/negatives in the data, thus allowing better comparison between classifiers trained on different datasets (Chicco et al., 2021). The best estimate of each accuracy metric or area estimate per model or region was then reported as the median value of 1,000 runs, alongside a 95% confidence interval.

In the case of SVM and RF, random CV models were implemented in Google Earth Engine (Gorelick et al., 2017). However, because ML is currently not supported by GEE, random CV with this algorithm was implemented in IDL-ENVI software, using a principal component analysis (PCA) to reduce the remote sensing products to six uncorrelated principal components to reduce computation time. All spatial CV models were implemented in R software (*superClass* function from the *RStoolbox* package, version 0.2.6), with PCA also applied in the case of ML only. All RF models were trained using 500 trees, with three input products used at each split in the forest (the default, the square root of the number of variables). All SVM model were implemented with a radial basis function kernel, with all other parameters set to default values.

5.4.4 Mapping seasonal inundation

To better understand the distribution of seasonally inundated peat swamp forests, I additionally mapped the frequency of inundation across a central part of the Congo Basin. This requires multi-temporal SAR data to identify standing water in forests at different times of the year (Bourgeau-Chavez et al., 2021). Various recent studies have shown the potential of using monthly variations in SAR backscatter coefficients to map inundation dynamics over the central Congo basin (e.g., Kim et al., 2017; Lee et al., 2015; Rosenqvist, 2009). However, none of these studies have specifically mapped inundation patterns over peatlands. Furthermore, all of these studies only focus on a limited sub-region of the Cuvette Centrale area. To map inundation over a wider peatland area, I made use of freely available georeferenced ALOS PALSAR (Level 1.5) HH images in ScanSAR wide-beam mode, downloaded from the Alaska Satellite Facility (ASF) (JAXA/METI, 2009). These images have a lower spatial resolution (100 m) than the fine-beam ALOS PALSAR imagery used for peatland distribution mapping, but cover a wider image swath of approximately 350 km per image.

Month	ALOS PALSAR ScanSAR path 271	ALOS PALSAR ScanSAR path 274	Approximate season
July 2007	18/07/2007	23/07/2007	Height of main dry season
September 2007	02/09/2007	07/09/2007	Start of main wet season
December 2007	03/12/2007	08/12/2007	End of main wet season
January 2008	18/01/2008	23/01/2008	Start of small dry season
March 2008	04/03/2008	09/03/2008	Start of small wet season
October 2008	20/10/2008	25/10/2008	Height of main wet season
January 2009	20/01/2009	25/01/2009	Height of small dry season
March 2009	07/03/2009	12/03/2009	Start of small wet season
April 2009	22/04/2009	27/04/2009	Height of small wet season

Table 5.2. Overview of ALOS PALSAR ScanSAR images for mapping inundation frequency. The list includes nine matching image pairs between 2007 and 2009. Note that there is a five-day delay between images taken along path 271 and path 274. The last column provides an indication of the prevailing season at each date.

Four swath blocks (paths 271-274 and frames 3600-3650) that cover the central Congo Basin region have multiple images available across different seasons between 2007 and 2009. These swath blocks overlap with approximately 127,400 km^2 (or 88%) of the total peatland area as predicted by Dargie et al. (2017). This area includes most of the likely seasonally inundated forest along the Congo's eastern tributaries in DRC, as well as a large peatland area predicted to be extensively palm-dominated around Lake Mai-Ndombe (Figure 5.5). This is particularly useful because these southern parts of the peatland complex have not been included in previous

inundation maps (c.f. Lee et al., 2015; Rosenqvist, 2009; see Chapter 2, Figure 2.1). Thus, using a multi-temporal combination of these four ScanSAR swaths makes it possible for the first time to map inundation patterns across the large majority of the central Congo Basin peatlands, including what is predicted to be an extensive palm-dominated peat swamp area in the southeast of the basin.

Although the ALOS satellite has a return cycle of 46 days, only nine dates between 2007 and 2009 have matching images available across all four swath blocks (Table 5.2). This includes images with a time difference of 5 days between the two satellite paths, meaning that the two eastern images (path 271) are taken five days earlier than the two western images (path 274).
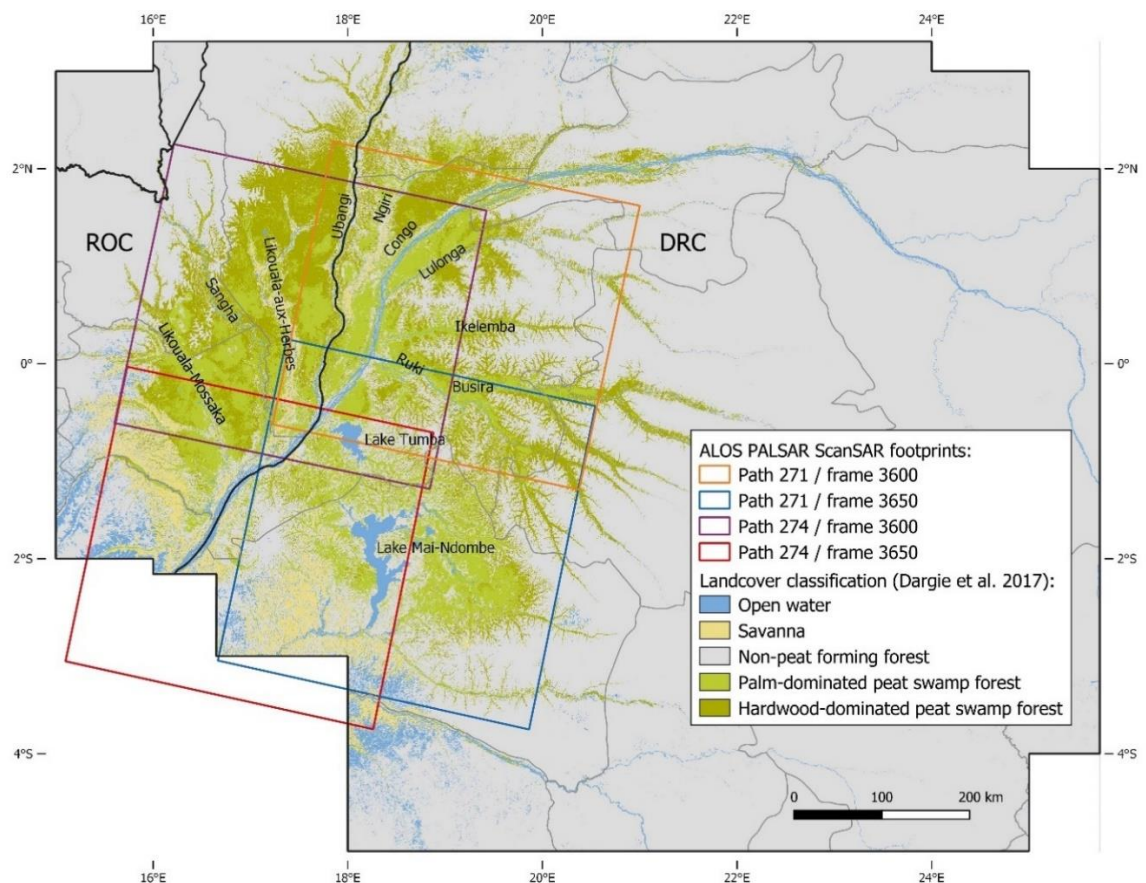
Figure 5.5. Map of the footprint of ALOS PALSAR ScanSAR images used for mapping seasonal inundation. *Because the exact image locations differ slightly between the nine selected dates, footprint extents indicate the minimal overlapping extent of each ScanSAR image across all nine dates. The top two swath blocks (pink and orange; frame 3600) largely correspond with the extent of previously developed inundation maps (e.g. Lee et al., 2015; Rosenqvist, 2009). The base map shows the predicted landcover classes by Dargie et al. (2017). National boundaries are black lines; sub-national boundaries are grey lines.*

All images were acquired in single-polarized HH polarization, as the backscatter difference between flooded and non-flood forest is generally higher with this polarization than with cross-polarized HV images or single-polarized VV images (Martinis & Rieke, 2015; Y. Wang et al., 1995). The images were radiometric terrain corrected and geocoded to Lat/Lon (WGS-84) projection using ASF MapReady software (version 3.2). As topographic reference source for terrain correction, I used the MERIT DEM topographic map, as this was thought to provide a more reliable elevation estimate in the forested areas than the SRTM DEM (Hawker et al., 2019). Like with the radar data used for mapping peatland distribution, all raw image data was then converted to backscatter values in dB by applying Eq. 5.4 in IDL-ENVI software (Shimada et al., 2009). Speckle and noise inherent in the radar signal were removed by applying a 3x3 median pixel filter, similar to the approach of Lee et al. (2015). I then mosaiced the four images from different paths/frames, but corresponding to the same month, into a single mosaic using the Seamless Mosaic tool in IDL-ENVI. Colour adjustment was applied to the entire image, and seamline feathering was applied to make the image boundaries less sharp, with a feathering distance of 6 pixels.

Each mosaiced image was then classified into three different classes based on each pixel's backscatter value: (i) open water, aquatic or herbaceous vegetation if $\sigma^0 \leq$ -11 dB, (ii) non-inundated forest if $\sigma^0 >$ -11 and $\leq$ -6 dB, and (iii) inundated forest is $\sigma^0 >$ -6 dB. The first threshold value of -11 dB is based on the low backscatter coefficients observed in the central Congo Basin for permanently open water, aquatic and herbaceous vegetation by Kim et al. (2017). The second threshold value of -6 dB is based on a statistical analysis by Lee et al. (2015) of the most optimal threshold to distinguish flooded and non-flooded forest across the region. I then stacked all nine classified images together in QGIS software and counted the number of times that each pixel belonged to the inundated forest class. This provides a proxy (ranging from 0-9 months) for inundation frequency between July 2007 and April 2009. This map was then clipped to the derived second-generation peatland distribution map (section 5.4.3) to create a map of inundation frequency in the peat swamp forests of the central Congo Basin.

I compared inundation frequencies for each of the 40 peat swamp forest plots that were clustered in four vegetation types in Chapter 3. Specifically, I looked at the range of inundation counts that are observed in the seasonally inundated, mixed peat swamp forest type associated with *Oubanguia africana* and *Guibourtia demeusei*, as this vegetation type was identified to be

primarily driven by water table fluctuations, and compared this with the other three clusters, whose differences appeared not to be directly driven by inundation patterns.

5.5 Results

5.5.1 Verification of DRC peat predictions

Of the 259 field locations sampled across all 11 transects in DRC (Chapter 2), 84.6% were correctly classified as either being peat swamp or not (overall accuracy) by the map developed by Dargie et al. (2017). Matthews correlation coefficient for this comparison is only 64.0%, largely because of an imbalance in the dataset between positives (peat presence) and negatives (no peat presence). These figures change to 77.7% and 54.4%, respectively, when including the other DRC data from along the Congo River mainstem, totalling 382 locations. This indicates that peat predictions by Dargie et al. (2017) are less accurate along the river-influenced Congo River mainstem, than along the river-influenced (blackwater) sites that straddle the Ruki and Ikelemba Rivers.

The reliability of this first-generation map's predictions (user's accuracy) was slightly lower for peat swamp forest classes (83.2%) than for non-peat swamp forest classes (88.0%). The lower user's accuracy for the peat swamp forest class is mostly caused by the false positive predictions of peat in the non-peat-forming seasonally inundated forest along the Congo River mainstem, or the Pombi and Boleke transects, which are either located on higher elevation or an island in the Ruki River. Inaccuracies for the non-peat swamp forest class were mostly caused by some false negatives (peat swamp forest being incorrectly classified as *terra firme* forest or non-peat-forming seasonally inundated forest) at the peatland's margins along Bondama, Mpeka and Lokolama transects.

5.5.2 Comparison of remote-sensing input products

Comparing Maximum Likelihood results based on either absolute elevation (DEM), relative elevation (height above the nearest drainage point; HAND), or their combination (DEM + HAND), shows that the combination of DEM+HAND outperforms models that are based on either DEM or HAND alone (Figure 5.6). The model combining both absolute and relative elevation has a median Matthews correlation coefficient of 79.7%, significantly higher than the median MCC of 77.8% or 75.6% that was measured for just DEM or HAND alone, respectively (One-way ANOVA, $p < 0.001$). Pair-wise comparison showed significant differences between all model combinations (Tukey multiple comparisons test, $p < 0.001$), with the DEM-based model also outperforming the model based on HAND alone.

Figure 5.6. Comparison of model performances based on absolute and relative elevation.
*Models include either absolute elevation (DEM only), relative elevation only (HAND only), or both
(DEM+HAND). Model performance is expressed as Matthews correlation coefficient (MCC) for
the binary classification (peat/non-peat). Each model estimate is based on 1,000 Maximum
Likelihood runs using an initial subset of 1,722 datapoints from DRC and ROC (2/3 training data
and 1/3 testing data). Horizontal black lines show the median of each class, boxes show the upper
and lower quartiles, and the vertical lines show maximum and minimum values. Circles represent
potential outlying values. All model combinations are significantly different from each other
(p<0.001).*

A comparison was made between the three models with either DEM, HAND or DEM+HAND, and

the model outcomes of Dargie et al. (2017), using the balanced accuracy metric (Table 5.3). This

shows that all three test models perform better than the first-generation model, which had a

median BA of 89.8% (95% CI, 86.0-93.4%), taking into account the fact that they were trained

and tested on different datasets. Thus, the addition of new datapoints from the DRC has

increased model accuracy, at least in map areas that are well-represented in the datasets. Like

with MCC, the model trained on both DEM and HAND elevation products also has the highest

balanced accuracy (92.5%). Interestingly, it's 95% confidence interval is considerably smaller

than that of the model by Dargie et al. (2017), reflecting a decrease in variation between

individual model runs.

Estimates of total peatland area are similar for the models based on DEM alone or DEM+HAND,

while the model based on HAND alone gives a much larger total peatland area (Table 5.3).

However, the three different models show strong spatial agreement in peat prediction in the

central part of the Cuvette Centrale, providing confidence in peat predictions in this area (white

in Figure 5.7). In terms of differences, the model based on relative elevation (HAND) alone

predicts large peatland areas in the eastern part of the central Congo Basin (blue in Figure 5.7), along the upper Congo and Lomami Rivers, which are not predicted as peat by those models based on DEM or DEM+HAND. I therefore use both DEM and HAND in the final model to predict the spatial distribution of peatland across the Cuvette Centrale.

Study	Elevation product used	Ground-truth data used	MCC (%)	BA (%)	Peatland area estimate (km^2)
This study	DEM	DRC + ROC	77.8 (74.2 – 81.9)	92.0 (90.3 – 93.8)	167,100 (158,700 – 173,600)
This study	DEM + HAND	DRC + ROC	79.7 (76.0 – 83.4)	92.5 (90.8 – 94.1)	166,700 (158,500 – 173,800)
This study	HAND	DRC + ROC	75.6 (71.7 – 79.0)	90.8 (88.9 – 92.5)	281,400 (266,100 – 293,800)
Dargie *et al.* (2017)	DEM	ROC	79.3 (71.9 – 86.4)	89.8 (86.0 – 93.4)	145,500 (131,900 – 156,400)

Table 5.3. Comparison of model performances and peatland area estimates between elevation products. Median Matthews correlation coefficients (MCC, %), median balanced accuracy (BA, %) and median peatland area estimates (km^2) are obtained from 1,000 Maximum Likelihood model runs in IDL-ENVI (95% confidence interval in parentheses), using an initial subset of 1,722 datapoints from DRC and ROC. Peatland areas are rounded to the nearest 100 km^2. MCC values of Dargie et al. (2017) were obtained by replicating that study with the exact same data. Balance accuracy is included for comparison between models with different datasets (Chicco et al., 2021).

When subsequently testing different combinations of remote sensing data sources (optical, radar, and topographic) in Maximum Likelihood models that included both DEM and HAND products, no improvement in model accuracy is found with respect to the datasources used by Dargie et al. (2017) (Figure 5.8). The models are significantly different from one another (One-way ANOVA, $p<0.001$), with pair-wise comparison showing significantly lower median MCC values in all new combinations, compared with the original band combinations of Landsat 7 ETM+, ALOS PALSAR and SRTM-derived dataproducts (Tukey multiple comparisons test, $p<0.05$ for ALOS PALSAR compared with ALOS-2 PALSAR-2; or $p<0.001$ for all other combinations).
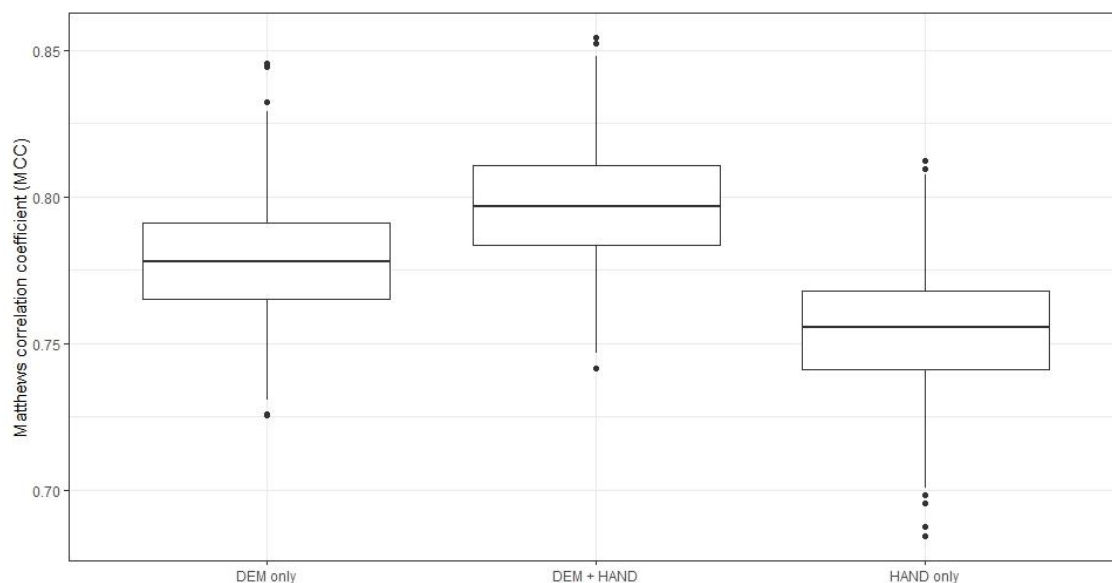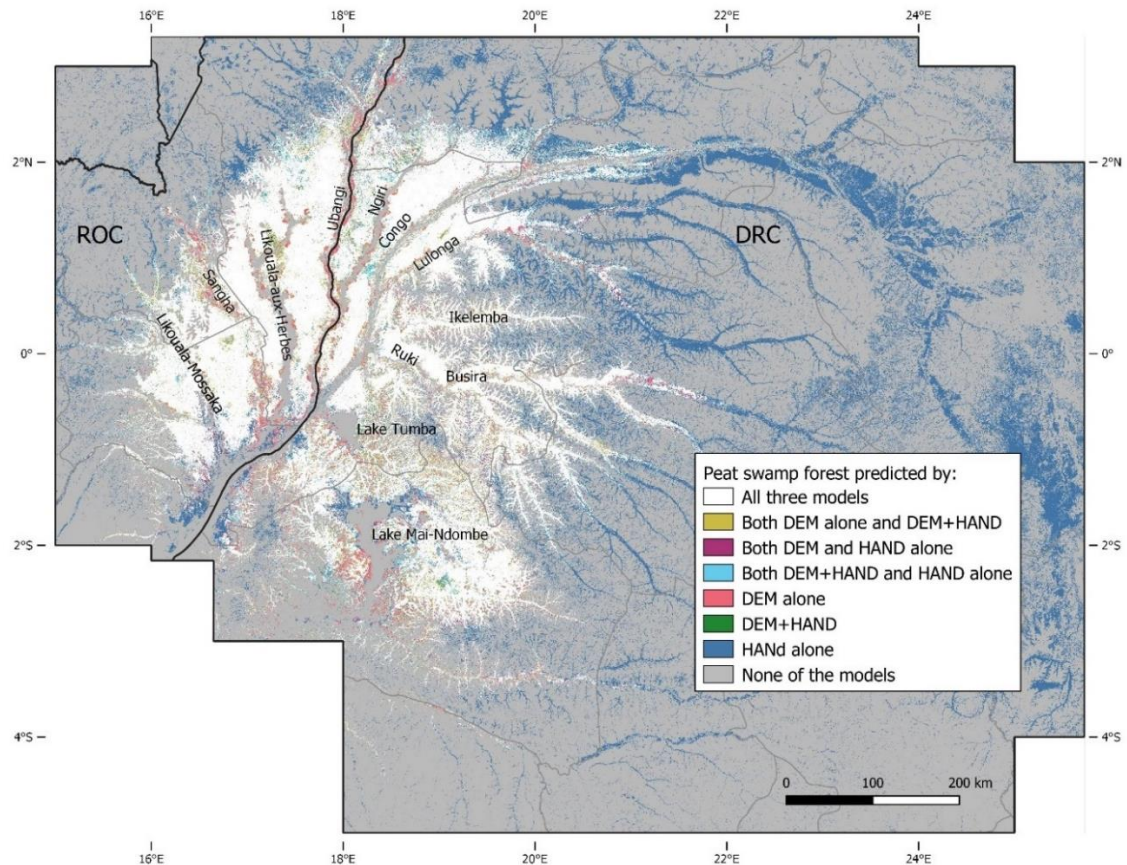
Figure 5.7. Comparison of peat predictions based on absolute and relative elevation. *Models include either absolute elevation (DEM alone), relative elevation only (HAND alone), or both (DEM+HAND). All models are based on Maximum Likelihood classification using the same ground-truth datapoints and optical, radar and slope products. White indicates agreement on peat prediction between all three model, yellow between DEM alone and DEM+HAND, cyan between DEM+HAND and HAND alone, and magenta between DEM and HAND alone. Red indicates peat predictions by DEM alone, green by DEM+HAND, and blue by HAND alone. Grey indicates that none of the models predicted peat. National boundaries are black lines; sub-national boundaries are grey lines.*

The model with older Landsat 7 ETM+ mosaics (2000-2010) performed better than a model with the more recent basin-wide automated cloud-free Sentinel-2 mosaics that I developed (bands 5, 8A, 11; composite of five years, 2016-2020). The median MCC of 80.9% for the Landsat 7 ETM+ mosaics is significantly higher than the 78.1% for the Sentinel-2 mosaics (p<0.005), likely because they contain less directional reflectance artefacts.

Similarly, the model with older ALOS PALSAR bands (2007-2009) performed better than a model with more recent radar ALOS-2 PALSAR-2 data (2015-2017), although the difference is less big than for the optical data (80.9% and 80.6% median MCC, respectively; p<0.01).

The NASADEM topographic dataset also leads to a reduction in overall median Matthews correlation coefficient, when keeping all other variables the same, compared with using the older SRTM-derived data (79.0% and 80.9% median MCC, respectively; p<0.001). More surprisingly, however, using topographic data derived from the error-adjusted MERIT DEM dataset results in particularly bad model performance when compared with a similar model based on SRTM-derived data (75.1% and 80.9% median MCC, respectively; p<0.001). This effect is larger than the reduction in accuracy caused by either changing the optical or radar data sources. Thus, I use the SRTM-derived elevation and slope dataproducts in the final model.
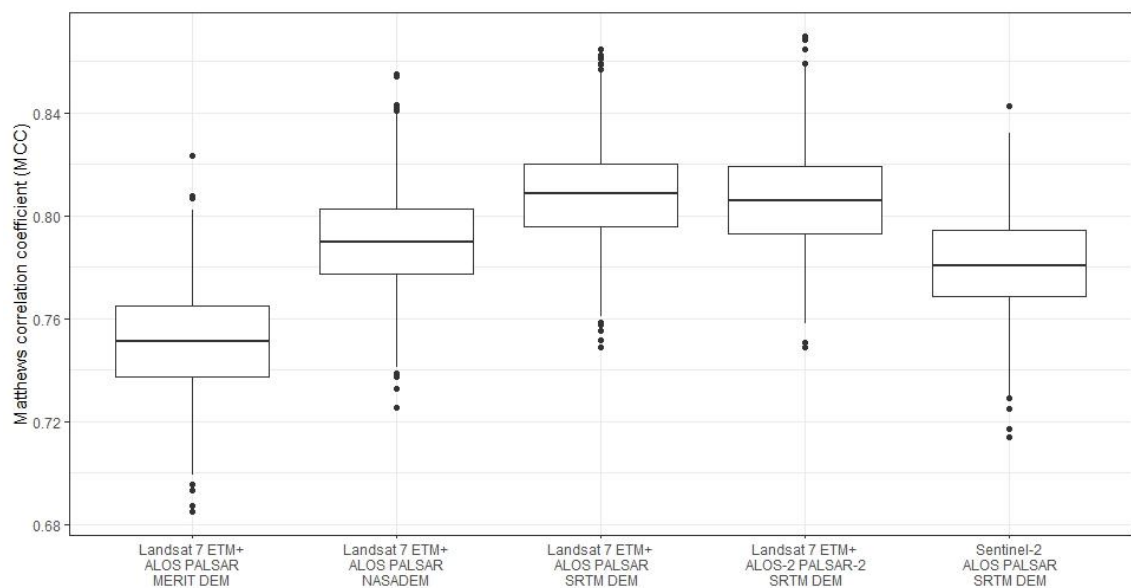
Figure 5.8. Comparison of model performances of five different combinations of remote sensing data sources. *Model performance is expressed as Matthews correlation coefficient (MCC) for the binary classification (peat/non-peat). Each model estimate is based on 1,000 Maximum Likelihood runs using an initial subset of 1,722 datapoints from DRC and ROC (2/3 training data and 1/3 testing data). Horizontal black lines show the median of each class, boxes show the upper and lower quartiles, and the vertical lines show maximum and minimum values. Circles represent potential outlying values. All model combinations are significantly different from each other (p<0.05).*

Spectral signatures of landcover classes

Figure 5.9 shows the spectral signatures of each of the five landcover classes in the best-performing model (combination of Landsat 7 ETM+, ALOS PALSAR and SRTM-derived products), by plotting boxplots of each class for each of the nine remote sensing bands. From this, it can be observed that all three Landsat 7 ETM+ bands have significantly different values in the two peat swamp forest classes than in the non-peat-forming forest class. Furthermore, the three SRTM-derived topographic bands are also significantly different in the two peat swamp forest classes than in the non-peat-forming forest. Absolute elevation (DEM), relative elevation (HAND) and

slope are all significantly lower in peat swamps than in non-peat forming forests (Kruskall-Wallis test, p<0.05). Additionally, ALOS PALSAR HH values are significantly higher in both peat swamp forest types than in non-peat-forming forest (p<0.05), as would be expected for inundated forest (Manavalan, 2018; Richards et al., 1987). However, HV/HH-ratios are not significantly different between hardwood-dominated peat swamp forest and non-peat-forming forest, likely because of the presence of peat-forming seasonally inundated forests (cluster 4 identified in Chapter 3), which are likely more similar to non-peat-forming seasonally inundated forests in terms of forest structure and inundation pattern. Nonetheless, the spectral signatures show that there are sufficient differences between the landcover classes, and in particular between peat swamp and non-peat swamp classes, to use these nine remote sensing products in a classification model of peatland distribution.
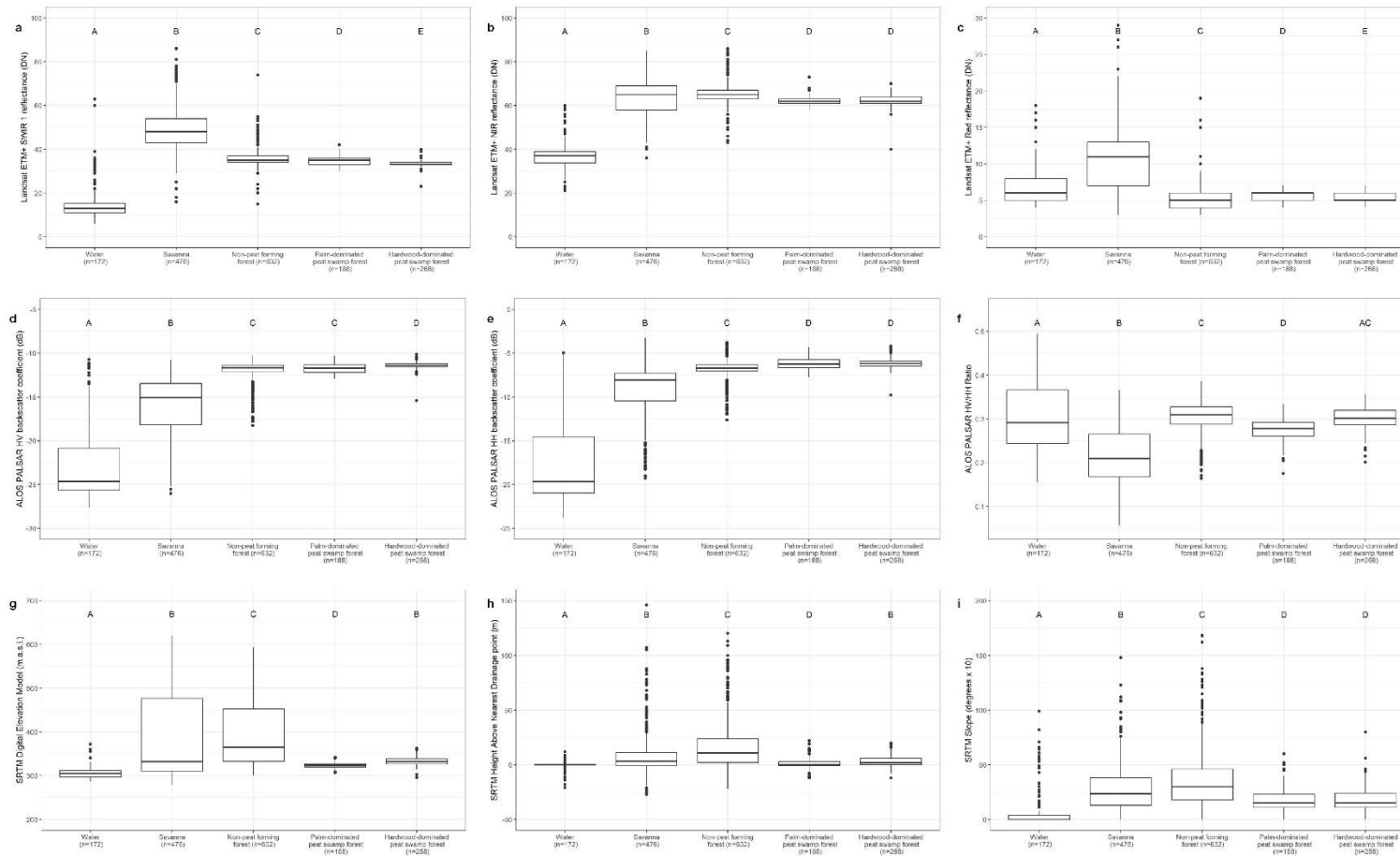
Figure 5.9. Boxplots of the spectral signatures of ground-truth landcover classes. a. *Landsat ETM+ SWIR 1 band (Digital Number [DN]).* ***b***. *Landsat ETM+ NIR band (DN).* ***c***. *Landsat ETM+ Red band (DN).* ***d***. *ALOS PALSAR HV backscatter coefficient (dB).* ***e***. *ALOS PALSAR HH backscatter coefficient (dB).* ***f***. *ALOS PALSAR HV/HH ratio.* ***g***. *SRTM Digital Elevation Model (DEM; m.a.s.l.).* ***h***. *SRTM Height Above Nearest Drainage point (HAND; m).* ***i***. *SRTM Slope (degrees x 10). Black lines show the median of each class, boxes show the upper and lower quartiles, and the vertical lines show maximum and minimum values. Circles represent potential outlying values. Land cover classes which do not share a common letter have significantly different means for the respective remote sensing product (p<0.05, Kruskall-Wallis multiple comparison [Dunn's] test with Benjamini–Hochberg adjustment). Non-peat forming forest includes both* terra firme *forest (n=535) and non-peat forming seasonally inundated forest (n=97).*

5.5.3 Comparison of machine learning algorithms

I used the best-performing dataset of remote sensing products that was identified in 5.5.2 to compare three different machine learning algorithms: Maximum Likelihood, Support Vector Machine and Random Forest. This model used three Landsat 7 ETM+ optical bands (SWIR 1, NIR and Red), three ALOS PALSAR radar bands (HV, HH and HV/HH) and three SRTM-derived topographic bands (DEM, HAND and slope) as input data.
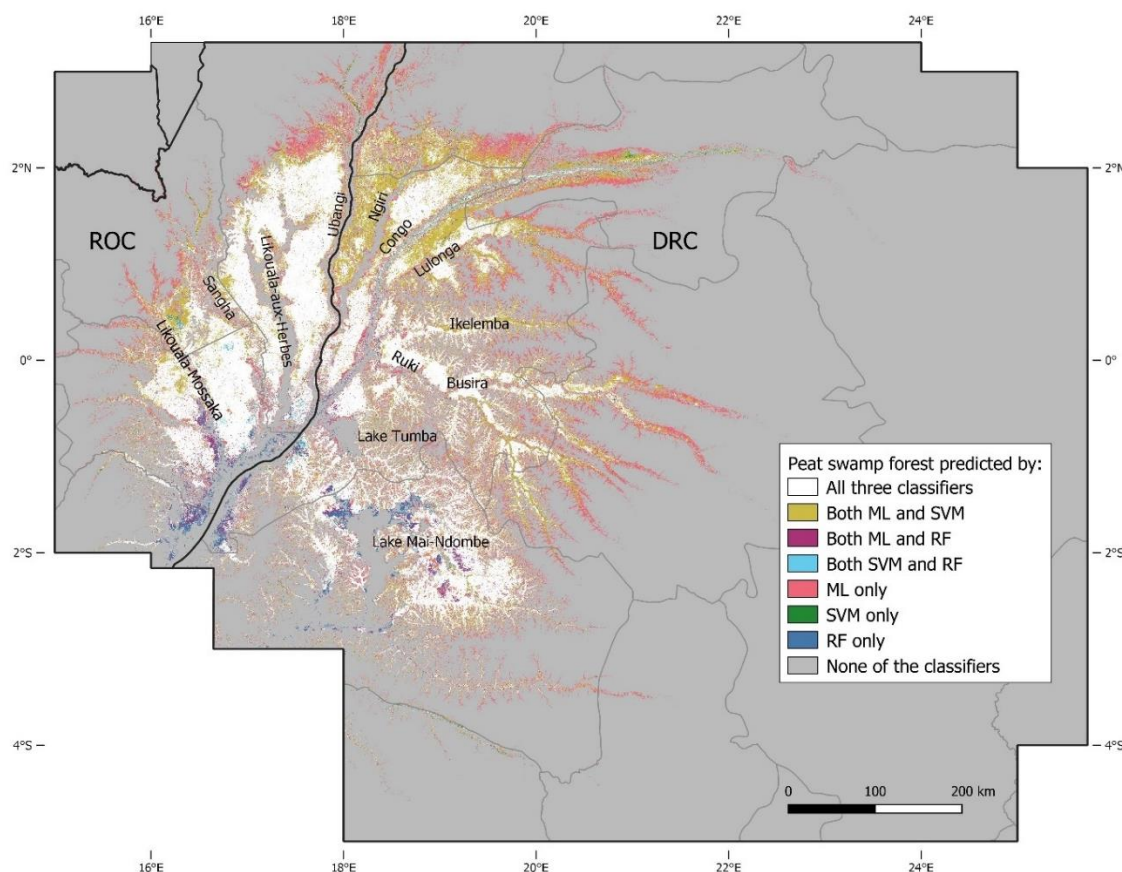
Figure 5.10. Comparison of peat predictions using Maximum Likelihood (ML), Support Vector Machine (SVM) and Random Forest (RF) classifiers. *White indicates agreement on peat prediction between all three classifiers, yellow between ML and SVM only, cyan between SVM and RF only, and magenta between ML and RF only. Red indicates peat predictions by ML only, green by SVM only, and blue by RF only. Grey indicates that none of the classifiers predicted peat. ML was implemented in IDL-ENVI. SVM and RF in Google Earth Engine. National boundaries are black lines; sub-national boundaries are grey lines.*

Figure 5.10 shows the spatial peat predictions as produced by each algorithm in either IDL-ENVI software (ML) or the GEE application (SVM and RF). Substantial agreement is found between all three algorithms in the central part of the Cuvette Centrale (white in Figure 5.10), but substantial disagreement can be seen on the peripheries of the basin. In particular, ML and SVM algorithms predict considerable peat deposits in the north and east of the Cuvette Centrale (red and

yellow), which is not predicted by the RF algorithm. On the other hand, RF predicts more peat deposits in the south of the basin (blue), which are not predicted by ML and SVM. It must also be noted that the ML classifier alone predicts considerably more peat on the periphery (red) than SVM does in those same regions (yellow). As a result, large differences in total peatland area are predicted by the three algorithms (Table 5.4), ranging from 102,000 km^2 (RF) to 167,600 km^2 (ML). Comparable differences between ML, SVM and RF were found for model runs in either R software (validation data only) or in GEE/IDL-ENVI (full map predictions), indicating that this variation is likely not caused by differences in implementation software.

Comparison of the ML, SVM and RF models with Dargie et al.'s (2017) model performance, using balanced accuracy estimates obtained from random cross-validation, shows improved results only in the case of the ML classifier (Table 5.4). Balanced accuracy of the Maximum Likelihood model is 91.9% (95% CI, 90.2-93.6), compared with 89.8% (95% CI, 86.0-93.4) for the first-generation model by Dargie et al. (2017). This shows that the combination of adding the HAND-index as input product and having an extended ground-truth dataset that covers a wider map region, has improved the model's performance. The substantially smaller BA interval of the improved ML model further indicates increased confidence in the new peatland predictions, despite only a small increase in median BA.

Comparing MCC using the spatial cross-validation approach across the three different machine learning algorithms, I found that the ML classifier is also most transferable to regions for which there is a lack of training data (Table 5.4). While the RF classifier results in slightly better MCC with random CV, when no regions are omitted, spatial CV shows particularly poor predictive performance of this classifier for the Congo and Ruki regions, when trained on data from the other regions. The SVM classifier results in the lowest MCC of all three models when assessed using random CV, and also performs worst of all three in the Congo region with spatial CV.

Additionally, assessing spatial CV for the largely interfluvial basin region in ROC (combining the Likouala-aux-Herbes and Ubangi regions; n=401), and the largely river-influenced region in DRC (combining the Congo and Ruki regions; n=540), also shows that the RF classifier performs particularly poorly (Table 5.4). This finding further supports selecting the Maximum Likelihood classifier as best algorithm to produce a second-generation map of peatland distribution in the central Congo Basin.

Model	Peatland area estimate (hardwood- and palm-dominated peat swamp forest, km^2)	Random cross-validation (BA, %)	Random cross-validation (MCC, %)	Spatial cross-validation per region (MCC, %)					
				Likouala-aux-Herbes, ROC (n=261)	Ubangi, ROC (n=140)	Congo, DRC (n=371)	Ruki, DRC (n=143)	Interfluvial basin peatlands, ROC (n=401)	River-influenced peatlands, DRC (n=540)
ML	167,648 (159,378 - 175,079)	91.9 (90.2 - 93.6)	78.0 (74.2 - 81.6)	78.1 (76.5 - 79.7)	66.6 (63.6 - 71.4)	41.9 (37.3 - 45.1)	73.2 (70.1 - 76.0)	73.9 (71.4 - 76.0)	65.0 (61.1 - 67.5)
SVM	135,359 (124,847 - 145,991)	87.0 (84.1 - 89.7)	77.5 (72.4 - 81.9)	76.6 (73.0 - 78.2)	75.1 (71.9 - 79.0)	34.9 (26.4 - 44.7)	74.0 (68.1 - 78.3)	73.2 (67.1 - 75.8)	68.2 (63.2 - 71.8)
RF	101,988 (92,596 - 111,358)	89.6 (86.7 - 93.3)	79.0 (73.5 - 84.1)	70.4 (60.1 - 76.6)	71.3 (64.7 - 78.4)	37.1 (25.9 - 46.8)	49.2 (39.5 - 58.5)	66.8 (58.0 - 74.1)	46.2 (39.2 - 52.5)

Table 5.4. Area estimates and random/spatial cross-validated accuracy results for ML, SVM and RF algorithms. *Binary classification performances (random and spatial Matthews correlation coefficient [MCC], %) are reported for supervised Maximum Likelihood (ML), Support Vector Machine (SVM) and Random Forest (RF) classification algorithms. Binary classification performance using balanced accuracy results (BA, %) from random cross-validation (CV) are additionally reported to facilitate correct comparison with the first-generation peatland map by Dargie et al. (2017) (median BA, 89.8%; 95% CI, 86.0-93.4). Random CV and area results are obtained from 1,000 randomly stratified two-thirds data splits of 1,736 datapoints. Spatial CV results are obtained for each region by selecting 1,000 randomly stratified two-thirds data splits as training data from all remaining datapoints, validated against all datapoints of the selected (omitted) region. The 'interfluvial basin peatlands' group comprises the Likouala-aux-Herbes and Ubangi regional groups in ROC; the 'river-influenced peatlands' group comprises the Congo and Ruki regional groups in DRC (see Figure 5.4). Models were implemented in IDL-ENVI (ML) or GEE (SVM/RF) for random CV and area calculations. All spatial CV analyses were implemented in R. All figures are median values with 95% confidence intervals in parentheses.*

5.5.4 Distribution of peat swamp forest area

The median total peatland area estimated by the best-performing algorithm (Maximum Likelihood classifier, based on its ability to most accurately predict in regions with no training data) is 167,600 km^2, an increase of 15% compared with Dargie et al. (2017). This figure is obtained from all the 50 m pixels in the peat probability map that indicates either palm- or hardwood-dominated peat swamp forests in at least 500 out of 1,000 runs (Figure 5.11). The map in Figure 5.11 uses the same colour scheme and classification as Dargie et al. (2017) to aid direct comparison. As a measure of statistical model uncertainty, the 95% confidence interval around this estimate, as tested by random Monte Carlo cross-validation, ranges from 159,400 to 175,100 km^2.
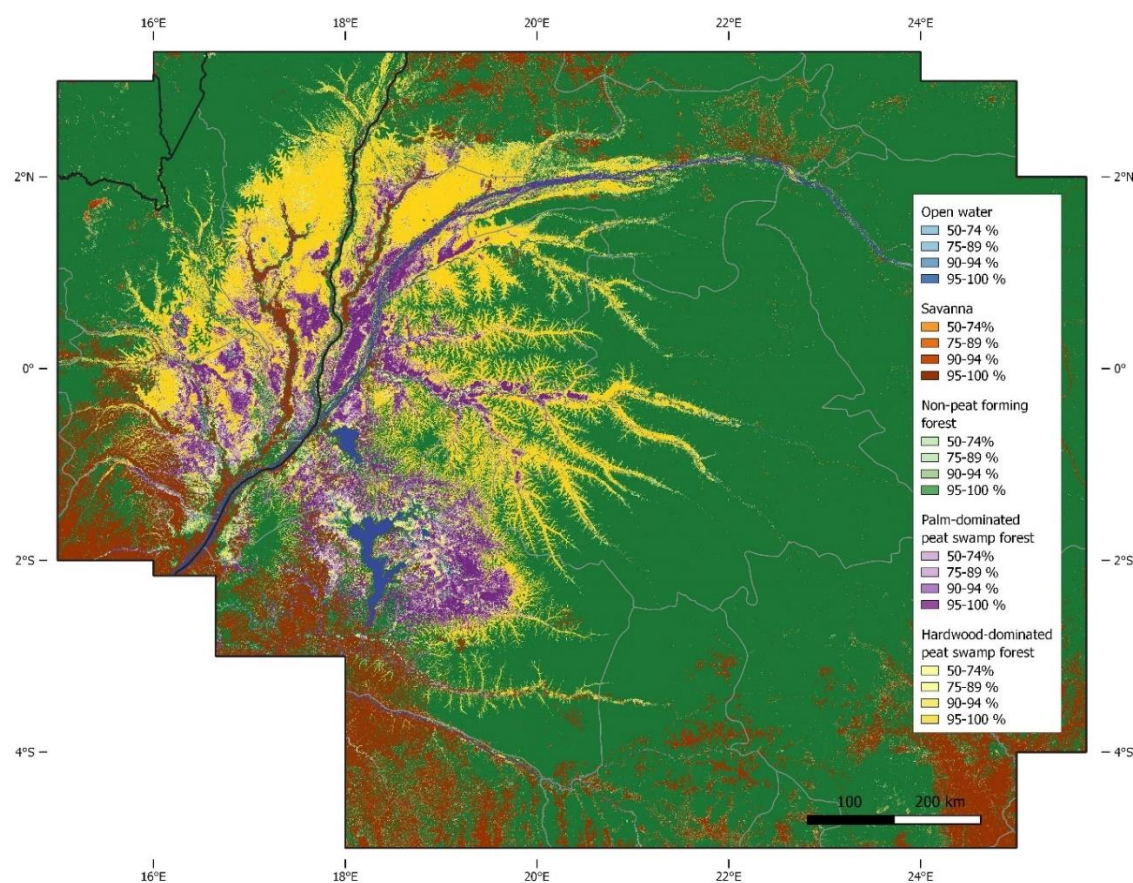
Figure 5.11. Probability map of peat swamp vegetation across the central Congo Basin. *Model predictions are based on the second-generation model using a supervised Maximum Likelihood classification, including the HAND-index, with 1,736 ground-truth datapoints. Prediction probabilities are indicated as the most likely class per pixel (>50%) out of 1,000 model runs, using a legend identical to Dargie et al. (2017) to facilitate comparison. National boundaries are black lines; sub-national boundaries are grey lines; non-peat forming forest includes both* terra firme *and non-peat forming seasonally inundated forests.*

It was found that 90% of all pixels that are predicted as peat in the median ML map result are predicted as peat in at least 950 out of 1,000 runs (i.e., with ≥ 95% probability, either as hardwood- or palm-dominated peat swamp forest; Figure 5.11). This shows that peat predictions are consistent across model runs and thus robust. Overall model performance of this model, as assessed using the Matthews correlation coefficient, is 78.0% (95% CI, 74.2-81.6%).
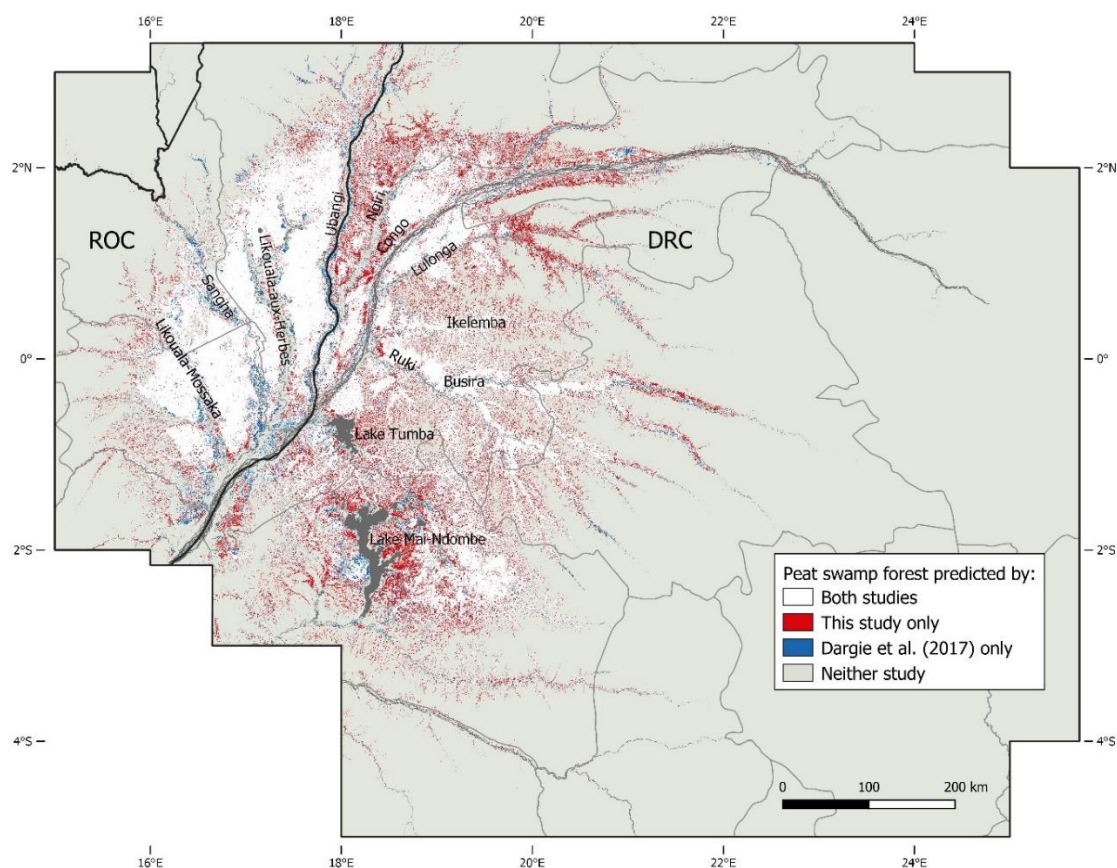
Figure 5.12. Comparison of peat swamp forest predictions between this study and Dargie et al. (2017). *Comparison is based on the most likely class (> 50% probability) per pixel. White indicates peat in both studies; red indicates peat in this study only; blue indicates peat only in Dargie et al. (2017); light grey indicates peat in neither study. Open water is dark grey. National boundaries are black lines; sub-national boundaries are grey lines; non-peat forming forest includes both* terra firme *and non-peat forming seasonally inundated forests.*

Comparing the second-generation peatland distribution map with the first-generation map by Dargie et al. (2017) shows large areas of agreement (white in Figure 5.12). However, the new map predicts areas of peat which were previously not mapped, particularly around Lake Mai-Ndombe in the south and the Ngiri and upper Congo/Lulonga Rivers further north in the DRC (red in Figure 5.12). In addition, small areas of previously predicted peat deposits are no longer predicted by the new model, particularly along the Sangha and Likouala-Mossaka Rivers in ROC

(blue in Figure 5.12). These areas of difference are likely areas of high uncertainty and should therefore be priorities for future fieldwork.

Of the total peatland area estimate of 167,600 km^2, approximately two-thirds is found in the DRC (113,200 km^2), while ROC is home to one-third of the Cuvette Centrale peatlands (55,100 km^2). DRC's Équateur province alone harbours an estimated 58,300 km^2 of peatlands, an area that is larger than is found in all of the Republic of the Congo. Secondly, the DRC's province of Mai-Ndombe has a peatland area of 29,800 km^2, approximately similar to what is found in the most-peatland-rich department in ROC, Likouala, which harbours about 28,600 km^2 of peatlands. More detailed sub-national peatland area estimates are provided in Table 6.3 in Chapter 6.

5.5.5 Distribution of seasonally inundated peat swamps

The landcover map in Figure 5.11 distinguishes only between hardwood- and palm-dominated peat swamp forest types. However, in Chapter 3, it was concluded that there are also a mixed peat swamp forest type and a seasonally inundated mixed peat swamp forest type in DRC. To map this last swamp type, which is primarily driven by inundation patterns, I developed a map of inundation frequency across most of the central Congo Basin peatland areas identified in section 5.5.4.

Figure 5.13 shows the number of times out of the total of nine selected months that peat swamp forests were identified from ALOS PALSAR data as having standing water beneath the canopy. Here, nine months indicates likely year-round inundation, while zero months indicate no inundation at all. From this map, it can be seen that there are large spatial differences in inundation frequency between regions of the peatland complex. Principally, an east-west gradient can be observed, with frequently inundated sites located in the eastern (mostly DRC) part of the Cuvette Centrale, and less frequently inundated sites located in the western (mostly ROC) part of the Cuvette Centrale. More specifically, four major peatland area can be identified, as indicated (numbers 1-4) in Figure 5.13. First, there appears to be an area of peat swamp forests in ROC, principally west and north of the Likouala-aux-Herbes River, that seems rarely inundated, even in wet season radar images. Second, there appears to be an area of seasonally inundated peat swamps straddling the Congo River mainstem with a medium inundation frequency of 4-6 inundations out of the 9 recorded months, and occasionally higher. These

inundations appear to extend across the peatland areas east and west of the Congo River towards the Ngiri and Lulonga Rivers. Third, there appears to be an area of seasonally inundated peat swamps along the Ikelemba, Ruki and Busira Rivers and their headwaters. This area has a similar medium inundation frequency of 4-6 inundations out of the 9 recorded months, although areas with greater numbers are also found. Fourth, there appears to be an area of peat swamp forest east of Lake Mai-Ndombe that appears heavily inundated year-round, with an inundation frequency of nine out of nine months.
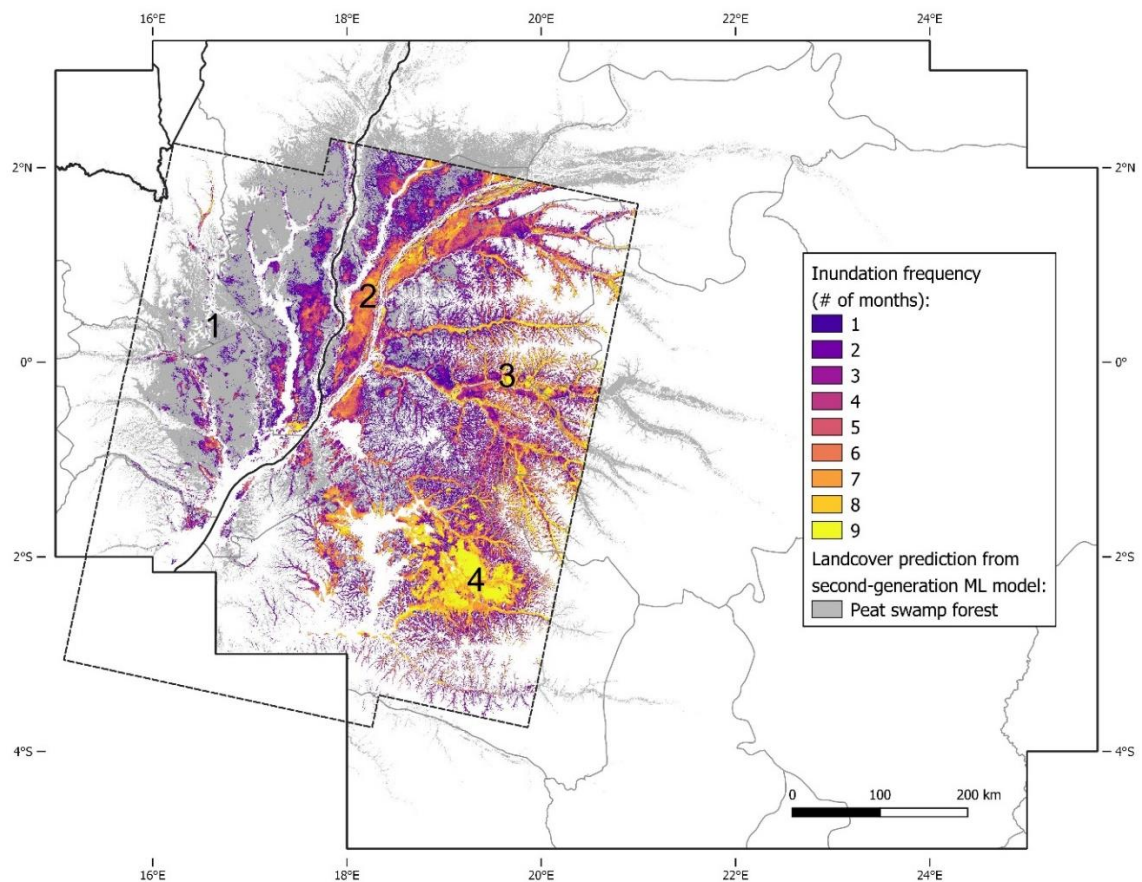
Figure 5.13. Map of inundation frequency in peat swamp forests of the central Congo Basin. *Inundation frequency is measured as the number of inundations recorded by the ALOS PALSAR ScanSAR (> -6 dB backscatter) out of nine selected months between 2007 and 2009. The baselayer shows the predicted peat swamp forest extent (in grey) from the second-generation Maximum Likelihood model (section 5.5.4). The dashed line indicates the footprint of the available multi-temporal radar data. National boundaries are black lines; sub-national boundaries are grey lines.*

In Figure 5.14, I compare the distribution of inundation frequencies as mapped for each of the 40 peat swamp vegetation plots that were analysed in Chapter 3. Although vegetation cluster 1 has a mean of inundation frequency of 6 out of 9 months, the shape of the violin plot highlights how these vegetation plots are either strongly inundated (≥ 7 out of 9), or hardly inundated (≤

2 out of 9). This could indicate that palm-dominated peat swamps are found in locations with little seasonality, which experience either almost permanently inundated conditions year-round, or very little inundation year-round. This contrasts with the distribution of vegetation cluster 4, the seasonally inundated mixed peat swamp forest, which has a mean inundation frequency of 4 months and 25 days out of 9, with a range from 2 to 6 months. This suggests inundation on a seasonal basis, rather than year-round. Finally, both cluster 2 and 3, the hardwood-dominated and mixed peat swamp forests, are characterized by low inundation frequencies of ≤ 3 out of 9 months, with means of 1 month and 9 days and 2 months and 7 days, respectively. This implies that it is difficult to separate cluster 2 and 3 based on inundation frequencies. In addition, it appears challenging to use inundation frequencies to differentiate these classes from at least part of the palm-dominated swamp, given some palm swamp has very low inundation frequencies. However, since seasonally inundated swamps alone are characterised by inundation frequencies of 4-6 out of 9 months, this range can be used to specifically map this peat swamp forest type.
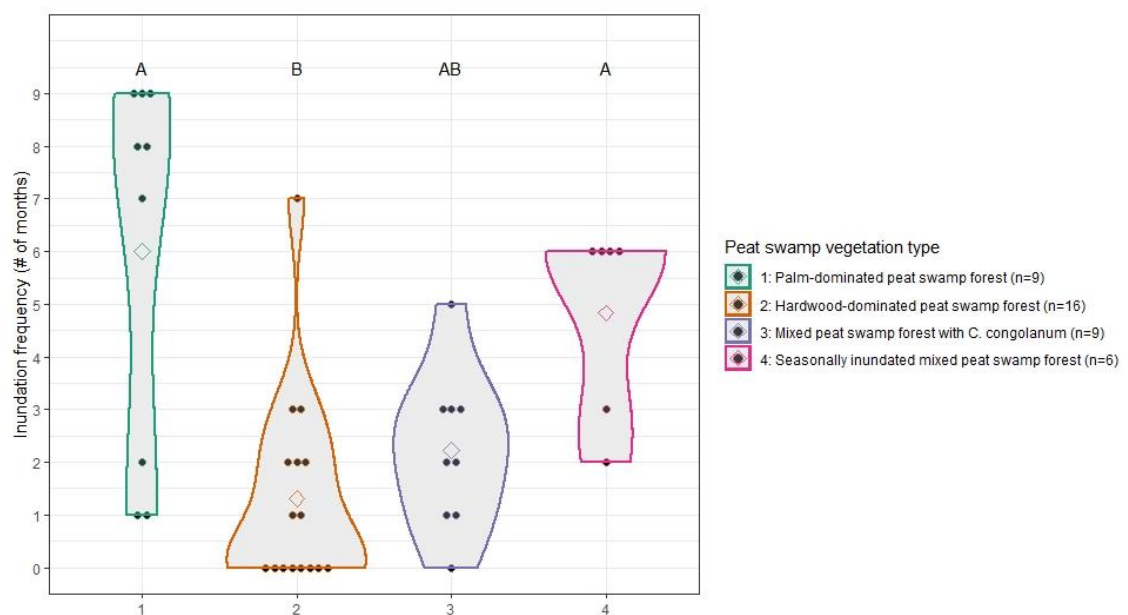
Figure 5.14. Violin plots of inundation frequency (# of months out of 9) across four peat swamp vegetation types. *The distribution includes 40 vegetation plots in peat swamp forests (represented by black dots), clustered into 4 distinct vegetation types (obtained from Chapter 3). Transparent diamonds indicate the mean per group. Transects that do not share a common letter are significantly different (p<0.05, Dunn's Kruskal-Wallis multiple comparison test, p-values adjusted with the Benjamini-Hochberg method).*

Figure 5.15 shows the distribution of peat swamp forests that experience this inundation frequency (in mint). This seasonally inundated vegetation is mostly located on either side of the Congo River mainstem, and in smaller river valleys along its eastern tributaries. Interestingly,

the western part of the Lokolama peatland area, is also highlighted as seasonally inundated, perhaps suggesting pooling of wet season rainfall in a shallow basin or potential river water input from the Congo River.
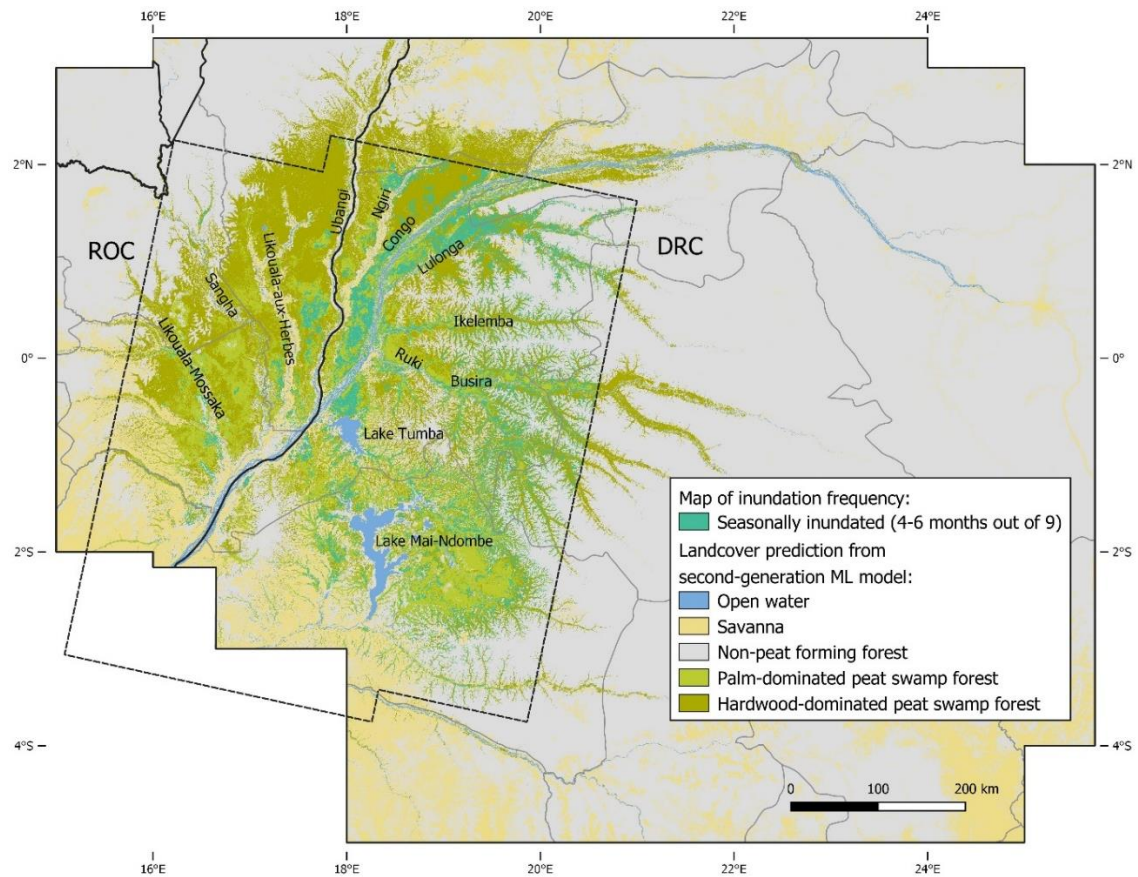
Figure 5.15. Map of seasonally inundated mixed peat swamp forest. *Seasonally inundated mixed peat swamp forest (mint) is assumed to be associated with an inundation frequency of 4-6 out of 9. The baselayer shows the predicted landcover classes from the second-generation Maximum Likelihood model (section 5.5.4). The dashed line indicates the footprint of the available multi-temporal radar data. National boundaries are black lines; sub-national boundaries are grey lines; non-peat forming forest includes both* terra firme *and non-peat forming seasonally inundated forests.*

Peat swamp forests with an inundation frequency of 4-6 out of 9 months cover approximately a quarter (23.7%) of the peatland area that is within the ALOS PALSAR ScanSAR footprint (Table 5.5). Scaling this proportion to the entire peatland area across the central Congo Basin, including outside the radar footprint, I estimate this vegetation type to cover approximately 39,800 km^2. Just over half (56.4%) of the peatland area experiences limited inundation ($\leq$ 3 out of 9 months), which equals approximately 94,400 km^2, most of which is found in ROC. Finally, I estimate that about a fifth (19.9%) of the peatland area is almost permanently inundated ($\geq$ 7 out of 9 months), which equals approximately 33,300 km^2 (Table 5.5).

Inundation frequency (# of inundations out of 9)	Peatland area within ScanSAR footprint (km²)	Proportion of total ScanSAR peatland area (%)	Estimated total peatland area across the basin (km²)	Combined proportion of total ScanSAR peatland area (%)	Combined estimated total peatland area across the basin (km²)
0	25,367	19.9	33,371	56.4	94,447
1	20,072	15.8	26,405		
2	14,364	11.3	18,897		
3	11,990	9.4	15,774		
4	10,489	8.2	13,799	23.7	39,839
5	9,821	7.7	12,919		
6	9,974	7.8	13,121		
7	9,021	7.1	11,867	19.9	33,314
8	8,764	6.9	11,530		
9	7,538	5.9	9,916		

Table 5.5. Overview of area estimates per inundation frequency. *Area estimates within the ScanSAR footprint are obtained by overlaying the map of inundation frequency with the second-generation peatland distribution map (section 5.5.4). Area estimates across the wider central Congo Basin area are then obtained by multiplying the relative proportions per inundation frequency with the median estimated peatland area of 167,600 km².*

5.6 Discussion

In this chapter, I developed a new map of peatland distribution across the central Congo Basin and assessed its statistical and systemic uncertainties. A best peatland area estimate of 167,700 km^2 was derived using a Maximum Likelihood model, with a 95% confidence interval ranging from 159,400 to 175,100 km^2. This confirms the central Congo Basin peatland complex as the world's largest tropical peatland area, accounting for approximately 36% of all tropical peatlands, given a total pantropical area of ~460,000 km^2 (440,000 km^2 from Page et al. (2022), plus the ~20,000 km^2 additionally predicted by my new Congo Basin map). Furthermore, the new model confirms the Democratic Republic of the Congo and the Republic of the Congo as the second and third most important countries in the tropics for peatland area after Indonesia, respectively (Page et al., 2011). Globally, they rank sixth and nineth for peatland area, respectively (Xu et al., 2018).

Maximum Likelihood was chosen out of three classification algorithms (the others being Support Vector Machine and Random Forest) because it produces the most accurate peat predictions in areas from which the model lacks any ground-truth data. Like Dargie et al. (2017), my Maximum Likelihood model makes use of the three Landsat 7 ETM+ optical bands, three ALOS PALSAR radar bands and SRTM-derived DEM and slope bands. Additionally, my model included the SRTM-derived HAND-index (relative elevation) as input layer, which was found to significantly improve model performances compared with only DEM- or HAND-based models. This is in line with other studies that indicate how the HAND-index is an important predictor of inundation potential, and hence peat formation (Aristizabal et al., 2020; Nobre et al., 2016; Gumbricht et al., 2017). Overall, median balanced accuracy increased for the new map, compared to the map produced by Dargie et al. (2017), highlighting increased confidence in the new peatland predictions. The considerable overlap in areas predicted to be peat by the old and new models shows that peat can be mapped with confidence in central Congo Basin region by combining ground-truth data on peat-vegetation associations and remotely-sensed data.

Regarding model configurations, it is worth pointing out that the spatial pattern of peat prediction from the HAND-only model shows considerable similarity with the peatland distribution as suggested by Gumbricht et al. (2017), including peatland areas further upstream and at higher elevations in the east of the basin. This indicates how the HAND-index reflects some of the hydro-geomorphological processes that were modelled by Gumbricht et al. (2017). However, predictions from this HAND-only model differed considerably from the predictions of

the two models containing the DEM, which are both more accurate (higher MCC) and restrict peat presence to the lower elevations of the Cuvette Centrale depression. Unfortunately, no ground-truth datapoints are available in the east of the Congo Basin from locations that are suggested as peat by the HAND-only model and Gumbricht et al. (2017), to verify whether these locations truly contain peat or not. Therefore, the presence of peat in this east of the central Congo Basin, particularly upstream on the Congo River and along the Lomami River south of Kisangani, cannot fully be excluded without further field verification. This adds considerable systemic uncertainty to the best peatland area prediction that is derived in this chapter. Following Meyer & Pebesma (2021, 2022), these areas likely need to be classified as outside the 'area of applicability' of the current dataset and should be high priorities for future field campaigns.

Apart from comparing absolute and relative elevation, I also compared different data sources of optical, radar and topographic products. These new data sources showed no improvements compared with those previously used by Dargie et al. (2017). Substitution of Landsat 7 ETM+ optical bands by Sentinel-2 bands did not improve model performance, even though the Sentinel-2 imagery is more recent and has higher spatial resolution. The Landsat 7 ETM+ bands likely performed better, because stripy artefacts as a result of bidirectional reflectance were corrected using normalised indices in the case of Sentinel-2, while they were corrected using relative normalizations from MODIS atmospherically corrected data inputs in the case of Landsat 7 ETM+ (Potapov et al., 2012; OSFAC, 2014). This likely produced smoother mosaics with less colour differences. Furthermore, as all remote-sensing products were resampled to 50 m resolution, any potential accuracy improvement that could have been derived from higher spatial resolution in Sentinel-2 (20 m) compared with the Landsat 7 ETM+ mosaics (60 m), was likely lost in the process.

Classification accuracy also decreased when substituting ALOS PALSAR radar data with more recent ALOS-2 PALSAR-2 imagery, although less so than when substituting optical bands. As the ALOS-2 PALSAR-2 bands were derived from the same type of synthetic-aperture radar data, and following the same post-acquisition processing as Dargie et al. (2017), there is no methodological reason to judge these new bands as less accurate than their predecessors. However, differences in classification accuracy between the two radar types could potentially be caused by the fact that the ALOS-2 PALSAR-2 bands used here only cover 3 years, instead of the 4 years that are covered by the initial ALOS PALSAR dataset. Thus, the ALOS-2 PALSAR-2

bands might be more sensitive to annual anomalies in surface wetness (such as the strong 2015-16 El Niño event). Larger temporal datasets could theoretically be used in the future, although the expected accuracy improvement from this is likely to be modest, compared with other sources of uncertainty that I highlight here.

In addition to substituting optical and radar data, I compared various topographic data sources (SRTM DEM, NASADEM and MERIT DEM). Even though NASADEM is thought to be a more accurate version of the older SRTM DEM, inclusion of this data source in the model caused a lower prediction accuracy. NASADEM has been judged to be only slightly more accurate in terms of vertical elevation than SRTM DEM (Uuemaa et al., 2020). By resampling from 30 m to 50 m resolution, much of this vertical improvement is likely lost, making the differences between either data product potentially very marginal. More surprisingly, the use of the error-adjusted MERIT DEM caused a large drop in classification accuracy, whereas this data product was expected to correct for potentially significant biases in ground surface elevation due to canopy height. The fact that MERIT DEM performs worse than SRTM DEM, is likely due to the fact that MERIT DEM has a lower spatial resolution of 3 arc-second (~90 m at the equator), which was resampled to 50 m. Like with the other data products, any potential accuracy improvement that resulted from less tree height bias in the Congo Basin floodplains was likely lost in the process. Once a new vegetation-corrected DEM at higher spatial resolution becomes available, that could be the topographic data source of choice. Recently released new topographic datasets such as the Copernicus DEM GLO-30 or the forest-removed FABDEM model (Hawker et al., 2022) should also be prime candidates for future model input.

From this analysis, it becomes clear that potential accuracy improvements that could be obtained with new remote sensing data products have to be balanced against the need to resample to a common resolution. Higher spatial resolutions are available in the case of Sentinel-2, ALOS-2 PALSAR-2, SRTM DEM and NASADEM. However, using a more fine-scale resolution as model input would increase computation times significantly given the size of the study area.

Furthermore, it is clear from the random and spatial cross-validations that most of the uncertainty in peatland area estimates derives from a lack of spatially representative ground-truth data, rather than from a lack of high-resolution remote sensing data. This can be seen from the fact that the confidence intervals in accuracy estimates of the models with different datasets in Figure 5.8 strongly overlap, while the regional area predictions from different classification

models in Tables 5.3 and 5.4 (DEM, HAND or DEM+HAND; and ML, SVM or RF, respectively) are very different.

Based on the above comparisons, I conclude that the original data sources used by Dargie et al. (2017) (Landsat 7 ETM+ optical, ALOS PALSAR radar and SRTM topographic data) are still the most useful for peat prediction in the central Congo Basin. Given the acquisition dates of these remote sensing products, the new peatland distribution map presented here forms a useful baseline description of the Congolese peatlands for approximately the years 2000-2010, as large-scale peatland deforestation has not occurred to date (Miles et al., 2017; Vancutsem et al., 2021).

Based on spatial cross-validation of three different classification algorithms (ML, SVM and RF), it was concluded that Maximum Likelihood is the most accurate classification algorithm, because it produces the most useful peat predictions in areas from which the model lacks any ground-truth data. The statistical uncertainty around the peatland area estimate of the Maximum Likelihood model, assessed via random Monte Carlo cross-validation, is limited, ranging from 157,579 to 172,586 km^2. However, the fact that this confidence interval does not overlap with the initial confidence interval of Dargie et al. (2017), and that large differences in estimated peatland area are found with the two other classification algorithms, suggest that systemic uncertainty is larger.

Furthermore, the balanced accuracy (BA) for the new model shows a substantially smaller confidence interval compared with Dargie et al. (2017), indicating improved confidence in the new peatland map. Nonetheless, median BA only showed a small increase, despite a three times larger ground-truth dataset. This is likely because the improvement caused by the larger dataset is partly offset by an increase in the spatial extent and ecological diversity of the datapoints. In particular, the new dataset now contains ground-truth datapoints from transects along the Congo River, where all algorithms that I tested are relatively underperforming (Table 5.4). Although appearing to produce the best results based on random CV alone, Random Forest specifically does not perform well in the Congo River region when using spatial CV. This is not surprising, given this classifier is known to be sensitive to sampling design and spatial autocorrelation (Belgiu & Drăgu, 2016; Sinha et al., 2019). The relative lack of prediction accuracy in the Congo River region by all three tested classification algorithms is suspected to be related to the different nutrient status of the mixed/white-water Congo River. This will likely

inhibit peat accumulation in seasonally inundated floodplains along the Congo mainstem. Thus, although the vegetation appears similar to typical peat swamp forest, these river-influenced sites along the Congo River likely do not always form peat (≥ 30 cm thickness of ≥ 65% organic matter) due to the higher nutrient status. Adding ground-truth data from these locations might have caused a blurring of the spectral signal of the different classes, resulting in poorer model performance for this region despite a greater overall quantity of input data. The Congo River region thus highlights limitations to the assumption that the specific hardwood- and palm-dominated swamp forest vegetations types mapped here always have peat underneath. It also shows the importance of verifying peat predictions in unsampled regions, particularly since nutrient status cannot be mapped as easily as a potential predictor variable using remote sensing. Critically, new field campaigns to the predicted peatlands surrounding Lake Mai Ndombe, which have yet to be sampled, are a high priority.

One way to further improve peatland mapping could be by adding a map of inundation period or inundation frequency. Unfortunately, the multi-temporal radar data that is freely available covers only a portion of the total peatland area. Therefore, this data was not included in the peatland area mapping of this study and only used separately to develop a distribution map of seasonally inundated peat swamps. The general distribution of inundated forests that was obtained corresponds with previous results over a smaller portion of the basin (Kim et al., 2017; Lee et al., 2015; Rosenqvist, 2009), attesting to the reliability of this wider map. Crucially, as far as I know, this is the first time that an inundation map has been extended towards the southern edge of the peatland complex, where heavily inundated swamp forests are observed.

It must be noted that inundation here refers only to standing water above the peat surface, which could result from precipitation and does not necessarily suggest river flooding from outside areas. For example, Dargie et al. (2017) showed how interfluvial basins in ROC likely receive only rainwater, yet some of these areas are seasonally inundated by standing water (4-6 months out of 9).

Nonetheless, potentially four distinct major peatland regions can be distinguished based on inundation frequency: (i) an area of limited inundation dominating in interfluvial basins in ROC; (ii) an area of seasonal inundation along the Congo River mainstem; (iii) an area of seasonal inundation along the Congo River's eastern tributaries; and (iv) a large area of almost permanent inundation east of Lake Mai-Ndombe.

First, the inundation map suggests that large parts of the swamp forests in ROC are rarely inundated. However, this does not mean that these areas are not waterlogged. Microtopographic data presented in Chapter 4 showed how the water table typically needs to be 10-20 cm above the peat surface to cover half of the 16 m^2 microtopography quadrats with water. Assuming that at least half of a pixel area similarly needs to be inundated to produce enough backscatter signal in the radar image, this suggest that the water level normally needs to be 10-20 cm above the peat surface to show up as inundated. Thus, if no inundation is recorded by the radar data, this does not necessarily mean that the soil is not waterlogged or that the water table is not close to the peat surface. The detection of large peatland areas in ROC that must be permanently waterlogged but are rarely inundated corresponds with the suggestion that these are shallow domed interfluvial basins (Davenport et al., 2020), with relatively low amplitude water table fluctuations (Dargie et al., 2017). In particular, Dargie et al. (2017) provide *in situ* datalogger data which shows that water tables of > 20 cm above the surface occur only a few days a year in interfluvial basins in ROC, typically after the largest rainfall events in the wet season. Therefore, half of the peatlands are likely permanently waterlogged swamps with relatively stable water tables close to the peat surface.

On the other hand, large areas of seasonal inundation are detected along the Congo mainstem and its eastern tributaries in DRC. These two areas likely differ by the fact that the Congo region is flooded with more nutrient-rich river water, which also appears to extend over a wider floodplain area. In contrast, the seasonally inundated peatlands along the Ruki and Ikelemba Rivers have been shown to receive nutrient-poor water (Chapter 4) and are constricted by the narrower width of the river valleys.

Finally, the fourth area east of Lake Mai-Ndombe highlights how some peatlands are likely permanently inundated by standing water above the peat surface. By comparing Figure 5.11 and Figure 5.13, this part of the peatland complex appears to correspond largely with a major area of palm-dominated peat swamp forest, suggesting a tolerance of *Raphia laurentii* for almost year-round anoxic conditions. However, it is unclear if this inundation results from local ponding of precipitation or if this water originates elsewhere. Furthermore, the relative overrepresentation of palm-dominated vegetation in permanently inundated locations could also be the result of a different double-bounce mechanism in the low-stature palm swamp, in contrast with typically taller hardwood swamps. More research is thus required to establish whether the -6 dB backscatter threshold that was applied is equally valid in palm-dominated and

hardwood-dominated forest. Field verification of the apparently permanently inundated palm-dominated peatlands east of Lake Mai-Ndombe is also urgently required, as this area has so far been excluded from most wetland and peatland research in the Cuvette Centrale.

5.7 Conclusion

In this chapter, I developed a more accurate map of peatland distribution across the central Congo Basin, using ground-truth data collected in the largely river-influenced swamp forests of the DRC. This model predicts a total peatland area of 167,600 km^2 (95% confidence interval, 159,400 - 175,100 km^2), which is an increase of 15% compared with Dargie et al. (2017). This model uses Landsat 7 ETM+ optical bands, ALOS PALSAR radar bands, and SRTM-derived topographic bands, which were found to provide more accurate results than alternative data sources. This is the same as Dargie et al.'s (2017) remote sensing products, except that I added the SRTM-derived HAND-index (relative elevation), which was found to improve the model's accuracy. The Maximum Likelihood classifier was further found to be the best-performing classifier out of three options (the others being Support Vector Machine and Random Forest). This is based on its ability to most accurately predict in regions with no training data, which I assessed via spatial cross-validation. Map areas where these classifiers disagree on the periphery of the peatland complex should be priorities for future fieldwork. Furthermore, more fieldwork is needed in the eastern parts of the central Congo Basin, particularly upstream on the Congo River and along the Lomami River near Kisangani, which appear to be areas that are outside the 'area of applicability' of the current dataset. In addition, the development of a map of inundation frequency highlights an understudied area of permanently inundated palm swamp forest east of Lake Mai-Ndombe in DRC, which requires more research. From this map of inundation frequency, it is estimated that about a quarter of the total peatland area is seasonally inundated, particularly along the Congo River and its eastern tributaries in DRC, while about a fifth of the peatlands is estimated to be permanently inundated by standing water. Just over half of the total peatland complex is rarely inundated, suggesting permanently waterlogged conditions that derive from stable water tables near the peat surface. Overall, new map based on field data from the DRC, including from river-influenced settings that have been studied for the first time, confirms the central Congo Basin peatland complex as the world's largest tropical peatland area, accounting for approximately 36% of all tropical peatlands. Furthermore, the DRC and ROC are confirmed to be the second and third most important countries in the tropics for peatland area after Indonesia, respectively.

Chapter 6: Modelling peat thickness, carbon density and carbon stocks of the central Congo Basin

6.1 Abstract

Peat thickness and carbon density in the central Congo Basin has so far only been estimated using a limited dataset from interfluvial basins in the Republic of the Congo. In this chapter, I used 463 field measurements of peat thickness across both river-influenced peatlands in DRC and interfluvial basin peatlands in ROC to train a Random Forest regression model of peat thickness, providing the first map of peat thickness across the central Congo Basin. This RF model was found to provide optimal results when trained using four predictor variables: distance from the peatland margin, precipitation seasonality, climatic water balance and distance to the nearest drainage point. The model performs well in areas that were included in the sampling (median R^2 = 82.2%, RMSE = 0.68 m), but spatial cross-validation shows that considerably systemic uncertainty remains in areas from which no data is available. This highlights the need for more field data on peat thickness, particularly from Mai Ndombe in DRC. Mean modelled peat thickness across the basin is 1.7 ± 0.9 m, slightly lower than the mean field estimate of 2.4 ± 1.5 m, as expected given that the transect sampling design is biased towards the deeper centres of peatland areas. I further used bulk density and carbon concentration values of 80 peat cores from across the peatland complex to develop a linear regression between peat thickness and carbon density per unit area. Based on the modelled values of peat thickness, I then generated the first map of peat carbon density across the central Congo Basin. Mean modelled carbon density is 1,712 ± 634 Mg C ha^{-1}, in line with the field-measured mean of 1,741 ± 1,186 Mg C ha^{-1}. Based on this map of carbon density, I estimate that the total peat carbon stock in the central Congo Basin is 29.0 Pg (95% CI, 26.3-32.2). This is similar to the median 30.6 Pg C reported by Dargie et al. (2017), but their lower 95% confidence interval was 6.3 Pg, which has increased to 26.3 Pg in this study. Thus, mapping peat thickness helps to significantly reduce uncertainty in peat carbon stocks. The new carbon stock estimates confirm the central Congo Basin peatland complex as a globally important store of carbon, storing ~28% of all tropical peat carbon. I estimate that only 8% of the carbon stored in the peat lies within formal national-level protected areas, while industrial logging, mining, or palm oil concessions together overlie 26% of total carbon stocks, suggesting a vulnerability of the peat carbon to future land-use changes.

6.2 Introduction

Although machine learning tools have long proven very useful for mapping peatlands (Minasny et al., 2019), only recently a handful of studies have used the same kind of tools to map peat thickness, most of which are situated in the temperate or boreal zone. For example, Parry et al. (2012) presented a method for mapping peat thickness of blanket bogs in the Dartmoor area of England. They developed regression analyses between elevation and slope, and peat thickness. Similarly, Young et al. (2018) developed regressions for British blanket bogs using elevation, slope, aspect, vegetation type and soil type. However, they additionally tested the use of spatial covariates (latitude/longitude), to make use of the spatial autocorrelation of measurements, which was found to improve the predictive accuracy. For tropical peatlands in Indonesia, Rudiyanto et al. (2016) also mapped peat thickness as a function of elevation, slope, aspect and spatial position, as well as a wetness index and distance to the nearest river. They again found that elevation was the best predictor. Vernimmen et al. (2020) build on this to map peat thickness in Sumatra, finding that it correlates well with accurate surface elevation derived from airborne LiDAR data. It thus appears that topographic variables, and in particular elevation, are the most useful predictors for peat thickness. However, all of these studies have in common that they were trained and applied on relatively small peatland areas, with relatively more ground-truth data than is available in the central Congo Basin. This high resolution makes the use of spatial covariates particularly useful, as spatial autocorrelation works at local scale. Given the lack of a similar high-resolution dataset for the Cuvette Centrale, it is questionable whether this method would be applicable here as well.

As peat accumulation is dependent on the balance between aerobic and anaerobic conditions, it could be hypothesized that radar data of soil wetness or hydroperiod would potentially correlate with peat thickness. However, as we saw in the previous chapter, large parts of the peatland complex do not appear as inundated in multi-temporal SAR data, even though they are very likely permanently waterlogged. Thus, it is unlikely that radar data alone would be a good predictor of peat thickness. This appears to be confirmed by Rudiyanto et al. (2016), who found that their surface wetness index did not contribute much to the model.

In addition to inundation patterns, nutrient gradients are likely to affect decomposition rates as well. However, in contrast to surface wetness, spatially-explicit data on nutrient availability is not easily available and can thus not be included in a model of peat thickness. Instead, likely

predictor variables of peat thickness will have to come from remotely-sensed data on vegetation, topography, hydrology and climatic variables.

In this chapter, I hypothesize that ALOS PALSAR radar data is correlated with peat thickness, as we have seen that shallow, seasonally inundated peat swamps have a distinctly different backscatter signal than deeper peat swamps with more stable water tables (see Chapter 5). Thus, the use of this data type can be expected to help differentiate between shallow seasonally inundated peat, and deeper permanently waterlogged peat. Similarly, optical Landsat 7 ETM+ data can likely help to differentiate between these peat swamp forests, as the vegetation structure of seasonally inundated forests has been found to differ (see Chapter 3).

Additionally, I hypothesize that distance from the peatland margin is an important predictor of peat thickness, as peat thickness was generally found to increase along transects when moving away from the *terra firme* edge (see Chapter 2). Since this also corresponds with distance to the river along some river-influenced peatlands, I additionally hypothesize that distance from the nearest drainage point is also an important driver of peat thickness.

Furthermore, I hypothesize that climatic variables such as total precipitation or precipitation seasonality play a role in predicting peat thickness. This is because peatlands in the central Congo Basin are likely closer to the their hydrological limit, given the relatively drier climate compared with other tropical peatland areas (Malhi & Wright, 2004). Thus, small differences in rainfall patterns could have a potentially important impact on peat thickness by shifting the balance between accumulation and decay.

Finally, I hypothesize that topographic variables are useful for predicting peat thickness in the central Congo Basin, given they have proven useful in other peatland studies and will likely help to identify depressions where water is expected to pond. In particular, I hypothesize the HAND-index to be an important driver of peat thickness, as it is hydrologically more relevant at the local scale than absolute elevation above sea level (Nobre et al., 2011).

Unlike the Maximum Likelihood classifier used for mapping landcover distribution in Chapter 5, the Random Forests algorithm has the advantage that it can be used for regression models as well. Additionally, this algorithm is capable of providing an estimate of variable importance, which can be useful in assessing the individual contributions of the hypothesized predictor

variables (Maxwell et al., 2018). However, how well an RF regression would work for predicting peat thickness over a large mapping area is unclear. As was also observed in Chapter 5, Random Forest is sensitive to overfitting due to spatial autocorrelation in the dataset (Nussbaum et al., 2018; Sinha et al., 2019). Thus, any such model requires a large enough dataset to prevent overfitting errors. Fortunately, peat thickness measurements are now available from across interfluvial basin peatlands and river-influenced peatlands. In this chapter, I therefore aim to develop a Random Forest regression model for predicting peat thickness, by using the combined dataset of peat thickness measurements in the DRC (this study) and ROC (Dargie et al. 2017). I will then use this model of peat thickness to scale the estimates of the amount of carbon stored belowground in peat across the central Congo Basin. In this way, developing a peat thickness model will contribute to reducing the current uncertainty in peat carbon stock estimates in the Cuvette Centrale.

6.3 Chapter aims

The overall aim of this chapter is to estimate the total carbon stocks of the central Congo Basin peatlands by combining field data on peat thickness and carbon density with remotely-sensed data. In addition, I develop the first model of peat thickness for the central Congo peatlands that is based on *in situ* measurements. The specific objectives of this chapter are: (i) to develop a map of peat thickness across the basin; (ii) to use this map of peat thickness to develop a first map of peat carbon density across the basin; and (iii) to estimate basin-wide peat carbon stocks.

6.4 Methods

6.4.1 Peat bulk density measurements

I estimated carbon density for 80 peat cores (OM ≥ 65%, thickness ≥ 0.3 m), located every other kilometre along 18 transects across both DRC and ROC. These included 25 peat cores from the seven transects used for hypothesis-testing in the Ruki River region in DRC (presented in Chapter 2), plus 14 cores from three transects in the Congo River region in DRC, collected by the CongoPeat project (S. Lewis, G. Dargie and the CongoPeat consortium, unpublished data). In addition, there were 43 cores from eight transects in the Likouala-aux-Herbes River region (26 cores from 5 transects) and Ubangi River regions (17 cores across 3 transects) in ROC, collected by Dargie et al. (2017).

Knowing the bulk density of peat, i.e. the mass per unit volume, is an important first step for quantifying peat carbon stocks (Chambers et al., 2011). Peat bulk density was measured for all 80 peat cores. Every other 0.1-m down-core, samples of a known peat volume were weighed after being dried for 24h in an oven at 105°C and cooled down in a desiccator (n=906). Bulk density (ρ, g cm^{-3}) was then calculated by dividing the oven-dry sample mass by the volume of the sample (Rowell, 1994), similar to Dargie et al. (2017):

$$\rho = \frac{m_{dry}}{V} \qquad \text{[Eq. 6.1]}$$

Here, m_{dry} is the calculated dry mass (g) of the entire sample and V is the volume (cm^3) of the 0.1-m thick peat sample. For samples that were subsampled, dry mass of the of the entire sample was calculated from the wet mass of the entire sample, minus the water content:

$$m_{dry} = m_{wet} - (m_{wet} * W) \qquad \text{[Eq. 6.2]}$$

Here, m_{wet} is the wet mass (g) of the entire sample and W is the water content fraction. W was calculated from the oven-dried subsample using:

$$W = \frac{m_{wet,sub} - m_{dry,sub}}{m_{wet,sub}} \qquad \text{[Eq. 6.3]}$$

Here, $m_{wet,sub}$ is the wet mass of the subsample and $m_{dry,sub}$ is the dry mass of the subsample. The sample volume (V) was taken from the peat corer dimensions (530 cm^3 per core; 106 cm^3 per sample). Within each core, linear interpolation was used to estimate bulk density for the alternate 0.1m-thick samples of the core that were not measured.

6.4.2 Peat carbon concentrations measurements

In addition to bulk density, knowing the carbon content of the peat is required to estimate carbon storage in each peat sample (Chambers et al., 2011). Total carbon concentrations (%) were measured only for the deepest core of each transect, plus one additional core from the Lokolama transect in DRC and three additionally cores from the Ekolongouma transect in ROC, because the carbon content of the peat is known to be relatively consistent, unlike bulk density which is more variable (Dargie, 2015). This totals 22 cores, including 11 from DRC (eight from the Ruki River region; three from the Congo River region) and 11 from ROC (five from the Likouala-aux-Herbes River region; six from the Ubangi River region) (Dargie et al. 2017).

Carbon concentrations of every other 0.1-m thick peat sample down-core were measured using an elemental analyser at the University of Leeds (manufacturer: Elementar UK Ltd, Handford, UK; model: Vario MICRO Cube with thermal conductivity detection). However, due to Covid-19 disruption, the cores from the three Congo River transects were analysed by Dr Arnoud Boom, Hollie Bean and Genna Tyrrell at the University of Leicester using isotope-ratio mass spectrometry (manufacturer: Sercon Instruments Ltd, Crewe, UK; model: ANCA GSL). All samples (n=422) were pre-dried for 48h at 40°C and ground to <100 µm using a MM301 mixer mill. Again, linear interpolation was used within each core for the alternate samples that were not measured.

The remaining 58 cores had less-intensive carbon concentration sampling, whereby typically only the surface sample was measured. I interpolated the carbon concentration for each 0.1-m thick down-core sample of these cores, following Dargie et al. (2017), because well-sampled cores showed a consistent pattern with depth: an increase to a depth of about 0.65 m, followed by a long, very weak decline, and finally a strong decline over the deepest approximately 0.5 m of the core. I used segmented regression on the 22 well-sampled cores (*segmented* package in *R,* version 1.3-1) to parameterize the three sections of each peat core. This generated mean values for the change in carbon content across each section (20.7, -3.3 and -33.6 % m^{-1}, respectively) which were used to interpolate the carbon concentrations for the less-intensively sampled 58 cores. If no surface sample had been measured (n=25), I used the mean intercept (50.54% carbon) as starting value to interpolate carbon concentrations.

To calculate peat carbon density (mass per unit area), estimates of carbon storage in each 0.1-m thick peat sample down-core (thickness × bulk density × carbon concentration) were summed

to provide an estimate of total carbon density per core (in Mg C ha^{-1}), identical to Dargie et al. (2017).

6.4.3 Modelling peat thickness

Generally, an increase in peat thickness was observed along most transects (Chapter 2), suggesting peat thickness increases with greater distance from the peatland margin. This trend can potentially be used to model peat thickness across the peatland complex. To test this, I analysed 447 measurements of peat thickness that were collected across 18 transects in the central Congo Basin. These included 236 measurements from the DRC, of which 163 were collected across the seven hypothesis-testing transects in the Ruki River region (this thesis, Chapter 2) and 73 across three transects in the Congo River region (sampled by the CongoPeat project, using the same protocol). In addition, 211 measurements collected by Dargie et al. (2017) in the ROC were added (141 across five transects in the Likoula-aux-Herbes River region; 70 across three transects in the Ubangi River region). All pole-method measurements were calibrated using Eq. 5.1 (Figure 5.2), which takes into account the greater offset between pole-method measurements and LOI-measurements that is found in the river-influenced peatlands of the DRC, compared with the interfluvial basin peatlands of the ROC. I then plotted the increase in peat thickness with distance from the peatland margin along each transect (Figure 6.1). For this, a map of distance from the peatland margin was developed in Google Earth Engine using the median second-generation peat probability map developed in Chapter 5 (i.e., the Maximum Likelihood map with > 500 hardwood- or palm-dominated peat swamp predictions out of 1,000 runs [>50%]). For each peat pixel in this binary map, a cost function was used in GEE to calculate the Euclidean distance to the nearest non-peat pixel, after speckle and noise were removed using a 5x5 squared-kernel majority filter. Using this distance map, transects were found to have markedly different relationships between peat thickness and distance from the peatland margin, i.e., significantly different regression slopes ranging between -0.79 m km^{-1} and 0.88 m km^{-1} (n=18, p<0.001). Additionally, a linear regression using all 447 datapoints provides only a modest fit (R^2 = 41.0%; RMSE = 1.21 m), which cautions against using a uniform regression between peat thickness and distance from the margin across the central Congo Basin.

Therefore, I instead developed a spatially-explicit Random Forest regression model to predict the uneven trends in peat thickness across the basin. The RF regression was implemented in GEE with 500 trees and all other parameters set to default values. As training data, I included all LOI-

verified and corrected pole-method thickness measurements that fell within the smoothed version of the second-generation peatland distribution model with >50% peat probability (n=463), including 13 records from archaeological measurements (Kiahtipes & Schefuß, 2019), as well as thickness measurements > 0 and < 0.3 m from non-peat sites that were likely to improve predictions of shallow peat deposits near the margins (n=12).
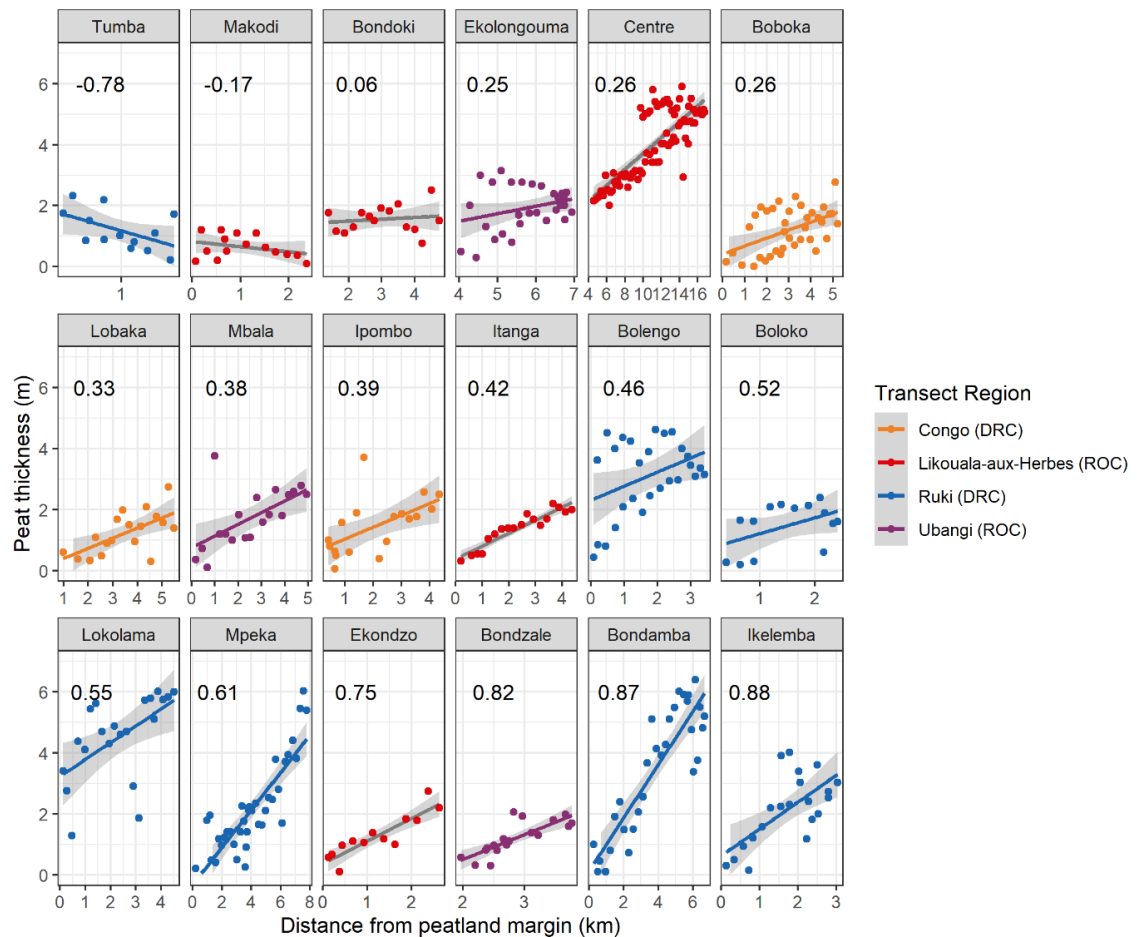
Figure 6.1. Plots showing the regression slope in peat thickness with distance from the margin for each transect. *In situ peat thickness measurements included both LOI and corrected pole-method measurements (n=463). Distance from the peatland margin is calculated as the shortest Euclidean distance to a non-peat pixel in any direction, based on a smoothed median Maximum Likelihood map of peatland extent (> 50% peat probability threshold). Transects are ordered by increasing regression slope (in m km^{-1}; upper left corner of each panel), with colours indicating the four transect regions used for spatial cross-validation. Note that the horizontal axes are different for each panel. Shaded grey shows 95% confidence intervals around each regression.*

As predictor variables, I collected a dataset of 14 remotely-sensed covariates that were hypothesized to potentially explain or be related to variations in peat thickness. These 14 variables included the nine optical (Landsat 7 EMT+), radar (ALOS PALSAR) and topographic (SRTM) products that were identified as most useful for predicting peatland distribution in

Chapter 5. In addition, I included distance from the peatland margin (derived from the binary smoothed peatland area map), distance from the nearest drainage point (using the same hydrological reference network as was used to develop the HAND-index; Lehner et al., 2008), precipitation seasonality (from the WorldClim2 database; Fick & Hijmans, 2017), live woody aboveground biomass (Baccini et al., 2012), and climatic water balance. Climatic water balance (CWB) was calculated by subtracting mean annual potential evapotranspiration (from the Global Aridity Index & Potential Evapotranspiration Database; Trabucco & Zomer, 2019) from mean annual precipitation across the basin (from the WorldClim2 database; Fick & Hijmans, 2017). All predictor variables were resampled to 50 m resolution. The map of inundation frequency developed in Chapter 5 from multi-temporal SAR data was not included because it did not cover the whole of the peatland complex.

I then applied a stepwise backward selection on all predictor variables out of these 14 that were found to be significantly correlated with peat thickness. In Google Earth Engine, I tested combinations of these significant variables by first running a model that included all significant variables, and then dropping one of them out of the model each time in order from low to high variable importance. The importance of each variable was assessed by calculating Mean Decrease Impurity (MDI), the total decrease in the residual sum of squares of the Random Forest regression after splitting on that variable, averaged over all decision trees in the random forest. Median MDI was calculated for each variable in GEE based on 100 random (two-thirds) cross-validations of the overall model containing all significant variables. As the optimal regression model, I selected the model with highest median R^2 and lowest median root mean square error (RMSE) obtained from 100 random (two-thirds) cross-validations for each model option.

To assess the accuracy of the optimal RF model, I tested if peat thickness is affected by spatial autocorrelation at scales similar to that of the transect length (~10 km). I estimated spatial variation in the peat thickness dataset by fitting a variogram model using the *gstat* package in *R* (version 2.0-7) and testing multiple fits using either exponential, spherical or Gaussian models. The best fist was found to be an exponential model with a range of 9.0 km, confirming that spatial autocorrelation is strong at the transect scale. Therefore, I also applied a spatial cross-validation approach to the Random Forest regression model. Like with the spatial cross-validation that was applied to peatland distribution models in Chapter 5, this is done to assess how well the model performs in faraway areas from which no training data is included.

For this spatial cross-validation, I used the same four transect regions as in Chapter 5 (see Figure 5.4), with datapoints from the Likoula-aux-Herbes River region and Ubangi River region combining into a larger interfluvial basin region, and datapoints from the Congo River region and the Ruki River region combining into a larger river-influenced region. For each region, I tested peat thickness predictions from the optimal RF model using 100 random selections of two-thirds of the remaining datapoints from the other regions as training data.

Furthermore, I assessed how uncertainty from the peatland area predictions affects the uncertainty around the peat thickness predictions, as distance from the peatland margin was found to be the most important predictor included in the optimal peat thickness model. For this, I ran 100 peat thickness models, each with a slightly different input layer of distance from the peatland margin. I first created 100 different maps of distance from the peatland margin, by randomly selecting (with replacement) a minimum peat probability threshold > 0% and < 100%, removing speckle and noise with a 5x5 squared-kernel majority filter, and re-calculating the closest distance to the nearest non-peat pixel. I then combined the 100 resulting maps of distance from the margin each time with the other significant predictors that were selected as input in the optimal RF model. This way, 100 different peat thickness maps could be developed based on varying peatland area predictions. For these model runs, I included all available thickness measurements (> 0 m) that fell within each derived distance map. Each output map was then masked to an area ≥ 0.3 m thickness, consistent with the peat definition. A map of median peat thickness and relative uncertainty (± half the width of the 95% CI as percentage of the median) was then calculated for each pixel based on the 100 available thickness estimates.

Finally, I compared the optimal RF model with a multiple linear regression model using the same predictor variables, including interaction effects. For this, all 463 datapoints were included (instead of a random two-thirds selection).

6.4.4 Modelling peat carbon density

To estimate carbon density from modelled peat thickness across the basin, I developed a regression model between peat thickness measurements and per-unit-area carbon density using the 80 sampled peat cores. I compared linear regressions for normal, logarithmic-, and square root-transformed peat thickness, selecting the model with lowest AICc and highest R^2. A linear model with square root-transformed peat thickness was found to provide the best fit ($R^2 = 0.86$;

p<0.001). Bootstrapping was applied (*boot* package in *R*, version 1.3-25) to assess uncertainty around the regression (Figure 6.2).
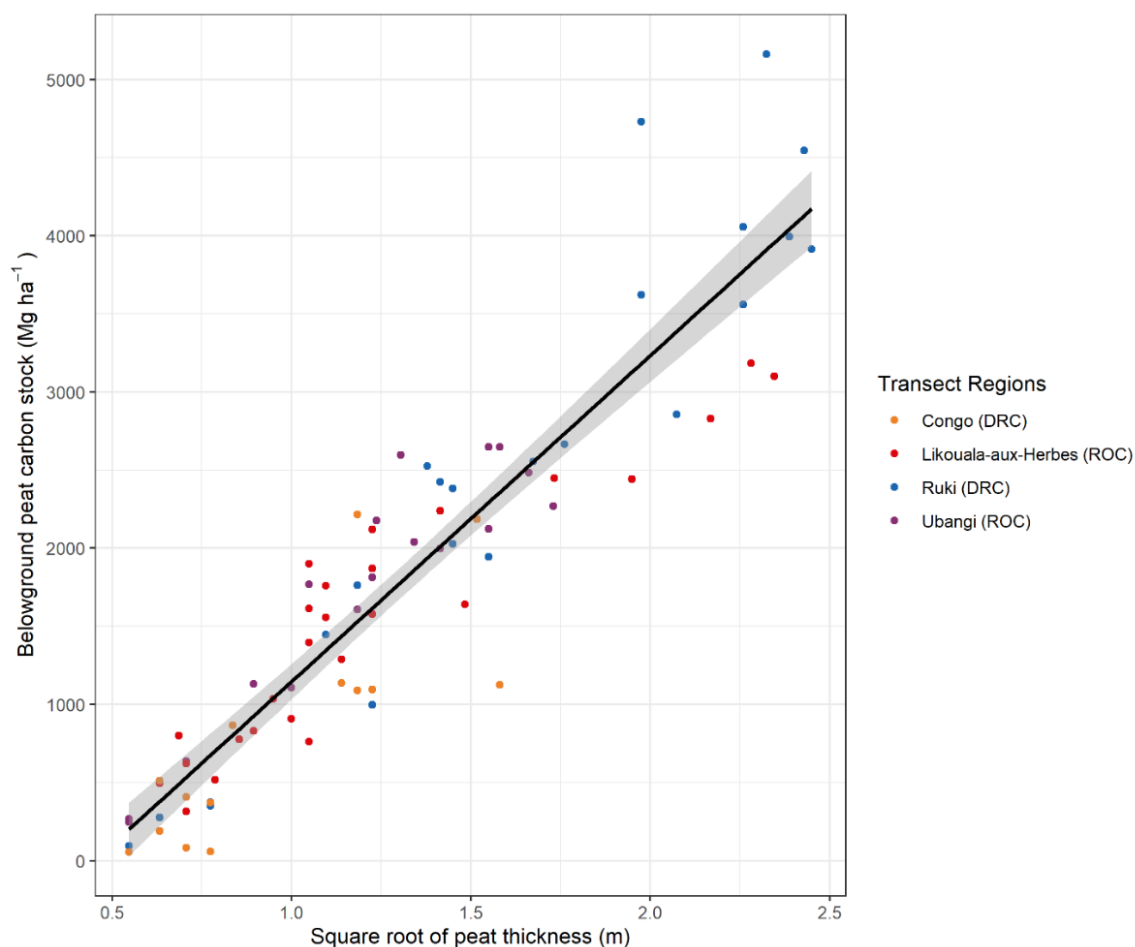
Figure 6.2. Linear regression between peat thickness and carbon density per unit area. *Dots are coloured by transect region. Best-fitting line: carbon density (in Mg ha^{-1}) = - 942.4 + 2088.4 x SqRt(peat thickness, in m); n=80, R^2 = 0.86; p<0.001. Shaded grey shows the 95% confidence interval. 20 bootstrapped regressions, normally distributed around the best-fitting line, were used to include this uncertainty when scaling peat thickness to carbon density estimates.*

Carbon density (mass per unit area) was then mapped across the central Congo Basin peatlands in GEE, by applying this thickness-carbon density regression to the median map of peat thickness developed in section 6.4.3. To include the uncertainty associated with the thickness-carbon density regression in this prediction, I used the bootstrapping of the regression to select 20 combinations of regression parameters that were normally distributed around the best fit (within shaded grey in Figure 6.2). I applied each of these 20 slightly different regression equations to the 100 peat thickness maps that were derived in section 6.4.3 by varying the peat probability threshold that served to generate the map of distance from the peatland margin. This generated a collection of 2,000 maps of carbon density estimates across the peatland area.

A map of median carbon density out of 2,000 estimates was subsequently derived as best-estimate, together with a map of relative (statistical) uncertainty (± half the width of the 95% CI as percentage of the median).

6.4.5 Estimating peat carbon stocks

Total peat carbon stocks were computed in GEE by summing the carbon density (in Mg ha^{-1}) over all 50 m grid squares defined as peat. To assess uncertainty around this estimate, I again combined the 100 peat thickness maps (i.e., uncertainty from area and thickness), with 20 bootstrapped thickness-carbon regressions (i.e., uncertainty from carbon density, including bulk density and carbon concentration). This way, I obtained 2,000 peat carbon stock estimates for the total central Congo Basin peatland complex, which I used to estimate the mean, median and 95% confidence interval.

A sensitivity analysis was performed by bootstrapping either the area, thickness, or carbon density component, whilst keeping the others constant. For area, I bootstrapped by using 100 randomly selected peatland area estimates; for thickness, I bootstrapped by using 100 randomly selected two-thirds subsets of all thickness measurements; for carbon density, I bootstrapped by using the 20 normally distributed regression equations obtained from bootstrapping the thickness-carbon density regression in Figure 6.2.

Regional carbon stock estimates were then obtained by overlaying the median carbon density map with maps of each sub-national administrative region (departments in ROC and provinces in DRC). Additionally, I assessed the amount of carbon that is currently covered by national-level protected areas (national parks and nature/biosphere/community reserves), or threatened by industrial logging, mining and palm oil concessions. National-level protected area maps were obtained from UNEP-WCMC/IUCN (2021). Maps of industrial logging, mining and palm oil concessions were obtained from Global Forest Watch (GFW, 2019a; GFW, 2019b; GFW 2019c; GFW, 2019d; GFW, 2019e), Map for Environment (2014) and Earthsight (2018). Since potential hydrocarbon concessions cover almost the whole peatland area (Dargie et al., 2019; Miles et al., 2017), they overlap with almost 100% of the central Congo peat carbon stocks and were not mapped separately.

6.5 Results

6.5.1 Peat thickness, bulk density and carbon content

Peat thickness was measured at 238 locations in DRC (≥ 0.3 m thickness with ≥ 65% organic matter). Based on the basin-wide calibration of pole-method measurements (see Chapter 5, Figure 5.2), I find a mean (± s.d.) thickness of 2.4 (± 1.6) m and a maximum of 6.4 m (Table 6.2). This is not significantly different from the mean value measured in ROC (2.4 ± 1.5 m; n=213), confirming that rivers-influenced peatlands attain similar peat thickness as rain-fed interfluvial basins reported in ROC by Dargie et al. (2017). The mean peat thickness of 451 measurements across the whole central Congo Basin is 2.4 (± 1.5) m.

Mean (± s.d) bulk density per core as measured across all central Congo Basin peat cores is 0.174 (± 0.063) g cm^{-3} (n=80), and mean carbon concentration per core is 55.7% (± 3.2) (n=80). Carbon concentration is very similar at 56.6% (± 4.5) if only the 22 well-sampled cores are included. Using the measurements of bulk density and carbon concentration to calculate carbon density for each peat sample, I find that the mean (± s.d) carbon density averaged per core is 0.096 (± 0.035) g C cm^{-3} (Table 6.2).

Summing carbon density values of all down-core samples per core, the mean (± s.d) total carbon density across the central Congo Basin peatlands, in terms of mass per unit area, is 1,741 (± 1,186) Mg C ha^{-1} (n=80). The maximum recorded carbon density is 5,162 Mg C ha^{-1} at 10 km along the Mpeka transect (5.40 m thick), a river-influenced peatland area next to the Ruki River tributary. The maximum recorded value in the interfluvial basin peatlands that dominate in ROC is only 3,183 Mg C ha^{-1}, recorded at 20 km along the Centre transect (5.2 m thick), in a wide but shallow domed peatland area that is bounded by the Likouala-aux-Herbes and Ubangi Rivers on either side (Davenport et al., 2020) . Minimum total carbon density in DRC is 56 Mg C ha^{-1} at 3 km along the Boboka transect along the Congo River (0.3 m thick), while the minimum in ROC is higher with 246 Mg C ha^{-1} at 2 km along the Bondzale transect along the Ubangi River (0.3 m thick).

Average peat bulk density per core is found to be significantly lower in the largely river-influenced sites in DRC (mean 0.150 ± 0.065 g cm^{-3}, n=37) than in the largely rain-fed interfluvial basins in ROC (mean 0.194 ± 0.055 g cm^{-3}, n=43; Welch's Two Sample T-test, p<0.01). Similarly, average carbon density per core is significantly lower in the river-influenced sites (mean 0.082

± 0.034 g C cm^{-3}) than in the interfluvial basin peatlands (mean 0.109 ± 0.030 g C cm^{-3}; Mann–Whitney U test, p<0.001). However, no significant difference between these two peatland types is found for either averaged carbon concentration per core (55.0 ± 3.6% and 56.2 ± 2.7%, respectively; Mann–Whitney U test, p=0.19) or total carbon density down-core (Mann–Whitney U test, p=0.80). Nonetheless, the range and variation in total carbon density is considerably larger in the river-influenced peatlands (1,883 ± 1,511 Mg C ha^{-1}) of the DRC, compared with interfluvial basin peatlands (1,619 ± 810 Mg C ha^{-1}) of the ROC (Table 6.2).

Furthermore, no significant differences are found for any of these variables between hardwood-dominated peat swamp forest (n=41) and palm-dominated peat swamp forest types (n=39). Mean peat bulk density in hardwood swamp forests is 0.175 (± 0.071) g cm^{-3}, compared with 0.171 (± 0.055) g cm^{-3} in palm swamp forests (Welch's Two Sample T-test, p=0.75). Mean averaged carbon concentration per peat core is 55.9% (± 2.5) in hardwood swamp forests and 55.5% (± 3.8) in palm swamp forests (Mann–Whitney U test, p=0.89), while mean carbon density averaged per core is 0.097 (± 0.039) g C cm^{-3} in hardwood swamp forests and 0.094 (± 0.030) g C cm^{-3} in palm swamp forests (Welch's Two Sample T-test, p=0.70). Finally, mean total carbon density down core is 1,710 (± 1,266) Mg C ha^{-1} in hardwood swamp forests and 1,696 (± 1,020) Mg C ha^{-1} in palm swamp forests (Mann–Whitney U test, p=0.86).

6.5.2 Map of peat thickness

To model peat thickness, I developed a Random Forest regression, using 463 thickness measurements (> 0 m) across both DRC and ROC. Ten of the 14 chosen variables were found to be significantly correlated with peat thickness (Kendall's τ, p<0.01). These included all three Landsat optical bands, all three ALOS PALSAR radar bands, distance from the peatland margin, distance from the nearest drainage point, precipitation seasonality, and climatic water balance (precipitation minus potential evapotranspiration). Live woody AGB and the three SRTM-derived topographic predictors (DEM, HAND and slope) were not significantly correlated with peat thickness (p=0.12, 0.87, 0.07 and 0.07, respectively) and therefore left out of further variable selection.

Analysis of variable importance in the overall model containing all ten significant variables shows that distance from the peatland margin, precipitation seasonality, climatic water balance and distance from the nearest drainage point are more important predictors than the Landsat 7 ETM+ or ALOS PALSAR radar bands (Figure 6.3).
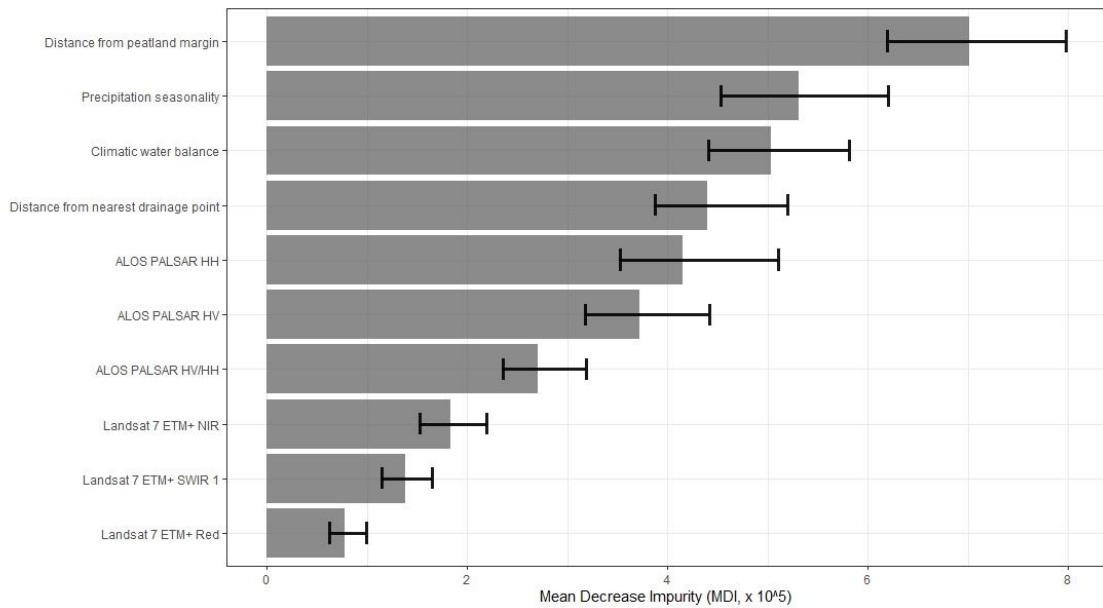
Figure 6.3. Barplot of variable importance for ten significant predictors of peat thickness in a Random Forest model. *Variable importance is assessed as the Mean Decrease Impurity (MDI), the total decrease in the residual sum of squares of the regression after splitting on that variable, averaged over all decision trees in the random forest. MDI was calculated for each variable using 100 random (two-thirds) cross-validations of the overall RF model containing all ten significant predictors. Note that the order of variables does not necessarily reflect the strength of the individual correlations of each predictor (Kendall's τ) with peat thickness.*

Using stepwise backward selection on these ten predictor variables, I derived an optimal model that contained the same four most important predictors only: distance from the peatland margin, distance to the nearest drainage point, climatic water balance (all positively correlated with peat thickness; Kendall's τ = 0.49, 0.15 and 0.13, respectively; p<0.001 for all), and precipitation seasonality (negatively correlated with thickness; Kendall's τ = -0.11, p<0.01). This model had the highest median R^2 (82.2%) and lowest median root mean square error (RMSE; 0.68 m) of all tested variable combinations, obtained from 100 random (two-thirds) cross-validations for each model option.

The spatial distribution of these four predictor variables across the peatland complex is shown in Figure 6.4. These maps indicate clear east-west gradients, either in the two precipitation variables (greater seasonality and greater climatic water balance in the eastern portion of the basin), or in the distance from the peatland margin (large distances associated with interfluvial basins in the west, shorter distances associated with river valleys in the east). On the other hand, distance from the nearest drainage point shows no large-scale gradient but varies instead on more local scale.
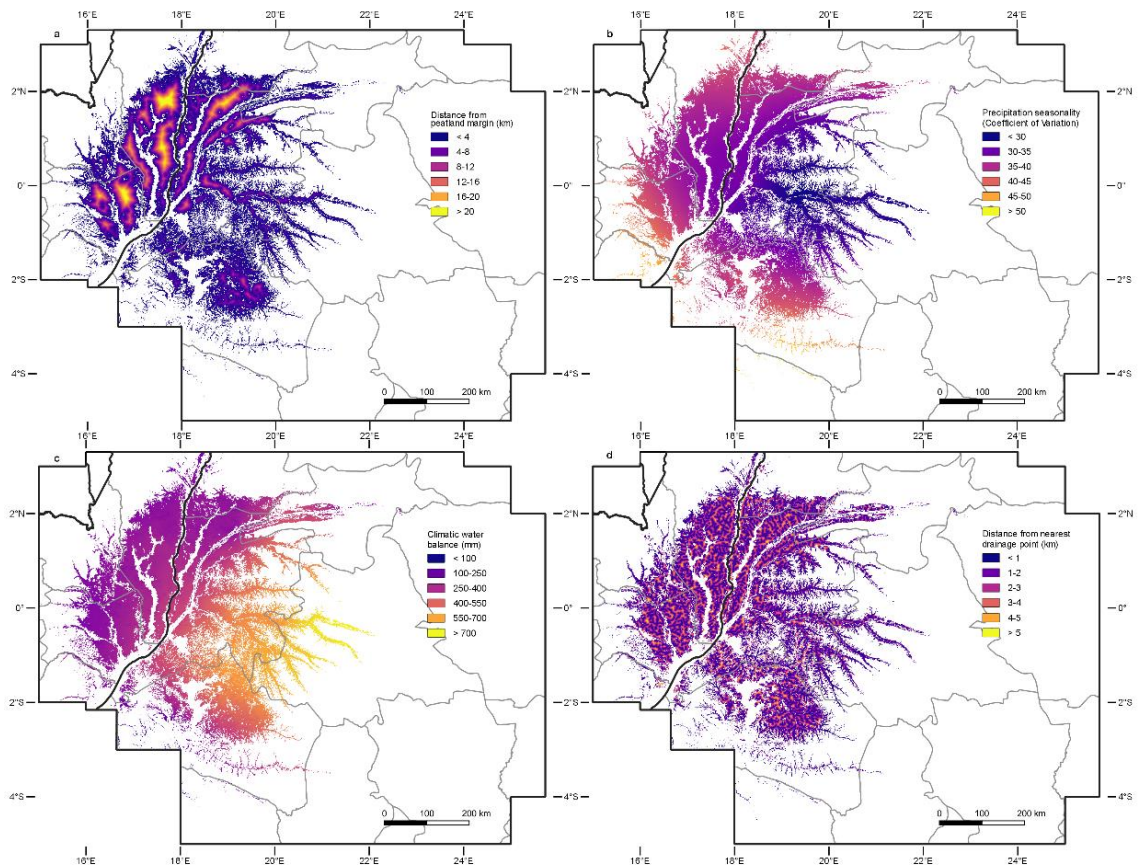
Figure 6.4. Spatial variability of four predictor variables retained in the optimal Random Forest regression model of peat thickness. a, Distance from the peatland margin (km). b, Precipitation seasonality (coefficient of variation). c, Climatic water balance (precipitation minus potential evapotranspiration; mm). d, Distance from the nearest drainage point (km). All maps have been masked to the smoothed median Maximum Likelihood peatland extent (> 50% peat probability). Black lines represent national boundaries; grey lines represent sub-national administrative boundaries.

Using these four predictors in a RF regression model that is trained on all 463 datapoints results in a R^2 of 93.4% and RMSE of 0.42 m. This model had consistently smaller residuals compared to a multiple linear regression model that contains the same four predictor variables, including interaction effects (adj-R^2 = 73.6%, RMSE = 0.80 m; Figure 6.5).

The RF model also outperformed the multiple linear regression model with interaction effects when testing out-of-sample performance, using 100 random two-thirds cross-validations of training data (median R^2 = 82.2%, RMSE = 0.68 m; and median adj-R^2 = 73.6%, RMSE = 0.85 m; for RF model and multiple linear regression, respectively).
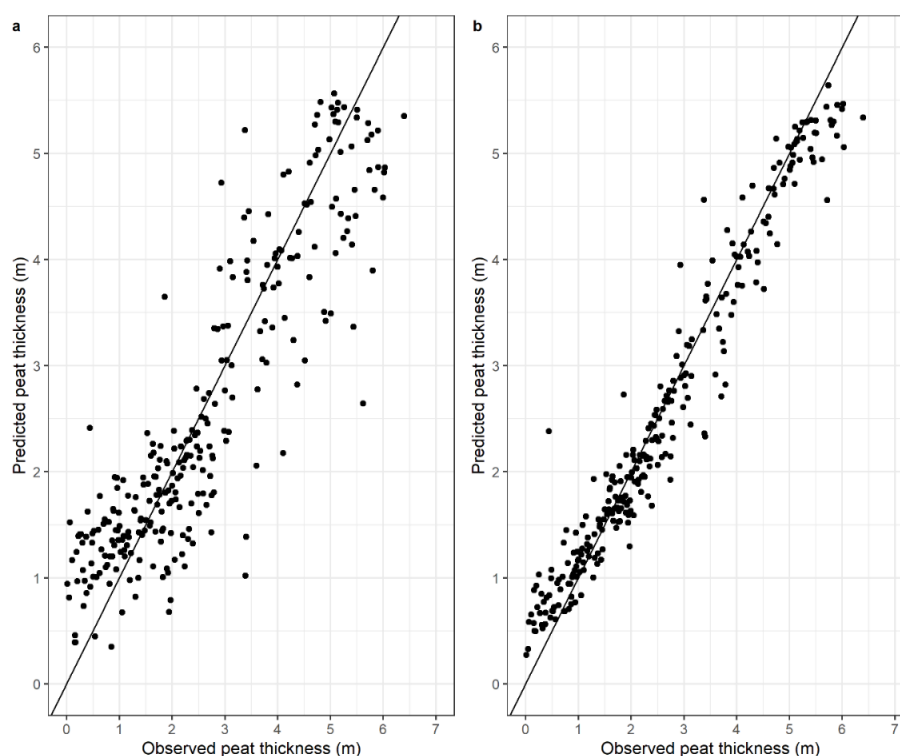
Figure 6.5. Comparison of observed and predicted values in Random Forest and linear peat thickness models. a, *Multiple linear regression model with interaction effects (adj-R^2 = 73.6%, RMSE = 0.80 m).* ***b,*** *Random Forest regression model (R^2 = 93.4%, RMSE = 0.42 m). Both models are trained and validated against all 463 field measurements and include the same four predictor variables: distance from the peatland margin, precipitation seasonality, climatic water balance, and distance from the nearest drainage point. Both panels show 277 aggregated means only to account for duplicates in observed values. The black lines indicate the 1:1 relationship.*

A spatial cross-validation of the RF model shows that spatial autocorrelation at the transect scale (~10 km) contributes to the success of this model, as performance is much reduced in left-out regions at greater distances from which no training data was included (Table 6.1). The average R^2 across the four left-out regions tested separately is only 29.6%, while the average RMSE is 1.42 m. R^2 is lowest in the Congo River region (17.0%), if trained only on datapoints from the other three regions, suggesting greater uncertainty in the model when extrapolating into this area. On the other hand, R^2 is highest in the Likouala-aux-Herbes River region (63.2%), suggesting there is less uncertainty when extrapolating into this region from the other three regions. Comparing the interfluvial basin with river-influenced peatlands, we see that the proportion of variation in peat thickness explained by training data from the other region is particularly low in the river-influenced peatlands (6.5%), compared to the interfluvial peatlands (38.5%). This is likely because there is greater variation in peat thickness over shorter distances in the river-influenced peatlands, meaning that the primary predictor variable in the RF model (distance from the peatland margin) is not as effective there if no river-influenced training data is included at all.

	Random cross-validation (overall)	Spatial cross-validation (regional)					
		Likouala-aux-Herbes, ROC (n=141)	Ubangi, ROC (n=71)	Congo, DRC (n=80)	Ruki, DRC (n=163)	Interfluvial basin peatlands, ROC (n=212)	River-influenced peatlands, DRC (n=243)
RMSE (m)	0.68 (0.59-0.79)	1.68 (1.54-1.84)	1.21 (1.08-1.36)	0.88 (78.8-102.5)	1.91 (1.79-2.03)	1.54 (1.30-1.69)	1.65 (1.59-1.74)
R^2 (%)	82.2 (74.6-86.4)	63.2 (37.7-78.1)	19.6 (16.9-22.9)	17.0 (12.1-20.8)	18.7 (2.8-41.0)	38.5 (14.0-53.0)	6.5 (0.5-13.6)

Table 6.1. Random and spatial cross-validation of the Random Forest regression model of peat thickness. Random CV results are obtained from 100 random Monte Carlo two-thirds data splits of all depth measurements (n=463), showing median values and 95% confidence interval (in parentheses). Spatial CV results are obtained for each region, by training on a random two-thrids of the remaining datapoints and validating against the selected left-out region only. The interfluvial basin peatlands (n=212) comprise the Likouala (n=141) and Ubangi (n=71) regions. The river-influenced peatlands (n=243) comprise the Congo (n=80) and Ruki (n=163) regions.

Nonetheless, by including datapoints from all four regions in the final model, the model results are consistent with the field data in areas from which peat thickness measurements are available. The model predicts thick peat deposits in the centres of the largest interfluvial basins (areas far from peatland margins), and in smaller, river-influenced valley-floor peatlands along the Ruki/Busira Rivers (areas with greater climatic water balance and lower precipitation seasonality) (Figure 6.6a). This is in line with field-measurements, as the two deepest peat thickness measurements are from the interfluvial Centre transect in ROC (5.9 m at 15.75 km), and the river-influenced Bondamba transect on the Busira River in DRC (6.4 m at 6.5 km; using the basin-wide pole-method calibration). Overall, mean (± s.d.) modelled peat thickness (1.7 ± 0.9 m) is lower than the field measurements (2.4 ± 1.5 m; Table 6.2), as expected given the linear transects that were used, which oversample deeper peat at the centre relative to the periphery in approximately ovoid peatlands. The mean modelled peat thickness in ROC (1.7 ± 0.9) is very similar to the mean modelled peat thickness in DRC (1.8 ± 0.8), suggesting no overall difference between the geomorphologically-distinct peatland areas in both countries. Areas of high uncertainty in peat thickness occur where distance from the margin is uncertain, such as in the south of the peatland complex near Lake Mai-Ndombe, as well as local hotspots in the north of the basin (Figure 6.6b).
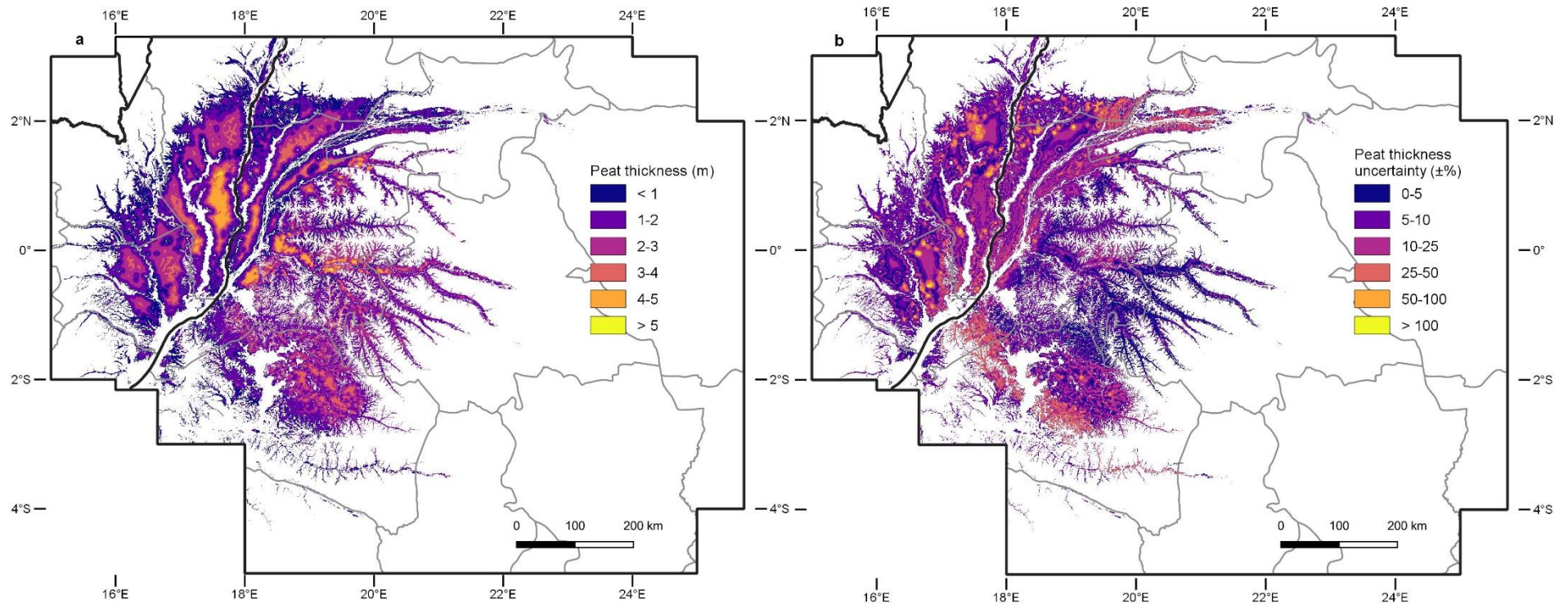
Figure 6.6. Maps of peat thickness and uncertainty across the central Congo Basin. a, *Median prediction of peat thickness (m) from 100 Random Forest regression models with four predictors: distance from the peatland margin, precipitation seasonality, climatic water balance, and distance from the nearest drainage point. b*, *Relative uncertainty (%) of the peat thickness estimate, expressed as ± half the width of the 95% confidence interval as percentage of the median. Black lines represent national boundaries; grey lines represent sub-national administrative boundaries.*

6.5.3 Map of peat carbon density

I developed a map of peat carbon density by applying a linear peat thickness-carbon density regression (Figure 6.4) to the map of peat thickness (Figure 6.6a). Modelled belowground peat carbon density for the central Congo Basin is 1,712 ± 634 Mg C ha^{-1}, similar to the field-measured mean of 1,741 ± 1,186 Mg C ha^{-1} (mean ± s.d., n=80; Table 6.2). Spatial patterns of peat carbon density (Figure 6.7a) and uncertainty (Figure 6.7b) follow similar patterns as peat thickness (Figure 6.6a and 6.6b). This results in slightly more carbon-dense peatlands in the DRC (1,740 ± 604 Mg C ha^{-1}) than in ROC (1,653 ± 687 Mg C ha^{-1}).

The maximum modelled carbon density across the central Congo Basin is 3,970 Mg C ha^{-1}, in the river-influenced peatlands of the DRC, compared with a slightly lower maximum of 3,852 Mg C ha^{-1} in the interfluvial basin peatlands of the ROC. This DRC value is considerably lower than the maximum field-measured carbon density in the DRC of 5,162 Mg C ha^{-1}, as expected given the lower maximum modelled peat thickness values. On the other hand, the maximum modelled ROC value is slightly larger than the maximum field-measured carbon density of 3,138 Mg C ha^{-1} in the ROC (Table 6.2), possibly because higher carbon densities from DRC dominate the upper range of peat thickness values in the thickness-carbon density regression (Figure 6.2).
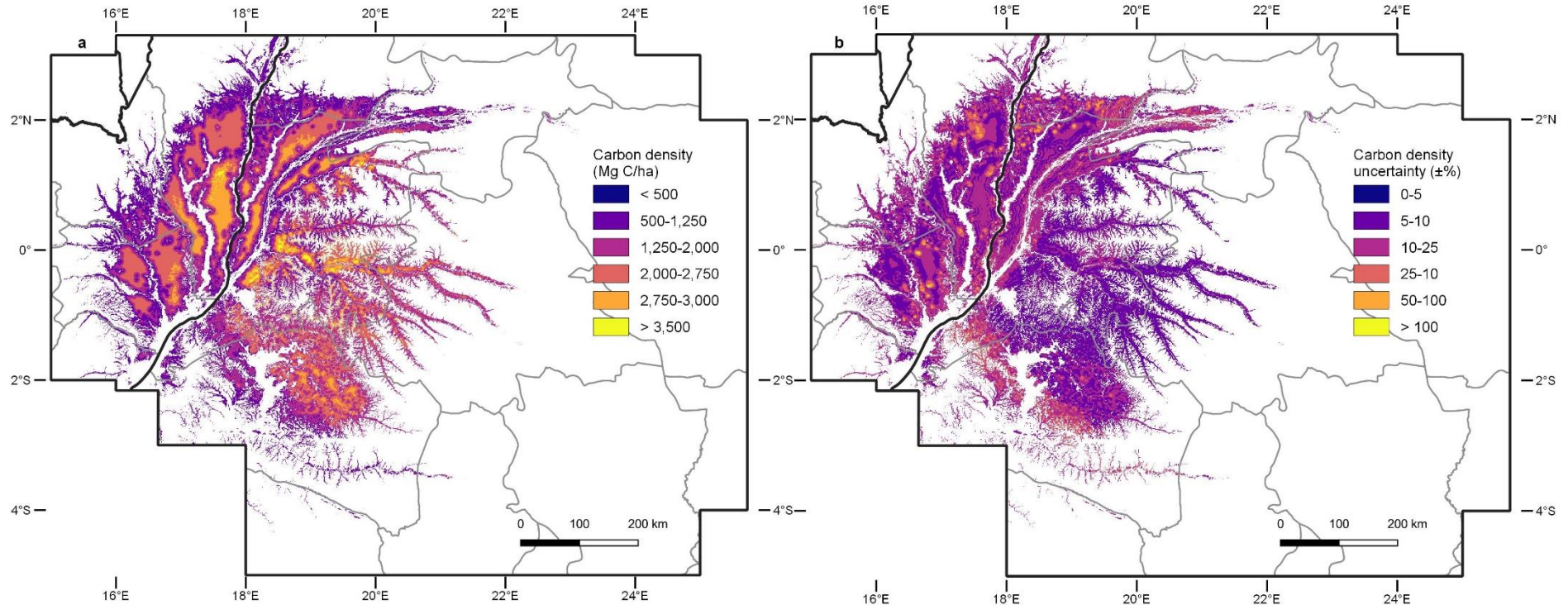
Figure 6.7. Maps of peat carbon density and uncertainty across the central Congo Basin. *a, Median prediction of belowground peat carbon density (Mg C ha^{-1}), obtained from applying 20 normally distributed thickness-carbon density regressions (Figure 6.4) to 100 peat thickness estimates (Figure 6.6a), generating 2,000 carbon density estimates. **b**, Relative uncertainty (%) of the carbon density estimate, expressed as ± half the width of the 95% confidence interval as percentage of the median. Black lines represent national boundaries; grey lines represent sub-national administrative boundaries.*

	Field measurements *														Spatial model †					
	Peat thickness (m) #			Peat bulk density (g cm⁻³) §				Peat carbon concentration (%) ‡				Total peat carbon density (Mg C ha⁻¹) ‡			Peat thickness (m) ¶			Total peat carbon density (Mg C ha⁻¹) $		
	Mean ± s.d.	Median	Max	Mean ± s.d.	Median	Min	Max	Mean ± s.d.	Median	Min	Max	Mean ± s.d.	Median	Max	Mean ± s.d.	Median	Max	Mean ± s.d.	Median	Max
Interfluvial basin peatlands (ROC)	2.4 (1.5)	2.1	5.9	0.19 (0.06)	0.19	0.10	0.31	56.2 (2.7)	56.5	49.6	61.8	1,619 (810)	1,640	3,183	1.7 (0.9)	1.3	5.4	1,653 (687)	1,402	3,852
River-influenced peatlands (DRC)	2.4 (1.6)	2.0	6.4	0.15 (0.07)	0.15	0.02	0.33	55.0 (3.6)	55.8	42.0	59.2	1,883 (1,511)	1,762	5,162	1.8 (0.8)	1.6	5.6	1,740 (604)	1,697	3,970
Central Congo Basin peatlands (ROC + DRC)	2.4 (1.5)	2.0	6.4	0.17 (0.06)	0.17	0.02	0.33	55.7 (3.2)	56.3	42.0	61.8	1,741 (1,186)	1,700	5,162	1.7 (0.9)	1.6	5.6	1,712 (634)	1,661	3,970

Table 6.2. Field-measured and spatially modelled estimates of peat thickness, bulk density, carbon concentration, and carbon density.

* Field measurement statistics include either the Likouala-aux-Herbes and Ubangi River groups of transects only ('Interfluvial basin peatlands'), or the Congo and Ruki River groups of transects only ('River-influenced peatlands'), or all groups ('Central Congo Basin peatlands').

† Spatial model statistics include all 50 m resolution pixels mapped in either Republic of the Congo only (ROC), Democratic Republic of the Congo only (DRC), or both countries (ROC + DRC).

 # In situ measurements (LOI and corrected pole-methods) from 213, 238 and 451 locations in ROC (Dargie et al., 2017), DRC (this study) and combined, respectively. Peat is ≥ 0.3 m thickness and ≥ 65% organic matter.

§ n=43, 37, and 80 well-sampled cores in ROC (Dargie et al., 2017), DRC (this study) and combined, respectively, based on 0.1-m thick samples.

‡ n=43, 37, and 80 well-sampled and interpolated cores in ROC (Dargie et al., 2017), DRC (this study) and combined, respectively, based on 0.1-m thick samples.

¶ Median estimate from 100 thickness estimates per 50 m resolution pixel across the median extent map, with thickness estimated from 100 RF regression models trained with four predictor variables, each with a randomly selected Maximum Likelihood peat probability threshold to derive distance from the peatland margin.

$ Median estimate from 2,000 carbon density estimates per 50 m resolution pixel across the median peat area map, with carbon density estimates derived from 20 normally distributed thickness-carbon regressions (Figure 6.4) applied to 100 peat thickness estimates.

6.5.4 Basin-wide peat carbon stock estimates

Median estimated total peat carbon stock in the central Congo Basin is 29.0 Pg (95% CI, 26.3-32.2; Figure 6.8a), based on bootstrapping the area estimate and peat thickness-carbon density regression. About two-thirds of this peat carbon is in DRC (19.6 Pg C; 95% CI, 17.9-21.9), and one-third in ROC (9.3 Pg C; 95% CI, 8.4-10.2). The high peat carbon stocks are found across several administrative regions in both countries (Table 6.3), with the largest stocks in DRC's Équateur province, storing 10.7 Pg C (95% CI, 9.9 - 11.7), more than is found in the entire ROC. This is followed by the Likouala department in ROC (5.4 Pg C; 95% CI, 4.8 - 5.8) and the Mai-Ndombe province in DRC (5.2 Pg C; 95% CI, 4.8 - 5.7).

Sensitivity analysis shows that statistical (aleatoric) uncertainty in total peat carbon stock is now mostly driven by uncertainty in peatland area, rather than peat thickness or carbon density (Figure 6.8b). Bootstrapping peatland area by randomly selecting a peatland probability threshold causes a range in peat carbon stocks of approximately 6 Pg C, in comparison with approximately 3 Pg C when bootstrapping the peat thickness-carbon density model, or approximately 2.5 Pg C when bootstrapping the peat thickness model. Thus, the uncertainty surrounding peatland area is the cause of the greatest uncertainty in my estimate of the total peat carbon stocks in the central Congo Basin.
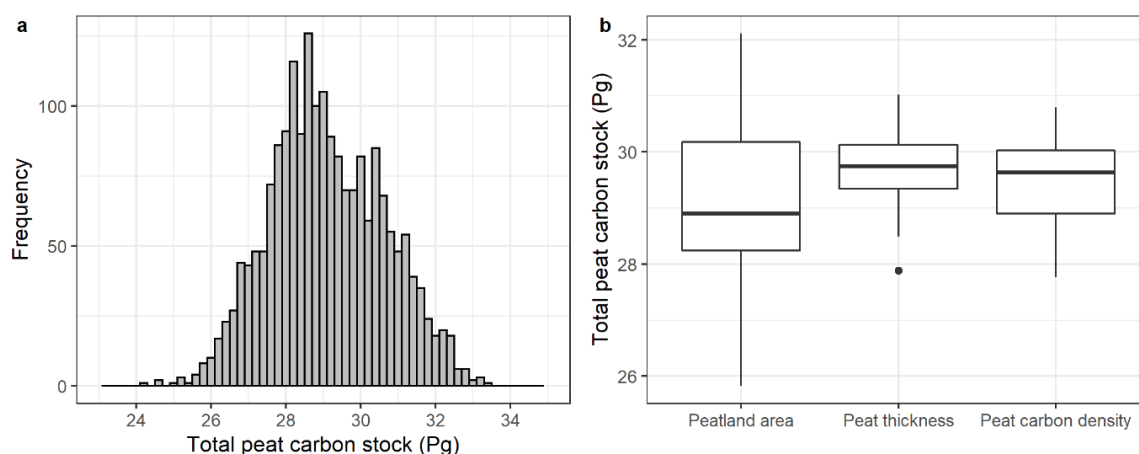
Figure 6.8. Distribution and sensitivity of peat carbon stock estimates in the central Congo Basin peatland complex. a, *Distribution of 2,000 peat carbon stock estimates, obtained by combining 100 random peat probability thresholds in the peatland extent model and computing the associated RF peat thickness map, with 20 normally-distributed equations from the bootstrapped peat thickness-carbon density regression. Median, 29.0 Pg C; mean, 29.1 Pg C; 95% CI, 26.3–32.2 Pg C.* ***b,*** *Sensitivity analysis by in turn bootstrapping peat area estimates (n=100), peat thickness measurements (n=100), or carbon density regressions (n=20), whilst keeping the other components constant. Central horizontal lines show the medians, box limits show the upper and lower quartiles, and the vertical lines show maximum and minimum values. Dots represent potential outlying values.*

Country	Region	Peatland area (km²)	Peat thickness (m)	Peat carbon density (Mg C ha⁻¹)	Peat carbon stock (Pg C)
Republic of the Congo (ROC)	Likouala	28,636	1.9 ± 1.0	1,815 ± 740	5.4 (4.8 - 5.8)
	Cuvette	17,757	1.6 ± 0.8	1,626 ± 624	2.9 (2.7 - 3.2)
	Sangha	7,465	1.1 ± 0.4	1,218 ± 325	0.9 (0.8 - 1.0)
	Plateaux	1,183	0.9 ± 0.1	1,059 ± 162	0.1 (0.1 - 0.1)
	Total ROC	55,072	1.7 ± 0.9	1,653 ± 687	9.3 (8.4 - 10.2)
Democratic Republic of the Congo (DRC)	Équateur	58,276	1.9 ± 0.9	1,822 ± 658	10.7 (9.9 - 11.7)
	Mai-Ndombe	29,825	1.8 ± 0.7	1,752 ± 548	5.2 (4.8 - 5.7)
	Tshuapa	11,628	1.9 ± 0.5	1,917 ± 343	2.1 (1.8 - 2.6)
	Sud-Ubangi	7,557	1.1 ± 0.4	1,243 ± 370	1.0 (0.8 - 1.2)
	Mongala	5,329	1.2 ± 0.4	1,259 ± 360	0.6 (0.5 - 0.8)
	Total DRC	113,201	1.8 ± 0.8	1,740 ± 604	19.6 (17.9 - 21.9)
ROC and DRC combined	**Total central Congo Basin peatlands**	167,648 (159,378 – 175,079)	1.7 ± 0.9	1,712 ± 634	29.0 (26.3 - 32.2)

Table 6.3. Estimated peatland area, peat thickness, carbon density and carbon stocks per administrative region. All values are regional means (± s.d.) of the median peat thickness and carbon density maps; or median estimates (with 95% confidence interval in parentheses) for total peatland area and peat carbon stock. For regional area estimates without confidence interval, the median peatland map (> 50% probability) was used. Sub-national administrative regions are provinces (DRC) or departments (ROC). Marginal peat predictions in other administrative regions (Kasaï, Tshopo, Kwilu, Nord-Ubangi in DRC; Cuvette-Ouest in ROC) are included in total country estimates, but not listed separately.

By overlaying the peat carbon density map with maps of protected areas, I estimate that only 2.4 Pg C stored in the peat, or just 8% of the total peat carbon stocks, currently lies within formal national-level protected areas (Figure 6.9 and Table 6.4). These are primarily the Tumba-Lediima and the Ngiri Nature Reserves in DRC and the Lake Télé Community Reserve in ROC. Meanwhile, logging, mining, or palm oil concessions together overlie 7.4 Pg C in peat, or 26% of total stocks. This high figure is mainly due to large logging concessions, most of which have not begun logging operations, particularly in DRC.
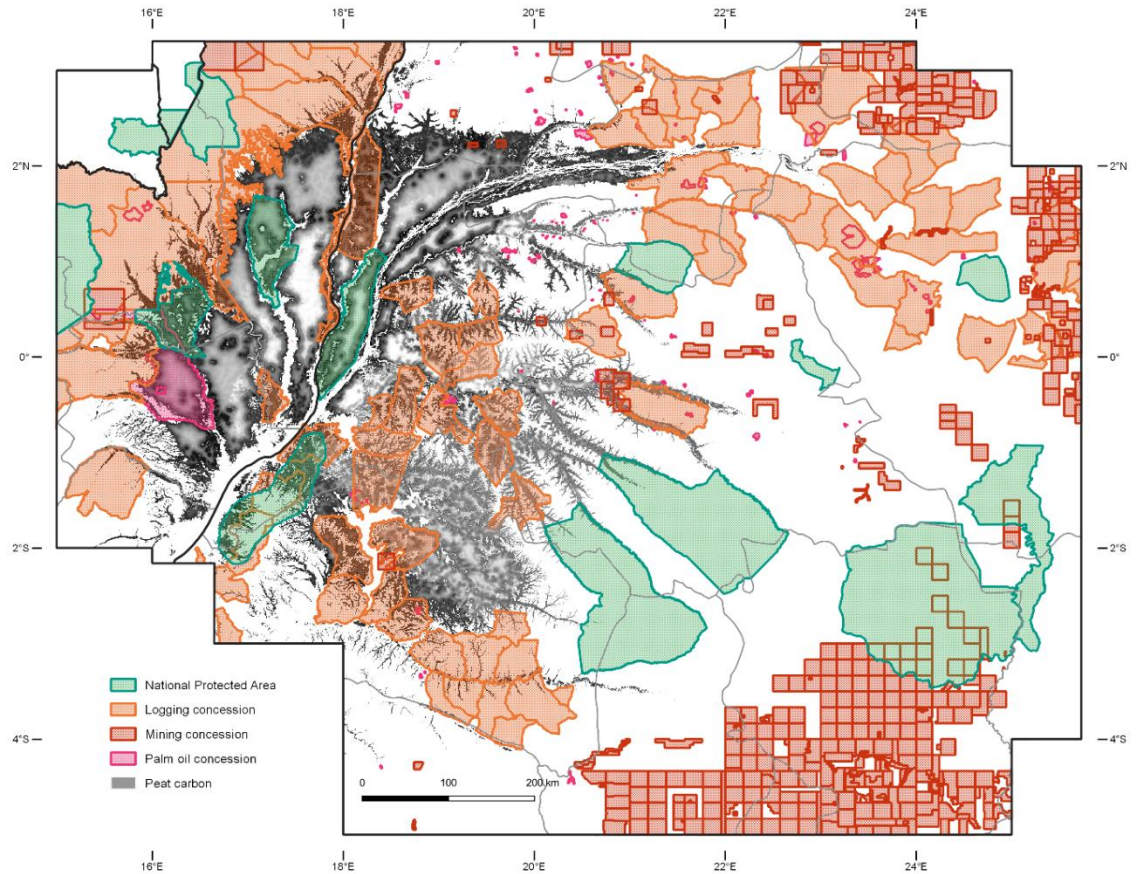
Figure 6.9. Map of national protected areas and industrial concessions across the central Congo Basin peatland complex. *The base map shows belowground peat carbon density (shaded grey; Figure 6.7), overlaid with protected areas at national-level (national parks and nature/biosphere/community reserves; UNEP-WCMC/IUCN, 2021)), or industrial logging, mining, and palm oil concessions (GFW 2019a, 2019b, 2019c, 2019d, 2019e; Map for Environment, 2014; Earthsight, 2018). Black lines represent national boundaries; grey lines represent sub-national administrative boundaries.*

Country	Concessions / Protected areas	Peatland area (km²)	Peat thickness (m)	Peat carbon density (Mg C ha⁻¹)	Peat carbon stock (Pg C)
Republic of the Congo (ROC)	Industrial logging / mining / palm oil concessions	13,539 (25%)	1.2 ± 0.6	1,299 ± 451	2.0 (22%)
	National-level protected areas	6,402 (12%)	1.4 ± 0.6	1,463 ± 478	1.0 (11%)
Democratic Republic of the Congo (DRC)	Industrial logging / mining / palm oil concessions	29,712 (26%)	1.6 ± 0.7	1,671 ± 567	5.4 (28%)
	National-level protected areas	8,105 (7%)	1.5 ± 0.8	1,552 ± 592	1.4 (7%)
ROC and DRC combined	Industrial logging / mining / palm oil concessions	43,250 (26%)	1.5 ± 0.7	1,551 ± 560	7.4 (26%)
	National-level protected areas	14,511 (9%)	1.5 ± 0.7	1,513 ± 547	2.4 (8%)

Table 6.4. Estimated peatland area, peat thickness, carbon density and carbon stocks in industrial concessions and protected areas. Estimates are calculated for all protected areas at national-level (national parks and nature/biosphere/community reserves; UNEP-WCMC/IUCN, 2021), or for industrial logging, mining, and palm oil concessions combined (GFW 2019a, 2019b, 2019c, 2019d, 2019e; Map for Environment, 2014; Earthsight, 2018). All values are means (± s.d.) of the median peat thickness and carbon density maps, or median estimates for total peatland area and peat carbon stock. Percentages show the proportion of total peatland area or peat carbon stock in ROC, DRC and combined that is found in either protected areas or industrial logging/mining/palm oil concessions (Figure 6.9).

6.6 Discussion

In this chapter I used newly collected ground-truth data from the Democratic Republic of the Congo to estimate the peat carbon stocks of the central Congo Basin peatlands. Firstly, I measured bulk density and carbon concentrations of 80 peat cores from both DRC and ROC. These measurements were used to develop a peat thickness-carbon density regression that is representative across the region. Based on 463 peat thickness measurements across the basin, I further developed a Random Forest regression to derive a first map of peat thickness across the peatland complex. By applying the thickness-carbon density regression to this map of peat thickness, I then generated a first map of peat carbon density for the central Congo Basin, allowing me to estimate total peat carbon stocks across the peatland complex.

I found that mean bulk density across the central Congo Basin is 0.174 ($\pm$ 0.063) g cm^{-3}, and mean carbon concentration is 55.7% ($\pm$ 3.2). Based on this, mean carbon density averaged per core is 0.096 ($\pm$ 0.035) g C cm^{-3}. These values are slightly lower than what was initially reported by Dargie et al. (2017) for the central Congo Basin based on data from interfluvial basins in just ROC alone. This is because average peat bulk density and carbon concentration per core are significantly lower in river-influenced peatlands in DRC, thereby reducing the overall mean across the whole region.

Nonetheless, my more representative values of peat carbon density in the central Congo Basin are still considerably higher than what has been reported for other tropical peatlands in either Indonesia or in the Peruvian Amazon. For example, the average peat bulk density in Indonesia is regarded as 0.1 g cm^{-3}, together with an average carbon content of 58% (Jaenicke et al., 2008), suggesting an average carbon density of 0.058 g C cm^{-3}. For Central Kalimantan on Borneo specifically, carbon density has been reported to be 0.061 g C cm^{-3}, while this is 0.044 g C cm^{-3} in coastal peatlands (Dommain et al., 2011). In the Peruvian Amazon, forested peatlands have been reported to have a bulk density of either 0.084 g cm^{-3} in pole (hardwood) forest or 0.099 g cm^{-3} in palm swamp, while carbon concentrations are either 50.5 or 44.0%, respectively (Draper et al., 2014). According to Dargie et al. (2017), this means a mean carbon density of 0.033 g C cm^{-3} in the Peruvian Amazon. Although the mean C content that I report here for the central Congo Basin is lower than that of Indonesia, bulk density and carbon density are typically higher than in other tropical peatland regions, sometimes by more than twice as much. This could reflect greater decomposition in the central Congo Basin, potentially as a result of the relatively

drier climate in Central Africa (Malhi & Wright, 2004), which would result in increased carbon storage per unit volume of peat.

The bulk density and C concentration values reported in this study are also higher than the values typically found in northern peatlands, which have an average bulk density of 0.118 ± 0.069 g cm^{-3} and C content of 46.8 ± 6.1% (Loisel et al., 2014). This results in almost twice as high carbon density values in the Congolese peatlands, compared with northern peatlands (on average 0.05-0.06 g C cm^{-3}; Loisel et al., 2014). This suggests that the central Congo Basin peatland complex is likely one of the most carbon dense peatlands on Earth, per unit volume of peat.

However, it must be noted that peat carbon concentrations as measured via isotope-ratio mass spectrometry at the University of Leicester were found to be consistently lower, by on average 7%, than peat C concentrations that were measured via an elemental analyser at the University of Leeds. This could mean that the carbon concentration of peatlands in the Congo River floodplain region, analysed via isotope-ratio mass spectrometry, is generally lower than that of the peatlands along either the Congo River's tributaries or in interfluvial basins. However, an alternative hypothesis is that this difference reflects a measurement bias from using two different analytical techniques that produce slightly different values. More comparative analysis is required across regions, and using both techniques, to establish whether this difference really reflects a natural pattern.

Furthermore, in this chapter, I developed a Random Forest regression model, which I used to map peat thickness. I predict thick peat deposits in both the interfluvial basin peatlands in ROC and river-influenced peatlands in DRC, in line with field measurements. Distance from the peatland margin was found to be the most important predictor of peat thickness. This is particularly the case in the interfluvial basins in ROC, where a clear increase in thickness is observed along the 20 km-long Centre transect. On the other hand, the river valley's thick deposits in DRC are most likely driven by greater climatic water balance and lower precipitation seasonality in the eastern part of the Cuvette Centrale region, as could be observed in Figure 6.4. These rainfall variables likely offset the shorter distances from peatland margins, which would have been expected to result in shallower peat deposits under similar rainfall conditions. However, potentially greater water input from upland runoff could also play a role in creating enough waterlogged conditions to allow significant peat formation to occur. The fact that

climatic water balance and precipitation seasonality were found to be the second and third most important variables in the RF model, out of ten significant predictors, reflects the relative importance of rainfall inputs in peat accumulation in central Congo. This appears to differ from smaller-scale assessments in temperate (Young et al., 2018) or other tropical peatlands, such as in Southeast Asia (Rudiyanto et al., 2016, 2018). In those regions, surface topography (elevation and slope) are primary predictors of peat thickness. However, this is potentially merely an artefact of differences in the spatial scales of the studies, as climate only varies over large scales. Alternatively, the relatively low rainfall in the central Congo Basin (~1700 mm yr^{-1}), compared to other tropical peatland regions (e.g., ~2,500-3,000 mm yr^{-1} in Northwest Amazonia and Southeast Asia; Malhi & Wright, 2004), may mean that peat thickness is more strongly related to climate in central Congo. On average, a drier climate implies greater exposure to (seasonal) drought conditions that may cross thresholds that negatively impact peat accumulation rates. This hypothesis appears to be in line with the relatively higher carbon density values that were observed in the central Congo Basin, suggesting greater decomposition from aerobic decay.

The peat thickness results from this chapter contrast strongly with an "expert system approach" that assigned peat thickness values based on hydrological terrain relief alone, essentially assuming that the height above the nearest drainage point (SRTM-derived HAND-index) represents the peat thickness of an interfluvial basin peat dome with respect to the elevation of the rivers that it is bounded by. Based on this, Gumbricht et al. (2017) estimated a mean thickness of 6.5 ± 3.5 m for the central Congo Basin peatlands, considerably larger than the field-trained modelled estimate of 1.7 ± 0.9 m that was found in this chapter. This shows the importance of collecting field data and verifying model predictions using field data.

However, even when using a unique dataset of peat thickness measurements across the Cuvette Centrale, spatial cross-validation of the RF model reveals considerable uncertainty in predicting peat thickness outside the sampled regions. This is especially the case when extrapolating into areas with a different hydro-geomorphology, such as the river-influenced peatlands based on data from interfluvial basin peatlands. This shows both the need for field data from a variety of hydro-geomorphological settings, and the underlying importance of better understanding the diversity of peatland types in the basin.

Because of this, even though the final RF model has low internal statistical uncertainty (median R^2 = 82.2%, RMSE = 0.68 m), true epistemic uncertainty is larger in areas that fall outside the

applicability of the dataset. However, given the lack of field data in these regions, this systemic uncertainty is hard to quantify. Here, I have aimed to incorporate some of this uncertainty from the peatland distribution model into the peat thickness model, as mapped in Figure 6.6b. However, this does not truly capture the uncertainty associated with extrapolating into unsampled areas with possibly distinct hydro-geomorphologies that affect peat thickness. The major limitation in the currently available field dataset, identified in this study, is the lack of sampling from the Mai Ndombe region in DRC, which potentially has a hydro-geomorphology that is very different from either the interfluvial basin or river-influenced peatlands identified so far. Thus, more fieldwork remains required in order to address this.

Nonetheless, because Random Forest by nature produces a consensus estimate based on an ensemble of bootstrapped models, peat thickness estimates in these unsampled areas tend to be in the range of 1-3 m, rather than the more extreme values mapped in areas from which training data is included. These medium modelled values are broadly consistent with the mean field estimates of 2.4 ± 1.5 m. Furthermore, given that mean modelled peat thickness is lower than the field-measured mean thickness, the model does not appear to overestimate peat thickness compared to the field-measured dataset. Thus, although unusually shallow or thick peat deposits are still possible in unsampled areas due to local conditions that are not captured by the model, such as in the Mai Ndombe region, it is unlikely that the overall modelled mean of 1.7 ± 0.9 m will alter considerably as more data is added.

Based on these values of peat thickness, I predict a mean carbon density per unit area of 1,712 ± 634 Mg C ha^{-1} in the central Congo Basin, in line with the field-measured mean of 1,741 ± 1,186 Mg C ha^{-1}. This spatially modelled carbon density value is approximately nine times the mean carbon stored in aboveground live tree biomass of African tropical moist forests (~198 Mg C ha^{-1}; Lewis et al., 2013). Compared with recently mapped peatlands in the lowland Peruvian Amazon (mean 867 Mg C ha^{-1}; Hastie et al., 2022), the central Congo peatlands store almost twice as much carbon per hectare. However, Southeast Asian peatlands are still the most carbon dense tropical peatlands per unit area, storing on average 2,775 Mg C ha^{-1}, mostly because of the presence of much thicker peat domes (Page et al., 2011).

Based on my new map of peat carbon density, I estimate the total peat carbon stock in the central Congo Basin to be 29.0 Pg (95% CI, 26.3-32.2). This is similar to the median 30.6 Pg C reported by Dargie et al. (2017), even though total peatland area increased by 15%, because the

mean modelled peat thickness in this study is lower than the mean *in situ* peat thickness that was measured by Dargie et al. (2017). However, the lower 95% confidence interval of Dargie et al.'s (2017) prediction was 6.3 Pg, which has increased to 26.3 Pg in this study. This considerable constraint on the carbon stock estimate is possible because the larger field-based dataset allowed a spatial modelling approach, so that I could sum carbon density evenly across all predicted peat pixels, rather than relying on the less representative sampling distribution of field samples only. Therefore, the possibility of low values of carbon storage in the central Congo peatlands can now confidently be discarded. This shows that the central Congo Basin peatlands are a globally important carbon stock, harbouring approximately a quarter to one-third (27.6%) of all the carbon stored in the world's tropical peatlands (best pan-tropical estimate: 105 Pg C, range 87–136 Pg; Page et al., 2022).

About two-thirds of this peat carbon is stored in DRC (19.6 Pg C; 95% CI, 17.9-21.9), and one-third in ROC (9.3 Pg C; 95% CI, 8.4-10.2), which is equivalent to approximately 82% and 238% of each country's aboveground forest carbon stock, respectively (Verhegghen et al., 2012). The 9.3 Pg C estimated for the ROC is larger than the peat carbon stock of 9.1 Pg C that is reported for Malaysia (Page et al., 2011). As such, in addition to peatland area (see Chapter 5), these new C stock estimates confirm the Democratic Republic of the Congo and the Republic of the Congo as the second and third most important countries in the tropics for peat carbon stocks after Indonesia (57 Pg C), respectively (Page et al., 2011).

Because the central Congo peatlands are relatively undisturbed (Miles et al., 2017; Vancutsem et al., 2021), the new maps of peatland extent, thickness and carbon density presented here form a baseline description for the decade 2000-2010, given the acquisition dates of the remotely-sensed data used. Today, the peatlands of the central Congo Basin are threatened by hydrocarbon exploration, logging, palm oil plantations, hydroelectric dams and climate change (Dargie et al., 2019; Miles et al., 2017). While the peatlands are largely within a UN Ramsar Convention transboundary wetland designation, hydrocarbon concessions cover almost the entire peatland complex (Dargie et al., 2019; Miles et al., 2017), thereby potentially threatening the whole ecosystem. In addition, I estimate that approximately a quarter of the total carbon stock (7.4 Pg C, or 26%) is threatened by industrial logging, mining or palm oil concessions. This contrasts with only 8% of the peat carbon (2.4 Pg C) that is found within national-level protected areas (Figure 6.9), suggesting the peat is vulnerable to future land use changes.

6.7 Conclusion

In this chapter, I produced spatial models of peat thickness and peat carbon density across the central Congo Basin. Using 463 field measurements of peat thickness from across DRC and ROC, I trained a Random Forest regression model of peat thickness, which I used to develop the first map of peat thickness for the Cuvette Centrale peatlands. This model was found to provide the best results when trained using only four predictors out of 14 selected variables: distance from the peatland margin, precipitation seasonality, climatic water balance and distance to the nearest drainage point. Although the model performed well in areas that were included in the sampling (median R^2 = 82.2%, RMSE = 0.68 m), spatial cross-validation showed that considerably systemic uncertainty remains in areas from which no data is available. Thus, more field measurements of peat thickness are required, particularly from the Mai Ndombe region in DRC. The mean modelled peat thickness of 1.7 ± 0.9 m across the basin is slightly lower than the mean field estimate of 2.4 ± 1.5 m, as expected given the transect sampling design is biased towards the deeper centres of peatland areas. Deep peat deposits are predicted in interfluvial basins in ROC, as well as in river-influenced peatlands in DRC. It is suggested that the deep deposits in ROC are related to the relatively large distances from the peatland margins that predominate there, while deep deposits in narrower river valleys in DRC are related to the relatively wetter climate (greater annual precipitation and less seasonality). Thus, it is concluded that rainfall input is a relatively important driver of peat accumulation in the central Congo Basin, at least on basin-wide scales. Furthermore, I measured bulk density and carbon concentration of 80 peat cores from across the peatland complex. This revealed the central Congo Basin peatlands to be relatively carbon dense, in terms of carbon per unit volume of peat, compared with other tropical peatlands. It is suggested that this might be an effect of the relatively drier climate, resulting in greater decomposition. I further used these measurements of carbon density to develop a linear regression model between peat thickness and carbon density per unit area. Based on the modelled values of peat thickness, I created the first map of peat carbon density across the Cuvette Centrale region. Mean modelled carbon density across the peatland complex is 1,712 ± 634 Mg C ha^{-1}, in line with the field-measured mean of 1,741 ± 1,186 Mg C ha^{-1}. Based on this model of carbon density, I estimated the total peat carbon stock in the central Congo Basin to be 29.0 Pg (95% CI, 26.3-32.2). This is similar to the median 30.6 Pg C reported by Dargie et al. (2017), but their lower 95% confidence interval was 6.3 Pg, which has increased to 26.3 Pg in this study. Thus, it is concluded that the mapping of peat thickness has helped to significantly reduce the uncertainty in peat carbon stocks. The new carbon stock estimates confirm the central Congo Basin peatland complex as a globally significant store of carbon, harbouring ~28%

of all tropical peat carbon. The DRC and ROC are also confirmed as the second and third most important countries in the tropics for peat carbon stocks, respectively, after Indonesia. By overlaying the map of carbon density with maps of protected areas and industrial concessions, I estimate that only 8% of the peat carbon stored in the central Congo Basin lies within formal national-level protected areas, while industrial logging, mining, or palm oil concessions together overlie 26% of total carbon stocks. This suggests a vulnerability of the peat carbon to future land-use changes.

Chapter 7: Conclusion

This thesis improves our understanding of tropical peat swamp forests in the central Congo Basin. Principally, it addresses major gaps in our knowledge of parts of this ecosystem in the Democratic Republic of the Congo, which hosts approximately two-thirds of the estimated peatland area. The objectives of this thesis were fulfilled, by confirming that peat forms in river-influenced swamp forests in the DRC; revealing that different peat swamp forest types can be distinguished based on inundation patterns; mapping the spatial distribution of peat and peat thickness across the central Congo Basin; and estimating the amount of carbon that is stored in peat. In this final chapter, I provide a summary of these key findings, explain the limitations of the work, explore important directions for future research, and finally address the wider implications of my research.

7.1 Key findings

Fieldwork conducted along 11 transects in the swamp forests that straddle the eastern tributaries of the Congo River provides the first direct field evidence that extensive peatlands exist in this part of the Democratic Republic of the Congo. My field campaigns validate the peat predictions made by Dargie et al. (2017), with large peatland areas found on either side of the river valleys, as well as further upstream along the dendritically-shaped stream network. Small discrepancies between the field verifications and Dargie et al.'s (2017) predictions were typically found in seasonally inundated swamps on the margins of larger peatland areas, showing that the predicted shape and distribution of the major peatland areas is generally correct, but is less accurate near the peatland's margins. Modest discrepancies were also found in higher-elevated areas, and on an island in the middle of the Ruki River.

A key output of this thesis is a new model of peatland distribution in the central Congo Basin, based on ground-truth data from both interfluvial basins in ROC and river valleys in DRC. This model predicts a peatland area of 167,600 km^2 across the basin (95% CI, 159,400-175,100 km^2), 15% more than was initially estimated by Dargie et al. (2017). Overall, the new peatland distribution map is in line with Dargie et al. (2017), except that I predict more peat in the DRC, particularly further upstream along the eastern tributaries and the Congo/Lulonga Rivers, as well as around Lake Mai-Ndombe and the Ngiri River. My mapping work confirms the central Congo Basin peatland complex as the most extensive peatland area in the tropics, accounting for approximately 36% of all the world's tropical peatland area, given a total pantropical area of

~460,000 km^2 (440,000 km^2 from Page et al. (2022), plus the ~20,000 km^2 additionally predicted by my new Congo Basin map).

Maximum Likelihood was found to be the most accurate machine learning classifier for mapping peatland distribution, compared with Support Vector Machine or Random Forest, based on its ability to most accurately predict peat in areas from which no training data is included in the model. Changing data sources for the optical, radar or topographic input bands did not improve model performance, as compared with the initial model by Dargie et al. (2017), although adding relative elevation, as measured by the HAND-index (heigh above the nearest drainage point), significantly improved model performance.

Confidence in the new peatland area estimate has increased, given I used three times (n=1,736) as many ground-truth datapoints as Dargie et al. (2017), including more than 400 new datapoints in swamps forest areas in different hydro-geomorphological settings in DRC. More formally, map accuracy as measured by median balanced accuracy has increased, while the range of the confidence interval around this metric decreased. BA is now 91.9% (95% CI, 90.2-93.6), compared with 89.8% (95% CI, 86.0-93.4) for the first-generation model by Dargie et al. (2017). Map accuracy as assessed via Matthews corelation coefficient is 78.0% (95% CI, 74.2 - 81.6).

Mean field-measured peat thickness along eleven transects in the Ruki region of the DRC is 3.2 ± 1.7 m (n=159, with ≥ 30 cm of ≥ 65% OM), significantly greater than the mean thickness of 2.4 ± 1.6 m reported for ROC (Dargie et al. 2017). The maximum peat thickness measured so far in the Cuvette Centrale (either 6.4 or 7.0 m at 6.5 km along the Bondamba transect, depending on the pole-method calibration used), is also larger than the maximum thickness reported for the ROC (5.9 m along the Centre transect). This reveals that peat deposits in river valley settings in DRC, contrary to what was expected, are even thicker than those of interfluvial basins in ROC. Because these river valley peatlands are also considerably narrower in width, it follows that peat thickness increases more sharply with distance from the peatland margin in the river valley peatlands of the DRC than in the interfluvial basin peatlands of the ROC. This is a crucial distinction for mapping peat thickness, which was one of the key aims of this thesis. No difference in peat thickness is observed between hardwood- and palm-dominated peat swamp vegetation, as both vegetation types are found in both hydro-geomorphological settings.

Furthermore, a major finding of this thesis is that peat deposits can also be found in swamp forests experiencing large wet season inundations, close to the major rivers or streams in DRC. This shows that peat formation in the central Congo Basin is not confined to permanently waterlogged swamps with relatively stable water tables, typical of shallow peat domes in interfluvial basins, but also occurs in swamps that experience larger water table fluctuations. These inundations are due to riverbank overflow during the wet season, and potentially upland runoff from higher *terra firme* grounds. However, this peat swamp vegetation type is typically characterized by shallower peat deposits than peat swamps further away from rivers.

Analysis of vegetation forest structure and species composition revealed that the seasonally inundated peat swamps have a distinct vegetation type: a mixed hardwood/palm swamp forest characterised by the presence of *Oubanguia africana* and *Guibourtia demeusei.* This vegetation type was previously described by Evrard (1968), but was not known to overlie peat soils. It was found that these seasonally inundated peat swamps are as acidic as other peatlands and can similarly be characterized as nutrient-poor. This is because the Ruki, Busira and Ikelemba Rivers are themselves blackwater rivers, characterized by low nutrient concentrations, high organic matter content and high acidity. This blackwater status is partly related to the large upland peat swamp area that these rivers drain, as shown by the lower pH values closer to the confluence with the Congo River. This highlights a strong interaction effect between rivers and peatlands that is still poorly understood.

Other distinct vegetation types that were observed in the DRC peat swamp forests are a hardwood-dominated peat swamp, a *Raphia laurentii* palm-dominated peat swamp, and a mixed hardwood/palm peat swamp characterized by the presence of *Cryptosepalum congolanum.* The first two of these classes, hardwood- and palm-dominated peat swamps, have also been observed extensively in the ROC (Dargie, 2015; Bocko et al., 2016; Dargie et al., 2017). However, the identification of a third – mixed – type suggests that these peat swamp forests possibly form a continuous gradient driven by differences in palm dominance. Together with the distinct *Raphia hookeri* palm-dominated peat swamp that was observed by Dargie et al. (2017) in abandoned fluvial channels, I conclude that there are at least five vegetation types that can be distinguished in the central Congo Basin peatland complex.

Moreover, based on radiocarbon dating of peat basal samples, I conclude that the earliest peat initiation in river-influenced settings of the DRC commenced ~42,000 years ago. This is over

20,000 years earlier than in interfluvial basin peatlands in ROC (Dargie et al., 2017; and G. Dargie, *unpublished data*). This reveals that parts of the central Congo Basin peatlands are of Late Pleistocene-age, rather than early Holocene age, and have survived throughout the Last Glacial Maximum.

Using multi-temporal radar data that covers most of the newly mapped peatland complex, I additionally developed a map of inundation frequency. From this, I estimate that approximately one-quarter (~40,000 km^2) of the peatlands experience seasonal inundation by standing surface water. This includes the typical river-influenced peatlands that I encountered in DRC, but possibly also areas that are seasonally inundated by water from non-riverine sources. Based on the first microtopography data collected in the central Congo Basin peatlands, it is assumed here that inundation derived from radar backscatter is indicative of on average at least 10-20 cm of standing water above the peat surface. Approximately one-fifth (~33,000 km^2) of the peatlands appear to be almost permanently inundated with standing water, particularly in what is likely a large area of palm-dominated peat swamps east of Lake Mai Ndombe in DRC, an understudied region. On the other hand, more than half of the peatlands (~95,000 km^2) are rarely inundated by standing water, suggesting water is near the surface to limit decomposition and allow peat formation, but must usually be lower than 20 cm above the surface. This is particularly the case in large interfluvial basins in ROC, as shown by Dargie et al. (2017) whose *in situ* datalogger data shows water tables of > 20 cm above the surface for only a few days a year, typically after the largest rainfall events in the wet season. Thus, these areas are thought to be permanently waterlogged peat swamps, with relatively stable water tables around the peat surface.

I developed the first map of peat thickness across the central Congo Basin, based on 463 peat thickness measurements from both interfluvial basins and river-influenced peatlands. After a stepwise backward selection of predictor variables, I conclude that distance from the peatland margin, climatic water balance, precipitation seasonality and distance to the nearest drainage point are the most useful predictors of peat thickness in the Cuvette Centrale. Distance from the peatland margin is a strong predictor of peat thickness in interfluvial basins in ROC, but less reliable in the narrower peatlands of the river valleys in DRC. On the other hand, the importance of climatic water balance and precipitation seasonality in the model suggests that rainfall is an important driver of peat thickness on a basin-wide scale. In particular, thick peat deposits in river valleys in DRC correspond with the wetter and less seasonal rainfall conditions over this part of the central Congo basin.

The mean modelled peat thickness in the central Congo Basin is 1.7 (± 0.9) m, with a maximum modelled value of 5.6 m. This is slightly lower than the mean field-measured peat thickness of 2.4 (± 1.5) m, and the maximum field-measured value of 6.4 m. This difference is not surprising, given that that the field sampling design oversamples deeper peat at the centre relative to the periphery of approximately ovoid peatlands. Thus, these figures give confidence in the peat thickness model, which correctly predicts deep peat deposits in interfluvial basins and river valleys, yet does not appear to overestimate peat thickness relative to the field-measured dataset. More formally, the peat thickness model performs well in areas that were included in the sampling (median R^2 = 82.2%, RMSE = 0.68 m), compared with a linear regression model including the same four predictors (median adj-R^2 = 73.6%, RMSE = 0.85 m).

I used this map of peat thickness to develop a first map of peat carbon density per unit area for the central Congo Basin. This map follows the same spatial pattern as peat thickness, as it is based on a linear regression between thickness and carbon density. The carbon density map reveals for the first time where the peat carbon that was predicted by Dargie et al. (2017) can be found exactly, a first and critical step towards the long-term protection of these peat carbon stocks.

Mean modelled peat carbon density in the central Congo Basin is 1,712 ± 634 Mg C ha^{-1}, in line with the field-measured mean of 1,741 Mg C ha^{-1}. Maximum modelled carbon density is 3,970 Mg C ha^{-1}, while the maximum field-measured value is 5,162 Mg C ha^{-1}. These results show that the central Congo Basin peatlands are one of the most carbon-dense ecosystems on Earth, storing approximately nine times the mean amount of carbon stored in aboveground live tree biomass of African tropical moist forests (~198 Mg C ha^{-1}; Lewis et al., 2013).

By summing carbon density across the predicted peat pixels, I estimate that 29.0 Pg C is stored belowground in peat across the region (95% confidence interval, 26.3-32.2 Pg C). This is very similar to the 30.6 Pg C that was predicted by Dargie et al. (2017), but critically, my estimate increases the lower confidence interval bound from, from 6.3 to 26.4 Pg C. These field-based constraints give high confidence of globally significant peat carbon stocks in the central Congo Basin, totalling approximately 28% of the world's tropical peat carbon (total tropical peat carbon 105 Pg C; Page et al., 2022). Furthermore, these results confirm the DRC and ROC as the second and third most important countries in the tropics, respectively, for both peatland area and peat carbon stocks, after Indonesia.

7.2 Limitations and future research directions

As with all studies, there are important limitations to this research. Most importantly, this thesis project is limited by a lack of field data across the central Congo Basin. One of the main aims of this thesis was to gather more *in situ* data and increase the representativeness of this sampling across the region, particularly in the DRC. Although this thesis involved a lot of fieldwork and has made major improvements in this direction, large areas of the peatland complex remain unsampled. Only 464 thickness measurements were used to model peat thickness across an area equivalent to more than the size of England and Wales combined. Compared with studies of typically well-sampled northern peatlands in the UK, this sample size is very small, relative to such a large area. More field verification of both peat presence and peat thickness is therefore urgently required across the Cuvette Centrale region. Specifically, focus should be given to areas further east of the basin, such as upstream along the Congo River and along the Lomami River, south of Kisangani in the province of Tshopo. This way, the 'area of applicability' of the peatland distribution model can be extended further east. Additionally, since the new peatland model presented in this thesis predicts more peatland areas further upstream along tributaries such as the Busira and Ikelemba Rivers, field verification of these upstream predictions is required in the province of Thsuapa. This applies to the Ngiri region as well, which is now predicted to contain more peat than was estimated by Dargie et al. (2017). Moreover, a large block of likely inundated palm-dominated peat swamp is consistently identified east of Lake Mai-Ndombe. This area has so far remained unsampled. As this region is possibly characterised by a different hydro-geomorphology than either the interfluvial basin peatlands in ROC or the river-influenced peatlands sampled so far in DRC, it should be an important research priority. In the ROC, on the other hand, limited field sampling has been undertaken in the south-western part of the peatland complex, located in the Cuvette department, again lacking confirmation of peat presence. Although this area is hypothesized to similarly be characterized by interfluvial basin peat domes as were recorded in the Likouala department (Dargie et al., 2017; Davenport et al., 2020), this remains to be verified. Flying of unmanned aerial vehicles equipped with LiDAR to measure topography and forest structure could help determine if there are peat domes in these regions, as well as in the river-influenced peatlands I visited in DRC (Davenport et al., 2020).

This thesis has shown how river valley peatlands in the DRC are characterized by seasonal inundations from riverbank overflow. Nonetheless, no *in situ* water table date could be presented from close (< 2 km) to the Ikelemba River, due to unforeseen technical problems with the water table dataloggers. Future research should ideally aim to quantify these water table

fluctuations by installing new water table dataloggers and monitoring them over a multi-year period. This applies to the Ruki or Ikelemba Rivers, as well as the floodplains along the Congo River itself, which have also been observed to experience large seasonal inundations. Again, field campaigns to the area east of Lake Mai Ndombe, where almost year-round inundation is seen by radar data, should be confirmed by *in situ* measurements as well. Having *in situ* water table measurements from different parts of the peatland complex will facilitate the corroboration and scaling of remotely-sensed inundation patterns.

Furthermore, in this thesis I had a particular focus on surface inundations, while sub-surface water table dynamics are likely equally important in driving species composition and peat accumulation. Although dry season water table depths below the surface were measured at each peat site, such measurements are often lacking from seasonally inundated non-peat forming forests. More measurements of maximum belowground water tables in non-peat forming forests would facilitate a comparison between peat-forming and non-peat-forming seasonally inundated forest types. This could ultimately shed more light on why some seasonally inundated forests form peat, while others do not.

Additionally, the analysis of forest structure and species composition presented here was restricted to peat swamp forests in the Ruki region of the DRC, where I collected the vegetation data. It would be very useful to extend this analysis across all vegetation data collected in the peat swamp forests of the Cuvette Centrale, including the data that has been sampled by Dargie et al. (2017) and Bocko et al. (2016) in ROC and the unpublished data collected by the CongoPeat consortium along the Congo River transects. This way, it would be possible to test more formally whether the distinction of five peat swamp forest vegetation types that has been identified in this thesis holds across the entire basin. Analyses of vegetation types could be helped further by the development of specific peat swamp forest allometric equations, more wood density data from swamp forest tree species, as well as the establishment of more and larger vegetation plots. Longer-term monitoring, using permanent vegetation plots in the standard method using common pan-tropical methods of 1 ha plots (e.g., Lewis et al., 2013) will be very useful to measure forest carbon fluxes in the live vegetation carbon pool and important for supporting the conservation and management of these forests (Baker et al., 2020). Furthermore, identification work on smaller plants, especially shrubs and herbs, is necessary, as those species typically have shorter generation times, which may make them the most likely to be endemic to the peatlands.

Once a formal classification of all vegetation plots has been established, peat swamp forest sites can be reclassified according to this new classification. With these classes, rather than the binary distinction between hardwood- and palm-dominated peat swamp forests, it might be possible to use landcover classifiers such as Maximum Likelihood to more accurately map these vegetation types across the peatland complex, and so refine my estimates of peatland area.

Such a more detailed approach to mapping peat swamp forest vegetation types might also be improved by the inclusion of an inundation map based on multi-temporal radar data. I have shown in this thesis how the seasonally inundated mixed peat swamp type characterized by *Oubanguia africana* and *Guibourtia demeusei* is associated with a medium number of inundations throughout the year. This contrasts with the other peat swamp forest types, which were found to be either rarely inundated more than 20 cm above the peat surface by standing water, or have almost permanent inundations at this level. Therefore, the development of an inundation map that covers the full peatland complex and captures this seasonal pattern is a key research priority.

Besides water table dynamics, understanding nutrient inputs into the peatlands are crucial for predicting peat thickness as well. Unfortunately, in this thesis I was only able to analyse a limited number of river water samples, while no rainwater samples were taken in DRC, due to technical problems with the filtration of samples. More data from across the basin is required, as nutrient status cannot be measured remotely by satellites. This is particularly necessary in the floodplains along the Congo River mainstem, where peat-associated swamp vegetation was encountered close to the river, but with only limited peat accumulation. It is very likely that a gradient in nutrient status exists when moving away from the Congo River into these swamps, unlike the peatlands along the Congo's tributaries such as the Ruki or Ikelemba, which showed no or very limited gradients in nutrient status.

Similarly, the geomorphology and shape of the bedrock underneath the peatlands is often unknown and cannot be easily mapped remotely. However, understanding the shape of the underlying bedrock, particularly in areas east of the Congo River that vary more in elevation than interfluvial basins, will help to model peat thickness. One critical step towards this, is the development of a digital terrain model for the Congo Basin, which essentially would represent the DEM but without the tree height. This way, the true ground surface elevation of the

peatlands can be mapped. Subsequently subtracting the measured peat thickness values could give an idea of the shape of the bedrock layer onto which peat has formed.

In addition, process-based models of peatland development are required to understand the drivers of peat formation and maintenance in the Cuvette Centrale. One model appears very promising for this: an adaptation and parameterisation of the DigiBog model (Baird et al., 2012; Morris et al., 2012; Young et al., 2017) for the Congo Basin peatlands, called DigiBogCongo. This model is currently being adapted by the CongoPeat consortium for application in the central Congo Basin, with the model tracking the production and decomposition of 'cohorts' of peat over time (via litter inputs and limitations on decomposition from waterlogging), hence making it possible to follow the build-up and decomposition of peat layers over long periods of time.

Finally, more radiocarbon dating of peat basal samples is required, especially in the river-influenced peat swamps of DRC. This thesis has revealed these peatlands to be over 20,000 years older than initially reported. However, this finding is based on only one peat core with an age of approximately 42,300 cal yr BP, which originates from only one sample on one transect. More replicates from other transects and other river systems are needed to confirm this is truly representative of the river valley peatlands that dominate in the DRC. Some of this work is currently being undertaken as part of the CongoPeat project.

7.3 Implications

This thesis has shown that extensive peatlands are found in river valley systems of the DRC, making the Cuvette Centrale peatland complex a globally significant store of carbon. This has major implications for forest conservation and climate change policy in the Congo Basin. The Cuvette Centrale peatlands have been shown to be sensitive to future climate change and land use changes. Thus, keeping the central Congo Basin peatlands wet is vital to prevent vast amounts of peat carbon being released to the atmosphere (Dargie et al., 2019; Miles et al., 2017; Cole et al., 2022).

In this work, I have shown where the peat carbon is located in detail. Based on this, I estimate that only 8% of the peat carbon lies within national-level protected areas. On the other hand, about a quarter (26%) of all peat carbon is covered by industrial logging, mining or palm oil concessions. Furthermore, virtually all the peat carbon is covered by hydrocarbon concessions,

the vast majority of which have so far not been issued yet. This suggests that the central Congo Basin peatlands are vulnerable to future land-use change. Given that the current areas of formal protection of peatlands are largely centred around interfluvial basins, I suggest that additional protective measures will be needed to safeguard the newly identified river-influenced peatlands of the central Congo Basin.

Furthermore, the identification of extensive nutrient-poor seasonally inundated peatlands in floodplains of the Congo River network reveals that there is more than one hydro-geomorphological setting where peat is formed and maintained. The discovery that these peatlands are of pre-Holocene age also indicate that there is more than one climatic setting in which peat formation has initiated in the central Congo Basin. This has many implications for our hydrological understanding of the peatlands, and how future climate change will impact the peatlands. If seasonally inundated peat swamps are not only dependent on rainfall but also riverbank overflow, upstream rainfall patterns, as well as infrastructural projects that affect river dynamics will have larger impacts on peatland functioning than previously thought.

For peatland research and conservation to be effective, it is important that consistent definitions are applied. In this thesis, I have chosen to define peat as at least 30 cm of soil with a minimum of 65% organic matter content, in line with previous studies (Page et al., 2011; Dargie et al., 2017). However, there is currently no formal government-approved definition of peat or peatlands in either the DRC or the ROC. Neither are there formal protocols for measuring or evaluating peat thickness and carbon stocks. As I have shown in this thesis, peat thickness measurements are variable due to the definitions and calibration equations used. Thus, there is an urgent need for the establishment of formal definitions that can support peatland research and conservation.

Lastly, keeping the central Congo Basin peatlands undisturbed would also help protect the rich biodiversity that characterises this ecosystem, including forest elephants, lowland gorillas, chimpanzees and bonobos (Maisels et al., 2013; Miles et al., 2017; Strindberg et al., 2018). Critically, efforts to map biodiversity and to overlie this with my map of peatland carbon density are needed to assess if there is a correlation between biodiversity and peat carbon stocks. If there is, then biodiversity protection and carbon protection can go hand-in-hand. There is a possibility of this positive relationship, because typically, the larger wildlife is more concentrated away from the peatland edges, in areas with less hunting pressure where the biodiversity is more

intact. The core peatland areas are also more likely to have deeper peat and therefore higher carbon storage. Investigations into this synergy of both more biodiversity and more carbon storage in the interior of the peatlands should be a future research priority. This could potentially fit with conservation efforts, for example through the assignment of buffer zones for sustainable forest use by local communities around the margins of the peatland, as is currently already being practiced, and core interior areas with stricter protections for the biodiversity of the peatlands.

References

Allen, J. D., & Castillo, M. M. (2007). *Stream Ecology: Structure and function of running waters* (2nd ed.). Springer: Dordrecht, the Netherlands.

Allen, S. E. (Ed.). (1989). *Chemical Analysis of Ecological Materials* (2nd ed.). Blackwell Scientific Publications: Oxford, UK.

Alongi, D. M. (2012). Carbon sequestration in mangrove forests. *Carbon Management*, *3*(3), 313–322. https://doi.org/10.4155/cmt.12.20

Alsdorf, Douglas, Beighley, E., Laraque, A., Lee, H., Tshimanga, R., O'Loughlin, F., Mahé, G., Dinga, B., Moukandi, G., & Spencer, R. G. M. (2016). Opportunities for hydrologic research in the Congo Basin. *Reviews of Geophysics*, *54*(2), 378–409. https://doi.org/10.1002/2016RG000517

Anderson, J. (1963). The flora of the peat swamp forests of Sarawak and Brunei, including a catalogue of all recorded species of flowering plants, ferns and fern allies. *Gardens Bulletin Singapore*, *29*, 131–228.

Anderson, M. J. (2001). A new method for non-parametric multivariate analysis of variance. *Austral Ecology*, *26*(1), 32–46. https://doi.org/10.1046/j.1442-9993.2001.01070.x

Anderson, M. J., Crist, T. O., Chase, J. M., Vellend, M., Inouye, B. D., Freestone, A. L., Sanders, N. J., Cornell, H. V., Comita, L. S., Davies, K. F., Harrison, S. P., Kraft, N. J. B., Stegen, J. C., & Swenson, N. G. (2011). Navigating the multiple meanings of β diversity: A roadmap for the practicing ecologist. *Ecology Letters*, *14*(1), 19–28. https://doi.org/10.1111/j.1461-0248.2010.01552.x

Andriesse, J. (1988). Nature and Management of Tropical Peat Soils. In *FAO Soils Bulletin* (Vol. 59). Food and Agriculture Organisation of the United Nations: Rome, Italy.

Anhuf, D., Ledru, M. P., Behling, H., Da Cruz, F. W., Cordeiro, R. C., Van der Hammen, T., Karmann, I., Marengo, J. A., De Oliveira, P. E., Pessenda, L., Siffedine, A., Albuquerque, A. L., & Da Silva Dias, P. L. (2006). Paleo-environmental change in Amazonian and African rainforest during the LGM. *Palaeogeography, Palaeoclimatology, Palaeoecology*, *239*(3–4), 510–527. https://doi.org/10.1016/j.palaeo.2006.01.017

Aristizabal, F., Judge, J., & Monsivais-Huertero, A. (2020). High-resolution inundation mapping for heterogeneous land covers with synthetic aperture radar and terrain data. *Remote Sensing*, *12*(6). https://doi.org/10.3390/rs12060900

Asefi-Najafabady, S., & Saatchi, S. (2013). Response of African humid tropical forests to recent rainfall anomalies. *Philosophical Transactions of the Royal Society of London. Series B, Biological Sciences*, *368*(20120306), 1–8. https://doi.org/10.1098/rstb.2012.0306

Baccini, A., Goetz, S. J., Walker, W. S., Laporte, N. T., Sun, M., Sulla-Menashe, D., Hackler, J., Beck, P. S. A., Dubayah, R., Friedl, M. A., Samanta, S., & Houghton, R. A. (2012). Estimated carbon dioxide emissions from tropical deforestation improved by carbon-density maps. *Nature Climate Change*, *2*(3), 182–185. https://doi.org/10.1038/nclimate1354

Bahn, V., & Mcgill, B. J. (2007). Can niche-based distribution models outperform spatial interpolation? *Global Ecology and Biogeography*, *16*(6), 733–742. https://doi.org/10.1111/j.1466-8238.2007.00331.x

Baird, A. J., Low, R., Young, D., Swindles, G. T., Lopez, O. R., & Page, S. (2017). High permeability explains the vulnerability of the carbon store in drained tropical peatlands. *Geophysical Research Letters*, *44*(3), 1333–1339. https://doi.org/10.1002/2016GL072245

Baird, A. J., Morris, P. J., & Belyea, L. R. (2012). The DigiBog peatland development model 1: rationale, conceptual model, and hydrological basis. *Ecohydrology*, *5*, 242–255. https://doi.org/10.1002/eco.230

Baker, T. R., Del Castillo Torres, D., Honorio Coronado, E. N., Lawson, I., Brañas, M. M., Montoya, M., & Roucoux, K. (2019). The challenges for achieving conservation and sustainable development within the wetlands of the Pastaza-Marañón Basin, Peru. In A. Chirif (Ed.), *Peru: Deforestation in times of climate change* (pp. 155–174). International Work Group for Indigenous Affairs: Lima, Peru.

Baker, T. R., Vicuña Miñano, E., Banda-R, K., del Castillo Torres, D., Farfan-Rios, W., Lawson, I. T., Loja Alemán, E., Pallqui Camacho, N., Silman, M. R., Roucoux, K. H., Phillips, O. L., Honorio Coronado, E. N., Monteagudo Mendoza, A., & Rojas Gonzáles, R. (2020). From plots to policy: How to ensure long-term forest plot data supports environmental management in intact tropical forest landscapes. *Plants People Planet*, *00*, 1–9. https://doi.org/10.1002/ppp3.10154

Barnosky, A. D., Koch, P. L., Feranec, R. S., Wing, S. L., & Shabel, A. B. (2004). Assessing the causes of late pleistocene extinctions on the continents. *Science*, *306*(70), 70–75. https://doi.org/10.1126/science.1101476

Barthelmes, A. (Ed.). (2018). Reporting greenhouse gas emissions from organic soils in the European Union: challenges and opportunities. In *Policy brief. Proceedings of the Greifswald Mire Centre 02/2018*.

Batumike, R., Imani, G., Urom, C., & Cuni-Sanchez, A. (2020). Bushmeat hunting around Lomami National Park, Democratic Republic of the Congo. *Oryx*, *55*(3), 1–11. https://doi.org/10.1017/S0030605319001017

Baugh, C. A., Bates, P. D., Schumann, G., & Trigg, M. A. (2013). SRTM vegetation removal and hydrodynamic modeling accuracy. *Water Resources Research*, *49*(9), 5276–5289. https://doi.org/10.1002/wrcr.20412

Bayon, G., Schefuß, E., Dupont, L., Borges, A. V., Dennielou, B., Lambert, T., Mollenhauer, G., Monin, L., Ponzevera, E., Skonieczny, C., & André, L. (2019). The roles of climate and human land-use in the late Holocene rainforest crisis of Central Africa. *Earth and Planetary Science Letters*, *505*, 30–41. https://doi.org/10.1016/j.epsl.2018.10.016

Becker, M., da Silva, J. S., Calmant, S., Robinet, V., Linguet, L., & Seyler, F. (2014). Water level fluctuations in the Congo Basin derived from ENVISAT satellite altimetry. *Remote Sensing*, *6*(10), 9340–9358. https://doi.org/10.3390/rs6109340

Belgiu, M., & Drăgu, L. (2016). Random forest in remote sensing: A review of applications and future directions. *ISPRS Journal of Photogrammetry and Remote Sensing*, *114*, 24–31. https://doi.org/10.1016/j.isprsjprs.2016.01.011

Bennett, A. C., Dargie, G. C., Cuni-Sanchez, A., Mukendi, J. T., Hubau, W., Mukinzi, J. M., Phillips, O. L., Malhi, Y., Sullivan, M. J. P., Cooper, D. L. M., Adu-Bredu, S., Affum-Baffoe, K., Amani, C. A., Banin, L. F., Beeckman, H., Begne, S. K., Bocko, Y. E., Boeckx, P., Bogaert, J., … Lewis, S. L. (2021). Resistance of African tropical forests to an extreme climate anomaly. *Proceedings of the National Academy of Sciences*, *118*(21), 1–12. https://doi.org/10.1073/pnas.2003169118

Berg, A. (1961). Rôle écologique des eaux de la Cuvette congolaise sur la croissance de la jacinthe d'eau [Eichhornia crassipes (Mart.) Solms]. *Académie Royale Des Sciences d'Outre-Mer*, *Memoires no. 8. Nouvelle série. Tome XII*, fasc. *3*.

Berner, E. K., & Berner, R. A. (2012). *Global Environment: Water, Air, and Geochemical Cycles* (2nd ed.). Princeton University Press: Princeton, US.

Berzaghi, F., Longo, M., Ciais, P., Blake, S., Bretagnolle, F., Vieira, S., Scaranello, M., Scarascia-Mugnozza, G., & Doughty, C. E. (2019). Carbon stocks in central African forests enhanced by elephant disturbance. *Nature Geoscience*, *12*(9), 725–729. https://doi.org/10.1038/s41561-019-0395-6

BESTOR. (2021). *Institut pour la Recherche scientifique en Afrique centrale*. Belgian Science and Technology Online Resources. https://www.bestor.be/wiki/index.php/Institut_pour_la_Recherche_scientifique_en_Afrique_centrale_-_Instituut_voor_Wetenschappelijk_Onderzoek_in_Centraal_Afrika

Betbeder, J., Gond, V., Frappart, F., Baghdadi, N. N., Briant, G., & Bartholomé, E. (2014). Mapping of Central Africa Forested Wetlands Using Remote Sensing. *IEEE Journal of Selected Topics in Applied Earth Observations and Remote Sensing*, *7*(2), 521–542. https://doi.org/10.1109/JSTARS.2013.2269733

Beven, K. (2016). Facets of uncertainty: Epistemic uncertainty, non-stationarity, likelihood, hypothesis testing, and communication. *Hydrological Sciences Journal*, *61*(9), 1652–1665. https://doi.org/10.1080/02626667.2015.1031761

Bhattacharyya, A., Schmidt, M. P., Stavitski, E., & Martínez, C. E. (2018). Iron speciation in peats: Chemical and spectroscopic evidence for the co-occurrence of ferric and ferrous iron in organic complexes and mineral precipitates. *Organic Geochemistry*, *115*, 124–137. https://doi.org/10.1016/j.orggeochem.2017.10.012

Bibi-Loumoni, J. A. (2019). *Densité spécifique de bois des espèces abandantes d'arbres de la tourbière forestière de la Likouala (Cuvette centrale du Bassin du Congo)*. BSc Thesis. Faculté des sciences et techniques, Université Marien Ngouabi, Republic of the Congo.

Biddulph, G. E., Bocko, Y. E., Bola, P., Crezee, B., Dargie, G. C., Emba, O., Georgiou, S., Girkin, N., Hawthorne, D., Jonay Jovani-Sancho, A., Joseph Kanyama, T., Mampouya, W. E., Mbemba, M., Sciumbata, M., & Tyrrell, G. (2021). Current knowledge on the Cuvette Centrale peatland complex and future research directions. *Bois et Forets Des Tropiques*, *350*, 3–14. https://doi.org/10.19182/bft2021.350.a36288

Bloemen, G. W. (1983). Calculation of hydraulic conductivities and steady state capillary rise in peat soils from bulk density and solid matter volume. *Zeitschrift Für Pflanzenernährung Und Bodenkunde*, *146*(4), 460–473. https://doi.org/10.1002/jpln.19831460407

Bocko, Y. E., Dargie, G., Suspense, I. A., Yoka, J., & Loumeto, J. J. (2016). Répartition spatiale de la richesse floristique des forêts marécageuses de la Likouala, Nord-Congo. *Afrique Science*, *12*(4), 200–212.

Bord na Móna. (1984). Fuel Peat in Developing Countries. In *World Bank Technical Paper 41*.

Borges, A. V., Darchambeau, F., Lambert, T., Morana, C., Allen, G. H., Tambwe, E., Toengaho Sembaito, A., Mambo, T., Wabakhangazi, J. N., Descy, J. P., Teodoru, C. R., & Bouillon, S. (2019). Variations in dissolved greenhouse gases (CO2, CH4, N2O) in the Congo River network overwhelmingly driven by fluvial-wetland connectivity. *Biogeosciences*, *16*(19), 3801–3834. https://doi.org/10.5194/bg-16-3801-2019

Bothwell, L. D., Selmants, P. C., Giardina, C. P., & Litton, C. M. (2014). Leaf litter decomposition rates increase with rising mean annual temperature in Hawaiian tropical montane wet forests. *PeerJ*, *2*(685), 12. https://doi.org/10.7717/peerj.685

Bouillon, S., Yambélé, A., Gillikin, D. P., Teodoru, C., Darchambeau, F., Lambert, T., & Borges, A. V. (2014). Contrasting biogeochemical characteristics of the Oubangui River and tributaries (Congo River basin). *Scientific Reports*, *4*(5402), 1–10. https://doi.org/10.1038/srep05402

Bourgeau-Chavez, L. L., Grelik, S. L., Battaglia, M. J., Leisman, D. J., Chimner, R. A., Hribljan, J. A., Lilleskov, E. A., Draper, F. C., Zutta, B. R., Hergoualc'h, K., Bhomia, R. K., & Lähteenoja, O. (2021). Advances in Amazonian Peatland Discrimination With Multi-Temporal PALSAR Refines Estimates of Peatland Distribution, C Stocks and Deforestation. *Frontiers in Earth Science*, *9*(676748), 1–19. https://doi.org/10.3389/feart.2021.676748

Brady, M. A. (1997). *Organic Matter Dynamics in Coastal Peat Deposits in Sumatra, Indonesia*. PhD Thesis. University of British Columbia: Vancouver, Canada.

Breiman, L. (2001). Random forests. *Machine Learning*, *45*(1), 5–32. https://doi.org/10.1023/A:1010933404324

Bronk Ramsey, C. (2008). Deposition models for chronological records. *Quaternary Science Reviews*, *27*(1–2), 42–60. https://doi.org/10.1016/j.quascirev.2007.01.019

Bronk Ramsey, C. (2009). Bayesian analysis of radiocarbon dates. *Radiocarbon*, *51*(1), 337–360. https://doi.org/10.1017/s0033822200033865

Bronk Ramsey, C., & Lee, S. (2013). Recent and Planned Developments of the Program OxCal. *Radiocarbon*, *55*(2–3), 720–730. https://doi.org/10.2458/azu_js_rc.55.16215

Burges, C. J. C. (1998). A tutorial on support vector machines for pattern recognition. *Data Mining and Knowledge Discovery*, *2*(2), 121–167. https://doi.org/10.1023/A:1009715923555

Bwangoy, J. R. B., Hansen, M. C., Roy, D. P., Grandi, G. De, & Justice, C. O. (2010). Wetland mapping in the Congo Basin using optical and radar remotely sensed data and derived topographical indices. *Remote Sensing of Environment*, *114*(1), 73–86. https://doi.org/10.1016/j.rse.2009.08.004

Cameron, C. C., Esterle, J. S., & Palmer, C. A. (1989). The geology, botany and chemistry of selected peat-forming environments from temperate and tropical latitudes. *International Journal of Coal Geology*, *12*(1–4), 105–156. https://doi.org/10.1016/0166-5162(89)90049-9

Campbell, D. (2005). The Congo River Basin. In L. H. Fraser & P. A. Keddy (Eds.), *The World's Largest Wetlands: Ecology and Conservation* (1st ed., pp. 149–165). Cambridge University Press: Cambridge, UK.

Chambers, F. M., Beilman, D. W., & Yu, Z. (2011). Methods for determining peat humification and for quantifying peat bulk density, organic matter and carbon content for palaeostudies of climate and peatland carbon dynamics. *Mires and Peat*, *7*(07), 1–10.

Chave, J., Coomes, D., Jansen, S., Lewis, S. L., Swenson, N. G., & Zanne, A. E. (2009). Towards a worldwide wood economics spectrum. *Ecology Letters*, *12*(4), 351–366. https://doi.org/10.1111/j.1461-0248.2009.01285.x

Chave, J., Réjou-Méchain, M., Búrquez, A., Chidumayo, E., Colgan, M. S., Delitti, W. B. C.,

Duque, A., Eid, T., Fearnside, P. M., Goodman, R. C., Henry, M., Martínez-Yrízar, A., Mugasha, W. A., Muller-Landau, H. C., Mencuccini, M., Nelson, B. W., Ngomanda, A., Nogueira, E. M., Ortiz-Malavassi, E., … Vieilledent, G. (2014). Improved allometric models to estimate the aboveground biomass of tropical trees. *Global Change Biology*, *20*(10), 3177–3190. https://doi.org/10.1111/gcb.12629

Chesworth, W., Cortizas, A. M., & García-Rodeja, E. (2006). The redox-pH approach to the geochemistry of the Earth's land surface, with application to peatlands. In *Developments in Earth Surface Processes* (Vol. 9, pp. 175–195). Elsevier: Amsterdam, Netherlands. https://doi.org/10.1016/S0928-2025(06)09008-0

Chicco, D., & Jurman, G. (2020). The advantages of the Matthews correlation coefficient (MCC) over F1 score and accuracy in binary classification evaluation. *BMC Genomics*, *21*(1), 1–13. https://doi.org/10.1186/s12864-019-6413-7

Chicco, D., Tötsch, N., & Jurman, G. (2021). The Matthews correlation coefficient (MCC) is more reliable than balanced accuracy, bookmaker informedness, and markedness in two-class confusion matrix evaluation. *BioData Mining*, *14*(13), 1–22. https://doi.org/10.1186/s13040-021-00244-z

Clarke, K. R. (1993). Non-parametric multivariate analyses of changes in community structure. *Australian Journal of Ecology*, *18*(1), 117–143. https://doi.org/10.1111/j.1442-9993.1993.tb00438.x

Clubb, F. J., Mudd, S. M., Milodowski, D. T., Valters, D. A., Slater, L. J., Hurst, M. D., & Limaye, A. B. (2017). Geomorphometric delineation of floodplains and terraces from objectively defined topographic thresholds. *Earth Surface Dynamics*, *5*(3), 369–385. https://doi.org/10.5194/esurf-5-369-2017

Clymo, R. (1987). The ecology of peatlands. *Science Progress*, *71*(4), 593–614.

Clymo, R. S. (2004). Hydraulic conductivity of peat at Ellergower Moss, Scotland. *Hydrological Processes*, *18*, 261–274. https://doi.org/10.1002/hyp.1374

Clymo, R. S., Turunen, J., & Tolonen, K. (1998). Carbon Accumulation in Peatland. *Oikos*, *81*(2), 368. https://doi.org/10.2307/3547057

Cobb, A. R., Hoyt, A. M., Gandois, L., Eri, J., Dommain, R., Abu Salim, K., Kai, F. M., Haji Su'ut, N. S., & Harvey, C. F. (2017). How temporal patterns in rainfall determine the geomorphology and carbon fluxes of tropical peatlands. *Proceedings of the National Academy of Sciences*, *1*, 10. https://doi.org/10.1073/pnas.1701090114

Cole, L. E. S., Åkesson, C. M., Hapsari, K. A., Hawthorne, D., Roucoux, K. H., Girkin, N. T., Cooper, H. V., Ledger, M. J., O'Reilly, P., & Thornton, S. A. (2022). Tropical peatlands in the anthropocene: Lessons from the past. *Anthropocene*, *37*(100324), 1–17. https://doi.org/10.1016/j.ancene.2022.100324

Collins, J. A., Prange, M., Caley, T., Gimeno, L., Beckmann, B., Mulitza, S., Skonieczny, C., Roche, D., & Schefuß, E. (2017). Rapid termination of the African Humid Period triggered by northern high-latitude cooling. *Nature Communications*, *8*(1372), 1–11. https://doi.org/10.1038/s41467-017-01454-y

Cook, K. H., Liu, Y., & Vizy, E. K. (2020). Congo Basin drying associated with poleward shifts of the African thermal lows. *Climate Dynamics*, *54*(1–2), 863–883. https://doi.org/10.1007/s00382-019-05033-3

Coynel, A., Seyler, P., Etcheber, H., Meybeck, M., & Orange, D. (2005). Spatial and seasonal

dynamics of total suspended sediment and organic carbon species in the Congo River. *Global Biogeochemical Cycles*, *19*(4), 1–17. https://doi.org/10.1029/2004GB002335

Daly, A. J., Baetens, J. M., & De Baets, B. (2018). Ecological diversity: Measuring the unmeasurable. *Mathematics*, *6*(7). https://doi.org/10.3390/math6070119

Damman, A. W. H. (1978). Distribution and Movement of Elements in Ombrotrophic Peat Bogs. *Oikos*, *30*(3), 480–495.

Dargie, G. C., Lawson, I. T., Rayden, T. J., Miles, L., Mitchard, E. T. A., Page, S. E., Bocko, Y. E., Ifo, S. A., & Lewis, S. L. (2019). Congo Basin peatlands: threats and conservation priorities. *Mitigation and Adaptation Strategies for Global Change*, *24*(4), 669–686. https://doi.org/10.1007/s11027-017-9774-8

Dargie, G. C., Lewis, S. L., Lawson, I. T., Mitchard, E. T. A., Page, S. E., Bocko, Y. E., & Ifo, S. A. (2017). Age, extent and carbon storage of the central Congo Basin peatland complex. *Nature*, *542*(7639), 86–90. https://doi.org/10.1038/nature21048

Dargie, G. C. (2015). *Quantifying and understanding the tropical peatlands of the central Congo basin*. PhD Thesis. School of Geography, University of Leeds, UK.

Datok, P., Fabre, C., Sauvage, S., Moukandi N'kaya, G. D., Paris, A., Dos Santos, V., Laraque, A., & Sanchez Perez, J. M. (2021). Investigating the role of the Cuvette Centrale in the hydrology of the Congo River Basin. In D. Alsdorf, G. Moukandi, & R. Tshimanga (Eds.), *Congo Basin Hydrology, Climate, and Biogeochemistry: A Foundation for the Future* (pp. 1–43). John Wiley & Sons Inc.: Hoboken, NJ, USA.

Davenport, I. J., McNicol, I., Mitchard, E. T., Dargie, G., Suspense, I., Milongo, B., Bocko, Y. E., Hawthorne, D., Lawson, I., Baird, A. J., Page, S., & Lewis, S. L. (2020). First Evidence of Peat Domes in the Congo Basin using LiDAR from a Fixed-Wing Drone. *Remote Sensing*, *12*(2196), 1–13. https://doi.org/10.3390/rs12142196

De Cáceres, M., Jansen, F., & Dell, N. (2020). *Package "indicspecies": Relationship Between Species and Groups of Sites* (1.7.9). https://cran.r-project.org/web/packages/indicspecies/index.html

De Cáceres, M., Legendre, P., & Moretti, M. (2010). Improving indicator species analysis by combining groups of sites. *Oikos*, *119*(10), 1674–1684. https://doi.org/10.1111/j.1600-0706.2010.18334.x

De Grandi, G. F., Mayaux, P., Rosenqvist, A., Rauste, Y., Saatchi, S., Simard, M., Leysen, M., & ESA. (1998). Flooded forest mapping at regional scale in the Central Africa Congo river basin: First thematic results derived by {ERS-1} and {JERS-1} radar mosaics. *Second International Workshop on Retrieval of Bio- & Geo-Physical Parameters From Sar Data For Land Applications*, *441*(1), 253–260.

De Vos, B., Lettens, S., Muys, B., & Deckers, J. A. (2007). Walkley-Black analysis of forest soil organic carbon: Recovery, limitations and uncertainty. *Soil Use and Management*, *23*(3), 221–229. https://doi.org/10.1111/j.1475-2743.2007.00084.x

Deffontaines, B., & Chorowicz, J. (1991). Principles of drainage basin analysis from multisource data: Application to the structural analysis of the Zaire Basin. *Tectonophysics*, *194*(3), 237–263. https://doi.org/10.1016/0040-1951(91)90263-R

Delvaux, D., Maddaloni, F., Tesauro, M., & Braitenberg, C. (2021). The Congo Basin: Stratigraphy and subsurface structure defined by regional seismic reflection, refraction and well data. *Global and Planetary Change*, *198*(103407), 1–32.

https://doi.org/10.1016/j.gloplacha.2020.103407

Dettmann, U., & Bechtold, M. (2016). Deriving effective soil water retention characteristics from shallow water table fluctuations in peatlands. *Vadose Zone Journal*, *15*(10), 1–13. https://doi.org/10.2136/vzj2016.04.0029

Dommain, R., Couwenberg, J., & Joosten, H. (2010). Hydrological self-regulation of domed peatlands in south-east Asia and consequences for conservation and restoration. *Mires & Peat*, *6*(05), 1–17.

Dommain, René, Cobb, A. R., Joosten, H., Glaser, P. H., Chua, A. F. L., Gandois, L., Kai, F.-M., Noren, A., Salim, K. A., Su'ut, N. S. H., & Harvey, C. F. (2015). Forest dynamics and tip-up pools drive pulses of high carbon accumulation rates in a tropical peat dome in Borneo (Southeast Asia). *Journal of Geophysical Research: Biogeosciences*, *120*, 617–640. https://doi.org/10.1002/2014JG002796

Dommain, René, Couwenberg, J., & Joosten, H. (2011). Development and carbon sequestration of tropical peat domes in south-east Asia: Links to post-glacial sea-level changes and Holocene climate variability. *Quaternary Science Reviews*, *30*(7–8), 999–1010. https://doi.org/10.1016/j.quascirev.2011.01.018

Draper, F. C., Honorio Coronado, E. N., Roucoux, K. H., Lawson, I. T., Nigel, N. C., Paul, P. V., Phillips, O. L., Torres Montenegro, L. A., Valderrama Sandoval, E., Mesones, I., García-Villacorta, R., Arévalo, F. R. R., & Baker, T. R. (2018). Peatland forests are the least diverse tree communities documented in Amazonia, but contribute to high regional beta-diversity. *Ecography*, *41*(8), 1256–1269. https://doi.org/10.1111/ecog.03126

Draper, F. C., Roucoux, K. H., Lawson, I. T., Mitchard, E. T. A., Honorio Coronado, E. N., Lähteenoja, O., Montenegro, L. T., Sandoval, E. V., Zaráte, R., & Baker, T. R. (2014). The distribution and amount of carbon in the largest peatland complex in Amazonia. *Environmental Research Letters*, *9*(124017), 1–12. https://doi.org/10.1088/1748-9326/9/12/124017

Dufrêne, M., & Legendre, P. (1997). Species assemblages and indicator species: The need for a flexible asymmetrical approach. *Ecological Monographs*, *67*(3), 345–366. https://doi.org/10.2307/2963459

Dupré, B., Gaillardet, J., Rousseau, D., & Allegre, C. J. (1996). Major and trace elements of river-borne material: The Congo Basin. *Geochimica et Cosmochimica Acta*, *60*(8), 1301–1321.

Dyer, E. L. E., Jones, D. B. A., Nusbaumer, J., Li, H., Collins, O., Vettoretti, G., & Noone, D. (2017). Congo Basin precipitation: Assessing seasonality, regional interactions, and sources ofmoisture. *Journal of Geophysical Research*, *122*(13), 6882–6898. https://doi.org/10.1002/2016JD026240

Earthsight. (2018). *The Coming Storm: How Secrecy and Collusion in Industrial Agriculture Spell Disaster for the Congo Basin's Forests*.

ESA. (2021). *Sentinel-2 MSI*. European Space Agency. https://sentinels.copernicus.eu/web/sentinel/user-guides/sentinel-2-msi

Evrard, C. (1968). *Recherches écologiques sur le peuplement forestier des sols hydromorphes de la Cuvette centrale congloaise*. Institut pour l'étude agronomique du Congo belge (INEAC): Bruxelles, Belgique.

FAO-Unesco. (1974). *Soil Map of the World 1:5 000 000: Vol. Volume 1* (Issue Legend). Food and Agriculture Organization of the United Nations: Paris, France.

https://doi.org/10.1038/1791168c0

FAO. (2006). World reference base for soil resources 2006. In *World Soil Resources Reports No. 103*. Food & Agriculture Organization of the United Nations: Rome, Italy. https://doi.org/10.1017/S0014479706394902

Fayolle, A., Ngomanda, A., Mbasi, M., Barbier, N., Bocko, Y., Boyemba, F., Couteron, P., Fonton, N., Kamdem, N., Katembo, J., Kondaoule, H. J., Loumeto, J., Maïdou, H. M., Mankou, G., Mengui, T., Mofack, G. I., Moundounga, C., Moundounga, Q., Nguimbous, L., … Medjibe, V. P. (2018). A regional allometry for the Congo basin forests based on the largest ever destructive sampling. *Forest Ecology and Management*, *430*, 228–240. https://doi.org/10.1016/j.foreco.2018.07.030

Fick, S. E., & Hijmans, R. J. (2017). WorldClim 2: new 1-km spatial resolution climate surfaces for global land areas. *International Journal of Climatology*, *37*(12), 4302–4315. https://doi.org/10.1002/joc.5086

Flugel, T. J., Eckardt, F. D., & Cotterill, F. P. D. (2015). The Present Day Drainage Patterns of the Congo River System and their Neogene Evolution. In M. J. de Wit, F. Guillocheau, & M. C. J. de Wit (Eds.), *Geology and Resource Potential of the Congo Basin* (pp. 315–337). Springer: Berlin, Germany. https://doi.org/10.1007/978-3-642-29482-2

Gallego-Sala, A. V., Charman, D. J., Brewer, S., Page, S. E., Prentice, I. C., Friedlingstein, P., Moreton, S., Amesbury, M. J., Beilman, D. W., Björck, S., Blyakharchuk, T., Bochicchio, C., Booth, R. K., Bunbury, J., Camill, P., Carless, D., Chimner, R. A., Clifford, M., Cressey, E., … Zhao, Y. (2018). Latitudinal limits to the predicted increase of the peatland carbon sink with warming. *Nature Climate Change*, *8*(10), 907–913. https://doi.org/10.1038/s41558-018-0271-1

Garcin, Y., Deschamps, P., Ménot, G., De Saulieu, G., Schefuß, E., Sebag, D., Dupont, L. M., Oslisly, R., Brademann, B., Mbusnum, K. G., Onana, J. M., Ako, A. A., Epp, L. S., Tjallingii, R., Strecker, M. R., Brauer, A., & Sachse, D. (2018). Early anthropogenic impact on Western Central African rainforests 2,600 y ago. *Proceedings of the National Academy of Sciences*, *115*(13), 3261–3266. https://doi.org/10.1073/pnas.1715336115

Garcin, Y., Schefuß, E., Dargie, G. C., Hawthorne, D., Lawson, I., Sebag, D., Bocko, Y. E., Ifo, S. A., Mampouya, W. Y. E., Mbemba, M., Biddulph, G., Tyrrell, G., Young, D., Girkin, N., Vane, C., Adatte, T., Baird, A., Boom, A., Gulliver, P., … Bola, P. (2022). Hydroclimatic vulnerability of peat carbon in the central Congo Basin. *Nature*, *612*, 277-282. https://doi.org/10.1038/s41586-022-05389-3.

Garzanti, E., Vermeesch, P., Vezzoli, G., Andò, S., Botti, E., Limonta, M., Dinis, P., Hahn, A., Baudet, D., De Grave, J., & Yaya, N. K. (2019). Congo River sand and the equatorial quartz factory. *Earth-Science Reviews*, *197*(102918), 1–23. https://doi.org/10.1016/j.earscirev.2019.102918

Gaudino, S., Galas, C., Belli, M., Barbizzi, S., De Zorzi, P., Jaćimović, R., Jeran, Z., Pati, A., & Sansone, U. (2007). The role of different soil sample digestion methods on trace elements analysis: A comparison of ICP-MS and INAA measurement results. *Accreditation and Quality Assurance*, *12*(2), 84–93. https://doi.org/10.1007/s00769-006-0238-1

GFW. (2019a). *Democratic Republic of the Congo forest titles*. Global Forest Watch. https://data.globalforestwatch.org/datasets/535eb1335c4841b0bff272b78e2cc2f4_6

GFW. (2019b). *Democratic Republic of the Congo mining permits*. Global Forest Watch. https://data.globalforestwatch.org/datasets/3b4c0c91306c47abaec0c3fd46088242_5/

GFW. (2019c). *Republic of the Congo logging concessions*. Global Forest Watch. https://data.globalforestwatch.org/datasets/gfw::republic-of-the-congo-logging-concessions/

GFW. (2019d). *Republic of the Congo mining permits*. Global Forest Watch. https://data.globalforestwatch.org/datasets/84fbbcc10c9f47f890750dd42426cbd2_18/

GFW. (2019e). *Republic of the Congo oil palm concessions*. Global Forest Watch. https://data.globalforestwatch.org/datasets/f1fb5773903244abbe8282cae189863e_17/

Giresse, P., Maley, J., & Chepstow-Lusty, A. (2020). Understanding the 2500 yr BP rainforest crisis in West and Central Africa in the framework of the Late Holocene: Pluridisciplinary analysis and multi-archive reconstruction. *Global and Planetary Change*, *192*(103257), 1–19. https://doi.org/10.1016/j.gloplacha.2020.103257

Gond, V., Fayolle, A., Pennec, A., Cornu, G., Mayaux, P., Camberlin, P., Doumenge, C., Fauvet, N., & Gourlet-Fleury, S. (2013). Vegetation structure and greenness in Central Africa from Modis multi-temporal data. *Philosophical Transactions of the Royal Society B: Biological Sciences*, *368*(1625), 1–8. https://doi.org/10.1098/rstb.2012.0309

Goodman, R. C., Phillips, O. L., Del Castillo Torres, D., Freitas, L., Cortese, S. T., Monteagudo, A., & Baker, T. R. (2013). Amazon palm biomass and allometry. *Forest Ecology and Management*, *310*, 994–1004. https://doi.org/10.1016/j.foreco.2013.09.045

Gorelick, N., Hancher, M., Dixon, M., Ilyushchenko, S., Thau, D., & Moore, R. (2017). Google Earth Engine: Planetary-scale geospatial analysis for everyone. *Remote Sensing of Environment*, *202*, 18–27. https://doi.org/10.1016/j.rse.2017.06.031

Goudie, A. S. (2005). The drainage of Africa since the Cretaceous. *Geomorphology*, *67*, 437–456. https://doi.org/10.1016/j.geomorph.2004.11.008

Grubbs, F. E. (1969). Procedures for Detecting Outlying Observations in Samples. *Technometrics*, *11*(1), 1–21. https://doi.org/https://doi.org/10.2307%2F1266761

Guillocheau, F., Chelalou, R., Linol, B., Dauteuil, O., Robin, C., Mvondo, F., Callec, Y., & Colin, J.-P. (2015). Cenozoic Landscape Evolution in and Around the Congo Basin: Constraints from Sediments and Planation Surfaces. In M. J. de Wit, F. Guillocheau, & M. C. J. de Wit (Eds.), *Geology and Resource Potential of the Congo Basin*. Springer: Berlin, Germany. https://doi.org/10.1007/978-3-642-29482-2

Gumbricht, T., Roman-Cuesta, R. M., Verchot, L., Herold, M., Wittmann, F., Householder, E., Herold, N., & Murdiyarso, D. (2017). An expert system model for mapping tropical wetlands and peatlands reveals South America as the largest contributor. *Global Change Biology*, *23*(9), 3581–3599. https://doi.org/10.1111/gcb.13689

Hagen, O., Skeels, A., Onstein, R., Jetz, W., & Pellissier, L. (2021). Earth history events shaped the evolution of uneven biodiversity across tropical moist forests. *Proceedings of the National Academy of Sciences*, *118*(40), 1–11. https://doi.org/10.1073/pnas.2026347118

Hardy, O. J., Born, C., Budde, K., Dainou, K., Dauby, G., Duminil, J., Ewedje, E., Gomez, C., Heuertz, M., Koffi, G. K., Lowe, A. J., Micheneau, C., Ndiade-Bourobou, D., Pineiro, R., & Poncet, V. (2013). Comparative phylogeography of African rain forest trees: A review of genetic signatures of vegetation history in the Guineo-Congolian region. *Comptes Rendus Geoscience*, *345*(7–8), 284–296. https://doi.org/10.1016/j.crte.2013.05.001

Harris, D. J., Ndolo Ebika, S. T., Sanz, C. M., Madingou, M. P. N., & Morgan, D. B. (2021a). Large trees in tropical rain forests require big plots. *Plants People Planet*, *3*(3), 282–294.

https://doi.org/10.1002/ppp3.10194

Harris, N. L., Gibbs, D. A., Baccini, A., Birdsey, R. A., de Bruin, S., Farina, M., Fatoyinbo, L., Hansen, M. C., Herold, M., Houghton, R. A., Potapov, P. V., Suarez, D. R., Roman-Cuesta, R. M., Saatchi, S. S., Slay, C. M., Turubanova, S. A., & Tyukavina, A. (2021b). Global maps of twenty-first century forest carbon fluxes. *Nature Climate Change*, *11*(3), 234–240. https://doi.org/10.1038/s41558-020-00976-6

Harrison, I. J., Brummett, R., & Stiassny, M. L. J. (2016). The Congo River Basin. In C. M. Finlayson, M. Everard, K. Irvine, R. McInnes, B. Middleton, A. van Dam, & N. . Davidson (Eds.), *The Wetland Book* (pp. 1–19). Springer: Dordrecht, the Netherlands. https://doi.org/10.1007/978-94-007-6173-5

Hastie, A., Honorio Coronado, E. N., Reyna, J., Mitchard, E. T. A., Åkesson, C. M., Baker, T. R., Cole, L. E. S., Oroche, C. J. C., Dargie, G., Dávila, N., De Grandi, E. C., Del Águila, J., Del Castillo Torres, D., De La Cruz Paiva, R., Draper, F. C., Flores, G., Grández, J., Hergoualc'h, K., Householder, J. E., … Lawson, I. T. (2022). Risks to carbon storage from land-use change revealed by peat thickness maps of Peru. *Nature Geoscience*, *15*, 369–374. https://doi.org/10.1038/s41561-022-00923-4

Hawker, L., Neal, J., & Bates, P. (2019). Accuracy assessment of the TanDEM-X 90 Digital Elevation Model for selected floodplain sites. *Remote Sensing of Environment*, *232*(July). https://doi.org/10.1016/j.rse.2019.111319

Hawker, L., Rougier, J., Neal, J., Bates, P., Archer, L., & Yamazaki, D. (2018). Implications of Simulating Global Digital Elevation Models for Flood Inundation Studies. *Water Resources Research*, *54*, 7910–7928. https://doi.org/10.1029/2018WR023279

Hawker, L., Uhe, P., Paulo, L., Sosa, J., Savage, J., Sampson, C., & Neal, J. (2022). A 30 m global map of elevation with forests and buildings removed. *Environmental Research Letters*, *17*(024016), 1–11. https://doi.org/10.1088/1748-9326/ac4d4f

Heaton, T. J., Blaauw, M., Blackwell, P. G., Bronk Ramsey, C., Reimer, P. J., & Scott, E. M. (2020). The IntCal20 Approach to Radiocarbon Calibration Curve Construction: A New Methodology Using Bayesian Splines and Errors-in-Variables. *Radiocarbon*, *62*(4), 821–863. https://doi.org/10.1017/RDC.2020.46

Heiri, O., Lotter, A. F., & Lemcke, G. (2001). Loss on ignition as a method for estimating organic and carbonate content in sediments: Reproducibility and comparability of results. *Journal of Paleolimnology*, *25*(1), 101–110. https://doi.org/10.1023/A:1008119611481

Hirano, T., Segah, H., Harada, T., Limin, S., June, T., Hirata, R., & Osaki, M. (2007). Carbon dioxide balance of a tropical peat swamp forest in Kalimantan, Indonesia. *Global Change Biology*, *13*(2), 412–425. https://doi.org/10.1111/j.1365-2486.2006.01301.x

Hirano, T., Segah, H., Kusin, K., Limin, S., Takahashi, H., & Osaki, M. (2012). Effects of disturbances on the carbon balance of tropical peat swamp forests. *Global Change Biology*, *18*, 3410–3422. https://doi.org/10.1111/j.1365-2486.2012.02793.x

Hirt, C. (2018). Artefact detection in global digital elevation models (DEMs): The Maximum Slope Approach and its application for complete screening of the SRTM v4.1 and MERIT DEMs. *Remote Sensing of Environment*, *207*, 27–41. https://doi.org/10.1016/j.rse.2017.12.037

Hodgkins, S. B., Richardson, C. J., Dommain, R., Wang, H., Glaser, P. H., Verbeke, B., Winkler, B. R., Cobb, A. R., Rich, V. I., Missilmani, M., Flanagan, N., Ho, M., Hoyt, A. M., Harvey, C. F.,

Vining, S. R., Hough, M. A., Moore, T. R., Richard, P. J. H., De La Cruz, F. B., … Chanton, J. P. (2018). Tropical peatland carbon storage linked to global latitudinal trends in peat recalcitrance. *Nature Communications*, *9*(1), 1–13. https://doi.org/10.1038/s41467-018-06050-2

Hogg, A. G., Heaton, T. J., Hua, Q., Palmer, J. G., Turney, C. S. M., Southon, J., Bayliss, A., Blackwell, P. G., Boswijk, G., Bronk Ramsey, C., Pearson, C., Petchey, F., Reimer, P., Reimer, R., & Wacker, L. (2020). SHCal20 Southern Hemisphere Calibration, 0-55,000 Years Cal BP. *Radiocarbon*, *62*(4), 759–778. https://doi.org/10.1017/RDC.2020.59

Honorio Coronado, E. N., Hastie, A., Reyna, J., Flores, G., Gr, J., Aguila, J. Del, Aguila, M. Del, Del, D., Torres, C., Ramírez, E., Ríos, M., Ríos, S., Rodriguez, L., & Roucoux, K. H. (2021). Intensive field sampling increases the known extent of carbon-rich Amazonian peatland pole forests. *Environmental Research Letters*, *16*(074048), 1–15.

Hooijer, A., Page, S., Canadell, J. G., Silvius, M., Kwadijk, J., Wösten, H., & Jauhiainen, J. (2010). Current and future CO2 emissions from drained peatlands in Southeast Asia. *Biogeosciences*, *7*(5), 1505–1514. https://doi.org/10.5194/bg-7-1505-2010

Hooijer, Aljosja. (2006). Tropical peatlands in south-east Asia. In Hakan Rydin & J. K. Jeglum (Eds.), *The Biology of Peatlands* (1st ed., pp. 233–238). Oxford University Press: Oxford, UK.

Householder, J. E., Janovec, J. P., Tobler, M. W., Page, S., & Lähteenoja, O. (2012). Peatlands of the madre de dios river of peru: Distribution, geomorphology, and habitat diversity. *Wetlands*, *32*(2), 359–368. https://doi.org/10.1007/s13157-012-0271-2

Hua, W., Zhou, L., Chen, H., Nicholson, S. E., Raghavendra, A., & Jiang, Y. (2016). Possible causes of the Central Equatorial African long-term drought. *Environmental Research Letters*, *11*(12). https://doi.org/10.1088/1748-9326/11/12/124002

Hubau, W., Lewis, S. L., Phillips, O. L., Affum-Baffoe, K., Beeckman, H., Cuní-Sanchez, A., Daniels, A. K., Ewango, C. E. N., Fauset, S., Mukinzi, J. M., Sheil, D., Sonké, B., & Sullivan, M. J. P. (2020). Asynchronous carbon sink saturation in African and Amazonian tropical forests. *Nature*, *579*(7797), 80–87. https://doi.org/10.1038/s41586-020-2035-0

Hughes, R. H., & Hughes, J. S. (1992). *A Directory of African Wetlands*. IUCN, Gland, Switzerland and Cambridge, UK; UNEP, Nairobi, Kenya; and WCMC, Cambridge, UK.

Huijnen, V., Wooster, M. J., Kaiser, J. W., Gaveau, D. L. A., Flemming, J., Parrington, M., Inness, A., Murdiyarso, D., Main, B., & Van Weele, M. (2016). Fire carbon emissions over maritime southeast Asia in 2015 largest since 1997. *Scientific Reports*, *6*(26886), 1–8. https://doi.org/10.1038/srep26886

Hüllermeier, E., & Waegeman, W. (2021). Aleatoric and Epistemic Uncertainty in Machine Learning: An Introduction to Concepts and Methods. *Machine Learning*, *110*(3). https://doi.org/https://doi.org/10.1007/s10994-021-05946-3

Ifo, S. A., Binsangou, S., Ibocko Ngala, L., Madingou, M., & Cuni-Sanchez, A. (2018). Seasonally flooded, and terra firme in northern Congo: Insights on their structure, diversity and biomass. *African Journal of Ecology*, *57*(1), 92–103. https://doi.org/10.1111/aje.12555

Imbole, I., Monkengo-mo-Mpenge, I., Boika, M., Nsala, M., Mulumba, K., & Yamba-Yamba, M. (2016). Analyse de la pluviosité annuelle dans la Réserve Scientifique de Mabali de 1980 à 2012. *Revue Congolaise Des Sciences*, *2*(1), 70–85.

Immirzi, C. P., Maltby, E., & Clymo, R. S. (1992). *The global status of peatlands and their role in*

carbon cycling. A report for Friends of the Earth by the Wetland Ecosystem Research Group, Department of Geography, University of Exeter.

Inogwabini, B.-I., Nzala, A. B., & Bokika, J. C. (2013). People and Bonobos in the Southern Lake Tumba Landscape, Democratic Republic of Congo. *American Journal of Human Ecology*, *2*(2), 44–53. https://doi.org/10.11634/216796221302309

Inogwabini, B. I. (2014). Bushmeat, over-fishing and covariates explaining fish abundance declines in the Central Congo Basin. *Environmental Biology of Fishes*, *97*(7), 787–796. https://doi.org/10.1007/s10641-013-0179-6

Inogwabini, B. I., Sandokan, B. M., & Ndunda, M. (2006). A dramatic decline in rainfall regime in the Congo Basin: Evidence from a thirty-four year data set from the Mabali Scientific Research Centre, Democratic Republic of Congo. *International Journal of Meteorology*, *31*(312), 278–285.

IPCC. (2014). *2013 Supplement to the 2006 IPCC Guidelines for National Greenhouse Gas Inventories: Wetlands* (T. Hiraishi, T. Krug, K. Tanabe, N. Srivastava, J. Baasansuren, M. Fukuda, & T. G. Troxler (Eds.)). Intergovernmental Panel on Climate Change (IPCC): Geneva, Switzerland.

Ise, T., Dunn, A. L., Wofsy, S. C., & Moorcroft, P. R. (2008). High sensitivity of peat decomposition to climate change through water-table feedback. *Nature Geoscience*, *1*(11), 763–766. https://doi.org/10.1038/ngeo331

Islam, M. A., Thenkabail, P. S., Kulawardhana, R. W., Alankara, R., Gunasinghe, S., Edussriya, C., & Gunawardana, A. (2008). Semi-automated methods for mapping wetlands using Landsat ETM+ and SRTM data. *International Journal of Remote Sensing*, *29*(24), 7077–7106. https://doi.org/10.1080/01431160802235878

Jaenicke, J., Rieley, J. O., Mott, C., Kimman, P., & Siegert, F. (2008). Determination of the amount of carbon stored in Indonesian peatlands. *Geoderma*, *147*(3–4), 151–158. https://doi.org/10.1016/j.geoderma.2008.08.008

James, R., Washington, R., & Rowell, D. P. (2013). Implications of global warming for the climate of African rainforests. *Philosophical Transactions of the Royal Society B: Biological Sciences*, *368*(1625), 20120298. https://doi.org/10.1098/rstb.2012.0298

JAXA/METI. (2009). *ALOS PALSAR L1.5*. Japan Aerospace Exploration Agency / Ministry of Economy, Trade, and Industry of Japan. https://asf.alaska.edu

JAXA. (1997). *Global PALSAR-2/PALSAR/JERS-1 Mosaics*. Japan Aerospace Exploration Agency / Ministry of Economy, Trade, and Industry of Japan. https://www.eorc.jaxa.jp/ALOS/en/dataset/fnf_e.htm

Jiang, Y., Zhou, L., Tucker, C. J., Raghavendra, A., Hua, W., Liu, Y. Y., & Joiner, J. (2019). Widespread increase of boreal summer dry season length over the Congo rainforest. *Nature Climate Change*, *9*(8), 617–622. https://doi.org/10.1038/s41558-019-0512-y

Joosten, H. (2016). Changing Paradigms in the History of Tropical Peatland Research. In M. Osaki & N. Tsuji (Eds.), *Tropical Peatland Ecosystems* (pp. 33–48). Springer Japan: Tokyo, Japan.

Joosten, H., & Clarke, D. (2002). *Wise Use of Mires and Peatlands: Background and Principles Including a Framework for Decision-Making*. International Mire Conservation Group and International Peat Society.

Joosten, H., Tapio-Biström, M.-L., & Tol, S. (2012). Peatlands - guidance for climate change mitigation through conservation, rehabilitation and sustainable use. In *Mitigation of Climate Change in Agriculture (MICCA) Programme series 5* (2nd ed.). FAO and Wetlands International: Rome, Italy.

Junk, W. J., Piedade, M. T. F., Schöngart, J., Cohn-Haft, M., Adeney, J. M., & Wittmann, F. (2011). A classification of major naturally-occurring Amazonian lowland wetlands. *Wetlands*, *31*(4), 623–640. https://doi.org/10.1007/s13157-011-0190-7

Kaat, A. (2009). *Factbook for UNFCCC policies on peat carbon emissions*. Wetlands International: Wageningen, the Netherlands.

Kassambara, A., & Mundt, F. (2020). *Package "factoextra": Extract and Visualize the Results of Multivariate Data Analyses* (1.0.7). https://cran.r-project.org/web/packages/factoextra/index.html

Kelly, T. J., Baird, A. J., Roucoux, K. H., Baker, T. R., Honorio Coronado, E. N., Ríos, M., & Lawson, I. T. (2014). The high hydraulic conductivity of three wooded tropical peat swamps in northeast Peru: Measurements and implications for hydrological function. *Hydrological Processes*, *28*(9), 3373–3387. https://doi.org/10.1002/hyp.9884

Kelly, T. J., Lawson, I. T., Roucoux, K. H., Baker, T. R., & Honorio Coronado, E. N. (2020). Patterns and drivers of development in a west Amazonian peatland during the late Holocene. *Quaternary Science Reviews*, *230*(106168), 1–18. https://doi.org/10.1016/j.quascirev.2020.106168

Kenfack, D. (2011). A synoptic revision of Carapa (Meliaceae). *Harvard Papers in Botany*, *16*(2), 171–231.

Kiahtipes, C. A., & Schefuß, E. (2019). Congo Basin peatlands as a baseline record for past hydrology and climate. *Earth and Space Science Open Archive*, *[W-68]*. https://doi.org/10.1002/essoar.10500726.1

Kiely, L., Spracklen, D. V., Arnold, S. R., Papargyropoulou, E., Conibear, L., Wiedinmyer, C., Knote, C., & Adrianto, H. A. (2021). Assessing costs of Indonesian fires and the benefits of restoring peatland. *Nature Communications*, *12*(1), 1–11. https://doi.org/10.1038/s41467-021-27353-x

Kiely, Laura, Spracklen, D. V., Wiedinmyer, C., Conibear, L., Reddington, C. L., Arnold, S. R., Knote, C., Khan, M. F., Latif, M. T., Syaufina, L., & Adrianto, H. A. (2020). Air quality and health impacts of vegetation and peat fires in Equatorial Asia during 2004-2015. *Environmental Research Letters*, *15*(9), 1–12. https://doi.org/10.1088/1748-9326/ab9a6c

Kim, D., Lee, H., Laraque, A., Tshimanga, R. M., Yuan, T., Jung, H. C., Beighley, E., & Chang, C. H. (2017). Mapping spatio-temporal water level variations over the central congo river using palsar scansar and envisat altimetry data. *International Journal of Remote Sensing*, *38*(23), 7021–7040. https://doi.org/10.1080/01431161.2017.1371867

Klingenfuß, C., Roßkopf, N., Walter, J., Heller, C., & Zeitz, J. (2014). Soil organic matter to soil organic carbon ratios of peatland soil substrates. *Geoderma*, *235–236*, 410–417. https://doi.org/10.1016/j.geoderma.2014.07.010

Korhola, A., Tolonen, K., Turunen, J., & Jungner, H. (1995). Estimating long-term carbon accumulation rates in boreal peatlands by radiocarbon dating. *Radiocarbon*, *37*(2), 575–584. https://doi.org/10.1017/S0033822200031064

Kurnianto, S., Warren, M., Talbot, J., Kauffman, B., Murdiyarso, D., & Frolking, S. (2015).

Carbon accumulation of tropical peatlands over millennia: A modeling approach. *Global Change Biology*, *21*(1), 431–444. https://doi.org/10.1111/gcb.12672

Lähteenoja, O., & Page, S. (2011). High diversity of tropical peatland ecosystem types in the Pastaza-Maraón basin, Peruvian Amazonia. *Journal of Geophysical Research*, *116*(G02025), 14. https://doi.org/10.1029/2010JG001508

Lähteenoja, O., Reátegui, Y. R., Räsänen, M., Torres, D. D. C., Oinonen, M., & Page, S. (2011). The large Amazonian peatland carbon sink in the subsiding Pastaza-Marañón foreland basin, Peru. *Global Change Biology*, *18*(1), 164–178. https://doi.org/10.1111/j.1365-2486.2011.02504.x

Lähteenoja, O., Ruokolainen, K., Schulman, L., & Alvarez, J. (2009a). Amazonian floodplains harbour minerotrophic and ombrotrophic peatlands. *Catena*, *79*(2), 140–145. https://doi.org/10.1016/j.catena.2009.06.006

Lähteenoja, O., Ruokolainen, K., Schulman, L., & Oinonen, M. (2009b). Amazonian peatlands: An ignored C sink and potential source. *Global Change Biology*, *15*, 2311–2320. https://doi.org/10.1111/j.1365-2486.2009.01920.x

Lampela, M., Jauhiainen, J., Kämäri, I., Koskinen, M., Tanhuanpää, T., Valkeapää, A., & Vasander, H. (2016). Ground surface microtopography and vegetation patterns in a tropical peat swamp forest. *Catena*, *139*, 127–136. https://doi.org/10.1016/j.catena.2015.12.016

Lampela, M., Jauhiainen, J., & Vasander, H. (2014). Surface peat structure and chemistry in a tropical peat swamp forest. *Plant and Soil*, *382*(1–2), 329–347. https://doi.org/10.1007/s11104-014-2187-5

Laraque, A., Bricquet, J. P., Pandi, A., & Olivry, J. C. (2009). A review of material transport by the Congo River and its tributaries. *Hydrological Processes*, *23*(22), 3216–3224. https://doi.org/10.1002/hyp.7395

Laraque, A., Mahé, G., Orange, D., & Marieu, B. (2001). Spatiotemporal variations in hydrological regimes within Central Africa during the XXth century. *Journal of Hydrology*, *245*(1–4), 104–117. https://doi.org/10.1016/S0022-1694(01)00340-7

Laraque, A., N'kaya, G. D. M., Orange, D., Tshimanga, R., Tshitenge, J. M., Mahé, G., Nguimalet, C. R., Trigg, M. A., Yepez, S., & Gulemvuga, G. (2020). Recent budget of hydroclimatology and hydrosedimentology of the congo river in central Africa. *Water*, *12*(2613), 1–36. https://doi.org/10.3390/w12092613

Laraque, A., Pouyaud, B., Rocchia, R., Robin, E., Chaffaut, I., Moutsambote, J. M., Maziezoula, B., Censier, C., Albouy, Y., Elenga, H., Etcheber, H., Delaune, M., Sondag, F., & Gasse, F. (1998a). Origin and function of a closed depression in equatorial humid zones: The Lake Telé in North Congo. *Journal of Hydrology*, *207*(3–4), 236–253. https://doi.org/10.1016/S0022-1694(98)00137-1

Lawson, I. T., Kelly, T. J., Aplin, P., Boom, A., Dargie, G., Draper, F. C. H., Hassan, P. N. Z. B. P., Hoyos-Santillan, J., Kaduk, J., Large, D., Murphy, W., Page, S. E., Roucoux, K. H., Sjögersten, S., Tansey, K., Waldram, M., Wedeux, B. M. M., & Wheeler, J. (2015). Improving estimates of tropical peatland area, carbon storage, and greenhouse gas fluxes. *Wetlands Ecology and Management*, *23*(3), 327–346. https://doi.org/10.1007/s11273-014-9402-2

Lawson, Ian T., Jones, T. D., Kelly, T. J., Coronado, E. N. H., & Roucoux, K. H. (2014). The

Geochemistry of Amazonian Peats. *Wetlands*, *34*(5), 905–915. https://doi.org/10.1007/s13157-014-0552-z

Lebrun, J. P. A., & Gilbert, G. (1954). *Une classification écologique des forêts du Congo*. Institut national pour l'étude agronomique du Congo belge (INEAC): Bruxelles, Belgique.

Lee, H., Beighley, R. E., Alsdorf, D., Jung, H. C., Shum, C. K., Duan, J., Guo, J., Yamazaki, D., & Andreadis, K. (2011). Characterization of terrestrial water dynamics in the Congo Basin using GRACE and satellite radar altimetry. *Remote Sensing of Environment*, *115*(12), 3530–3538. https://doi.org/10.1016/j.rse.2011.08.015

Lee, H., Yuan, T., Jung, H. C., & Beighley, E. (2015). Mapping wetland water depths over the central Congo Basin using PALSAR ScanSAR, Envisat altimetry, and MODIS VCF data. *Remote Sensing of Environment*, *159*, 70–79. https://doi.org/10.1016/j.rse.2014.11.030

Legendre, P. (1993). Spatial Autocorrelation: Trouble or New Paradigm? *Ecology*, *74*(6), 1659–1673. https://doi.org/https://doi.org/10.2307/1939924

Lehner, B., & Döll, P. (2004). Development and validation of a global database of lakes, reservoirs and wetlands. *Journal of Hydrology*, *296*(1–4), 1–22. https://doi.org/10.1016/j.jhydrol.2004.03.028

Lehner, B., Verdin, K., & Jarvis, A. (2008). New Global Hydrography Derived From Spaceborne Elevation Data. *Eos, Transactions of the American Geophysical Union*, *89*(10), 93–94. https://doi.org/10.1029/2008EO100001

Leifeld, J., & Menichetti, L. (2018). The underappreciated potential of peatlands in global climate change mitigation strategies. *Nature Communications*, *9*(1071), 1–7. https://doi.org/10.1038/s41467-018-03406-6

Lewis, C., Albertson, J., Xu, X., & Kiely, G. (2012). Spatial variability of hydraulic conductivity and bulk density along a blanket peatland hillslope. *Hydrological Processes*, *26*, 1527–1537. https://doi.org/10.1002/hyp.8252

Lewis, S. L., Sonke, B., Sunderland, T., Begne, S. K., Lopez-Gonzalez, G., van der Heijden, G. M. F., Phillips, O. L., Affum-Baffoe, K., Baker, T. R., Banin, L., Bastin, J.-F., Beeckman, H., Boeckx, P., Bogaert, J., De Canniere, C., Chezeaux, E., Clark, C. J., Collins, M., Djagbletey, G., … Zemagho, L. (2013). Above-ground biomass and structure of 260 African tropical forests. *Philosophical Transactions of the Royal Society B: Biological Sciences*, *368*(1625), 1–14. https://doi.org/10.1098/rstb.2012.0295

Lindersson, S., Brandimarte, L., Mård, J., & Di Baldassarre, G. (2020). A review of freely accessible global datasets for the study of floods, droughts and their interactions with human societies. *WIREs Water*, *7*(1424), 1–20. https://doi.org/10.1002/wat2.1424

Liski, J., Nissinen, a, Erhard, M., & Taskinen, O. (2003). Climatic effects on litter decomposition from arctic tundra to tropical rainforest. *Global Change Biology*, *9*(4), 575–584. https://doi.org/10.1046/j.1365-2486.2003.00605.x

Liu, H., & Lennartz, B. (2019). Hydraulic properties of peat soils along a bulk density gradient—A meta study. *Hydrological Processes*, *33*(1), 101–114. https://doi.org/10.1002/hyp.13314

Loisel, J., Gallego-Sala, A. V., Amesbury, M. J., Magnan, G., Anshari, G., Beilman, D. W., Benavides, J. C., Blewett, J., Camill, P., Charman, D. J., Chawchai, S., Hedgpeth, A., Kleinen, T., Korhola, A., Large, D., Mansilla, C. A., Müller, J., van Bellen, S., West, J. B., … Wu, J. (2021). Expert assessment of future vulnerability of the global peatland carbon

sink. *Nature Climate Change*, *11*, 70–77. https://doi.org/10.1038/s41558-020-00944-0

Loisel, Julie, Yu, Z., Beilman, D. W., Camill, P., Alm, J., Amesbury, M. J., Anderson, D., Andersson, S., Bochicchio, C., Barber, K., Belyea, L. R., Bunbury, J., Chambers, F. M., Charman, D. J., De Vleeschouwer, F., Fiałkiewicz-Kozieł, B., Finkelstein, S. A., Gałka, M., Garneau, M., … Zhou, W. (2014). A database and synthesis of northern peatland soil properties and Holocene carbon and nitrogen accumulation. *The Holocene*, *24*(9), 1028–1042. https://doi.org/10.1177/0959683614538073

Lopes, A., Touzi, R., & Nezry, E. (1990). Adaptive Speckle Filters and Scene Heterogeneity. *IEEE Transactions on Geoscience and Remote Sensing*, *28*(6), 992–1000. https://doi.org/10.1109/36.62623

Lopez-Gonzalez, G., Lewis, S. L., Burkitt, M., Baker, T. R., & Phillips, O. L. (2009). *ForestPlots.net Database*. www.forestplots.net

Lopez-Gonzalez, G., Lewis, S. L., Burkitt, M., & Phillips, O. L. (2011). ForestPlots.net: A web application and research tool to manage and analyse tropical forest plot data. *Journal of Vegetation Science*, *22*(4), 610–613. https://doi.org/10.1111/j.1654-1103.2011.01312.x

Lopez, O. R., & Kursar, T. A. (2003). Does flood tolerance explain tree species distribution in tropical seasonally flooded habitats? *Oecologia*, *136*(2), 193–204. https://doi.org/10.1007/s00442-003-1259-7

Lv, M., Xu, Z., Yang, Z. L., Lu, H., & Lv, M. (2021). A Comprehensive Review of Specific Yield in Land Surface and Groundwater Studies. *Journal of Advances in Modeling Earth Systems*, *13*(2), 1–24. https://doi.org/10.1029/2020MS002270

Lyons, M. B., Keith, D. A., Phinn, S. R., Mason, T. J., & Elith, J. (2018). A comparison of resampling methods for remote sensing classification and accuracy assessment. *Remote Sensing of Environment*, *208*, 145–153. https://doi.org/10.1016/j.rse.2018.02.026

Mainali, K. P., Slud, E., Singer, M. C., & Fagan, W. F. (2022). A better index for analysis of co-occurrence and similarity. *Science Advances*, *8*(4), 9204.

Maisels, F., Strindberg, S., Blake, S., Wittemyer, G., Hart, J., Williamson, E. A., Aba'a, R., Abitsi, G., Ambahe, R. D., Amsini, F., Bakabana, P. C., Hicks, T. C., Bayogo, R. E., Bechem, M., Beyers, R. L., Bezangoye, A. N., Boundja, P., Bout, N., Akou, M. E., … Warren, Y. (2013). Devastating Decline of Forest Elephants in Central Africa. *PLoS ONE*, *8*(3), 1–13. https://doi.org/10.1371/journal.pone.0059469

Maley, J., Doumenge, C., Giresse, P., Mahé, G., Philippon, N., Hubau, W., Lokonda, M. O., Tshibamba, J. M., & Chepstow-Lusty, A. (2018). Late Holocene forest contraction and fragmentation in central Africa. *Quaternary Research*, *89*(1), 43–59. https://doi.org/10.1017/qua.2017.97

Malhi, Y., & Wright, J. (2004). Spatial patterns and recent trends in the climate of tropical rainforest regions. *Philosophical Transactions of the Royal Society B: Biological Sciences*, *359*(1443), 311–329. https://doi.org/10.1098/rstb.2003.1433

Manavalan, R. (2018). Review of synthetic aperture radar frequency, polarization, and incidence angle data for mapping the inundated regions. *Journal of Applied Remote Sensing*, *12*(02), 1. https://doi.org/10.1117/1.jrs.12.021501

Map for Environment. (2014). *DRC Agriculture Plantations*. DIAF/WRI Working Layer. https://mapforenvironment.org/layer/info/80/#5.24/-1.263/19.467

Martinez Arbizu, P. (2020). *Package "pairwiseAdonis": Pairwise multilevel comparison using adonis* (0.4). https://github.com/pmartinezarbizu/pairwiseAdonis

Martínez Cortizas, A., García-Rodeja Gayoso, E., & Weiss, D. (2002). Peat bog archives of atmospheric metal deposition. *Science of the Total Environment*, *292*(1–2), 1–5. https://doi.org/10.1016/S0048-9697(02)00024-4

Martinis, S., & Rieke, C. (2015). Backscatter analysis using multi-temporal and multi-frequency SAR data in the context of flood mapping at River Saale, Germany. *Remote Sensing*, *7*(6), 7732–7752. https://doi.org/10.3390/rs70607732

Master, S. (2010). Lac Télé structure, Republic of Congo: Geological setting of a cryptozoological and biodiversity hotspot, and evidence against an impact origin. *Journal of African Earth Sciences*, *58*(4), 667–679. https://doi.org/10.1016/j.jafrearsci.2009.07.017

Maxwell, A. E., Warner, T. A., Fang, F., Maxwell, A. E., Warner, T. A., Implementation, F. F., Maxwell, A. E., & Warner, T. A. (2018). Implementation of machine-learning classification in remote sensing: an applied review. *International Journal of Remote Sensing*, *39*(9), 2784–2817. https://doi.org/10.1080/01431161.2018.1433343

Mayaux, P., De Grandi, G. F., Rauste, Y., Simard, M., & Saatchi, S. (2002). Large-scale vegetation maps derived from the combined L-band GRFM and C-band CAMP wide area radar mosaics of Central Africa. *International Journal of Remote Sensing*, *23*(7), 1261–1282. https://doi.org/10.1080/01431160110092894

McLennan, S. M. (2001). Relationships between the trace element composition of sedimentary rocks and upper continental crust. *Geochemistry, Geophysics, Geosystems*, *2*, 1–24. https://doi.org/10.1038/scientificamerican0983-130

Medina-Lopez, E. (2020). Machine learning and the end of atmospheric corrections: A comparison between high-resolution sea surface salinity in coastal areas from top and bottom of atmosphere Sentinel-2 imagery. *Remote Sensing*, *12*(18), 1–21. https://doi.org/10.3390/RS12182924

Meyer, H., & Pebesma, E. (2021). Predicting into unknown space? Estimating the area of applicability of spatial prediction models. *Methods in Ecology and Evolution*, *12*(9), 1620–1633. https://doi.org/10.1111/2041-210X.13650

Meyer, H., & Pebesma, E. (2022). Machine learning-based global maps of ecological variables and the challenge of assessing them. *Nature Communications*, *13*(1), 1–4. https://doi.org/10.1038/s41467-022-29838-9

Meyer, H., Reudenbach, C., Wöllauer, S., & Nauss, T. (2019). Importance of spatial predictor variable selection in machine learning applications – Moving from data reproduction to spatial prediction. *Ecological Modelling*, *411*(108815), 1–11. https://doi.org/10.1016/j.ecolmodel.2019.108815

Mezbahuddin, M., Grant, R. F., & Hirano, T. (2015). How hydrology determines seasonal and interannual variations in water table depth, surface energy exchange, and water stress in a tropical peatland: Modeling versus measurements. *Journal of Geophysical Research: Biogeosciences*, *120*(11), 2132–2157. https://doi.org/10.1002/2015JG003005

Miettinen, J., Hooijer, A., Vernimmen, R., Liew, S. C., & Page, S. E. (2017). From carbon sink to carbon source: Extensive peat oxidation in insular Southeast Asia since 1990. *Environmental Research Letters*, *12*(2). https://doi.org/10.1088/1748-9326/aa5b6f

Miles, L., Ravilious, C., García-Rangel, S., de Lamo, X., Dargie, G., & Lewis, S. (2017). *Carbon, biodiversity and land-use in the Central Congo Basin Peatlands*. United Nations Environment Programme (UNEP): Nairobi, Kenya.

Minasny, B., Berglund, Ö., Connolly, J., Hedley, C., de Vries, F., Gimona, A., Kempen, B., Kidd, D., Lilja, H., Malone, B., McBratney, A., Roudier, P., O'Rourke, S., Rudiyanto, Padarian, J., Poggio, L., ten Caten, A., Thompson, D., Tuve, C., & Widyatmanti, W. (2019). Digital mapping of peatlands – A critical review. *Earth-Science Reviews*, *196*(102870), 1–38. https://doi.org/10.1016/j.earscirev.2019.05.014

Mitsch, W. J., Nahlik, A., Wolski, P., Bernal, B., Zhang, L., & Ramberg, L. (2010). Tropical wetlands: Seasonal hydrologic pulsing, carbon sequestration, and methane emissions. *Wetlands Ecology and Management*, *18*(5), 573–586. https://doi.org/10.1007/s11273-009-9164-4

Molliex, S., Kettner, A. J., Laurent, D., Droz, L., Marsset, T., Laraque, A., Rabineau, M., & Moukandi N'Kaya, G. D. (2019). Simulating sediment supply from the Congo watershed over the last 155 ka. *Quaternary Science Reviews*, *203*, 38–55. https://doi.org/10.1016/j.quascirev.2018.11.001

Momo, S. T., Ploton, P., Martin-Ducup, O., Lehnebach, R., Fortunel, C., Sagang, L. B. T., Boyemba, F., Couteron, P., Fayolle, A., Libalah, M., Loumeto, J., Medjibe, V., Ngomanda, A., Obiang, D., Pélissier, R., Rossi, V., Yongo, O., Bocko, Y., Fonton, N., … Barbier, N. (2020). Leveraging Signatures of Plant Functional Strategies in Wood Density Profiles of African Trees to Correct Mass Estimations From Terrestrial Laser Data. *Scientific Reports*, *10*(1), 1–11. https://doi.org/10.1038/s41598-020-58733-w

Moore, S., Evans, C. D., Page, S. E., Garnett, M. H., Jones, T. G., Freeman, C., Hooijer, A., Wiltshire, A. J., Limin, S. H., & Gauci, V. (2013). Deep instability of deforested tropical peatlands revealed by fluvial organic carbon fluxes. *Nature*, *493*, 660–663. https://doi.org/10.1038/nature11818

Morley, R. J. (1981). Development and Vegetation Dynamics of a Lowland Ombrogenous Peat Swamp in Kalimantan Tengah, Indonesia. *Journal of Biogeography*, *8*(5), 383–404. https://doi.org/10.2307/2844758

Morris, P. J., Baird, A. J., & Belyea, L. R. (2012). The DigiBog peatland development model 2: ecohydrological simulations in 2D. *Ecohydrology*, *5*, 256–268.

Morris, P. J., Swindles, G. T., Valdes, P. J., Ivanovic, R. F., Gregoire, L. J., Smith, M. W., Tarasov, L., Haywood, A. M., & Bacon, K. L. (2018). Global peatland initiation driven by regionally asynchronous warming. *Proceedings of the National Academy of Sciences*, *115*(19), 4851–4856. https://doi.org/10.1073/pnas.1717838115

Muller, J., Wüst, R. A. J., Weiss, D., & Hu, Y. (2006). Geochemical and stratigraphic evidence of environmental change at Lynch's Crater, Queensland, Australia. *Global and Planetary Change*, *53*(4), 269–277. https://doi.org/10.1016/j.gloplacha.2006.03.009

Mushi, C. A., Ndomba, P. M., Trigg, M. A., Tshimanga, R. M., & Mtalo, F. (2019). Assessment of basin-scale soil erosion within the Congo River Basin: A review. *Catena*, *178*, 64–76. https://doi.org/10.1016/j.catena.2019.02.030

NASA/JPL. (2020). *NASADEM Merged DEM Global 1 arc second V001*. United States National Aeronautics and Space Administration / Jet Propulsion Laboratory. https://doi.org/10.5067/MEaSUREs/NASADEM/NASADEM_HGT.001

NASA/METI. (2011). *The Advanced Spaceborne Thermal Emission and Reflection Radiometer (ASTER) Global Digital Elevation Model (GDEM) version 2*. United States National Aeronautics and Space Administration / Ministry of Economy, Trade, and Industry of Japan. http://earthexplorer.usgs.gov/

Négrel, P., Allègre, C. J., Dupré, B., & Lewin, E. (1993). Erosion sources determined by inversion of major and trace element ratios and strontium isotopic ratios in river: The Congo Basin case. *Earth and Planetary Science Letters*, *120*(1–2), 59–76. https://doi.org/10.1016/0012-821X(93)90023-3

Nobre, A. D., Cuartas, L. A., Hodnett, M., Rennó, C. D., Rodrigues, G., Silveira, A., Waterloo, M., & Saleska, S. (2011). Height Above the Nearest Drainage - a hydrologically relevant new terrain model. *Journal of Hydrology*, *404*(1–2), 13–29. https://doi.org/10.1016/j.jhydrol.2011.03.051

Nobre, A. D., Cuartas, L. A., Momo, M. R., Severo, D. L., Pinheiro, A., & Nobre, C. A. (2016). HAND contour: A new proxy predictor of inundation extent. *Hydrological Processes*, *30*(2), 320–333. https://doi.org/10.1002/hyp.10581

Novak, M., Zemanova, L., Voldrichova, P., Stepanova, M., Adamova, M., Pacherova, P., Komarek, A., Krachler, M., & Prechova, E. (2011). Experimental evidence for mobility/immobility of metals in peat. *Environmental Science and Technology*, *45*(17), 7180–7187. https://doi.org/10.1021/es201086v

Nussbaum, M., Spiess, K., Baltensweiler, A., Grob, U., Keller, A., Greiner, L., Schaepman, M. E., & Papritz, A. (2018). Evaluation of digital soil mapping approaches with large sets of environmental covariates. *Soil*, *4*(1), 1–22. https://doi.org/10.5194/soil-4-1-2018

O'Loughlin, F. E., Neal, J., Schumann, G. J. P., Beighley, E., & Bates, P. D. (2020). A LISFLOOD-FP hydraulic model of the middle reach of the Congo. *Journal of Hydrology*, *580*(124203), 1–14. https://doi.org/10.1016/j.jhydrol.2019.124203

O'Loughlin, F. E., Paiva, R. C. D., Durand, M., Alsdorf, D. E., & Bates, P. D. (2016). A multi-sensor approach towards a global vegetation corrected SRTM DEM product. *Remote Sensing of Environment*, *182*, 49–59. https://doi.org/10.1016/j.rse.2016.04.018

Observatoire Satellital des Forêts d'Afrique Centrale (OSFAC). (2014). *Forêts d'Afrique Centrale Evaluées par Télédétection*. https://osfac.net/data-products/facet/

Oksanen, J., Guillaume Blanchet, F., Friendly, M., Kindt, R., Legendre, P., McGlinn, D., Minchin, P. R., O'Hara, R. B., Simpson, G. L., Solymos, P., Stevens, M. H. H., Szoecs, E., & Wagner, H. (2020). *Package "vegan": Community Ecology Package* (2.5-7). https://cran.r-project.org/web/packages/vegan/index.html

Olofsson, P., Foody, G. M., Herold, M., Stehman, S. V., Woodcock, C. E., & Wulder, M. A. (2014). Good practices for estimating area and assessing accuracy of land change. *Remote Sensing of Environment*, *148*, 42–57. https://doi.org/10.1016/j.rse.2014.02.015

Osaki, M., Hirose, K., Segah, H., & Helmy, F. (2016). Tropical Peat and Peatland Definition in Indonesia. In M. Osaki & N. Tsuji (Eds.), *Tropical Peatland Ecosystems* (pp. 137–147). Springer Japan: Tokyo, Japan.

Osaki, M., & Tsuji, N. (Eds.). (2016). *Tropical Peatland Ecosystems*. Springer Japan: Tokyo, Japan.

Ottinger, M., & Kuenzer, C. (2020). Spaceborne L-Band synthetic Aperture Radar Data for geoscientific analyses in coastal land applications: A review. *Remote Sensing*, *12*(14).

https://doi.org/10.3390/rs12142228

Otypková, Z., & Chytrý, M. (2006). Effects of plot size on the ordination of vegetation samples. *Journal of Vegetation Science*, *17*(4), 465. https://doi.org/10.1658/1100-9233(2006)17[465:eopsot]2.0.co;2

Owusu Agyemang, P. C., Roberts, E. M., & Jelsma, H. A. (2016). Late Jurassic-Cretaceous fluvial evolution of central Africa: Insights from the Kasai-Congo Basin, Democratic Republic Congo. *Cretaceous Research*, *67*, 25–43. https://doi.org/10.1016/j.cretres.2016.06.013

Page, S. E., Rieley, J. O., & Wüst, R. (2006). Lowland tropical peatlands of Southeast Asia. In I. P. Martini, A. Martinez Cortizas, & E. Chesworth (Eds.), *Peatlands: Evolution and Records of Environmental and Climate Changes* (9th ed., pp. 146–172). Elsevier: Amsterdam, Netherlands. https://doi.org/10.1016/S0928-2025(06)09007-9

Page, S., Mishra, S., Agus, F., Anshari, G., Dargie, G., Evers, S., Jauhiainen, J., Jaya, A., Jovani-Sancho, A. J., Laurén, A., Sjögersten, S., Suspense, I. A., Wijedasa, L. S., & Evans, C. D. (2022). Anthropogenic impacts on lowland tropical peatland biogeochemistry. *Nature Reviews Earth & Environment*, *0123456789*. https://doi.org/10.1038/s43017-022-00289-6

Page, S.E., Rieley, J. O., Shotyk, Ø. W., & Weiss, D. (1999). Interdependence of peat and vegetation in a tropical peat swamp forest. *Philosophical Transactions of the Royal Society B: Biological Sciences*, *354*, 1885–1897. https://doi.org/10.1098/rstb.1999.0529

Page, S.E., Wüst, R. A. J., Weiss, D., Rieley, J. O., Shotyk, W., & Limin, S. H. (2004). A record of Late Pleistocene and Holocene carbon accumulation and climate change from an equatorial peat bog (Kalimantan, Indonesia): implications for past , present and future carbon dynamics. *Journal of Quaternary Science*, *19*(7), 625–635. https://doi.org/10.1002/jqs.884

Page, Susan E., Rieley, J. O., & Banks, C. J. (2011). Global and regional importance of the tropical peatland carbon pool. *Global Change Biology*, *17*(2), 798–818. https://doi.org/10.1111/j.1365-2486.2010.02279.x

Page, Susan E., Siegert, F., Rieley, J. O., Boehm, H. D. V., Jaya, A., & Limin, S. (2002). The amount of carbon released from peat and forest fires in Indonesia during 1997. *Nature*, *420*(6911), 61–65. https://doi.org/10.1038/nature01131

Parmentier, I., Harrigan, R. J., Buermann, W., Mitchard, E. T. A., Saatchi, S., Malhi, Y., Bongers, F., Hawthorne, W. D., Leal, M. E., Lewis, S. L., Nusbaumer, L., Sheil, D., Sosef, M. S. M., Affum-Baffoe, K., Bakayoko, A., Chuyong, G. B., Chatelain, C., Comiskey, J. A., Dauby, G., … Hardy, O. J. (2011). Predicting alpha diversity of African rain forests: Models based on climate and satellite-derived data do not perform better than a purely spatial model. *Journal of Biogeography*, *38*(6), 1164–1176. https://doi.org/10.1111/j.1365-2699.2010.02467.x

Parmentier, I., Malhi, Y., Senterre, B., Whittaker, R. J., N, A. T. N., Alonso, A., Balinga, M. P. B., Bakayoko, A., Bongers, F., Chatelain, C., Comiskey, J. A., Cortay, R., Kamdem, M. N. D., Doucet, J. L., Gautier, L., Hawthorne, W. D., Issembe, Y. A., Kouamé, F. N., Kouka, L. A., … Wöll, H. (2007). The odd man out? Might climate explain the lower tree α-diversity of African rain forests relative to Amazonian rain forests? *Journal of Ecology*, *95*(5), 1058–1071. https://doi.org/10.1111/j.1365-2745.2007.01273.x

Parry, L. E., Charman, D. J., & Noades, J. P. W. (2012). A method for modelling peat depth in blanket peatlands. *Soil Use and Management*, *28*(4), 614–624.

https://doi.org/10.1111/j.1475-2743.2012.00447.x

Patakamuri, S. K. (2021). *Package 'modifiedmk': Modified Versions of Mann Kendall and Spearman's Rho Trend Tests* (1.6). https://cran.r-project.org/web/packages/modifiedmk/index.html

Peh, K. S. H., Sonké, B., Lloyd, J., Quesada, C. A., & Lewis, S. L. (2011). Soil does not explain monodominance in a Central African tropical forest. *PLoS ONE*, *6*(2), 1–9. https://doi.org/10.1371/journal.pone.0016996

Phillips, O. L., Sullivan, M. J. P., Baker, T. R., Monteagudo Mendoza, A., Vargas, P. N., & Vásquez, R. (2019). Species Matter: Wood Density Influences Tropical Forest Biomass at Multiple Scales. *Surveys in Geophysics*, *40*(4), 913–935. https://doi.org/10.1007/s10712-019-09540-0

Phillips, S., & Bustin, R. M. (1998). Accumulation of organic rich sediments in a dendritic fluvial/lacustrine mire system at Tasik Bera, Malaysia: implications for coal formation. *International Journal of Coal Geology*, *36*(1–2), 31–61. https://doi.org/10.1016/S0166-5162(97)00031-1

Plotkin, J. B., Potts, M. D., Yu, D. W., Bunyavejchewin, S., Condit, R., Foster, R., Hubbell, S., LaFrankie, J., Manokaran, N., Seng, L. H., Sukumar, R., Nowak, M. A., & Ashton, P. S. (2000). Predicting species diversity in tropical forests. *Proceedings of the National Academy of Sciences*, *97*(20), 10850–10854. https://doi.org/10.1073/pnas.97.20.10850

Ploton, P., Mortier, F., Réjou-Méchain, M., Barbier, N., Picard, N., Rossi, V., Dormann, C., Cornu, G., Viennois, G., Bayol, N., Lyapustin, A., Gourlet-Fleury, S., & Pélissier, R. (2020a). Spatial validation reveals poor predictive performance of large-scale ecological mapping models. *Nature Communications*, *11*(1), 1–11. https://doi.org/10.1038/s41467-020-18321-y

Ploton, P., Takoudjou Momo, S., Sonke, B., Boyemba, F., Loumeto, J., Medjibe, V., Ngomanda, A., Obiang, D., & Yongo, O. (2020b). *Wood density data of central African rainforest trees*. DataSuds, V1. https://doi.org/https://doi.org/10.23708/8DUWUC

Porankiewicz, B., Iskra, P., Sandak, J., Tanaka, C., & Jóźwiak, K. (2006). High-speed steel tool wear during wood cutting in the presence of high-temperature corrosion and mineral contamination. *Wood Science and Technology*, *40*(8), 673–682. https://doi.org/10.1007/s00226-006-0084-7

Potapov, P. V., Turubanova, S. A., Hansen, M. C., Adusei, B., Broich, M., Altstatt, A., Mane, L., & Justice, C. O. (2012). Quantifying forest cover loss in Democratic Republic of the Congo, 2000-2010, with Landsat ETM+ data. *Remote Sensing of Environment*, *122*, 106-116. https://doi.org/10.1016/j.rse.2011.08.027

Powers, D. M. W. (2011). Evaluation: From Precision, Recall and F-Measure to ROC, Informedness, Markedness and Correlation. *Journal of Machine Learning Technologies*, *2*(1), 37–63.

Powers, J. S., Montgomery, R. A., Adair, E. C., Brearley, F. Q., Dewalt, S. J., Castanho, C. T., Chave, J., Deinert, E., Ganzhorn, J. U., Gilbert, M. E., González-Iturbe, J. A., Bunyavejchewin, S., Grau, H. R., Harms, K. E., Hiremath, A., Iriarte-Vivar, S., Manzane, E., De Oliveira, A. A., Poorter, L., … Lerdau, M. T. (2009). Decomposition in tropical forests: A pan-tropical study of the effects of litter type, litter placement and mesofaunal exclusion across a precipitation gradient. *Journal of Ecology*, *97*(4), 801–811. https://doi.org/10.1111/j.1365-2745.2009.01515.x

Probst, J. L., Mortatti, J., & Tardy, Y. (1994). Carbon river fluxes and weathering CO2 consumption in the Congo and Amazon river basins. *Applied Geochemistry*, *9*(1), 1–13. https://doi.org/10.1016/0883-2927(94)90047-7

R Core Team. (2019). *R: A Language and Environment for Statistical Computing*. R Foundation for Statistical Computing.

Rainey, H. J., Iyenguet, F. C., Malanda, G. A. F., Madzoké, B., Santos, D. Dos, Stokes, E. J., Maisels, F., & Strindberg, S. (2009). Survey of Raphia swamp forest, Republic of Congo, indicates high densities of Critically Endangered western lowland gorillas (Gorilla gorilla gorilla). *Oryx*, *44*(1), 124–132. https://doi.org/10.1017/S003060530999010X

Rajashekhar Rao, B. K., Bailey, J., & Wingwafi, R. W. (2011). Comparison of three digestion methods for total soil potassium estimation in soils of papua New Guinea derived from varying parent materials. *Communications in Soil Science and Plant Analysis*, *42*(11), 1259–1265. https://doi.org/10.1080/00103624.2011.571740

Ramsar Convention on Wetlands. (2002). *Guidelines for Global Action on Peatlands (GAP)*. 8th Meeting of the Conference of the Contracting Parties to the Convention on Wetlands. Valencia, Spain.

Rebelo, L. M., McCartney, M. P., & Finlayson, C. M. (2010). Wetlands of Sub-Saharan Africa: Distribution and contribution of agriculture to livelihoods. *Wetlands Ecology and Management*, *18*(5), 557–572. https://doi.org/10.1007/s11273-009-9142-x

Rebelo, Lisa Maria. (2010). Eco-Hydrological Characterization of Inland Wetlands in Africa Using L-Band SAR. *IEEE Journal of Selected Topics in Applied Earth Observations and Remote Sensing*, *3*(4), 554–559. https://doi.org/10.1109/JSTARS.2010.2070060

Reimer, P. J., Austin, W. E. N., Bard, E., Bayliss, A., Blackwell, P. G., Bronk Ramsey, C., Butzin, M., Cheng, H., Edwards, R. L., Friedrich, M., Grootes, P. M., Guilderson, T. P., Hajdas, I., Heaton, T. J., Hogg, A. G., Hughen, K. A., Kromer, B., Manning, S. W., Muscheler, R., … Talamo, S. (2020). The IntCal20 Northern Hemisphere Radiocarbon Age Calibration Curve (0-55 cal kBP). *Radiocarbon*, *62*(4), 725–757. https://doi.org/10.1017/RDC.2020.41

Reimer, P. J., Bard, E., Bayliss, A., Beck, J. W., Blackwell, P. G., Bronk Ramsey, C., Buck, C. E., Cheng, H., Edwards, R. L., Friedrich, M., Grootes, P. M., Guilderson, T. P., Haflidason, H., Hajdas, I., Hatté, C., Heaton, T. J., Hoffmann, D. L., Hogg, A. G., Hughen, K. A., … van der Plicht, J. (2013). IntCal13 and Marine13 Radiocarbon Age Calibration Curves 0–50,000 Years Cal BP. *Radiocarbon*, *55*(4), 1869–1887. https://doi.org/10.2458/azu_js_rc.55.16947

Rezanezhad, F., Price, J. S., Quinton, W. L., Lennartz, B., Milojevic, T., & Van Cappellen, P. (2016). Structure of peat soils and implications for water storage, flow and solute transport: A review update for geochemists. *Chemical Geology*, *429*, 75–84. https://doi.org/10.1016/j.chemgeo.2016.03.010

Ribeiro, K., Pacheco, F. S., Ferreira, J. W., de Sousa-Neto, E. R., Hastie, A., Krieger Filho, G. C., Alvalá, P. C., Forti, M. C., & Ometto, J. P. (2021). Tropical peatlands and their contribution to the global carbon cycle and climate change. *Global Change Biology*, *27*(3), 489–505. https://doi.org/10.1111/gcb.15408

Richards, J. A., Woodgate, P. W., & Skidmore, A. K. (1987). An explanation of enhanced radar backscattering from flooded forests. *International Journal of Remote Sensing*, *8*(7), 1093–1100. https://doi.org/10.1080/01431168708954756

Richards, John A., & Jia, X. (2006). Remote sensing digital image analysis: An introduction. In *Remote Sensing Digital Image Analysis: An Introduction* (4th ed.). Springer Verlag: Berlin, Germany.

Ricotta, C., & Podani, J. (2017). On some properties of the Bray-Curtis dissimilarity and their ecological meaning. *Ecological Complexity*, *31*, 201–205. https://doi.org/10.1016/j.ecocom.2017.07.003

Riley, J., & Huchzermeyer, F. W. (1999). African Dwarf Crocodiles in the Likouala Swamp Forests of the Congo Basin: Habitat, Density, and Nesting. *Copeia*, *1999*(2), 313–320.

Roberts, D. R., Bahn, V., Ciuti, S., Boyce, M. S., Elith, J., Guillera-Arroita, G., Hauenstein, S., Lahoz-Monfort, J. J., Schröder, B., Thuiller, W., Warton, D. I., Wintle, B. A., Hartig, F., & Dormann, C. F. (2017). Cross-validation strategies for data with temporal, spatial, hierarchical, or phylogenetic structure. *Ecography*, *40*(8), 913–929. https://doi.org/10.1111/ecog.02881

Rosenqvist, A. (2009). Mapping of seasonal inundation in the Congo River basin - Prototype study using ALOS PALSAR. *Proceedings of the 33rd International Symposium on Remote Sensing of Environment, May 4-8, 2009, Stresa, Italy*, *ISRSE 33*, 709–712.

Roucoux, K. H., Lawson, I. T., Jones, T. D., Baker, T. R., Coronado, E. N. H., Gosling, W. D., & Lähteenoja, O. (2013). Vegetation development in an Amazonian peatland. *Palaeogeography, Palaeoclimatology, Palaeoecology*, *374*, 242–255. https://doi.org/10.1016/j.palaeo.2013.01.023

Rowell, D. L. (1994). *Soil Science Methods and Applications*. Longman Scientific & Technical: Harlow, UK.

Rudiyanto, Minasny, B., Setiawan, B. I., Arif, C., Saptomo, S. K., & Chadirin, Y. (2016). Digital mapping for cost-effective and accurate prediction of the depth and carbon stocks in Indonesian peatlands. *Geoderma*, *272*, 20–31. https://doi.org/10.1016/j.geoderma.2016.02.026

Rudiyanto, Minasny, B., Setiawan, B. I., Saptomo, S. K., & McBratney, A. B. (2018). Open digital mapping as a cost-effective method for mapping peat thickness and assessing the carbon stock of tropical peatlands. *Geoderma*, *313*, 25–40. https://doi.org/10.1016/j.geoderma.2017.10.018

Runge, J. (2008). The Congo River, Central Africa. In A. Gupta (Ed.), *Large rivers: geomorphology and management* (pp. 293–311). John Wiley & Sons Ltd.: Hoboken, NJ, USA.

Ruwaimana, M., Anshari, G. Z., Silva, L. C. R., & Gavin, D. G. (2020). The oldest extant tropical peatland in the world: a major carbon reservoir for at least 47 000 years. *Environmental Research Letters*, *15*(11). https://doi.org/10.1088/1748-9326/abb853

Rydin, Håkan, & Jeglum, J. K. (2006). *The Biology of Peatlands*. Oxford University Press: Oxford, UK.

Sakabe, A., Itoh, M., Hirano, T., & Kusin, K. (2018). Ecosystem-scale methane flux in tropical peat swamp forest in Indonesia. *Global Change Biology*, *24*, 5123–5136. https://doi.org/10.1111/gcb.14410

Samba, G., Nganga, D., & Mpounza, M. (2008). Rainfall and temperature variations over Congo-Brazzaville between 1950 and 1998. *Theoretical and Applied Climatology*, *91*(1–4), 85–97. https://doi.org/10.1007/s00704-007-0298-0

Scharlemann, J. P. W., Tanner, E. V. J., Hiederer, R., & Kapos, V. (2014). Global soil carbon: understanding and managing the largest terrestrial carbon pool. *Carbon Management*, *5*(1), 81–91. https://doi.org/10.4155/cmt.13.77

Schefuß, E., Eglinton, T. I., Spencer-Jones, C. L., Rullkötter, J., De Pol-Holz, R., Talbot, H. M., Grootes, P. M., & Schneider, R. R. (2016). Hydrologic control of carbon cycling and aged carbon discharge in the Congo River basin. *Nature Geoscience*, *9*(9), 687–690. https://doi.org/10.1038/ngeo2778

Schmidt, M. W. I., Torn, M. S., Abiven, S., Dittmar, T., Guggenberger, G., Janssens, I. A., Kleber, M., Kögel-Knabner, I., Lehmann, J., Manning, D. A. C., Nannipieri, P., Rasse, D. P., Weiner, S., & Trumbore, S. E. (2011). Persistence of soil organic matter as an ecosystem property. *Nature*, *478*, 49–56. https://doi.org/10.1038/nature10386

Seidensticker, D. (2020, December 27). *dirkseidensticker/HumActCentralAfrica_Paper: Codebase (Version v1.0)*. Zenodo. https://doi.org/10.5281/ZENODO.4394894

Seidensticker, D., Hubau, W., Verschuren, D., Fortes-Lima, C., de Maret, P., Schlebusch, C. M., & Bostoen, K. (2021). Population collapse in Congo rainforest from 400 CE urges reassessment of the Bantu Expansion. *Science Advances*, *7*(7), 1–13. https://doi.org/10.1126/sciadv.abd8352

Sen, P. K. (1968). Estimates of the Regression Coefficient Based on Kendall's Tau. *Journal of the American Statistical Association*, *63*(324), 1379–1389.

Shanahan, T. M., Mckay, N. P., Hughen, K. A., Overpeck, J. T., Otto-Bliesner, B., Heil, C. W., King, J., Scholz, C. A., & Peck, J. (2015). The time-transgressive termination of the African humid period. *Nature Geoscience*, *8*(2), 140–144. https://doi.org/10.1038/ngeo2329

Shimada, M., Isoguchi, O., Tadono, T., & Isono, K. (2009). PALSAR Radiometric and Geometric Calibration. *IEEE Transactions on Geoscience and Remote Sensing*, *47*(12), 3915–3932. https://doi.org/10.1109/TGRS.2009.2023909

Shotyk, W. (1996). Peat bog archives of atmospheric metal deposition: Geochemical evaluation of peat profiles, natural variations in metal concentrations, and metal enrichment factors. *Environmental Reviews*, *4*(2), 149–183. https://doi.org/10.1139/a96-010

Shotyk, W., Wayne Nesbitt, H., & Fyfe, W. S. (1990). The behaviour of major and trace elements in complete vertical peat profiles from three Sphagnum bogs. *International Journal of Coal Geology*, *15*(3), 163–190. https://doi.org/10.1016/0166-5162(90)90050-9

Sinha, P., Gaughan, A. E., Stevens, F. R., Nieves, J. J., Sorichetta, A., & Tatem, A. J. (2019). Assessing the spatial sensitivity of a random forest model: Application in gridded population modeling. *Computers, Environment and Urban Systems*, *75*, 132–145. https://doi.org/10.1016/j.compenvurbsys.2019.01.006

Sjöström, J. K., Martínez Cortizas, A., Hansson, S. V., Silva Sánchez, N., Bindler, R., Rydberg, J., Mörth, C. M., Ryberg, E. E., & Kylander, M. E. (2020). Paleodust deposition and peat accumulation rates – Bog size matters. *Chemical Geology*, *554*(July), 119795. https://doi.org/10.1016/j.chemgeo.2020.119795

Steinmann, P., & Shotyk, W. (1997). Chemical composition, pH, and redox state of sulfur and iron in complete vertical porewater profiles from two Sphagnum peat bogs, Jura Mountains, Switzerland. *Geochimica et Cosmochimica Acta*, *61*(6), 1143–1163.

Stevens, J. P. (1984). Outliers and Influential Data Points in Regression Analysis. *Psychological Bulletin*, *95*(2), 334–344. https://doi.org/10.1037/0033-2909.95.2.334

Strindberg, S., Maisels, F., Williamson, E. A., Blake, S., Stokes, E. J., Aba'a, R., Abitsi, G., Agbor, A., Ambahe, R. D., Bakabana, P. C., Bechem, M., Berlemont, A., De Semboli, B. B., Boundja, P. R., Bout, N., Breuer, T., Campbell, G., De Wachter, P., Akou, M. E., … Wilkie, D. S. (2018). Guns, germs, and trees determine density and distribution of gorillas and chimpanzees in Western Equatorial Africa. *Science Advances*, *4*(4), 1–14. https://doi.org/10.1126/sciadv.aar2964

Sullivan, M. J. P., Talbot, J., Lewis, S. L., Phillips, O. L., Qie, L., Begne, S. K., Chave, J., Cuni-Sanchez, A., Hubau, W., Lopez-Gonzalez, G., Miles, L., Monteagudo-Mendoza, A., Sonké, B., Sunderland, T., Ter Steege, H., White, L. J. T., Affum-Baffoe, K., Aiba, S. I., De Almeida, E. C., … Zemagho, L. (2017). Diversity and carbon storage across the tropical forest biome. *Scientific Reports*, *7*(39102), 1–12. https://doi.org/10.1038/srep39102

Swindles, G. T., Morris, P. J., Whitney, B., Galloway, J. M., Gałka, M., Gallego-Sala, A., Macumber, A. L., Mullan, D., Smith, M. W., Amesbury, M. J., Roland, T. P., Sanei, H., Patterson, R. T., Sanderson, N., Parry, L., Charman, D. J., Lopez, O., Valderamma, E., Watson, E. J., … Lähteenoja, O. (2018). Ecosystem state shifts during long-term development of an Amazonian peatland. *Global Change Biology*, *24*(2), 738–757. https://doi.org/10.1111/gcb.13950

Takada, M., Shimada, S., & Takahashi, H. (2016). Tropical Peat Formation. In M. Osaki & N. Tsuji (Eds.), *Tropical Peatland Ecosystems* (1st ed., pp. 127–136). Springer Japan: Tokyo, Japan.

Tan, P.-N., Steinbach, M., Karpatne, A., & Kumar, V. (2019). Cluster Analysis: Basic Concepts and Algorithms. In *Introduction to Data Mining* (Second). Pearson Education Limited: Harlow, UK.

Tang, A. C. I., Melling, L., Stoy, P. C., Musin, K. K., Aeries, E. B., Waili, J. W., Shimizu, M., Poulter, B., & Hirata, R. (2020). A Bornean peat swamp forest is a net source of carbon dioxide to the atmosphere. *Global Change Biology*, *26*, 6931–6944. https://doi.org/10.1111/gcb.15332

Targhetta, N., Kesselmeier, J., & Wittmann, F. (2015). Effects of the hydroedaphic gradient on tree species composition and aboveground wood biomass of oligotrophic forest ecosystems in the central Amazon basin. *Folia Geobotanica*, *50*(3), 185–205. https://doi.org/10.1007/s12224-015-9225-9

Tathy, J. P., Cros, B., Delmas, R. A., Marenco, A., Servant, J., & Labat, M. (1992). Methane emission from flooded forest in Central Africa. *Journal of Geophysical Research*, *97*(D6), 6159–6168.

Tavares da Costa, R., Mazzoli, P., & Bagli, S. (2019). Limitations posed by free DEMs in watershed studies: The case of river Tanaro in Italy. *Frontiers in Earth Science*, *7*(141), 1–15. https://doi.org/10.3389/feart.2019.00141

Ter Steege, H., Henkel, T. W., Helal, N., Marimon, B. S., Marimon-Junior, B. H., Huth, A., Groeneveld, J., Sabatier, D., Coelho, L. de S., Filho, D. de A. L., Salomão, R. P., Amaral, I. L., Matos, F. D. de A., Castilho, C. V., Phillips, O. L., Guevara, J. E., Carim, M. de J. V., Cárdenas López, D., Magnusson, W. E., … Melgaço, K. (2019). Rarity of monodominance in hyperdiverse Amazonian forests. *Scientific Reports*, *9*(1), 13822. https://doi.org/10.1038/s41598-019-50323-9

Theimer, B. D., Nobes, D. C., & Warner, B. G. (1994). A study of the geoelectrical properties of peatlands and their influence on ground-penetrating radar surveying. *Geophysical Prospecting*, *42*(3), 179–209. https://doi.org/10.1111/j.1365-2478.1994.tb00205.x

Thomas, S. C., & Martin, A. R. (2012). Carbon Content of Tree Tissues: A synthesis. *Forests*, *3*(2), 332–352. https://doi.org/10.3390/f3020332

Trabucco, A., & Zomer, R. J. (2019). *Global Aridity Index and Potential Evapotranspiration (ET0) Climate Database v2*. Figshare. https://doi.org/https://doi.org/10.6084/m9.figshare.7504448.v3

Treat, C. C., Kleinen, T., Broothaerts, N., Dalton, A. S., Dommaine, R., Douglas, T. A., Drexler, J. Z., Finkelstein, S. A., Grosse, G., Hope, G., Hutchings, J., Jones, M. C., Kuhry, P., Lacourse, T., Lähteenoja, O., Loisel, J., Notebaert, B., Payne, R. J., Peteet, D. M., … Brovkin, V. (2019). Widespread global peatland establishment and persistence over the last 130,000 y. *Proceedings of the National Academy of Sciences*, *116*(11), 4822–4827. https://doi.org/10.1073/pnas.1813305116

Tuley, P. (1995). *The Palms of Africa*. Trendrine Press: St Ives, Cornwall, UK.

Tuomisto, H. (2010). A consistent terminology for quantifying species diversity? Yes, it does exist. *Oecologia*, *164*(4), 853–860. https://doi.org/10.1007/s00442-010-1812-0

Uda, S. K., Hein, L., & Sumarga, E. (2017). Towards sustainable management of Indonesian tropical peatlands. *Wetlands Ecology and Management*, *25*(6), 683–701. https://doi.org/10.1007/s11273-017-9544-0

UNEP-WCMC/IUCN. (2021). *Protected Planet: The World Database on Protected Areas (WDPA) and World Database on Other Effective Area-based Conservation Measures (WD-OECM)*. UNEP-WCMC and IUCN: Cambridge, UK. https://www.protectedplanet.net

USGS. (2006). *Shuttle Radar Topography Mission (SRTM) 1 arc-second Digital Elevation Model (DEM)*. United States Geological Survey. http://earthexplorer.usgs.gov/

Uuemaa, E., Ahi, S., Montibeller, B., Muru, M., & Kmoch, A. (2020). Vertical accuracy of freely available global digital elevation models (ASTER, AW3D30, MERIT, TanDEM-X, SRTM, and NASADEM). *Remote Sensing*, *12*(3482), 1–23. https://doi.org/10.3390/rs12213482

Vancutsem, C., Achard, F., Pekel, J. F., Vieilledent, G., Carboni, S., Simonetti, D., Gallego, J., Aragão, L. E. O. C., & Nasi, R. (2021). Long-term (1990–2019) monitoring of forest cover changes in the humid tropics. *Science Advances*, *7*(10), 1–21. https://doi.org/10.1126/sciadv.abe1603

Vancutsem, C., Pekel, J. F., Evrard, C., Malaisse, F., & Defourny, P. (2009). Mapping and characterizing the vegetation types of the Democratic Republic of Congo using SPOT VEGETATION time series. *International Journal of Applied Earth Observation and Geoinformation*, *11*(1), 62–76. https://doi.org/10.1016/j.jag.2008.08.001

Verhegghen, A., Mayaux, P., De Wasseige, C., & Defourny, P. (2012). Mapping Congo Basin vegetation types from 300 m and 1 km multi-sensor time series for carbon stocks and forest areas estimation. *Biogeosciences*, *9*(12), 5061–5079. https://doi.org/10.5194/bg-9-5061-2012

Vernimmen, R., Hooijer, A., Akmalia, R., Fitranatanegara, N., Mulyadi, D., Yuherdha, A., Andreas, H., & Page, S. (2020). Mapping deep peat carbon stock from a LiDAR based DTM and field measurements, with application to eastern Sumatra. *Carbon Balance and Management*, *15*(1), 1–18. https://doi.org/10.1186/s13021-020-00139-2

Wadoux, A. M. J. C., Heuvelink, G. B. M., de Bruin, S., & Brus, D. J. (2021). Spatial cross-validation is not the right way to evaluate map accuracy. *Ecological Modelling*, *457*(109692), 1–5. https://doi.org/10.1016/j.ecolmodel.2021.109692

Walker, M., Johnsen, S., Rasmussen, S., Popp, T., Steffensen, J.-P., Gibbard, P., Hoek, W., Lowe, J., Andrews, J., Bjorck, S., Cwynar, L. C., Hughen, K., Kershaw, P., Kromer, B., Litt, T., Lowe, D. J., Nakagawa, T., Newnham, R., & Schwander, J. (2009). Formal definition and dating of the GSSP (Global Stratotype Section and Point) for the base of the Holocene using the Greenland NGRIP ice core, and selected auxiliary records. *Journal of Quaternary Science*, *24*(1), 3–17. https://doi.org/10.1002/jqs.1227

Wang, F., Shao, W., Yu, H., Kan, G., He, X., Zhang, D., Ren, M., & Wang, G. (2020). Re-evaluation of the Power of the Mann-Kendall Test for Detecting Monotonic Trends in Hydrometeorological Time Series. *Frontiers in Earth Science*, *8*(14), 1–12. https://doi.org/10.3389/feart.2020.00014

Wang, H., Tian, J., Chen, H., Ho, M., Vilgalys, R., Bu, Z.-J., Liu, X., & Richardson, C. J. (2021). Vegetation and microbes interact to preserve carbon in many wooded peatlands. *Communications Earth & Environment*, *2*(1), 1–8. https://doi.org/10.1038/s43247-021-00136-4

Wang, Y., Hess, L. L., Filoso, S., & Melack, J. M. (1995). Understanding the radar backscattering from flooded and nonflooded Amazonian forests: Results from canopy backscatter modeling. *Remote Sensing of Environment*, *54*(3), 324–332. https://doi.org/10.1016/0034-4257(95)00140-9

Washington, R., James, R., Pearce, H., Pokam, W. M., & Moufouma-Okia, W. (2013). Congo basin rainfall climatology: Can we believe the climate models? *Philosophical Transactions of the Royal Society B: Biological Sciences*, *368*(20120296), 1–7. https://doi.org/10.1098/rstb.2012.0296

Weiss, D., Shotyk, W., Rieley, J., Page, S., Gloor, M., Reese, S., & Martinez-Cortizas, A. (2002). The geochemistry of major and selected trace elements in a forested peat bog, Kalimantan, SE Asia, and its implications for past atmospheric dust deposition. *Geochimica et Cosmochimica Acta*, *66*(13), 2307–2323. https://doi.org/10.1016/S0016-7037(02)00834-7

Wetlands International. (2010). *A Quick Scan of Peatlands in Malaysia*. Wetlands International - Malaysia: Petaling Jaya, Malaysia.

Wheeler, B. D., & Proctor, M. C. F. (2000). Ecological gradients, subdivisions and terminology of north-west European mires. *Journal of Ecology*, *88*(2), 187–203. https://doi.org/10.1046/j.1365-2745.2000.00455.x

White, F. (1983). *The vegetation of Africa: a descriptive memoir to accompany the Unesco/AETFAT/UNSO vegetation map of Africa*. UNESCO: Paris, France.

Winston, R. B. (1994). Models of the geomorphology, hydrology, and development of domed peat bodies. *Geological Society of America Bulletin*, *106*(12), 1594–1604. https://doi.org/10.1130/0016-7606

Wong, L. S., Hashim, R., & Ali, F. H. (2009). A Review on Hydrauli Conductivity and Compressibility of Peat. *Journal of Applied Sciences*, *9*(18), 3207–3218.

Wood, C. M., Matsuo, A. Y. O., Wilson, R. W., Gonzalez, R. J., Patrick, M. L., Playle, R. C., & Val, A. L. (2003). Protection by natural blackwater against disturbances in ion fluxes caused by low pH exposure in freshwater stingrays endemic to the Rio Negro. *Physiological and Biochemical Zoology*, *76*(1), 12–27. https://doi.org/10.1086/367946

Wösten, J. H. M., Clymans, E., Page, S. E., Rieley, J. O., & Limin, S. H. (2008). Peat-water

interrelationships in a tropical peatland ecosystem in Southeast Asia. *Catena*, *73*(2), 212–224. https://doi.org/10.1016/j.catena.2007.07.010

Wüst, R. A. J., & Bustin, R. M. (2004). Late Pleistocene and Holocene development of the interior peat-accumulating basin of tropical Tasek Bera, Peninsular Malaysia. *Palaeogeography, Palaeoclimatology, Palaeoecology*, *211*(3–4), 241–270. https://doi.org/10.1016/j.palaeo.2004.05.009

Wüst, R. A. J., Bustin, R. M., & Lavkulich, L. M. (2003). New classification systems for tropical organic-rich deposits based on studies of the Tasek Bera Basin, Malaysia. *Catena*, *53*(2), 133–163. https://doi.org/10.1016/S0341-8162(03)00022-5

Xu, J., Morris, P. J., Liu, J., & Holden, J. (2018). PEATMAP: Refining estimates of global peatland distribution based on a meta-analysis. *Catena*, *160*, 134–140. https://doi.org/10.1016/j.catena.2017.09.010

Yamazaki, D., Ikeshima, D., Sosa, J., Bates, P. D., Allen, G. H., & Pavelsky, T. M. (2019). MERIT Hydro : A High-Resolution Global Hydrography Map Based on Latest Topography Dataset. *Water Resources Research*, *55*, 5053–5073. https://doi.org/10.1029/2019WR024873

Yamazaki, D., Ikeshima, D., Tawatari, R., Yamaguchi, T., Loughlin, F. O., Neal, J. C., Sampson, C. C., Kanae, S., & Bates, P. D. (2017). A high-accuracy map of global terrain elevations. *Geophysical Research Letters*, *44*, 5844–5853. https://doi.org/10.1002/2017GL072874

Young, D. M., Baird, A. J., Charman, D. J., Evans, C. D., Gallego-Sala, A. V., Gill, P. J., Hughes, P. D. M., Morris, P. J., & Swindles, G. T. (2019). Misinterpreting carbon accumulation rates in records from near-surface peat. *Scientific Reports*, *9*(1), 1–8. https://doi.org/10.1038/s41598-019-53879-8

Young, D. M., Baird, A. J., Gallego-Sala, A. V., & Loisel, J. (2021). A cautionary tale about using the apparent carbon accumulation rate (aCAR) obtained from peat cores. *Scientific Reports*, *11*(1), 1–12. https://doi.org/10.1038/s41598-021-88766-8

Young, D. M., Baird, A. J., Morris, P. J., & Holden, J. (2017). Simulating the long-term impacts of drainage and restoration on the ecohydrology of peatlands. *Water Resources Research*, *53*(8), 6510–6522. https://doi.org/10.1002/2016WR019898

Young, D. M., Parry, L. E., Lee, D., & Ray, S. (2018). Spatial models with covariates improve estimates of peat depth in blanket peatlands. *PLoS ONE*, *13*(9), 1–19. https://doi.org/10.1371/journal.pone.0202691

Yu, Z. C. (2012). Northern peatland carbon stocks and dynamics: a review. *Biogeosciences*, *9*, 4071–4085. https://doi.org/10.5194/bg-9-4071-2012

Yu, Z., Loisel, J., Brosseau, D. P., Beilman, D. W., & Hunt, S. J. (2010). Global peatland dynamics since the Last Glacial Maximum. *Geophysical Research Letters*, *37*(13), 1–5. https://doi.org/10.1029/2010GL043584

Yue, S., & Wang, C. Y. (2004). The Mann-Kendall test modified by effective sample size to detect trend in serially correlated hydrological series. *Water Resources Management*, *18*(3), 201–218. https://doi.org/10.1023/B:WARM.0000043140.61082.60

Yule, C. M., & Gomez, L. N. (2009). Leaf litter decomposition in a tropical peat swamp forest in Peninsular Malaysia. *Wetlands Ecology and Management*, *17*(3), 231–241. https://doi.org/10.1007/s11273-008-9103-9

Yule, C. M., Lim, Y. Y., & Lim, T. Y. (2018). Recycling of phenolic compounds in Borneo's tropical

peat swamp forests. *Carbon Balance and Management*, *13*(1), 14.
https://doi.org/10.1186/s13021-018-0092-6

Zanne, A. E., Lopez-Gonzalez, G., Coomes, D. A., Ilic, J., Jansen, S., Lewis, S. L., Miller, R. B.,
Swenson, N. G., Wiemann, M. C., & Chave, J. (2009). *Data from: Towards a worldwide
wood economics spectrum*. Dryad Digital Repository. https://doi.org/10.5061/dryad.234

Zulkifley, M. T. M., Ng, T. F., Raj, J. K., Hashim, R., Ghani, A., Shuib, M. K., & Ashraf, M. A.
(2013). Definitions and engineering classifications of tropical lowland peats. *Bulletin of
Engineering Geology and the Environment*, *72*(3–4), 547–553.
https://doi.org/10.1007/s10064-013-0520-5

Appendix I: Overview of field campaigns

Field campaign	Transect name (code; purpose)	Community name	Field team members	Measurement / sample collection for
January - March 2018	Lokolama (LOK; testing hypotheses)	Lokolama	- Bart Crezee - Simon Lewis - Corneille Ewango - Jean-Bosco Ndjango - Ovide Emba - Bolivard Bongwemisa - Papy Bosange	- basic field sampling (see 2.4.2) - *in situ* water table measurements - peat pore water inorganic chemistry - surface peat inorganic chemistry - downcore inorganic chemistry - radiocarbon dating
	Ikelemba (IKE; testing hypotheses)	Bosukela (Mweko camp)	- Bart Crezee - Corneille Ewango - Ovide Emba - Bolivard Bongwemisa - Yannick Mbangana - Juress Sando - Felly Mongonga	- basic field sampling (see 2.4.2) - *in situ* water table measurements - peat pore water inorganic chemistry - surface peat inorganic chemistry - downcore inorganic chemistry - radiocarbon dating
	Boloko (BEL; testing hypotheses)	Mpama and Befale	- Bart Crezee - Corneille Ewango - Jean-Bosco Ndjango - Ovide Emba - Bolivard Bongwemisa - Papy Bosange	- basic field sampling (see 2.4.2)
	Tumba (TUM; testing hypotheses)	Bonsole	- Bart Crezee - Corneille Ewango - Jean-Bosco Ndjango - Bolivard Bongwemisa - Papy Bosange	- basic field sampling (see 2.4.2)
June - August 2019	Mpeka (PEK; testing hypotheses)	Mpeka	- Bart Crezee - Greta Dargie - Corneille Ewango - Joseph Kanyama - Ovide Emba - Pierre Bola - Nicholas Girkin - Juress Sando - Felly Mongonga - Roger Kendewa	- basic field sampling (see 2.4.2) - peat pore water inorganic chemistry - surface peat inorganic chemistry
	Bondamba (BDM; testing hypotheses)	Bondamba		- basic field sampling (see 2.4.2) - peat pore water inorganic chemistry - surface peat inorganic chemistry
	Bolengo (BNG; testing hypotheses)	Bolengo		- basic field sampling (see 2.4.2) - peat pore water inorganic chemistry - surface peat inorganic chemistry

	Boleke (BLK; assessing mapping capabilities)	Boleke		- basic field sampling (see 2.4.2)
	Pombi (POM; assessing mapping capabilities)	Pombi		- basic field sampling (see 2.4.2)
	Bondamba 2 (BDM2; assessing mapping capabilities)	Bondamba		- basic field sampling (see 2.4.2)
	Bondamba 3 (BDM3; assessing mapping capabilities)	Bondamba		- basic field sampling (see 2.4.2)
January 2020	Lokolama (LOK; testing hypotheses)	Lokolama	- Bart Crezee - Corneille Ewango - Ovide Emba - Joseph Kanyama - Papy Bosange,	- *in situ* water table measurements - surface microtopography - radiocarbon dating (LOK_5.0 only)
	Ikelemba (IKE; testing hypotheses)	Bosukela (Mweko camp)	- Bart Crezee - Simon Lewis - Joseph Kanyama - Ovide Emba - Juress Sando - Felly Mongonga	- *in situ* water table measurements - surface microtopography
	Centre de Recherche en Écologie et Foresterie (CREF), Mabali		- Bart Crezee - Papy Bosange	- long-term temperature data - long-term precipitation data

NB: See section 2.4.2 for the difference in basic field sampling along transects used for testing hypotheses and transects used for assessing mapping capabilities.

Appendix II: Alphabetical list of plant species

Name	Family	Botanical authority
Albizia altissima	Fabaceae	Hook.f.
Albizia glaberrima	Fabaceae	(Schumach. & Thonn.) Benth.
Alchornea cordifolia	Euphorbiaceae	(Schumach. & Thonn.) Müll.Arg.
Baphia laurentii	Fabaceae	De Wild.
Carapa palustris	Meliaceae	(G.C.C.Gilbert) Kenfack
Carapa procera	Meliaceae	DC.
Chionanthus sp.	Oleaceae	L. (for genus)
Cleistanthus mildbraedii	Phyllanthaceae	Jabl.
Cleistanthus polystachyus	Phyllanthaceae	Hook.f. ex Planch.
Cleistopholis patens	Annonaceae	(Benth.) Engl. & Diels
Coelocaryon botryoides	Myristicaceae	Vermoesen
Crotonogynopsis sp.	Euphorbiaceae	Pax (for genus)
Cryptosepalum congolanum	Fabaceae	(De Wild.) J.Léonard
Cynometra simplicifolia	Fabaceae	Harms
Daniellia pynaertii	Fabaceae	De Wild.
Dichostemma glaucescens	Euphorbiaceae	Pierre
Diospyros crassiflora	Ebenaceae	Hiern
Diospyros mespiliformis	Ebenaceae	Hochst. ex A.DC.
Donella pruniformis	Sapotaceae	(Engl.) Pierre ex Engl.
Elaeis guineensis	Arecaceae	Jacq.
Englerophytum laurentii	Sapotaceae	(De Wild.) L.Gaut.
Entandrophragma palustre	Meliaceae	Staner
Eremospatha haullevilleana	Arecaceae	De Wild.
Eremospatha wendlandiana	Arecaceae	Dammer ex Becc.
Garcinia ovalifolia	Clusiaceae	Oliv.
Garcinia smeathmannii	Clusiaceae	(Planch. & Triana) Oliv.
Guibourtia demeusei	Leguminosae	(Harms) J.Leonard
Homalium africanum	Salicaceae	(Hook.f.) Benth.
Hypselodelphys scandens	Marantaceae	Louis & Mullend.
Isoberlinia doka	Fabaceae	Craib & Stapf
Laccosperma secundiflorum	Arecaceae	(P.Beauv.) Kuntze
Macaranga sp.	Euphorbiaceae	Thouars (for genus)
Manilkara obovata	Sapotaceae	(Sabine & G.Don) J.H.Hemsl.
Musanga cecropioides	Urticaceae	R.Br. ex Tedlie
Oubanguia africana	Lecythidaceae	Baill.
Palisota mannii	Commelinaceae	C.B.Clarke
Pandanus candelabrum	Pandanaceae	P.Beauv.
Prioria buchholzii	Fabaceae	(Harms) Breteler
Pseudagrostistachys ugandensis	Euphorbiaceae	(Hutch.) Pax & K.Hoffm.
Raphia hookeri	Arecaceae	G.Mann & H.Wendl.
Raphia laurentii	Arecaceae	De Wild.
Raphia sese	Arecaceae	De Wild.
Sclerosperma mannii	Arecaceae	H.Wendl.
Staudtia kamerunensis	Myristicaceae	Warb.
Symphonia globulifera	Clusiaceae	L.f.
Uapaca corbisieri	Phyllanthaceae	De Wild.

Uapaca guineensis	Phyllanthaceae	Müll.Arg.
Uapaca paludosa	Phyllanthaceae	Aubrév. & Leandri
Xylopia rubescens	Annonaceae	Oliv.

NB: Voucher curation of field collections is still ongoing at the time of submission of this thesis. Therefore, no voucher numbers are provided in this table. All collected vouchers are located at the herbarium of the Faculty of Sciences of the University of Kisangani in DRC.